The Possibility of Primordial Black Hole Direct Detection

José Laurindo de Góis Nóbrega Sobrinho

Thesis submitted to obtain the PhD degree in

Mathematics

(speciality of Mathematical–Physics)

Supervisor:

Pedro Manuel Edmond Reis da Silva Augusto

May 2011

UNIVERSIDADE da MADEIRA

The Possibility of Primordial Black Hole Direct Detection

José Laurindo de Góis Nóbrega Sobrinho

Thesis presented and unanimously approved in public session, on 20 June 2011, to obtain the PhD Degree in Mathematics (speciality of Mathematical–Physics)

Jury

Chairman: Rector of the Universidade da Madeira

Members of the Committee (in alphabetical order)**:**

Doctor Anne Marie Green
Associate Professor, University of Nottingham, United Kingdom

Doctor Carlos Paulo da Câmara Crawford do Nascimento
Professor Auxiliar com Agregação, Universidade de Lisboa

Doctor José Pizarro de Sande e Lemos
Professor Associado com Agregação, Universidade Técnica de Lisboa

Doctor Pedro Manuel Edmond Reis da Silva Augusto
Professor Auxiliar com Agregação, Universidade da Madeira

Abstract

This thesis explores the possibility of directly detecting blackbody emission from Primordial Black Holes (PBHs). A PBH might form when a cosmological density fluctuation with wavenumber k, that was once stretched to scales much larger than the Hubble radius during inflation, reenters inside the Hubble radius at some later epoch. By modeling these fluctuations with a running–tilt power–law spectrum ($n(k) = n_0 + a_1(k)n_1 + a_2(k)n_2 + a_3(k)n_3$; $n_0 = 0.951$; $n_1 = -0.055$; n_2 and n_3 unknown) each pair (n_2,n_3) gives a different $n(k)$ curve with a maximum value (n_+) located at some instant (t_+). The (n_+,t_+) parameter space [(1.20,10^{-23} s) to (2.00,10^9 s)] has $t_+ = 10^{-23}$ s–10^9 s and $n_+ = 1.20$–2.00 in order to encompass the formation of PBHs in the mass range 10^{15} g–$10^{10} M_\odot$ (from the ones exploding at present to the most massive known). It was evenly sampled: n_+ every 0.02; t_+ every order of magnitude. We thus have $41 \times 33 = 1353$ different cases. However, 820 of these ($\approx 61\%$) are excluded (because they would provide a PBH population large enough to close the Universe) and we are left with 533 cases for further study.

Although only sub–stellar PBHs ($\ll 1 M_\odot$) are hot enough to be detected at large distances we studied PBHs with 10^{15} g–$10^{10} M_\odot$ and determined how many might have formed and still exist in the Universe. Thus, for each of the 533 (n_+,t_+) pairs we determined the fraction of the Universe going into PBHs at each epoch (β), the PBH density parameter (Ω_{PBH}), the PBH number density (n_{PBH}), the total number of PBHs in the Universe (N), and the distance to the nearest one (d). As a first result, $\approx 14\%$ of these (72 cases) give, at least, one PBH within the observable Universe, one–third being sub–stellar and the remaining evenly spliting into stellar, intermediate mass and supermassive. Secondly, we found that the nearest stellar mass PBH might be at 32 pc, while the nearest intermediate mass and supermassive PBHs might be 100 and 1000 times farther, respectively.

Finally, for 6% of the cases (four in 72) we might have substellar mass PBHs within 1 pc. One of these cases implies a population of $\sim 10^5$ PBHs, with a mass of $\sim 10^{18}$ g (similar to Halley's comet), within the Oort cloud, which means that the nearest PBH might be as close as $\sim 10^3$ AU. Such a PBH could be directly detected with a probability of $\sim 10^{-21}$ (cf. $\sim 10^{-32}$ for low–energy neutrinos). We speculate in this possibility.

Key words: black hole physics – early Universe – cosmological parameters – Oort cloud – dark matter – Galaxy: halo

Resumo

Esta tese explora a possibilidade de detetar diretamente a emissão de corpo negro de Buracos Negros Primordiais (BNPs). Um BNP pode formar-se quando uma flutuação de densidade cosmológica de número de onda k, esticada para uma escala muito superior ao raio de Hubble durante a inflação, reentra dentro do raio de Hubble numa época posterior. Modelando estas flutuações com um espectro da forma $n(k) = n_0 + a_1(k)n_1 + a_2(k)n_2 + a_3(k)n_3$ ($n_0 = 0.951$; $n_1 = -0.055$; n_2 e n_3 desconhecidos), cada par (n_2,n_3) dá lugar a uma curva $n(k)$ com um máximo (n_+) localizado num determinado instante (t_+). O espaço de parâmetros (n_+,t_+) [(1.20,10^{-23} s) a (2.00,10^9 s)] tem $t_+ = 10^{-23}$ s–10^9 s e $n_+ = 1.20$–2.00 de forma a incluir a formação de BNPs na gama de 10^{15} g–$10^{10} M_\odot$ (desde os que estão a explodir no presente aos maiores conhecidos). Fez-se uma amostragem uniforme: n_+ em passos de 0.02; t_+ para todas as ordens de magnitude. Ficamos, assim, com $41 \times 33 = 1353$ casos diferentes. Contudo, 820 destes ($\approx 61\%$) foram excluídos (pois dariam lugar a uma população de BNPs suficiente para fechar o Universo) sobrando 533 casos para estudo posterior.

Embora apenas os BNPs de massa subestelar ($\ll 1 M_\odot$) sejam suficientemente quentes para que possam ser detetados a grandes distâncias, estudamos BNPs com 10^{15} g–$10^{10} M_\odot$ e determinamos quantos podem ter-se formado e continuar a existir no Universo. Assim, para cada um dos 533 pares (n_+,t_+) determinamos a fração do Universo convertida em BNPs em cada época (β), a densidade numérica de BNPs (n_{PBH}), o número total de BNPs no Universo (N) e a distância para o mais próximo (d). Um primeiro resultado sugere que $\approx 14\%$ destes (72 casos) dão, pelo menos, um BNP no Universo observável, sendo um terço subestelares e os restantes igualmente distribuídos pelos estelares, de massa intermédia e supermassivos. Além disso, o BNP estelar mais próximo poderá estar a 32 pc enquanto que o de massa intermédia e supermassivo mais próximos podem estar, respectivamente, 100 e 1000 vezes mais distantes.

Finalmente, para 6% dos casos (quatro em 72) podemos ter BNPs de massa subestelar a distâncias inferiores a 1 pc. Um destes casos dá-nos uma população de $\sim 10^5$ BNPs com $\sim 10^{18}$ g (semelhante ao cometa Halley) dentro da nuvem de Oort, o que significa que o BNP mais próximo pode estar a $\sim 10^3$ AU. Tal BNP pode ser detetado diretamente com uma probabilidade de $\sim 10^{-21}$ (cf. $\sim 10^{-32}$ no caso de neutrinos de baixa energia). Especulamos sobre esta possibilidade.

Palavras chave: Física de buracos negros – Universo primordial – parâmetros cosmológicos – nuvem de Oort – matéria escura – Galáxia: halo

To Elda Sobrinho
and
Carlos Daniel

Contents

List of Figures

List of Tables

List of Equations

Acronyms

2dFGRS – 2 degree Field Galaxy Redshift Survey

ACBAR – Arcminute Cosmology Bolometer Array Receiver

AMSB – Anomaly–Mediated Susy Breaking

AGILE – Astro–revilatore Gamma a Immagini LEggero

BH – Black Hole

CBI – Cosmic Background Imager

CDM – Cold Dark Matter

CMB – Cosmic Microwave Background

EoS – Equation of State

EW – ElectroWeak

FUSE – Far Ultraviolet Spectroscopic Explorer

FLRW – Friedmann–Lemaître–Robertson–Walker

GALLEX – GALLium EXperiment

GMSB – Gauge–Mediated Susy Breaking

GUT – Grand Unification Theory

HDM – Hot Dark Matter

HESS – High Energy Stereoscopic System

HG – Hadron Gas

HST – Hubble Space Telescope

IIE – Innovative Interstellar Explorer

IMBH – Intermediate Mass Black Hole ($10^2 M_\odot < M_{BH} < 10^6 M_\odot$)

INTEGRAL – INTErnational Gamma–Ray Astrophysics Laboratory

ΛCDM – Lambda–Cold Dark Matter Model

LEP – Large Electron Positron collider

LGT – Lattice Gauge Theory

LHC – Large Hadron Collider

LSP – Lightest Supersymmetric Particle

LSS – Large Scale Structure

LTE – Local Thermodynamic Equilibrium

MSSM – Minimal Supersymmetric extension of the Standard Model

mSUGRA – minimal SUperGRAvity

XMM – X–ray Multi–mirror Mission.

PBH – Primordial Black Hole

PDG – Particle Data Group

QCD – Quantum ChromoDynamics

QGP – Quark–Gluon Plasma

RHIC – Relativistic Heavy Ion Collider

SBH – Stellar mass Black Hole ($1M_{\odot} \leq M_{BH} \leq 10^2 M_{\odot}$)

SDSS – Sloan Digital Sky Survey

SLC – Stanford Linear Collider

SMBH – SuperMassive Black Hole ($M_{BH} \geq 10^6 M_{\odot}$)

SMPP – Standard Model of Particle Physics

SOFIA – Stratospheric Observatory For Infrared Astronomy

SPS – Snowmass Points and Slopes

SST – Spitzer Space Telescope

SSBH – Sub–Stellar mass Black Hole ($10^{-5}\text{g} < M_{BH} < 1M_{\odot}$)

SUSY – SUperSYmmetry

VLA – Very Large Array

WIMP – Weakly Interacting Massive Particle

WMAP – Wilkinson Microwave Anisotropy Probe

Physical Constants and Parameters (*)

Speed of light	c	2.99792458×10^{8} ms^{-1}
Planck constant	h	$6.6260755(40) \times 10^{-34}$ Js
Gravitation constant	G	$6.67259(85) \times 10^{-11}$ m^{3}kg^{-1}s^{-2}
Boltzmann constant	k	$1.380658(12) \times 10^{-23}$ JK^{-1}
Electron charge	e	$1.60217733(49) \times 10^{-19}$ C
Planck mass	m_P	$2.17671(14) \times 10^{-8}$ kg
Planck length	l_P	$1.61605(10) \times 10^{-35}$ m
Planck time	t_P	$5.39056(34) \times 10^{-44}$ s
Astronomical Unit	AU	$1.4959787066 \times 10^{11}$ m
Parsec	pc	3.0856776×10^{16} m
Solar mass	$M_\odot$	1.9891×10^{30} kg
Jupiter mass	m_J	1.8987×10^{27} kg
Earth mass	m_T	5.9742×10^{24} kg

Pluto orbital semi–major axis	39.5 AU
Radius of the Oort Cloud	≈ 0.4 pc (†)
Distance to the galactic centre	8.5 kpc
Radius of the galactic halo	16 kpc (‡)
Distance to the Large Magellanic Cloud (LMC)	55 kpc
Distance to the Andromeda galaxy (M31)	0.725 Mpc
Size of the Observable Universe	10^{26} m (⋄)

(*) The values were taken from Cox (2000), except otherwise noted. For some of the values the standard error of the last digits follows in parentheses.

(†) Dones et al. (2004).

(‡) We considered, in our integrations, the radius of the galactic halo approximately equal to the radius of the galactic disc (e.g. Unsöld & Bascheck, 2002).

(⋄) cf. Section 1.1.3.

xxx

Conventions

α – relation between the mass variance and δ_H;
α_{sp} – ratio of the sound speed with respect to the background value $(1/\sqrt{3})$ at a given moment;
β – the fraction of the Universe going into PBHs;
δ – fluctuation amplitude;
δ_k – fluctuation amplitude at the horizon crossing time;
δ_c – the threshold for PBH formation;
δ_{c1} – the threshold for PBH formation at the beginning of a phase transition;
δ_{c2} – the threshold for PBH formation at the end of a phase transition;
κ – spatial curvature of the observable Universe;
Λ – cosmological constant;
ω – adiabatic index;
ρ – density of the overdense region;
$\bar{\rho}$ – Universe average density;
ρ_0 – Universe density at the present time;
ρ_1, ρ_2 – density of the overdense region, respectively, at the beginning and at the end of a first–order phase transition;
ρ_c – critical density;
ρ_{HG} – HG density;
ρ_{QGP} – QGP density;
ρ_k – density at the horizon crossing time;
ρ_{PBH} – PBH mass density;
σ – mass variance;
Ω_κ – curvature density parameter;
Ω_Λ – cosmological constant density parameter;
Ω_b – baryon density parameter;
Ω_{CDM} – CDM density parameter;
Ω_m – matter density parameter;
Ω_{PBH} – PBH density parameter;
B – bag constant;
c_s – sound speed;
c_{s_0} – background sound speed for a radiation–dominated Universe;
d – the minimum distance to the nearest PBH;
f – the fraction of the overdense region spent in the dust–like phase;
f_A, f_B, f_C, f_E, f_F – the function f for fluctuations of classes A, B, C, E or F (QCD Bag Model);
$f_{A_{Lat}}$, $f_{B_{Lat}}$, $f_{C_{Lat}}$ – the function f for fluctuations of classes A, B or C (QCD Lattice Fit model);
g – number of degrees of freedom;
g'_{ep}, g_{ep} – number of degrees of freedom, respectively, before and after the electron–positron annihilation epoch;
g'_{EW}, g_{EW} – number of degrees of freedom, respectively, before and after the EW phase transition;

g_{HG} – number of degrees of freedom for the HG;
g_{QGP} – number of degrees of freedom for the QGP;
H – Hubble parameter;
h – normalized Hubble constant ($H_0/100$ kms^{-1}Mpc^{-1});
H_0 – Hubble constant;
k – wavenumber;
k_+ – the wavenumber for which the power spectrum shows a maximum;
k_c – pivot scale (the wavenumber at which the normalized scalar and tensor spectra cross);
k_e – wavenumber at the end of inflation;
k_r – wavenumber during radiation domination;
l – latent heat;
M_H – horizon mass;
M_{PBH} – PBH mass;
n – spectral index;
n_+ – the maximum value of the power spectrum;
n_0 – tilt of the spectrum for the running–tilt power–law spectrum;
n_1 – running of tilt for the running–tilt power–law spectrum;
n_2, n_3 – unknown parameters (running–tilt power–law spectrum);
n_{PBH} – PBH number density;
N – the number of PBHs within the observable Universe;
P – primordial power spectrum for the density fluctuations;
p – pressure;
p_{QGP} – QGP pressure;
p_{HG} – HG pressure;
R – scale factor;
R_0 – present day value of the scale factor (normalized to unity);
R_k – scale factor at the horizon crossing time;
R_H – Hubble radius;
R_l – strength of a first–order phase transition;
R_J – Jeans length;
R_s – Schwarzschild radius;
S – the scale factor for the perturbed region;
S_1, S_2 – the scale factor for the perturbed region, respectively, at the beginning and at the end of a first–order phase transition;
S_c – the scale factor for the perturbed region at the turnaround point;
s – entropy density;
s_{QGP} – QGP entropy density;
s_{HG} – HG entropy density;
t_+ – the epoch at which the power spectrum attains its maximum value (n_+);
t_{QCD-}, t_{QCD+} – the age of the Universe, respectively, at the beginning and at the end of the QCD;
t_0 – the age of the Universe (present time);
t_1 – beginning of the QCD Lattice Fit or QCD Crossover;
t_2 – the end of the QCD Crossover;

t_c – turnaround point;
t_{eq} – the age of the Universe at radiation–matter equality;
t_{EW-}, t_{EW+} – the age of the Universe, respectively, at the beginning and at the end of the EW;
t_H – Hubble time;
t_i, t_e – the age of the Universe, respectively, at the beginning and at the end of inflation;
t_k – horizon crossing time;
t_{SN} – the age of the Universe at matter–Λ equality (i.e., the instant when the expansion of the Universe starts to accelerate according to the high redshift SuperNovae Ia data);
T – temperature;
T_* – temperature at which the inflection point in the Higgs field appears;
T_0 – present day background temperature;
T_c – critical temperature;
W_{TH} – top–hat window function;
z – redshift.

Non–negligible contributions to β (†):

B	QCD Bag Model
BE	QCD Bag Model and EW Bag Model
BL	QCD Bag Model or QCD Lattice Fit
BLE	(QCD Bag Model or QCD Lattice Fit) and EW Bag Model
E	EW Bag Model
ea	e^-e^+ annihilation
L	QCD Lattice Fit
R	Radiation
RB	Radiation and QCD Bag Model
RBE	Radiation and QCD Bag Model and EW Bag Model
RBea	Radiation and QCD Bag Model and e^-e^+ annihilation
RBL	Radiation and (QCD Bag Model or QCD Lattice Fit)
RBLC	Radiation and (QCD Bag Model or QCD Lattice Fit or QCD Crossover)
RBLCE	Radiation and (QCD Bag Model or QCD Lattice Fit or QCD Crossover) and EW Bag Model
RBLCea	Radiation and (QCD Bag Model or QCD Lattice Fit or QCD Crossover) and e^-e^+ annihilation
RBLE	Radiation and (QCD Bag Model or QCD Lattice Fit) and EW Bag Model
RC	Radiation and QCD Crossover
RCea	Radiation and QCD Crossover and e^-e^+ annihilation
RE	Radiation and EW Bag Model
Rea	Radiation and e^-e^+ annihilation
RL	Radiation and QCD Lattice Fit
RLea	Radiation and QCD Lattice Fit and e^-e^+ annihilation

(†) We might also have situations with one or more contributions exceeding the observational limits (these are labeled with an $*$). For example, RB^*LCE^*, represents a case for which we have, besides the contribution from radiation R, contributions from the QCD Lattice Fit (L) or from the QCD Crossover (C). The QCD Bag Model is excluded due to observational constraints (B^*). The same happens for the EW Bag Model (E^*). The contribution from the electron–positron annihilation epoch is negligible, in this case.

Preface

BHs are objects predicted by the Laws of Physics. They arise as a natural consequence of the Theory of General Relativity. Within the present day Universe we are aware of the processes that can lead to the formation of BHs with masses ranging from $\sim 1\mathrm{M}_{\odot}$ up to $\sim 10^{10}\mathrm{M}_{\odot}$ and, in fact, in the past decades, we have identified several BH candidates in all of these mass ranges. All those candidates were identified by indirect means (i.e. measuring the effects they cause in their neighborhoods). The direct detection of a BH might be a giant step ahead in Astronomy and, in a more general sense, in Science itself.

According to Quantum Field Theory a BH should radiate like a black–body with a temperature inversely proportional to its own mass (i.e. smaller BHs are hotter than larger ones). The existence of this radiation, usually called Hawking radiation, could lead to the evaporation of the BH (if it is not balanced by the accretion of matter and radiation). During the evaporation process the BH emits electromagnetic waves (photons), neutrinos, gravitons and, in more advanced stages, electrons, positrons and other particles.

We decided to concentrate in the possible detection of the elecromagnetic component of this Hawking emission. In Sobrinho (2003)[1] we have considered BHs of all masses and determined the distances at which their electromagnetic emission can be detected at different wavelenghts using present day technology (i.e. the most sensitive telescopes operating at each electromagnetic spectrum band). As a result we found out that, for example, a BH with $\sim 10^{16}$ g could be detected, in γ–rays, at a maximum distance of $\sim 10^{10}$ m and that a BH with $\sim 10^{18}$ g could be detected, in X–rays, at a maximum distance of $\sim 10^{9}$ m. More massive BHs could be detected in ultraviolet, visible, infrared and radio wavelengths but only within laboratorial distances (for example a BH with $\sim 10^{20}$ g could be detected, in the ultraviolet, at a maximum distance of $\sim 10^{6}$ m and a BH with $\sim 10^{26}$ g could be detected, in the radio, at a maximum distance of $\sim 10^{2}$ m).

Thus it seemed that, if one wanted to consider the realistic detection of the electromagnetic radiation emitted by a BH then one should think of sub–stellar mass BHs (i.e. BHs with less than $1M_{\odot}$). As far as we know BHs with masses smaller than $\approx 3M_{\odot}$, cannot form in the present day Universe except, possibly, for the production of BHs in particle accelerators (in the speculative framework of branes) or, eventually, when high–energy cosmic–rays collide with the upper layers of the atmosphere. However, at the beginning of the expansion of the Universe the same fluctuations that originated the observed structure of the present day Universe could have lead, also, to the production of BHs of all masses (i.e. ranging from the Planck mass up to $\sim 10^{10}\mathrm{M}_{\odot}$). This BHs are called primordial BHs (PBHs) due to their origin.

Bearing in mind this idea we decided to enter deeper into Cosmology and determine the PBH density in the present day Universe and, consequently, the minimum distance to the nearest PBH. In order to have a better picture of this early BH for-

[1] See Appendix P for a summary in English.

mation epoch we decided to study not only the formation of sub–stellar mass PBHs but also the formation of PBHs of all masses.

This PhD thesis is organized as follows. In Chapter 1 we review several aspects about the early Universe and PBH formation that we found relevant for the present study. We finish this section with the expressions giving the fraction of the Universe going into PBHs at a given epoch and the PBH density parameter at that epoch as well as at the present day epoch. Being aware of the importance that cosmological phase transitions might have taken in PBH formation we have determined their location and duration within the Universe timeline. We do that, in Chapter 2, for the QCD phase transition, EW phase transition and electron–positron annihilation epoch. In Chapter 3 we consider the evolution of density fluctuations during cosmological phase transitions adopting some results from the literature and deriving our own results whenever necessary. In Chapter 4 we determine the behaviour of the PBH formation threshold during the QCD phase transition, EW phase transition and electron–positron annihilation epoch. In Chapter 5 we determine, assuming a running–tilt power–law spectrum for the fluctuations, the fraction of the Universe going into PBHs at each epoch of interest. First we consider a radiation–dominated universe and then we show how the results are altered when one considers cosmological phase transitions. In Chapter 6 we determine the present day values for the PBH density parameter, their number density and the minimum distance to the nearest PBH of a given mass. We then compile the results taking into account the different cosmological phase transitions (QCD, EW and electron–positron annihilation) and the different kinds of BHs (with respect to their masses). Finally, in Chapter 7 we summarize and discuss the results and, in Chapter 8 we present our conclusions as well as some ideas for the future.

I have a graduation in Physics from the University of Madeira (1995). In 2003 I have completed my PAPCC (Provas de Aptidão Pedagógica e Capacidade Científica) that consisted on giving a lesson (*Emulação da Máquina URM no Mathematica*) and defending an original thesis (*Possibilidade de detecção directa de buracos negros por radiação electromagnética*). In more than one sense this is equivalent to a M.Sc. thesis.

I am an Assistant at the recently created *Centro de Ciências Exactas e da Engenharia* (CCEE) in UMa. Prior to that, I have taught at the *Departamento de Física* of the UMa (1995/97), at *Escola Secundária de Jaime Moniz* (1994/95, 1997/98), at *Escola Básica e Secundária de Machico* (1998/99) and at the *Departamento de Matemática* (1999/2010) (later *Departamento de Matemática e Engenharias*, now incorporated into the new CCEE).

I have started working with BHs back in 1994 having as supervisor Professor Hanna Nencka then at the Departamento de Física. We have worked on the *Two–Bodies Problem* within the context of General Relativity. As a result we have presented a poster, at the conference (in memory of W. K. Clifford) *New Trends in Geometrical and Topological Methods* (UMa, 1995) with the title *Space–Time Geometry of a Pair of Reissner–Nordström Black Holes*. In 2000, already as an assistant at the Depar-

tamento de Matemática, I have started to work under the supervision of Professor Pedro Augusto on my PAPCC. The main objective was to determine the possibility of directly detecting BHs through their electromagnetic emission. I have concluded the PAPCC in 2003 and then I have started writing this PhD thesis on the same topic.

I am a founding member of the *Grupo de Astronomia da Universidade da Madeira* (GAUMa) created in 2000 in order to promote the research, outreach and teaching on Astronomy on Madeira. Since then I have been responsible and/or collaborator on many outreach activities in the area of Astronomy held here in Madeira (e.g. public/school lectures (about 30), observation sessions (about 20) hands–on activities with high school students (about 10), original posters (about 20)). An important mark in the Astronomy outreach in Madeira took place in 2009 with the International Year of Astronomy (IYA). I was an active member of the regional organization for Madeira, coordenated by Prof. Pedro Augusto. Within the 365 days of 2009 we have organized 229 different events in Madeira (including the islands of Porto Santo and Desertas)!

This work would not have been possible without the constant support and understanding from my wife Elda Maria Camacho Sobrinho and from our son Carlos Daniel Camacho Sobrinho. To them, that helped me in overcoming some of the most difficult moments, I dedicate this work. A special thanks to my parents who always supported me in my studies since the first day at school in October 1975 up to the present. I am also grateful to all relatives and colleagues who, in one way or another, helped me over these past years. In particular to my colleagues at the CCEE that were working on their own PhD thesis during these past years I would like to say that is was a pleasure and a privilege to share with them those high moments that only happen to those who endeavour in writing a PhD thesis in fundamental areas such as Mathematics and Physics. I am also deeply grateful to my supervisor (and colleague) Professor Pedro Augusto for his availability, support and advice during the writing up of this thesis.

This thesis was written in *LaTeX*. The numerical calculations were made using *Mathematica 5.1* from Wolfram Research. All graphics and original figures were also generated with the help of Mathematica 5.1. I have chosen to work with Mathematica because it is the software that we use in the classes of *Paradigmas da Programação* (an introductory computer programming course that I have been teaching since 1999).

José Laurindo de Góis Nóbrega Sobrinho

May 2011

1 Introduction: PBHs and the Early Universe

Black Holes (BHs) are objects predicted by the laws of Physics. In fact, they arise as a natural consequence by solving the field equations of General Relativity. BHs with stellar mass can form through the collapse of the iron cores of massive stars, of mass M, after they have reached the end of their thermonuclear evolution (e.g. Misner et al., 1973). If the core radius shrinks to the so called Schwarzschild radius

$$R_s = \frac{2GM}{c^2}$$

then a BH is formed. The spherical surface formed at this radius is called the event horizon. As the matter continues to collapse inside the event horizon it will form a singularity (i.e., a point with infinite curvature and density where the theory of General Relativity should be replaced by a (still lacking) theory of Quantum Gravity). Inside the event horizon light is trapped.

Stellar mass BHs could have masses from three to hundreds of solar masses. However, gravitational collapse allows for the formation of BHs with much greater or smaller masses (down to the Planck mass; $\sim 10^{-5}$ g — e.g. Lemos (1996)). In the centre of galactic nuclei gravitational collapse could lead to the formation of Super-Massive BHs (SMBHs). In fact, it is now well–established that SMBHs with masses in the range $10^6 M_\odot$–$10^{10} M_\odot$ reside in the centres of galaxies (e.g. Mack et al., 2007) including our own galaxy with a $4 \times 10^6 M_\odot$ SMBH (e.g. Gillessen et al., 2009).

Intermediate mass BHs (IMBHs), i.e., BHs with masses in the range $10^3 M_\odot$–$10^5 M_\odot$, might form either in the core of star clusters (e.g. Portegies Zwart et al., 2004) or galaxies (e.g. Greene & Ho, 2004).

As far as we know BHs with masses smaller than about $3M_\odot$, cannot form in the present Universe, except, possibly, for the production of BHs in accelerators such as the *Large Hadron Collider* (LHC) in the speculative framework of branes (e.g. Dimopoulos & Landsberg, 2001; Cavaglia et al., 2003) or, eventually, when cosmic–rays collide with the upper layers of the atmosphere (e.g. Anchordoqui et al., 2002).

However, the observed structure of the Universe on the scale of galaxies and smaller formations, requires that, at the beginning of the expansion of the Universe, there should have existed fluctuations which lead to the formation of such structures. It is plausible that some regions might have got so compressed that they did not continue to expand with the rest of the Universe but rather underwent gravitational collapse and produced Primordial Black Holes (PBHs). The first person to realize that was Hawking (1971)[2].

Hawking (1974) has shown that, when quantum effects are taken into account, BHs radiate like a blackbody. This process hardly affects stellar mass BHs, but it could be very significant in the case of smaller mass PBHs. In fact, PBHs with initial masses below 10^{15}g ($\sim 10^{-18} M_\odot$) should have completely evaporated by now and

[2]Zeldovich & Novikov (1967) also discussed the inhnomogenities in the early Universe but they were considering 'retarded cores' rather than BHs (e.g. Carr, 2003).

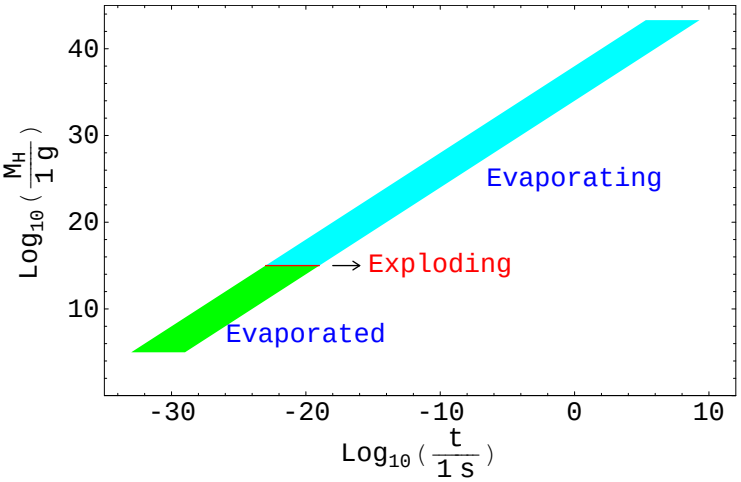

Figure 1: According to numerical simulations PBHs may form, at a given epoch, with masses ranging from $10^{-4}M_H$ up to M_H (Section 1.4.2). PBHs with initial masses smaller than 10^{15}g should have completely evaporated by now, PBHs with $\approx 10^{15}$g should be exploding and those with initial masses greater than 10^{15}g are still evaporating or accreting matter (Sobrinho & Augusto, 2007).

PBHs with initial masses of order 10^{15}g might be exploding right now (see Figure 1), contributing to the γ–ray background (e.g. Page & Hawking, 1976; Carr, 1976; MacGibbon & Carr, 1991; Barrau, 1999).

PBHs are interesting for several reasons (e.g. Carr, 2005). For example, within the context of Cosmology, they can act as probes to scales which are many orders of magnitude smaller than the scales probed by *Large Scale Structure* (LSS) surveys and *Cosmic Microwave Background* (CMB) angular anisotropy observations, giving the possibility to probe a very distinct part of the inflaton potential (e.g. Polarski, 2001) as well as the spectrum of primordial density fluctuations (e.g. Carr & Goymer, 1999). Within the context of Fundamental Physics they are the only BHs small enough for quantum emission effects to be important (e.g. MacGibbon & Carr, 1991) and thus they would play a key role in studying quantum gravitational effects. However, even if PBHs never formed, their nonexistence provides useful cosmological information (e.g. MacGibbon & Carr, 1991).

Being aware of the important role that BHs play in the Universe, and taking into account that up to now they only have been detected indirectly (see e.g. Kormendy & Richstone, 1995; Bennett et al., 2002; Zhang et al., 1997), we decided to investigate the possibility of BH direct detection by means of their electromagnetic emission. The ones that offer the best chances, in terms of electromagnetic detection, are the smallest ones and as far as we know BHs with such masses could form only in the early Universe. Thus, we decided to concentrate our studies in determining first how many PBHs formed and still exist in the Universe lurking around us.

1.1 The Primordial Universe

1.1.1 Relativistic Cosmology preliminaries

According to observation we live in a flat, homogeneous and isotropic (on scales larger than 100 Mpc) expanding Universe (e.g. Jones & Lambourne, 2004). Thus, *Cosmology*, i.e. the study of the dynamical structure of the Universe as a whole, is based on the (e.g. d'Inverno, 1993)

Cosmological Principle – At each epoch, the Universe presents the same aspect from every point, except for local irregularities,

which is in essence, a generalization of the *Copernican Principle* that the Earth is not at the centre of the Solar System. We are assuming that there is a *cosmic time* t with the Cosmological Principle valid for each spacelike hypersurface $t = const$. The statement that each hypersurface has no privileged points means that it is homogeneous. The principle also requires that each hypersurface has no privileged directions about any point, i.e., the spacelike hypersurfaces are isotropic and necessarily spherically symmetric about each point. The concepts of homogeneity and isotropy, however, do not apply to the Universe in detail (e.g. d'Inverno, 1993).

Assuming that there is a privileged class of observers in the Universe, namely, those associated with the smeared–out motion of the galaxies[3], Weyl introduced a fluid pervading space, which he called *the substractum*, in which the galaxies move like particles in a fluid. These ideas are contained in the (e.g. d'Inverno, 1993)

Weyl's Postulate – The particles of the substractum lie in space–time on a congruence of timelike geodesics diverging from a point in the finite or infinite past.

The postulate requires that the geodesics do not intersect except at a singular point in the past and possibly at a similar singular point in the future. There is, therefore, one and only one geodesic passing through each point of space–time, and consequently the matter at any point possesses a unique velocity. This means that the substractum may be taken to be a *perfect fluid*. Although galaxies do not follow this motion exactly, the deviations appear to be random and less than one–thousandth of the velocity of light (e.g. d'Inverno, 1993).

Weyl's postulate requires that the geodesics of the substractum are orthogonal to a family of spacelike hypersurfaces. We introduce coordinates (t, x^1, x^2, x^3) such that these spacelike hypersurfaces are given by constant t and such that the space coordinates (x^1, x^2, x^3) are constant along the geodesics. Such coordinates are called *comoving coordinates* (e.g. d'Inverno, 1993). Comoving observers are also called *fundamental observers*.

[3]We can work with this smeared–out motion because the relative velocities in each group of galaxies are, according to observation, small (e.g. d'Inverno, 1993).

Relativistic Cosmology is based on three assumptions: (1) the Cosmological Principle, (2) Weyl's postulate and (3) General Relativity[4].

A flat, homogeneous and isotropic expanding universe can be described by the *Friedmann–Lemaître–Robertson–Walker* (FLRW) metric (e.g. d'Inverno, 1993)

$$ds^2 = dt^2 - R^2(t)\left[\frac{dr^2}{1-\kappa r^2} + r^2\left(d\theta^2 + sin^2\theta d\phi^2\right)\right] \tag{1}$$

where $R(t)$ is the so called *scale factor* which describes the time dependence of the geometry (the distance between any pair of galaxies, separated by more than 100 Mpc, is proportional to $R(t)$) and κ is a constant which fixes the sign of the spatial curvature ($\kappa = 0$ for Euclidean space, $\kappa > 0$ for a closed elliptical space of finite volume and $\kappa < 0$ for an open hyperbolic space). Notice that, whatever the physics of the expansion, the space–time metric must be of the FLRW form, because of the isotropy and homogeneity (e.g. Longair, 1998).

Considering the FLRW metric (1), Weyl's postulate, General Relativity (with a *cosmological constant* term Λ) and a comoving coordinate system it turns out that the field equations lead to two independent equations sometimes called the *Friedmann–Lemaître equations* (e.g. Yao et al., 2006; Unsöld & Bascheck, 2002)

$$\left(\frac{\dot{R}}{R}\right)^2 = \frac{8\pi G\rho}{3} - \frac{\kappa}{R^2} + \frac{\Lambda}{3} \tag{2}$$

$$\frac{\ddot{R}}{R} = \frac{\Lambda}{3} - \frac{4\pi G}{3}(\rho + 3p) \tag{3}$$

where we have used relativistic units ($c = 1$) and a dot denotes differentiation with respect to cosmic time t. Equation (3) involves a second time derivative of R and so it can be regarded as an equation of motion, whereas equation (2), sometimes called the *Friedmann equation*, only involves a first time derivative of R and so may be considered an integral of motion, i.e., an energy equation.

The addition of a cosmological constant term Λ is equivalent to assume that matter is not the only source of gravity. The Λ term was introduced by Einstein with the purpose of constructing a static cosmological model for the Universe. However, with the discovery of the expansion of the Universe (Slipher, 1917) the model became obsolete. More recently, a $\Lambda > 0$ term was introduced again in order to account for the remarkable discovery that the expansion of the Universe is, in fact, accelerating rather than retarding (Section 1.1.3). Taking into account that, according to observation, we live in a flat universe, we consider $\kappa = 0$ (e.g. Yao et al., 2006).

[4]For an introductory text on the Theory of General Relativity see (e.g. Schutz, 1985; d'Inverno, 1993).

Energy conservation leads to a third equation, which can also be derived from equations (2) and (3), and is just a consequence of the *First Law of Thermodynamics* (e.g. Yao et al., 2006)

$$\dot{\rho} = -3\frac{\dot{R}}{R}(\rho + p). \tag{4}$$

We need also an *equation of state* (EoS) relating the pressure p to the energy density ρ at a given epoch. This relation is, in general, non–trivial. However, in Cosmology, where one deals with dilute gases, the EoS can be written in a simple linear form (e.g. Carr, 2003; Ryden, 2003)

$$p = w\rho \tag{5}$$

where the dimensionless quantity w is the so–called *adiabatic index*. Normally w is a constant such that $0 \leq w \leq 1$. If $w = 0$ we are in the case of a pressureless matter–dominated universe and, if $w = 1$ we have a stiff EoS which may be the case if the Universe is dominated by a *scalar field*[5] (e.g. Harada & Carr, 2005).

In the case of cosmological perturbations the radiation fluid behaves as a perfect (i.e. dissipationless) fluid, the entropy (S) in a comoving volume is conserved and, one has a reversible process. The isentropic[6] sound speed can be written as (e.g. Schmid et al., 1999)

$$c_s^2 = \left(\frac{\partial p}{\partial \rho}\right)_S = w. \tag{6}$$

In the early hot and dense primordial Universe it is appropriate to assume an EoS corresponding to a gas composed of radiation and relativistic massive particles with $w = 1/3$ (e.g. Carr, 2003)

$$p = \frac{\rho}{3}$$

which means that, in the case of a radiation–dominated universe, the sound speed is given by

$$c_s = \frac{1}{\sqrt{3}}. \tag{7}$$

However, during inflation (Section 1.1.2) or in a universe dominated by a cosmological constant, w becomes negative and may not even be constant (e.g. Yao et al.,

[5] A scalar field is a field that associates a scalar value to every point in space. On the other hand, a vector field associates a vector to every point in space. In Quantum Field Theory, a scalar field is associated with spin 0 particles (scalar bosons) and a vector field is associated with spin 1 particles (vector bosons).

[6] A thermodynamic process that occurs at a constant entropy (S) is sayd to be isentropic. If it is a reversible process then it is identical to an adiabatic process, i.e., a thermodynamic process in which there is no energy added or subtracted from the system.

2006). If $w < 0$ the sound speed is imaginary (cf. equation 6). In this case we have perturbations with negative pressure that will not propagate as stable sound waves, but will have amplitudes that grow or decay with time (e.g. Ryden, 2003). The case $w < -1/3$ is of special interest because it provides a positive acceleration to the Universe. Current measurements give $w = -0.967 \pm 0.073$ (Spergel et al., 2007) which means that the expansion of the Universe is accelerating by the present time. We thus consider, for simplicity, $w = -1$.

Inserting equation (5) into equation (4) we have

$$\dot{\rho} = -3(1+w)\rho\frac{\dot{R}}{R}. \tag{8}$$

Putting $w = -1$ in equation (8) one gets $\dot{\rho} = 0$ which means that in a universe dominated by a cosmological constant the energy density remains constant (or almost constant, if one considers $w \gtrsim -1$ and $w \neq -1$). Integration of equation (8) yields

$$\rho(t) \propto R(t)^{-3(1+w)}. \tag{9}$$

Another important thermodynamic relation is the *Second Law of Thermodynamics*, which connects pressure and energy density. It can be written, in the case of a fluid without chemical potential, that (e.g. Schmid et al., 1999; Schwarz, 2003)

$$\rho = T\frac{dp}{dT} - p. \tag{10}$$

The entropy density for such a fluid is given by the Maxwell relation for the free energy (e.g. Schmid et al., 1999; Schwarz, 2003)

$$s = \frac{dp}{dT}. \tag{11}$$

The sound speed (equation 6) can be written, from equations (10) and (11), also in the form (e.g. Schmid et al., 1999)

$$c_s^2 = \left(\frac{d\ln s}{d\ln T}\right)^{-1}. \tag{12}$$

During a first–order phase transition, for a fluid with negligible chemical potential, the entropy is conserved and, hence, $c_s^2 = 0$ during the transition (see Section 1.2). In the following we consider the solutions of equation (2) when a single component dominates the energy density.

Inserting equation (9) into equation (2), with $\kappa = 0$ and $\Lambda = 0$, one obtains (e.g. Yao et al., 2006)

$$R(t) \propto t^{\frac{2}{3(1+w)}}. \tag{13}$$

For a radiation–dominated universe ($w = 1/3$), equation (13) becomes

$$R(t) \propto t^{1/2}. \tag{14}$$

The radiation and matter densities in the Universe decrease as the expansion dilutes the number of atoms and photons. Radiation is also diminished due to the *cosmological redshift*, so its density falls faster than that of matter. When the age of the Universe was $\sim 10^6$ years it became matter–dominated (see Appendix A). Now it is appropriate to assume an EoS corresponding to a pressureless gas ($w = 0$). For this matter–dominated universe, equation (13) becomes

$$R(t) \propto t^{2/3}. \tag{15}$$

This might also be the case if the Universe experienced a dust–like phase during a phase transition in the radiation–dominated epoch (e.g. Carr et. al., 1994).

If the Universe is dominated by a positive cosmological constant Λ then we have an EoS with $w < 0$. We consider, for simplicity and observational consistency, $w = -1$. In this case the integration of equation (2) with $\kappa = 0$ and $\Lambda > 0$ leads to (e.g. Yao et al., 2006)

$$R(t) \propto \exp\left(\sqrt{\frac{\Lambda}{3}}ct\right) \tag{16}$$

which corresponds to an exponential expansion of the Universe.

Assuming that light propagates in Relativistic Cosmology in the same way as it does in General Relativity we consider now how an observer O receives light from a receding galaxy. Without loss of generality we take O to be at the origin of coordinates $r = 0$. Inserting the conditions for a radial null geodesic into the line element (1) we have (e.g. d'Inverno, 1993)

$$\frac{dt}{R(t)} = \pm\frac{dr}{(1-\kappa r^2)^{1/2}} \tag{17}$$

where the $+$ sign corresponds to a receding light ray and the $-$ sign to an aproaching light ray. Consider a light ray emanating from a galaxy P with world line $r = r_1$, at coordinate t_1, and received by O at coordinate time t_0. Using equation (17) we have (e.g. d'Inverno, 1993)

$$\int_{t_1}^{t_0}\frac{dt}{R(t)} = -\int_{r_1}^{0}\frac{dr}{(1-\kappa r^2)^{1/2}}.$$

Next, consider a second light ray emanating from P at time $t_1 + dt_1$ and received at O at time $t_0 + dt_0$. Thus, we have

$$\int_{t_1+dt_1}^{t_0+dt_0}\frac{dt}{R(t)} = -\int_{r_1}^{0}\frac{dr}{(1-\kappa r^2)^{1/2}}.$$

Comparing the two results and taking into account that $R(t)$ does not vary greatly over the intervals dt_1 and dt_0 we have (e.g. d'Inverno, 1993)

$$\frac{dt_0}{R(t_0)} = \frac{dt_1}{R(t_1)}.$$

All fundamental particles of the substractum have world lines on which the spatial coordinates are constant and, hence, the metric reduces to $ds^2 = dt^2$. Here t measures the *proper time* along the substractum world lines. The intervals dt_1 and dt_0 are, respectively, the proper time intervals between the rays as measured at the source and observer. In an expanding universe we have that $t_0 > t_1$ and so $R(t_0) > R(t_1)$ which means that the observer O will experience a *redshift* z given by (e.g. d'Inverno, 1993)

$$1 + z = \frac{\nu_1}{\nu_0} = \frac{R(t_0)}{R(t_1)} = \frac{dt_0}{dt_1} \tag{18}$$

where ν_1 and ν_0 are the frequencies measured by the emitter and the receiver, respectively. In a contracting universe O will detect instead a *blue shift*.

The *Hubble parameter* H is defined as (e.g. d'Inverno, 1993)

$$H(t) = \frac{\dot{R}(t)}{R(t)} \tag{19}$$

and the *Hubble time* is defined as (e.g. Boyanovsky et al., 2006)

$$t_H(t) = \frac{1}{H(t)} = \frac{R(t)}{\dot{R}(t)}.$$

Multiplying t_H by the speed of light c one obtains the so called *Hubble radius* R_H (e.g. Boyanovsky et al., 2006)

$$R_H(t) = \frac{c}{H(t)} = c\frac{R(t)}{\dot{R}(t)} \tag{20}$$

which is closely related to the size of the *Observable Universe*[7]. The mass contained inside a region with size R_H is called the *horizon mass* and it is given by

$$M_H(t) = \frac{4}{3}\pi R_H(t)^3 \rho(t).$$

Here we consider for $M_H(t)$ the approximation given by (e.g. Carr, 2005)

$$M_H(t) \approx \frac{c^3 t}{G} \approx 10^{15} \left(\frac{t}{10^{-23}\ \mathrm{s}}\right) \mathrm{g} \tag{21}$$

[7]The Hubble radius, R_H, represents the size of the region surrounding an observer beyond which objects recede at a rate greater than the speed of light due to the expansion of the Universe. On the other hand, the observable Universe (or particle horizon), R_U, represents the part of the Universe that we can observe because light signals from those objects had time to reach us since the beginning of the expansion. After inflation it is $R_H \lesssim R_U$.

where c is the speed of light in the vacuum and G is the Gravitational constant. This expression is useful in the context of the study of PBHs. It is natural to assume that the mass of a PBH, when it forms, is of the order of M_H at that epoch (e.g. Carr, 2005). When $t \approx 10^{-23}$ s we have $M_H \approx 10^{15}$ g. These values represent, respectively, the time of formation and the initial mass of the PBHs that are presumed to be explodind by the present time (e.g. Page & Hawking, 1976).

1.1.2 Inflation

There are some problems that the stantard *Big Bang model*[8] could not give a satisfactory answer. In order to identify such problems let us start by dividing equation (2) by H^2

$$1 = \frac{8\pi G}{3H^2}\rho - \frac{\kappa}{R^2H^2} + \frac{c^2\Lambda}{3H^2}. \tag{22}$$

Consider the case $\Lambda = 0$. If $\kappa < 0$ the Universe will expand forever and if $\kappa > 0$ the expansion will eventually give way to contraction. Between the two possibilities we have the critical case $\kappa = 0$. In this case one obtains from equation (22) the following expression for the density

$$\rho_c = \frac{3H^2}{8\pi G} \tag{23}$$

which is called the *critical density*. The *matter density parameter* is defined as (e.g. Unsöld & Bascheck, 2002)

$$\Omega_m = \frac{\rho}{\rho_c} \tag{24}$$

where ρ is the matter density of the Universe. We introduce here also the quantities (e.g. Covi, 2003)

$$\Omega_\kappa = -\frac{\kappa}{H^2R^2} \tag{25}$$

$$\Omega_\Lambda = \frac{c^2\Lambda}{3H^2}. \tag{26}$$

With this definitions we can rewrite equation (22) in the simple form (e.g. Covi, 2003)

$$1 = \Omega = \Omega_m + \Omega_\kappa + \Omega_\Lambda. \tag{27}$$

[8]For more information about the Big Bang model and the Universe timeline see Appendix A.

In the standard Big Bang theory we have always $\ddot{R} < 0$ (cf. equation (3) with $\Lambda = 0$) which implies that the term R^2H^2 in equation (22) will always decrease. This indicates that Ω tends to shift away from unity with the expansion of the Universe. However, present observations suggest that $\Omega \sim 1$, i.e., Ω should have been very close to unity in the past. This turns out to be an extreme fine tuning of initial conditions. Unless initial conditions are chosen very accurately, the Universe soon collapses, or expands quickly before any structure formation. This is known as the *flatness problem* (e.g. Tsujikawa, 2003).

The CMB[9] radiation was released when the Universe was ~ 380000 years old. At that epoch the Universe had cooled enough so that the opaque plasma neutralized into a transparent gas, allowing photons to, finally, travel freely. These CMB photons have been travelling mostly in straight lines since then, so they provide an image of what the Universe looked like at that epoch. Observation shows that the CMB is nearly homogeneous and isotropic (with anisotropies at the 10^{-5} level, Appendix B) which, therefore, implies that the observed Universe had become uniform in temperature by that time. In standard FLRW Cosmology, a simple calculation shows that the uniformity could be established that quickly only if signals could propagate at 100 times the speed of light, a proposition clearly contradicting the known laws of Physics. This is known as the *horizon problem* (e.g. Guth, 2000).

From the view point of Particle Physics, *symmetry breaking*[10] leads to the production of many unwanted relics such as *magnetic monopoles*, *cosmic strings*, and other *topological defects*. If these particles existed in the early stage of the Universe then their massive relics should be the dominant materials in the Universe (they would outweigh everything else in the Universe by a factor of about 10^{12}), which contradicts observations. This problem is generally called the *monopole problem* (e.g. Tsujikawa, 2003; Guth, 2000).

In order to explain problems such as 'flatness', 'horizon' and 'monopole' the present paradigm makes use of an inflationary stage of expansion in the very early Universe. During inflation the scale factor $R(t)$ behaves like (e.g. Narlikar & Padmanabhan, 1991)

$$R(t) = R(t_i) \exp\left(H(t - t_i)\right).$$

The scale factor grows exponentially from an initial value $R_i = R(t_i)$, corresponding to the instant $t_i \sim 10^{-35}$ s when the EW and strong forces separate (e.g. Narlikar

[9]For more details about the CMB temperature see Appendix B.

[10]The basic idea underlying unified theories of the weak, strong, and electromagnetic interactions is that, prior to symmetry breaking, all vector bosons (which mediate these interactions) are massless, and there are no fundamental differences among the interactions. As a result of the symmetry breaking, however, some of the vector bosons acquire mass, and their corresponding interactions become short–range, thereby destroying the symmetry between the various interactions. For example, prior to the appearance of the constant scalar Higgs field H, the Glashow–Weinberg–Salam model was symmetrical, and ElectroWeak (EW) interactions were mediated by massless vector bosons. With the Higgs field, some of the vector bosons (W^-, Z^0 and W^+) acquire masses of ~ 100 GeV, and the corresponding interactions become short–range (weak interactions), whereas the electromagnetic field boson (i.e., the photon) remains massless (e.g. Linde, 2005).

& Padmanabhan, 1991, cf. Table A-1) to a value $R_e = R(t_e)$ according to (e.g. d'Inverno, 1993)

$$\frac{R_e}{R_i} = e^{N(t_e)} \tag{28}$$

where (e.g. Tsujikawa, 2003)

$$N(t_e) = \ln \frac{R_e}{R_i} = \int_{t_i}^{t_e} H dt \approx H t_e \tag{29}$$

gives the number of *e–folds* that elapsed during inflation. For example, the value $N = 70$ means that during inflation the scale factor have grown up by a factor of e^{70} ($\approx 10^{30}$). Although the exact value of $N(t_e)$ is unknown, in order to solve the mentioned problems, the inflationary stage must last a time interval such that $50 < N(t_e) < 70$ (e.g. Narlikar & Padmanabhan, 1991; Boyanovsky et al., 2006).

During inflation the scale factor $R(t)$ has a positive acceleration $\ddot{R}(t) > 0$ which means that the R^2H^2 term in equation (22) increases during inflation. As a result Ω rapidly approaches unity (see equation 27). After the inflationary period, the evolution of the Universe is followed by the conventional Big Bang phase (Appendix A) and, despite this, Ω stays of order unity even in the present epoch, solving the flatness problem (e.g. Tsujikawa, 2003).

Inflation gives rise to a remarkable phenomenon: physical wavelengths grow faster than the size of the Hubble radius (see equation 20). This means that the region where the causality works is stretched on scales much larger than the Hubble radius, i.e., once a physical wavelength becomes larger than the Hubble radius, it is causally disconnected from physical processes. This solves the horizon problem (e.g. Boyanovsky et al., 2006). Notice that Inflationary Cosmology suggests that, even though the observed Universe is incredibly large, it is only an infinitesimal fraction of the entire Universe (e.g. Guth, 2000).

Inflation is, perhaps, the simplest known mechanism to eliminate monopoles from the visible Universe, even though they are still in the spectrum of possible particles. The monopoles are eliminated simply by arranging the parameters so that inflation takes place after (or during) monopole production, so the monopole density is diluted to a completely negligible level (e.g. Guth, 2000).

The inflationary era is followed by the radiation–dominated and matter–dominated stages where the acceleration of the scale factor becomes negative. With a negative acceleration of the scale factor, the Hubble radius grows faster than the scale factor, and wavelengths that were outside, can now re–enter the Hubble radius. This is the main concept behind the inflationary paradigm for the generation of temperature fluctuations as well as for providing the seeds for LSS formation (e.g. Boyanovsky et al., 2006).

Inflation gives a possible solution to the crucial problem of where the primordial fluctuations leading to the observed LSS come from. In fact, they have their origin

in the ubiquitous vacuum fluctuations. The seed of the LSS has been observed in the form of tiny fluctuations imprinted in the CMB at the time of decoupling (e.g. Bringmann et al., 2002).

There are various inflationary scenarios (e.g. slow roll inflation, old inflation, chaotic inflation, hybrid inflation, eternal inflation) differing essentially only in the choice of the potential $V(\phi)$ where ϕ represents the *inflaton*, i.e., the scalar field responsible for inflation (e.g. Boyanovsky et al., 2006). Each inflationary model makes precise predictions about the spectrum of its primordial fluctuations and this is how these models can be constrained by observations (e.g. Bringmann et al., 2002).

The inflaton ϕ is an homogeneous scalar field, whose potential energy $V(\phi)$ leads to the exponential expansion of the Universe. The energy density and the pressure density of the inflaton can be described, respectively, as (e.g. Liddle & Lyth, 1993)

$$\rho = \frac{1}{2}\dot{\phi}^2 + V(\phi) \tag{30}$$

$$p = \frac{1}{2}\dot{\phi}^2 - V(\phi). \tag{31}$$

Substituting equations (30) and (31) for equations (2) and (4) we get (e.g. Liddle & Lyth, 1993)[11]

$$H^2 = \frac{8\pi G}{3}\left(\frac{1}{2}\dot{\phi}^2 + V(\phi)\right) = \frac{8\pi}{3m_{pl}^2}\left(\frac{1}{2}\dot{\phi}^2 + V(\phi)\right) \tag{32}$$

$$\ddot{\phi} + 3H\dot{\phi} + V'(\phi) = 0 \tag{33}$$

where we have considered $\kappa = 0$ and $\Lambda = 0$ in equation (32). Here, the prime denotes the derivative of the potential with respect to the inflaton field.

Amongst the wide variety of inflationary scenarios, slow roll inflation provides a simple and generic description of inflation consistent with the *Wilkinson Microwave Anisotropy Probe* (WMAP) data (e.g. Boyanovsky et al., 2006). The basic premise of slow roll inflation is that the potential is fairly flat during the inflationary stage. This flatness not only leads to a slowly varying inflaton and Hubble parameter, hence ensuring a sufficient number of e–folds, but also provides an explanation for the gaussianity of the fluctuations as well as for the almost scale invariance of their power spectrum. Departures from scale invariance and gaussianity are determined by the departures from flatness of the potential, namely by derivatives of the potential with respect to the inflaton field (e.g. Boyanovsky et al., 2006). The slow roll approximation corresponds to (e.g. Carr, 2005)

$$\xi \ll 1, \quad |\eta| \ll 1 \tag{34}$$

[11] We have written equation (32) also in terms of the Planck mass $m_{pl} = (\hbar c/G)^{1/2}$ with $\hbar = c = 1$.

where ξ and η are the so called *slow–roll parameters* which are determined by the derivatives of the inflaton potential in the following manner (e.g. Carr, 2005)

$$\xi = \frac{m_{pl}^2}{16\pi}\left(\frac{V'}{V}\right)^2$$

$$\eta = \frac{m_{pl}^2}{8\pi}\frac{V''}{V}.$$

The inflationary era ends when ξ and $|\eta|$ grow to order unity (e.g. Tsujikawa, 2003). At that time the scalar field starts to roll faster and finally to oscillate around the minimum and finally it decays producing radiation and reheating the Universe (e.g. Covi, 2003). If the conditions (34) are valid then equations (32) and (33) are approximately given by (e.g. Boyanovsky et al., 2006)

$$H^2 = \frac{8\pi}{3m_{pl}^2}V(\phi)$$

$$3H\dot{\phi} + V'(\phi) = 0.$$

Inflation is now an established part of Cosmology with several important aspects, such as the superhorizon origin of density perturbations, having been spectacularly validated by WMAP (e.g. Boyanovsky et al., 2006). The gaussian and nearly scale invariant spectrum of primordial fluctuations generically predict by most inflationary models fits with high precision the data provided by WMAP (e.g. Spergel et al., 2007).

1.1.3 The Lambda–Cold Dark Matter Model

In the last few years there has been a wealth of observational evidence from CMB, LSS, and high redshift supernovae Ia data that leads to the remarkable conclusions that: i) the spatial geometry of the Universe is flat ($\kappa = 0$), ii) the Universe is accelerating today, and iii) most of the matter is in the form of dark matter. The current understanding of Cosmology is based on the so called *Lambda–Cold Dark Matter Model* (ΛCDM) in which the total energy density of the Universe has as main ingredients: 4% of baryonic matter, 24% of dark matter and 76% of dark energy (e.g. Boyanovsky et al., 2006).

Baryonic matter

Ordinary matter is mainly composed of protons and neutrons (which are baryons) and electrons (which are leptons). Since the baryons vastly outweigth the electrons, in the context of Cosmology, ordinary matter is called *baryonic matter* (e.g. Lyth, 1993). The luminous matter in the Universe accounts for only 10% of all baryonic matter which means that there exists a great amount of *baryonic dark matter* in the Universe.

Non–Baryonic Dark Matter

If $\Omega_m \approx 0.24$ as measured by WMAP (Spergel et al., 2007) then, besides baryonic matter (luminous and dark), there might exist a huge amount of *non–baryonic dark matter* (e.g. Lyth, 1993).

We can estimate the total amount of matter in a bound system, such as a galaxy or galaxy cluster, through its gravitational field, which can be deduced from the velocities of its components. One finds that each galaxy is surrounded by a dark halo accounting for most of its mass. Soon after the need for dark matter came to be widely accepted in the early 1980s, it became clear that the hypothesis fails completely if the dark matter consists of massive neutrinos, because their thermal motion wipes out small scale structure. Given the failure of this *Hot Dark Matter* (HDM) model, attention turned to the other extreme, of matter which has, by definition, negligible random motion, the so called *Cold Dark Matter* (CDM) (e.g. Liddle & Lyth, 1993).

As implied by its name, the CDM is assumed to be cold, which, for most purposes, means non–relativistic. By definition, dark matter does not interact significantly with more conventional forms of matter by any means other than gravity, and, in particular, is beneficial for structure formation in that it is not subject to pressure forces from interaction with radiation which prevent baryonic density inhomogeneities on scales smaller than superclusters from collapsing before radiation decouples from matter (e.g. Liddle & Lyth, 1993).

The current best candidate for CDM are the so–called *weakly interacting massive particles* (WIMPs) that might have been produced in the very early Universe (e.g. Bertone et al., 2005).

PBHs are also a potential CDM candidate. However, there are some mass ranges in which PBHs are constrained down to some limits in our galactic halo (e.g. Carr, 2005). Searches for microlensing of stars in the Large Magellanic Cloud have shown that objects with masses in the range $0.3 - 10 M_\odot$ cannot make up more than 40% of the CDM halo (Alcock et al., 2001), those with masses in the range $10^{-4} - 0.03 M_\odot$ cannot make up more than 20% (Alcock et al., 1997) and those with masses in the range 10^{-7}–$10^{-3} M_\odot$ cannot make up more than 25% (Alcock et al., 1998). Femtolensing of gamma-ray bursts by PBHs precludes those in the mass range $10^{17} - 10^{20}$ g from having a critical density (e.g. Carr, 2005). For a recent update on cosmological constraints on PBHs see Carr et al. (2010).

Dark energy

Independent measurements of Type Ia supernovae have revealed that the expansion of the Universe is undergoing a non–linear acceleration rather than following strictly Hubble's law. To explain this acceleration, General Relativity requires that much of the Universe consist of an energy component with large negative pressure. Its true nature remains unknown, although the present observations indicate that this

Table 1: The best fit values for the ΛCDM model free parameters according to the WMAP data (Spergel et al., 2007).

Parameter	Value	Description
h	$0.734^{+0.028}_{-0.038}$	Normalized Hubble constant
$100\Omega_b h^2$	$2.233^{+0.072}_{-0.091}$	Baryon density
$\Omega_m h^2$	$0.1268^{+0.0072}_{-0.0095}$	Total matter density
τ	$0.088^{+0.043}_{-0.054}$	Optical depth to reionization
A_s	$0.801^{+0.043}_{-0.054}$	Scalar fluctuation amplitude at $k = 0.002$ Mpc^{-1}
n_s	$0.951^{+0.015}_{-0.019}$	Scalar spectral index at $k = 0.002$ Mpc^{-1}

dark energy can be described by a cosmological constant Λ (e.g. Boyanovsky et al., 2006).

The model assumes a nearly scale–invariant spectrum of primordial perturbations and a universe without spatial curvature ($\kappa = 0 \Rightarrow \Omega_\kappa = 0$). It also assumes that it has no observable topology, so that the Universe is much larger than the observable particle horizon. Those are predictions of cosmic inflation (Section 1.1.2).

The ΛCDM model has six parameters: the Hubble constant H_0, the baryon density Ω_b, the total matter density Ω_m (which includes baryons plus dark matter), the optical depth to reionization τ (which determines the redshift of reionization), the amplitude of the primordial fluctuations A_s and the slope for the scalar perturbation spectrum n_s (which measures how fluctuations change with scale; $n_s = 1$ corresponds to a scale–invariant spectrum). The values of these six free parameters as obtained from the WMAP data (Spergel et al., 2007) are presented in Table 1. The Hubble constant h is given in normalized units of 100 kms^{-1}Mpc^{-1} and the densities Ω_m and Ω_b are given as functions of h. Thus, the present value of the Hubble parameter H_0 is, according to the WMAP observations

$$H_0 = 73.4\,\text{kms}^{-1}\,\text{Mpc}^{-1} \approx 2.38 \times 10^{-18}\ \text{s}^{-1} \tag{35}$$

and

$$\Omega_m \approx 0.24$$

$$\Omega_b \approx 0.042.$$

The dark matter density is given by

$$\Omega_{CDM} = \Omega_m - \Omega_b \approx 0.198 \tag{36}$$

Notice that the dark energy density Ω_Λ (cf. equation 26) is not a free parameter because, since the ΛCDM model assumes a flat universe ($\Omega = 1$), we have, according to equation (27)

$$\Omega_\Lambda = 1 - \Omega_m \approx 0.76. \tag{37}$$

Other derived parameters are the age of the Universe t_0 (Section 1.1.4) and the critical density ρ_c (cf. equation 23). Inserting the value of H_0 into equation (23) one obtains

$$\rho_c = \rho_0 \approx 1.013 \times 10^{-26} \text{ kgm}^{-3}.$$

The Hubble radius (cf. equation 20), at the present time, is given by

$$R_H(t_0) = \frac{c}{H_0} \approx 1.3 \times 10^{26} \text{ m}.$$

The cosmological constant, which is also a derived parameter, is given by (see equation 26)

$$\Lambda = \frac{3H_0^2\Omega_\Lambda}{c^2}. \tag{38}$$

Inserting the obtained values for H_0 (equation 35) and Ω_Λ (equation 37) into equation (38) one obtains[12]

$$\Lambda \approx 1.44 \times 10^{-52} \text{ m}^{-2}.$$

1.1.4 The scale factor

The metric (1) leaves room for choice of a normalization. One common choice is to make the scale factor equal to unity at the present time (e.g. Liddle & Lyth, 1993)

$$R_0 = R(t_0) = 1. \tag{39}$$

This is convenient because, at any time, the scale factor will be related to the redshift z simply by (cf. equation 18)

$$R(t) = \frac{1}{1 + z(t)}. \tag{40}$$

We can now determine the Hubble parameter (equation 19) for the different epochs of the Universe. During the radiation–dominated epochs we have, according to expression (14), that

$$H(t) = \frac{1}{2t} \tag{41}$$

[12]When one calculates the theoretical value of Λ one ends up with a value about 120 orders of magnitude larger than the experimentally measured one. This has been called the worst mismatch between theory and experiment in the whole of science (e.g. Weinberg, 2000).

and during the dust–like phases or mater–dominated epochs we have, according to expression (15), that

$$H(t) = \frac{2}{3t}. \tag{42}$$

When the Universe becomes dominated by dark energy ($\Lambda > 0$) the Hubble parameter becomes constant in time (cf. expression 16)

$$H(t) = c\sqrt{\frac{\Lambda}{3}}. \tag{43}$$

Since inflation only lasts a few e–folds (see Section 1.1.2), the Hubble parameter can be taken as a constant during this period (e.g. Huang, 2007; Narlikar & Padmanabhan, 1991). From equation (29) we have

$$H(t) = \frac{N(t_e)}{t_e}. \tag{44}$$

Considering the normalisation (39) we can determine the proportionality constant in expression (16), yielding, for the scale factor of a universe dominated by a positive cosmological constant, the result

$$R(t) = \exp\left(c\sqrt{\tfrac{\Lambda}{3}}(t - t_0)\right), \quad t_{SN} \leq t \leq t_0 \tag{45}$$

where t_0 is the present time (i.e. the age of the Universe) and t_{SN} is the age of the Universe at matter–Λ equality (corresponding to the instant when the expansion starts to accelerate). The dark energy domination is preceded by a matter–dominated stage (see Appendix A). During matter domination the scale factor behaves according to expression (15). Considering that R is a continuous function of time we write, for the matter–dominated stage

$$R(t) = \exp\left(c\sqrt{\tfrac{\Lambda}{3}}(t_{SN} - t_0)\right)\left(\tfrac{t}{t_{SN}}\right)^{2/3}, \quad t_{eq} \leq t \leq t_{SN} \tag{46}$$

where t_{eq} is the age of the Universe at radiation–matter equality. Before that time, the Universe was radiation–dominated up to the end of inflation at some instant $t = t_e$. During radiation domination the scale factor behaves according to expression (14). During the period ($t_e \leq t \leq t_{eq}$) the Universe experienced two phase transitions during which it might have been, for brief instants, dust–like (Section 1.2). When one goes backwards in time the first phase transition is the QCD phase transition. Considering that t_{QCD+} corresponds to the age of the Universe at the end of the QCD phase transition we write

$$R(t) = \exp\left(c\sqrt{\tfrac{\Lambda}{3}}(t_{SN} - t_0)\right)\left(\tfrac{t_{eq}}{t_{SN}}\right)^{2/3}\left(\tfrac{t}{t_{eq}}\right)^{1/2}, \quad t_{QCD+} \leq t \leq t_{eq}. \tag{47}$$

We consider that during the QCD epoch ($t_{QCD-} \leq t \leq t_{QCD+}$) the scale factor is given by

$$R(t) = \exp\left(c\sqrt{\frac{\Lambda}{3}}(t_{SN} - t_0)\right)\left(\frac{t_{eq}}{t_{SN}}\right)^{2/3}\left(\frac{t_{QCD+}}{t_{eq}}\right)^{1/2} \times \\ \times \left(\frac{t}{t_{QCD+}}\right)^{n_{qcd}}, t_{QCD-} \leq t \leq t_{QCD+} \tag{48}$$

where $n_{qcd} = 2/3$ if the Universe experiences a dust–like phase during the QCD phase transition and $n_{qcd} = 1/2$ if the Universe continues to be radiation–dominated during that era. Between the end of the EW transition ($t = t_{EW+}$) and the beginning of the QCD phase transition ($t = t_{QCD-}$) the Universe is radiation–dominated. Thus, we write

$$R(t) = \exp\left(c\sqrt{\frac{\Lambda}{3}}(t_{SN} - t_0)\right)\left(\frac{t_{eq}}{t_{SN}}\right)^{2/3}\left(\frac{t_{QCD+}}{t_{eq}}\right)^{1/2}\left(\frac{t_{QCD-}}{t_{QCD+}}\right)^{n_{qcd}} \times \\ \times \left(\frac{t}{t_{QCD-}}\right)^{1/2}, t_{EW+} \leq t \leq t_{QCD-}. \tag{49}$$

During the EW transition ($t_{EW-} \leq t \leq t_{EW+}$) we consider that the scale factor is given by

$$R(t) = \exp\left(c\sqrt{\frac{\Lambda}{3}}(t_{SN} - t_0)\right)\left(\frac{t_{eq}}{t_{SN}}\right)^{2/3}\left(\frac{t_{QCD+}}{t_{eq}}\right)^{1/2}\left(\frac{t_{QCD-}}{t_{QCD+}}\right)^{n_{qcd}} \times \\ \times \left(\frac{t_{EW+}}{t_{QCD-}}\right)^{1/2}\left(\frac{t}{t_{EW+}}\right)^{n_{ew}}, t_{EW-} \leq t \leq t_{EW+} \tag{50}$$

where $n_{ew} = 2/3$ if the Universe experiences a dust–like phase during that epoch and $n_{ew} = 1/2$ if the Universe continues to be radiation–dominated. Between the end of inflation ($t = t_e$) and the beginning of the EW phase transition ($t = t_{EW-}$) the Universe is radiation–dominated. We write

$$R(t) = \exp\left(c\sqrt{\frac{\Lambda}{3}}(t_{SN} - t_0)\right)\left(\frac{t_{eq}}{t_{SN}}\right)^{2/3}\left(\frac{t_{QCD+}}{t_{eq}}\right)^{1/2}\left(\frac{t_{QCD-}}{t_{QCD+}}\right)^{n_{qcd}} \times \\ \times \left(\frac{t_{EW+}}{t_{QCD-}}\right)^{1/2}\left(\frac{t_{EW-}}{t_{EW+}}\right)^{n_{ew}}\left(\frac{t}{t_{EW-}}\right)^{1/2}, t_e \leq t \leq t_{EW-}. \tag{51}$$

The change on the scale factor during a dust–like QCD transition is not very significant because the term t_{QCD-}/t_{QCD+} is ~ 1 (cf. Section 2.1) and, thus, it can be neglected in equations (48) to (51) unless one is working locally (i.e., near t_{QCD-} and t_{QCD+}). The same idea is valid for the term t_{EW-}/t_{EW+} (cf. Section 2.2). According to this, we can replace equations (47) to (51) by the single equation

$$R(t) = \exp\left(c\sqrt{\tfrac{\Lambda}{3}}(t_{SN} - t_0)\right)\left(\tfrac{t_{eq}}{t_{SN}}\right)^{2/3}\left(\tfrac{t}{t_{eq}}\right)^{1/2}, \quad t_e \leq t \leq t_{eq} \tag{52}$$

while equations (45) and (46) remain unchanged.

The scale factor R, the background temperature T and the redshift z at a given epoch are related according to the expression (e.g. Unsöld & Bascheck, 2002)

$$\frac{T(t)}{T_0} = \frac{R_0}{R(t)} = 1 + z \tag{53}$$

where T_0 represents the present day background temperature ($T_0 \approx 2.725$ K). The value of t_0, i.e., the age of the Universe, can be obtained with the help of expression (e.g. Yao et al., 2006)

$$H_0 t_0 = \frac{2}{3\sqrt{\Omega_\Lambda}} \ln \frac{1 + \sqrt{\Omega_\Lambda}}{\sqrt{1 - \Omega_\Lambda}}, \quad \Omega_m < 1. \tag{54}$$

valid in the case of a flat universe ($\Omega_m + \Omega_\Lambda = 1$). Inserting H_0 (see equation 35) into equation (54) with $\Omega_\Lambda = 0.76$ we obtain, for the age of the Universe

$$t_0 \approx 4.3 \times 10^{17} \text{ s.}$$

Considering that during the cosmological constant domination the Hubble parameter stays constant (cf. equation 43) we have that $H(t_{SN}) = H_0$. Thus, inserting H_0 into equation (42) we obtain

$$t_{SN} \approx 2.8 \times 10^{17} \text{ s.}$$

Notice that if $\Lambda = 0$ this would correspond to t_0. This means that, in the absence of dark energy, the Universe would be younger by a factor of ≈ 1.5 (e.g. Jones & Lambourne, 2004).

The value of t_{eq} can be obtained with the help of equations (40) and (46) considering that $z \approx 3200$ at radiation–matter equality (e.g. Hinshaw et al., 2009)

$$t_{eq} \approx 2.5 \times 10^{12} \text{ s.}$$

Proceding the same way, one obtains, for the age of the Universe at photon decoupling ($z \approx 1090$)

$$t_{dec} \approx 1.2 \times 10^{13} \text{ s.}$$

Taking $t_i = 10^{-35}$ s we have, from equations (41) and (44), that

$$t_e \sim 10^{-33} \text{ s}$$

valid for both $N(t_e) = 50$ and $N(t_e) = 70$. The calculation of numerical values to t_{QCD-}, t_{QCD+}, t_{EW-} and t_{EW+} will be discused in Sections 2.1 and 2.2.

1.1.5 Fluctuations

It was already realized many years ago that a spectrum of primordial fluctuations can lead to the formation of PBHs (e.g. Carr & Hawking, 1974; Carr, 1975; Novikov et al., 1979). What was initially considered was a spectrum of classical fluctuations instead of a spectrum of quantum fluctuations. We have now in Cosmology a paradigm based on the existence of Inflation (Section 1.1.2) which allows us to consider the quantum origin of the fluctuations (Polarski, 2001). During inflation fluctuations of quantum origin, of the *inflaton* (i.e. the scalar field driving inflation) are produced. These fluctuations are then stretched to scales much larger than the Hubble radius R_H (equation 20) at the time when they were produced.

Once a physical wavelength becomes larger than R_H, it is causally disconnected from physical processes. The inflationary era is followed by a radiation–dominated stage and matter–dominated stage with the acceleration of the scale factor becoming negative (see Section 1.1.1 and Appendix A). With a negative acceleration of the scale factor, the Hubble radius grows faster than the scale factor, and wavelengths that were outside, can re–enter the Hubble radius. This is the main concept behind the inflationary paradigm for the generation of temperature fluctuations as well as for providing the seeds for LSS formation (e.g. Boyanovsky et al., 2006).

WMAP has provided perhaps the most striking validation of inflation as a mechanism for generating superhorizon fluctuations, through the measurement of an anticorrelation peak in the temperature–polarization angular power spectrum at $l \sim 150$ corresponding to superhorizon scales (e.g. Boyanovsky et al., 2006, see also Appendix B).

Although there is a great diversity of inflationary models (Section 1.1.2), they generically predict a gaussian and nearly scale invariant spectrum of primordial fluctuations which is an excellent fit to the highly precise wealth of data provided by the WMAP (e.g. Boyanovsky et al., 2006). The inhomogeneities that we observe today do not display any property typical of their quantum origin. On the large cosmological scales probed by the observations, the fluctuations appear to us as random classical quantities. This means that there was, at some time in the past, a *quantum–to–classical* transition (see Appendix F). In fact, for all PBHs produced after $\sim 10^{-23}$ s, the quantum–to–classical transition is already extremely effective. Taking into account that we are interested in PBHs that formed at that epoch or later, we will consider only classical fluctuations during the rest of the text.

The simplest way to describe a classical fluctuation is in terms of an overdensity or density contrast (e.g. Carr, 1975)

$$\delta(m) = \frac{\Delta m}{m}$$

where m is the average mass of the perturbed region and Δm is the excess of mass associated with the perturbation. If we want to treat the evolution of the spectrum of fluctuations we must consider instead $\delta(\vec{r})$; which can be defined as (e.g. Musco

et al., 2005)

$$\delta(\vec{r}) = \frac{\rho(\vec{r},t) - \overline{\rho}}{\overline{\rho}}$$

where $\rho(\vec{r},t)$ represents the density evolution inside a region of radius r and $\overline{\rho}$ represents the average cosmological density. It may be useful to write this last expression in the form

$$\rho = \overline{\rho}(1+\delta). \tag{55}$$

Each physical scale $\lambda(t)$ is defined by some comoving wavenumber k and evolves with time according to (Blais et al., 2003; Bringmann et al., 2002)

$$\lambda(t) = 2\pi\frac{R(t)}{k}$$

where $R(t)$ is the scale factor (Section 1.1.4). For a given physical scale, the horizon crossing time t_k is conventionally defined by (e.g. Blais et al., 2003; Bringmann et al., 2002)

$$ck = R(t_k)H(t_k) \tag{56}$$

where H is the *Hubble parameter* (Section 1.1.1). This corresponds to the time when that scale reenters the Hubble radius which will inevitably happen after inflation for scales that are larger than the Hubble radius at the end of inflation (e.g. Blais et al., 2003; Bringmann et al., 2002).

If there is a perturbation associated with the scale entering the horizon at time t_k and if that perturbation is large enough, then it will begin to collapse into a PBH at a later time $t_c > t_k$. We refer to this instant t_c as the *turnaround point*.

For a perturbation of a fixed size, its collapse cannot begin before it goes through the cosmological horizon. The size of a PBH when it forms, therefore, is related to the horizon size, or, equivalently, to the horizon mass M_H (equation 21) when the collapsing perturbation enters the horizon.

Next we determine the relation between the size of the overdense region at turnaround $S_c(t_c)$ and the scale factor at horizon crossing $R_k(t_k)$. In the unperturbed region we consider the FLRW metric (Section 1.1.1). The evolution of the scale factor, for a FLRW universe can be written in the form (Carr, 1975)

$$\left(\frac{dR}{dt}\right)^2 = \frac{8\pi G}{3}\overline{\rho}(t)R(t)^2$$

where $\overline{\rho}$ represents the average cosmological density. Note that this is just one of the Friedmann–Lemaître equations (Section 1.1.1, equation 2) where we have considered $\kappa = 0$ (flat universe) and we have neglected the cosmological constant term (which is a reasonable choice at early epochs).

In the perturbed region we consider the metric (Carr, 1975)

$$ds^2 = d\tau^2 - S^2(\tau)\left[\frac{dr^2}{1-\Delta\epsilon r^2} + r^2\left(d\theta^2 + sin^2\theta d\phi^2\right)\right]$$

where $\Delta\epsilon$ is the perturbed total energy per unit mass and τ is the proper time as measured by comoving observers. Here $S(\tau)$ plays the role of a scale factor for the perturbed region. The evolution of $S(\tau)$ can be written in the form (Carr, 1975)

$$\left(\frac{dS}{d\tau}\right)^2 = \frac{8\pi G}{3}\rho(\tau)S(\tau)^2 - \Delta\epsilon \tag{57}$$

where $\rho(\tau)$ represents the density in the perturbed region.

Considering that initially the overdense region is comoving with the unperturbed background we consider $\tau_k = t_k$ (here the subscript k denotes a quantity evaluated when the fluctuation crosses the horizon), $S_k = R_k$ and $(dS/d\tau)_k = (dR/dt)_k$ (Carr, 1975) . With these choices we obtain for $\Delta\epsilon$ the expression

$$\Delta\epsilon = \frac{8\pi G}{3}R_k^2\left(\rho_k - \overline{\rho}_k\right)$$

Inserting this into equation (57) and taking into account that $\rho_k = \overline{\rho}_k(1+\delta_k)$ (cf. equation 55) we obtain

$$\left(\frac{dS}{d\tau}\right)^2 = \frac{8\pi G}{3}\left(\rho(\tau)S(\tau)^2 - \rho_k R_k^2\frac{\delta_k}{1+\delta_k}\right). \tag{58}$$

which describes the evolution of the perturbed region.

1.1.6 Degrees of freedom

In the early Universe collision and decay processes are continuously creating and destroying particles (see Appendixes A and C). Considering thermal equilibrium (i.e., each process is taking place at the same rate as its inverse) then the number of particles of a given species i, per momentum state, is given by (e.g. Lyth, 1993)

$$f(p) = g_i(T)\left[e^{\frac{E-\mu}{T}} \pm 1\right]^{-1}$$

where $g_i(T)$ counts the effective number of relativistic *degrees of freedom* of that particle species at a given photon temperature T; p is the momentum, E is the energy ($E = \sqrt{p^2+m^2}$) and the sign is $+$ for fermions and $-$ for bosons. The quantity $\mu = \mu(T)$ is the *chemical potential*[13] of the species. The chemical potential is conserved in every collision. If the charges are all zero then all of the chemical

[13]In the context of Particle Physics the chemical potential measures the tendency of particles to diffuse. Particles tend to diffuse from regions of high chemical potential to those of low chemical

potentials are zero and $f(p)$ turns out to be some sort of generalized blackbody distribution (e.g. Lyth, 1993)

$$f(p) = g_i(T) \left[e^{\frac{E}{T}} \pm 1 \right]^{-1}. \tag{59}$$

The particle number density n and the energy density ρ of particles of a particular species i are given by (e.g. Lyth, 1993)

$$n_i = \frac{g_i(T)}{(2\pi)^3} \int_0^\infty f(p) 4\pi p^2 dp \tag{60}$$

$$\rho_i = \frac{g_i(T)}{(2\pi)^3} \int_0^\infty E f(p) 4\pi p^2 dp. \tag{61}$$

If the mass m of the species in question is such that $T \gg m$ then one is in the relativistic regime and it is a good approximation to consider $E = p$. Taking this into account and inserting (59) into equations (60) and (61) we obtain, separately for fermions and bosons (e.g. Lyth, 1993)

$$\rho_{B,i} = \frac{\pi^2}{30} g_i(T) T^4$$

$$\rho_{F,i} = \frac{7}{8} \frac{\pi^2}{30} g_i(T) T^4$$

$$n_{B,i} = \frac{\zeta(3)}{\pi^2} g_i(T) T^3$$

$$n_{F,i} = \frac{3}{4} \frac{\zeta(3)}{\pi^2} g_i(T) T^3$$

where $\zeta(3) \approx 1.2021$. According to the generalized blackbody distribution each relativistic species contributes with $\sim T^4$ to ρ and $\sim T^3$ to n. When $T < m$ we are in the non–relativistic regime and we have ρ and n falling rapidly. The reason is that the energy available in a collision is now insufficient to create the species (e.g. Lyth, 1993).

---

potential. In a system with many particle species each of them has its own chemical potential. The chemical potential of the i-th particle species is defined as

$$\mu_i = \left(\frac{\partial U}{\partial N_i} \right)_{S,V,N_{j \neq i}}$$

where U is the total internal energy of the system, S is the entropy, V is the volume and N_i is the number of particles of the i-th species. Being a function of internal energy, the chemical potential applies equally to both fermion and boson particles. That is, in theory, any fundamental particle can be assigned a value of chemical potential, depending upon how it changes the internal energy of the system into which it is introduced. QCD matter is a prime example of a system in which many such chemical potentials appear (e.g. Baierlein, 2001).

As the temperature T falls below the mass m of a given species, particle–antiparticle pairs rapidly annihilate. Then the small particle–antiparticle imbalance $(n - \bar{n})$ becomes significant, and annihilation soon stops because only particles (or only antiparticles) survive. As a result μ no longer vanishes. However, even if the surviving particles do not decay, their contribution to ρ and n during the radiation–dominated era are negligible (e.g. Lyth, 1993).

If we are interested in the total energy density (i.e., in the energy density due to all the particle species for which $T \gg m$) then it may be useful to consider the *effective number of degrees of freedom* at a particular epoch (i.e., characterized by a given temperature T) defined as (e.g. Yao et al., 2006)

$$g(T) = \sum_{bosons} g_i(T) + \frac{7}{8} \sum_{fermions} g_i(T) \tag{62}$$

where the sum goes over all particle species with $T \gg m$. Notice that the fermionic degrees of freedom are suppressed by a factor of 7/8 with respect to bosonic degrees of freedom. This is due to the difference between Fermi–Dirac statistics and Bose–Einstein statistics (e.g. Hands, 2001).

We may write, with the help of equation (62), the total energy density for a radiation–dominated universe as (e.g. Schwarz, 2003)

$$\rho = \frac{\pi^2}{30} g(T) T^4.$$

In particle physics the *helicity* h is the projection of the angular momentum of the particle in the direction of motion. Because angular momentum with respect to an axis has discrete values, helicity is discrete too. For a relativistic particle ($T \gg m$) there are two possible helicity eigenstates usually referred to as *left–handed* and *right–handed* states (e.g. Hands, 2001).

For each quark flavour (see Appendix C) we have to count two electric charges (quark + anti–quark), two helicity states and three colour states. This gives a total of $2 \times 2 \times 3 = 12$ degrees of freedom per quark. In the case of gluons we have to consider that each one of the eight colour charges could have one of two helicity states. Thus, gluons contribute with $2 \times 8 = 16$ degrees of freedom.

Each neutral lepton (i.e. neutrino) contributes with two degrees of freedom corresponding to two possible helicity states[14]. On the other hand each charged lepton contibutes with four degrees of freedom corresponding to two helicity states $\times$ two charges (lepton and anti–lepton). The photon contributes with two degrees of freedom corresponding to two possible helicity states.

The Higgs boson contributes with 4 degrees of freedom corresponding to the two possible helicity states of the *scalar doublet*. The $W^{\pm}$ and Z^0 bosons contribute with 6 degrees of freedom corresponding to three species times two possible helicity

[14]The antineutrinos observed so far all have right–handed helicity, while the neutrinos are left–handed.

states. However at the EW transition (Section 1.2.2) the W and Z contribution becomes 9. This is due to the Higgs mechanism during which the W and Z bosons acquire mass and a third polarization degree of freedom (e.g. Ignatius, 1993).

The meson π contributes with 3 degrees of freedom (one for each kind of π meson: π^-, π^0 and π^+). We may have to consider also the contribution of kaons. This would be 4 degrees of freedom (e.g. Boyanovsky et al., 2006).

As it was already mentioned it is a good approximation to treat all particles with $T \gg m$ as though they were massless. The contribution of all other particles can be neglected in the total energy density (e.g Schwarz, 2003). This is why we did not consider the contribution of composite particles such as protons and neutrons. For example, in the case of the proton we have $m_p \approx 900$ MeV. Considering that protons form at the QCD epoch when the temperature of the Universe was $T_c = 170$ MeV it turns out that in this case we do not have $T \gg m$ and thus, we can safely neglect the contribution of the proton to the total number of degrees of freedom.

At very high temperatures ($T > m_t \sim 172.5$ GeV) all the particles of the Standard Model of Particle Physics (SMPP) contribute to the effective number of degrees of freedom $g(T)$ (cf. equation 62) giving (e.g. Ignatius, 1993)

$$\begin{aligned} g(T) &= g_\gamma + g_{W^\pm,Z^0} + g_g + g_H + \tfrac{7}{8}\left[\, g_{e,\mu,\tau} + g_\nu + g_q \,\right] = \\ & 2 + 3 \times 2 + 8 \times 2 + 4 + \tfrac{7}{8}\left[3 \times 4 + 3 \times 2 + 6 \times 12\right] = 106.75. \end{aligned} \tag{63}$$

As the expansion of the Universe goes on, the temperature decreases and it will equal, successively, the threshold of each particle leading to smaller values of $g(T)$. This evolution is represented in Table 2 where we have, in the first row, the case when all the particles are present and, in the final row, the present day case with only neutrinos and photons.

At temperatures above 1 MeV, electrons, photons and neutrinos have the same temperature. Below this temperature the three neutrino flavours are decoupled chemically and kinetically from the radiation plasma. This early decoupling from thermal evolution with the rest of the Universe is due to the fact that neutrinos interact with other particles only via weak interactions (e.g. Gynther, 2006). As a result, the entropy of the relativistic electrons is transferred to the photon entropy, but not to the neutrino entropy when electrons and positrons annihilate. This leads to an increase of the photon temperature relative to the neutrino temperature by (e.g Schwarz, 2003)

$$T_\nu = \left(\frac{4}{11}\right)^{1/3} T_\gamma.$$

As a result, below $T \sim 1$ MeV we have to consider the effective number of degrees of freedom of the energy density, g_ρ, and the number of degrees of freedom of the entropy density, g_s (e.g Schwarz, 2003). The present value of g_ρ is (e.g. Coleman &

Table 2: The evolution of the number of degrees of freedom $g(T)$ in the Universe according to the SMPP (equation 62). As the expansion goes on, and the temperature T decreases, some particle species cease to exist (because T eventually gets below the particle threshold) decreasing the value of $g(T)$.

Temperature	Leptons	Quarks	g_F	*Bosons*		g_B	$g(T)$
$T > m_t$	$\nu\ e^-\ \mu\ \tau$	$u\ d\ s\ c\ b\ t$	90	$\gamma\ g\ W\ H$		28	106.75
$m_H < T < m_t$	$\nu\ e^-\ \mu\ \tau$	$u\ d\ s\ c\ b$	78	$\gamma\ g\ W\ H$		28	96.25
$m_{W,Z} < T < m_H$	$\nu\ e^-\ \mu\ \tau$	$u\ d\ s\ c\ b$	78	$\gamma\ g\ W$		27	95.25
$m_b < T < m_{W,Z}$	$\nu\ e^-\ \mu\ \tau$	$u\ d\ s\ c\ b$	78	$\gamma\ g$		18	86.25
$m_\tau < T < m_b$	$\nu\ e^-\ \mu\ \tau$	$u\ d\ s\ c$	66	$\gamma\ g$		18	75.75
$m_c < T < m_\tau$	$\nu\ e^-\ \mu$	$u\ d\ s\ c$	62	$\gamma\ g$		18	72.25
$m_s < T < m_c$	$\nu\ e^-\ \mu$	$u\ d\ s$	50	$\gamma\ g$		18	61.75
$T_c < T < m_s$	$\nu\ e^-\ \mu$	$u\ d$	38	$\gamma\ g$		18	51.25
$m_\pi < T < T_c$	$\nu\ e^-\ \mu$		14	γ	π	5	17.25
$m_\mu < T < m_\pi$	$\nu\ e^-\ \mu$		14	γ		2	14.25
$m_e < T < m_\mu$	$\nu\ e^-$		10	γ		2	10.75
$T < m_e$	ν		6	γ		2	7.25

Ross, 2003)

$$g_\rho(T) = g_\gamma + 6 \times \frac{7}{8}\left(\frac{4}{11}\right)^{4/3} \approx 3.363.$$

On the other hand we have $g_s(T) \approx 3.909$ at the present (e.g Schwarz, 2003).

At the temperature of the QCD transition ($T_c \approx 170$ MeV, see Section 1.2.1) the number of degrees of freedom changes very rapidly, since quarks and gluons are coloured. Before the QCD transition we have $g = 61.75$ and after the transition we have $g = 17.25$ (cf. Table 2) which gives $\Delta g \approx 45$. At still higher temperatures, heavier particles are excited, but within the SMPP nothing so spectacular as the QCD transition happens. Within the SMPP the EW transition is only a tiny effect (e.g. Schwarz, 2003) with $\Delta g = 96.25 - 95.25 = 1$.

This situation is drastically changed if one considers the Minimal Supersymmetric extension of the Standard Model (MSSM) (see Appendix D). In Table D-4 we list the contribution that each particle and each sparticle species might give to $g(T)$. Note that the contributions from squarks, sleptons and gluinos are identical to that of, respectively, quarks, leptons and gluons (apart from the factor 7/8). The Higgs sector now is formed by two doublets which gives 2×4 degrees of freedom. Each neutralino contributes with two degrees of freedom corresponding to two possible helicity states and each chargino contributes with four degrees of freedom (two charges $\times$ two helicity states).

In order to account for these extra degrees of freedom we replace equation (62) by the more general

$$g(T) = \sum_{bosons} g_i(T) + \frac{7}{8} \sum_{fermions} g_i(T) + \\ + \sum_{sfermions} g_i(T) + \frac{7}{8} \sum_{bosinos} g_i(T). \tag{64}$$

At very high temperatures when all the particles contribute to the effective number of degrees of freedom we have, according to equation (64)

$$\begin{aligned} g(T) &= g_\gamma + g_{W^\pm,Z^0} + g_g + g_H + \frac{7}{8}\left[\, g_{e,\mu,\tau} + g_\nu + g_q \,\right] + \\ &+ g_{\tilde{e},\tilde{\mu},\tilde{\tau}} + g_{\tilde{\nu}} + g_{\tilde{q}} + \frac{7}{8}\left[\, g_{\tilde{g}} + g_{\tilde{N}} + g_{\tilde{C}^\pm} \,\right] = \\ &= 2 + 3\times 2 + 8\times 2 + 8 + \frac{7}{8}\left[3\times 4 + 3\times 2 + 6\times 12\right] + \\ &+ 3\times 4 + 3\times 2 + 6\times 12 + \frac{7}{8}\left[8\times 2 + 4\times 2 + 2\times 4\right] = \\ &= \frac{443}{4} + 118 = \frac{915}{4} = 228.75. \end{aligned} \tag{65}$$

The SMPP has $g = 106.75$ when the temperature is larger than all particle masses (cf. equation 63) while the MSSM has $g = 228.75$ (which is more than twice 106.75). In Figure 2 we sketch the curve $g(T)$. Notice the drastic change in $g(T)$ during the QCD transition. During the EW transition the change in the value of $g(T)$ is significant only when considering the MSSM.

In Table D-5 we show the evolution of $g(T)$ for the MSSM, starting with $g(T) = 228.75$, which corresponds to the case when all particles are present (cf. equation 65), down to $g(T) = 95.25$, when the temperature equals the threshold of the *Lightest Supersymmetric Particle* (LSP). From that point on, the evolution of $g(T)$ proceeds within the SMPP, according to Table 2. As already mentioned, the Higgs sector of the MSSM contributes with eight real scalar degrees of freedom (cf. Appendix D). Three of them get swallowed (during the EW transition) by the $W^\pm$ and Z^0 bosons. The other five are distributed by the mass eigenstates H^+, H^-, H^0, A^0 and h^0.

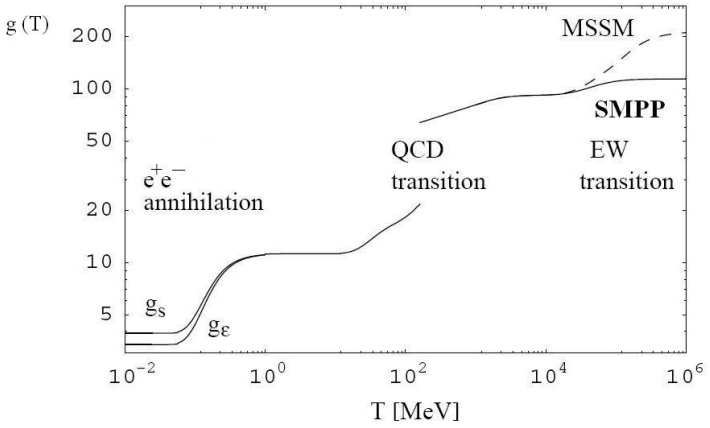

Figure 2: The effective number of degrees of freedom $g(T)$. The full line is the prediction of the SMPP, the dashed line shows the MSSM, according to the SPS1a scenario (see Appendix D). Below $T \sim 1$ MeV we have to consider, separately, the effective number of degrees of freedom of the energy density here represented by g_ε, and the number of degrees of freedom of the entropy density, g_s (adapted from Schwarz, 2003).

1.2 Cosmological phase transitions

The inflationary stage is followed by a radiation–dominated era after a short period of reheating during which the energy stored in the inflaton field decays into quanta of other fields, which, through scattering processes, reach a state of *Local Thermodynamic Equilibrium* (LTE). This period is followed by deccelerated expansion and cooling, with the Universe successively visiting the different energy scales at which particle and nuclear physics predict symmetry breaking phase transitions (e.g. Boyanovsky et al., 2006).

If a thermodynamic quantity changes discontinuously (for example as a function of temperature) we have a *first–order phase transition*. This happens because, at the point at which the transition occurs, there are two separate thermodynamic states in equilibrium. Any thermodynamic quantity that undergoes such a discontinuous change at the phase transition is referred to as an *order parameter*. Whether or not a first–order phase transition occurs often depends on other parameters that enter the theory. It is possible that, while another parameter is varied, the change in the order parameter of the phase transition decreases until it, together with all other thermodynamic quantities, become continuous (i.e., it shows a thermodynamic behaviour without discontinuities or singularities in the free energy or any of its derivatives) at the phase transition point. In this case we refer to a *second–order phase transition* (e.g. Trodden, 1999). An alternative to a first–order or second–order transition is a simple *crossover* in thermodynamic behaviour without discontinuities or singularities in the free energy or any of its derivatives. If the crossover is smooth the system will evolve in LTE. However, if the crossover is relatively sharp, the situation may not be too different from a first–order phase transition (e.g. Boyanovsky et al., 2006).

Phase transitions are one of the most important phenomena in particle Cosmology since, without them, the history of the Universe would simply be one of gradual cooling. In the absence of phase transitions, the only departure from thermal equilibrium is provided by the expansion of the Universe (e.g. Trodden, 1999).

The SMPP (Appendix C) predicts two phase transitions. The first one, at temperatures of ~ 100 GeV, is the EW phase transition (Section 1.2.2) which was responsible for the spontaneous breaking of the EW symmetry, which gives the masses to the elementary particles (e.g. Aoki et al., 2006b). The second transition occurs at $T \approx 170$ MeV. It is related to the spontaneous breaking of the *chiral symmetry*[15] of the QCD when quarks and gluons become confined in hadrons (e.g. Schmid et al., 1999).

The QCD phase transition was pointed out, for a long time, as a prime candidate for a first–order phase transition (e.g. Jedamzik & Niemeyer, 1999). Recent results (e.g. Aoki et al., 2006b) provide strong evidence that the QCD transition may be a simple Crossover instead. Here we consider the two possibilities.

1.2.1 The QCD phase transition

When the age of the Universe was $\sim 10^{-5}$ s ($T \approx 170$ MeV) a spontaneous breaking of the chiral symmetry of QCD occured. As a result, quarks and gluons became confined in hadrons (e.g. Boyanovsky et al., 2006). In recent years most attention has focussed on the possibility of recreating the *Quark–Gluon Plasma* (QGP) in terrestrial laboratories in relativistic heavy–ion collisions. Extensive experimental work is currently being done with heavy ion collisions to study the QCD transition (most recently at the *Relativistic Heavy Ion Collider*, RHIC) (e.g. Aoki et al., 2006b).

At the QCD epoch the Universe can be treated as a radiation fluid made up of quarks, gluons, leptons and photons (e.g. Boyanovsky et al., 2006). Baryons are tightly coupled to the radiation fluid at the QCD scale. Their energy density is negligible with respect to that of the other relativistic particles and their *chemical potential* is negligible $\mu_B \approx 0$ (e.g. Schwarz, 2003).

There is some apparent similarity in Cosmology and heavy–ion collision physics. From present observations of remote objects in the Universe, we look into the past. Combining observational facts, like the distribution and the redshift of galaxies, one can develop a picture of the early stages of the Universe. The situation in heavy–ion collision physics is very similar to this one. Observing the created hadrons at a very late stage, one tries to extrapolate back to the hottest and densest stages. Due to this similarity the process of heavy–ion collision is sometimes called the *Little Bang*. Notice, however, that we are dealing with different scales in both cases and that in the case of the Big Bang we are also dealing with an expanding universe (e.g.

[15] Chiral symmetry is a symmetry of QCD in the limit of vanishing quark masses. We know, however, that quark masses are finite (see Table C-2). But compared with hadronic scales the masses of the two lightest quarks, up and down, are very small, so that chiral symmetry may be considered an approximate symmetry of the strong interactions (e.g. Koch, 1997).

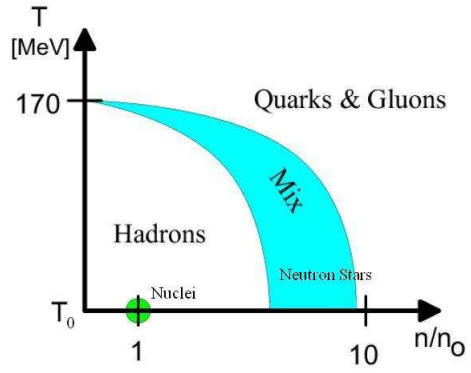

Figure 3: Naive phase diagram of strongly interacting matter in the $T - n$ plane. Here n is the baryon density, n_0 is the present value of n, $T_c = 170$ MeV, and $T_0 = 2.725$ K is the CMB temperature. At the present time the mixed phase occurs, in the Universe, only at the level of atomic nuclei (green circle) or within compact objects such as neutron stars (adapted from Kämpfer, 2000).

Kämpfer, 2000).

The critical temperature T_c is one of the most fundamental quantities in QCD thermodynamics. Several groups have tried to determine T_c near the physical mass parameter in $2 + 1$ flavour QCD. According to the results obtained, a tentative conclusion is that the critical temperature is in the range 164 MeV $-$ 186 MeV. In order to improve the results further, simulations at lighter quark masses are necessary (Ejiri, 2007). In Figure 3 we have a naive phase diagram of strongly interacting matter in the $T - n$ plane (n is the baryon density) where we consider $T_c = 170$ MeV.

In a first–order phase transition the QGP supercools until hadronic bubbles are formed at some temperature $T_{sc} \approx 0.95 T_c$. The crucial parameters for *supercooling* are the surface tension σ (i.e. the work that has to be done per unit area to change the phase interface at fixed volume) and the *latent heat* (e.g. Schmid et al., 1997)

$$l = T_c \Delta s. \tag{66}$$

The value of the latent heat which is avaliable only from *quenched lattice QCD* (gluons only, no quarks) is given by (e.g. Schmid et al., 1999)

$$l \approx 1.4 T_c^4.$$

The latent heat should be compared with the difference in entropy density between an ideal *Hadron Gas* (HG) and an ideal QGP. This defines the ratio (e.g. Schmid et al., 1997)

$$R_l = \frac{l}{(T_c \Delta s)^{ideal}}. \tag{67}$$

A first–order phase transition is classified as strong if $R_l \approx 1$. The Bag Model gives $R_l = 1$ and from quenched lattice QCD we have $R_l \approx 0.2$ (e.g. Schmid et al., 1999).

Without 'dirt' (e.g. PBHs, axions) the bubbles *nucleate* due to thermal fluctuations in a process called *homogeneous nucleation* (e.g. Schmid et al., 1999). Hadronic bubbles grow very fast, within $\Delta t_{nuc} \sim 10^{-6} t_H$ until the released heat has reheated the Universe to T_c and prohibits further bubble formation (e.g. Schmid et al., 1999). By that time, only a small fraction of the volume of the observable Universe has gone through the transition (e.g. Boyanovsky et al., 2006). For the remaining 99% of the transition, both phases (QGP and HG) coexist at constant pressure (e.g. Schmid et al., 1999):

$$p_c = p_{QGP}(T_c) = p_{HG}(T_c). \tag{68}$$

Bubbles can grow only if they are created with radii greater than the critical bubble radius R_{crit}. Smaller bubbles disappear again due to the fact that the energy gained from the bulk of the bubble is more than compensated by the surface energy in the bubble wall. The value of R_{crit} is given by (e.g. Schmid et al., 1999)

$$R_{crit} = \frac{2\sigma}{p_{HG}(T) - p_{QGP}(T)},$$

which diverges at $T = T_c$ meaning that bubble formation should stop after reheating.

During the period of coexistence hadronic bubbles grow slowly (due to the expansion of the Universe only) causing a continuous growth of the volume fraction occupied by the hadron phase, at the expense of the quark–gluon phase. The latent heat released from the bubbles is distributed into the surrounding QGP keeping the Universe at constant temperature T_c. This reheats the QGP to T_c and prohibits further bubble formation. The transition is completed when all space is occupied by the hadron phase (e.g. Jedamzik, 1998; Schmid et al., 1999; Boyanovsky et al., 2006). In Figure 4 it is represented the qualitative behaviour of the temperature T as a function of the scale factor R during a first–order phase transition.

For a first–order transition at coexistence temperature T_c, the conditions of thermodynamic equilibrium are the equality of pressure p and temperature T between high–energy and low–energy density phases. This will be correct as long as we assume the Universe as a fluid with no chemical potential ($\mu = 0$), i.e., a fluid with no relevant conserved quantum number (e.g. Schmid et al., 1999). One may consider a region sufficiently large ($\gg R_H$) to include material in both phases such that the pressure response of matter to slow adiabatic expansion, compression, or collapse in that region is negligible. This may be expressed by defining an effective isentropic speed of sound c_s (see equation 12) for the matter in a state of phase mixture. In thermodynamic equilibrium (Jedamzik, 1997)

$$c_s^2 = \left(\frac{\partial p}{\partial \rho}\right)_s = 0$$

holds exactly during the entire transition and suddenly rises back to $1/\sqrt{3}$ (cf. equation 7) at the end of the transition (e.g. Schwarz, 2003).

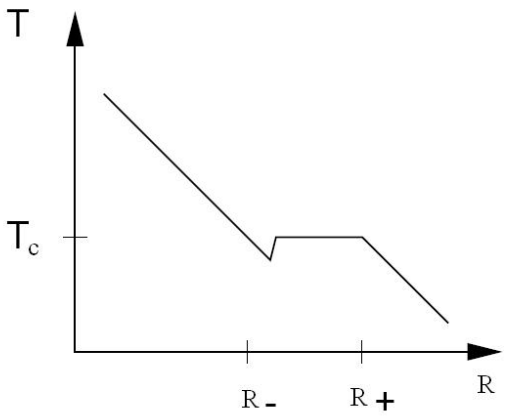

Figure 4: Qualitative behaviour of the temperature T as a function of the scale factor R during a first–order QCD transition. Above the critical temperature T_c the Universe cools down thanks to its expansion ($R < R_-$). After a tiny period of supercooling (in the figure the amount of supercooling and its duration are exaggerated) bubbles of the new phase nucleate. During the rest of the transition both phases coexist in pressure and temperature equilibrium ($R_- < R < R_+$). Therefore the temperature is constant. For $R > R_+$ the temperature decreases again due to the expansion of the Universe (adapted from Schwarz, 2003).

In the case of the QCD transition the isentropic condition applies after initial supercooling, bubble nucleation, and sudden reheating to T_c. During this part of the transition, which takes about 99% of the transition time, the fluid is extremely close to thermal equilibrium. That is because the expansion of the Universe is very slow compared to the strong, electromagnetic and weak interactions around T_c (e.g. Schmid et al., 1999).

In the case of a Crossover, instead of a first–order phase transition, the sound speed decreases but does not vanish completely (e.g. Kämpfer, 2000). If the Crossover is smooth, then no out–of–equilibrium aspects are expected as the system will evolve in LTE (e.g. Boyanovsky et al., 2006).

If there is some cosmic dirt in the Universe such as PBHs, monopoles, strings, and other kinds of defects, then the typical nucleation distance may differ significantly from the scenario of homogeneous nucleation. That is because, in a first–order phase transition, the presence of impurities lowers the energy barrier and, thereby, the maximum amount of superccoling achieved during the transition (Christiansen & Madsen, 1996). The basic idea in inhomogeneous bubble nucleation is that temperature inhomogeneities determine the location of bubble nucleation. In cold regions, bubbles nucleate first. However, if the mean distance between bubbles is larger than the amplitude of the fluctuations, then the temperature inhomogeneities are negligible and the phase transition proceeds via homogeneous nucleation (Boyanovsky et al., 2006).

There are three main models often used in the study of the QCD transition: the *Bag Model*, the *Lattice Fit* and the *Crossover*. Although recent results provide strong evidence that the QCD transition may be just a smooth crossover (Aoki et al.,

2006b) we describe, in the following sections, all three models.

The Bag Model

The MIT Bag Model provides a semiphenomenological description of an EoS that features a quark–hadron transition (e.g. Boyanovsky et al., 2006). It gives a simple parametrization for the pressure p, energy density ρ and entropy density s at the QCD scale. The Bag Model represents the short distance–dynamics by an ideal gas of quarks and gluons and the long–distance confinement effects by a constant negative contribution to the pressure, the *bag constant* B (e.g. Schwarz, 2003; Schmid et al., 1999).

The simplest version of the model considers the thermodynamics in two different regions: a high temperature region ($T > T_c$) where we have a gas of massless quarks and gluons (QGP) and a low temperature region ($T < T_c$) where we have a gas of free massless hadrons (HG). At $T = T_c$ quarks, gluons and hadrons coexist in equilibrium at constant pressure and temperature (e.g. Boyanovsky et al., 2006).

The pressure for the high temperature region, which corresponds to a QGP is given, for vanishing chemical potential ($\mu = 0$), by (e.g. Schmid et al., 1999)

$$p_{QGP}(T) = p_{QGP}^{ideal}(T) - B \tag{69}$$

where we have, considering that gluons and existing quarks are effectively massless at $T \approx T_c$, that (e.g. Schmid et al., 1999)

$$p_{QGP}^{ideal}(T) = \frac{\pi^2}{90} g_{QGP} T^4$$

where g_{QGP} corresponds to the number of degrees of freedom of the QGP at the beginning of the transition (see Section 1.1.6). The low temperature region, which corresponds to an HG, can be modeled as a gas of massless hadrons with (e.g. Schmid et al., 1999)

$$p_{HG}(T) = \frac{\pi^2}{90} g_{HG} T^4 \tag{70}$$

where g_{HG} represents the number of degrees of freedom of the HG at the end of the transition (see Section 1.1.6).

Taking into account the pressure coexistence condition (cf. equation 68) we obtain, from equations (69) and (70), the following expression for the bag constant (e.g. Cardall & Fuller, 1998; Schmid et al., 1999)

$$B = \frac{\pi^2}{90} \left(g_{QGP} - g_{HG} \right) T_c^4. \tag{71}$$

The energy density ρ and entropy density s for the Bag Model follow from equations (10), (11) and (69). In the case of the energy density we have, for the QGP phase (e.g. Schmid et al., 1999)

$$\rho_{QGP}(T) = \rho_{QGP}^{ideal}(T) + B = \frac{\pi^2}{30} g_{QGP} T^4 + B \tag{72}$$

and for the HG phase we get (e.g. Boyanovsky et al., 2006)

$$\rho_{HG}(T) = \frac{\pi^2}{30} g_{HG} T^4. \tag{73}$$

The evolution of the average energy density ρ as a function of time during a first–order QCD transition is given by (Jedamzik, 1997)

$$\rho(t) = \left(\frac{R(t_{QCD-})}{R(t)} \right)^3 \left(\rho_{QGP}(T_c) + \frac{1}{3}\rho_{HG}(T_c) \right) - \frac{1}{3}\rho_{HG}(T_c).$$

With the help of equations (71), (72), and (73) this becomes

$$\rho(t) = \frac{1}{3}\frac{\pi^2}{30} T_c^4 \left[4 g_{QGP} \left(\frac{R(t_{QCD-})}{R(t)} \right)^3 - g_{HG} \right]. \tag{74}$$

In the case of the entropy density, we have, for the QGP (e.g. Schmid et al., 1999; Jedamzik, 1997)

$$s_{QGP}(T) = s_{QGP}^{ideal}(T) = \frac{2\pi^2}{45} g_{QGP} T^3$$

and for the HG

$$s_{HG}(T) = s_{HG}^{ideal}(T) = \frac{2\pi^2}{45} g_{HG} T^3.$$

In this model, the entropy density, jumps at the critical temperature T_c. This is due to the fact that on the coexistence line both, pressure and temperature, are constant. This jump in the entropy density (which is depicted in Figure 5), means that the Bag Model leads to a strong first–order phase transition ($R_l \approx 1$) with a latent heat (equation 66, e.g. Boyanovsky et al., 2006; Schmid et al., 1999)

$$l = T_c \Delta s = \frac{2\pi^2}{45} (g_{QGP} - g_{HG}) T_c^4 = 4B. \tag{75}$$

It is useful to write a single expression for the entropy density in the Bag Model as (Schwarz, 1998)

$$s(T) = \frac{2\pi^2}{45} g_{HG} T^3 \left[1 + \frac{\Delta g}{g_{HG}} \Theta(T - T_c) \right] \tag{76}$$

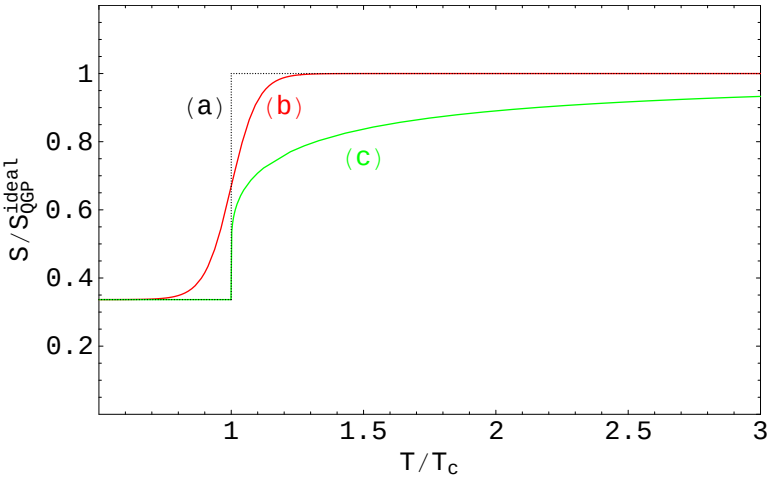

Figure 5: The entropy density of hot QCD relative to the entropy density of an ideal QGP for the: (a) Bag Model – equation (76), (b) Lattice Fit – equation (78), and (c) smooth Crossover – equation (80) (adapted from Schmid et al., 1999).

where $\Delta g = g_{QGP} - g_{HG}$ and the function Θ is defined as (Schwarz, 1998)

$$\Theta(T - T_c) = \begin{cases} 0 & \text{if } T < T_c \\ 1 & \text{if } T > T_c. \end{cases} \tag{77}$$

The typical value for the bag constant is given by $B^{1/4} \sim 200$ MeV (e.g. Boyanovsky et al., 2006). Inserting $B^{1/4} = 200$ MeV into equation (75) one gets, considering two quark flavours ($g_{QGP} = 51.25$, cf. Section 1.1.6) and three massless pions ($g_{HG} = 17.25$, cf. Section 1.1.6), that $T_c \approx 145$ MeV, which is not too far from the lattice result $T_c \sim 170$ MeV (e.g. Boyanovsky et al., 2006). In the Bag Model the sound speed stays at $c_s^2 = 1/3$ before and after the transition and vanishes during the transition (e.g. Schwarz, 2003).

Lattice Fit

Lattice Gauge Theory (LGT) is the study of *Gauge Theories* in a space–time that as been discretized onto a lattice. One hopes that performing simulations on larger and larger lattices, while making the lattice spacing, a, smaller and smaller, the behaviour of the continuum theory can be recovered. In the case of the QCD transition the critical temperature T_c is calculated in the chiral limit using $T = (N_t a)^{-1}$ where N_t represents the temporal lattice size (e.g. Ejiri, 2007).

The only known first principle method to study QCD non–perturbatively in a wide temperature range is LGT (e.g. Boyanovsky et al., 2006). Lattice QCD discretises the Lagrangian on a four–dimensional lattice and extrapolates the results to vanishing lattice spacing (e.g. Aoki et al., 2006a).

It has been established that lattice QCD without dynamical quarks exhibits a thermal first–order phase transition at a critical temperature of $T_c \approx 270$ MeV. For

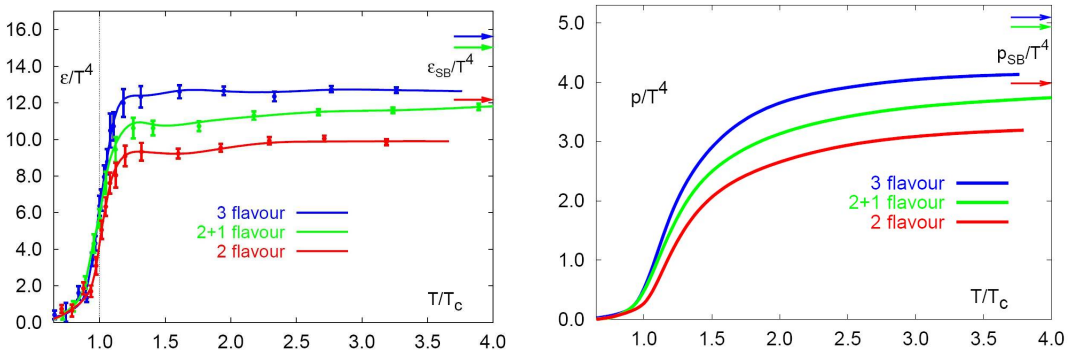

Figure 6: The energy density ε and pressure p (both divided by T^4 to compare to a free gas of massless quarks and gluons) as a function of T/T_c for the QCD transition in an LGT. The arrows mark the Stephan-Boltzmann result (Karsch, 2002; Karsch et al., 2000).

dynamical quarks, lattice QCD calculations provide a range of estimates for T_c. In the case of two–flavour QCD, $T_c \approx 175$ MeV, whereas for three–flavour QCD, $T_c \approx 155$ MeV, almost independently of the quark mass. For the most interesting case of two light quark flavours (up and down) and the more massive strange quark, a value of $T_c \approx 170$ MeV has been obtained. We adopt a transition temperature $T_c = 170$ MeV, bearing in mind that the systematic uncertainty is probably of the order 10 MeV (e.g. Boyanovsky et al., 2006).

Particular attention has been devoted on determining the order of the QCD phase transition and the correct value of T_c. For massless quarks, the theoretical expectation is a second order transition for two quark flavours and a first–order transition for three and more quark flavours. In the lattice, for two light quarks the results are inconclusive. The consensus that seems to be emerging is that for the physical masses of two light (up and down) and one heavier (strange) quark there is a sharp crossover between a high temperature gas of quarks and gluons and a low temperature hadronic phase without any thermodynamic discontinuities. This is displayed in Figure 6 which summarizes results from LGT for the energy density and pressure (both divided by T^4 to compare to a free gas of massless quarks and gluons) as a function of T/T_c. Notice the sharp decrease in the energy density and pressure at $T = T_c$ (e.g. Boyanovsky et al., 2006).

A strong decrease in the sound speed, already above T_c, has been observed in lattice QCD with $c_s^2(T_c) \approx 0.1$. Figure 7 displays the sound speed for quenched QCD, clearly showing a dramatic decrease for $T < 2T_c$ and approaching $1/\sqrt{3}$ for $T \gg T_c$ in agreement with an ultrarelativistic gas of quarks and gluons (e.g. Boyanovsky et al., 2006).

The high temperature behaviour is not quite given by the Stephan–Boltzmann law (cf. Figure 6) suggesting that even at high temperatures the plasma is not described by free quarks and gluons up to temperatures $T \sim 4T_c \sim 700$ Mev (e.g. Boyanovsky et al., 2006).

We need a suitable analytic representation for the Lattice QCD data. Schmid et al.

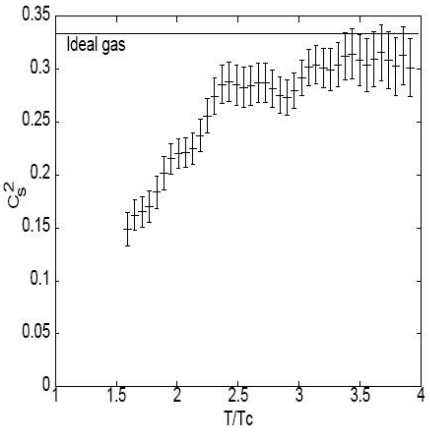

Figure 7: The square of the speed of sound c_s^2 as a function of T/T_c for the QCD transition in a LGT (Gupta, 2003).

(1999) had considered to fit the entropy density with

$$s(T) = \frac{2\pi^2}{45} T^3 \left[g_{HG} + \Delta g \Theta(T - T_c) \left(R_l + (1 - R_l) \left(1 - \frac{T_c}{T} \right)^{\gamma} \right) \right] \tag{78}$$

which is valid for $T > T_c$. Here Θ and R_l are given by equations (77) and (67) respectively, $\Delta g = g_{QGP} - g_{HG}$ and a good fit is obtained for $0.3 < \gamma < 0.4$. We consider, for the rest of the text, $\gamma = 1/3$. In Figure 5 we show the curve of $s(T)$.

The other thermodynamic quantities (for $T > T_c$) can be derived from equation (78). Below T_c again is valid the equation for an ideal HG as in the case of the Bag Model (Schmid et al., 1999).

Inserting the entropy density fit given by equation (78) into equation (12) we obtain (Schmid et al., 1999)

$$c_s^2 \propto \left(1 - \frac{T_c}{T} \right)^{1-\gamma} \tag{79}$$

valid for $T \geq T_c$.

Crossover

The value of T_c for the QCD Crossover is not unique. Different observables lead to different numerical T_c values ranging between 151 MeV and 176 MeV (Bernard et al., 2005; Aoki et al., 2006b).

The entropy density for a Crossover can be written as (e.g. Schmid et al., 1999; Schwarz, 1998)

$$s(T) = \frac{2\pi^2}{45} g_{HG} T^3 \left[1 + \frac{1}{2} \frac{\Delta g}{g_{HG}} \left(1 + \tanh \left(\frac{T - T_c}{\Delta T} \right) \right) \right] \tag{80}$$

where $\Delta g = g_{QGP} - g_{HG}$ and the value of ΔT must be chosen in order to fit the modeled results. When $\Delta T \longrightarrow 0$ we recover the Bag Model, i.e., a first–order phase transition. Both models coincide at temperatures far away from T_c (Schwarz, 1998). QCD Lattice data indicate that $0 \leq \Delta T < 0.1 T_c$ (e.g. Schmid et al., 1999; Bernard et al., 1997). In Figure 5 we show the curve of $s(T)$ for the limiting case $\Delta T = 0.1 T_c$.

The other thermodynamic quantities can be derived from equation (80). For example, inserting the entropy density (80) into equation (12) we obtain, for the sound speed during a QCD Crossover, the following result

$$c_s^2(T) = \left[3 + \frac{\Delta g T \mathrm{sech}\left(\frac{T-T_c}{\Delta T}\right)^2}{\Delta T \left(g_{HG} + g_{QGP} + \Delta g \tanh\left(\frac{T-T_c}{\Delta T}\right)\right)} \right]^{-1} . \tag{81}$$

1.2.2 The EW phase transition

The first phase transition predicted by the SMPP is the *EW phase transition* which occurs at a temperature $T_{EW} \sim 100$ GeV and at a time scale $t_{EW} \sim 10^{-10}$ s (e.g. Unsöld & Bascheck, 2002). At this temperature, which corresponds to an energy scale of the order of the masses of the Z^0 and $W^{\pm}$ vector bosons (Table C-3), the weak interaction become short ranged after a symmetry breaking phase transition. For $T < T_{EW}$ the Z^0 and $W^{\pm}$ vector bosons acquire masses through the Higgs mechanism while the photon remains massless, corresponding to the unbroken symmetry of the electromagnetic interactions (e.g. Boyanovsky et al., 2006).

In the EW standard model (*Glashow–Salam–Weinberg model*) the Higgs field is responsible for the dynamical mass generation via spontaneous symmetry breaking. At sufficiently high temperatures, $T > T_{EW}$, the expectation value of the Higgs field is zero, i.e., the symmetry is restored and particles are massless. At $T < T_{EW}$ the symmetry breakes and particle masses become finite (e.g. Kämpfer, 2000). During this transition, according to the SMPP, all particles except the Higgs acquire their mass by the mechanism of spontaneous symmetry breaking (e.g. Schwarz, 2003).

According to the SMPP the EW phase transition is modeled by a Crossover model. A first–order phase transition is allowed only within the context of some extensions of the SMPP such as the MSSM (Appendix D). Here we consider the two situations, taking in both cases $T_c = 100$ GeV (see Appendix E).

1.2.3 The electron–positron annihilation epoch

During a first–order cosmological phase transition the Universe experiences a drastic reduction in the sound speed. Less dramatic reductions may also occur during particle annihilation periods in the early Universe (e.g. Jedamzik & Niemeyer, 1999; Kämpfer, 2000).

This is the case, for example, of the electron–positron (e^+e^-) annihilation process which becomes predominant as soon as the radiation temperature drops below the mass of the electron (~ 1 MeV). A reduction in the sound speed value of order $10-20\%$ for a few Hubble times does occur during the cosmic e^+e^- annihilation. There is the possibility of an enhancement in PBH formation on the e^+e^- annihilation horizon mass scale of approximately, $M \sim 10^5 M_\odot$ (Jedamzik, 1997).

The neutrino degrees of freedom are not affected at all by this process. As a result, we have the disappearance of four fermionic degrees of freedom, i.e., the ones corresponding to electrons and positrons (e.g. Zimdahl & Pavón, 2001). Thus, we have (cf. Table 2) $\Delta g = 10.75 - 7.25 = 3.5$.

There are other annihilation processes that could lead to an equivalent reduction in the speed of sound (e.g. muon annihilation). In this work we concentrate on the electron–positron annihilation process and on its eventual consequences in the context of PBH production.

1.3 The primordial power spectrum

The primordial power spectrum of the density contrast is operationally defined by (e.g. Blais et al., 2003)

$$P(k) = \left\langle |\delta_k|^2 \right\rangle$$

where the brackets can be taken as representing classical averages over small regions of k–space. In fact the brackets refer to quantum expectation values, but as it was already mentioned (Section 1.1.5) as long as we are interested in PBHs that form for $t \geq 10^{-23}$s then, due to an effective quantum–to–classical transition, it is sufficient to deal with classical averages. The fluctuations as well as their Fourier transforms are all classical stochastic quantities and the power spectrum can be treated as a classical power spectrum (Polarski, 2001).

Notice that what is meant by primordial power spectrum is the power spectrum on *superhorizon scales* (scales much bigger than the Hubble radius for which $k \ll RH$). In these scales, the scale dependence of the power spectrum is unaffected by cosmic evolution. In subhorizon scales this is not the case. For such scales the power spectrum $P(k)$ must involve convolution with a *Transfer Function* $T = T(k,t)$ (Blais et al., 2003, Section 1.4.4).

Let us introduce here the quantity $\delta_H^2(k,t)$ defined as (Bringmann et al., 2002)

$$\delta_H^2(k,t) = \frac{(RH)^4}{k^4}\frac{k^3}{2\pi^2}P(k,t) \tag{82}$$

which has the peculiarity of being time independent in superhorizon scales being equal in very good approximation to the value at the horizon crossing time t_k. At the horizon crossing time ($t = t_k$ and $k = RH$) we have that

$$\delta_H^2(k,t_k) = \frac{k^3}{2\pi^2}P(k,t_k).$$

The quantity $\delta_H^2(k_0, t_0)$ (where the subscript 0 stands for a quantity evaluated at present time) at the present Hubble radius scale can be derived using the large angular scale CMB anisotropy data (Appendix B). It is that quantity that comes from observations which fixes the overall amplitude of the fluctuations spectrum.

Since the primordial scalar power spectrum is an unknown function one is forced to parametrize it with a *spectral index* n which specifies the dependence of the power spectrum on the comoving wavenumber k (e.g. Carr et. al., 1994; Bridle et al., 2003). In general n is a function of scale (i.e. $n = n(k)$) and is determined by the magnitude of the inflaton potential and its first and second derivatives (i.e., determined by the slow–roll parameters – cf. Section 1.1.2) (e.g. Carr, 2005)

$$1 - n = 6\xi_k - 2\eta_k.$$

Many models of inflation predict a significant gravity wave background caused by tensor fluctuations generated during inflation. These tensor fluctuations have their largest effects on large angular scales (e.g. Spergel et al., 2003). The spectral index, n_T, for the gravitational wave (i.e. tensor) spectrum relates to the slow–roll parameters according to (e.g. Bunn et al., 1996; Habib et al., 2005)

$$n_T(k) = -2\xi_k$$

Scales relevant for LSS lie in the range $1 - 10^4$ Mpc and correspond to only 9 e–foldings of inflationary expansion. Since the scalar field must roll down its potential very slowly during inflation, only a very narrow region of V is relevant for these scales. It is therefore consistent to expand the potential as a Taylor series about a given scale and this is equivalent to assuming that the spectral index n is constant over a sufficiently small range (e.g. Carr et. al., 1994).

The simplest models of inflation predict a *power–law primordial power spectrum*. However, there are also viable models of inflation which predict primordial power spectra which cannot be parametrized by a simple power law (e.g. *Broken scale invariance spectrum*, Blais et al., 2003).

In the case of a power–law spectrum we need to specify the amplitudes and spectral indices only at a single scale. It is best to choose this scale near the centre of the available data in order to reduce the propagation of fitting errors. This scale k_c, known as the *pivot point* or *pivot scale*, is defined to be the point at which the normalized scalar and tensor spectra cross (e.g. Bunn et al., 1996; Liddle et al., 2006).

1.3.1 Scale–free power law spectrum

The fact that gravity does not have a characteristic scale, leads us to postulate for the fluctuations a power–law spectrum (e.g. Combes et al., 2002; Bringmann et al., 2002; Green & Liddle, 1997; Longair, 1998)

$$P(k, t) = A(t)k^n \tag{83}$$

where n is the so called *spectral index* and A is a function of time. The simplest case for the power spectrum, which is usually considered, is the one which is *scale–free*, i.e., the case where n is equal to a constant. This choice is made in the assumption that the spectrum of the initial fluctuations must have been very broad with no prefered scales (e.g. Longair, 1998).

Harrison (1970) and Zeldovich (1970) argued that in order to explain the development of primordial fluctuations into protogalaxies, n must exactly, or very closely, equal unity and that we should have at the horizon crossing time

$$P(k, t_k) \propto k^{-3}.$$

That is because in that case the density contrast $\delta(m)$ has the same amplitude on all scales when the perturbations entered the horizon (e.g. Carr, 1975; Longair, 1998; Combes et al., 2002). When $n = 1$, the power spectrum (83) is called the *Harrison–Zeldovich Spectrum* (e.g. Longair, 1998). In this particular case when the fluctuation enters the horizon we have $A(t_k) \sim k^{-4}$ (e.g. Bringmann et al., 2002). In the more general case we may write the power spectrum as (e.g. Narlikar, 2002)

$$P(k, t_k) \propto k^{n-4}. \tag{84}$$

The value of the constant of proportionality in equation (84) depends on the kind of universe we are dealing with (radiation–dominated universe or matter–dominated universe). Thus, we may write the power spectrum (84) as

$$P(k, t_k) = \Gamma^2(\omega) k^{n-4} \tag{85}$$

where Γ is a function of the adiabatic index ω (see equation 5) given by the expression (see Liddle & Lyth (1993) for more details)

$$\Gamma(\omega) = \frac{2(1+\omega)}{5+3\omega}. \tag{86}$$

In the case of a radiation–dominated universe ($\omega = 1/3$) we have $\Gamma(1/3) = 4/9$ and in the case of a matter–dominated universe ($\omega = 0$) we have $\Gamma(0) = 2/5$. We can now relate, with the help of equations (85), (86) and (82) the value of $\delta_H(k_r)$ evaluated at some instant during the radiation–dominated era with the value of $\delta_H(k_c)$ evaluated at some instant t_{k_c}, where k_c is some suitable pivot scale. Doing so we obtain the following result

$$\delta_H^2(k_r, t_{k_r}) = \Theta^2(k_c) \delta_H^2(k_c, t_{k_c}) \left(\frac{k_r}{k_c}\right)^{n-1} \tag{87}$$

where we have considered

$$\Theta(k_c) = \frac{\Gamma(\frac{1}{3})}{\Gamma(\omega_{k_c})} = \begin{cases} \frac{10}{9} & k_{SN} < k_c < k_{eq} \text{ (matter domination)} \\ 1 & k_c \geq k_{eq} \text{ (radiation domination).} \end{cases}$$

The amplitude of the density perturbation spectrum at some pivot scale k_c is given, according to WMAP observations, by (e.g. Easther, 2005)

$$\delta_H^2(k_c) = \left(\frac{5}{3}\right)^2 \frac{800\pi^2}{T^2} A(k_c) \tag{88}$$

where T is the CMB temperature in units of μK (i.e., $T = 2.725 \times 10^6\ \mu K$ – e.g. Verde et al., 2003) and $A(k_c)$ is the normalization of the amplitude at the pivot scale k_c. Inserting the CMB temperature into equation (88) we obtain (e.g. Verde et al., 2003; Easther, 2005)

$$\delta_H^2(k_c) = 2.95 \times 10^{-9} A(k_c). \tag{89}$$

A common pivot scale often used is $k_c = 0.002\mathrm{Mpc}^{-1} \approx 6.5 \times 10^{-26}\mathrm{m}^{-1}$ (e.g. Spergel et al., 2003). Taking into account that this scale is well within the matter–dominated epoch we write equation (87) in the form

$$\delta_H^2(k_r, t_{k_r}) = \left(\frac{10}{9}\right)^2 \delta_H^2(k_c, t_{k_c}) \left(\frac{k_r}{k_c}\right)^{n-1}. \tag{90}$$

It is clear from equations (87) or (90) that in the case of a power law spectrum the quantity δ_H behaves at horizon crossing like (e.g. Bringmann et al., 2002)

$$\delta_H^2(k, t_k) \propto k^{n-1}.$$

The simplest models of inflation predict a nearly scale–free power law primordial spectrum with $n \lesssim 1$. Although this kind of spectrum explains quite well the formation of LSS, according to it the fraction of the Universe going into PBHs is pratically zero (Section 5.1). If we want to have a non–negligible amount of PBHs then we must consider a spectrum with more power on small scales. In fact, it is required a *blue spectrum* (i.e. a spectrum with $n > 1$) in the early Universe (at least during some epochs).

As a first approach one can introduce a step on the index of the scale–free power law spectrum. This step is characterized by two additional (unknown) parameters: location and amplitude. The location must be long before the period of LSS formation and the amplitude value must not lead to an amount of PBHs exceeding the observational constraints (Blais et al., 2003; Sobrinho & Augusto, 2007).

A more natural primordial spectrum is the *Broken Scale Invariance* spectrum based in an inflationary model with a jump in the first derivative of the inflaton potential $V(\phi)$ at some scale k_s. Again we have two additional (unknown) parameters giving the location and the amplitude of the jump (Starobinsky, 1992; Blais et al., 2003; Sobrinho & Augusto, 2007).

A very promissing spectrum is the so called *running–tilt–power–law spectrum* which is based in recent observations of the anisotropy in the CMB. Here we work with this spectrum.

1.3.2 Running–tilt power–law spectrum

Some inflationary models predict that the spectral index of fluctuations n should be a slowly varying function of scale (i.e. $n = n(k)$). Fits of observations of LSS and CMB usually employ a power–law spectrum

$$P(k) = P(k_c)\left(\frac{k}{k_c}\right)^{n(k)} \tag{91}$$

where k_c is some pivot scale and $n(k)$ represents the running of the spectral index. We may write $n(k)$ in the form (e.g. Düchting, 2004)

$$n(k) = n_0 + \sum_{i\geq 1}\frac{n_i}{(i+1)!}\left(\ln\frac{k}{k_c}\right)^i. \tag{92}$$

The value of n_0 depends on the pivot scale used, and represents the *tilt* of the spectrum. It is given by (e.g. Spergel et al., 2003)

$$n_0 = n_s(k) = \frac{d\ln(P(k))}{d\ln(k)}.$$

The value of n_1 represents the *running of tilt* of the spectrum for the chosen pivot scale. It is given by (e.g. Düchting, 2004)

$$n_1 = \alpha_s(k) = \frac{dn_s(k)}{d\ln(k)}.$$

Typical *slow–roll* models predict that the running of the spectal index α_s is unobservably small. However, this issue has generated recent interest after the WMAP team claimed that $\alpha_s < 0$ was favoured over $\alpha_s = 0$ (e.g. Tegmark et al., 2004). The evidence for the running comes, predominantly, from the very largest scales multipoles. Excluding $l < 5$ multipoles from the WMAP temperature we obtain $\alpha_s \approx 0$ (Bridle et al., 2003).

The observational input needed for the running–tilt power–law spectrum is, besides the value of $\delta_H^2(k_0, t_{k_0})$, the values for the parameters n_i evaluated at some pivot scale k_c. According to the results from the WMAP mission we have (e.g. Spergel et al., 2007)

$$\begin{aligned} n_0 &= n_s(k_c) = 0.951^{+0.015}_{-0.019} \\ n_1 &= \alpha_s(k_c) = -0.055^{+0.029}_{-0.035} \end{aligned} \tag{93}$$

where the pivot scale is $k_c = 0.002\mathrm{Mpc}^{-1} \approx 6.5\times10^{-26}\mathrm{m}^{-1}$. The values for the other parameters (i.e. the values of n_i, $i \geq 2$) are unknown at the present. A definitive measurement of n_1, and possibly also of n_2 and n_3 is expected from surveys such as the Planck satellite mission (e.g. Düchting, 2004).

1.4 PBH formation

1.4.1 The condition for PBH formation

The collapse of an overdense region, forming a BH, is possible only if the *root mean square* of the primordial fluctuations, averaged over a Hubble volume, is larger than a threshold δ_{min}. There is also an upper bound δ_{max} corresponding to the case for which a separate universe will form[16]. Thus a PBH will form when the density contrast δ, averaged over a volume of the linear size of the Hubble radius, satisfies (Carr, 1975)

$$\delta_{min} \leq \delta \leq \delta_{max}.$$

The lower and upper bounds of δ can be determined following analytic arguments (see Carr, 1975; Kiefer, 2003). The expansion of an overdense region will, eventually, come to an halt, at some stage, followed by a collapse. The collapse leads to a PBH provided that the size of the region, when it stops expanding, is bigger than the *Jeans Length*[17] R_J (e.g. Kiefer, 2003)

$$R \geq R_J = \sqrt{\frac{1}{3G\rho}}.$$

In order to prevent the formation of a separate universe we must ensure, also, that the overdense region is smaller in size than the particle horizon at the moment of collapse. In particular, when the fluctuation enters the horizon in a radiation–dominated universe, one gets (e.g. Carr, 1975; Kiefer, 2003)

$$\delta_{min} \equiv \frac{1}{3} \leq \delta < 1 \equiv \delta_{max}.$$

The extreme δ_{max} corresponds to the situation for which a separate universe forms and δ_{min} corresponds to the threshold of PBH formation. If $\delta < \delta_{min}$ the fluctuation dissipates and there is no PBH formation.

The value $\delta_{min} = 1/3$ is suggested by analytic arguments. However, numerical simulations considering critical phenomena in the PBH formation (see Section 1.4.2) reveal a higher value, $\delta_{min} \approx 0.7$, which is almost twice the old value (Niemeyer & Jedamzik, 1999a; Musco et al., 2005). Another study using *peaks theory*[18] (Green et al., 2004) leads to $\delta_{min} \approx 0.3 - 0.5$, which is in good agreement with the analytic approach ($\delta_{min} = 1/3$). Taking into account that the threshold δ_{min} arises from critical behaviour, we refer to δ_{min} in the rest of the text as δ_c.

[16]It was originally thought that fluctuations with $\delta > 1$ would collapse to form a separate closed Universe rather than a PBH (Carr, 1975). More recently, Kopp et al. (2011) argue that an upper limit arises for other reasons, and argue that curvature fluctuations should be used for PBH abundance calculations. However, the fraction of the Universe going into PBHs at a given epoch is only weakly dependent in the value of this upper limit (cf. Section 1.4.4).

[17]The Jeans Length is the critical radius of a region where thermal energy, which causes the region to expand, is counteracted by gravity; this causes the region to collapse.

[18]See Bardeen et al. (1986).

The value of the threshold δ_c is constant, with some exceptions, throughout the radiation–dominated universe. Exceptions are phase transitions and annihilation processes (Section 1.2). During these epochs the speed of sound vanishes or, at least, diminishes and, as a result, δ_c becomes smaller (Chapter 4). This is very important because a smaller δ_c will favour PBH production (Chapter 5). Thus, we write the condition for PBH formation in the form

$$\delta_c \leq \delta < 1. \tag{94}$$

For radiation domination ($w = 1/3$), the size of the overdense region at turnaround (i.e. at the moment when the kinetic energy of the expansion is zero), its Schwarzschild radius, the Jeans length, and the cosmological horizon size are all of the same order of magnitude. On the contrary, for dust domination ($w = 0$), the Jeans length is much smaller than the horizon size. For an overdense region that experiences a radiation phase for much of its evolution and a dust–like phase for the rest we define an *effective Jeans length* (e.g. Cardall & Fuller, 1998)

$$R_{J,eff} = \sqrt{\frac{1}{3G\rho_c}(1-f)}$$

where f denotes the fraction of the overdense region spent in the dust–like phase of the transition.

1.4.2 PBH initial mass

It was belived for a long time that the PBH mass, at the time of formation, was aproximately equal to the mass of the collapsing region and thus to the horizon mass M_H (equation 21) at the epoch of formation (Niemeyer & Jedamzik, 1998). A particularly interesting development has been the application of *critical phenomena* to PBH formation.

Studies of the collapse of various types of spherically symmetric matter fields have shown that there is always a critical solution which separates those configurations which form a PBH from those which disperse to an asymptotically flat state. The configurations are described by some index δ and, as the critical index δ_c is approached, the PBH mass is found to scale as $(\delta - \delta_c)^\gamma$ for some exponent γ. It is possible to set up families of initial data such that if $\delta < \delta_c$ the scalar field completely disperses, while if $\delta \geq \delta_c$ a PBH forms (e.g. Choptuik, 1993; Niemeyer & Jedamzik, 1998; Gundlach, 1998).

Choptuik (1993) demonstrated that on the case of a massless scalar field the PBH masses are well–fit by a scaling law with an exponent $\gamma \approx 0.36 - 0.37$. Similar results were subsequently demonstrated for radiation and more general fluids (e.g. Evans & Coleman, 1994; Koike et al., 1995; Maison, 1996; Koike et al., 1999). In all of these studies spacetime was assumed to be asymptotically flat. Niemeyer & Jedamzik (1998) have reached similar results applying the same idea to the study of PBH formation under the context of an expanding universe.

It was then possible to show that when the perturbation overdensity is sufficiently close to the critical overdensity, δ_c, the final mass of the resulting PBH may be an arbitrarily small fraction of the horizon mass given as function of the distance from the threshold, $\delta - \delta_c$ (Niemeyer & Jedamzik, 1998)

$$M_{PBH} = K M_H \left(\delta - \delta_c\right)^{\gamma} \tag{95}$$

where K and γ are dimensionless quantities to be determined according to the perturbation characteristics and M_H is the cosmological horizon mass at the horizon–crossing time (equation 21). The value of K strongly depends on the shape of perturbation ($K \approx 11.9$– Gaussian perturbation; $K \approx 2.9$– mexican–hat perturbation; Niemeyer & Jedamzik, 1999a). On the other hand, the value of γ seems to be universal ($\gamma \approx 0.36$; Koike et al., 1995; Niemeyer & Jedamzik, 1999a; Musco et al., 2005).

Since $M \to 0$ as $\delta \to \delta c$, this suggests that PBHs may be much smaller than the particle horizon at the epoch of formation (e.g. Green & Liddle, 1999; Kribs et al., 1999; Yokoyama, 1998).

An important problem is to determine if the scaling law for PBH masses, given by equation (95) continues valid down to vanishingly small masses or if it stops at some finite value (Choptuik, 1998). This is a very challenging problem from the numerical calculation point of view because when $\delta \to \delta_c$ we have the appearance of strong shocks and deep voids outside the region where the PBH is forming (Musco et al., 2005). Hawke & Stewart (2002) addressed this problem using a purpose–built code and have claimed that the formation of shocks prevents BHs forming on scales below $10^{-4} M_H$, i.e., for smaller BH masses the scaling law (95) appears not to hold. However, this may not be true for all initial data (e.g. Musco et al., 2005; Gundlach & Martín-García, 2007).

In Figure 1 we have represented the allowed masses for PBHs as a function of (forming) time assuming that $10^{-4} M_H \leq M_{PBH} \leq M_H$. PBHs with initial masses of $\sim 10^{15}$g are supposed to be exploding by now. Ligther PBHs should have already completely evaporated.

1.4.3 PBHs from collapsing density perturbations

The dynamics of PBH formation from the collapse of density perturbations[19] in the early Universe are fully described by the general relativistic hydrodynamical equations of a perfect fluid, the field equations, the first law of Thermodynamics, and a suitable EoS (e.g. Niemeyer & Jedamzik, 1999a).

The idea is to introduce into the equations, as an initial condition, a density perturbation $\epsilon(R_s)$ superimposed in a uniform background with constant density ϵ_0 and then see the subsequent evolution of that perturbation.

[19]For other proposed mechanisms for PBH formation see (e.g. Carr, 2005; Mack et al., 2007).

Niemeyer & Jedamzik (1999a) considered three families of curvature perturbations expressed in the form of perturbations on the energy density. The first family of perturbations is described by a Gaussian–shaped overdensity that asymptotically approaches the FLRW solution, the second is described by a mexican–hat function and the third by a sixth order polynomial (see Appendix G for more details).

Niemeyer & Jedamzik (1999a) finded similar values of δ_c for all the three families of perturbations considered – $\delta_c = 0.67$ (mexican–hat), $\delta_c = 0.70$ (Gaussian), and $\delta_c = 0.71$ (polynomial) – suggesting a universal value of $\delta_c \approx 0.7$. The results were confirmed by Musco et al. (2005) when considering perturbations on length–scales much larger than the horizon scale and well within the linear regime. However, when considering growing–mode perturbations Musco et al. (2005) encountered very similar curves and almost identical values of γ but substantially different values for the critical threshold: $\delta_c \simeq 0.43$ for mexican–hat perturbations and $\delta_c \simeq 0.47$ for polynomial perturbations (see Appendix G for examples).

The pressure response of a radiation fluid is given by equation (12). Any decrease of the pressure response of the radiation fluid may yield a reduction of the threshold δ_c. Such a behaviour is expected to occur during cosmological first–order phase transitions (e.g. Jedamzik & Niemeyer, 1999).

A reduction of the PBH formation threshold for fluctuations which enter the cosmological horizon during first–order phase transitions may have cosmological implications. The slightest reduction of δ_c may result in the formation of PBHs with masses of the order of the horizon mass during the first–order phase transition, yielding a highly peaked PBH mass function (e.g. Jedamzik & Niemeyer, 1999).

1.4.4 The fraction of the Universe going into PBHs

If the primordial fluctuations obey Gaussian statistics then the probability P_δ that a spherical region of initial mass m has a density contrast in the range $[\delta, \delta + d\delta]$ will also obey a Gaussian statistics (e.g. Green et al., 2004). Thus we may write (Carr, 1975)

$$P_\delta d\delta = \frac{1}{\sqrt{2\pi}\sigma(m)} \exp\left(-\frac{\delta^2}{2\sigma^2(m)}\right) d\delta \tag{96}$$

which represents a Gaussian normal distribution about zero with standard deviation or mass variance $\sigma(m)$. The probability $\beta(t_k)$ that a region of comoving size $r = (RH)^{-1}_{t=t_k} = (ck)^{-1}$ (see equation 56) has an averaged density contrast at horizon crossing in the range $\delta_c \leq \delta \leq \delta_{max}$, which is the condition for PBH formation (Section 1.4.1), is given by (e.g. Bringmann et al., 2002)[20]

$$\beta(t_k) = \frac{1}{\sqrt{2\pi}\sigma(t_k)} \int_{\delta_c}^{\delta_{max}} \exp\left(-\frac{\delta^2}{2\sigma^2(t_k)}\right) d\delta \tag{97}$$

[20]Taking into account that $M_H(t_k)$ represents the horizon mass evaluated at the instant t_k when the fluctuation with wavenumber k crosses the horizon we may write also $\beta(M_H)$ or $\beta(k)$ meaning exactly the same as $\beta(t_k)$. The idea applies also to other quantities (e.g. mass variance).

where

$$\sigma^2(t_k) = \sigma^2(k) = \sigma^2(r)\big|_{t=t_k} .$$

If $\delta_c \gg \sigma(t_k)$ and $\delta_{max} - \delta_c \gg \sigma(t_k)$ we have the approximation (e.g. Bringmann et al., 2002)

$$\beta(t_k) \approx \frac{\sigma(t_k)}{\sqrt{2\pi}\delta_c} \exp\left(-\frac{\delta_c^2}{2\sigma^2(t_k)}\right). \tag{98}$$

Remember that for the smallest scales we cannot speak anymore about classical fluctuations (see Section 1.1.5) and that is why the equations (96), (97) and (98) do not apply anymore on that case. As it was mentioned for all PBHs produced after approximately 10^{-23}s, the quantum–to–classical transition is already extremely effective which means that one can really work to tremendously high accuracy with classical probability distributions (Polarski, 2001).

The main problem in calculating the production rate for PBHs is the correct evaluation of $\sigma(r)$ at a given epoch (e.g. Blais et al., 2003; Green & Liddle, 1997). The mass variance can be generically written as (e.g. Liddle & Lyth, 1993; Longair, 1998)

$$\sigma^2(r) = \left\langle \left(\frac{\delta M}{M}\right)_r^2 \right\rangle = \frac{1}{(2\pi)^3} \int_0^\infty P(k) d^3k$$

where $P(k)$ is the power spectrum of the density fluctuations averaged over a small region of k–space. Assuming spherical symmetry, the volume element of k–space d^3k turns out to be $4\pi k^2 dk$ and we are left with

$$\sigma^2(r) = \frac{1}{2\pi^2} \int_0^\infty k^2 P(k) dk.$$

If we want to examine specific mass ranges, we have to smooth the density distribution, introducing a suitable window function W (e.g. Green & Liddle, 1997). Different window functions have been proposed in the literature, namely the top–hat window function (e.g. Blais et al., 2003) and the Gaussian window function (e.g. Green et al., 2004).

The choice of a suitable window function turns out to be a very important problem. It must be done in accordance with the results one uses. For example, if one uses $\delta_c \approx 0.7$ as found by Niemeyer & Jedamzik (1999a) then one must also use the top–hat window function in order to be consistent with their numerical results (Bringmann et al., 2002).

Despiste the fact that a Gaussian window would be more convenient for theoretical calculations (e.g. Liddle & Lyth, 1993) it would erroneously yield too small values for the mass variance (Blais et al., 2003). Actually the top–hat window function is accepted as the most physical choice to study the formation of PBHs. With this choice the smoothed density contrast δ describes directly the average density

contrast in the region relevant to PBH formation (Blais et al., 2003), i.e., it is sensitive to scales well within the horizon (Green et al., 2004). Thus, we adopt a top–hat window function. The Fourier transform of the top–hat window function divided by the probed volume is given by (e.g. Blais et al., 2003; Bringmann et al., 2002)

$$W_{TH}(kr) = \frac{3}{(kr)^3}\left(\sin(kr) - kr\cos(kr)\right). \tag{99}$$

The mass variance can now be rewritten in order to accomodate (99) as (e.g. Blais et al., 2003; Bringmann et al., 2002)

$$\sigma^2(r) = \frac{1}{2\pi^2}\int_0^\infty k^2 W_{TH}^2(kr)P(k)dk. \tag{100}$$

There is a natural upper cut–off in k–space for the power spectrum, namely k_e, corresponding to the Hubble radius at the end of inflation t_e. In fact the smallest scale generated by inflation (Blais et al., 2003). The lower limit can be taken to be zero if we assume that the number of e–folds during inflation (cf. equations (28) and (29)) amply solves the cosmological horizon problem (Bringmann et al., 2002). Thus we rewrite equation (100) as

$$\sigma^2(r) = \frac{1}{2\pi^2}\int_0^{k_e} k^2 W_{TH}^2(kr)P(k)dk.$$

Considering that k represents the scale entering the horizon at time t_k and that k' represents all scales, i.e $0 \leq k' \leq k_e$ we introduce here the variable $x = k'/k$ such that $0 \leq x \leq k_e/k$ and $x = 1$ at horizon crossing. Considering this variable change, this becomes

$$\sigma^2(r) = \frac{1}{2\pi^2}\int_0^{\frac{k_e}{k}} k^3 x^2 W_{TH}^2(x)P(kx)dx. \tag{101}$$

Considering the same variable change in equation (82) we have that

$$P(kx,t) = \frac{2\pi^2 kx}{(RH)^4}\delta_H^2(kx,t).$$

Inserting this into equation (101) we have

$$\sigma^2(r) = \int_0^{\frac{k_e}{k}} \frac{k^4x^3}{(RH)^4}\delta_H^2(kx,t)W_{TH}^2(x)dx. \tag{102}$$

But we are interested in the instant $t = t_k$ when the fluctuation with wavenumber k enters the horizon. Thus, inserting (56) into equation (102) we have that

$$\sigma^2(k) = \int_0^{\frac{k_e}{k}} x^3\delta_H^2(kx,t_k)W_{TH}^2(x)dx.$$

On superhorizon scales ($ck \ll RH$) the scale dependence of the power spectrum is unafected by cosmic evolution. However on subhorizon scales the power spectrum must involve convolution with a Transfer function $T = T(k,t)$ (e.g. Blais et al., 2003).

This transfer function must be taken at the time t_k of interest and not today. That is because at each stage of the cosmological evolution, the correct use of the transfer function takes into account the dynamics of the fluctuations after horizon–entry. This leads effectivelly to very different spectra on small scales at different times. The transfer function is defined through (Blais et al., 2003)

$$T^2(k,t) = \frac{P(k,t)}{P(k,t_u)} \frac{P(0,t_u)}{P(0,t)}$$

where t_u represents some initial time when all scales are outside the Hubble radius, i.e., when $ck < RH$. Taking as a reference the end of inflation we consider $t_u = t_e$. Notice that when $k \to 0$ (superhorizon scales) we have that $T(k,t) \to 1$ as expected. The transfer function can be computed analytically yelding (Blais et al., 2003)

$$T^2(kx, t_k) = W_{TH}^2(c_s x) = W_{TH}^2\left(\frac{x}{\sqrt{3}}\right)$$

where $c_s = 1/\sqrt{3}$ denotes the speed of sound in the radiation–dominated era. We see that actually $T^2(kx, t_k)$ does not depend on the wavenumber k. This will be true for scales very deep inside the radiation era ($t_e \ll t_k \ll t_{eq}$, $k_e \gg k \gg k_{eq}$), which are the ones we are interested in (Blais et al., 2003).

We are now in position to write an accurate general formula for the mass variance valid when the fluctuation with wavenumber k enters the horizon (Blais et al., 2003)

$$\sigma^2(k) = \int_0^{\frac{k_e}{k}} x^3 \delta_H^2(kx) W_{TH}^2(x) W_{TH}^2(\frac{x}{\sqrt{3}}) dx.$$

It may be useful to consider the following relation where all the quantities are evaluated at the time t_k (Blais et al., 2003; Bringmann et al., 2002)

$$\sigma^2(t_k) = \alpha^2(k) \delta_H^2(k, t_k) \tag{103}$$

with the function α given by (e.g. Blais et al., 2003)

$$\alpha^2(k) = \int_0^{\frac{k_e}{k}} x^3 \frac{\delta_H^2(kx)}{\delta_H^2(k)} W_{TH}^2(x) W_{TH}^2(\frac{x}{\sqrt{3}}) dx. \tag{104}$$

In the case of a power–law spectrum we have (cf. equation 90)

$$\frac{\delta_H^2(kx)}{\delta_H^2(k)} = x^{n-1}$$

allowing us to write the function $\alpha(k)$ (equation 104) in the form (e.g. Blais et al., 2003)

$$\alpha^2(k) = \int_0^{\frac{k_e}{k}} x^{n+2} W_{TH}^2(x) W_{TH}^2(\frac{x}{\sqrt{3}}) dx. \tag{105}$$

It is crucial to distinguish both quantities $\sigma^2(t_k)$ and $\delta_H^2(k, t_k)$. As seen from equation (103) the quantity $\sigma^2(t_k)$, which depends on the averaging, is related to the non–averaged quantity $\delta_H^2(k, t_k)$ in a non–trivial way by means of $\alpha(k)$. The quantity $\delta_H^2(k, t_k)$ can be reconstructed at the time t_k from its present value $\delta_H^2(k_0, t_0)$. This is not the case for the quantity $\sigma^2(t_k)$ because the deformation of the power spectrum is different at the time t_k and today (Polarski, 2002).

The problem in evaluating $\alpha(k)$ comes from the evolution of the perturbations for scales k' inside the Hubble radius: $k = RH \leq k' \leq k_e$ or equivalently $1 \leq x \leq \frac{k_e}{k}$. This small scale evolution is encoded in the transfer function $T(k, t)$. Clearly, an accurate value of $\alpha(k)$ can be obtained only numerically and with an explicit knowledge of $T(k, t)$ (Bringmann et al., 2002).

It is clear at this point that the problem in evaluating $\beta(k)$ is transfered to the evaluation of the function $\alpha(k)$. Knowing $\alpha(k)$ (equation 104) it is straightforward to find $\sigma(k)$ (equation 103) and $\beta(k)$ (equation 97) as long as we have the needed observational input and a suitable expression for the primordial power spectrum $P(k)$.

In Table 3 we have, for several epochs of interest, the values of the wavenumber k (equation 56) corresponding to the fluctuations crossing the horizon at that times as well as the corresponding horizon mass M_H (equation 21). The selected epochs are: $t_e \sim 10^{-33}$ s (end of inflation, Section 1.1.4), $t_* \approx 10^{-23}$ s (formation of PBHs that are exploding by the present time, e.g. Green & Liddle, 1997), $t = 10^{-10}$ s (EW phase transition, Section 1.2.2), $t = 10^{-5}$ s (QCD phase transition, Section 1.2.1), $t = 3$ s (electron–positron annihilation epoch, Section 1.2.3), $t = 20$ s (corresponding to the maximum mass allowed for PBH in the CDM context, Afshordi et al., 2003), $t = 10^5$ s (corresponding to the mass of the biggest SMBH known candidates, e.g. Kormendy, 2004), $t_{eq} = 2.5 \times 10^{12}$ s (matter–radiation equality, Section 1.1.4), $t_{dec} = 1.2 \times 10^{13}$ s (photon decoupling, Section 1.1.4), $t_{SN} = 2.8 \times 10^{17}$ s (matter–dark energy equality, Section 1.1.4), and $t_0 = 4.3 \times 10^{17}$ s (present time, Section 1.1.4).

The mass variance $\sigma(k)$ can be determiend with the help of equation (103) with $\alpha(k)$ given by equation (105) and δ_H given by equation (90). It may be useful to express the mass variance in terms of masses instead of wavenumbers. Making use of equations (41), (42), (46), (52), and (56) we have

$$\frac{k}{k_c} = \frac{R(t_k)H(t_k)}{R(t_{k_c})H(t_{k_c})} = \frac{3}{4}\left(\frac{t_{k_c}}{t_{eq}}\right)^{1/3}\left(\frac{t_{eq}}{t_k}\right)^{1/2}. \tag{106}$$

Table 3: The wavenumber k (equation 56) for the fluctuation crossing the horizon at different epochs t_k and the corresponding horizon mass M_H (equation 21).

	t_k(s)	k(m^{-1})	M_H(g)	$M_H(M_\odot)$
t_e	10^{-33}	10^{-2}	10^{5}	5.0×10^{-29}
t_*	10^{-23}	1.1×10^{-7}	10^{15}	5.0×10^{-19}
	10^{-10}	3.3×10^{-14}	10^{28}	5.0×10^{-6}
	10^{-5}	1.1×10^{-16}	10^{33}	0.5
	3	1.9×10^{-19}	3×10^{38}	1.5×10^{5}
	20	7.4×10^{-20}	2×10^{39}	10^{6}
	10^{5}	1.1×10^{-21}	10^{43}	5.0×10^{9}
t_{eq}	2.5×10^{12}	2.8×10^{-25}	2.5×10^{50}	1.3×10^{17}
t_{dec}	1.2×10^{13}	1.7×10^{-25}	1.2×10^{51}	6.0×10^{17}
t_{SN}	2.8×10^{17}	5.8×10^{-27}	2.8×10^{55}	1.4×10^{22}
t_0	4.3×10^{17}	5.2×10^{-27}	4.3×10^{55}	2.2×10^{22}

Taking now into account that $M_H(t) \propto t$ (cf. equation 21) and considering the result (106), equation (90) and equation (103) it turns out that the mass variance can be written as (e.g. Blais et al., 2003; Bringmann et al., 2002)

$$\sigma^2(t_k) = \frac{100}{81}\alpha^2(k)\delta_H^2(t_{k_c}) \left(\frac{3}{4}\right)^{n-1} \left[\frac{M_H(t_{k_c})}{M_H(t_{eq})}\right]^{\frac{n-1}{3}} \left[\frac{M_H(t_{eq})}{M_H(t_k)}\right]^{\frac{n-1}{2}}. \tag{107}$$

In the case $n = 1$ (Harrison–Zeldovich spectrum) this simplifies considerably and we are left with

$$\sigma^2(t_k) = \frac{100}{81}\alpha^2(k)\delta_H^2(t_{k_c}). \tag{108}$$

The observational input needed in equations (107) and (108) is the numerical value of $\delta_H^2(t_{k_c})$ which is found using the CMB anisotropy data for large angular scales (Blais et al., 2003).

1.4.5 The PBH density parameter

The *PBH density parameter* for PBHs formed at a given instant $t = t_k$ is defined as (e.g. Niemeyer & Jedamzik, 1998)

$$\Omega_{PBH}(t_k) = \frac{\rho_{PBH}(t_k)}{\rho_c(t_k)}$$

where $\rho_{PBH}(t_k)$ represents the mass density of PBHs formed at $t = t_k$ and $\rho_c(t_k)$ is the Universe critical density evaluated at the same instant of time. This can also be

written as (e.g. Niemeyer & Jedamzik, 1998)

$$\Omega_{PBH}(t_k) = \frac{1}{M_H(t_k)} \int_{\delta_c}^{1} M_{PBH}(\delta, t_k) P(\delta, t_k) d\delta \tag{109}$$

where M_H is given by equation (21), M_{PBH} is given by equation (95), and $P(\delta, t_k)$ is given by equation (96).

If we want to determine correctly the value of $\Omega_{PBH}(t_k)$ then one must use, for $M_{PBH}(\delta, t_k)$, the continuous distribution of PBH masses given by equation (95). In so doing, we implicitly assume that equation (95) is valid for δ as large as unity; this is never the case (as mentioned in Section 1.4.2, equation (95) is only valid in the immediate neighborhood of δ_c). However, the largest contribution to the integral (109) comes from $\delta \approx \delta_c$ due to the exponential form of $P(\delta)$, and, thus, the assumption is well justified (Niemeyer & Jedamzik, 1998).

When $\delta = \delta_c$ we get, from equation (95), that $M_{PBH} = 0$. Once again, taking into account that the main contribution to the integral (109) comes from $\delta \approx \delta_c$ we can extend the upper limit of the integral to infinity. Taking these assumptions into account and noting from equation (95) that

$$d\delta = \frac{1}{\gamma} \left(\frac{M_{PBH}}{K M_H} \right)^{1/\gamma} \frac{dM_{PBH}}{M_{PBH}}$$

we write the integral (109) in the form (e.g. Yokoyama, 1998)

$$\Omega_{PBH}(t_k) = \frac{1}{M_H(t_k)} \int_0^{\infty} \frac{M_{PBH}}{\gamma} P\left(\delta(M_{PBH})\right) \left(\frac{M_{PBH}}{K M_H(t_k)} \right)^{\frac{1}{\gamma}} \frac{dM_{PBH}}{M_{PBH}} \tag{110}$$

with

$$P\left(\delta(M_{PBH})\right) = \frac{1}{\sqrt{2\pi}\sigma(t_k)} \exp\left[-\frac{1}{2\sigma^2(t_k)} \left[\delta_c + \left(\frac{M_{PBH}}{K M_H(t_k)} \right)^{1/\gamma} \right]^2 \right].$$

It is common to write equation (110) in the form of a differential mass spectrum (e.g. Yokoyama, 1998; Niemeyer & Jedamzik, 1998)

$$\begin{aligned} \frac{d\Omega_{PBH}(t_k)}{d \ln M_{PBH}} = \frac{1}{\sqrt{2\pi}\sigma(t_k)\gamma} \frac{M_{PBH}}{M_H(t_k)} \left(\frac{M_{PBH}}{K M_H(t_k)} \right)^{1/\gamma} \times \\ \times \exp\left[-\frac{1}{2\sigma^2(t_k)} \left[\delta_c + \left(\frac{M_{PBH}}{K M_H(t_k)} \right)^{1/\gamma} \right]^2 \right]. \end{aligned} \tag{111}$$

This mass spectrum exhibits a peak at

$$M_{PBH}^{max} = \frac{K M_H}{2^\gamma} \left(-\delta_c + \sqrt{\delta_c^2 + 4(1+\gamma)\sigma^2} \right)^\gamma. \tag{112}$$

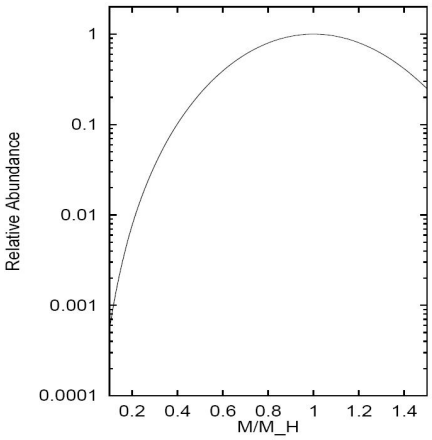

Figure 8: The relative abundance of PBHs formed at some epoch when one takes the scaling relation (equation 95) into account (Yokoyama, 1998).

Taking into account that $\sigma^2(t_k) \gtrsim 10^{-4}$ at all epochs relevant for PBH formation (cf. Section 5.4 and Appendix L), remembering that $\gamma \approx 0.36$ (cf. Section 1.4.2), considering $K = 11.9$ (which corresponds to the numerical value obtained for gaussian fluctuations, cf. Section 1.4.2) and assuming $1/3 \leq \delta_c \leq 0.7$ (cf. Section 1.4.1) it turns out from equation (112) that

$$M_{PBH}^{max} \approx M_H .$$

It is not surprising that the value of M_{PBH}^{max} at a fixed epoch coincides with the value of M_H, evaluated at the same epoch, since the latter determines the mass scale for collapse. However, depending in the value of σ, a fraction of all PBHs formed at each epoch will have masses significantly smaller than M_H (Niemeyer & Jedamzik, 1998).

The mass spectrum given by equation (111) is depicted in Figure 8 where we find that the abundance of smaller–mass PBHs is very suppressed even in the presence of the critical behaviour (see Section 1.4.2).

If one wants to study the presence of PBHs in the present day Universe then one needs to evaluate the present day value of the density parameter $\Omega_{PBH}(t_0)$. Taking into account only the PBHs formed at a given epoch $t = t_k$ this relation turns out to be (e.g. Ricotti et al., 2008)

$$\Omega_{PBH}(t_k)\,[1 + z(t_k)] = \Omega_{PBH}(t_0, t_k)\,[1 + z(t_{eq})]\,, \tag{113}$$

valid for non–evaporated PBHs (cf. Figure 1).

1.5 This thesis

Having as motivation the possibility of direct detection of BHs by their electromagnetic emission, we endeavoured into finding out, first, how many PBHs could exist in

the Universe. We consider PBHs because only sub-stellar mass BHs can be detected directly at realistic distances; furthermore, as far as we know, BHs with such masses could have formed only in the early Universe (i.e, PBHs). In order to determine the PBH number density in the present day Universe or, equivalently, the present day value of the PBH density parameter we first need to know the fraction of the Universe going into PBHs as a function of time –$\beta(t_k)$.

Our study begins when the Universe was 10^{-23} s old. PBHs formed at that particular epoch are exploding right now and PBHs formed earlier have completely evaporated by now. Only PBHs formed after 10^{-23} s are still lurking around evaporating and accreting matter (we show this in Figure 1). We decided to investigate the existence of, not only, sub–stellar mass PBHs, but also of PBHs of all masses up to the most massive PBHs ($\sim 10^{10} M_{\odot}$) that might have formed when the Universe was $\sim 10^5$ s old.

During this interval (10^{-23}–10^5 s) the Universe was radiation–dominated with, perhaps, the exception of two epochs predicted by the SMPP: the EW phase transition and the QCD phase transition. Such epochs are very important, within the context of PBH formation, in the sense that during those the sound speed vanishes or, at least, decreases for a brief period, decreasing the PBH formation threshold δ_c which, in turn, favours PBH formation. In addition to the EW and QCD phase transitions we consider the electron–positron annihilation epoch, during which the decrease of the sound speed value might have favoured PBH formation as well.

This thesis is organized as follows. In Chapter 1 we review several aspects about the early Universe and PBH formation that we found relevant for this thesis. We begin with some preliminaries on Relativistic Cosmology and review some key aspects of Inflation, ΛCDM, the scale factor, primordial fluctuations, and degrees of freedom. Next we move on to cosmological phase transitions and present some aspects about the QCD and the EW epochs that we found relevant for this work. We do the same for the electron–positron annihilation epoch. We then introduce the primordial power spectrum for density fluctuations refering to the scale–free power–law spectrum (enough to explain LSS formation but insuficient to assure PBH formation) and to the running–tilt power–law spectrum (suitable for PBH formation). Finally, at the end of the section, we consider the mechanism of PBH formation. We then introduce the PBH formation threshold (δ_c) and the PBH initial mass concepts. We finish the section with the expressions giving the fraction of the Universe going into PBHs ($\beta(t_k)$) and the PBH density parameter ($\Omega_{PBH}(t_k)$), both playing a central role on this thesis, since it is from these that we estimate the probability of direct detection of PBHs.

Being aware of the importance that cosmological phase transitions might have taken in PBH formation we have determined their location and duration within the Universe timeline. We do that for the QCD phase transition, EW phase transition and electron–positron annihilation epoch in Chapter 2.

In Chapter 3 we consider the evolution of density fluctuations during cosmological phase transitions. In the case of a first–order phase transition (QCD Bag Model,

QCD Lattice Fit or EW Bag Model) we adopted and developed a model proposed in the literature in which fluctuations are divided into six different classes depending on the instant t_k at which they cross the horizon (before, during or after the transition) and the instant t_c, called the turnaround point, at which they start collapsing. In the case of a Crossover–like transition we derive our own expressions. We modeled the electron–positron annihilation epoch as a Crossover–like transition.

In Chapter 4 we determine, using the results obtained from Chapters 2 and 3, the values giving the decreasing of the PBH formation threshold (δ_c) during the QCD phase transition (Bag Model, Lattice Fit and Crossover), EW phase transition (Bag Model and Crossover) and electron–positron annihilation epoch. In the case of the QCD Bag Model and EW Bag Model we adopted the same approach used in the literature in which the decrease of the δ_c threshold is given by means of a function f that accounts for the fraction ot time during which the perturbed region is in the dust–like phase. For the Crossover–like transitions (QCD, EW and electron–positron annihilation) we constructed a new (and more general) function f that takes into account the continuous change in the sound speed during the transition (equation 183). For the QCD Lattice Fit case we have a dust–like epoch during which the sound speed vanishes (resembling the QCD Bag Model) preceded by an epoch during which the sound speed value decreases (resembling the QCD Crossover). Thus, for this situation, we constructed a new function f based in the ones that we considered for the Bag Model–like transitions and for the Crossover–like transitions (equations 186, 189 and 192). The main result from this Chapter consists in sets of points giving the behaviour of the treshold δ_c during the Universe timeline (Figures 31, 33, 40, 42, 43, 45; Tables I-1 to I-6).

In Chapter 5 we determine the fraction of the Universe going into PBHs at each epoch of interest. First, we confirm that for a scale–free power–law spectrum the value of $\beta(t_k)$ is negligible at all epochs and we show that this picture does not change even if we consider a strong first–order phase transition such as the QCD Bag Model. Then, we look into the running–tilt power–law spectrum and consider an expansion with up to four terms. These include two known parameters (n_0 and n_1) and two unknown parameters (n_2 and n_3). We then show that these last two can be related to the parameters t_+ (giving the location of the maximum of the spectral index $n(k)$) and n_+ (corresponding to $n(k(t_+))$). Thus, we decided to work on the (n_+, t_+) parameter space searching for *cases* favouring PBH formation. We then proceed to calculate $\beta(t_k)$. First, we consider a radiation–dominated universe and searched for the cases giving non–zero values (i.e. cases for which $\beta(t_k) > 10^{-100}$ at least during some time interval) as well as the cases that are excluded due to observational constraints. Then we show how this is altered when one considers cosmological phase transitions: QCD (Bag Model, Lattice Fit and Crossover), EW Bag Model and electron–positron annihilation. In the case of an EW Crossover we confirm that the results are negligible. The main result from this section consists in sets of points giving the curve $\beta(t_k)$ for the different cases (Figures 53 to 64).

In Chapter 6 we determine the present day values for the PBH density parameter, PBH number density and the minimum distance to the nearest PBH of a given

mass. We perform the calculations for the different cases identified in Chapter 5. We consider as observationally relevant only the cases that give, at least, one PBH in the observable Universe. We then compile the results taking into account the different cosmological phase transitions: i) QCD (Bag Model – Table 20, Figures 71 to 73; Lattice Fit model – Table 21, Figures 74 to 76; Crossover – Table 22, Figures 77 and 78); ii) EW (Table 23, Figures 79 to 81); electron–positron annihilation (Table 19, Figures 68 to 70). We also compile the results taking into account the different classes of BHs in terms of mass: SMBHs (Table 18, Figures 66 and 67), IMBHs (Table 24), SBHs (Table 25), SSBHs (Tables 26 and 27, Figures 83 to 85). At the end of the Chapter we consider two important topics: the contribution from PBHs to CDM (Table 28) and the existence of PBHs in the neighborhood of the Solar System.

In Chapter 7 we summarize and discuss the results obtained. First, in Section 7.1 we resume the background theory on PBH formation, and, in Section 7.2 we resume the methodology that we followed in order to determine the PBH density parameter. In Sections 7.3 to 7.7 we discuss the results obtained taking into account the contributions from radiation, from the cosmological phase transitions (QCD, EW) as well as from the electron–positron annihilation epoch. In Section 7.8 we define a mechanism that allows us to compare, between themselves, PBHs of different masses and located at different distances from us. In Section 7.9 we show that, according to our results, it is possible to directly detect PBHs. In particular, we show that we could have a $\sim 10^{18}$ g PBH within a distance of $\sim 10^{14}$ m and that it could be detected by an X–ray telescope with the probability $\sim 10^{-15}$.

Finally, in Chapter 8, we present our final conclusions as well as some ideas for future work. We concluded that, provided some fine–tuning to the initial conditions, it is very reasonable to assume the formation and existence of PBHs in observationally relevant numbers in the Universe. In particular we got situations giving important contributions to CDM with relevant populations of PBHs within the galactic halo peaking at 10^{27} g (in the case of the EW contribution) or $0.5 M_{\odot}$ (in the case of the QCD contribution). We also got cases giving important numbers in terms of IMBHs and SMBHs. Finally, we list some objectives and ideas for future work.

2 Duration of the cosmological phase transitions

2.1 QCD phase transition

If one wants to study how a given fluctuation behaves during the QCD phase transition then it is of crucial importance to know the duration of the transition. This means that, if we want to perform numerical integrations then we need to define a specific beginning $t = t_{QCD-}$ and a specific end $t = t_{QCD+}$ to the QCD transition. Here t_{QCD-} and t_{QCD+} are the limits for the time interval during which the speed of sound vanishes. This is aplicable in the case of a first–order transition (Bag Model and Lattice Fit). In the case of a Crossover we will define an effective duration instead.

Taking into account that the temperature of the Universe during the QCD phase transition is T_c we can obtain, with the help of equation (53) a numerical value for $R(t_{QCD+})$ (i.e. the value of the scale factor at the end of the transition)

$$R(t_{QCD+}) = \frac{T_0}{T_c}. \tag{114}$$

On the other hand, equation (48) becomes, for $t = t_{QCD+}$

$$R(t_{QCD+}) = \exp\left(c\sqrt{\frac{\Lambda}{3}}(t_{SN} - t_0)\right)\left(\frac{t_{eq}}{t_{SN}}\right)^{2/3}\left(\frac{t_{QCD+}}{t_{eq}}\right)^{1/2}. \tag{115}$$

Inserting equation (114) into equation (115) we obtain for the instant when the transition ends

$$t_{QCD+} = t_{SN}\left(\frac{t_{eq}}{t_{SN}}\right)^{-1/3}\exp\left(-2c\sqrt{\frac{\Lambda}{3}}(t_{SN} - t_0)\right)\left(\frac{T_0}{T_c}\right)^2. \tag{116}$$

The evolution of the scale factor during the QGP and HG coexistence in a first–order QCD transition, i.e., during the $c_s^2 = 0$ part, is determined by the entropy conservation (e.g. Schwarz, 2003; Schmid et al., 1997)

$$\Delta R = \frac{R(t_{QCD+})}{R(t_{QCD-})} = \left(\frac{s(t_{QCD-})}{s(t_{QCD+})}\right)^{1/3} = \left(1 + R_l\frac{\Delta g}{g_{HG}}\right)^{1/3} \tag{117}$$

where R_l is given by equation (67), $\Delta g = g_{QGP} - g_{HG}$, $g_{QGP} = 61.75$ (51.25) with (without) strange quarks and $g_{HG} = 21.25$ (17.25) with (without) kaons (cf. Section 1.1.6). Inserting these values into equation (117) it turns out that, in the case of a Bag Model ($R_l = 1$), the Universe expands by a factor of $\Delta R \approx 1.44$ until all QGP has been converted into the HG, whereas for a Lattice Fit ($R_l = 0.2$) the Universe expands by a factor of $\Delta R \approx 1.1$ (see e.g. Schwarz, 2003).

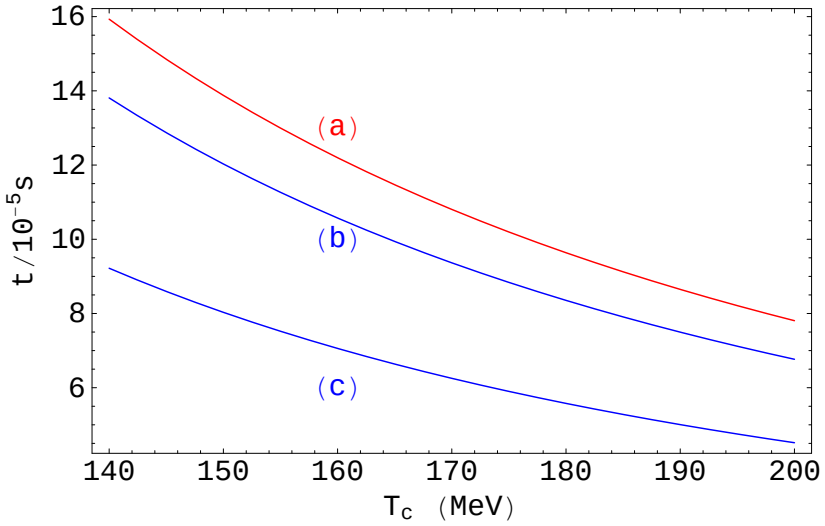

Figure 9: The beginning (t_{QCD-}) and the end (t_{QCD+}) of the QCD phase transition as a function of the transition temperature T_c: (a) t_{QCD+}, valid for both the Bag Model and the Lattice Fit; (b) t_{QCD-} for the Lattice Fit and (c) t_{QCD-} for the Bag Model.

When $t = t_{QCD-}$ equation (48) becomes

$$R(t_{QCD-}) = \exp\left(c\sqrt{\frac{\Lambda}{3}}(t_{SN} - t_0)\right)\left(\frac{t_{eq}}{t_{SN}}\right)^{2/3}\left(\frac{t_{QCD+}}{t_{eq}}\right)^{1/2}\left(\frac{t_{QCD-}}{t_{QCD+}}\right)^{2/3} \quad (118)$$

where we have considered $n_{qcd} = 2/3$. From equations (115), (117) and (118) we obtain

$$t_{QCD-} = \frac{t_{QCD+}}{\sqrt{\Delta R^3}}. \quad (119)$$

For example, when $T_c = 170$ MeV we obtain, from equation (116), the value $t_{QCD+} \approx 1.08 \times 10^{-4}$ s which is valid (according to the assumptions made in the preceding paragraphs) for both the Bag Model and the Lattice Fit. Inserting this value into equation (119) one obtains $t_{QCD-} \approx 6.25 \times 10^{-5}$ s in the case of the Bag Model and $t_{QCD-} \approx 9.37 \times 10^{-5}$ s in the case of the Lattice Fit. In Figure 9 we present the curves for t_{QCD+} and t_{QCD-} as functions of the critical temperature T_c.

According to the Lattice Fit the sound speed decreases until it vanishes at some instant t_{QCD-}. In order to recover $c_s^2 = 1/3$ when $T \gg T_c$ we write equation (79) in the form

$$c_s^2 = \frac{1}{3}\left(1 - \frac{T_c}{T}\right)^{1-\gamma}. \quad (120)$$

For $T = T_c$ we have $c_s^2 = 0$ and for $T < T_c$ we get, once again, $c_s^2 = 1/3$. In Figure 10 we show expression (120), as well as the results obtained for quenched QCD (Figure 7), for $T \geq T_c$ with $T_c = 170$ MeV. The analytic approach given by

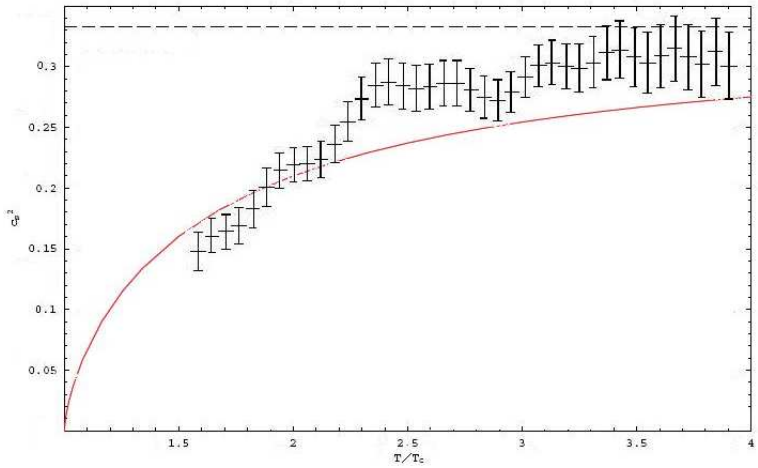

Figure 10: The behaviour of the sound speed c_s^2 as a function of T/T_c during the QCD transition according to the Lattice Fit model (solid line – equation 120) and the numerical results obtained from quenched QCD — adapted from Gupta (2003). The dashed line represents the ideal gas case, i.e., $c_s^2 = 1/3$. When $T = T_c$ the sound speed vanishes.

equation (120) and the numerical results obtained from quenched QCD both show a similar behaviour, in particular, when T gets below $\sim 2T_c$.

It is useful to know not only the interval during which $c_s = 0$, but also, the interval during which c_s^2 makes its way down from $1/3$ to zero. For this purpose we need to write c_s^2 as a function of time t. Inserting expression (53) into expression (120) we obtain

$$c_s^2(t) = \frac{1}{3}\left(1 - \frac{R(t)}{R(t_{QCD-})}\right)^{1-\gamma} \tag{121}$$

valid for $t \leq t_{QCD-}$ where t_{QCD-} corresponds to the beginning of the phase transition. Considering equation equation (49) we may write equation (121) in the form

$$c_s^2(t) = \frac{1}{3}\left[1 - \left(\frac{t}{t_{QCD-}}\right)^{1/2}\right]^{1-\gamma}. \tag{122}$$

Therefore, we define $T_1 > T_c$ as the temperature for which c_s^2 equals 95% of its 'background' value: $c_{s,0}^2 = 1/3$. This corresponds to some instant of time $t_1 < t_{QCD-}$. From equation (120), with $T_c = 170$ MeV and $\gamma = 1/3$, one obtains $T_1 \approx 2296$ MeV $\approx 13.5T_c$. Similarly, from equation (122), with $t_{QCD-} = 9.37 \times 10^{-5}$ s and $\gamma = 1/3$ one obtains $t_1 \approx 5.1 \times 10^{-7}$ s.

For the Crossover case we consider that the sound speed minimum value is attained for $t \approx t_{QCD+}$ (corresponding to $T \approx T_c$). During the QCD Crossover the Universe continues to be radiation–dominated with the scale factor given by equation (52). Inserting equation (52) into equation (53) we obtain an expression for the

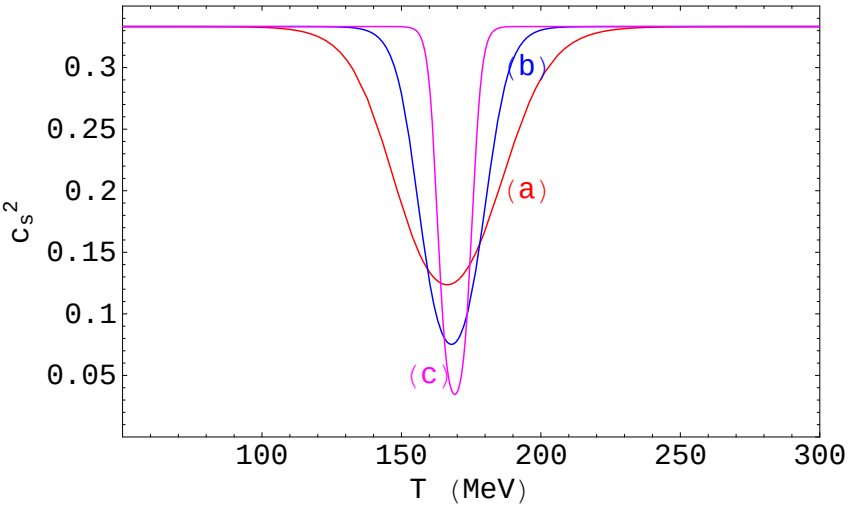

Figure 11: The sound speed $c_s^2(T)$ for the QCD Crossover with $T_c = 170$ MeV and different values for the parameter ΔT: (a) $\Delta T = 0.1T_c$, (b) $\Delta T = 0.05T_c$ and (c) $\Delta T = 0.02T_c$. Notice that the sound speed decreases around T_c but does not reach zero (with the exception of the limiting case $\Delta T \longrightarrow 0$ – see Figure 17).

temperature T as a function of the time t valid for the QCD Crossover:

$$T(t) = T_0 \left[\exp\left(c\sqrt{\frac{\Lambda}{3}}(t_{SN} - t_0) \right) \left(\frac{t_{eq}}{t_{SN}} \right)^{2/3} \left(\frac{t}{t_{eq}} \right)^{1/2} \right]^{-1} . \tag{123}$$

On the Bag Model and Lattice Fit cases, the temperature remains constant ($T = T_c$) for a while. The same does not occur during a Crossover where the temperature continues to decrease with time. Inserting expression (123) into equation (81) we obtain, for the speed of sound during the QCD Crossover, the following expression

$$c_s^2(t) = \left[3 + \frac{\Delta g T(t) \mathrm{sech}\left(\frac{T(t)-T_c}{\Delta T} \right)^2}{\Delta T \left(g_{HG} + g_{QGP} + \Delta g \tanh\left(\frac{T(t)-T_c}{\Delta T} \right) \right)} \right]^{-1} . \tag{124}$$

In Figure 11 we show the curve for c_s^2 as a function of temperature with $T_c = 170$ MeV and with ΔT assuming different values. As it was already mentioned, when $\Delta T \longrightarrow 0$ we recover the Bag Model sound speed profile. Notice that, for a Crossover, the speed of sound decreases but does not reach zero. The minimum value for the sound speed is attained for $T \approx T_c$. Thus, considering $T = T_c$ in equation (81) we obtain the following expression giving an approximate value for the minimum sound speed during a QCD Crossover

$$c_{s,min}^2 \approx \left[3 + \frac{g_{QGP} - g_{HG}}{\frac{\Delta T}{T_c}(g_{QGP} + g_{HG})} \right]^{-1} . \tag{125}$$

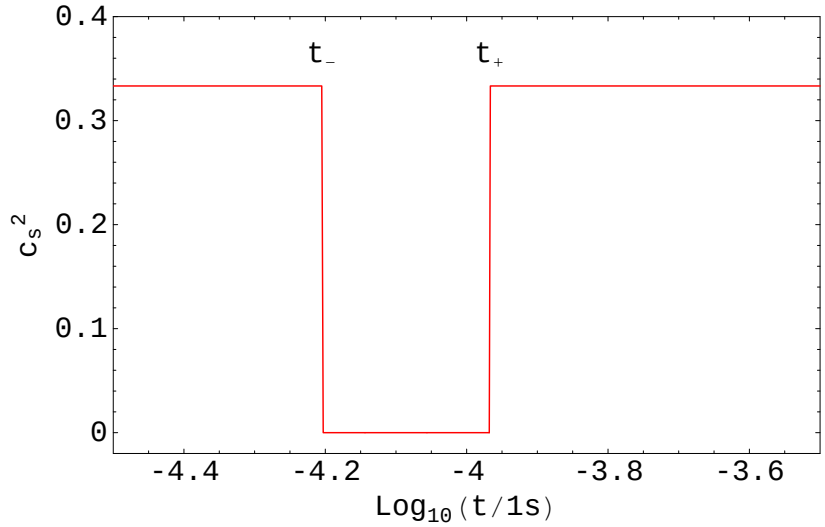

Figure 12: The sound speed $c_s^2(t)$ for the QCD phase transition according to the Bag Model with $T_c = 170$ MeV. During the coexistence phase, which occurs between the instants $t_{QCD-} = 6.25 \times 10^{-5}$ s and $t_{QCD+} = 1.08 \times 10^{-4}$ s, the sound speed drops to zero.

In Figure 17 we have the curve for $c^2_{s,min}$ as a function of the ΔT parameter when $T_c = 170$ MeV. Notice that when $\Delta T = 0$ we have $c^2_{s,min} = 0$ and when $\Delta T = 0.1T_c$ we have $c^2_{s,min} \approx 0.38 c^2_{s,0} \approx 0.13$ ($c^2_{s,0} = 1/3$ is the sound speed for an ideal gas).

For the QCD Crossover we define an effective duration as the interval for which the sound speed stays below 95% of its 'background' value $c^2_{s,0} = 1/3$. We want to determine the temperatures T_1 and T_2 such that

$$c_s^2(T_1) = c_s^2(T_2) = 0.95 c^2_{s,0}, \quad T_2 < T_c < T_1.$$

The duration or width of the QCD Crossover in terms of temperature is, then, given by $T_2 - T_1$. It is useful to have also the width of the QCD Crossover in terms of time. In that case, the transition width will be given by $t_2 - t_1$ with the instants t_1 and t_2 satisfying the condition

$$c_s^2(t_1) = c_s^2(t_2) = 0.95 c^2_{s,0} \quad , t_1 < t_c < t_2$$

where $t_c = t_{QCD+}$.

We are now able to present the sound speed profile for the QCD phase transition for a given temperature T_c as a function of time. In Figure 12, 13 and 14 we show the curve $c_s^2(t)$ for, respectively, the Bag Model, the Lattice Fit and the Crossover for a QCD temperature of $T_c = 170$ MeV.

In Table 4 we present a sum up of the results for the duration of the QCD phase transition according to the different models.

In Figure 15 we show the evolution of the scale factor $R(t)$ during the QCD transition according to the different models.

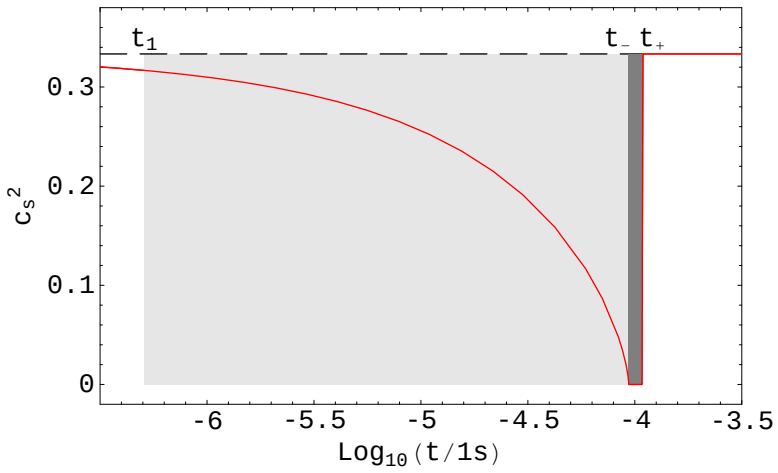

Figure 13: The sound speed $c_s^2(t)$ for the QCD phase transition according to the Lattice Fit with $T_c = 170$ MeV. During the coexistence phase, which occurs between the instants $t_{QCD-} = 9.37 \times 10^{-5}$ s and $t_{QCD+} = 1.08 \times 10^{-4}$ s the sound speed drops to zero (dark gray zone). For $t_1 = 5.1 \times 10^{-7}$ s the sound speed equals 95% of its 'background' value. The dashed line represents the ideal gas case for which $c_s^2 = 1/3$.

Table 4: The width of the QCD phase transition according to the Bag Model, Lattice Fit and Crossover when $T_c = 170$ MeV. The sound speed vanishes in the interval $t_{QCD-} < t < t_{QCD+}$ and is below 95% of its 'background' value $c_{s,0}^2 = 1/3$ in the interval $t_1 < t < t_2$. Here Δt represents the interval during which the sound speed value is less than 95% of $\sqrt{1/3}$.

Model	$t_1(\times 10^{-5}$ s)	$t_{QCD-}(\times 10^{-5}$ s)	$t_{QCD+}(\times 10^{-5}$ s)	$t_2(\times 10^{-5}$ s)	$\Delta t(\times 10^{-5}$ s)	$\frac{\Delta t}{\Delta t_{BAG}}$
Bag	–	6.25	10.8	–	4.6	1
Lattice	0.051	9.37	10.8	–	10.7	2.33
Crossover ($\Delta T = 0.01 T_c$)	10.1	–	–	11.7	1.6	0.35
Crossover ($\Delta T = 0.05 T_c$)	8.5	–	–	15.0	6.5	1.41
Crossover ($\Delta T = 0.1 T_c$)	7.1	–	–	19.6	12.5	2.72

2.2 EW phase transition

2.2.1 Crossover (SMPP)

We adopt, for the EW Crossover, the results obtained for the QCD Crossover (Section 1.2.1). Thus, we write the entropy density as (cf. equation 80)

$$s(T) = \frac{2\pi^2}{45} g_{EW} T^3 \left[1 + \frac{1}{2} \frac{\Delta g}{g_{EW}} \left(1 + \tanh \left(\frac{T - T_c}{\Delta T} \right) \right) \right] \tag{126}$$

where $\Delta g = 96.25 - 95.25 = 1$ and $g_{EW} = 95.25$ is the number of degrees of freedom after the EW Crossover (cf. Section 1.1.6).

The other thermodynamic quantities can be derived from equation (126). For example, inserting the entropy density (126) into equation (12) we obtain, for the sound

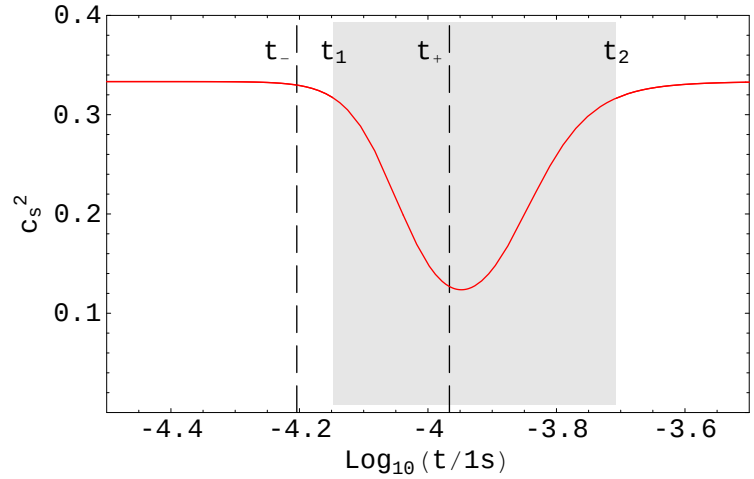

Figure 14: The sound speed $c_s^2(t)$ for the QCD phase transition in the case of a Crossover with a reference temperature $T_c = 170$ MeV and $\Delta T = 0.1 T_c$. The dashed lines represent, for reference, the location of the first–order phase transition according to the Bag Model ($t_{QCD-} = 6.25 \times 10^{-5}$ s, $t_{QCD+} = 1.08 \times 10^{-4}$ s). Between the instants $t_1 \approx 7.1 \times 10^{-5}$ s and $t_2 \approx 1.96 \times 10^{-4}$ s the sound speed stays below 95% of its 'background' value ($c_{s,0}^2 = 1/3$).

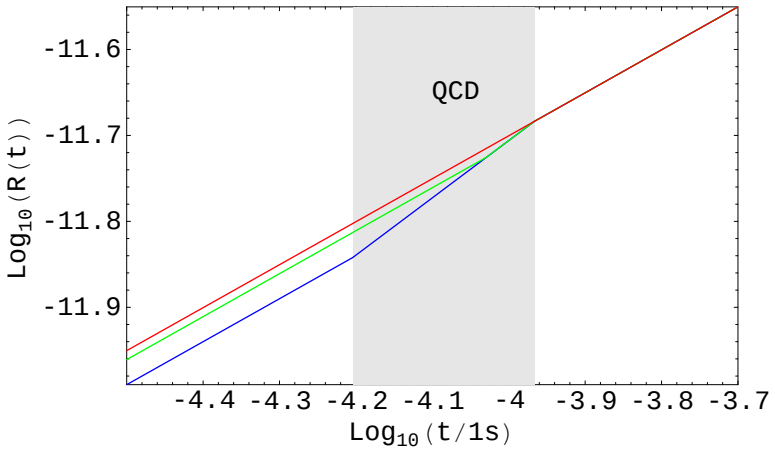

Figure 15: The scale factor during the QCD transition as a function of time. The gray region corresponds to the dust–like epoch, according to the Bag Model. The curves correspond, from top to bottom, to the: crossover case ($n_{qcd} = 1/2$), Lattice Fit ($n_{qcd} = 2/3$ and $t_{QCD-} = 9.37 \times 10^{-5}$ s) and Bag Model ($n_{qcd} = 2/3$ and $t_{QCD-} = 6.25 \times 10^{-5}$ s).

speed during a EW Crossover, the following result (cf. equation 81)

$$c_s^2(T) = \left[3 + \frac{\Delta g T \mathrm{sech}\left(\frac{T-T_c}{\Delta T}\right)^2}{\Delta T \left(g_{EW} + g'_{EW} + \Delta g \tanh\left(\frac{T-T_c}{\Delta T}\right)\right)} \right]^{-1} \tag{127}$$

where $g'_{EW} = 96.25$ is the number of degrees of freedom existing before the EW Crossover.

The value of ΔT must be chosen in order to fit eventual results. The lowest value for δ_c during the EW Crossover is attained when $\Delta T \approx 0.013 T_c$ (see Section 4.4).

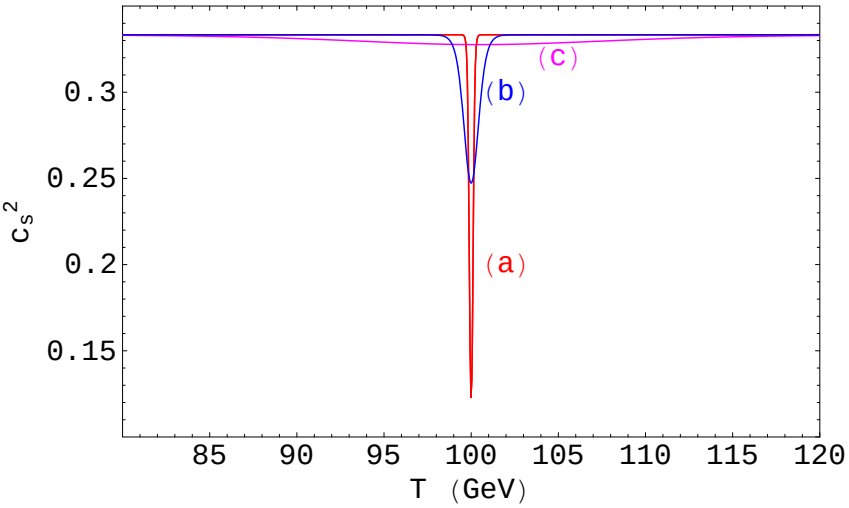

Figure 16: The sound speed $c_s^2(T)$ for the EW Crossover with $T_c = 100$ GeV and: (a) $\Delta T = 0.001T_c$; (b) $\Delta T = 0.005T_c$; (c) $\Delta T = 0.1T_c$. Notice that the sound speed decreases around T_c but does not reaches zero (with the exception of the limiting case $\Delta T \longrightarrow 0$).

In Figure 16 we show the curve for c_s^2 as a function of the temperature with $T_c = 100$ GeV and with ΔT assuming different values. Notice that when $\Delta T \longrightarrow 0$ the sound speed aproaches zero but only for an instant. For larger values of ΔT the sound speed decreases less. The minimum value for the sound speed is attained for $T \approx T_c$. Thus, considering $T = T_c$ in equation (127), we obtain the following expression giving an approximate value for the minimum sound speed during an EW Crossover

$$c_{s,min}^2 \approx \left[3 + \frac{g'_{EW} - g_{EW}}{\frac{\Delta T}{T_c}(g'_{EW} + g_{EW})}\right]^{-1} . \tag{128}$$

In Figure 17 we show the curve for $c_{s,min}^2$ as a function of the ΔT parameter for the EW Crossover ($T_c = 100$ GeV) and, for comparison purposes, the corresponding curve for the QCD Crossover ($T_c = 170$ MeV). It is clear that during the EW Crossover the effects due to the reduction in the sound speed are less obvious than for the QCD case.

For the EW Crossover case, we consider that the sound speed minimum value is attained for $t \approx t_{EW+}$ (corresponding to $T \approx T_c$). During the EW Crossover the Universe continues to be radiation–dominated with the scale factor given by equation (52). Recalling equation (123) that gives the temperature as a function of time during the EW Crossover and inserting it into equation (127), we obtain, for the speed of sound during the EW Crossover, the following expression

$$c_s^2(t) = \left[3 + \frac{\Delta g T(t) \mathrm{sech}\left(\frac{T(t)-T_c}{\Delta T}\right)^2}{\Delta T\left(g_{EW} + g'_{EW} + \Delta g \tanh\left(\frac{T(t)-T_c}{\Delta T}\right)\right)}\right]^{-1} . \tag{129}$$

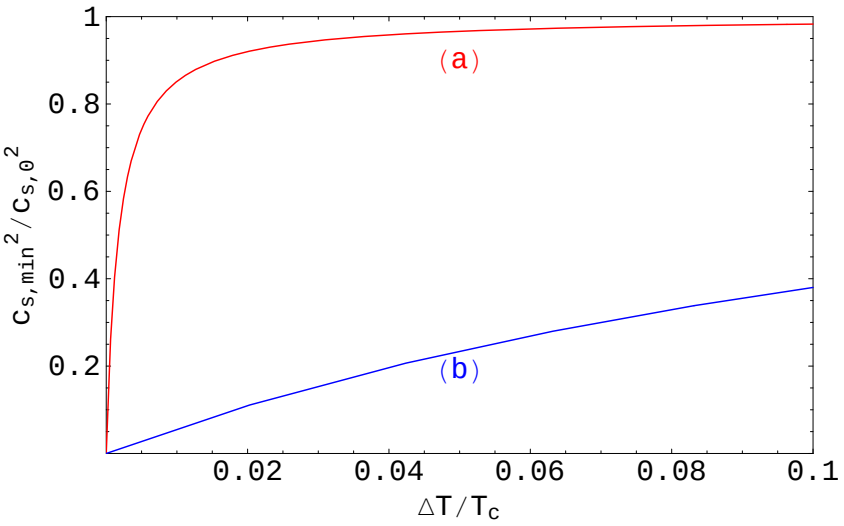

Figure 17: The minimum value attained by the sound speed, $c^2_{s,min}$, as a function of the parameter ΔT during: (a) the EW Crossover (see equation 128); (b) the QCD Crossover (see equation 125).

Taking into account that $T_c = 100$ GeV $\approx 7.7 \times 10^{14}$ K, we obtain, from equation (123), that $t_c \approx 3.12 \times 10^{-10}$ s. This corresponds to the instant of time when the sound speed reaches its minimum value.

We consider the effective duration of the QCD Crossover the interval for which the sound speed stays below[21] 99% of its 'background' value $c^2_{s,0} = 1/3$. When $\Delta T = 0.013 T_c$ and $t_c = 3.12 \times 10^{-10}$ s this occurs between the instants $t_1 = 2.97 \times 10^{-10}$ s and $t_2 = 3.29 \times 10^{-10}$ s.

2.2.2 Bag Model (MSSM)

Now we are going to determine the duration of the EW phase transition in the case of a Bag model. We need to define a specific beginning $t = t_{EW-}$ as well as a specific end $t = t_{EW+}$ to the EW transition. Here t_{EW-} and t_{EW+} are the limits for the time interval during which the sound speed vanishes. Although the temperature of the Universe is not constant during the EW phase transition, is stays all the time near the critical value T_c. Thus, the value of $R(t_{EW+})$ (i.e. the value of the scale factor at the end of the transition) is given, approximately, by (see equation 53)

$$R(t_{EW+}) \approx \frac{T_0}{T_c}. \tag{130}$$

On the other hand, for $t = t_{EW+}$ equation (52) becomes

$$R(t_{EW+}) = \exp\left(c\sqrt{\frac{\Lambda}{3}}(t_{SN} - t_0)\right)\left(\frac{t_{eq}}{t_{SN}}\right)^{2/3}\left(\frac{t_{EW+}}{t_{eq}}\right)^{1/2}. \tag{131}$$

[21] We do not consider 95%, as we did in the QCD case, because the reduction of the sound speed during the EW Crossover is much less significant than it was in the QCD case.

Inserting equation (130) into equation (131) we obtain, for the instant when the transition ends

$$t_{EW+} = t_{SN}\left(\frac{t_{eq}}{t_{SN}}\right)^{-1/3} \exp\left(-2c\sqrt{\frac{\Lambda}{3}}(t_{SN}-t_0)\right)\left(\frac{T_0}{T_c}\right)^2. \tag{132}$$

The evolution of the scale factor while the high and low temperature phases coexist in a first–order EW phase transition, i.e., during the $c_s^2 = 0$ part, may be determined by the entropy conservation as long as we assume that the transition evolves close to equilibrium (e.g. Jedamzik & Niemeyer, 1999). Thus, we here adopt equation (117) from the QCD case, writing it in the form

$$\Delta R = \frac{R(t_{EW+})}{R(t_{EW-})} = \left(\frac{s(t_{EW-})}{s(t_{EW+})}\right)^{1/3} = \left(1+\frac{\Delta g}{g_{EW}}\right)^{1/3}. \tag{133}$$

When $t = t_{EW-}$ equation (50) becomes

$$R(t_{EW-}) = \exp\left(c\sqrt{\frac{\Lambda}{3}}(t_{SN}-t_0)\right)\left(\frac{t_{eq}}{t_{SN}}\right)^{2/3}\left(\frac{t_{EW+}}{t_{eq}}\right)^{1/2}\left(\frac{t_{EW-}}{t_{EW+}}\right)^{2/3} \tag{134}$$

where we consider $n_{ew} = 2/3$ and $n_{qcd} = 1/2$. From equations (131), (133) and (134) we obtain

$$t_{EW-} = \frac{t_{EW+}}{\sqrt{\Delta R^3}}. \tag{135}$$

Considering $T_c = 100$ GeV we obtain, with the help of equation (132), the value $t_{EW+} = 3.15 \times 10^{-10}$ s. In order to determine the value of t_{EW-} one must determine first the value of ΔR. This is a problem, because we need to know the value of $\Delta g = g'_{EW} - g_{EW}$ (see equation 133). We consider, for g_{EW} (i.e., the number of degrees of freedom at the end of the transition), in accordance with the SMPP, the value $g_{EW} = 95.25$. However, we do not have any clue for the real value of g'_{EW}. In the context of the MSSM it may be as large as 228.75 when all particles and superpartners are present (cf. Table D-5) and, in the context of the SMPP it is $g'_{EW} = 96.25$. Within this range of values ΔR varies between ≈ 1.0035 and ≈ 1.3392. Inserting these values into equation (135) with $t_{EW+} = 3.15 \times 10^{-10}$ s it turns out that t_{EW-} should be between 2.03×10^{-10} s and 3.13×10^{-10} s.

We consider here $t_{EW-} = 2.3 \times 10^{-10}$ s, corresponding to $\Delta g \approx 80$. In Figure 18 we show the sound speed profile for the EW transition, according to these results. It must be noted, however, that the value of t_{EW-} was introduced only with the purpose of giving an example. At this stage, we do not have any observational evidence supporting this or any other value. In fact, we do not have any conclusive results on the existence of extensions of the SMPP beyond the EW cosmological phase transition.

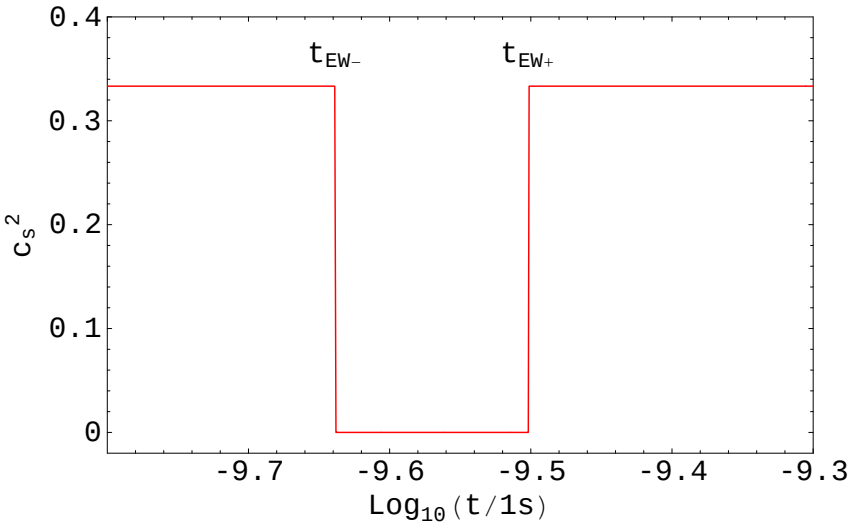

Figure 18: The sound speed $c_s^2(t)$ for the EW phase transition according to the Bag Model with $T_c = 100$ GeV. During the coexistence phase, which occurs between the instants $t_{EW-} = 2.3 \times 10^{-10}$ s (see text for more details) and $t_{EW+} = 3.15 \times 10^{-10}$ s, the sound speed drops to zero.

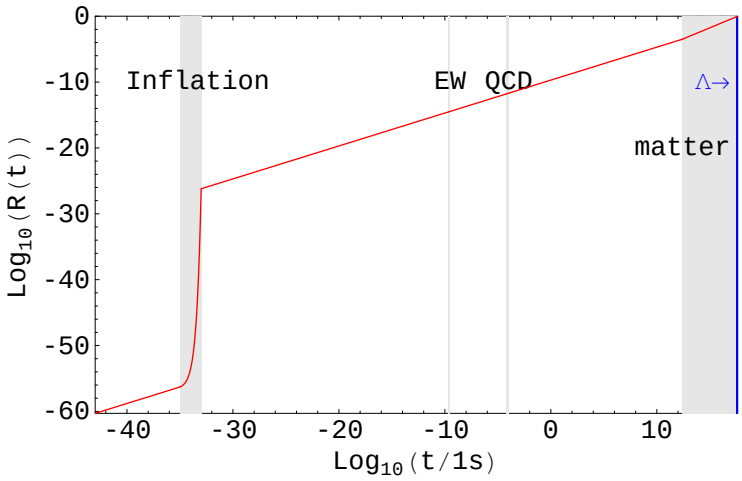

Figure 19: The scale factor as a function of time. The gray regions correspond to the inflationary period, the EW and QCD transitions and the matter–dominated era. In blue (right side) we have the dark energy–dominated era. The other regions (in white) correspond to radiation–dominated periods.

In Table 5 we show the evolution of the scale factor taking into account the QCD and the EW phase transitions. Notice that some of the values may be slightly different, depending in the values one chooses for n_{qcd}, n_{ew} and t_{QCD-}. In Figure 19 we show $R(t)$ for the entire Universe timeline (i.e., from the Planck time t_p up to the present time t_0).

Table 5: The Scale Factor (equations 45–51) for different instants of time during the evolution of the Universe: t_p (Planck time), t_i (beginning of inflation), t_e (end of inflation), t_{EW-} (beginning of the EW transition), t_{EW+} (end of the EW transition), t_{QCD-} (beginning of the QCD transition), t_{QCD+} (end of the QCD transition), t_{eq} (last scattering surface), t_{SN} (the instant when the Universe starts to accelerate) and t_0 (present time). Notice that we have indicated two values for t_{QCD-}. The first one corresponds to the Bag Model results and the second one to the Lattice Fit results.

	t(s)	$R(t)$	
t_p	$\sim 10^{-43}$	$\sim 10^{-60}$	
t_i	$\sim 10^{-35}$	$\sim 10^{-56}$	
t_e	$\sim 10^{-33}$	$\sim 10^{-27}$	
t_{EW-}	2.30×10^{-10}	2.9×10^{-15}	
t_{EW+}	3.15×10^{-10}	3.5×10^{-15}	
t_{QCD-}	6.25×10^{-5}	1.4×10^{-12}	(QCD Bag)
t_{QCD-}	9.37×10^{-5}	1.9×10^{-12}	(QCD Lattice)
t_{QCD+}	1.08×10^{-4}	2.1×10^{-12}	
t_{eq}	2.5×10^{12}	3.2×10^{-4}	
t_{SN}	2.8×10^{17}	0.73	
t_0	4.3×10^{17}	1	

2.3 Electron–positron annihilation

Taking into account that the value of Δg for the e^+e^- annihilation epoch is very small (cf. Section 1.2.3) we assumed that during this period the sound speed has a 'Crossover'–like profile. Doing so we adopt for the sound speed during the e^+e^- annihilation process an expression similar to (81) or (127). Thus, we consider

$$c_s^2(T) = \left[3 + \frac{\Delta g T \mathrm{sech}\left(\frac{T-T_c}{\Delta T}\right)^2}{\Delta T\left(g_{ep} + g'_{ep} + \Delta g \tanh\left(\frac{T-T_c}{\Delta T}\right)\right)}\right]^{-1} \tag{136}$$

where $g'_{ep} = 10.75$ and $g_{ep} = 7.25$. We also consider a critical temperature $T_c = 1$ MeV. The parameter ΔT must be determined in order to achieve results: reductions of order $10 - 20\%$ in the sound speed must take place.

The minimum value for the sound speed is attained for $T \approx T_c$. Considering $T = T_c$ in equation (136) we obtain the following expression giving an approximate value for the minimum speed of sound during the e^+e^- annihilation process:

$$c_{s,min}^2 \approx \left[3 + \frac{g'_{ep} - g_{ep}}{\frac{\Delta T}{T_c}(g'_{ep} + g_{ep})}\right]^{-1}. \tag{137}$$

Table 6: The reduction of the speed of sound during the electron–positron annihilation and the corresponding values for the parameter ΔT ($T_c = 1$ MeV).

c_s reduction	$\frac{\Delta T}{T_c}$
20%	0.115
15%	0.169
10%	0.276
5%	0.600

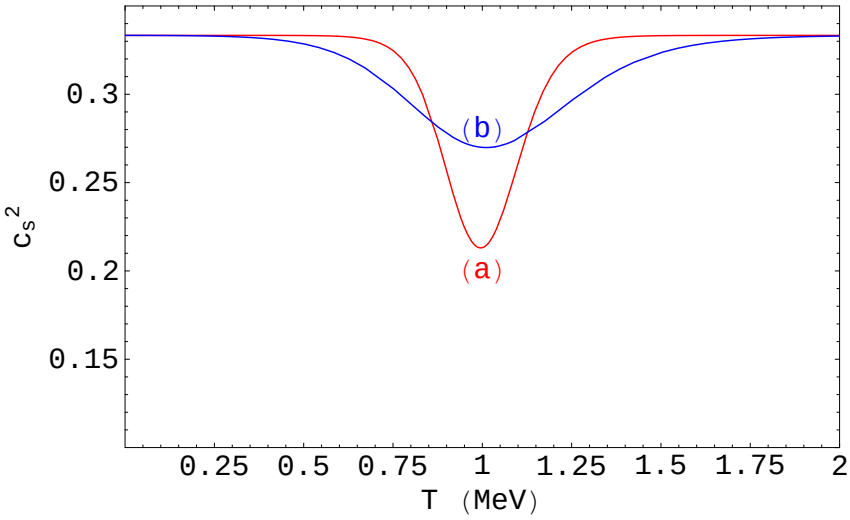

Figure 20: The sound speed $c_s^2(T)$ during the electron–positron annihilation with $T_c = 1$ MeV and: (a) $\Delta T = 0.115 T_c$ (reduction of 20%), (b) $\Delta T = 0.276 T_c$ (reduction of 10%).

Assuming different reductions, in the range 5%–20%, in the value of the speed of sound we have obtained, from equation (137), the corresponding values for the parameter ΔT (see Table 6).

In Figure 20 we show the curve for the sound speed as a function of the temperature with $T_c = 1$ MeV and with ΔT assuming the values corresponding to a reduction of 10% and 20% in the sound speed value (Table 6). For the temperature as a function of time during the electron–positron annihilation epoch we recover here equation (123). Inserting expression (123) into equation (136) we obtain, for the sound speed during the electron–positron annihilation, the following:

$$c_s^2(t) = \left[3 + \frac{\Delta g T(t) \mathrm{sech}\left(\frac{T(t)-T_c}{\Delta T}\right)^2}{\Delta T \left(g_{ep} + g'_{ep} + \Delta g \tanh\left(\frac{T(t)-T_c}{\Delta T}\right)\right)} \right]^{-1} , \tag{138}$$

with $T_c = 1$ MeV. Taking into account that 1 MeV $\approx 7.7 \times 10^9$ K we obtain from

Table 7: The width of the cosmological electron–positron annihilation in terms of time as a function of the parameter ΔT (cf. equation 138) when $T_c = 1$ MeV. t_1 represents the instant when the sound speed gets less than 99% of its 'background' value 1/3 and t_2 represents the instant when the sound speed reaches, once again, 99% of 1/3 ($t_1 < t < t_2$). The effective width of the process is given by $t_2 - t_1$.

$\frac{\Delta T}{T_c}$	t_2(s)	t_1(s)	$t_2 - t_1$(s)
0.115	7.39	1.71	5.61
0.169	8.67	1.49	7.18
0.276	15.42	1.08	14.3
0.600	50.0	0.57	49.4

equation (123) $t_c \approx 3.15$ s. This corresponds to the instant of time for which the speed of sound reaches its minimum value.

We have considered as a reasonable effective duration for the e^+e^- annihilation process the interval for which the sound speed stays below 99% of its 'background' value $c_{s,0}^2 = 1/3$. With the help of equations (136) and (138) we have obtained this effective width for the values of the parameter ΔT that we have already considered in Table 6. The results obtained are shown Table 7.

3 Fluctuations and phase transitions

3.1 QCD phase transition

3.1.1 Bag Model

Let us consider how a fluctuation evolves in the presence of a QCD phase transition according to the Bag Model. Here we follow very closely the model proposed by Cardall & Fuller (1998). Let ρ_1 and ρ_2 ($\rho_2 < \rho_1$) represent the energy densities at the start and at the end of the phase transition, respectively. Here we are assuming, for simplicity, that we have for $\rho > \rho_1$ a pure quark–gluon radiation plasma ($w = 1/3$), for $\rho < \rho_2$ a pure hadron radiation plasma ($w = 1/3$) and for $\rho_2 < \rho < \rho_1$ a mixed phase that can be treated as dust ($w = 0$).

Fluctuation dynamics in the presence of a phase transition are dependent on the strength of the transition, as well as on the exact time t_k at which the fluctuation crosses the horizon; in particular, if shortly before onset, during, or shortly after completion of the transition (Jedamzik & Niemeyer, 1999). In order to characterize the horizon crossing time and the turnaround point in terms of density we introduce here the quantities, x and y, defined as

$$x = \frac{\overline{\rho}_k}{\rho_1} \tag{139}$$

$$y = \frac{\rho_1}{\rho_2}. \tag{140}$$

When $x = 1$ ($\overline{\rho}_k = \rho_1$) we are at the beginning of the phase transition and when $x = y^{-1}$ ($\overline{\rho}_k = \rho_2$) we are at the end of the phase transition. A given fluctuation has $x > 1$ if it crosses the horizon before the beginning of the phase transition, $y^{-1} < x < 1$ if it crosses the horizon during the phase transition and $x < y^{-1}$ if it crosses the horizon after the completion of the phase transition. For each situation we must consider also the possible locations of the turnaround point. As a result, we have six different classes of density fluctuations as shown in Table 8.

It is very useful to use x as a function of time. We can obtain this with the help of equation (74). We start with the expressions for ρ_1 and ρ_2

$$\rho_1 = \rho(t_{QCD-}) = \frac{1}{3}\frac{\pi^2}{30} T_c^4 \left(4 g_{QGP} - g_{HG}\right), \tag{141}$$

$$\rho_2 = \rho(t_{QCD+}) = \frac{1}{3}\frac{\pi^2}{30} T_c^4 \left[4 g_{QGP} \left(\frac{t_{QCD-}}{t_{QCD+}}\right)^2 - g_{HG}\right],$$

Table 8: Classification of overdense regions according to the state of matter at the horizon crossing time and at the turnaround point for the QCD phase transition (Cardall & Fuller, 1998).

Class	Horizon crossing phase	Turnaround phase
A	quark–gluon	quark–gluon
B	quark–gluon	mixed
C	quark–gluon	hadron
D	mixed	mixed
E	mixed	hadron
F	hadron	hadron

where we have used, in the case of ρ_2, equation (48) for $R(t_{QCD+})$ and equation (49) for $R(t_{QCD-})$. We can now write, with the help of equations (74) and (141):

$$x(t) = \frac{\rho(t)}{\rho_1} = \frac{4g_{QGP}\left(\frac{R(t_{QCD-})}{R(t)}\right)^3 - g_{HG}}{4g_{QGP} - g_{HG}} \tag{142}$$

where $R(t_{QCD-})$ is given by equation (49) and $R(t)$ is given by: i) equation (47) if $x \leq y^{-1}$; ii) equation (48) if $y^{-1} < x < 1$; iii) equation (49) if $x \geq 1$. The value of y, which defines the end of the transition, can now be determined evaluating $x(t_{QCD+})$. It turns out that for the Bag Model case, with $g_{QGP} = 61.75$ and $g_{HG} = 21.25$, one obtains

$$y^{-1} = x(t_{QCD+}) = \frac{4g_{QGP}\left(\frac{t_{QCD-}}{t_{QCD+}}\right)^2 - g_{HG}}{4g_{QGP} - g_{HG}} \approx 0.272. \tag{143}$$

Notice that, equation (142) is to be used only during the first–order QCD transition: more precisely, in the neighborhood of the transition. For example, if one considers $x \ll y^{-1}$ then x will eventually become negative which does not make sense.

It will also be useful to know the expression which gives the turnaround point for each class of fluctuations. For that we first deduce a general expression for the turnaround point. The density $\rho(\tau)$ can be written as (cf. Section 1.1.1, equation 9)

$$\rho(\tau) = K_s S(\tau)^{-3(1+w)} \tag{144}$$

where K_s is a constant and $S(\tau)$ represents the evolution of the scale factor for the perturbed region. In the case of $\rho_k(t_k)$ we have

$$\rho_k = K_k R_k^{-3(1+w_k)} \tag{145}$$

where K_k is a constant and w_k is the adiabatic index when the fluctuation crosses the horizon. Inserting expressions (144) and (145) into equation (58) we obtain

$$\left(\frac{dS}{d\tau}\right)^2 = \frac{8\pi G}{3}\frac{K_s}{1+\delta_k}\left(\frac{1+\delta_k}{S(\tau)^{1+3w}} - \frac{K_k}{K_s}\frac{\delta_k}{R_k^{1+3w_k}}\right). \tag{146}$$

The turnaround point is reached when the perturbed region stops expanding, i.e., when $dS/d\tau = 0$. Thus, the evaluation of equation (146) at the turnaround point gives

$$S_c^{1+3w_c} = \frac{K_s}{K_k}R_k^{1+3w_k}\left(\frac{1+\delta_k}{\delta_k}\right) \tag{147}$$

where the subscript c denotes a quantity evaluated at the turnaround point.

For classes A and F, which evolve completely during a radiation–dominated phase ($w = w_k = w_c = 1/3$), we obtain, taking into account that $S_k = R_k$, that $K_s/K_k = 1$. In this case we have, from equation (147) the result

$$S_{c,A} = S_{c,F} = R_k\left(\frac{1+\delta_k}{\delta_k}\right)^{1/2}. \tag{148}$$

For class D, which evolves completely during the dust phase ($w = w_k = w_c = 0$) we have, according to equation (147)

$$S_{c,D} = R_k\frac{1+\delta_k}{\delta_k}. \tag{149}$$

For classes B, C and E the value of the adiabatic index w varies during the fluctuation. For example, in the case of class B we have $w_k = 1/3$ and $w_c = 0$. The change in the value of w occurs when $t = t_{QCD-}$, or equivalently, when $x = 1$ (i.e., at the beginning of the transition). Considering that $\rho(\tau)$ is a continuous function, we write

$$K_k S_1^{-3(1+w_k)} = K_s S_1^{-3(1+w_c)}$$

where S_1 represents the size of the overdense region at the beginning of the transition. This leads to

$$\frac{K_s}{K_k} = \frac{S_1^{3w_c}}{S_1^{3w_k}} = \frac{1}{S_1}. \tag{150}$$

In the case of class E we have $w_k = 0$ and $w_c = 1/3$. Now the change of w occurs when $t = t_{QCD+}$ or, equivalently, when $x = y^{-1}$ (i.e., at the end of the transition). The continuity of the density, ρ, now leads to

$$\frac{K_s}{K_k} = \frac{S_2^{3w_c}}{S_2^{3w_k}} = S_2 \tag{151}$$

where S_2 represents the size of the overdense region at the end of the transition. Finally, in the case of fluctuations of class C, we have $w_k = w_c = 1/3$ with an intermediate period during which $w = w' = 0$. Applying the continuity condition for ρ successively at $t = t_{QCD+}$ and $t = t_{QCD-}$ we obtain, in the case of class C

$$\frac{K_s}{K_k} = \frac{S_2^{3w_c}}{S_1^{3w_k}} \frac{S_1^{3w'}}{S_2^{3w'}} = \frac{S_2}{S_1}. \tag{152}$$

The expression for S_1, which is valid and useful for fluctuations of classes B and C, can be obtained considering that ρ_1 is reached from radiation domination (i.e. $\rho_1 \propto S_1^{-4}$ and $\rho_k \propto R_k^{-4}$). From energy conservation we have the condition $\rho_1 S_1^4 = \rho_k R_k^4$ which can be combined with equation (55) in order to obtain

$$S_1 = x^{1/4}(1+\delta_k)^{1/4} R_k. \tag{153}$$

Considering the energy conservation during the dust–like phase (i.e. $\rho_1 \propto S_1^{-3}$ and $\rho_2 \propto S_2^{-3}$) and recalling that $y = \rho_1/\rho_2$ we get the useful relation

$$\frac{S_2}{S_1} = y^{1/3}. \tag{154}$$

On the other hand, an expression for S_2 suitable for fluctuations of class E, can be obtained considering that ρ_2 is reached from the dust–like phase (i.e. $\rho_2 \propto S_2^{-3}$ and $\rho_k \propto R_k^{-3}$). From energy conservation we have the condition $\rho_2 S_2^3 = \rho_k R_k^3$ which can be combined with equation (55) in order to obtain

$$S_{2_E} = (xy)^{1/3}(1+\delta_k)^{1/3} R_k. \tag{155}$$

Finally, an expression for S_2 suitable for fluctuations of class F, can be obtained considering the energy conservation in a radiation–dominated universe (i.e. $\rho_2 \propto S_2^{-4}$ and $\rho_k \propto R_k^{-4}$) yelding

$$S_{2_F} = (xy)^{1/4}(1+\delta_k)^{1/4} R_k. \tag{156}$$

We are now ready to determine expressions for the turnaround points of classes B, C and E. From equation (147), with the constant K_s/K_k given by equation: (150)–class B, (152)–class C, and (151)–class E; and with S_1 given by equation (153) and S_2 given by equation (154) in the case of fluctuations of class C and by equation (155) in the case of fluctuations of class E, we obtain

$$S_{c,B} = R_k x^{-1/4} \frac{(1+\delta_k)^{3/4}}{\delta_k}, \tag{157}$$

$$S_{c,C} = R_k y^{1/6} \left(\frac{1+\delta_k}{\delta_k}\right)^{1/2}, \text{ and} \tag{158}$$

$$S_{c,E} = R_k (xy)^{1/6} \frac{(1+\delta_k)^{2/3}}{\delta_k^{1/2}}. \tag{159}$$

The separation between classes A,B,C and classes D,E is given by the condition $\rho_1 = \rho_k$. With the help of equation (55) this becomes

$$\delta_k = x^{-1} - 1. \tag{160}$$

On the other hand the separation between classes D,E and class F is given by the condition $\rho_2 = \rho_k$. With the help of equation (55) this becomes

$$\delta_k = (xy)^{-1} - 1. \tag{161}$$

The separation between classes A and B can be obtained noting that what distinguishes these classes is the location of the turnaround point. Thus, considering $S_{c,A}$ (equation 148) equal to $S_{c,B}$ (equation 157), we obtain

$$x = \frac{1+\delta_k}{\delta_k^2}. \tag{162}$$

The same idea can be applied in order to determine the separation between classes B and C. Thus, considering $S_{c,B} = S_{c,C}$ we obtain

$$xy^{2/3} = \frac{1+\delta_k}{\delta_k^2}. \tag{163}$$

Finally, the separation between classes D and E can be determined considering $S_{c,D} = S_{c,E}$ which yields

$$xy = \frac{(1+\delta_k)^2}{\delta_k^3}. \tag{164}$$

Solving the equation $S_{c,C} = S_{c,D}$ we obtain

$$y = \left(\frac{1+\delta_k}{\delta_k} \right)^3 \tag{165}$$

which means that classes C and D have only a single point in common on the (δ,x) plane. Putting $y^{-1} = 0.272$ (cf. equation 143) it turns out that $\delta_k \approx 1.84$. This result means that class D fluctuations do not exist for $\delta_k < 1.84$ and that class C fluctuations do not exist for $\delta_k > 1.84$.

In Figure 21 we represent the regions in the (δ_k, $\log_{10} x$) plane corresponding to the classes of perturbations listed in Table 8. Notice that we must distinguish

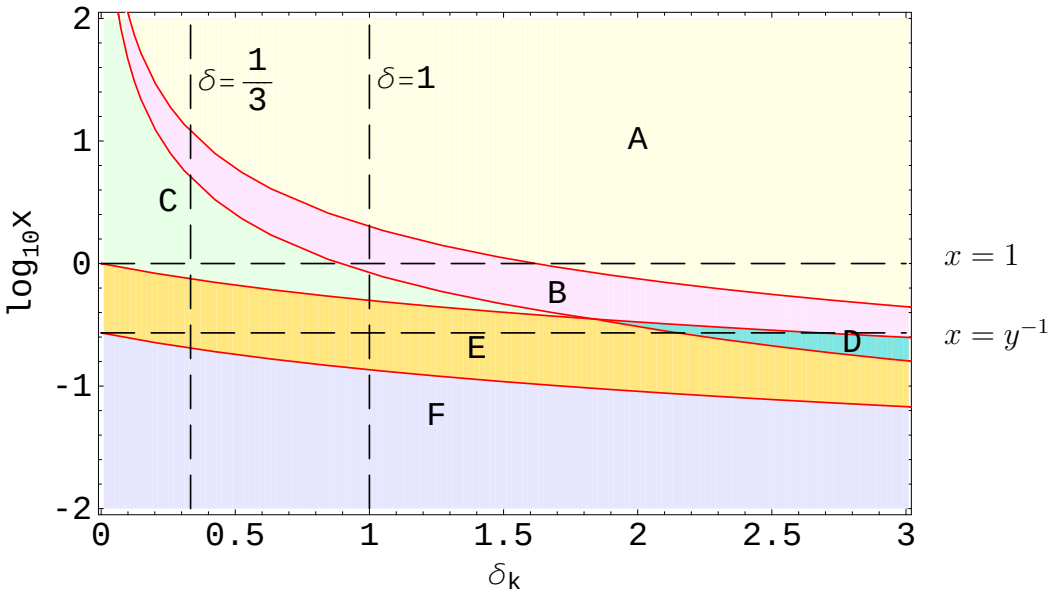

Figure 21: Regions in the (δ_k, $\log_{10} x$) plane corresponding to the classes of perturbations listed in Table 8 for the QCD Bag Model case. The variable x identifies the epoch when a perturbation enters the horizon: $x > 1$ ($x < 1$) corresponds to overdense regions that enter the horizon before (after) the average cosmological density begins the transition from the QGP to the HG. The quantity δ_k is the overdensity of the perturbation at horizon crossing. A PBH will form if $1/3 \leq \delta_k < 1$ (adapted from Cardall & Fuller, 1998).

between the average cosmological background and the state of matter on a particular overdense region. For example, when $x = 10^{-0.6} \approx 0.25$ the average cosmological background is already in the hadron phase ($0.25 < y^{-1}$) but an overdense region with, for example, $\delta_k = 0.9$ continues to be in the mixed phase. This is because overdense regions do not expand with the rest of the background Universe and, so, the state of matter on those regions evolve slower. That is why the border between classes E and F (for example) is a function of δ_k (i.e. depends on the amplitude of the fluctuation) instead of being just a simple horizontal line.

3.1.2 Lattice Fit

Let us now consider how a fluctuation evolves during a first–order QCD phase transition according to the Lattice Fit. We adopt a model similar to the one considered for the Bag Model. One difference is that, in the case of the Lattice Fit, the mixed phase period is shorter. Another difference is that before the mixed phase (i.e. during the last instants of the quark–gluon phase) the reduction in the sound speed value is not abrupt (see e.g. Figure 13).

In order to characterize the horizon crossing time and the turnaround point we make use, once again, of x and y as defined by equations (139) and (140). We consider also the six different classes of fluctuations shown in Table 8. Equation (142), which gives x as a function of time, continues to be valid here (as long as we do not move

too far away from the transition epoch). The end of the transition is now given by

$$y^{-1} = x(t_{QCD+}) = \frac{4g_{QGP}\left(\frac{t_{QCD-}}{t_{QCD+}}\right)^2 - g_{HG}}{4g_{QGP} - g_{HG}} \approx 0.729 \tag{166}$$

which differs from the Bag Model value (cf. equation 143) because in the case of the Lattice Fit we have a different value for t_{QCD-} (cf. Table 4).

Equations (148) to (159), which give the turnaround point for each class of fluctuation, and the values of S_1 and S_2 are still valid here as long as we use the correct value for y (cf. equation 166). The same goes for equations (160) and (161), which give the separations between classes C, E, and F. However, the separations between classes A, B, and C, in the case of the Lattice Fit, are not given by equations (162) and (163). We have to derive a new set of equations in order to account for the influence of the period $t_1 < t < t_{QCD-}$ (see Section 4.3).

In Figure 22 we show the regions in the (δ_k, $\log_{10} x$) plane corresponding to the classes of fluctuations listed in Table 8 for the Lattice Fit case. We have considered that the sound speed stays equal to $1/\sqrt{3}$ outside the interval $t_{QCD-} < t < t_{QCD+}$ and vanishes inside (c.f. Bag Model – Figure 21). Note that by inserting $y^{-1} = 0.729$ into equation (165) we conclude that fluctuations of class D cannot exist, in the context of the Lattice Fit, for $\delta_k < 9.0$ and that fluctuations of class C cannot exist above $\delta_k \approx 9.0$.

As we mentioned above (classes A, B, and C) Figure 22 does not exactly say the truth. We show it only for comparison purposes.

3.1.3 Crossover

We now consider the evolution of a fluctuation during the QCD Crossover. In this case there is no dust–like stage between the QGP plasma phase and the HG phase but rather a smooth change from one phase to the other. We assume that during the Crossover the Universe continues to be radiation–dominated[22]. Taking $w_k = w_c = 1/3$, equation (147), relating the size of the perturbed region at the horizon crossing time with the respective size at the turnaround point, can be written as[23]

$$S_c = R_k \left(\frac{1+\delta_k}{\delta_k}\right)^{1/2}. \tag{167}$$

[22]Although the adiabatic index decreases a bit during the transition, we assume $w = 1/3$ as a good approximation. During a first–order transition, the decrease in the value of w is more pronounced and although it does not reach zero (pure dust–like phase) we assume $w = 0$ (see e.g. Schmid et al., 1999).

[23]Here, we consider $K_s/K_k = 1$. If one uses the correct values for w_k and w_c then, we would have K_s/K_k, very close, but not necessarily equal to unity.

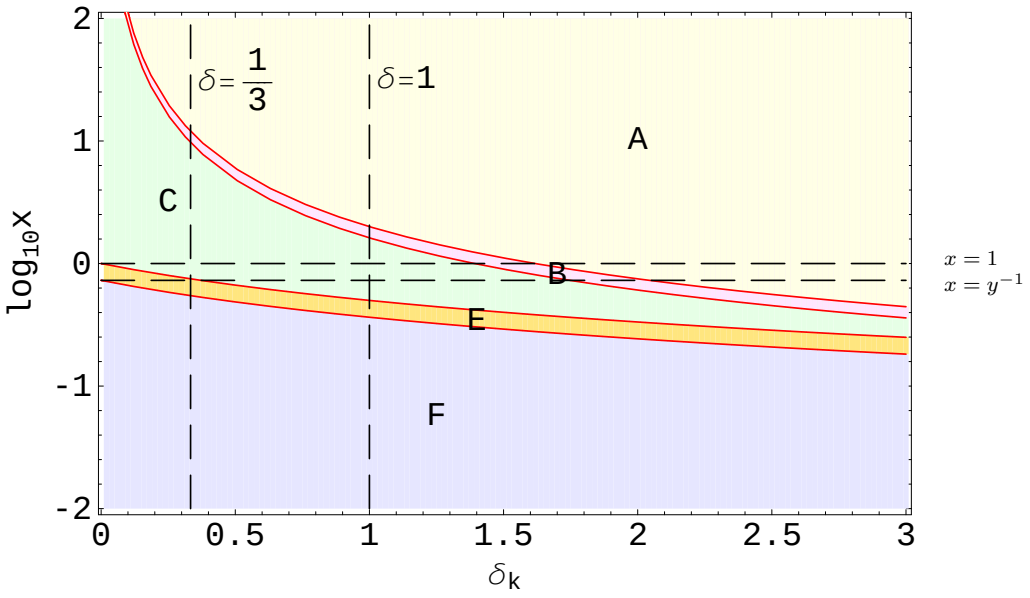

Figure 22: Regions in the $(\delta_k, \log_{10} x)$ plane corresponding to the classes of perturbations listed in Table 8 for the QCD Lattice Fit case (cf. Bag Model in Figure 21) – correct, except for A, B, and C (Section 4.3 gives the correct graph). Here we are considering that the sound speed vanishes in the interval $t_{QCD-} < t < t_{QCD+}$ and is equal to $1/\sqrt{3}$ outside this interval. Fluctuations of class D (not represented) cannot exist for $\delta_k < 9.0$. On the other hand fluctuations of class C cannot exist above $\delta_k \approx 9.0$ (see text for more details).

We use this result for the entire Crossover. Here it does not make sense to consider different classes of fluctuations as we did for the Bag Model and the Lattice Fit (cf. Table 8). Expressions for S_c and R_k are obtained from the scale factor $R(t)$. In the case of a QCD Crossover, the scale factor $R(t)$ is given by equation (52). Thus, we have

$$R_k = R(t_k) = \exp\left(c\sqrt{\frac{\Lambda}{3}}(t_{SN} - t_0)\right)\left(\frac{t_{eq}}{t_{SN}}\right)^{2/3}\left(\frac{t_k}{t_{eq}}\right)^{1/2} \tag{168}$$

and

$$S_c = R(t_c) = \exp\left(c\sqrt{\frac{\Lambda}{3}}(t_{SN} - t_0)\right)\left(\frac{t_{eq}}{t_{SN}}\right)^{2/3}\left(\frac{t_c}{t_{eq}}\right)^{1/2}. \tag{169}$$

Inserting expressions (168) and (169) into equation (167) we obtain a relation between the horizon crossing time t_k and the turnaround time t_c as

$$t_c = t_k \frac{1+\delta_k}{\delta_k}. \tag{170}$$

Table 9: Classification of overdense regions according to the state of matter at the horizon crossing and at turnaround for the EW first–order phase transition.

Class	Horizon crossing phase	Turnaround phase
A	high	high
B	high	mixed
C	high	low
D	mixed	mixed
E	mixed	low
F	low	low

3.2 EW phase transition

3.2.1 Crossover (SMPP)

We now describe the evolution of a fluctuation during the EW Crossover in the same way that we did for the QCD Crossover case (cf. Section 3.1.3). Thus, R_k and S_c are given, once again, by expressions (168) and (169). In addition, the relation between the turnaround instant t_c and the horizon crossing time t_k is given by expression (170).

3.2.2 Bag Model (MSSM)

Let us consider how a fluctuation evolves in the presence of a first–order EW phase transition according to the Bag Model. Here we continue to follow the model proposed by Cardall & Fuller (1998) for the QCD first–order phase transition (see Section 3.1.1). Considering the possible locations of t_k and t_c, we define six different classes of density fluctuations (Table 9).

It is very useful to have x as a function of time. We get this by adapting equation (142) derived for the QCD case. Thus, we have

$$x(t) = \frac{4g'_{EW}\left(\frac{R(t_{EW-})}{R(t)}\right)^3 - g_{EW}}{4g'_{EW} - g_{EW}} \tag{171}$$

which is valid only in the neighborhood of the EW transition. Here $R(t_{EW-})$ is given by equation (51) and $R(t)$ is given by: i) equation (49) if $x \leq y^{-1}$; ii) equation (50) if $y^{-1} < x < 1$; iii) equation (51) if $x \geq 1$.

The value of y, which defines the end of the EW transition, can now be determined evaluating $x(t_{EW+})$. If one assumes $\Delta g \approx 80$ and $g_{EW} = 95.25$ (see Section 2.2.2),

then one obtains

$$y^{-1} = x(t_{EW+}) = \frac{4g'_{EW}\left(\frac{t_{EW-}}{t_{EW+}}\right)^2 - g_{EW}}{4g'_{EW} - g_{EW}} \approx 0.460.$$

Equations (148) to (165), derived for the QCD transition, are quite general and, hence, we simply adopt them here without making any changes.

Inserting $y^{-1} = 0.460$ into equation (165) it turns out that $\delta_k \approx 3.4$. This result means that class D fluctuations do not exist for $\delta_k < 3.4$ and that class C fluctuations do not exist for $\delta_k > 3.4$.

3.3 Fluctuations during the e^+e^- annihilation

We now describe the evolution of a fluctuation during the cosmological electron–positron annihilation process in the same way that we did for the QCD Crossover case (cf. Section 3.1.3). Thus, R_k and S_c are, once again, given by expressions (168) and (169). In addition, the relation between the turnaround instant t_c and the horizon crossing time t_k is given by expression (170).

4 The threshold δ_c for PBH formation

4.1 QCD Bag Model

During a first–order QCD phase transition we replace the lower limit in the condition (94) by (e.g. Cardall & Fuller, 1998)

$$\delta_c \to \delta_c(1-f) \tag{172}$$

where f denotes the fraction of the overdense region spent in the dust–like phase. Therefore, the larger the fraction of time a fluctuation spends in the mixed phase regime, the smaller the required amplitude of the perturbation (at horizon crossing) for collapse into a BH (e.g. Cardall & Fuller, 1998). Next, we present the expressions for f for each class of fluctuations of interest to us (cf. Table 8, e.g. Cardall & Fuller, 1998)

$$f_A = 0 \tag{173}$$

$$f_B = \frac{S_{c,B}^3 - S_1^3}{S_{c,B}^3} = 1 - \frac{x^{3/2}\delta_k^3}{(1+\delta_k)^{3/2}} \tag{174}$$

$$f_C = \frac{S_{2_C}^3 - S_1^3}{S_{c,C}^3} = \frac{x^{3/4}\delta_k^{3/2}}{y^{1/2}(1+\delta_k)^{3/4}}(y-1) \tag{175}$$

$$f_E = \frac{S_{2_E}^3 - S_1^3}{S_{c,E}^3} = \frac{(xy)^{1/2}\delta_k^{3/2}}{1+\delta_k}(1-y^{-1}) \tag{176}$$

$$f_F = \frac{S_{2_F}^3 - S_1^3}{S_{c,F}^3} = \frac{(xy)^{3/4}\delta_k^{3/2}}{(1+\delta_k)^{3/4}}(1-y^{-1}) \tag{177}$$

where the quantities S_1, S_2, S_{2_E}, S_{2_F}, $S_{c,B}$, $S_{c,C}$, $S_{c,E}$, and $S_{c,F}$ are given by equations (153), (154), (155), (156) (157), (158), (159), and (148), respectively.

When $x \geq 1$ we are dealing with fluctuations of classes A, B or C (cf. Figure 21). For a given x we can determine, with the help of equations (162) and (163), the range of amplitudes which correspond to each class.

For example, for the case $x = 2$, we have from equation (162), that[24] $\delta = 1$, and from equation (163) that $\delta \approx 0.58$. This means that when $x = 2$ the overdensity will be of class C if $0 < \delta < 0.58$, of class B if $0.58 < \delta < 1$ and of class A if $\delta > 1$.

[24] In order to simplify the writing we represent the density constrast at the horizon crossing time t_k by δ (instead of δ_k).

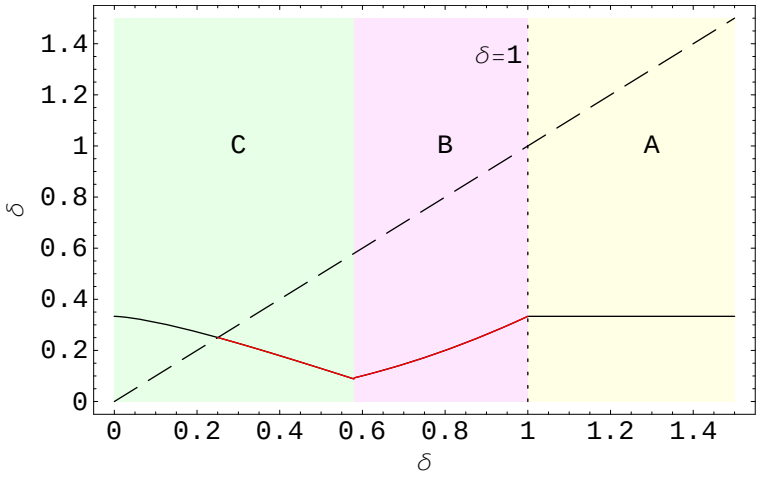

Figure 23: PBH formation during the QCD transition according to the Bag Model for the case $x = 2$ and $\delta_c = 1/3$. The solid curve corresponds to the function $(1 - f)\delta_c$ and the dashed curve to the identity δ. The pink region corresponds to fluctuations of class B (see text). To the left of this region we have fluctuations of class C (green) and to the right fluctuations of class A (yellow). The borders between the different classes are given by $\delta_{AB} = 1$ and $\delta_{BC} \approx 0.58$. Collapse to a PBH occurs for values of δ for which the dashed line is above the solid curve (while $\delta < 1$). The intersection point at $\delta \approx 0.25$ marks a new threshold δ_{c1} for PBH formation (adapted from Cardall & Fuller, 1998).

In order to identify the values of δ for which collapse to a PBH occurs (when $x = 2$ and $\delta_c = 1/3$), we plot in Figure 23 both $(1 - f)\delta_c$ and δ itself as functions of δ. Notice that one should use the function f appropriate to each class (i.e. f_A – equation 173; f_B – equation 174; f_C – equation 175). We can, then, have PBHs formed from fluctuations of classes B and C only, since fluctuations of class A would lead to the formation of a separate universe (since for them we always have $\delta > 1$) – Section 1.4.1.

Fluctuations of class C with $\delta < 0.25$ dissipate before forming a PBH. This point $\delta_{c1} \approx 0.25$ marks a new and lower threshold for PBH formation during the QCD phase transition when $x = 2$.

In Figure 24 we plot the cases: (a) $x = 15$, (b) $x = 30$, and (c) $x = 90$ with $\delta_c = 1/3$ for all the three cases. In the case $x = 15$ there are two regions for which PBH formation is allowed: i) a region for $\delta \geq 1/3$, which corresponds to PBH formation from fluctuations of class A during the radiation–dominated universe; ii) a region between $\delta_{c1} \approx 0.15$ and $\delta_{c2} \approx 0.27$ corresponding to the formation of PBHs from fluctuations of classes B and C. The gap between $\delta = 0.27$ and $\delta = 1/3$ corresponds to: i) fluctuations of class A which dissipate because they have $\delta < 1/3$; ii) fluctuations of class B which dissipate because they do not spend enough time in the dust–like phase, allowing collapse to begin.

The case $x = 30$ is similar to the case $x = 15$. Notice, however, that now the region $[\delta_{c1}, \delta_{c2}]$ is much smaller. In the case $x = 90$ the fluctuations of classes B and C do not lead any longer to the formation of PBHs.

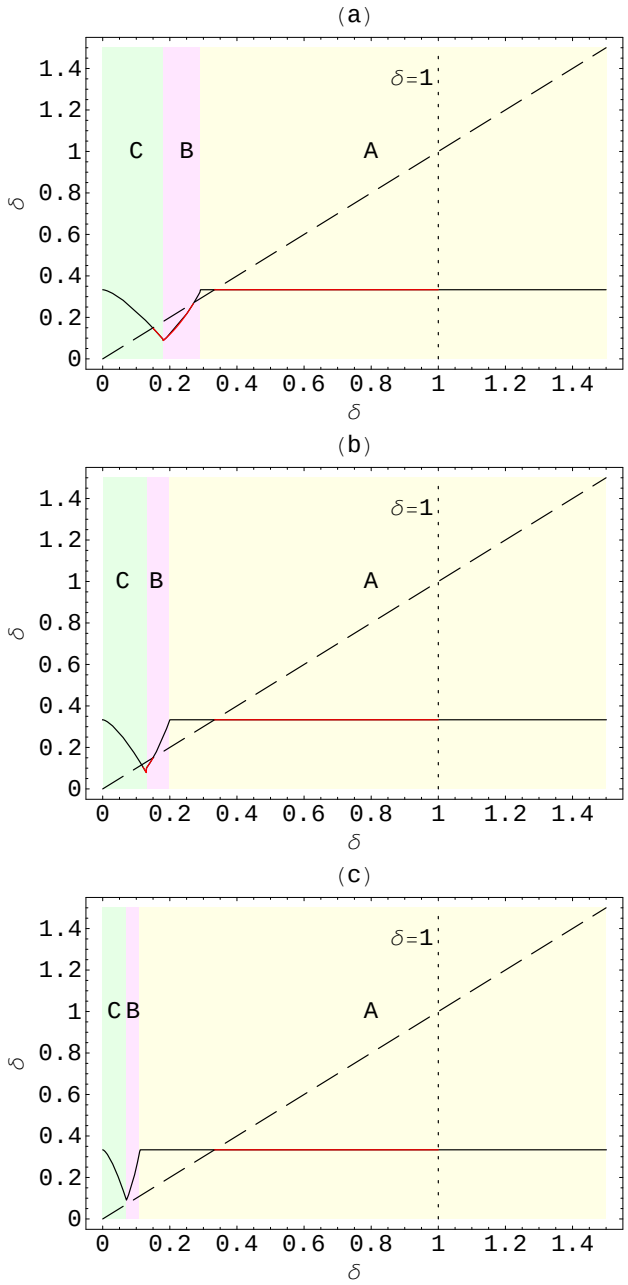

Figure 24: PBH formation during the QCD transition according to the Bag Model for the cases: (a) $x = 15$, (b) $x = 30$, and (c) $x = 90$; with $\delta_c = 1/3$. The solid curve corresponds to the function $(1 - f)\delta_c$ and the dashed curve corresponds to the identity δ. The borders between the different classes are given by: (a) $\delta_{AB} \approx 0.29$, $\delta_{BC} \approx 0.18$; (b) $\delta_{AB} \approx 0.20$, $\delta_{BC} \approx 0.13$; and (c) $\delta_{AB} \approx 0.11$, $\delta_{BC} \approx 0.07$. Collapse to a PBH occurs for values of δ for which the dashed line is above the solid curve (while $\delta < 1$). In the case $x = 15$ we have three intersections points: $\delta_{c1} \approx 0.15$, $\delta_{c2} \approx 0.27$ and $\delta_c = 1/3$. This means that we now have two regions for PBH formation: $0.15 \leq \delta \leq 0.27$ and $1/3 \leq \delta < 1$. In the case $x = 30$ we have $\delta_{c1} \approx 0.12$ and $\delta_{c2} \approx 0.15$ (see text and Figure 23 for more details, adapted from Cardall & Fuller, 1998).

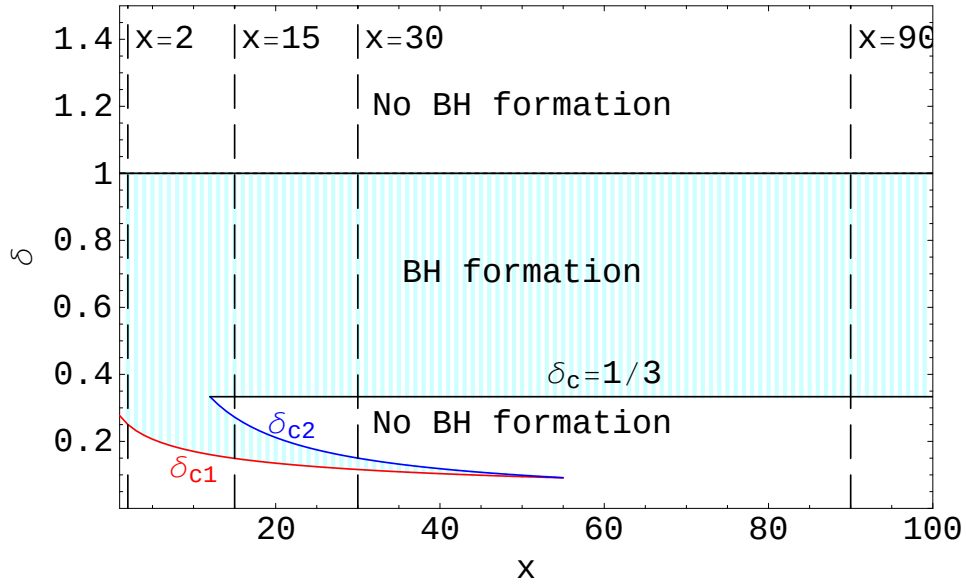

Figure 25: The curve in the (x, δ) plane indicating which parameter values lead to collapse to a PBH, according to the QCD Bag Model, in the case $x > 1$ and $\delta_c = 1/3$. We show the values of x corresponding to the cases presented in Figures 23 and 24. The intersection point $\delta_{c1} = \delta_{c2}$ corresponds to $x \approx 55$ and the intersection point $\delta_{c2} = \delta_c = 1/3$ corresponds to $x = 12$. (adapted from Cardall & Fuller, 1998).

Figure 25 indicates the region in the $(x,\ \delta)$ plane for which collapse to a PBH occurs ($x > 1$ and $\delta_c = 1/3$). Without the phase transition, this would be a straight horizontal line at $\delta = 1/3$. The intersection points $\delta_{c1} = \delta_{c2}$ ($x \approx 55$) and $\delta_{c2} = \delta_c = 1/3$ ($x = 12$) turn out to be very important for the calculation of β (see Chapter 5).

When $y^{-1} < x < 1$ we are dealing with fluctuations of classes B, C or E (cf. Figure 21). Notice that fluctuations of class A could reach also the range $y^{-1} < x < 1$ but only if they have $\delta > 1$ which leads to the formation of a separate universe. For a given x we can determine, with the help of equations (160) and (163), the range of amplitudes which correspond to each class.

For example, for the case $x = 0.927$, we have, from equation (160), that $\delta \approx 0.079$ and from equation (163) that $\delta \approx 0.94$. This means that when $x = 0.927$ the overdensity will be of class E if $\delta < 0.079$, of class C if $0.079 < \delta < 0.94$ and of class B if $\delta > 0.94$. The division between class B and A occurs according to equation (162) when $\delta \approx 1.7$.

In Figure 26 we plot both $(1 - f)\delta_c$ and δ itself as functions of δ for the cases: (a) $x = 0.927$, (b) $x = 0.6$, and (c) $x = 0.308$ with $\delta_c = 1/3$ for all the three cases. The appropriate function f was used for each class (i.e. f_B – equation 174; f_C – equation 175; f_E – equation 176). In the case $x = 0.927$ PBHs are formed from fluctuations of classes B and C. Fluctuations of class C with $\delta < 0.28$ dissipate without forming a PBH. This point $\delta_{c1} \approx 0.28$ marks the new threshold for PBH formation during the QCD phase transition when $x = 0.927$.

In the case $x = 0.6$ PBHs can form from fluctuations of class C or class E, but no longer from fluctuations of class B. The new threshold for PBH formation is $\delta_{c1} \approx 0.29$. Finally, in the case $x = 0.308$ PBHs can only form from fluctuations of class E (the separation between classes E and C occurs for $\delta_{CE} \approx 2.24$). The new threshold for PBH formation is $\delta_{c1} \approx 0.30$.

Figure 27 indicates the region in the $(x,\, \delta)$ plane for which collapse to a PBH occurs when $y^{-1} < x < 1$ and $\delta_c = 1/3$. Without the phase transition, this would be a straight horizontal line at $\delta = 1/3$.

When $x < y^{-1}$ we are dealing with fluctuations of classes E or F (cf. Figure 21). For a given x we can determine, with the help of equation (161) the range of amplitudes which corresponds to each class. We consider the cases $x = 0.26$, $x = 0.22$, and $x = 0.11$. In Figure 28 we show the plots for $\delta_c = 1/3$. When $x = 0.26$ or $x = 0.22$ we have PBH formation from fluctuations of class E, and when $x = 0.11$, from fluctuations of class F. In Figure 29 we show the region in the $(x,\, \delta)$ plane for which collapse to a PBH occurs when $x < y^{-1}$ and $\delta_c = 1/3$.

We now compile the results obtained for the QCD Bag Model. In particular, we have joined Figures 25, 27 and 29 in a single one in order to have a full picture of the QCD phase transition on the $(x,\, \delta)$ plane: Figure 30. With the help of equation (142) we move from the$(\log_{10} x,\, \delta)$ plane into the $(\log_{10} t_k,\, \delta)$ plane. As a result, we get Figure 31 where we have also indicated the lines $t_k = t_{QCD-}$ and $t_k = t_{QCD+}$ (which mark the location of the transition, Section 2.1). During the QCD transition the threshold for PBH formation experiences a reduction. As a result, a new window for PBH formation (between δ_{c1} and δ_c or between δ_{c1} and δ_{c2}) is opened for a brief period. In Table I-1 we present some values giving this new threshold for PBH formation during the QCD transition according to the Bag Model when $\delta_c = 1/3$.

Here we considered the case $\delta_c = 1/3$. In Appendix H we repeat the same examples for different values of δ_c up to 0.7. As a general conclusion we see that the window for PBH formation is larger for smaller values of δ_c.

4.2 QCD Crossover

During the QCD Crossover a reduction in the value of the threshold δ_c is expected, due to the reduction in the sound speed. We need to determine the analogous of function f (see condition 172) for the QCD Crossover. This function f should account for the fact that we have a variable sound speed value during the Crossover and that a smaller value of $c_s(t)$ contributes more significantly to the reduction of δ_c than a larger one. We then introduce the time function α_{sp} such that

$$\alpha_{sp}(t) = 1 - \frac{c_s(t)}{c_{s0}} \tag{178}$$

where $c_{s0} = 1/\sqrt{3}$. In the case of the Bag Model we have $\alpha_{sp}(t) = 1$ during the mixed phase and $\alpha_{sp}(t) = 0$ otherwise. Now we consider for the function f a more

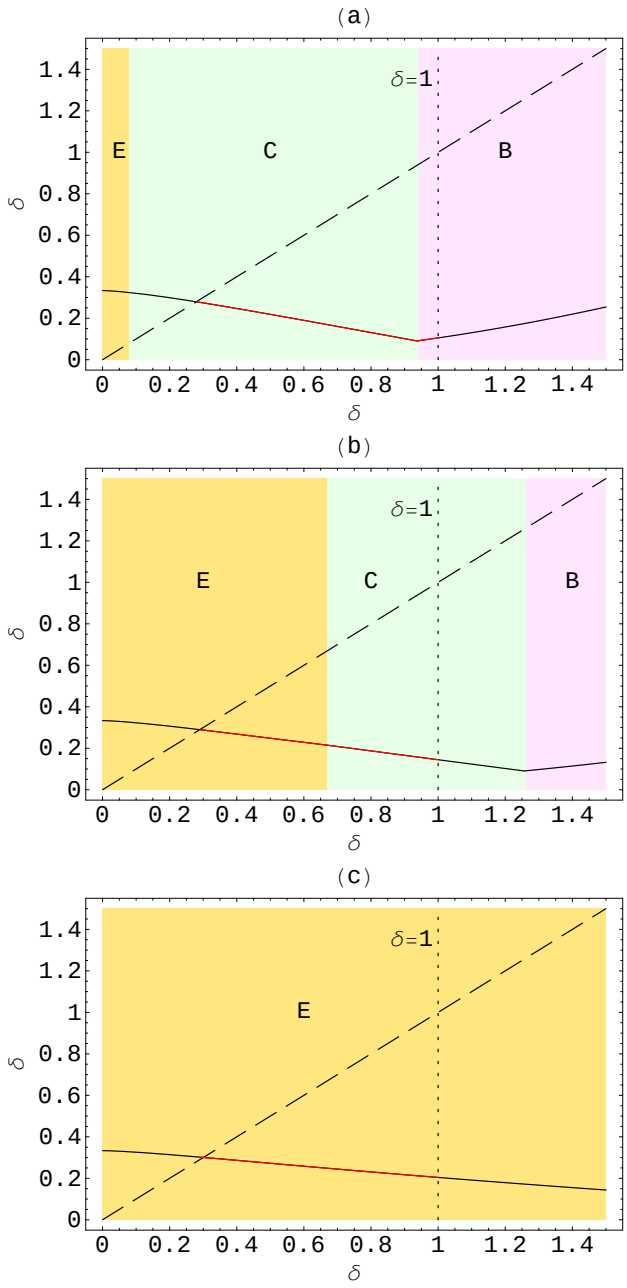

Figure 26: PBH formation during the QCD transition according to the Bag Model for the cases: (a) $x = 0.927$, (b) $x = 0.6$, and (c) $x = 0.308$ with $\delta_c = 1/3$ for all the three cases. The solid curve corresponds to the function $(1 - f)\delta_c$ and the dashed curve corresponds to the identity δ. The borders between the different classes are given by: (a) $\delta_{CE} \approx 0.079$, $\delta_{BC} \approx 0.94$; (b) $\delta_{CE} \approx 0.67$, $\delta_{BC} \approx 1.26$; and (c) $\delta_{CE} \approx 2.24$ (not shown). The new threshold for PBH formation is: (a) $\delta_{c1} \approx 0.28$, (b) $\delta_{c1} \approx 0.29$, and (c) $\delta_{c1} \approx 0.30$.

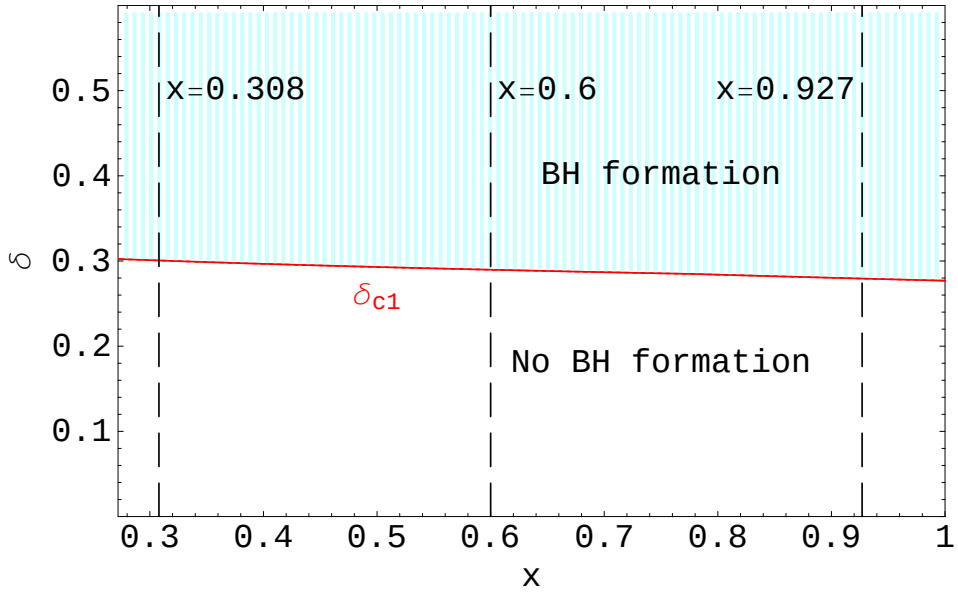

Figure 27: The curve in the (x, δ) plane indicating which parameter values lead to collapse to a PBH, within the QCD Bag Model, in the case $y^{-1} < x < 1$ and $\delta_c = 1/3$ (note that the PBH formation region extends up to $\delta = 1$). We show the values of x corresponding to the cases presented in Figure 26.

general expression:

$$f = \frac{1}{S_c^3} \int_{S_i}^{S_c} \alpha_{sp}(t) dS^3, \tag{179}$$

where S_i corresponds to the size of the region when the transition begins. In particular, this expression is valid for the Bag Model. For example, for a fluctuation of class B we recover equation (174)

$$f = \frac{1}{S_{c,B}^3} \int_{S_1}^{S_{c,B}} 1 \times dS^3 = \frac{S_{c,B}^3 - S_1^3}{S_{c,B}^3}.$$

In order to apply equation (179) to the QCD Crossover we start by transforming it into an expression where all the quantities are given as a function of time. Thus, taking into account that $S = S(t)$ represents the evolution of the scale factor during the QCD Crossover (equation 52) and that

$$dS^3 = 3S^2 dS = 3S^2 \frac{dS}{dt} dt, \tag{180}$$

we obtain

$$dS^3 = \frac{3}{2} \left[\exp\left(c\sqrt{\frac{\Lambda}{3}} (t_{SN} - t_0) \right) \left(\frac{t_{eq}}{t_{SN}} \right)^{2/3} \right]^3 \frac{\sqrt{t}}{t_{eq}^{3/2}} dt. \tag{181}$$

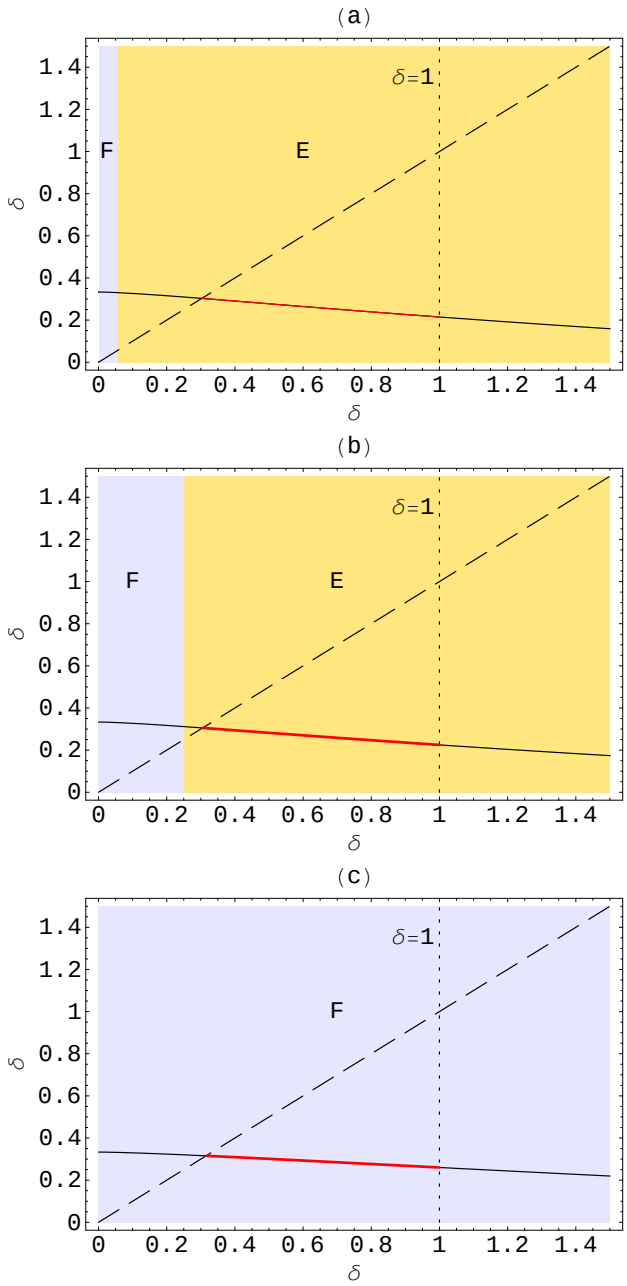

Figure 28: PBH formation during the QCD transition according to the Bag Model for the cases: (a) $x = 0.26$, (b) $x = 0.22$, and (c) $x = 0.11$ with $\delta_c = 1/3$ for all the three cases. The solid curve corresponds to the function $(1 - f)\delta_c$ and the dashed curve corresponds to the identity δ. Notice that one should use the function f appropriate to each class (i.e., f_E – equation 176 or f_F – equation 177). The borders between the different classes are given by: (a) $\delta_{EF} \approx 0.053$; (b) $\delta_{EF} \approx 0.25$, and (c) $\delta_{EF} \approx 1.5$ (not shown). The new threshold for PBH formation is: (a) $\delta_{c1} \approx 0.30$, (b) $\delta_{c1} \approx 0.31$, and (c) $\delta_{c1} \approx 0.32$. (adapted from Cardall & Fuller, 1998).

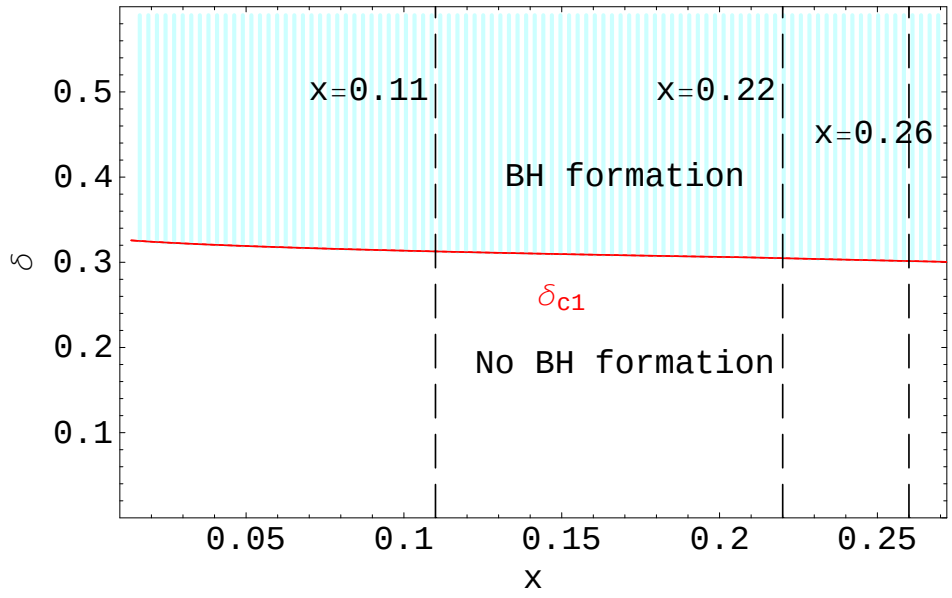

Figure 29: The curve in the (x, δ) plane indicating which parameter values lead to collapse to a PBH, within the QCD Bag Model, in the case $x < y^{-1}$ and $\delta_c = 1/3$ (note that the PBH formation region extends up to $\delta = 1$). We have indicated the values of x corresponding to the cases presented in Figure 28.

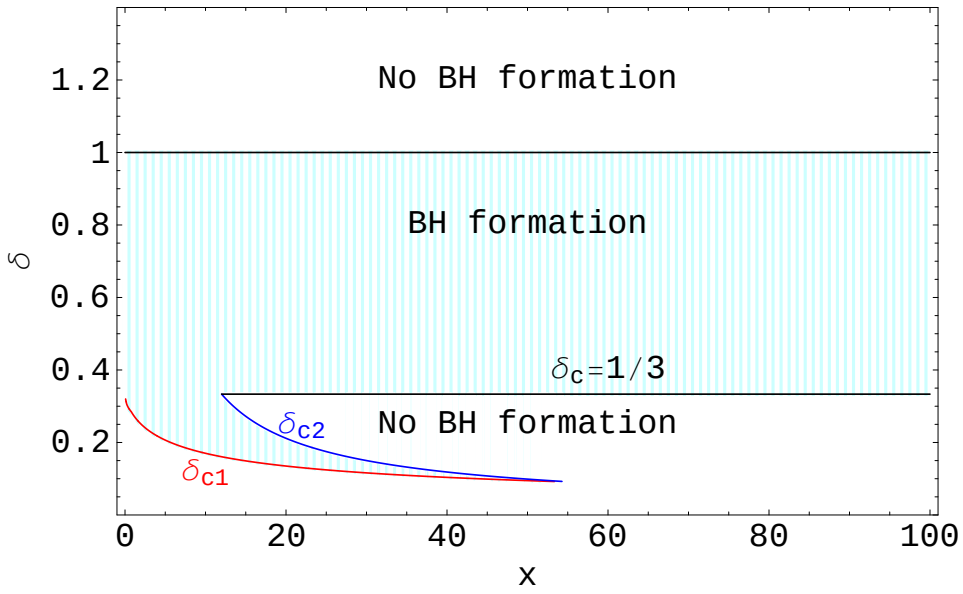

Figure 30: The curve in the (x, δ) plane indicating which parameter values lead to collapse to a PBH when $\delta_c = 1/3$ (full QCD Bag Model). This Figure was obtained by joining Figures 25, 27 and 29.

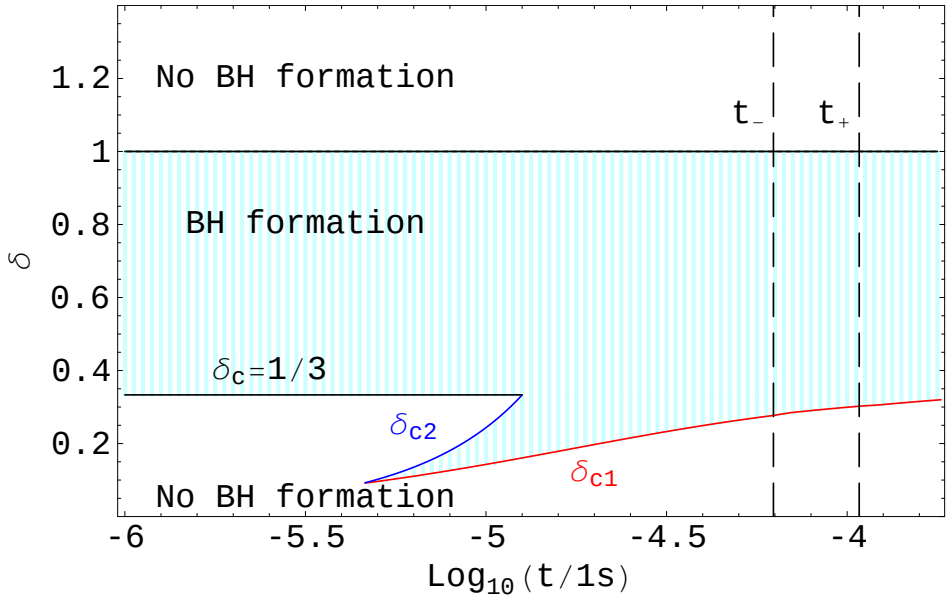

Figure 31: The same as in Figure 30 but now with δ as a function of $\log_{10}(t_k/1\text{ s})$. We also represent the lines corresponding to the beginning ($t_k = t_{QCD-}$) and end ($t_k = t_{QCD+}$) of the QCD phase transition.

Considering equations (52) and (181) and that $S_c = R(t_c)$ (see equation 169) one obtains, from equation (179), the following result:

$$f = \frac{3}{2}\frac{1}{t_c^{3/2}}\int_{t_k}^{t_c}\left(1-\frac{c_s(t)}{c_{s0}}\right)\sqrt{t}dt \tag{182}$$

where we have taken into account that $S_1 \equiv t_k$ and $S_c \equiv t_c$. Notice that this result is valid also in the case $t_k < t_1$ because f vanishes in the interval $[t_k, t_1]$.

Considering the relation (170), we may write expression (182) in the form

$$f = \frac{3}{2}\left(t_k\frac{1+\delta}{\delta}\right)^{-3/2}\int_{t_1}^{t_k\frac{1+\delta}{\delta}}\left(1-\frac{c_s(t)}{c_{s0}}\right)\sqrt{t}dt. \tag{183}$$

We now study the changes in the value of the threshold δ_c during a QCD Crossover. We do that by considering examples of fluctuations that cross the horizon before ($t_k \leq t_1$), during ($t_1 < t_k < t_2$) and after ($t_k > t_2$) the transition. Here we consider only the case $\Delta T = 0.1T_c$ for which (cf. Table 4) $t_1 = 7.1 \times 10^{-5}$ s and $t_2 = 19.6 \times 10^{-5}$ s.

In order to identify the values of δ for which collapse to a PBH occurs we plot in Figure 32 both, $(1-f)\delta_c$ and δ itself as functions of δ, (f is given by expression 183) for different values of t_k.

As a first example we consider the case of a fluctuation that crosses the horizon at $t_k = 1.5 \times 10^{-5}$ s (i.e., before t_1) (Figure 32a). We conclude that the evolution of perturbations entering the horizon at this epoch are not affected by the presence of a Crossover transition (t_k occurs well before the transition).

As a second example we consider a fluctuation that crosses the horizon at $t_k = 3.5 \times 10^{-5}$ s. In this case we still have $t_k < t_1$ but now there is a visible effect in the value of δ_c. In fact, we now have a lower threshold for PBH formation $\delta_{c1} \approx 0.275$ (Figure 32b).

In Figure 32c we show the case $t_k \approx t_1 = 7.1 \times 10^{-5}$ s. The threshold for PBH formation is now $\delta_{c1} \approx 0.307$. Notice that, although we are considering a fluctuation that crosses the horizon at the beginning of the transition, the value of δ_c is less affected than in the previous case.

In Figures 32d to 32h we represent the cases $t_k = 10^{-4}$ s ($t_1 < t_k < t_{min}$ where t_{min} represents the instant for which the sound speed reaches its minimum value during the Crossover, Section 2.1), $t_k = 1.2 \times 10^{-4}$ s ($t_k \gtrsim t_{min}$), $t_k = 1.5 \times 10^{-4}$ s ($t_{min} < t_k < t_2$), $t_k = 2.0 \times 10^{-4}$ s ($t_k \approx t_2$) and, finally, $t_k = 2.3 \times 10^{-4}$ s ($t_k > t_2$). For all these cases it is clear that the effect of the QCD Crossover, in terms of the reduction of the value of δ_c, is not as significant as it was for fluctuations crossing the horizon a little bit before the beginning of the transition. The value of δ_{c1} smoothly aproaches $\delta_c = 1/3$ as one uses larger values of t_k.

Figure 33 shows the region on the $(\log_{10}(t_k/1\text{s}), \delta)$ plane for which collapse to a PBH occurs in the case of a QCD Crossover with $\Delta T = 0.1 T_c$ and $\delta_c = 1/3$. Without the phase transition, this would be a straight horizontal line at $\delta = 1/3$ (in Figure H-7 we consider also the case $\delta_c = 0.7$).

Due to the QCD Crossover, the PBH formation threshold δ_c experiences a reduction in its value. In Table I-2 we present a few examples of these new values, δ_{c1}, as a function of time.

4.3 QCD Lattice Fit

In the case of the Lattice Fit we have a dust–like period ($t_{QCD-} < t < t_{QCD+}$) during which the sound speed vanishes. However, this does not occur instantaneously as it does for the Bag Model. In fact, there is a period ($t_1 \leq t \leq t_{QCD-}$) during which the sound speed value drops from $1/\sqrt{3}$ to zero (cf. Figure 13).

We need to write a function f suitable to the Lattice Fit. For the period $t_1 \leq t \leq t_{QCD-}$ we adopt the ideas from the Crossover case (Section 4.2); for the period $t_{QCD-} \leq t \leq t_{QCD+}$ we consider the Bag Model results (Section 4.1).

Let us start with fluctuations of class A. We have $f_A = 0$, as in the Bag Model case, only if $t_c < t_1$. In general, for a fluctuation of class A we write (cf. equation 179)

$$f_{A_{Lat}} = \frac{1}{S_{c,A}^3} \int_{S_k}^{S_{c,A}} \alpha_{sp}(t) dS^3 \tag{184}$$

where $S_{c,A}$, the size of the overdense region at turnaround, is given by equation (148), and $S_k \equiv R(t_k)$, the size of the overdense region when the fluctuation crosses the horizon, is given by equation (49) with $n_{qcd} = 2/3$. Here $\alpha_{sp}(t)$ is given by

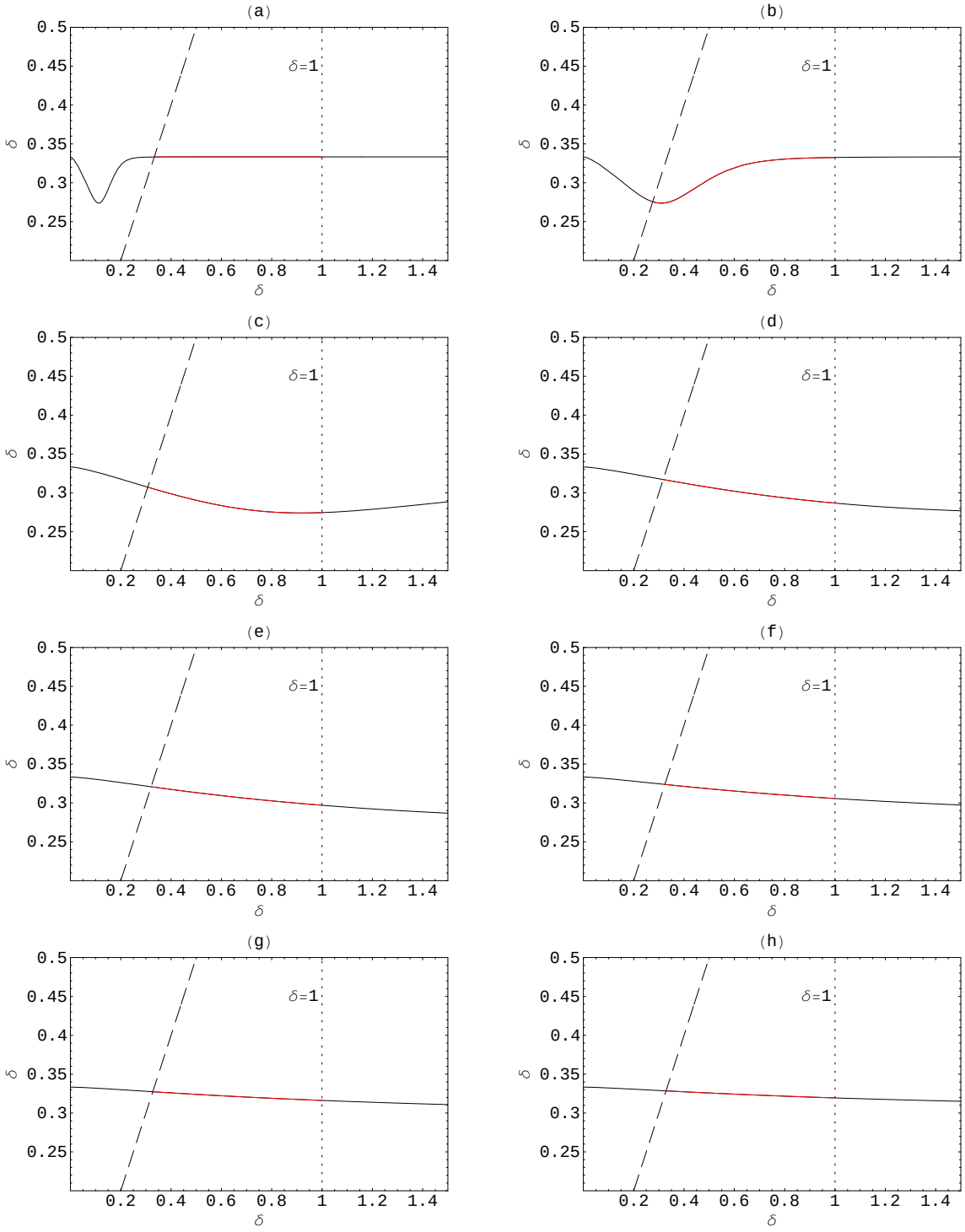

Figure 32: PBH formation during the QCD transition according to the Crossover model for the case $\delta_c = 1/3$ and: (a) $t_k = 1.5 \times 10^{-5}$ s; (b) $t_k = 3.5 \times 10^{-5}$ s; (c) $t_k = 7.1 \times 10^{-5}$ s; (d) $t_k = 10^{-4}$ s; (e) $t_k = 1.2 \times 10^{-4}$ s; (f) $t_k = 1.5 \times 10^{-4}$ s; (g) $t_k = 2.0 \times 10^{-4}$ s; (h) $t_k = 2.3 \times 10^{-4}$ s. The solid curve corresponds to the function $(1 - f)\delta_c$ and the dashed curve (on the left) corresponds to the identity δ. The intersection point between the lines $(1 - f)\delta_c$ and δ (giving the new threshold, δ_{c1}, for PBH formation) is: (a) $\delta_{c1} \approx 0.333$; (b) $\delta_{c1} \approx 0.275$; (c) $\delta_{c1} \approx 0.307$; (d) $\delta_{c1} \approx 0.317$; (e) $\delta_{c1} \approx 0.321$; (f) $\delta_{c1} \approx 0.324$; (g) $\delta_{c1} \approx 0.327$; (h) $\delta_{c1} \approx 0.328$ (see text for more details).

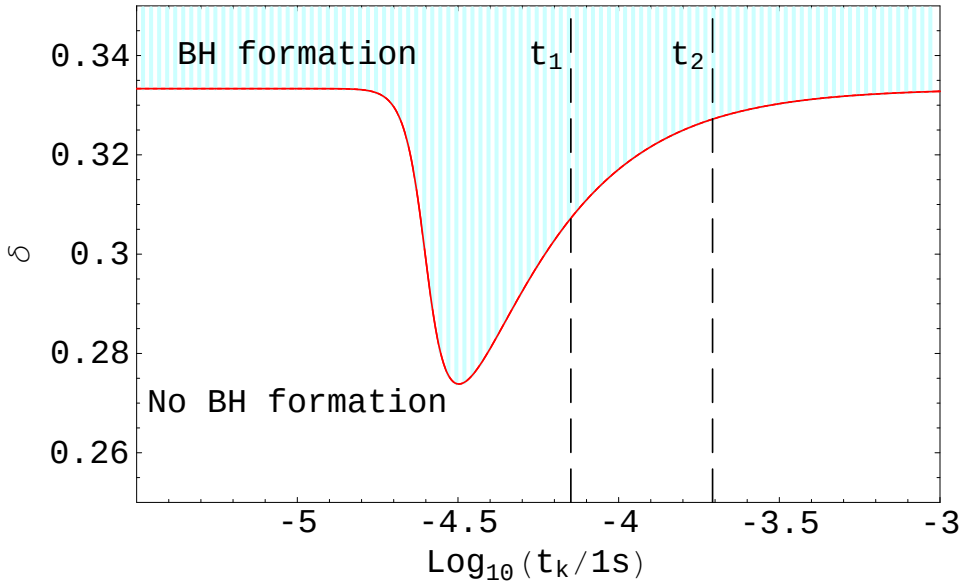

Figure 33: The curve in the $(\log_{10}(t_k/1\text{s}), \delta)$ plane indicating which parameter values lead to collapse to a PBH in the case $\delta_c = 1/3$ for a QCD Crossover. We have also represented, for reference, the values of t_1 and t_2 giving the locus of the transition (note that the PBH formation region extends up to $\delta = 1$).

equation (178), as in the Crossover case, but now with the sound speed $c_s(t)$ given by equation (122). Taking into account that the volume element dS^3 (see equation 180) must be evaluated in the radiation–dominated period ($t_k \leq t \leq t_{QCD-}$), we have, from equation (49), with $n_{qcd} = 2/3$ that

$$dS^3 = \frac{3}{2}\left[\exp\left(c\sqrt{\frac{\Lambda}{3}}(t_{SN} - t_0)\right)\left(\frac{t_{eq}}{t_{SN}}\right)^{2/3}\left(\frac{t_{QCD+}}{t_{eq}}\right)^{1/2} \times \right. \\ \left. \times \left(\frac{t_{QCD-}}{t_{QCD+}}\right)^{2/3}\right]^3 \frac{\sqrt{t}}{t_{QCD-}^{3/2}} dt. \tag{185}$$

Inserting expression (185) into equation (184) and replacing $R(t_k)$, as given by equation (49), with $n_{qcd} = 2/3$ in $S_{c,A}$ we obtain

$$f_{A_{Lat}} = \frac{3}{2}\left(t_k \frac{1+\delta}{\delta}\right)^{-3/2} \int_{t_k}^{t_k \frac{1+\delta}{\delta}} \alpha_{sp}(t)\sqrt{t}dt. \tag{186}$$

In the case of a fluctuation of class B we write

$$f_B = f_{B_{Lat}} + \frac{S_{c,B}^3 - S_1^3}{S_{c,B}^3} \tag{187}$$

with

$$f_{B_{Lat}} = \frac{1}{S_{c,B}^3}\int_{S_k}^{S_1} \alpha_{sp}(t) dS^3 \tag{188}$$

where S_1 and $S_{c,B}$ are given by expressions (153) and (157), respectively. Inserting expression (185) into equation (188), replacing $R(t_k)$ in $S_{c,B}$ and considering that $S_1 \equiv R(t_{QCD-})$, we obtain

$$f_{B_{Lat}} = \frac{3}{2}\left(t_k^{-1/2} x^{-1/4} \frac{(1+\delta)^{3/4}}{\delta}\right)^{-3} \int_{t_k}^{t_{QCD-}} \alpha_{sp}(t)\sqrt{t}dt \tag{189}$$

where $x = x(t_k)$. In the case of a fluctuation of class C we have

$$f_C = f_{C_{Lat}} + \frac{S_2^3 - S_1^3}{S_{c,C}^3} \tag{190}$$

with

$$f_{C_{Lat}} = \frac{1}{S_{c,C}^3} \int_{S_k}^{S_1} \alpha_{sp}(t) dS^3 \tag{191}$$

where S_{2_C} and $S_{c,C}$ are given by expressions (154) and (158) respectively. Inserting expression (185) into equation (191), replacing $R(t_k)$ in $S_{c,C}$ and considering that $S_1 \equiv R(t_{QCD-})$, we obtain

$$f_{C_{Lat}} = \frac{3}{2}\left(t_k \frac{1+\delta}{\delta}\right)^{-3/2} y^{-1/2} \int_{t_k}^{t_{QCD-}} \alpha_{sp}(t)\sqrt{t}dt \tag{192}$$

with $y^{-1} \approx 0.729$ (Section 3.1.2). In the case of fluctuations of classes E and F ($t_k > t_{QCD-}$) we continue to use, respectively, for f_E and f_F, the expressions (176) and (177) of the Bag Model.

When $x \geq 1$ ($t_k \leq t_{QCD-}$) we are dealing with fluctuations of classes A, B or C. For a given x we can determine the range of amplitudes corresponding to each class. More precisely, the solution of the equation $f_B(\delta) = f_C(\delta)$ gives the boundary between classes B and C and the solution of the equation $f_A(\delta) = f_B(\delta)$ the boundary between classes B and A.

Let us start with the case $x = 15$ ($t_k \approx 1.6 \times 10^{-5}$ s) and $\delta_c = 1/3$. The boundaries between the different classes are $\delta_{AB} \approx 0.25$ and $\delta_{BC} \approx 0.21$. In order to identify the values of δ for which collapse to PBH occurs we plot in Figure 34 both $(1-f)\delta_c$ and δ itself as functions of δ. Notice that one should use the function f appropriate to each class (i.e. f_A – equation 186; f_B – equation 187; f_C – equation 190). As it is clear we could have, in this case, PBHs from fluctuations of classes A (provided that $\delta < 1$), B and C (provided that $\delta > 0.18$ because otherwise the fluctuation will dissipate without forming a PBH). This point $\delta_{c1} \approx 0.18$ marks a new and lower threshold for PBH formation during the QCD phase transition when $x = 15$ and $\delta_c = 1/3$.

We have also represented in Figure 34 the curve $(1 - f_{Bag})\delta_c$ where f_{Bag} regards only to the contribution within the Bag Model (i.e., we are considering $f_{A_{Lat}} = f_{B_{Lat}} =$

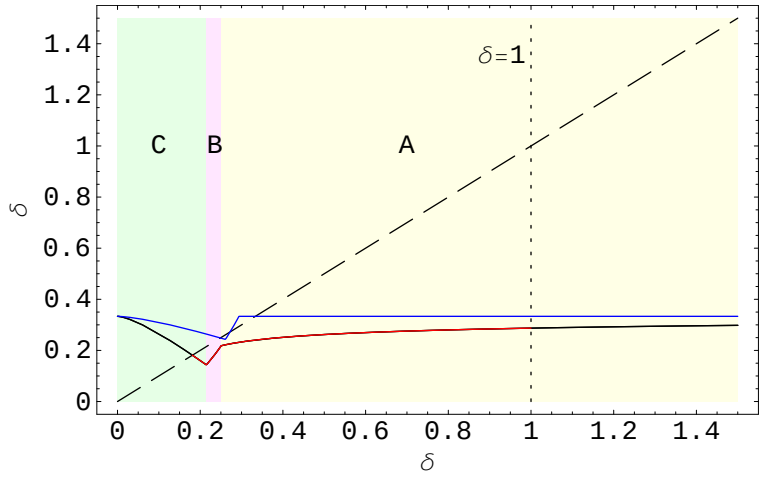

Figure 34: PBH formation during the QCD transition according to the Lattice Fit for the case $x = 15$ ($t_k \approx 1.6 \times 10^{-5}$ s) with $\delta_c = 1/3$. The bottom solid curve (in black and red) corresponds to the function $(1 - f)\delta_c$ and the dashed curve corresponds to the identity δ. The intersection point between these two curves at $\delta_{c1} \approx 0.18$ marks a new threshold for PBH formation. The borders between the different classes of fluctuations are $\delta_{AB} \approx 0.25$ and $\delta_{BC} \approx 0.21$. The top solid curve (in blue) corresponds to the case for which f regards only to the contribution, within the Bag Model, of the period $t_{QCD-} < t < t_{QCD+}$ (see text for more details).

$f_{C_{Lat}} = 0$) of the period $t_{QCD-} < t < t_{QCD+}$ (i.e., the period during which the sound speed vanishes). We have done this in order to show that the contribution from the period $t_k < t < t_{QCD-}$ is important. The reduction in the sound speed during this period leads to a shift in the boundaries between different classes of fluctuations towards the left (i.e., to lower values of δ). For example δ_{AB} moves from ≈ 0.29 to ≈ 0.25.

In Figure 35 we show the case $x = 2$ ($t_k \approx 6.1 \times 10^{-5}$ s) with $\delta_c = 1/3$. This case illustrates an interesting result. For small values of x ($x < 5$) we only have fluctuations of classes A and C. Fluctuations of class B cannot exist (at least according to the assumptions we made when deducing expressions for f). A fluctuation that crosses the horizon near t_{QCD-} ($x \approx 1$) evolves as a fluctuation of class A ($t_c < t_{QCD-}$) if it is strong enough or, otherwise, it will evolve as a fluctuation of class C ($t_c > t_{QCD+}$). In Figure 36 we have represented the regions on the (δ_k, $\log_{10} x$) plane corresponding to the classes of perturbations listed in Table 8 (compare this with Figure 22).

In Figure 37a we plot the case $x = 25$ ($t_k \approx 1.1 \times 10^{-5}$ s) with $\delta_c = 1/3$. Now there are two regions for which PBH formation is allowed: i) a region for $\delta \geq 0.25$, which corresponds to PBH formation from fluctuations of class A during the radiation–dominated universe; ii) a region between $\delta_{c1} \approx 0.15$ and $\delta_{c2} \approx 0.17$, corresponding to the formation of PBHs from fluctuations of classes B and C. The gap between $\delta = 0.17$ and $\delta = 0.25$ corresponds to fluctuations of class A which dissipate because they are not strong enough, and fluctuations of class B which dissipate because they do not spend enough time in the dust–like phase allowing collapse to begin.

In Figure 37b we plot the case $x = 50$ ($t_k \approx 7.3 \times 10^{-6}$ s) with $\delta_c = 1/3$. In this

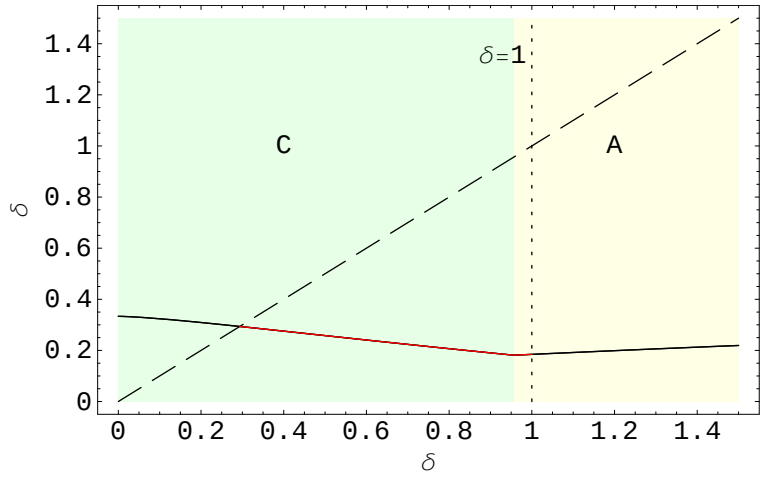

Figure 35: PBH formation during the QCD transition according to the Lattice Fit for the case $x = 2$ ($t_k \approx 6.1 \times 10^{-5}$ s) with $\delta_c = 1/3$. The solid curve corresponds to the function $(1 - f)\delta_c$ and the dashed curve corresponds to the identity δ. The new threshold for PBH formation is now $\delta_{c1} \approx 0.29$ and the border between fluctuations of classes A and C is $\delta_{AC} \approx 0.95$.

case PBH formation is allowed only from fluctuations of class A. The new threshold for PBH formation is now $\delta_{c1} \approx 0.27$. As one moves to larger values of x (smaller values of t_k) δ_{c1} will approach $1/3$.

When $y^{-1} < x < 1$ we are dealing with fluctuations of classes C or E (cf. Figure 36). In Figure 38a we plot both $(1 - f)\delta_c$ and δ itself as functions of δ for the case $x = 0.985$ ($t_k \approx 9.5 \times 10^{-5}$ s) when $\delta_c = 1/3$. In this case, PBHs could form only from fluctuations of class C, provided that $0.318 \lesssim \delta_k < 1$. Fluctuations of class C with $\delta < 0.318$ dissipate without forming a PBH. This point $\delta_{c1} \approx 0.318$ marks the new threshold for PBH formation during the QCD phase transition when $x = 0.985$. As a second example we show in Figure 38b the plot for the case $x \approx 0.871$ ($t_k \approx 1.0 \times 10^{-4}$ s) with $\delta_c = 1/3$. In this case the new threshold for PBH formation is $\delta_{c1} \approx 0.319$.

When $x < y^{-1}$ we are dealing with fluctuations of classes E, F or C (cf. Figure 36). In Figure 39 we plot $(1 - f)\delta_c$ and δ itself as functions of δ for the case $x = 0.70$ ($t_k \approx 1.2 \times 10^{-4}$ s) when $\delta_c = 1/3$. PBHs could form, in this case, from fluctuations of classes C and E. Fluctuations of class F dissipate without forming a PBH. Fluctuations of class E also dissipate when $\delta < 0.322$. This point $\delta_{c1} \approx 0.322$ marks the new threshold for PBH formation during the QCD phase transition when $x = 0.70$.

As a second example we show in Figure 39b the plot for the case $x \approx 0.47$ ($t_k \approx 1.5 \times 10^{-4}$ s), when $\delta_c = 1/3$. In this case PBHs could form from fluctuations of class E and F but no longer from fluctuations of class C. The new threshold for PBH formation is now $\delta_{c1} \approx 0.326$.

We now compile the results obtained. We have determined the threshold δ_c for the entire QCD phase transition according to the Lattice Fit model. As a result we obtain Figure 40 for the case $\delta_c = 1/3$ (in Figure H-8 we consider the case $\delta_c = 0.7$).

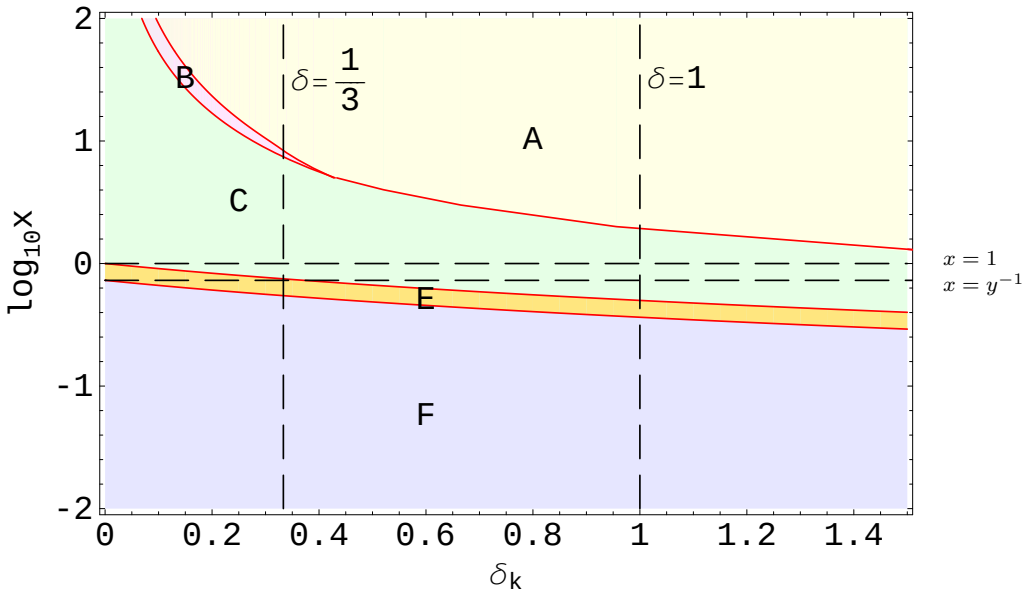

Figure 36: Regions in the (δ_k, $\log_{10} x$) plane corresponding to the classes of perturbations listed in Table 8 for the QCD Lattice Fit. The variable x identifies the epoch a perturbation enters the horizon and the quantity δ_k represents the corresponding overdensity at that time (see Section 3.1.2 for more details).

During the QCD transition, the threshold for PBH formation (δ_c) experiences a reduction. As a result, a new window for PBH formation (between δ_{c1} and δ_c, between δ_{cA} and δ_c or between δ_{c1} and δ_{c2}) is opened for a brief period. Note that the window between δ_{cA} and δ_c does not exist for the Bag Model case (Section 4.1) because, in that case, we have $f_A = 0$. In Table I-3 we present some values for this new threshold for PBH formation during the QCD transition according to the Lattice Fit, when $\delta_c = 1/3$.

4.4 EW Crossover (SMPP)

During the EW Crossover it is expected a reduction in the value of the PBH formation threshold δ_c due to the decrease in the sound speed. We adopt for f expression (183) derived for the QCD Crossover (Section 4.2) but now with the sound speed, $c_s(t)$, given by equation (129). First, however, we must determine which values of ΔT we will use. We are particularly interested in a value of ΔT for which the threshold δ_c attains a minimum value (because lower values of δ_c favour PBH formation).

For a given ΔT we determine, with the help of funtion $(1-f)\delta_c$, the new threshold δ_{c1} as a function of the horizon crossing time t_k. When $t_k \ll t_{EW-}$ or, when $t_k \gg t_{EW+}$, we get $\delta_{c1} = \delta_c$. Between these two extremes there is a value of t_k for which δ_{c1} attains a minimum value $\delta_{c1,min}$. For example, when $\Delta T = 0.001 T_c$ and $\delta_c = 1/3$, we obtain $\delta_{c1,min} \approx 0.33213$ with $t_k \approx 8.32 \times 10^{-11}$ s.

We repeated this procedure for different values of ΔT ($0 < \Delta T \leq T_c$) and concluded that, in the $\delta_c = 1/3$ case, our best value is $\delta_{c1,min} \approx 0.33186$, corresponding to

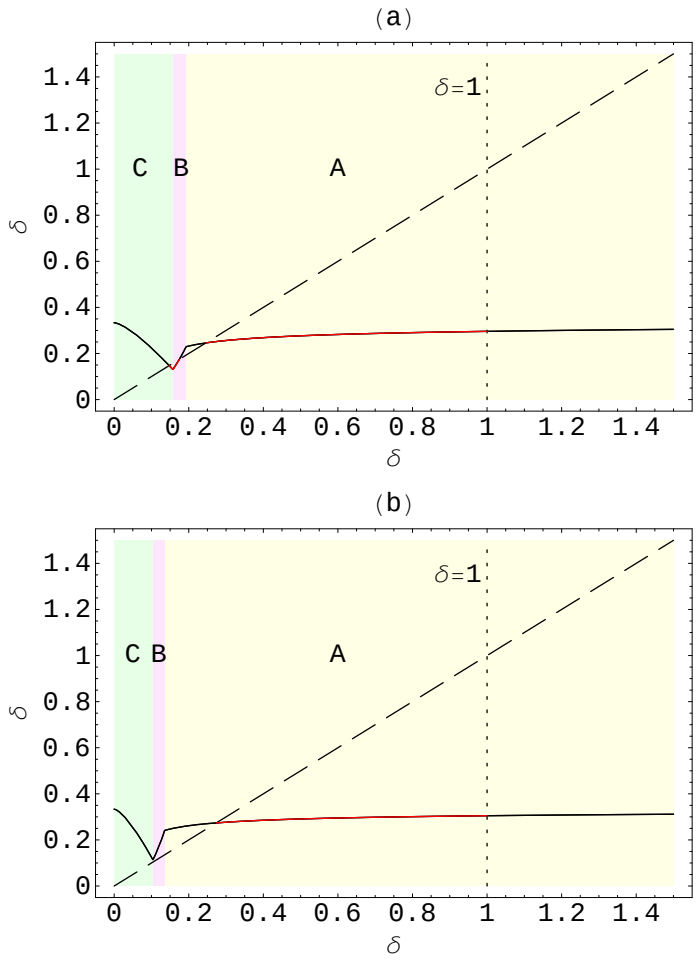

Figure 37: PBH formation during the QCD transition according to the Lattice Fit for the cases: (a) $x = 25$, and (b) $x = 50$; with $\delta_c = 1/3$. The solid curve corresponds to the function $(1 - f)\delta_c$ and the dashed curve corresponds to the identity δ. The borders between the different classes are given by: (a) $\delta_{AB} \approx 0.19$, $\delta_{BC} \approx 0.16$; (b) $\delta_{AB} \approx 0.14$, $\delta_{BC} \approx 0.10$. Collapse to PBH occurs for values of δ for which the dashed line is above the solid curve (while $\delta < 1$). In the case $x = 25$ we have three intersections points: $\delta_{c1} \approx 0.15$, $\delta_{c2} \approx 0.17$ and $\delta_c = 0.25$. This means that, in this case, there are two regions for PBH formation: $0.15 \leq \delta \leq 0.17$ and $0.25 \leq \delta < 1$. In the case $x = 50$ PBHs form if $0.27 \leq \delta < 1$.

having $\Delta T \approx 0.013 T_c$ and $t_k \approx 8.32 \times 10^{-11}$ s (see Appendix J for a selection of the results obtained).

In this section we study the changes in the value of the threshold δ_c during an EW Crossover, through examples of fluctuations that cross the horizon at different epochs. We are mostly interested in the case $\Delta T = 0.013 T_c$ (because it is the one that leads to the lowest value of δ_c) but we also consider the cases $\Delta T = 0.001 T_c$ and $\Delta T = 0.1 T_c$, with the purpose of comparing the results.

Let us start with $\delta_c = 1/3$ and with a fluctuation that crosses the horizon at $t_k = 5.0 \times 10^{-11}$ s (i.e., before $t_1 = 2.97 \times 10^{-10}$ s, cf. Section 2.2.1). In order to identify the values of δ for which collapse to PBH will occur, in this case, we plot, in Figure

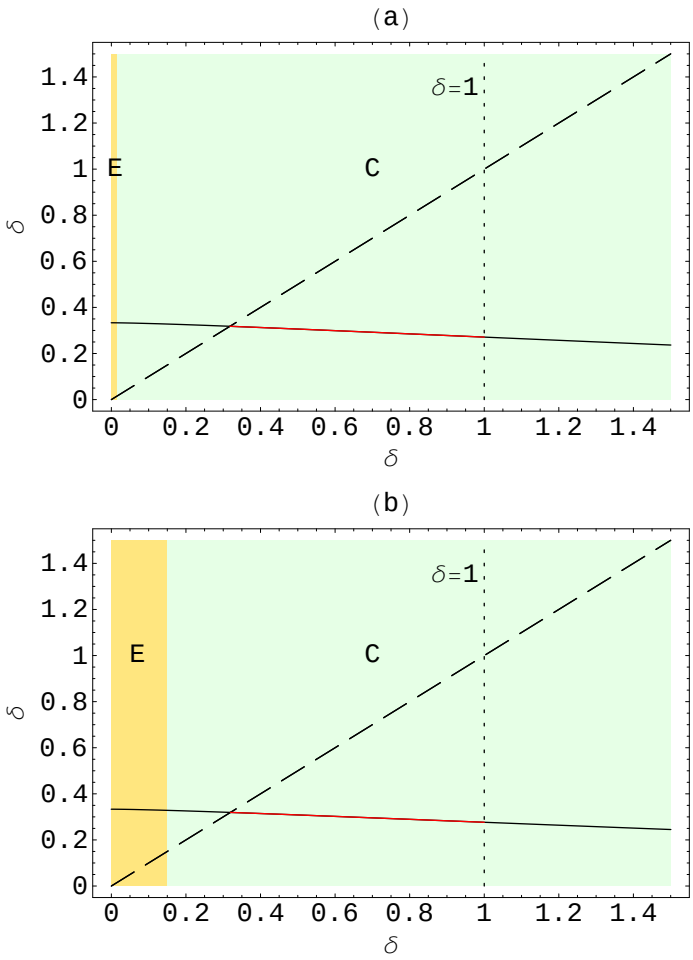

Figure 38: PBH formation during the QCD transition according to the Lattice Fit, when $\delta_c = 1/3$, for the cases: (a) $x = 0.985$ ($t_k \approx 9.5 \times 10^{-5}$ s); (b) $x = 0.871$ ($t_k \approx 1.0 \times 10^{-4}$ s). The solid curve corresponds to the function $(1-f)\delta_c$ and the dashed curve corresponds to the identity δ. The new threshold for PBH formation is, in both cases, $\delta_{c1} \approx 0.32$. The borders between classes C and E are: (a) $\delta_{CE} \approx 0.015$; (b) $\delta_{CE} \approx 0.15$.

41a, both $(1-f)\delta_c$ and δ itself as functions of δ. We conclude that the evolution of perturbations entering the horizon at this epoch are not affected by the presence of a Crossover transition. That is because t_k occurs sufficiently before the transition.

As a second example, we consider a fluctuation that crosses the horizon at $t_k = 7.0 \times 10^{-11}$ s. In this case, we do have a lower threshold for PBH formation $\delta_{c1} \approx 0.3330$ if $\Delta T = 0.1 T_c$ but not if $\Delta T = 0.001 T_c$ or $\Delta T = 0.013 T_c$ as it is clear from Figure 41b. In Figure 41c we have the case $t_k \approx 8.32 \times 10^{-11}$ s. This corresponds to the case for which a minimal value for $\delta_{c1} \approx 0.33186$ is achieved and that occurs for $\Delta T = 0.013 T_c$.

We considered also the cases $t_k = 1.5 \times 10^{-10}$ s – Figure 41d ($t_k < t_1$), $t_k = 2.3 \times 10^{-10}$ s – Figure 41e ($t_1 < t_k < t_2$, see Section 2.2.1), and $t_k = 3.5 \times 10^{-10}$ s – Figure 41f ($t_k > t_2$). For all these cases it is clear that the effect of the EW Crossover, in terms of the reduction of the value of δ_c, is not as significant as it was for fluctuations

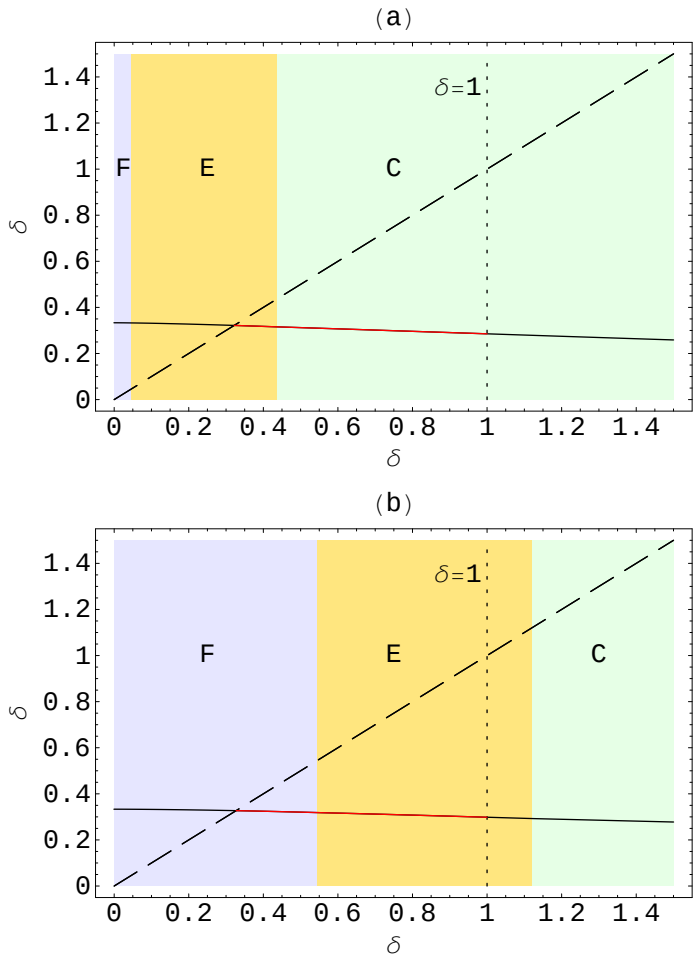

Figure 39: PBH formation during the QCD transition according to the Lattice Fit, when $\delta_c = 1/3$, for the cases: (a) $x = 0.70$ ($t_k \approx 1.2 \times 10^{-4}$ s); (b) $x = 0.47$ ($t_k \approx 1.5 \times 10^{-4}$ s). The solid curve corresponds to the function $(1-f)\delta_c$ and the dashed curve corresponds to the identity δ. The new threshold for PBH formation is: (a) $\delta_{c1} \approx 0.322$; (b) $\delta_{c1} \approx 0.326$. The borders between classes C, E, and F are given by: (a) $\delta_{CE} \approx 0.44$, $\delta_{EF} \approx 0.045$; (b) $\delta_{CE} \approx 1.12$, $\delta_{EF} \approx 0.54$.

crossing the horizon a little bit before the beginning of the transition (cf. Figures 41a and 41b). The value of δ_{c1} smoothly aproaches $\delta_c = 1/3$ as one moves to larger values of t_k for all the considered values of ΔT.

Figure 42 shows the region on the $(\log_{10}(t_k/1\text{s}), \delta)$ plane for which collapse to PBH occurs in the case of the EW Crossover with $\delta_c = 1/3$ and when ΔT assumes the values $0.001T_c$, $0.013T_c$ and $0.1T_c$. Without the phase transition, these would be three straight horizontal lines at $\delta = 1/3$. We have also represented, for reference, the location of the EW Crossover (in Figure H-9 we show also the case $\delta_c = 0.7$). It is clear that the case $\Delta T = 0.013T_c$ is the most important in the context of PBH production (with $\delta_c = 1/3$). For that reason we consider, from now on, for the EW Crossover, only this case.

Due to the EW Crossover the PBH formation threshold δ_c experiences a reduction in its background value. In Table I-4 we present some of these new values δ_{c1} as a

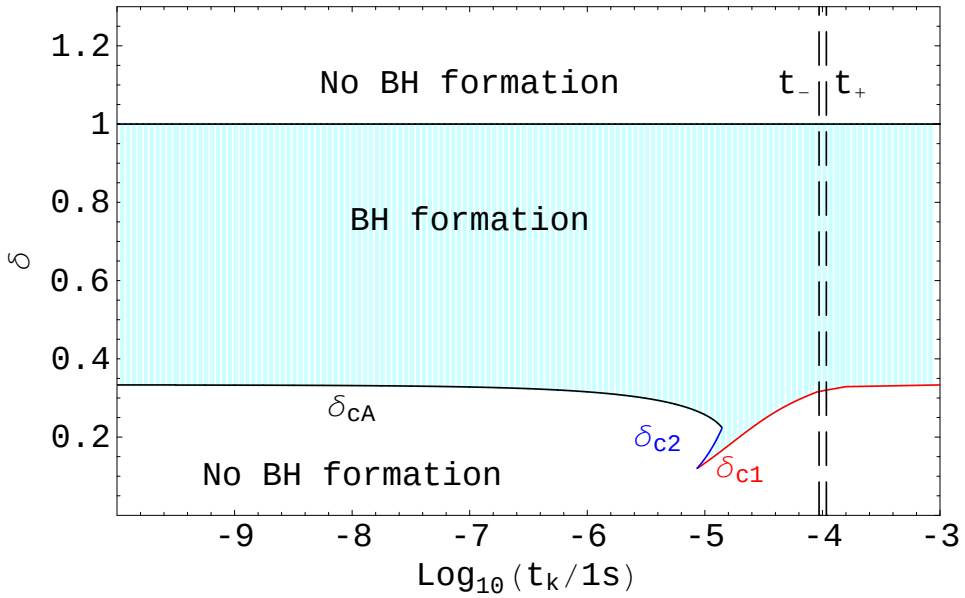

Figure 40: The curve in the $(\log_{10}(t_k/1s),\ \delta)$ plane indicating which parameter values lead to collapse to a PBH in the case of the QCD Lattice Fit when $\delta_c = 1/3$. The vertical dashed lines correspond to $t_k = t_{QCD-}$ and $t_k = t_{QCD+}$.

function of time for the case $\delta_c = 1/3$.

4.5 EW Bag Model (MSSM)

In the case of an EW first–order phase transition we replace the lower limit in the condition (94) by expression (172). The quantity f, which represents the fraction of the overdense region spent in the dust–like phase, will be given, once again, by expressions (173) to (177), in accordance with the class of fluctuation we are dealing with.

For the QCD Bag Model case we have studied with some detail fluctuations crossing the horizon before the mixed phase, during the mixed phase, and after the mixed phase (Section 4.1). Here, in the EW Bag Model case, we just point out that one obtains similar results. For example, one should obtain situations similar to the ones represented in Figure 24 (naturally with different values for x, δ_{c1}, δ_{c2},...).

In Figure 43a we show the region in the (x, δ) plane for which BH formation is allowed in the case $\delta_c = 1/3$. Without the phase transition this would be a straight horizontal line at $\delta = 1/3$. In Figure 43b we show the same situation but now represented on the $(\log_{10}(t_k/1\text{ s}),\ \delta)$. We have represented also, for reference, the values t_{EW-} and t_{EW+} (in Figure H-10 we show the case $\delta_c = 0.7$).

In Table I-5 we present some of these new values for the threshold of PBH formation during a EW first–order phase transition within the MSSM according to the Bag Model for the case $\delta_c = 1/3$.

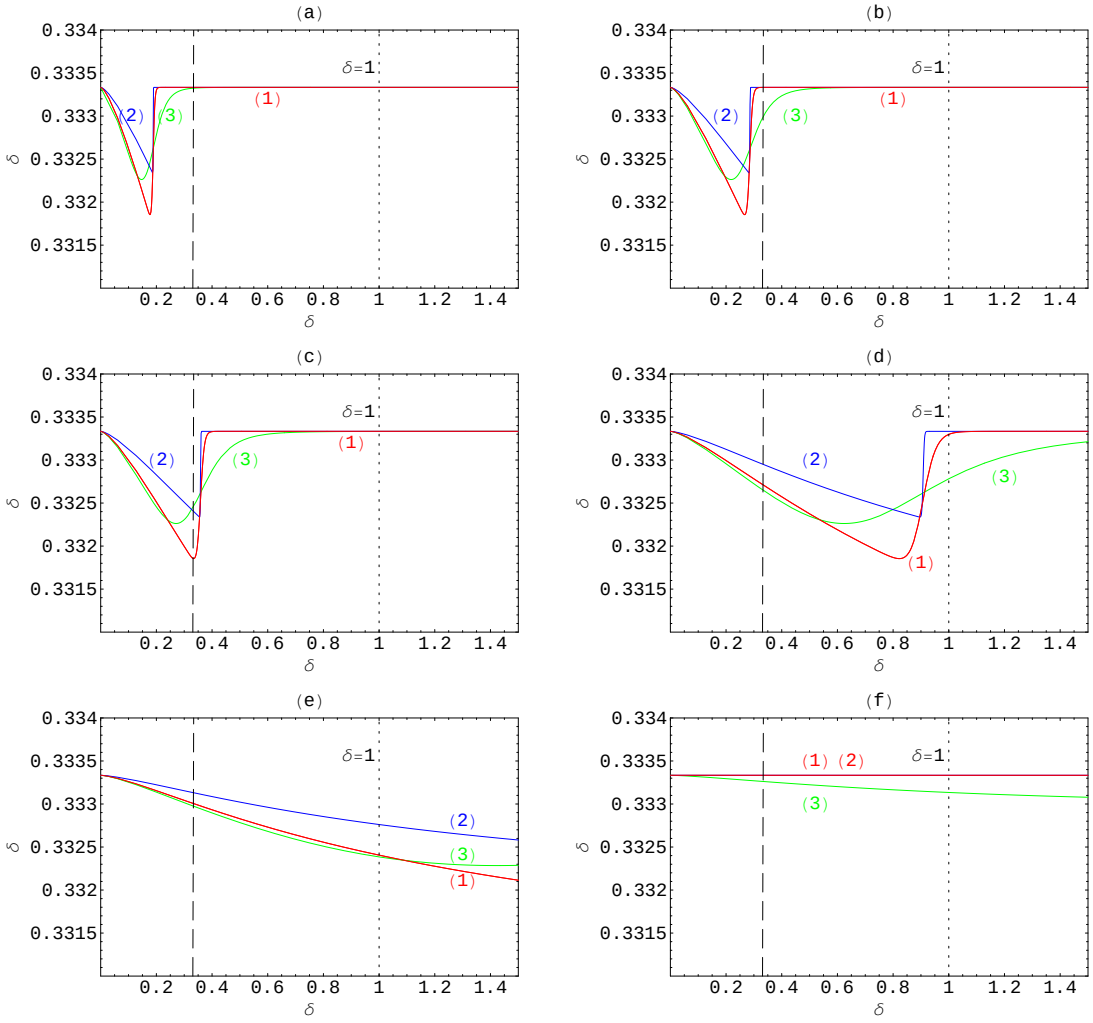

Figure 41: PBH formation during the EW transition according to the Crossover model for the case $\delta_c = 1/3$ and: (a) $t_k = 5.0 \times 10^{-11}$ s, (b) $t_k = 7.0 \times 10^{-11}$ s, (c) $t_k = 8.32 \times 10^{-11}$ s, (d) $t_k = 1.5 \times 10^{-10}$ s, (e) $t_k = 2.3 \times 10^{-10}$ s, and (f) $t_k = 3.5 \times 10^{-10}$ s. The solid curves correspond to the function $(1 - f)\delta_c$ when: (1) $\Delta T = 0.013 T_c$, (2) $\Delta T = 0.001 T_c$ and (3) $\Delta T = 0.1 T_c$. The dashed curve in the left represents the identity δ (which appears to be a vertical line due to the scales chosen for each axis). Collapse to PBH occurs for values of δ between this line and the line $\delta = 1$.

4.6 Electron–positron annihilation

In this section we study the changes in the value of the threshold δ_c during the cosmological electron–positron annihilation epoch. We do that by considering examples of fluctuations that cross the horizon at different epochs. We consider here the cases $\Delta T = 0.115 T_c$ (reduction of the sound speed value up to 20%, cf. Table 6) and $\Delta T = 0.276 T_c$ (reduction of the sound speed value up to 10%).

Let us start with $\delta_c = 1/3$ and with a fluctuation that crosses the horizon at $t_k = 0.20$ s. In order to identify the values of δ for which collapse to a BH will occur in this case, we plot in Figure 44a both $(1 - f)\delta_c$ and δ itself as functions of δ. Now, f

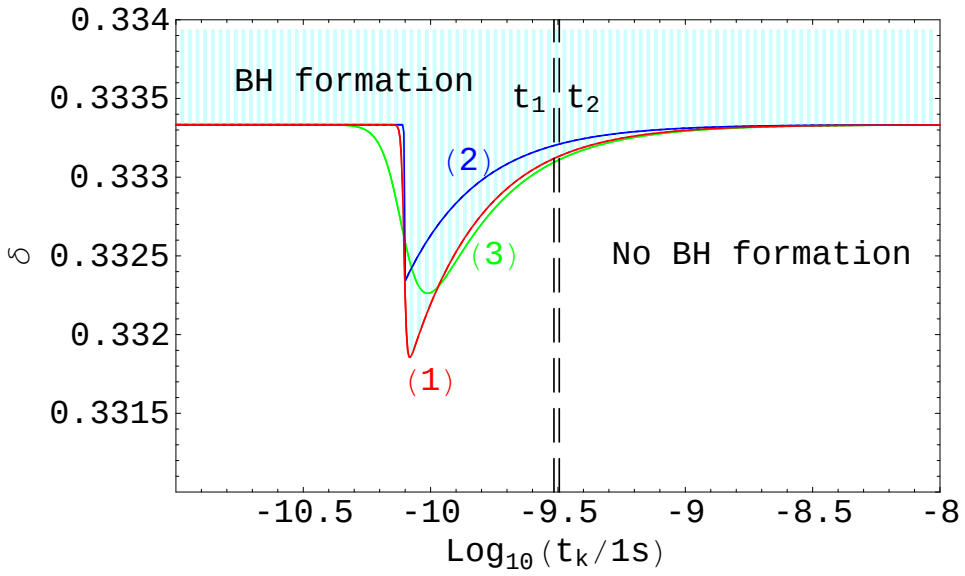

Figure 42: The curve in the $(\log_{10}(t_k/1\text{s}),\ \delta)$ plane indicating which parameter values lead to collapse to a PBH in the case $\delta_c = 1/3$ for the EW Crossover with (1) $\Delta T = 0.013T_c$, (2) $\Delta T = 0.001T_c$ and (3) $\Delta T = 0.1T_c$. Without the transition, these would be three straight horizontal lines at $\delta = 1/3$. We show the PBH formation region for the case $\Delta T = 0.013T_c$ (note that this region extends up to $\delta = 1$). We have also represented, for reference, the values of t_1 and t_2 giving the locus of the transition (vertical dashed lines).

is given by expression (183) with the sound speed $c_s(t)$ given by equation (138). We conclude that the evolution of perturbations entering the horizon at this epoch is not affected by the annihilation process. That is because t_k occurs suficiently before t_1 ($t_1 \approx 1.7$ s if $\Delta T = 0.115T_c$ and $t_1 \approx 1.1$ s if $\Delta T = 0.276T_c$ – cf. Table 7).

As a second example we show in Figure 44b the case of a fluctuation that crosses the horizon at $t_k = 0.9$ s. In this case we have a lower threshold for PBH formation $\delta_{c1} \approx 0.3041$ if $\Delta T = 0.115T_c$ and $\delta_{c1} \approx 0.3125$ if $\Delta T = 0.276T_c$.

In Figure 44c we show the case $t_k = 2.3$ s for which $\delta_{c1} \approx 0.3221$ if $\Delta T = 0.115T_c$ and $\delta_{c1} \approx 0.3193$ if $\Delta T = 0.276T_c$. As a final example we show in Figure 44d the case $t_k = 8.0$ s for which the effects are much less significant.

Figure 45 shows the region on the $(\log_{10} t_k, \delta)$ plane for which collapse to a BH occurs during the cosmological electron–positron annihilation with $\delta_c = 1/3$ and with ΔT assuming the values $0.115T_c$ and $0.276T_c$. Without the annihilation process these would be straight horizontal lines at $\delta = 1/3$. It is clear that the case $\Delta T = 0.115T_c$ is the most important in the context of PBH production because it leads to a more significant reduction in the value of δ_c (in Figure H-11 we show also the case $\delta_c = 0.7$ with $\Delta T = 0.115T_c$).

As a consequence of the cosmological electron–positron annihilation, the PBH formation threshold δ_c experiences a reduction in its background value. In Table I-6 we present some of these new values, δ_{c1}, in function of time for the case $\delta_c = 1/3$ with $\Delta T = 0.115T_c$.

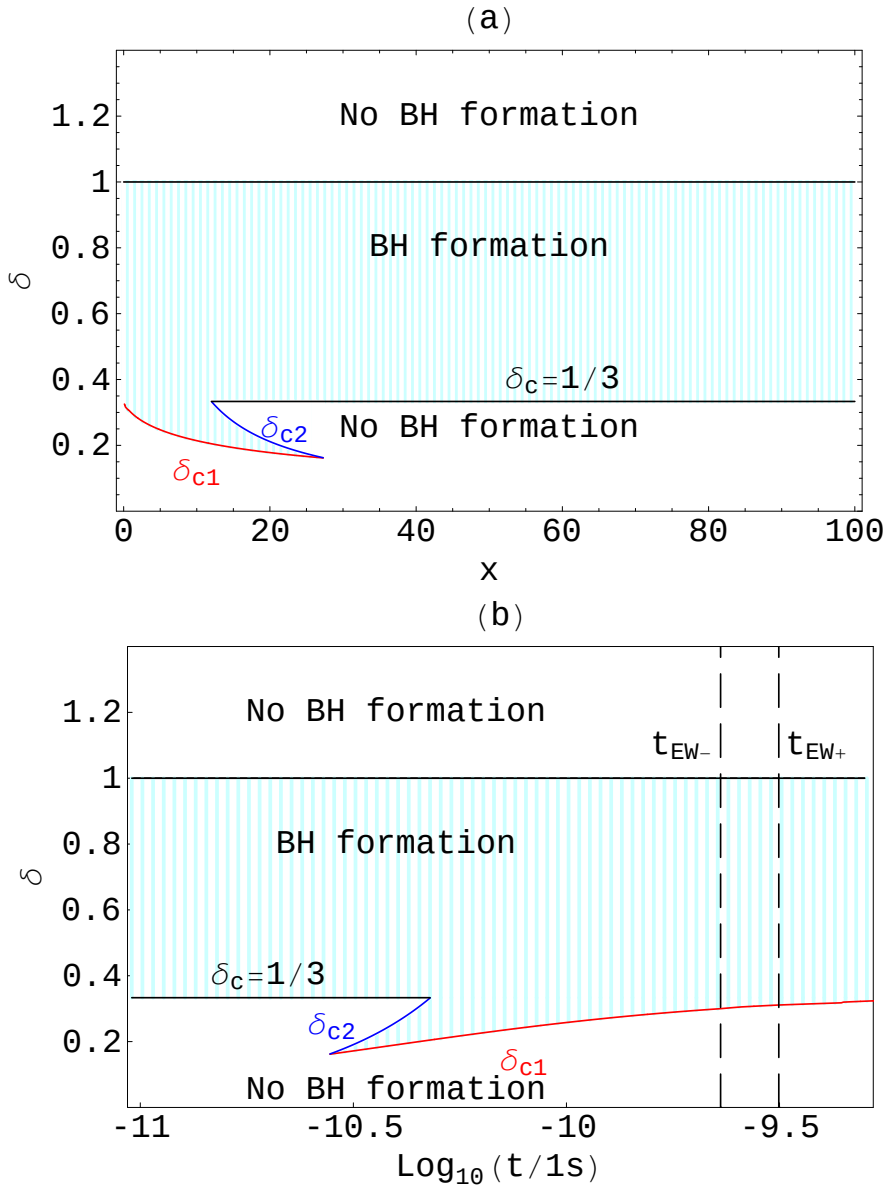

Figure 43: The curve indicating which parameter values lead to collapse to a PBH when $\delta_c = 1/3$ during the EW transition within the MSSM: (a) in the (x, δ) plane; (b) in the $(\log_{10}(t_k/1\text{ s}), \delta)$ plane.

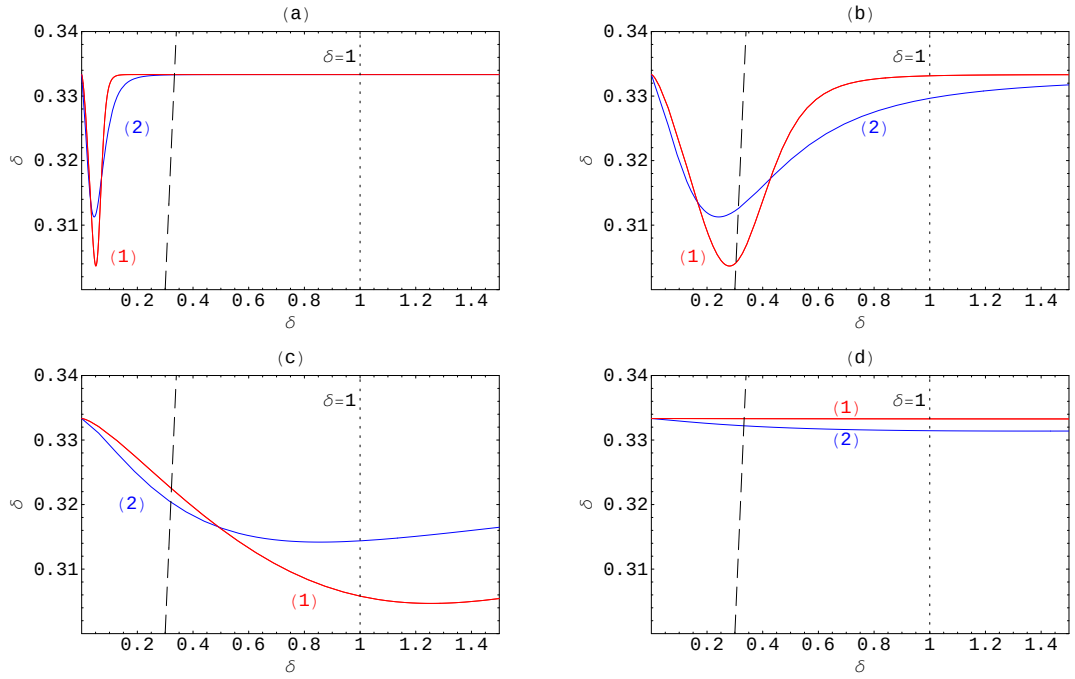

Figure 44: PBH formation during the cosmological electron–positron annihilation when $\delta_c = 1/3$ and: (a) $t_k = 0.2$ s; (b) $t_k = 0.9$ s; (c) $t_k = 2.3$ s; (d) $t_k = 8.0$ s. The solid curve corresponds to the function $(1-f)\delta_c$ when: (1) $\Delta T = 0.115 T_c$ and (2) $\Delta T = 0.276 T_c$. The dashed curve on the left corresponds to the identity δ. Collapse to a BH occurs for values of δ for which the dashed line is above the solid curve (while $\delta < 1$). The new thresholds for PBH formation are: (b)–(1) $\delta_{c1} \approx 0.3041$ and (2) $\delta_{c1} \approx 0.3125$; (c)–(1) $\delta_{c1} \approx 0.3221$ and (2) $\delta_{c1} \approx 0.3193$; (d)–(1) $\delta_{c1} \approx 0.3315$ and (2) $\delta_{c1} \approx 0.3301$. In case (a) the threshold remains $\delta_c = 1/3$ for both curves.

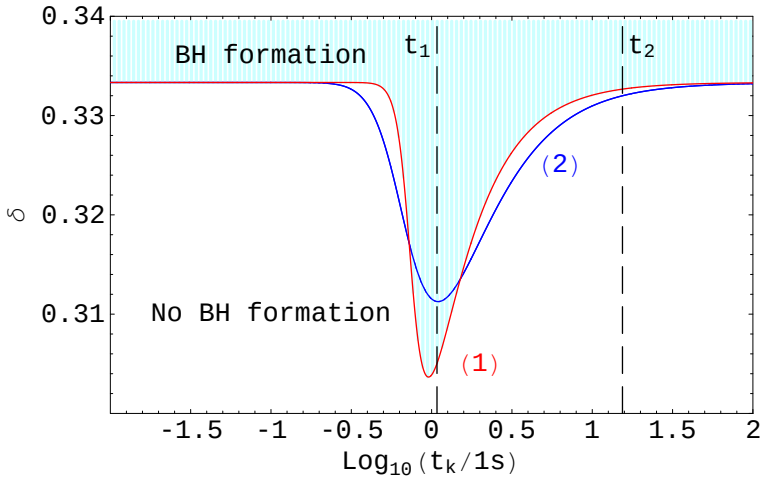

Figure 45: The curve on the $(\log_{10}(t_k/1\text{s}),\ \delta)$ plane indicating which parameter values lead to collapse to a BH in the case $\delta_c = 1/3$ for the cosmological electron–positron annihilation with (1) $\Delta T = 0.115 T_c$ and (2) $\Delta T = 0.276 T_c$. Without the annihilation process, these would be straight horizontal lines at $\delta = 1/3$. We have also represented, for reference, the location of the annihilation epoch for the case $\Delta T = 0.276 T_c$ (vertical dashed lines).

5 The fraction of the Universe going into PBHs

5.1 Scale–free power law spectrum

We consider here the case $n = 0.951$ which corresponds to the best fit of the results obtained by the WMAP mission[25] (Spergel et al., 2007). For the amplitude of the density fluctuations, evaluated at the pivot scale $k_c = 0.002\text{Mpc}^{-1} \approx 6.5\times10^{-26}\text{m}^{-1}$, we have the value $A(k_c) = 0.801$ (cf. Table 1). Inserting this into equation (89) we obtain

$$\delta_H^2(k_c, n = 0.951) \approx 2.4 \times 10^{-9}.$$

We now evaluate the integral (105). The value of $x_{max} = k_e/k$ depends on the moment that we are interested in. For example, if we want to determine the value of $\alpha(k)$ right at the end of inflation we should take $x_{max} = 1$ ($k = k_e$). On the other hand, if we are interested in the present day value of $\alpha(k)$ then we should take $x_{max} = k_e/k_0 \sim 10^{24}$ (cf. Table 3). In Figure 46 we show the plot of $\alpha^2(t_k)$ for $t_e \leq t_k \leq t_{eq}$. On the limit $x_{max} \to \infty$ (or equivalently $k \to 0$) we have the value

$$\alpha^2(0) \approx 5.17.$$

Numerical calculations and inspection of Figure 46 show us that this value is very accurately aproximated already for relatively small values of x_{max}. For example when $x_{max} = 50$, which corresponds to $k = k_e/50 \sim 10^{-4}$ m^{-1}, we already have $\alpha^2(k) \approx 5.17$. This happens well before the quantum–to–classical transition ($k \sim 10^{-7}$ m^{-1} or, equivalently, $t_k \sim 10^{-23}$ s – cf. Table 3) and as long as we are interested in events that took place after that particular epoch we may consider (e.g. Blais et al., 2003)

$$\alpha^2(k) \approx 5.17.$$

From $t_k = 10^{-23}$ s up to the present the value of $\sigma^2(t_k)$ (equation 105) increases only by an order of magnitude ($\sigma^2(10^{-23}\text{ s}) \approx 2.0 \times 10^{-9}$, $\sigma^2(t_0) \approx 1.9 \times 10^{-8}$). Notice also that $\sigma^2(t_0)$ agrees with the value presented in the literature (e.g. Bringmann et al. (2002), $\sigma^2(t_0) \simeq 10^{-8}$).

Assuming $\delta_c = 1/3$ and taking into account the values obtained for the mass variance we can use equation (98) in order to determine the fraction of the Universe going into PBHs at some particular epoch t_k. We find out that, for all the epochs of interest, we have

$$\beta(t_k) \approx 0.$$

That is because $(\delta_c^2/2\sigma^2) \sim 10^6$–$10^7$ and $e^{-10^6} \approx 0$. In the presence of a first–order phase transition, such as the QCD (Section 1.2.1) one obtains similar results for $\sigma(t_k)$ and for $\beta(t_k)$.

[25] Using WMAP data only the best fit value for the spectral index, in the context of a power law flat ΛCDM model, is $n = 0.951^{+0.015}_{-0.019}$ (cf. Table 1).

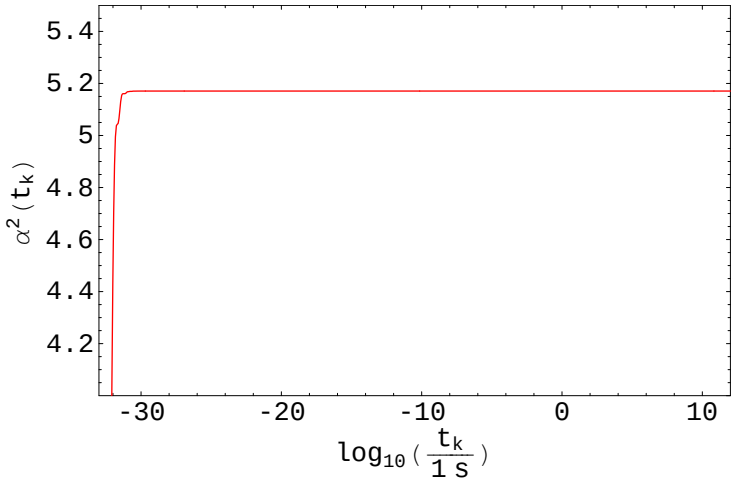

Figure 46: The behaviour of $\alpha^2(t_k)$ for a scale–free power law spectrum (equation 105) with $n = 0.951$.

In order to obtain more interesting values we have to move to a *blue spectrum*, i.e., to a spectrum with $n > 1$, at least during some epoch. The idea is to use a power spectrum model with more power in the smaller scales which are the ones relevant to PBH formation.

5.2 Running–tilt power–law spectrum

Here, we consider a running–tilt power–law spectrum $n(k)$ in the form

$$n(k) = n_0 + \frac{n_1}{2} \ln \frac{k}{k_c} + \frac{n_2}{6} \left(\ln \frac{k}{k_c} \right)^2 + \frac{n_3}{24} \left(\ln \frac{k}{k_c} \right)^3 \tag{193}$$

which is an expansion of equation (92) up to $i = 3$. For the parameters n_0 and n_1 we consider the observational values (cf. equation 93). The values of the parameters n_2 and n_3 remain unknown. The main idea is to find out sets of values (for n_2 and n_3) leading to interesting values in terms of PBH formation. Doing so we are determining which values lead to the *fine–tuning* required for PBH formation.

The simplest models of inflation suggest that the coefficients n_i scale as powers ϵ^i of some slow–roll parameter $\epsilon \approx 0.1$. This means that the expansion (193) can be expected to be accurate to 10% for about 16 e–foldings around the pivot scale (e.g. Düchting, 2004). This implies sensitivity down to scales probing the QCD epoch. For smaller scales (e.g. EW epoch) we have less accuracy and, in that cases, we will regard expression (193) as a phenomenological one.

If $n_2 = 0$ and $n_3 = 0$ then $n(k) < 1$ for all epochs. Giving other values to n_2 and n_3, provided that $4n_2^2 - 9n_1n_3 > 0$, the function (193) shows a maximum and a minimum located at

$$k_{\mp} = k_c \exp\left(-\frac{4n_2}{3n_3} \mp \frac{2}{3n_3} \sqrt{4n_2^2 - 9n_1n_3} \right).$$

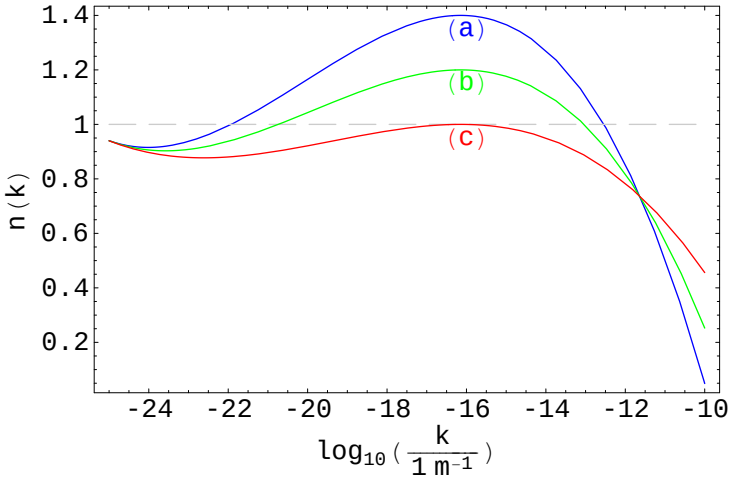

Figure 47: The behaviour of $n(k)$ (equation 193) with a maximum located at $k_+ = 7.1\times10^{-17}$ m^{-1} ($t_k \approx 2.2\times10^{-5}$ s). The cases represented correspond to: (a) $n(k_+) = 1.4$, $n_2 = 0.0345$, $n_3 = -0.00391$; (b) $n(k_+) = 1.2$, $n_2 = 0.0262$, $n_3 = -0.00285$ and (c) $n(k_+) = 1$, $n_2 = 0.0179$, $n_3 = -0.00178$.

We are interested in the location of k_+ (because that is the case for which we have a blue spectrum). Given a location k_+ (or, in terms of time, t_+) to the maximum of $n(k)$ it turns out that the corresponding value of n_3 is given by equation

$$n_3 = -\frac{4\left(3n_1 + 2n_2 \ln\frac{k_+}{k_c}\right)}{3\left(\ln\frac{k_+}{k_c}\right)^2}$$

where k_c represents the pivot scale at which the values of n_0 and n_1 have been measured. Inserting this expression of n_3 into the expression of $n(k)$ (equation 193) with $k = k_+$ and $n(k_+) = n_+$ we obtain for n_2 the expression

$$n_2 = -\frac{6\left(3n_0 - 3n_+ + n_1 \ln\frac{k_+}{k_c}\right)}{\left(\ln\frac{k_+}{k_c}\right)^2}.$$

In Figure 47 we have an example of the curve $n(k)$ and in Table K-1 we present (as an example) the values for n_2 and n_3 for the case $n_+ = 1.4$.

We now show, with a pair of examples, the behaviour of $\alpha^2(t_k)$ (equation 105) in the case of a running–tilt power–law spectrum as given by equation (193). In Figure 48 we show the curve of $\alpha^2(t_k)$ when $n(k_+) = 1.4$ with k_+ assuming the values 3.3×10^{-14} m^{-1} ($t_+ \approx 10^{-10}$ s), 1.1×10^{-16} m^{-1} ($t_+ \approx 10^{-5}$ s) and 3.3×10^{-19} m^{-1} ($t_+ \approx 1$ s), and in Figure 49 we show the curve of $\alpha^2(t_k)$ when $k_+ = 1.1\times10^{-16}$ m^{-1} ($t_+ \approx 10^{-5}$ s) but now with $n(k_+)$ assuming the values 1.2, 1.3 and 1.4.

In Figures 50 and 51 we show the curves of $\sigma^2(t_k)$ (equation 107) for the same examples that we have considered for $\alpha^2(t_k)$ (Figures 48 and 49). Notice that any peculiar features present in the curves of $\alpha^2(t_k)$ are smeared out when one calculates

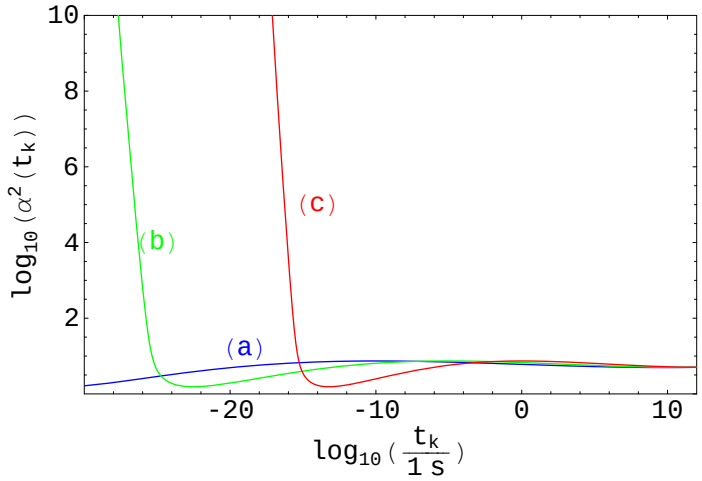

Figure 48: $\alpha^2(t_k)$ for the running–tilt power–law spectrum when the spectral index has the maximum value $n(k_+) = 1.4$ with: (a) $k_+ = 3.3 \times 10^{-14}$ m^{-1} ($t_+ \approx 10^{-10}$ s), (b) $k_+ = 1.1 \times 10^{-16}$ m^{-1} ($t_+ \approx 10^{-5}$ s) and (c) $k_+ = 3.3 \times 10^{-19}$ m^{-1} ($t_+ \approx 1$ s).

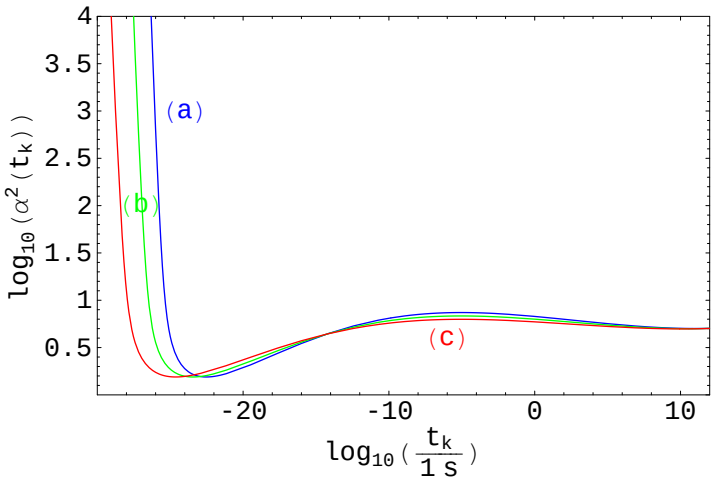

Figure 49: $\alpha^2(t_k)$ for the running–tilt power–law spectrum when the spectral index presents a maximum located at $k_+ = 1.1 \times 10^{-16}$ m^{-1} ($t_+ \approx 10^{-5}$ s) with: (a) $n(k_+) = 1.4$, (b) $n(k_+) = 1.3$ and (c) $n(k_+) = 1.2$.

$\sigma^2(t_k)$. It is clear from Figures 50 and 51 that when $t \sim 10^{12}$ s the value of $\sigma^2(t_k)$ is already very close to the present day value ($\sigma^2(t_0) \sim 10^{-8}$).

5.3 The different scenarios

The fraction of the Universe going into PBHs at a given epoch t_k is given by equation (97). The value of δ_c is, in the case of a radiation–dominated universe, a constant somewhere between 1/3 and 0.7 (Section 1.4.1). However, if the Universe experiences a phase transition, the value of δ_c experiences a reduction which favours PBH formation (Chapter 4). In this section, we consider that, during radiation domination, $\delta_c = 1/3$ and that, during the QCD transition, the EW transition, and the

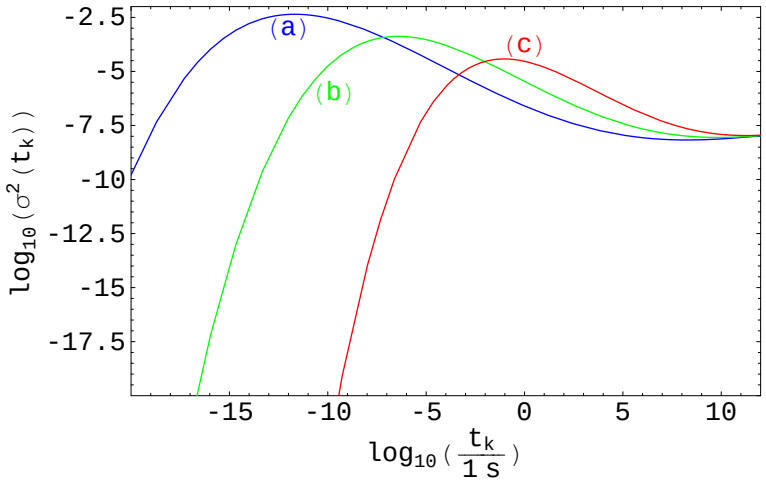

Figure 50: The mass variance $\sigma^2(t_k)$ for the running–tilt power–law spectrum when the spectral index presents the maximum value $n(k_+) = 1.4$ with: (a) $k_+ = 3.3 \times 10^{-14}$ m^{-1} ($t_+ \approx 10^{-10}$ s), (b) $k_+ = 1.1 \times 10^{-16}$ m^{-1} ($t_+ \approx 10^{-5}$ s) and (c) $k_+ = 3.3 \times 10^{-19}$ m^{-1} ($t_+ \approx 1$ s).

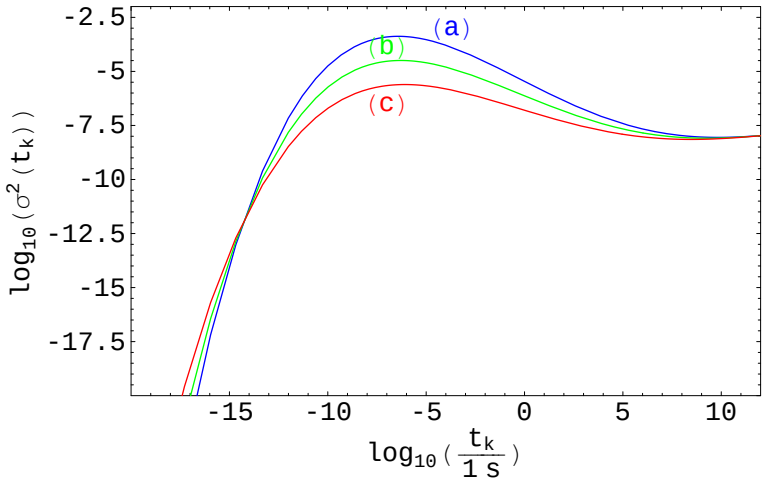

Figure 51: The mass variance $\sigma^2(t_k)$ for the running–tilt power–law spectrum when the spectral index presents a maximum located at $k_+ = 1.1 \times 10^{-16}$ m^{-1} ($t_+ \approx 10^{-5}$ s) with: (a) $n(k_+) = 1.4$, (b) $n(k_+) = 1.3$ and (c) $n(k_+) = 1.2$.

electron–positron annihilation epoch, δ_c assumes the values obtained in Chapter 4.

In the presence of a Crossover–like transition, such as the QCD Crossover, the EW Crossover or the electron–positron annihilation (see Section 1.2), equation (97) must be replaced by

$$\beta_1(t_k) = \frac{1}{\sqrt{2\pi}\sigma(t_k)} \int_{\delta_{c1}}^{\delta_c} \exp\left(-\frac{\delta^2}{2\sigma^2(t_k)}\right) d\delta + \frac{1}{\sqrt{2\pi}\sigma(t_k)} \int_{\delta_c}^{1} \exp\left(-\frac{\delta^2}{2\sigma^2(t_k)}\right) d\delta \tag{194}$$

where the additional integral accounts for the contribution from the Crossover epoch. We refer to the second integral, which is equal to the integral in expression (97), as the *contribution from radiation*. Denoting this integral by $\beta_{Rad}(t_k)$ equation (194) becomes

$$\beta_1(t_k) = \frac{1}{\sqrt{2\pi}\sigma(t_k)} \int_{\delta_{c1}}^{\delta_c} \exp\left(-\frac{\delta^2}{2\sigma^2(t_k)}\right) d\delta + \beta_{Rad}(t_k). \tag{195}$$

Naturally, if we are dealing with epochs sufficiently apart from the transition such that $\delta_{c1} \approx \delta_c$ then equation (97) remains valid.

On the other hand, in the presence of a Bag Model–like transition, such as the QCD Bag Model transition (Section 1.2.1) or the EW Bag Model transition (Section 1.2.2), equation (97) is valid only up to some instant after which there is an additional window $[\delta_{c1}, \delta_{c2}]$ allowing PBH formation (cf. Figure 31 and Table I-1 for the QCD, Figure 43 and Table I-5 for the EW). For these cases equation (97) must be replaced by

$$\beta_2(t_k) = \frac{1}{\sqrt{2\pi}\sigma(t_k)} \int_{\delta_{c1}}^{\delta_{c2}} \exp\left(-\frac{\delta^2}{2\sigma^2(t_k)}\right) d\delta + \beta_{Rad}(t_k).$$

Eventually, we reach some point where there is no more δ_{c2} (see e.g. Figure 31). In that case there is a single window $[\delta_{c1}, 1]$ for PBH formation and we must use, instead, equation (195).

Finally, in the case of a QCD Lattice Fit (Section 1.2.1) we must consider another extra window $[\delta_{cA}, \delta_c]$ allowing PBH formation (cf. Figure 40, Table I-3). In this case we must replace equation (97) by

$$\beta_3(t_k) = \frac{1}{\sqrt{2\pi}\sigma(t_k)} \int_{\delta_{cA}}^{\delta_c} \exp\left(-\frac{\delta^2}{2\sigma^2(t_k)}\right) d\delta + \beta_{Rad}(t_k).$$

Over a brief period we might have to consider the window $[\delta_{c1}, \delta_{c2}]$ (cf. Figure 40). For that period we must use, instead

$$\beta_4(t_k) = \frac{1}{\sqrt{2\pi}\sigma(t_k)} \int_{\delta_{c1}}^{\delta_{c2}} \exp\left(-\frac{\delta^2}{2\sigma^2(t_k)}\right) d\delta +$$

$$+ \frac{1}{\sqrt{2\pi}\sigma(t_k)} \int_{\delta_{cA}}^{\delta_c} \exp\left(-\frac{\delta^2}{2\sigma^2(t_k)}\right) d\delta + \beta_{Rad}(t_k).$$

Moving to later epochs we reach some point after which there is no more δ_{c2} available (see e.g. Figure 40). In that case there is a single window $[\delta_{c1}, 1]$ for PBH formation and we use equation (195).

Taking into account the considered models for the EW phase transition (Section 1.2.2), for the QCD transition (Section 1.2.1), and for the electron–positron annihilation (Section 1.2.3), there are six different possible scenarios (2 EW models $\times$ 3

Table 10: The different scenarios concerning the calculation of β.

Scenario	EW model	QCD model	e^-e^+ model
1	Crossover	Bag Model	Crossover
2	Crossover	Lattice Fit	Crossover
3	Crossover	Crossover	Crossover
4	Bag Model	Bag Model	Crossover
5	Bag Model	Lattice Fit	Crossover
6	Bag Model	Crossover	Crossover

QCD models $\times$ 1 e^-e^+ model) concerning the determination of the curve $\beta(t_k)$. We list those scenarios in Table 10.

For a given scenario, and for a given instant t_k, one must choose the appropriate expression to determine the value $\beta(t_k)$. Proceding this way, for different values of t_k, one can determine the curve $\beta(t_k)$ for that particular scenario.

In Sections 5.4 to 5.8 we make use of a few abreviations concerning different contributions to $\beta(t_k)$ (see Conventions). For example, RBE, represents a case for which there are non–negligible contributions from radiation (R), from the QCD Bag Model (B), and from the EW Bag Model (E) but with negligible contributions from the electron–positron annihilation as well as from the QCD Lattice Fit and from the QCD Crossover (if one chooses one of these models instead of the Bag Model).

We might have also situations with one or more contributions exceeding the observational limits (these are labeled with an $*$). For example, RB^*LCE^*, represents a case for which we have, besides the contribution from radiation R, contributions from the QCD Lattice Fit (L) or from the QCD Crossover (C). The QCD Bag Model is excluded due to observational constraints (B^*). The same happens for the EW Bag Model (E^*). The contribution from the electron–positron annihilation epoch is negligible in this case.

5.4 Radiation–dominated universe

In this section we determine the fraction of the Universe going into PBHs at different epochs for a radiation–dominated universe with a running–tilt power–law spectrum (Sections 1.3.2 and 5.2). We are interested in a blue spectrum, i.e, a spectrum for which $n > 1$. In fact, if we want to have interesting values for β, then we should have, at least, $n \gtrsim 1.22$. As an upper limit we consider $n \approx 2.0$. This corresponds to a cut–off at $t_k \sim 10^5$ s (see Figure 52) which excludes PBHs with masses larger than $\sim 10^{10} M_\odot$ (which is equivalent to the mass of the present day largest SMBH candidates; e.g. Kormendy, 2004; Natarajan & Treister, 2009). We consider, for t_+,

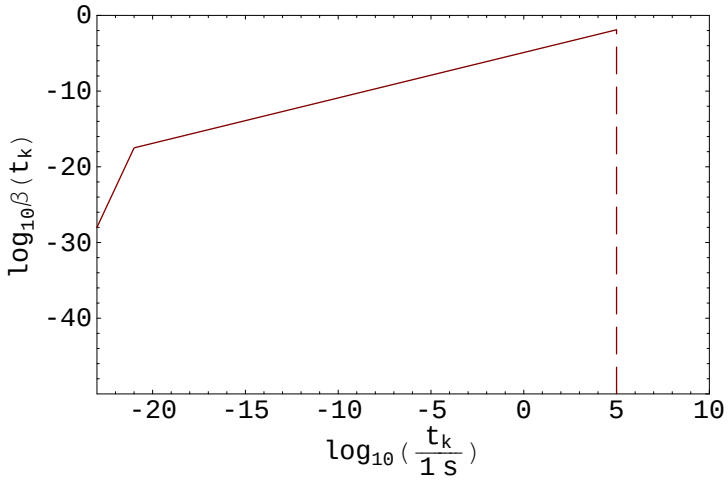

Figure 52: Observational constraints on $\beta(t_k)$. The vertical dashed line ($t_k = 10^5$ s) corresponds to an horizon mass of $\sim 10^{10} M_\odot$ (adapted from Carr, 2005).

all orders of magnitude between 10^{-23} s (we are interested in non–exploded PBHs) and 10^8 s (above this limit we get negligible results).

Each pair of the form (t_+, n_+) determines a different location and a different value for the maximum value of $\beta(t_k)$. In general one of three things might occur:

(1) $\beta(t_k)$ exceeds the observational constraints $\Rightarrow$ the pair (t_+, n_+) must be rejected.

(2) $\beta(t_k)$ is negligible ($< 10^{-100}$) for all values of t_k, in which case we take $\beta(t_k) = 0$.

(3) $\beta(t_k)$ is always below the observational constraints and, at least during some epoch, above 10^{-100}; these are the cases of interest to us.

Let us consider, as an example, the case $n_+ = 1.30$. If $t_+ = 10^{-17}$ s, then $\beta(t_k)$ exceeds the observational constraints as it is clear from Figure 53a. On the other hand, if $t_+ = 10^{-16}$ s we obtain a valid curve for $\beta(t_k)$ (see Figure 53b) with $\beta_{max} \sim 10^{-17}$. As one moves t_+ to later epochs the value of β_{max} becomes smaller (see Figure 53b) until, for $t_+ = 10^{-10}$ s, we reach $\beta_{max} \sim 10^{-133}$ (see Figure 53c). Thus, we consider that, in the case of $n_+ = 1.30$, there is a window 10^{-16} s $\leq t_+ \leq 10^{-11}$ s which is suitable for PBH formation. Cases with $t_+ < 10^{-16}$ s are not allowed and cases with $t_+ > 10^{-11}$ s are allowed but with negligible results.

We studied the intervals of this permitted window for different values of n_+ (between 1.20 and 2.00). The window moves to later epochs as one moves to larger values of n_+. As a lower limit, for $n < 1.22$, we get $\beta(t_k) \approx 0$ (no matter t_k or t_+). We selected 151 cases suitable for PBH production, in a radiation–dominated universe, that we show in Table 11 (these cases are marked by 'R').

On the lower right corner of Table 11 we show the cases for which $\beta(t_k)$ reaches values to the right of the cut–off line at $t_k = 10^5$ s ('R' with a gray background). We selected

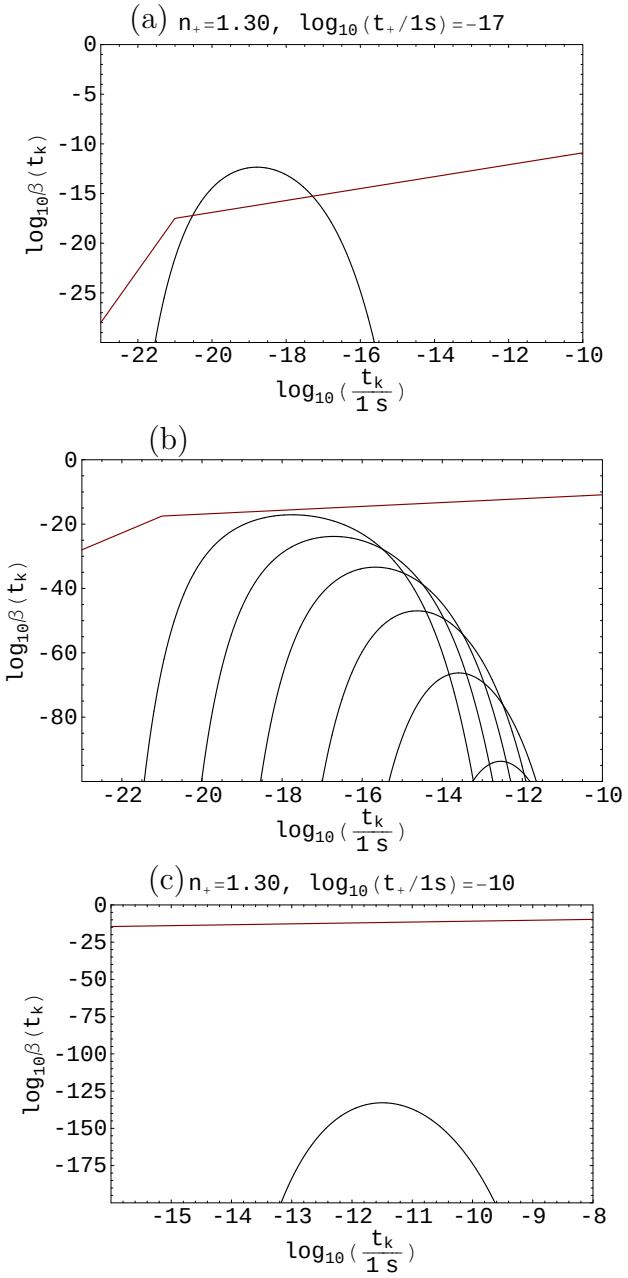

Figure 53: The fraction of the Universe going into PBHs in a radiation–dominated universe with a running–tilt power–law spectrum when $n_+ = 1.30$ and: (a) $t_+ = 10^{-17}$ s – not allowed since the curve $\beta(t_k)$ – black – does not respect the observational constraints (maroon); (b) from left to right: $t_+ = 10^{-16}$ s, $t_+ = 10^{-15}$ s, $t_+ = 10^{-14}$ s, $t_+ = 10^{-13}$ s, $t_+ = 10^{-12}$ s, and $t_+ = 10^{-11}$ s; (c) $t_+ = 10^{-10}$ s.

three examples, in order to ilustrate this particular situation (see Figure 54). In the case when $t_+ = 10^7$ s and $n_+ = 2.00$, represented in Figure 54c, the maximum of $\beta(t_k)$ is attained when $t_k \approx 10^{-6.5}$ s which corresponds to an horizon mass of $10^{11} M_\odot$ ($> 10^{10} M_\odot$).

For each case marked with 'R' in Table 11 we determined the corresponding maximum value of $\sigma^2(t_k)$ (equation 107). In Table L-1 we show the maximum values reached by $\sigma^2(t_k)$ for each considered value of n_+ (which corresponds to the value of t_+ right below the forbidden red region). For most of the cases we have $\sigma^2_{max}(t_k) \sim 10^{-4}$ (in fact $\sigma^2_{max}(t_k)$ never exceeds 6.5×10^{-4}). This means that, whatever the value of $\delta_c \in [1/3, 0.7]$ we consider, we have $\sigma^2(t_k) \ll \delta_c$ for all the relevant cases. This turns out to be an important result because it permits very useful simplifications of the equations (see e.g. equations 97 and 98).

5.5 EW Crossover

It was already mentioned that, in the context of the SMPP, the EW transition is a very smooth Crossover (Section 1.2.2). As a consequence of this, the contribution from the EW Crossover to the value of $\beta(t_k)$ is very small. In fact, in this case, the new threshold δ_{c1} stays always very close to δ_c (see Table I-4).

We consider, as an example, $t_+ = 10^{-8}$ s and $n_+ = 1.40$. In this case, the contribution from the EW Crossover to the total value of $\beta(t_k)$ is negligible (of order unity – Figure 55). On the face of this, we neglect all contributions from the EW Crossover.

5.6 Electron–positron annihilation

The cosmological electron–positron annihilation ocurred when the age of the Universe was ~ 1 s. Thus, the additional contribution from this epoch to the global value of β is more relevant when $t_+ \sim 1$ s. Integrating equation (195), with the threshold δ_{c1} replaced by the appropriate values (see Table I-6), we find that the cases with a non–zero contribution from the electron–positron annihilation are in the range $-2 \leq \log_{10}(t_+/1s) \leq 2$ and $1.52 \leq n_+ \leq 1.72$, as shown in Table 12.

Let us start with $t_+ = 1$ s. In this case the contribution from the electron–positron annihilation epoch is almost equal in magnitude to the contribution from radiation (although with peaks at different epochs). In Figure 56a we show, as a first example, the case $t_+ = 1$ s and $n_+ = 1.56$. From the radiation contribution we have $\beta_{max} \sim 10^{-29}$ located at $t_k \sim 10^{-1.14}$ s and from the electron–positron annihilation contribution we have $\beta_{max} \sim 10^{-34}$ located at $t_k \sim 10^{-0.07}$ s. As a second example we show in Figure 56b the case $t_+ = 1$ s and $n_+ = 1.62$. Now, we have from the radiation contribution $\beta_{max} \sim 10^{-10}$ located at $t_k \approx 10^{-1.2}$ s and from the electron–positron annihilation contribution $\beta_{max} \sim 10^{-12}$ located at $t_k \approx 10^{-0.08}$ s.

When $t_+ \approx 10$ s the contribution from the electron–positron annihilation epoch exceeds the contribution from radiation. As a first example let us consider the case

Table 11: The cases for which $\beta > 10^{-100}$ for a radiation–dominated universe with a running–tilt power–law spectrum when $\delta_c = 1/3$. Here n_+ represents the maximum value of the spectral index $n(k)$, and t_+ gives the location of that maximum (see Section 5.2). In cyan we show the cases for which $\beta(t_k) \approx 0$ and in red the cases for which $\beta(t_k)$ exceeds the observational constraints (cf. Figure 52). The cases suitable for PBH production are marked by 'R' (in white or gray). In gray we show the cases for which $\beta(t_k)$ crosses the $\approx 10^{10} M_\odot$ line.

	n_+																																							
$\log_{10}(t_+/1\text{s})$	1.20	1.22	1.24	1.26	1.28	1.30	1.32	1.34	1.36	1.38	1.40	1.42	1.44	1.46	1.48	1.50	1.52	1.54	1.56	1.58	1.60	1.62	1.64	1.66	1.68	1.70	1.72	1.74	1.76	1.78	1.80	1.82	1.84	1.86	1.88	1.90	1.92	1.94	1.96	1.98	2.00
-23	🟦	R	R	🟥	🟥	🟥	🟥	🟥	🟥	🟥	🟥	🟥	🟥	🟥	🟥	🟥	🟥	🟥	🟥	🟥	🟥	🟥	🟥	🟥	🟥	🟥	🟥	🟥	🟥	🟥	🟥	🟥	🟥	🟥	🟥	🟥	🟥	🟥	🟥	🟥	🟥
-22	🟦	R	R	🟥	🟥	🟥	🟥	🟥	🟥	🟥	🟥	🟥	🟥	🟥	🟥	🟥	🟥	🟥	🟥	🟥	🟥	🟥	🟥	🟥	🟥	🟥	🟥	🟥	🟥	🟥	🟥	🟥	🟥	🟥	🟥	🟥	🟥	🟥	🟥	🟥	🟥
-21	🟦	R	R	🟥	🟥	🟥	🟥	🟥	🟥	🟥	🟥	🟥	🟥	🟥	🟥	🟥	🟥	🟥	🟥	🟥	🟥	🟥	🟥	🟥	🟥	🟥	🟥	🟥	🟥	🟥	🟥	🟥	🟥	🟥	🟥	🟥	🟥	🟥	🟥	🟥	🟥
-20	🟦	🟦	R	🟥	🟥	🟥	🟥	🟥	🟥	🟥	🟥	🟥	🟥	🟥	🟥	🟥	🟥	🟥	🟥	🟥	🟥	🟥	🟥	🟥	🟥	🟥	🟥	🟥	🟥	🟥	🟥	🟥	🟥	🟥	🟥	🟥	🟥	🟥	🟥	🟥	🟥
-19	🟦	🟦	R	R	🟥	🟥	🟥	🟥	🟥	🟥	🟥	🟥	🟥	🟥	🟥	🟥	🟥	🟥	🟥	🟥	🟥	🟥	🟥	🟥	🟥	🟥	🟥	🟥	🟥	🟥	🟥	🟥	🟥	🟥	🟥	🟥	🟥	🟥	🟥	🟥	🟥
-18	🟦	🟦	R	R	R	🟥	🟥	🟥	🟥	🟥	🟥	🟥	🟥	🟥	🟥	🟥	🟥	🟥	🟥	🟥	🟥	🟥	🟥	🟥	🟥	🟥	🟥	🟥	🟥	🟥	🟥	🟥	🟥	🟥	🟥	🟥	🟥	🟥	🟥	🟥	🟥
-17	🟦	🟦	🟦	R	R	🟥 Fig. 53a	🟥	🟥	🟥	🟥	🟥	🟥	🟥	🟥	🟥	🟥	🟥	🟥	🟥	🟥	🟥	🟥	🟥	🟥	🟥	🟥	🟥	🟥	🟥	🟥	🟥	🟥	🟥	🟥	🟥	🟥	🟥	🟥	🟥	🟥	🟥
-16	🟦	🟦	🟦	R	R	R Fig. 53b	🟥	🟥	🟥	🟥	🟥	🟥	🟥	🟥	🟥	🟥	🟥	🟥	🟥	🟥	🟥	🟥	🟥	🟥	🟥	🟥	🟥	🟥	🟥	🟥	🟥	🟥	🟥	🟥	🟥	🟥	🟥	🟥	🟥	🟥	🟥
-15	🟦	🟦	🟦	🟦	R	R Fig. 53b	🟥	🟥	🟥	🟥	🟥	🟥	🟥	🟥	🟥	🟥	🟥	🟥	🟥	🟥	🟥	🟥	🟥	🟥	🟥	🟥	🟥	🟥	🟥	🟥	🟥	🟥	🟥	🟥	🟥	🟥	🟥	🟥	🟥	🟥	🟥
-14	🟦	🟦	🟦	🟦	R	R Fig. 53b	R	🟥	🟥	🟥	🟥	🟥	🟥	🟥	🟥	🟥	🟥	🟥	🟥	🟥	🟥	🟥	🟥	🟥	🟥	🟥	🟥	🟥	🟥	🟥	🟥	🟥	🟥	🟥	🟥	🟥	🟥	🟥	🟥	🟥	🟥
-13	🟦	🟦	🟦	🟦	R	R Fig. 53b	R	🟥	🟥	🟥	🟥	🟥	🟥	🟥	🟥	🟥	🟥	🟥	🟥	🟥	🟥	🟥	🟥	🟥	🟥	🟥	🟥	🟥	🟥	🟥	🟥	🟥	🟥	🟥	🟥	🟥	🟥	🟥	🟥	🟥	🟥
-12	🟦	🟦	🟦	🟦	🟦	R Fig. 53b	R	R	🟥	🟥	🟥	🟥	🟥	🟥	🟥	🟥	🟥	🟥	🟥	🟥	🟥	🟥	🟥	🟥	🟥	🟥	🟥	🟥	🟥	🟥	🟥	🟥	🟥	🟥	🟥	🟥	🟥	🟥	🟥	🟥	🟥
-11	🟦	🟦	🟦	🟦	🟦	R Fig. 53b	R	R	R	🟥	🟥	🟥	🟥	🟥	🟥	🟥	🟥	🟥	🟥	🟥	🟥	🟥	🟥	🟥	🟥	🟥	🟥	🟥	🟥	🟥	🟥	🟥	🟥	🟥	🟥	🟥	🟥	🟥	🟥	🟥	🟥
-10	🟦	🟦	🟦	🟦	🟦	🟦 Fig. 53c	R	R	R	🟥	🟥	🟥	🟥	🟥	🟥	🟥	🟥	🟥	🟥	🟥	🟥	🟥	🟥	🟥	🟥	🟥	🟥	🟥	🟥	🟥	🟥	🟥	🟥	🟥	🟥	🟥	🟥	🟥	🟥	🟥	🟥
-9	🟦	🟦	🟦	🟦	🟦	🟦	🟦	R	R	R	🟥	🟥	🟥	🟥	🟥	🟥	🟥	🟥	🟥	🟥	🟥	🟥	🟥	🟥	🟥	🟥	🟥	🟥	🟥	🟥	🟥	🟥	🟥	🟥	🟥	🟥	🟥	🟥	🟥	🟥	🟥
-8	🟦	🟦	🟦	🟦	🟦	🟦	🟦	R	R	R	R	🟥	🟥	🟥	🟥	🟥	🟥	🟥	🟥	🟥	🟥	🟥	🟥	🟥	🟥	🟥	🟥	🟥	🟥	🟥	🟥	🟥	🟥	🟥	🟥	🟥	🟥	🟥	🟥	🟥	🟥
-7	🟦	🟦	🟦	🟦	🟦	🟦	🟦	🟦	R	R	R	R	🟥	🟥	🟥	🟥	🟥	🟥	🟥	🟥	🟥	🟥	🟥	🟥	🟥	🟥	🟥	🟥	🟥	🟥	🟥	🟥	🟥	🟥	🟥	🟥	🟥	🟥	🟥	🟥	🟥
-6	🟦	🟦	🟦	🟦	🟦	🟦	🟦	🟦	🟦	R	R	R	R	🟥	🟥	🟥	🟥	🟥	🟥	🟥	🟥	🟥	🟥	🟥	🟥	🟥	🟥	🟥	🟥	🟥	🟥	🟥	🟥	🟥	🟥	🟥	🟥	🟥	🟥	🟥	🟥
-5	🟦	🟦	🟦	🟦	🟦	🟦	🟦	🟦	🟦	🟦	R	R	R	R	🟥	🟥	🟥	🟥	🟥	🟥	🟥	🟥	🟥	🟥	🟥	🟥	🟥	🟥	🟥	🟥	🟥	🟥	🟥	🟥	🟥	🟥	🟥	🟥	🟥	🟥	🟥
-4	🟦	🟦	🟦	🟦	🟦	🟦	🟦	🟦	🟦	🟦	R	R	R	R	R	🟥	🟥	🟥	🟥	🟥	🟥	🟥	🟥	🟥	🟥	🟥	🟥	🟥	🟥	🟥	🟥	🟥	🟥	🟥	🟥	🟥	🟥	🟥	🟥	🟥	🟥
-3	🟦	🟦	🟦	🟦	🟦	🟦	🟦	🟦	🟦	🟦	🟦	R	R	R	R	R	R	🟥	🟥	🟥	🟥	🟥	🟥	🟥	🟥	🟥	🟥	🟥	🟥	🟥	🟥	🟥	🟥	🟥	🟥	🟥	🟥	🟥	🟥	🟥	🟥
-2	🟦	🟦	🟦	🟦	🟦	🟦	🟦	🟦	🟦	🟦	🟦	🟦	🟦	R	R	R	R	R	🟥	🟥	🟥	🟥	🟥	🟥	🟥	🟥	🟥	🟥	🟥	🟥	🟥	🟥	🟥	🟥	🟥	🟥	🟥	🟥	🟥	🟥	🟥
-1	🟦	🟦	🟦	🟦	🟦	🟦	🟦	🟦	🟦	🟦	🟦	🟦	🟦	🟦	R	R	R	R	R	R	🟥	🟥	🟥	🟥	🟥	🟥	🟥	🟥	🟥	🟥	🟥	🟥	🟥	🟥	🟥	🟥	🟥	🟥	🟥	🟥	🟥
0	🟦	🟦	🟦	🟦	🟦	🟦	🟦	🟦	🟦	🟦	🟦	🟦	🟦	🟦	🟦	R	R	R	R	R	R	R	🟥	🟥	🟥	🟥	🟥	🟥	🟥	🟥	🟥	🟥	🟥	🟥	🟥	🟥	🟥	🟥	🟥	🟥	🟥
1	🟦	🟦	🟦	🟦	🟦	🟦	🟦	🟦	🟦	🟦	🟦	🟦	🟦	🟦	🟦	🟦	🟦	R	R	R	R	R	R	R	R	🟥	🟥	🟥	🟥	🟥	🟥	🟥	🟥	🟥	🟥	🟥	🟥	🟥	🟥	🟥	🟥
2	🟦	🟦	🟦	🟦	🟦	🟦	🟦	🟦	🟦	🟦	🟦	🟦	🟦	🟦	🟦	🟦	🟦	🟦	🟦	R	R	R	R	R	R	R	R	🟥	🟥	🟥	🟥	🟥	🟥	🟥	🟥	🟥	🟥	🟥	🟥	🟥	🟥
3	🟦	🟦	🟦	🟦	🟦	🟦	🟦	🟦	🟦	🟦	🟦	🟦	🟦	🟦	🟦	🟦	🟦	🟦	🟦	🟦	🟦	R	R	R	R	R	R	R	R	R	🟥	🟥	🟥	🟥	🟥	🟥	🟥	🟥	🟥	🟥	🟥
4	🟦	🟦	🟦	🟦	🟦	🟦	🟦	🟦	🟦	🟦	🟦	🟦	🟦	🟦	🟦	🟦	🟦	🟦	🟦	🟦	🟦	🟦	🟦	R	R	R	R	R	R	▨ R	▨ R	▨ R	▨ R Fig. 54a	▨ R	🟥	🟥	🟥	🟥	🟥	🟥	🟥
5	🟦	🟦	🟦	🟦	🟦	🟦	🟦	🟦	🟦	🟦	🟦	🟦	🟦	🟦	🟦	🟦	🟦	🟦	🟦	🟦	🟦	🟦	🟦	🟦	🟦	🟦	R	R	▨ R	▨ R	▨ R	▨ R	▨ R	▨ R	▨ R Fig. 54b	▨ R	▨ R	▨ R	🟥	🟥	🟥
6	🟦	🟦	🟦	🟦	🟦	🟦	🟦	🟦	🟦	🟦	🟦	🟦	🟦	🟦	🟦	🟦	🟦	🟦	🟦	🟦	🟦	🟦	🟦	🟦	🟦	🟦	🟦	🟦	🟦	🟦	▨ R	▨ R	▨ R	▨ R	▨ R	▨ R	▨ R	▨ R	▨ R	▨ R	▨ R
7	🟦	🟦	🟦	🟦	🟦	🟦	🟦	🟦	🟦	🟦	🟦	🟦	🟦	🟦	🟦	🟦	🟦	🟦	🟦	🟦	🟦	🟦	🟦	🟦	🟦	🟦	🟦	🟦	🟦	🟦	🟦	🟦	🟦	🟦	▨ R	▨ R	▨ R	▨ R	▨ R	▨ R	▨ R Fig. 54c
8	🟦	🟦	🟦	🟦	🟦	🟦	🟦	🟦	🟦	🟦	🟦	🟦	🟦	🟦	🟦	🟦	🟦	🟦	🟦	🟦	🟦	🟦	🟦	🟦	🟦	🟦	🟦	🟦	🟦	🟦	🟦	🟦	🟦	🟦	🟦	🟦	🟦	🟦	🟦	▨ R	▨ R
9	🟦	🟦	🟦	🟦	🟦	🟦	🟦	🟦	🟦	🟦	🟦	🟦	🟦	🟦	🟦	🟦	🟦	🟦	🟦	🟦	🟦	🟦	🟦	🟦	🟦	🟦	🟦	🟦	🟦	🟦	🟦	🟦	🟦	🟦	🟦	🟦	🟦	🟦	🟦	🟦	🟦

Table 12: The contribution to β from the electron–positron annihilation epoch. In yellow we show the cases for which there is a non–negligible contribution to β from the electron–positron annihilation epoch. For more details see Table 11 and the Conventions.

	n_+															
$\log_{10}(t_+/1\text{s})$	1.50	1.52	1.54	1.56	1.58	1.60	1.62	1.64	1.66	1.68	1.70	1.72	1.74	1.76	1.78
-3	RB*L*C	RB*L*C*													
-2	RBLC	RB*L*C	RB*L*Cea Fig. 58												
-1	R	Rea	RBLCea	RBLCea Fig. 57	RBLCea										
0	R	Rea	Rea	Rea Fig. 56a	Rea	Rea	Rea Fig. 56b								
1		ea	Rea Fig. 56c	Rea	Rea	Rea	Rea	Rea	Rea Fig. 56d	Rea*					
2					Rea	Rea Fig. 56e	Rea	Rea	Rea	Rea Fig. 56f	Rea	Rea			
3							R	R	R	R	R	R	R	R	R

$t_+ = 10$ s and $n_+ = 1.54$ (Figure 56c). Now we have a modest contribution from the electron–positron annihilation epoch with $\beta_{max} \sim 10^{-67}$ located at $t_k \sim 10^{-0.02}$ s and an even smaller contribution from radiation with $\beta_{max} \sim 10^{-80}$ located at $t_k \sim 10^{-0.045}$ s. As a second example we consider the case $t_+ = 10$ s and $n_+ = 1.66$ (Figure 56d). We now have more interesting values with $\beta_{max} \sim 10^{-8}$ located at $t_k \sim 10^{-0.025}$ s from the electron–positron annihilation epoch contribution and $\beta_{max} \sim 10^{-10}$ located at $t_k \sim 10^{-0.09}$ s from the radiation contribution (the peaks nearly overlap).

When $t_+ \approx 100$ s the contribution from the electron–positron annihilation epoch appears as an extension to the left on the curve of $\beta(t_k)$ as can be seen in Figures 56e and 56f.

In the case $t_+ = 10^{-1}$ s we might simultaneously have contributions from the electron–positron annihilation epoch and from the QCD phase transition ($RBLCea$ in Table 12). However, in these cases the main contribution always comes from radiation. As an example we have the case $t_+ = 10^{-1}$ s and $n_+ = 1.56$ represented in Figure[26] 57.

When $t_+ = 10^{-2}$ s and $n_+ = 1.54$ we also simultaneously have contributions from the electron–positron annihilation epoch and from the QCD epoch (Figure 58). However, in this case the main contribution to $\beta(t_k)$ comes from radiation and from the QCD Crossover (if one adopts for the QCD the Bag Model or the Lattice Fit, then this case is excluded due to observational constraints, see Section 5.7).

5.7 QCD phase transition

The contribution from the QCD phase transition to the global value of β depends on the model one adopts. There are some cases which are allowed when one considers only the contribution from radiation but which must be excluded when one takes into account the QCD phase transition because of the observational limits (cf. Tables 13, 14 and 15).

Consider, for example, the case $t_+ = 10^{-4}$ s and $n_+ = 1.48$, represented in Figure 59. It is clear that if one adopts a Bag Model or a Lattice Fit for the QCD transition, this case must be excluded. However, if one adopts the Crossover model, then it remains valid.

As a peculiar example we show the case $t_+ = 10^{-3}$ s and $n_+ = 1.52$, which is allowed when one takes into account only the contribution from radiation domination but must be excluded whatever the model one adopts for the QCD phase transition (Figure 60).

[26] In order to interpret correctly the curves in Figure 57, assuming a QCD Bag Model, start on the left over the blue line, then move to the black line (contribution from radiation) and, finally, move to the cyan line (contribution from the electron–positron annihilation). In the case of a QCD Lattice Fit start, instead, with the line in magenta and in the case of a QCD Crossover start with the green line.

Table 13: The contribution to β from the QCD Bag Model. In yellow we show the cases for which there is a non–negligible contribution to β from the QCD Bag Model. For more details see Table 11 and the Conventions.

	n_+																		
$\log_{10}(t_+/1\text{s})$	1.28	1.30	1.32	1.34	1.36	1.38	1.40	1.42	1.44	1.46	1.48	1.50	1.52	1.54	1.56	1.58	1.60	1.62	1.64
-11		R	R	R	R														
-10			R	R	RB														
-9				RB	RB	RB													
-8			B	RB	RB	RB	RB												
-7		B	B	B	RB	RB	RB	RB*											
-6		B Fig. 61c	B	B	B	RB	RB*	RB*	RB*										
-5		B	B	B	B	B	RB* Fig. 61d	RB*	RB*	RB*									
-4		B	B	B	B	B Fig. 61b	RB Fig. 61a	RB*	RB*	RB*	RB* Fig. 59								
-3				B	B	B	B	RB	RB* Fig. 61e	RB*	RB*	RB*	RB* Fig. 60						
-2							B	B	B	RB	RB	RB Fig. 61f	RB*	RB*ea					
-1											R	R	Rea	RBea	RBea	RBea			
0												R	Rea	Rea	Rea	Rea	Rea	Rea	

Table 14: The contribution to β from the QCD Lattice Fit. In yellow we show the cases for which there is a non–negligible contribution to β from the QCD Lattice Fit. For more details see Table 11 and the Conventions.

	n_+																		
$\log_{10}(t_+/1\text{s})$	1.28	1.30	1.32	1.34	1.36	1.38	1.40	1.42	1.44	1.46	1.48	1.50	1.52	1.54	1.56	1.58	1.60	1.62	1.64
-11		R	R	R	R														
-10			R	R	R														
-9				R	R	RL													
-8				R	RL	RL	RL												
-7				L	RL	RL	RL	RL											
-6			L	L	L	RL	RL	RL	RL*										
-5			L	L	L	L	RL Fig. 61d	RL	RL*	RL*									
-4			L	L	L	L Fig. 61b	RL Fig. 61a	RL	RL*	RL*	RL* Fig. 59								
-3				L	L	L	L	RL	RL Fig. 61e	RL*	RL*	RL*	RL* Fig. 60						
-2							L	L	L	RL	RL	RL Fig. 61f	RL*	RL*ea					
-1											R	R	Rea	RLea	RLea	RLea			
0												R	Rea	Rea	Rea	Rea	Rea	Rea	

Table 15: The contribution to β from the QCD Crossover. In yellow we show the cases for which there is a non–negligible contribution to β from the QCD Crossover. For more details see Table 11 and the Conventions.

	n_+																		
$\log_{10}(t_+/1\text{s})$	1.28	1.30	1.32	1.34	1.36	1.38	1.40	1.42	1.44	1.46	1.48	1.50	1.52	1.54	1.56	1.58	1.60	1.62	1.64
-11		R	R	R	R														
-10			R	R	R														
-9				R	R	R													
-8				R	R	R	R												
-7					R	R	R	RC											
-6						R	RC	RC	RC										
-5							RC Fig. 61d	RC	RC	RC									
-4							RC Fig. 61a	RC	RC	RC	RC Fig. 59								
-3								RC	RC Fig. 61e	RC	RC	RC	RC* Fig. 60						
-2										RC	RC	RC Fig. 61f	RC	RCea					
-1											R	R	Rea	RCea	RCea	RCea			
0												R	Rea	Rea	Rea	Rea	Rea	Rea	

In Figure 61a we show the case $t_+ = 10^{-4}$ s and $n_+ = 1.40$. In this case we have important contributions from the QCD transition ($\beta_{max} \sim 10^{-9}$ in the case of a Bag Model, $\beta_{max} \sim 10^{-14}$ in the case of a Lattice Fit and $\beta_{max} \sim 10^{-75}$ in the case of a Crossover) and an almost negligible contribution from radiation ($\beta_{max} \sim 10^{-97}$).

We have also to consider new cases for which the contribution from radiation is negligible ($\beta < 10^{-100}$ for all t_k, cases represented in Table 11 in cyan) but with some contribution from the QCD phase transition (cf. Table 13 – cases marked with 'B', and Table 14 – cases marked with 'L').

In Figure 61b we show the case $t_+ = 10^{-4}$ s and $n_+ = 1.38$, for which we have only meaningful contributions from the QCD Bag Model ($\beta_{max} \sim 10^{-13}$) or from the QCD Lattice Fit ($\beta_{max} \sim 10^{-22}$). In Figure 61c we show the case $t_+ = 10^{-6}$ s and $n_+ = 1.30$, for which the only relevant contribution comes from the QCD Bag Model, with $\beta_{max} \sim 10^{-69}$.

In the example of Figure 61d we show the case $t_+ = 10^{-5}$ s and $n_+ = 1.40$. Notice that we now have a visible contribution from radiation ($\beta_{max} \sim 10^{-61}$) as well as an important contribution from the QCD Lattice Fit ($\beta_{max} \sim 10^{-12}$). The contribution from the QCD Crossover ($\beta_{max} \sim 10^{-74}$) is very small, compared with the others. In this case the QCD Bag Model is excluded, due to observational constraints.

In Figure 61e we show, as a similar example, the case $t_+ = 10^{-3}$ s and $n_+ = 1.44$, now with a more important contribution from the QCD Crossover ($\beta_{max} \sim 10^{-43}$). The contribution from the Lattice Fit remains important ($\beta_{max} \sim 10^{-11}$) and the QCD Bag Model remains excluded. Finally, in Figure 61f we show the case $t_+ = 10^{-2}$ s and $n_+ = 1.50$. In this case we might have contributions from the QCD Bag Model ($\beta_{max} \sim 10^{-9}$), from the QCD Lattice Fit ($\beta_{max} \sim 10^{-11}$) or from the QCD Crossover ($\beta_{max} \sim 10^{-28}$).

We might have cases with simultaneous contributions from both QCD and EW transitions. Those are considered in Section 5.8. We might also have cases with simultaneous contributions from the QCD phase transition and from the electron–positron annihilation epoch. We have already presented two examples of these in Figures 57 and 58.

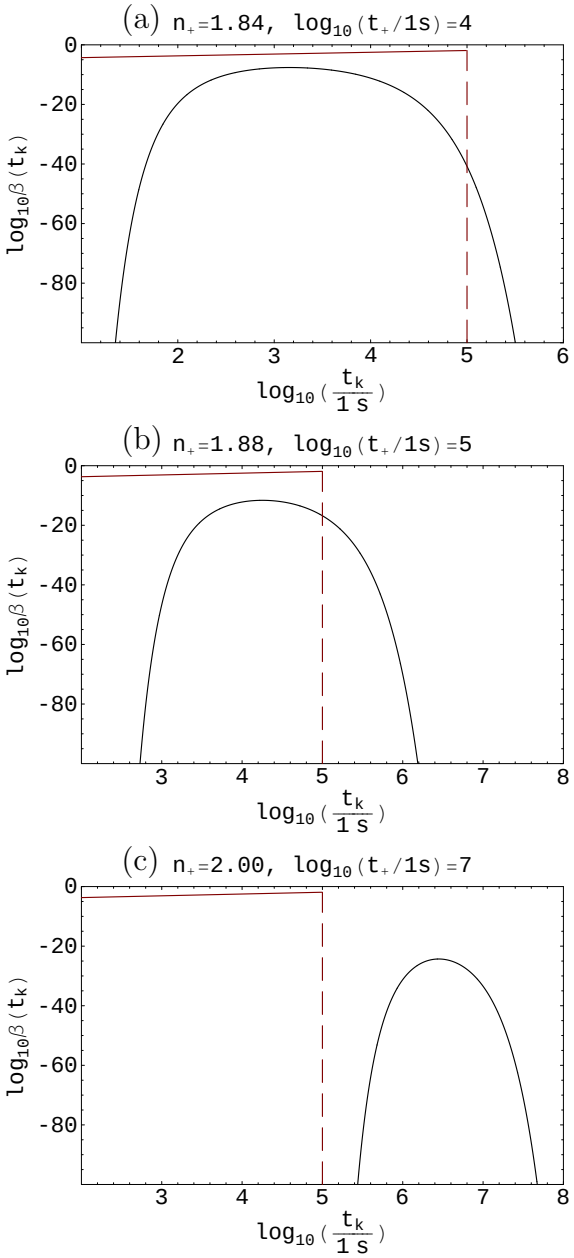

Figure 54: The fraction of the Universe going into PBHs in a radiation–dominated universe with a running–tilt power–law spectrum when: (a) $n_+ = 1.84$, $t_+ = 10^4$ s; (b) $n_+ = 1.88$, $t_+ = 10^5$ s; (c) $n_+ = 2.00$, $t_+ = 10^7$ s. In (a) and (b) some values go over the $\sim 10^{10} M_\odot$ line (cf. Figure 52) and, in (c) the peak, and all 'non–zero' values, fall on the $> 10^{10} M_\odot$ region.

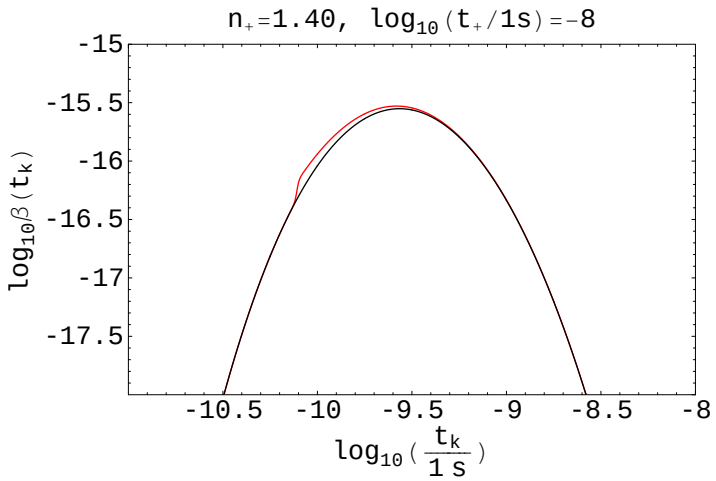

Figure 55: The fraction of the Universe going into PBHs for a running–tilt power–law spectrum with $n_+ = 1.40$ and $t_+ = 10^{-8}$ s. The red line corresponds to the contribution from the EW Crossover while the black line represents the contribution from the radiation domination. The maximum difference between the two in $\beta(t_k)$ is of order unity ($\simeq 10^{0.1}$). In order to properly read this graphic start on the left and move across the black line (contribution from radiation), then move to the red line (EW Crossover contribution) and, finally, move once again to the black line.

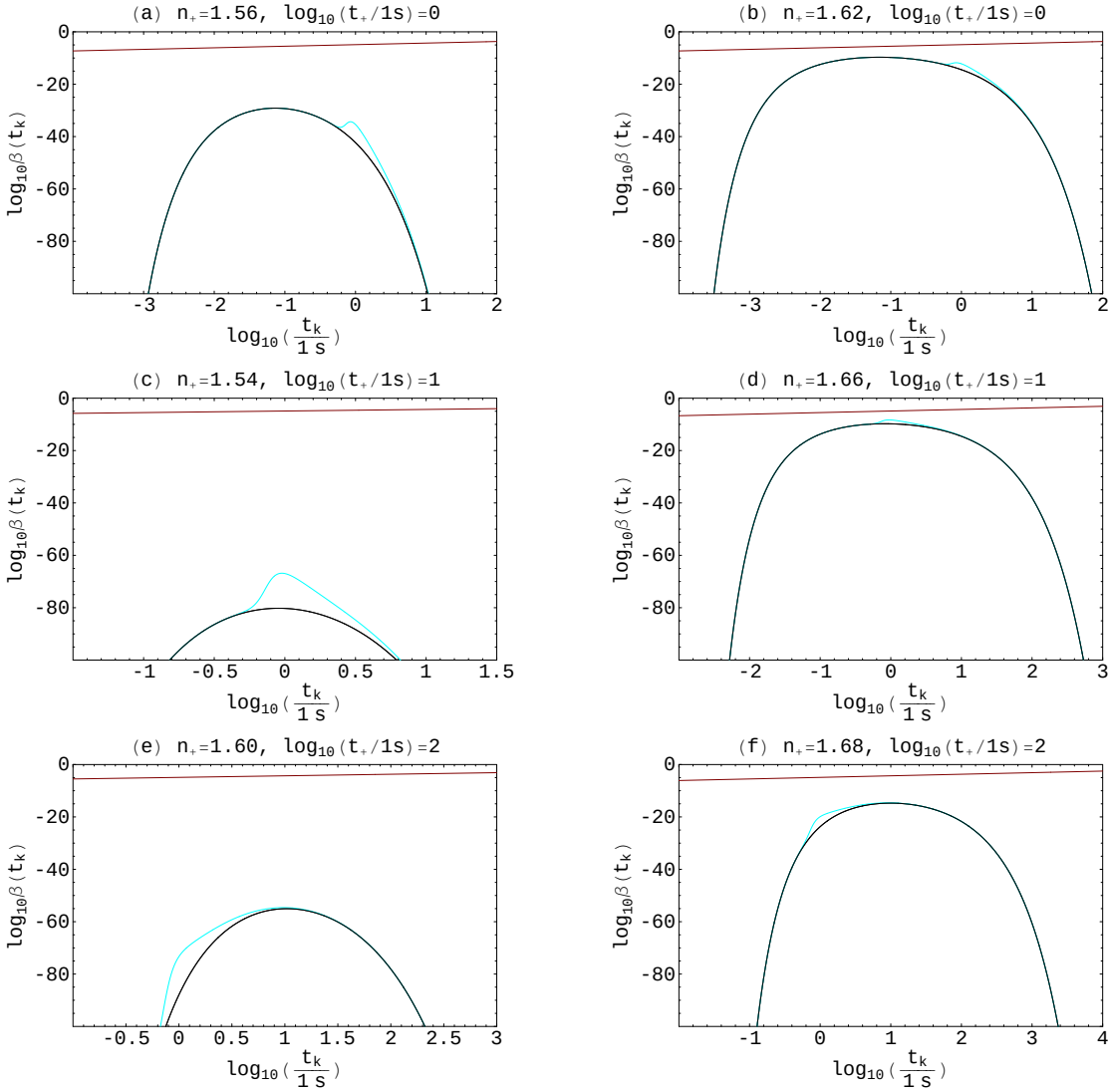

Figure 56: The fraction of the Universe going into PBHs in a universe with a running–tilt power–law spectrum when: (a) $n_+ = 1.56$ and $t_+ = 1$ s; (b) $n_+ = 1.62$ and $t_+ = 1$ s; (c) $n_+ = 1.54$ and $t_+ = 10$ s; (d) $n_+ = 1.66$ and $t_+ = 10$ s; (e) $n_+ = 1.60$ and $t_+ = 100$ s; (f) $n_+ = 1.68$ and $t_+ = 100$ s. The dark curve represents the radiation contribution and the cyan curve represents the contribution from the electron–positron annihilation epoch. Also shown (top of figure, in maroon) is the observational limit.

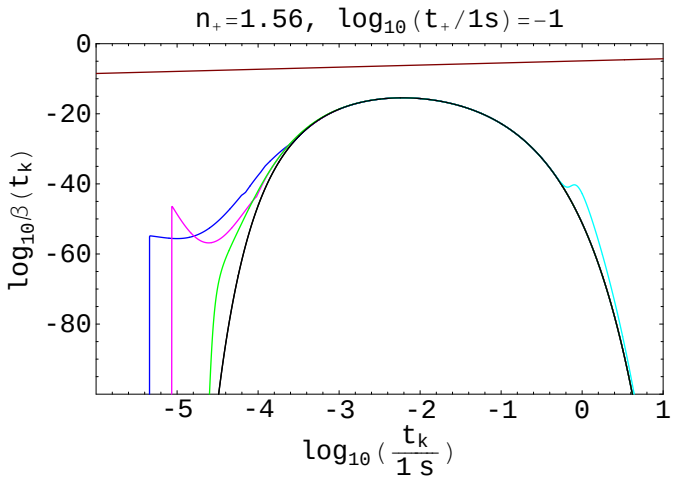

Figure 57: The fraction of the Universe going into PBHs in a universe with a running–tilt power–law spectrum when $n_+ = 1.56$ and $t_+ = 10^{-1}$ s. The dark curve represents the radiation contribution and the cyan curve (on the right) represents the aditional contribution from the electron–positron annihilation epoch. In this case we have also possible contributions from the QCD phase transition: Bag Model (blue curve on the left), Lattice Fit (in magenta), and Crossover (in green). Also shown (top of figure, in maroon) is the observational limit.

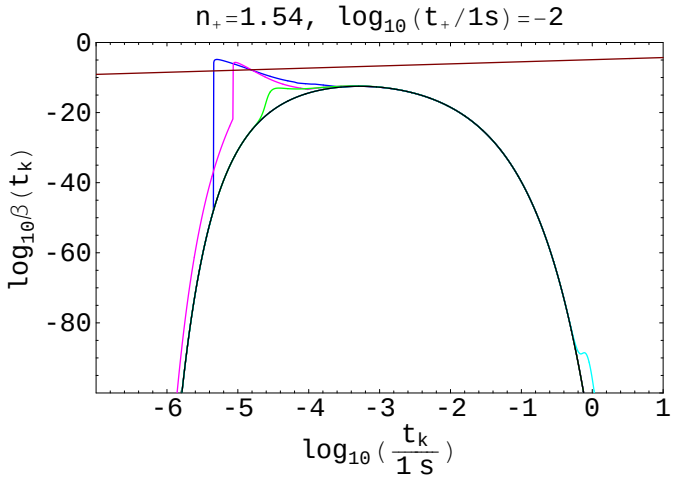

Figure 58: The fraction of the Universe going into PBHs in a universe with a running–tilt power–law spectrum when $n_+ = 1.54$ and $t_+ = 10^{-2}$ s. In this case the QCD Bag Model and the QCD Lattice Fit are excluded due to observational constraints (for more details see Figure 57).

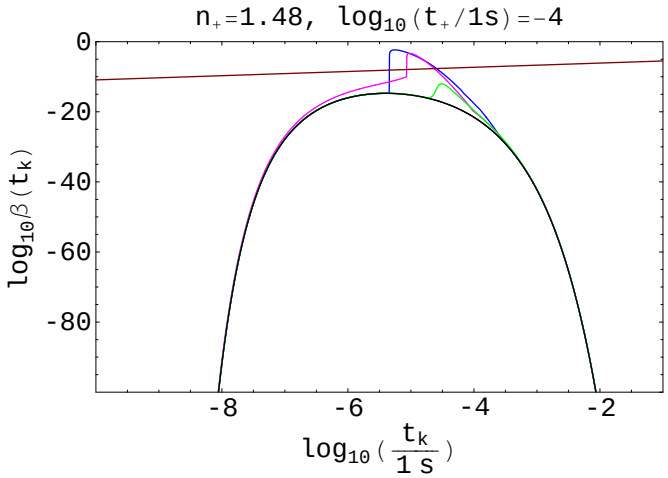

Figure 59: The fraction of the Universe going into PBHs in a universe with a running–tilt power–law spectrum when $n_+ = 1.48$ and $t_+ = 10^{-4}$ s. The dark curve represents the radiation contribution and the maroon line the observational constraints. The other curves represent the contribution from the QCD phase transition: Crossover (green), Lattice Fit (magenta) and Bag Model (blue). The latter two models for the QCD phase transition are excluded, due to observational constraints.

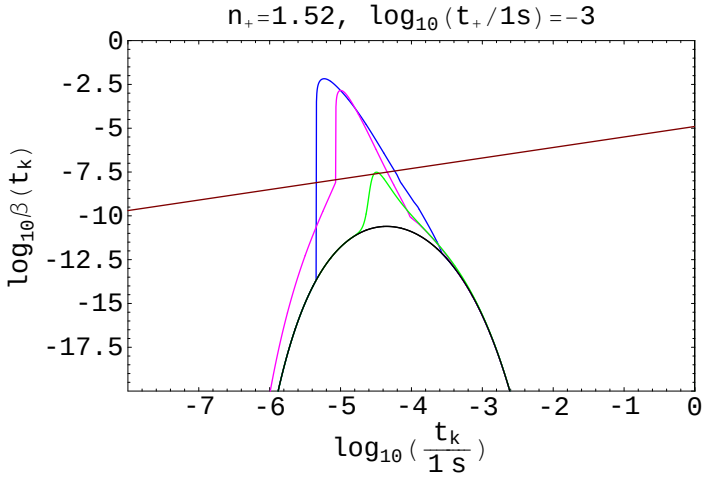

Figure 60: The fraction of the Universe going into PBHs in a universe with a running–tilt power–law spectrum when $n_+ = 1.52$ and $t_+ = 10^{-3}$ s (see Figure 59 for more details). Whatever the model adopted for the QCD phase transition this case must be excluded, due to observational constraints.

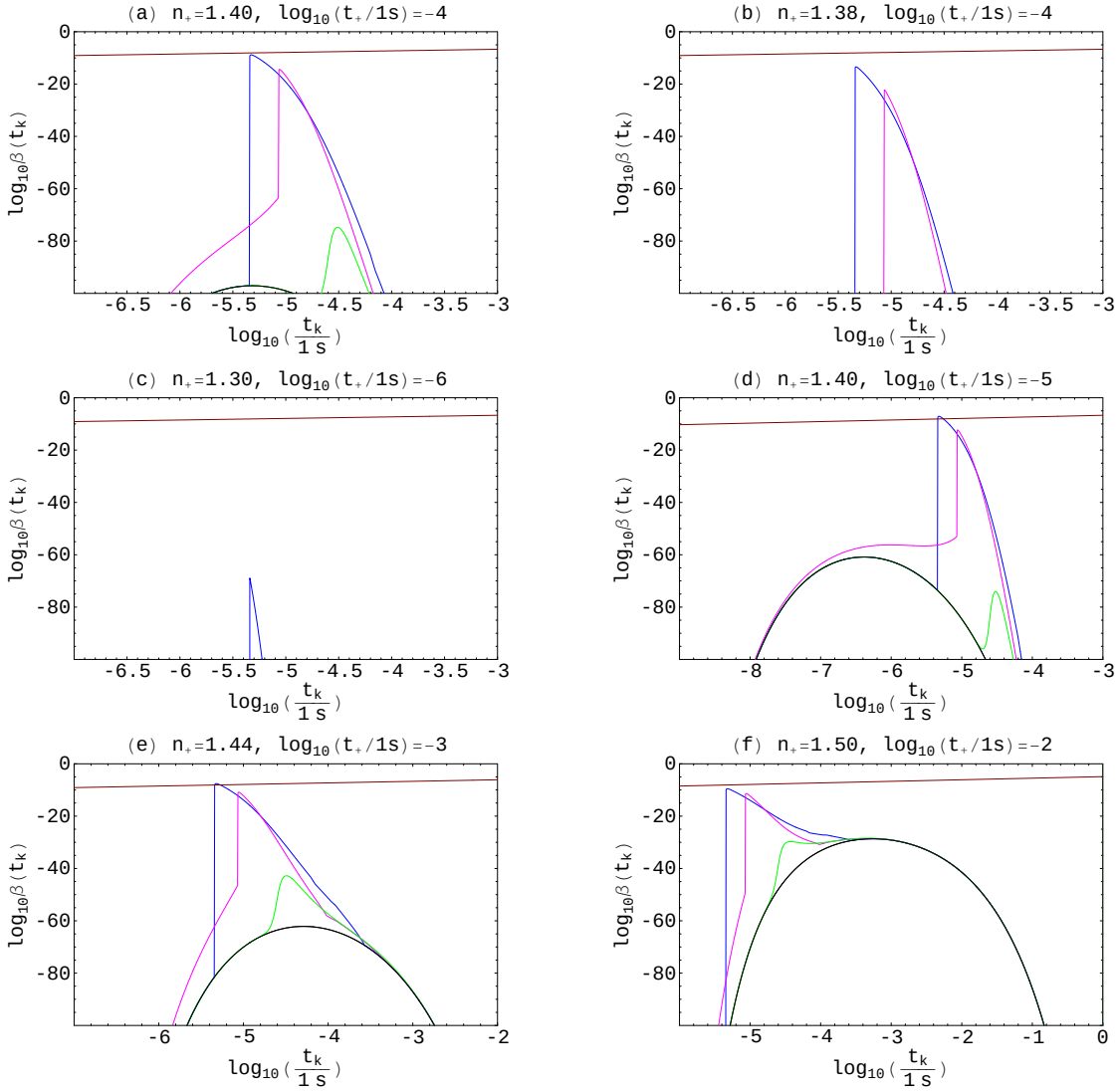

Figure 61: The fraction of the Universe going into PBHs, during the QCD phase transition, in a universe with a running–tilt power–law spectrum when: (a) $n_+ = 1.40$ and $t_+ = 10^{-4}$ s; (b) $n_+ = 1.38$ and $t_+ = 10^{-4}$ s; (c) $n_+ = 1.30$ and $t_+ = 10^{-6}$ s; (d) $n_+ = 1.40$ and $t_+ = 10^{-5}$ s; (e) $n_+ = 1.44$ and $t_+ = 10^{-3}$ s; (f) $n_+ = 1.50$ and $t_+ = 10^{-2}$ s (see Figure 59 and text for more details).

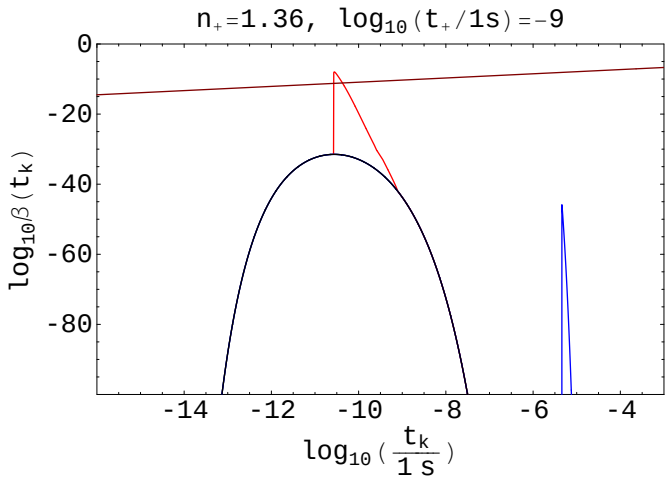

Figure 62: The fraction of the Universe going into PBHs in a universe with a running–tilt power–law spectrum when $n_+ = 1.36$ and $t_+ = 10^{-9}$ s. The curves represent the contribution from the EW phase transition (red), from the QCD phase transition (blue, Bag Model) and from radiation (black). The maroon line represents the observational constraints, which are violated here by the EW phase transition contribution.

5.8 EW phase transition (MSSM)

In this section we consider the contribution from the EW phase transition to the global value of β (in the context of the MSSM and taking into account the assumptions made at the end of Section 2.2.2). In Table 16 we point out the cases for which there is a non–negligible contribution from the EW phase transition.

There are some cases allowed when one considers only the contribution from radiation but which must be excluded when one takes into account the EW phase transition. For example, the case $t_+ = 10^{-9}$ s and $n_+ = 1.36$, represented in Figure 62. This case is not allowed in the context of a first–order EW phase transition. However, if there is no such transition (or if this is not strong enough) then this case becomes valid, with a possible contribution also from the QCD transition (Bag Model).

There are a few cases for which the contribution from radiation is negligible (i.e., cases shown in cyan in Table 11) but with an appreciable contribution from the EW phase transition. These cases are labeled in Table 16 with 'E', 'BE' and 'BLE'. In Figures 63a and 63b we present, as examples, the cases $t_+ = 10^{-10}$ s and $n_+ = 1.28$, and $t_+ = 10^{-9}$ s and $n_+ = 1.32$, with, respectively, $\beta_{max} \sim 10^{-60}$ and $\beta_{max} \sim 10^{-23}$.

There are also a lot of cases for which we have a contribution from the EW phase transition as well as from radiation (cf. Table 16, labeled 'RE'). In Figures 63c and 63d, we show as examples of this, the cases $t_+ = 10^{-13}$ s and $n_+ = 1.32$, and $t_+ = 10^{-12}$ s and $n_+ = 1.34$. Notice that in both cases the two contributions are quite comparable (in terms of β_{max}). In the first case we have $\beta_{max} \sim 10^{-24}$ from radiation and $\beta_{max} \sim 10^{-28}$ from the EW transition, and in the second case we have $\beta_{max} \sim 10^{-18}$ from radiation and $\beta_{max} \sim 10^{-12}$ from the EW transition.

Table 16: The contribution to β from the EW Bag Model (MSSM). In yellow we show the cases for which there is a non–negligible contribution to β from the EW Bag Model. For more details see Table 11 and the Conventions.

	n_+											
$\log_{10}(t_+/1\text{s})$	1.26	1.28	1.30	1.32	1.34	1.36	1.38	1.40	1.42	1.44	1.46	1.48
-15		R	R									
-14		R	RE	RE								
-13		RE	RE	RE Fig. 63c								
-12		E	RE Fig. 63e	RE	RE Fig. 63d							
-11		E	RE	RE	RE	RE*						
-10		E Fig. 63a	E	RE Fig. 63f	RE	RBE*						
-9		E	E	E Fig. 63b	RBE	RBE* Fig. 62	RBLE*					
-8			E	BE	RBE	RBLE	RBLE*	RBLE*				
-7			B	B	BLE Fig. 64a	RBLE Fig. 64b	RBLE	RBLE Fig. 64c	RB*LCE*			
-6			B	BL	BL	BL	RBL	RB*LCE	RB*LCE	RB*L*CE Fig. 64d		
-5			B	BL	BL	BL	BL	RB*LC	RB*LC	RB*L*C	RB*L*C	

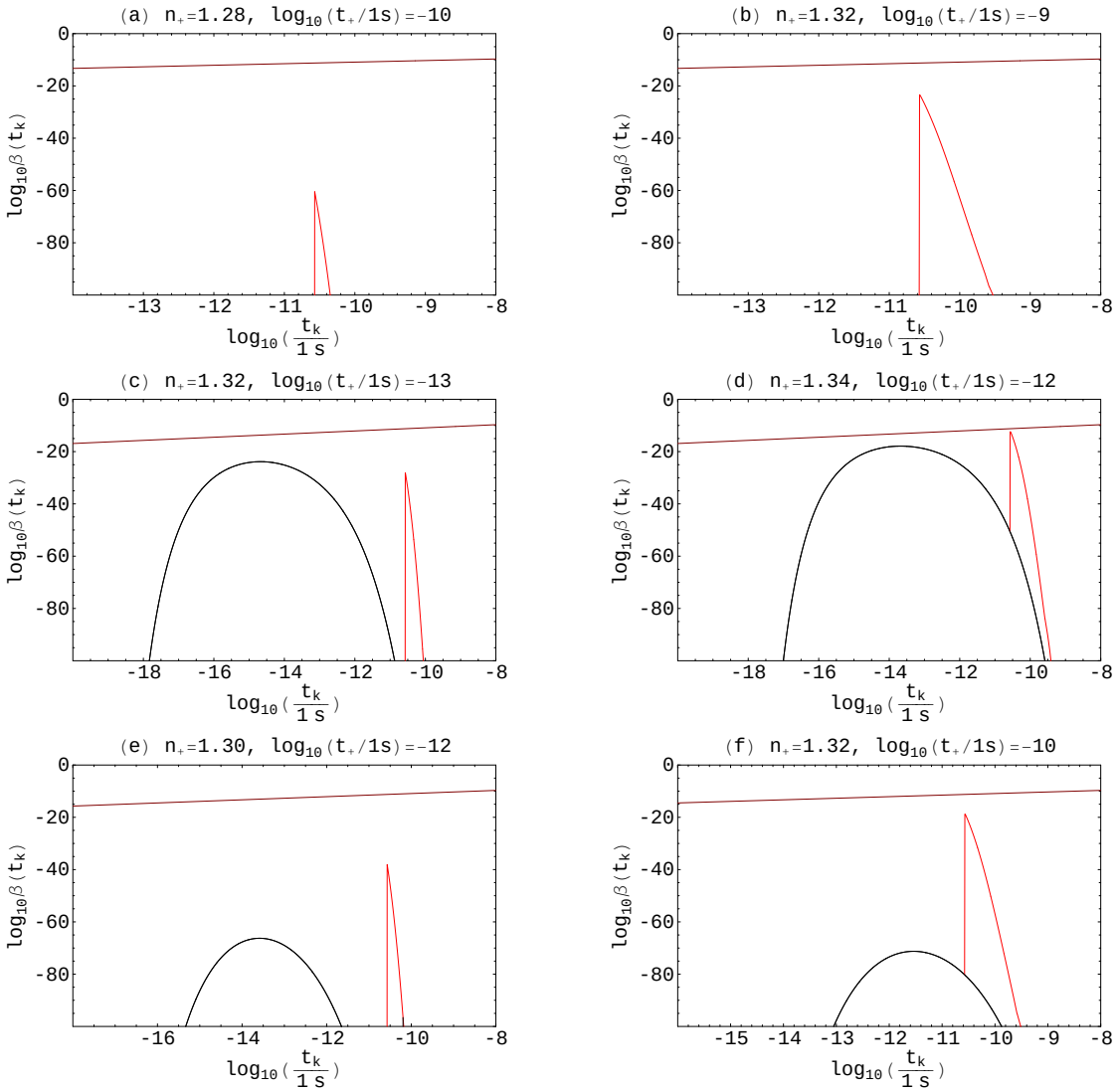

Figure 63: The fraction of the Universe going into PBHs in a universe with a running–tilt power–law spectrum when: (a) $n_+ = 1.28$ and $t_+ = 10^{-10}$ s; (b) $n_+ = 1.32$ and $t_+ = 10^{-9}$ s; (c) $n_+ = 1.32$ and $t_+ = 10^{-13}$ s; (d) $n_+ = 1.34$ and $t_+ = 10^{-12}$ s; (e) $n_+ = 1.30$ and $t_+ = 10^{-12}$ s; (f) $n_+ = 1.32$ and $t_+ = 10^{-10}$ s. The curves represent the contribution from the EW phase transition (red) and the contribution from radiation (black). Also shown (top of figures, in maroon) are the observational constraints.

In Figures 63e and 63f we present two mores cases with contributions from radiation and from the EW phase transition. Notice that in these cases the contribution from the EW phase transition is a lot more relevant than the contribution from radiation. For example, in the case $t_+ = 10^{-10}$ s and $n_+ = 1.32$, represented in Figure 63f, we have that the contribution from radiation gives $\beta_{max} \sim 10^{-71}$ and the contribution from the EW transition $\beta_{max} \sim 10^{-19}$.

Finally, we consider a few examples of a set of cases that have possible contributions from both the EW and QCD phase transitions (cf. Table 16, labeled BE, RBE, BLE, $RBLE$, RB^*LCE, and RB^*L^*CE). We start with the case $t_+ = 10^{-7}$ s

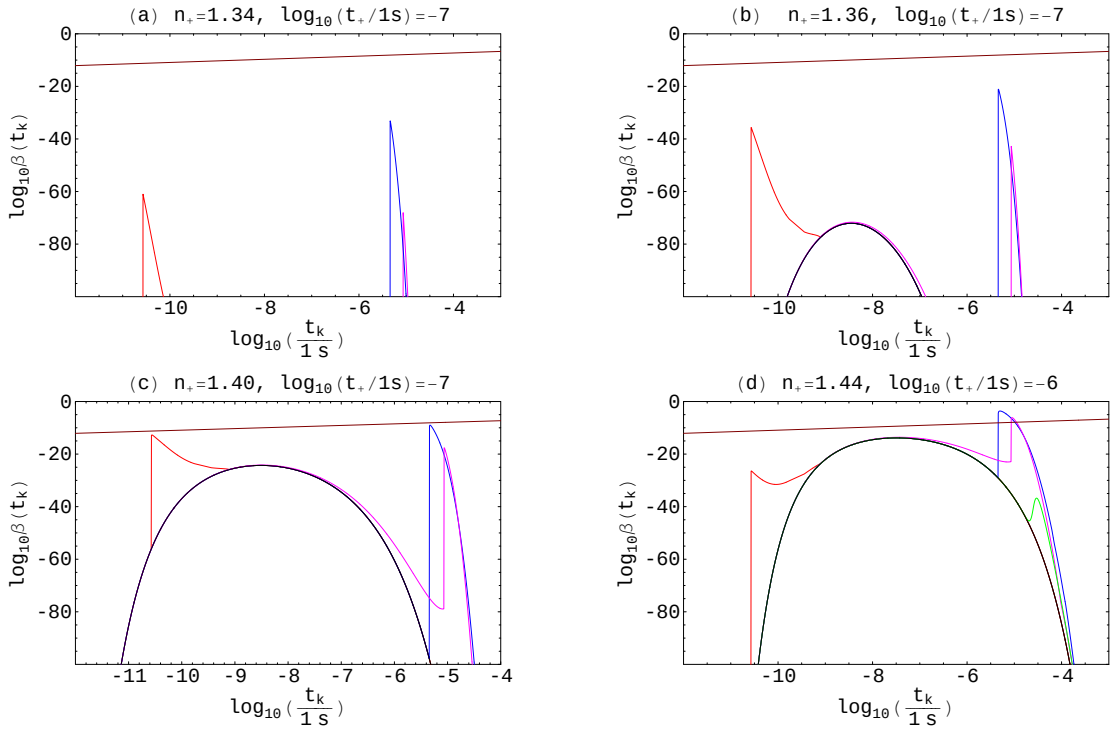

Figure 64: The fraction of the Universe going into PBHs in a universe with a running–tilt power–law spectrum when: (a) $n_+ = 1.34$ and $t_+ = 10^{-7}$ s; (b) $n_+ = 1.36$ and $t_+ = 10^{-7}$ s (see also Table M-1 and Figure M-1); (c) $n_+ = 1.40$ and $t_+ = 10^{-7}$ s; (d) $n_+ = 1.44$ and $t_+ = 10^{-6}$ s. The curves represent the contribution from the QCD phase transition (blue – Bag Model; magenta – Lattice Fit; green – Crossover), from the EW phase transition (red), and from radiation (black). Also shown (top of figures, in maroon) are the observational constraints.

and $n_+ = 1.34$, represented in Figure 64a. In this case we have contributions from the EW phase transition ($\beta_{max} \sim 10^{-61}$) and from the QCD phase transition (Bag Model – $\beta_{max} \sim 10^{-33}$, Lattice Fit – $\beta_{max} \sim 10^{-68}$).

In figures 64b and 64c we show the cases $t_+ = 10^{-7}$ s and $n_+ = 1.36$ (see also Table M-1 and Figure M-1), and $t_+ = 10^{-7}$ s and $n_+ = 1.40$, respectively. These are examples of cases characterized by contributions from the EW phase transition, QCD phase transition (Bag Model and Lattice Fit only) as well as from radiation. In particular, the second one (Figure 64c) shows very interesting values for β with two noticeable peaks ($\beta_{max} \sim 10^{-13}$ from the EW and $\beta_{max} \sim 10^{-9}$ from the QCD Bag Model or $\beta_{max} \sim 10^{-17}$ from the QCD Lattice Fit).

In Figure 64d we present the case $t_+ = 10^{-6}$ s and $n_+ = 1.44$. In this case, the main contribution to β comes from radiation ($\beta_{max} \sim 10^{-14}$), because the QCD Bag Model and Lattice Fit are excluded. We also have contributions from the EW phase transition and from the QCD phase transition (Crossover only).

In Table M-2 we list the peaks of the curve $\beta(t_k)$, as well as their locations, for the various cases (and different scenarios) studied in Sections 5.4 to 5.8.

When one considers PBH formation during cosmological phase transitions (QCD,

EW) in a radiation–dominated universe, assuming, for example, $\delta_c = 0.7$, the results are quite similar to the ones obtained with $\delta_c = 1/3$ (cf. Section N). Thus, we use, throughout this thesis, the $\delta_c = 1/3$ value as representative of all in the range $\delta_c \in [1/3, 0.7]$.

6 The PBH density parameter

6.1 The present day value of the PBH density parameter

If one wants to study the distribution of PBHs in the present day Universe then one needs to determine the present day value of the PBH density parameter $\Omega_{PBH}(t_0)$ (Section 1.4.5). In order to do that we start by writing expression (110) in the form

$$\Omega_{PBH}(t_k) = \frac{K}{\gamma}\int_0^\infty \frac{1}{\sqrt{2\pi}\sigma(t_k)} \exp\left[-\frac{1}{2\sigma^2(t_k)}\left(\delta_c + x^{1/\gamma}\right)^2\right] x^{1/\gamma} dx \tag{196}$$

where

$$x = \frac{M_{PBH}}{KM_H}.$$

Taking into account that $\sigma^2(t_k) \gtrsim 10^{-4}$ at all epochs relevant for PBH formation (cf. Section 5.4), which means that, for that epochs we always have $\delta_c \gg \sigma(t_k)$, we may rearrange the terms in equation (196) in order to obtain

$$\frac{\Omega_{PBH}(t_k)}{\beta(t_k)} = \frac{K}{\gamma}\frac{\delta_c}{\sigma^2(t_k)}\int_0^\infty \exp\left[-\frac{1}{\sigma^2(t_k)}\left(\delta_c x^{1/\gamma} + \frac{x^{2/\gamma}}{2}\right)^2\right] x^{1/\gamma} dx \tag{197}$$

with $\beta(t_k)$ given by equation (98). Assuming $\gamma \approx 0.36$ (cf. Section 1.4.2) and $K = 11.9$ (gaussian fluctuations, cf. Section 1.4.2) we performe a few numerical integrations to the right hand side of equation (197) with δ_c and $\sigma^2(t_k)$ assuming different values (see Table 17). As a general conclusion we note that

$$\Omega_{PBH}(t_k) \lesssim \beta(t_k)$$

which means that the value of the PBH density parameter, evaluated at a given epoch, does not change significantly even if we take into account equation (95). Thus, we consider, as a first approximation, the assumption that only horizon–mass PBHs are produced at each epoch, i.e., we write[27]

$$\Omega_{PBH}(t_k) = \beta(t_k). \tag{198}$$

Taking into account equation (40) and the assumption (198) we can write equation (113) in the form

$$\Omega(t_0, t_k) = \beta(t_k)\frac{R(t_{eq})}{R(t_k)}. \tag{199}$$

[27]Note that this would be the case if one considers $M_{PBH}(\delta, t_k) = M_H(t_k)$ in equation (109).

Table 17: $\Omega_{PBH}(t_k)/\beta(t_k)$ for different values of $\sigma^2(t_k)$ and δ_c (cf. equation 197).

δ_c	$\sigma^2(t_k)$			
	2×10^{-4}	3×10^{-4}	4×10^{-4}	5×10^{-4}
$\frac{1}{3}$	0.73	0.84	0.94	1.00
0.4	0.69	0.79	0.88	0.95
0.5	0.63	0.73	0.81	0.88
0.6	0.59	0.69	0.76	0.82
0.7	0.56	0.65	0.72	0.78

The global value of Ω_{PBH} evaluated at the present day (i.e. the present day value of the PBH density parameter which takes into account all non–evaporated PBHs) is given by

$$\Omega_{PBH}(t_0) = R(t_{eq}) \int_{t_*}^{t'} \frac{\beta(t_k)}{R(t_k)} dt_k \tag{200}$$

where $t_* = 10^{-23}$ s (PBHs formed before t_* have already evaporated) and t' represents a cut–off for PBH formation (we consider $t' \sim 10^5$ s which corresponds to PBHs with $\sim 10^{10} M_\odot$; for more details see Section 5.4). The current mass density of such PBHs, of course, must not exceed the total mass density of the Universe.

6.2 The distance to the nearest PBH

In this section we estimate the distance to the nearest PBH for different cases and scenarios. We start by determining the curve for the PBH density parameter $\Omega_{PBH}(t_0, t_k)$ (equation 199) as well as the corresponding global value at the present time $\Omega_{PBH}(t_0)$ (equation 200). With these values we can determine the PBH mass density ρ_{PBH} as well as the PBH number density n_{PBH}. If we are interested in PBHs formed at a particular epoch ($t = t_k$) then we write

$$\rho_{PBH}(t_0, t_k) = \rho_c(t_0)\Omega_{PBH}(t_0, t_k)$$

$$n_{PBH}(t_0, t_k) = \rho_c(t_0)\frac{\Omega_{PBH}(t_0, t_k)}{M_H(t_k)}$$

where ρ_c is the critical density and M_H is the horizon mass at that particular epoch (cf. Section 1.1). We recall that we assume the PBH mass at the moment of formation equal to the corresponding horizon mass (cf. Section 6.1). On the other

hand, if we are interested in global values then we consider instead

$$\rho_{PBH}(t_0) = \rho_c(t_0)\Omega_{PBH}(t_0)$$

$$n_{PBH}(t_0) = \rho_c(t_0)\int_{t_*}^{t'} \frac{\Omega_{PBH}(t_0,t_k)}{M_H(t_k)}dt_k \tag{201}$$

where $t_* = 10^{-23}$ s and $t' \sim 10^5$ s (see Section 6.1). Equation (201) is, of course, valid for more narrow mass ranges. If we are interested, for example, in the value of $n_{PBH}(t_0)$ with respect to PBHs formed between the intants t_1 and t_2 ($t_* \leq t_1 < t_2 \leq t'$) we write

$$n_{PBH}(t_0) = \rho_c(t_0)\int_{t_1}^{t_2} \frac{\Omega_{PBH}(t_0,t_k)}{M_H(t_k)}dt_k.$$

Assuming that PBHs, formed at a particular epoch, are uniformly distributed throughout the Universe, then the corresponding number N of PBHs inside a sphere of radius d is given by

$$N(t_0,t_k) = n_{PBH}(t_0,t_k)\frac{4}{3}\pi d(t_0,t_k)^3$$

Putting $N = 1$ we get for the distance

$$d(t_0,t_k) = \left(\frac{3}{4\pi}\frac{1}{n_{PBH}(t_0,t_k)}\right)^{1/3} \tag{202}$$

which can be regarded as representing the present day *minimum distance* to a PBH of mass $M_H(t_k)$. For a given case, the minimum of the curve $d(t_0,t_k)$ gives the minimum distance to the nearest PBH.

We have determined the curve $d(t_0,t_k)$ for all the cases considered in Chapter 5 (cf. Tables 11, 12, 13, 14, 15 and 16) and compiled the minimum of the curve, for each case, in Table O-1. We found out that for some of the cases the minimum distance could be larger than the size of the observable Universe ($\sim 10^{26}$ m). To better illustrate this we present, in Figure 65, the curve corresponding to the case $n_+ = 1.34$ and $t_+ = 10^{-8}$ s. In this case we might have contributions from the EW, QCD Bag Model and Radiation (cf. Table 16). However, only the EW contribution leads to an observationally interesting PBH number density (cf. Section 6.6, Table 23) with the nearest PBH at $\sim 10^{20}$ m (from the QCD Bag Model we get $\sim 10^{31}$ m and from the radiation contribution $\sim 10^{41}$ m). In all that follows, we consider as *observationally relevant* the cases giving at least one PBH inside the observable Universe which corresponds to ≈ 72 cases (a number that stays practically the same for all the six scenarios; cf. Table 29).

In order to present the results we decided to divide the (n_+, t_+) parameter space into different regions. A natural division arises when one takes into account the effects of cosmological phase transitions. For example, the effects of the electron–positron

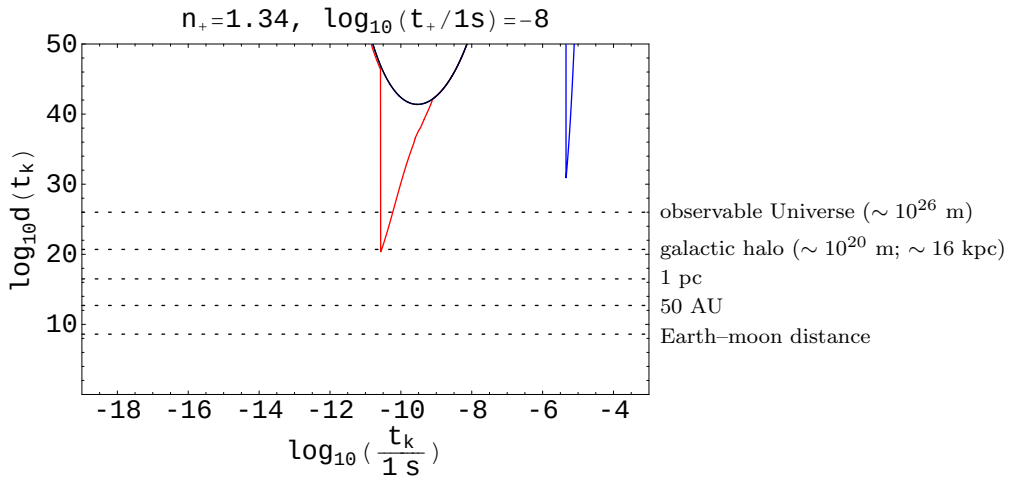

Figure 65: The minimum distance $d(t_0, t_k)$ (equation 202) to PBHs formed when $n_+ = 1.34$ and $t_+ = 10^{-8}$ s due to the: EW phase transition (red), QCD Bag Model (blue) and radiation–dominated universe (black). The dotted lines represent specific distances, as shown.

annihilation are present in the cases belonging to the region $1.60 \leq n_+ \leq 1.72$ and $1 \text{ s} \leq t_+ \leq 10^2$ s (Section 6.4). The effects from the EW Bag Model are present in the region $1.30 \leq n_+ \leq 1.44$ and 10^{-13} s $\leq t_+ \leq 10^{-6}$ s (Section 6.6). Between these two we have the region corresponding to the effects of the QCD phase transition (Section 6.5). Besides these three there are two other regions for which the results are due from only the radiation contribution. Namely, the region $1.72 \leq n_+ \leq 2.00$ and 10^3 s $\leq t_+ \leq 10^6$ s giving SMBHs (Section 6.3) and the region $1.24 \leq n_+ \leq 1.32$ and 10^{-23} s $\leq t_+ \leq 10^{-14}$ s giving SSBHs (Section 6.9). The upper limits of this second region are extended to $n_+ = 1.36$ and $t_+ = 10^{-10}$ s if the EW phase transition is described by a Crossover model (SMPP) instead of a Bag Model (MSSM).

6.3 Supermassive PBHs

The origin of the SMBHs, that are observed at the centre of many galaxies, remains unknown. They might form inside an existing galaxy or they might have formed long before the epoch of galaxy formation, in the primordial stages of the Universe. If that was the case, then SMBHs are PBHs.

Considering that a SMBH is characterized by a mass $10^6 M_\odot \leq M_{BH} \leq 10^{10} M_\odot$ we found out, from our sample of cases, that 20 ($\approx 28\%$ of the observationally relevant cases) allow SMBH formation. In six of the cases the mass spectrum spans from the IMBH mass range to the SMBH mass range and in 17 of the cases the peak of the mass spectrum is located in the SMBH range. In Table 18 we show the location of these 17 cases on the (n_+, t_+) parameter space ('yellow' cases) and, for each case, the PBH density parameter $\Omega_{PBH}(t_0)$ (equation 200), the PBH number density $n_{PBH}(t_0)$ (equation 201), the distance to the nearest PBH as well as the corresponding mass.

Table 18: The 17 cases (in yellow) giving observationally relevant results with the mass spectrum peak located in the SMBH range. For each case we show the PBH density parameter $\Omega_{PBH}(t_0)$ (equation 200), the PBH number density $n_{PBH}(t_0)$ (equation 201), the distance to the nearest PBH as well as the corresponding mass. For more details see Table 11 and the Conventions.

	n_s														
$\log_{10}(t_e/\mathrm{ls})$	1.72	1.74	1.76	1.78	1.80	1.82	1.84	1.86	1.88	1.90	1.92	1.94	1.96	1.98	2.00
2	Rea														
3	R $\Omega \sim 10^{-13}$ $n \approx 6.4 \times 10^{-9}$ Mpc^{-3} $d \sim 10^{25}$ m $5 \times 10^6 M_\odot$	R $\Omega \sim 10^{-8}$ $n \approx 2.3 \times 10^{-4}$ Mpc^{-3} $d \sim 10^{23}$ m $5 \times 10^6 M_\odot$ Fig. 67a	R $\Omega \sim 10^{-5}$ $n \approx 0.5$ Mpc^{-3} $d \sim 10^{22}$ m $5 \times 10^6 M_\odot$ Fig. 66a	R $\Omega \sim 10^{-3}$ $n \approx 1.6 \times 10^2$ Mpc^{-3} $d \sim 10^{21}$ m $5 \times 10^6 M_\odot$ Fig. 67b											
4				R $\Omega \sim 10^{-13}$ $n \approx 2.7 \times 10^{-10}$ Mpc^{-3} $d \sim 10^{25}$ m $5 \times 10^7 M_\odot$	R $\Omega \sim 10^{-9}$ $n \approx 4.3 \times 10^{-6}$ Mpc^{-3} $d \sim 10^{24}$ m $5 \times 10^7 M_\odot$	R $\Omega \sim 10^{-6}$ $n \approx 6.1 \times 10^{-3}$ Mpc^{-3} $d \sim 10^{23}$ m $5 \times 10^7 M_\odot$	R $\Omega \sim 10^{-3}$ $n \approx 1.5$ Mpc^{-3} $d \sim 10^{22}$ m $5 \times 10^7 M_\odot$ Fig. 66b	R $\Omega \sim 10^{-2}$ $n \approx 9.3 \times 10^1$ Mpc^{-3} $d \sim 10^{21}$ m $5 \times 10^7 M_\odot$ Fig. 67c						
5								R $\Omega \sim 10^{-12}$ $n \approx 9.1 \times 10^{-10}$ Mpc^{-3} $d \sim 10^{25}$ m $5 \times 10^8 M_\odot$	R $\Omega \sim 10^{-8}$ $n \approx 2.1 \times 10^{-6}$ Mpc^{-3} $d \sim 10^{24}$ m $5 \times 10^8 M_\odot$	R $\Omega \sim 10^{-6}$ $n \approx 8.6 \times 10^{-4}$ Mpc^{-3} $d \sim 10^{23}$ m $5 \times 10^8 M_\odot$	R $\Omega \sim 10^{-4}$ $n \approx 8.9 \times 10^{-2}$ Mpc^{-3} $d \sim 10^{22}$ m $5 \times 10^8 M_\odot$	R $\Omega \sim 10^{-2}$ $n \approx 3.3$ Mpc^{-3} $d \sim 10^{22}$ m $5 \times 10^8 M_\odot$ Fig. 66c		
6													R $\Omega \sim 10^{-10}$ $n \approx 6.3 \times 10^{-9}$ Mpc^{-3} $d \sim 10^{25}$ m $5 \times 10^9 M_\odot$	R $\Omega \sim 10^{-7}$ $n \approx 2.3 \times 10^{-6}$ Mpc^{-3} $d \sim 10^{24}$ m $5 \times 10^9 M_\odot$	R $\Omega \sim 10^{-5}$ $n \approx 2.5 \times 10^{-4}$ Mpc^{-3} $d \sim 10^{23}$ m $5 \times 10^9 M_\odot$
7															

We can interpret the curve $n_{PBH}(t_0, t_k)$ as a mass spectrum: the *PBH mass spectrum*. In order to have a better understanding of this we divided the curve $n_{PBH}(t_0, t_k)$ into different portions, each corresponding to an order of magnitude, and integrated these in order to obtain the total number of PBHs of a given mass order within a given volume.

In Figure 66 we show the mass spectrum for the cases: (a) $n_+ = 1.76$ and $t_+ = 10^3$ s; (b) $n_+ = 1.84$ and $t_+ = 10^4$ s; (c) $n_+ = 1.94$ and $t_+ = 10^5$ s. These are interesting, from the observational point of view, because they suggest a number of PBHs $\sim 10^{11}$, which corresponds to the number of galaxies known to exist in the observable Universe. For example, when $n_+ = 1.76$ and $t_+ = 10^3$ s (Figure 66a) we have $\sim 10^{11}$ PBHs in the observable Universe with masses $\sim 5 \times 10^6 M_\odot$. In the case $n_+ = 1.84$ and $t_+ = 10^4$ s (Figure 66b) we have a similar N but now with masses $\sim 5 \times 10^7 M_\odot$ and in the case $n_+ = 1.94$ and $t_+ = 10^5$ s (Figure 66c) the same, with masses $\sim 5 \times 10^8 M_\odot$.

There are, however, a few cases with more modest values. For example when $n_+ = 1.74$ and $t_+ = 10^3$ s we get $\sim 10^7$ PBHs in the observable Universe (one PBH for each $\sim 10^4$ galaxies) which means that, in this case, perhaps, only a small fraction of all existing SMBHs could be, in fact, PBHs (see Figure 67a). On the other extreme we have cases leading to a number of PBHs much larger than the number of galaxies. That is, for example, the situation with the case $n_+ = 1.78$ and $t_+ = 10^3$ s (the case with the highest value of n_{PBH} in Table 18) that leads to $\sim 10^{13}$ PBHs with $5 \times 10^6 M_\odot$ in the observable Universe (Figure 67b). In this case the mass spectrum extends to the IMBH region giving $\sim 10^{12}$ PBHs with $5 \times 10^5 M_\odot$. When $n_+ = 1.86$ and $t_+ = 10^4$ s we get, also, $\sim 10^{13}$ PBHs mainly with $5 \times 10^7 M_\odot$ (see Figure 67c).

6.4 The effect of the electron–positron annihilation

In this section we consider the contribution from the electron–positron annihilation epoch to the PBH density in the present Universe. We have tested all the 27 'yellow' cases shown in Table 12 and found out that for ten of them (37%) we have observationally relevant values for the PBH density. In Table 19 we show these ten cases, indicating, for each one, the corresponding values of $\Omega_{PBH}(t_0)$ (equation 200), $n_{PBH}(t_0)$ (equation 201) as well as the the minimum value of the curve $d(t_0, t_k)$ (equation 202) and the corresponding PBH mass ($M_H(t_k)$). We show also the results for the case $n_+ = 1.58$ and $t_+ = 1$ s (a single case between the QCD and the electron–positron annihilation regions, on the (n_+, t_+) parameter space, but with negligible contributions from both, cf. Tables 19, 20, 21 and 22).

In Figure 68 we show the PBH mass spectrum for the cases: (a) $n_+ = 1.62$ and $t_+ = 1$ s; (b) $n_+ = 1.66$ and $t_+ = 10$ s and (c) $n_+ = 1.72$ and $t_+ = 10^2$ s. These are the three cases, out of the ten, with the largest values of Ω_{PBH} ($\sim 10^{-3}$, cf. Table 19). For the rest of the cases the values are more modest with Ω_{PBH} never exceeding $\sim 10^{-5}$. The case $n_+ = 1.62$ and $t_+ = 1$ s gives $\sim 10^{16}$ PBHs (mainly with $\sim 5 \times 10^3 M_\odot$) in the observable Universe (Figure 68a), or a number density of

Table 19: The contribution to Ω_{PBH} from the electron–positron annihilation epoch (cf. Table 12). In yellow we show the 10 cases for which there is an observationally relevant contribution. For each case we show the corresponding values of $\Omega_{PBH}(t_0)$ (cf. Section 1.4.5 – equation 200), $n_{PBH}(t_0)$ (equation 201) as well as the the minimum value of the curve $d(t_0, t_k)$ (equation 202) and the corresponding PBH mass. For more details see Table 11 and the Conventions.

	n_+								
$\log_{10}(t_+/1\text{s})$	1.58	1.60	1.62	1.64	1.66	1.68	1.70	1.72	1.74
-1	RBLC								
0	R $\Omega \sim 10^{-14}$ $n \approx 1.2 \times 10^{-6}$ Mpc^{-3} $d \sim 10^{24}$ m $5 \times 10^3\ M_\odot$	Rea $\Omega \sim 10^{-8}$ $n \approx 2.3$ Mpc^{-3} $d \sim 10^{22}$ m $5 \times 10^3\ M_\odot$	Rea $\Omega \sim 10^{-3}$ $n \approx 4.8 \times 10^4$ Mpc^{-3} $d \sim 10^{20}$ m $5 \times 10^3\ M_\odot$ Fig. 68a						
1		Rea $\Omega \sim 10^{-22}$ $n \approx 7.1 \times 10^{-12}$ Mpc^{-3} $d \sim 10^{25}$ m $5 \times 10^4\ M_\odot$	Rea $\Omega \sim 10^{-11}$ $n \approx 4.4 \times 10^{-5}$ Mpc^{-3} $d \sim 10^{23}$ m $5 \times 10^4\ M_\odot$ Fig. 69a	Rea $\Omega \sim 10^{-6}$ $n \approx 2.6$ Mpc^{-3} $d \sim 10^{22}$ m $5 \times 10^4\ M_\odot$ Fig. 69b	Rea $\Omega \sim 10^{-3}$ $n \approx 6.1 \times 10^3$ Mpc^{-3} $d \sim 10^{21}$ m $5 \times 10^4\ M_\odot$ Fig. 68b	Rea*			
2					Rea $\Omega \sim 10^{-15}$ $n \approx 5.4 \times 10^{-10}$ Mpc^{-3} $d \sim 10^{25}$ m $5 \times 10^5\ M_\odot$	Rea $\Omega \sim 10^{-10}$ $n \approx 2.5 \times 10^{-4}$ Mpc^{-3} $d \sim 10^{23}$ m $5 \times 10^5\ M_\odot$	Rea $\Omega \sim 10^{-5}$ $n \approx 3.0$ Mpc^{-3} $d \sim 10^{22}$ m $5 \times 10^5\ M_\odot$ Fig 70	Rea $\Omega \sim 10^{-3}$ $n \approx 2.7 \times 10^3$ Mpc^{-3} $d \sim 10^{21}$ m $5 \times 10^5\ M_\odot$ Fig. 68c	
3								R	R

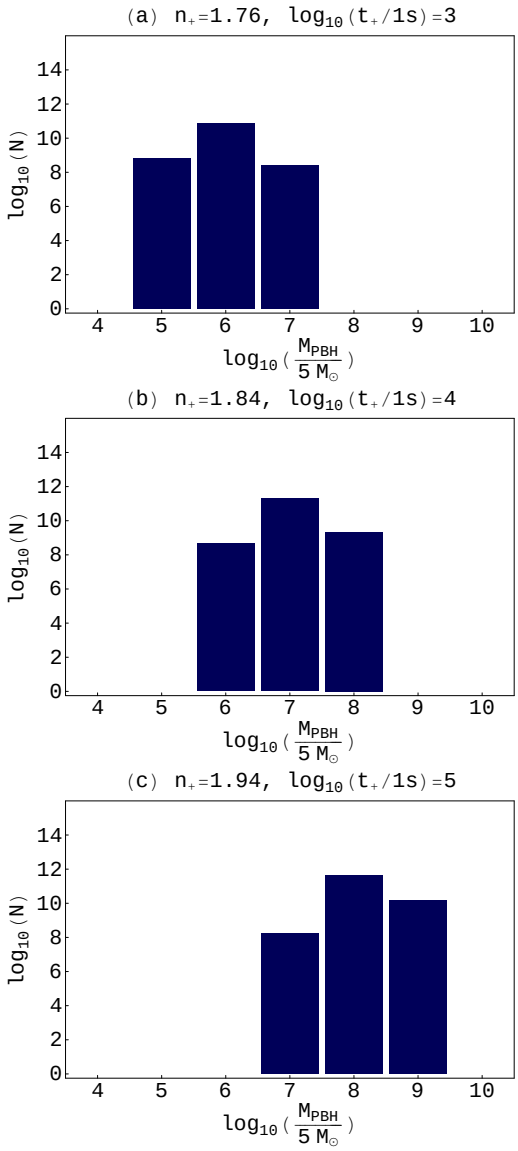

Figure 66: The PBH mass spectrum in the observable Universe when: (a) $n_+ = 1.76$ and $t_+ = 10^3$ s; (b) $n_+ = 1.84$ and $t_+ = 10^4$ s; (c) $n_+ = 1.94$ and $t_+ = 10^5$ s.

$\sim 10^4$ PBHs/Mpc^3 (corresponding to, at least, one PBH in our galactic halo). In the case $n_+ = 1.66$ and $t_+ = 10$ s we have $\sim 10^{15}$ PBHs (mainly with $\sim 5{\times}10^4 M_\odot$) in the observable Universe which corresponds to a number density of $\sim 10^4$ PBHs/Mpc^3 and, finally, in the case $n_+ = 1.72$ and $t_+ = 10^2$ s we have $\sim 10^{14}$ PBHs (mainly with $\sim 5 \times 10^5 M_\odot$) in the observable Universe which corresponds to a number density of $\sim 10^3$ PBHs/Mpc^3.

In the case $n_+ = 1.66$ and $t_+ = 10$ s (Figure 68b) $\approx 85\%$ of the PBHs are due to the effect of the electron–positron annihilation. There are two other cases for which the contribution from the electron–positron annihilation is even more significant when compared with the contribution from radiation. These are, respectively, the case $n_+ = 1.62$ and $t_+ = 10$ s (Figure 69a) with 99.6% and the case $n_+ = 1.64$ and

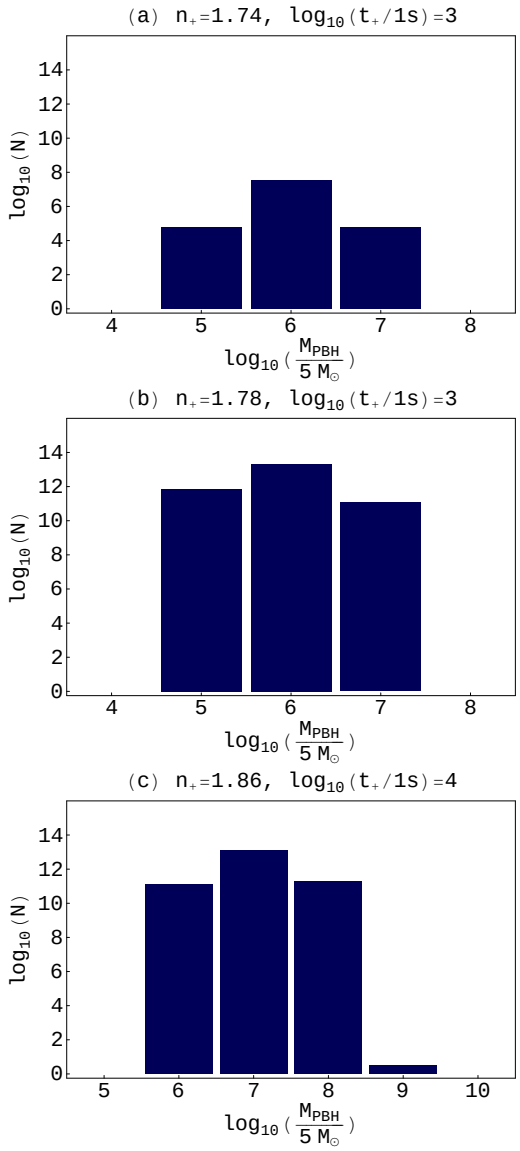

Figure 67: The PBH mass spectrum in the observable Universe when: (a) $n_+ = 1.74$ and $t_+ = 10^3$ s; (b) $n_+ = 1.78$ and $t_+ = 10^3$ s; (c) $n_+ = 1.86$ and $t_+ = 10^4$ s.

$t_+ = 10$ s (Figure 69b) with 96.7%. When $n_+ = 1.62$ this corresponds to $\sim 10^7$ PBHs (mainly with $\sim 5 \times 10^4 M_\odot$) distributed in the whole observable Universe which makes it a quite small density (less than 10^{-4} PBHs/Mpc^3) when compared with the one of galaxies. When $n_+ = 1.64$ we have $\sim 10^{11}$ PBHs (mainly with $\sim 5 \times 10^4 M_\odot$) distributed in the whole observable Universe which makes it an observationally interesting result (≈ 2 PBHs/Mpc^3).

In Figure 70 we show the mass spectrum for the case $n_+ = 1.70$ and $t_+ = 10^2$ s. In this case the electron–positron annihilation gives $\approx 36\%$ of the $\sim 10^{11}$ PBHs formed. However, if we consider only PBHs with $5 \times 10^4 M_\odot$ then the contribution from the electron–positron rises to $\approx 80\%$. This corresponds to the effect of the extension to the left on the curve of $\beta(t_k)$ that we have already mentioned (Section 5.6, Figure

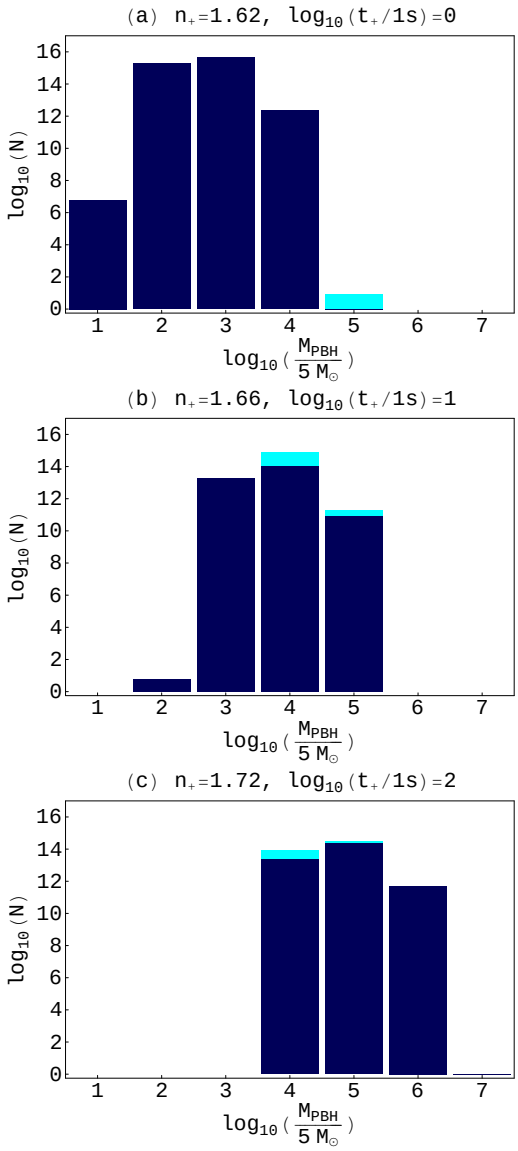

Figure 68: The PBH mass spectrum in the observable Universe when: (a) $n_+ = 1.62$ and $t_+ = 1$ s; (b) $n_+ = 1.66$ and $t_+ = 10$ s; (c) $n_+ = 1.72$ and $t_+ = 10^2$ s. In cyan we show the contribution from the electron–positron annihilation epoch only and in dark–blue the contribution from radiation only. Both add up to the totals shown.

56). The other cases with $t_+ = 10^2$ s exhibit similar mass spectra. For example when $n_+ = 1.72$ (see Figure 68c) the electron–positron annihilation contributes with $\approx 36\%$ to the total number of PBHs and with $\approx 72\%$ to the number of $5 \times 10^4 M_\odot$ PBHs.

In Section 5.6 we have identified a few cases for which we might have simultaneous contributions from the electron–positron annihilation and from the QCD phase transition (cf. Figure 57, Table 12 – cases labeled *RBLCea*). It turns out that, for all these cases, the contributions from the electron–positron annihilation lead to non–observationally relevant values within the observable Universe.

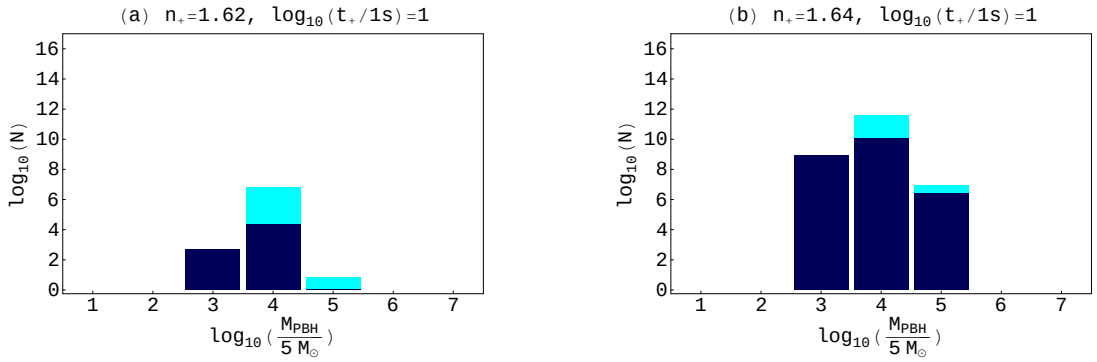

Figure 69: The PBH mass spectrum in the observable Universe when: (a) $n_+ = 1.62$ and $t_+ = 10$ s; (b) $n_+ = 1.64$ and $t_+ = 10$ s. For more details see Figure 68.

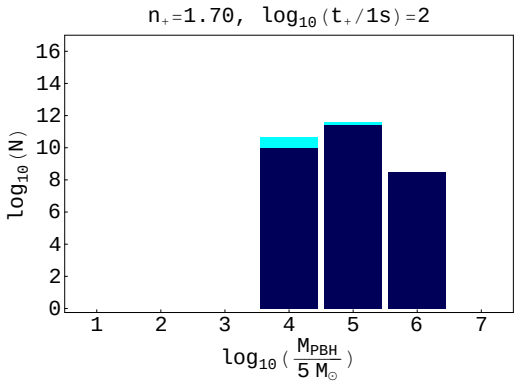

Figure 70: The PBH mass spectrum in the observable Universe when $n_+ = 1.70$ and $t_+ = 10^2$ s. For more details see Figure 68.

6.5 The effect of the QCD phase transition

We now consider the contribution from the QCD phase transition to the PBH density in the present day Universe. This contribution depends on the model one adopts.

6.5.1 Bag Model

In the case of the Bag Model we tested all the 45 'yellow' cases presented in Table 13 and found out that, for 24 of them (53%), Ω_{PBH} is observationally relevant (see Table 20). Within this scenario the PBH mass spectrum shows, in general, a peak located at $\sim 10^{33}$ g ($\sim 0.5 M_\odot$). The amplitude of this peak varies from case to case.

There are seven cases, out of the 24 (29%), for which Ω_{PBH} exceeds $\sim 10^{-5}$ (cf. Table 20). We start with the three cases giving $\Omega_{PBH} \sim 10^{-2}$. When $n_+ = 1.40$ and $t_+ = 10^{-7}$ s (Figure 71a) the mass spectrum shows two peaks: one located at $0.5 M_\odot$ ($N \sim 10^{21}$ PBHs), due to the QCD Bag Model, and another, located at $5 \times 10^{-5} M_\odot$ ($N \sim 10^{12}$ PBHs), due to the the radiation contribution. Although almost 100% of the PBHs formed, in this case, due to the QCD Bag Model, the

Table 20: The contribution to Ω_{PBH} from the QCD Bag Model. For more details see Table 19, Table 11 and the Conventions.

	n_+														
$\log_{10}(t_+/1\text{s})$	1.32	1.34	1.36	1.38	1.40	1.42	1.44	1.46	1.48	1.50	1.52	1.54	1.56	1.58	1.60
-10			R												
-9			R	RB $\Omega \sim 10^{-6}$ $n \approx 10^{11}$ Mpc^{-3} $d \sim 10^{18}$ m $5 \times 10^{-7} M_\odot$											
-8			B $\Omega \sim 10^{-23}$ $n \approx 10^{-11}$ Mpc^{-3} $d \sim 10^{25}$ m $0.5 M_\odot$	RB $\Omega \sim 10^{-12}$ $n \approx 1.3$ Mpc^{-3} $d \sim 10^{22}$ m $0.5 M_\odot$	RB $\Omega \sim 10^{-5}$ $n \approx 3.8 \times 10^{11}$ Mpc^{-3} $d \sim 10^{18}$ m $5 \times 10^{-6} M_\odot$ Fig. 73										
-7			B $\Omega \sim 10^{-14}$ $n \approx 6.6 \times 10^{-3}$ Mpc^{-3} $d \sim 10^{22}$ m $0.5 M_\odot$	B $\Omega \sim 10^{-7}$ $n \approx 2.8 \times 10^{5}$ Mpc^{-3} $d \sim 10^{20}$ m $0.5 M_\odot$	RB $\Omega \sim 10^{-2}$ $n \approx 1.7 \times 10^{10}$ Mpc^{-3} $d \sim 10^{18}$ m $0.5 M_\odot$ Fig. 71a	RB*									
-6		B $\Omega \sim 10^{-20}$ $n \approx 1.2 \times 10^{-8}$ Mpc^{-3} $d \sim 10^{24}$ m $0.5 M_\odot$	B $\Omega \sim 10^{-10}$ $n \approx 10^{2}$ Mpc^{-3} $d \sim 10^{21}$ m $0.5 M_\odot$	B $\Omega \sim 10^{-4}$ $n \approx 1.4 \times 10^{8}$ Mpc^{-3} $d \sim 10^{19}$ m $0.5 M_\odot$	RB*	RB*	RB*								
-5		B $\Omega \sim 10^{-19}$ $n \approx 9.2 \times 10^{-8}$ Mpc^{-3} $d \sim 10^{24}$ m $0.5 M_\odot$	B $\Omega \sim 10^{-9}$ $n \approx 3.8 \times 10^{2}$ Mpc^{-3} $d \sim 10^{21}$ m $0.5 M_\odot$	B $\Omega \sim 10^{-3}$ $n \approx 3.5 \times 10^{8}$ Mpc^{-3} $d \sim 10^{19}$ m $0.5 M_\odot$	RB*	RB*	RB*	RB*							
-4			B $\Omega \sim 10^{-14}$ $n \approx 1.4 \times 10^{-2}$ Mpc^{-3} $d \sim 10^{22}$ m $0.5 M_\odot$	B $\Omega \sim 10^{-6}$ $n \approx 5.2 \times 10^{5}$ Mpc^{-3} $d \sim 10^{20}$ m $0.5 M_\odot$	B $\Omega \sim 10^{-2}$ $n \approx 2.9 \times 10^{10}$ Mpc^{-3} $d \sim 10^{18}$ m $0.5 M_\odot$ Fig. 71b	RB*	RB*	RB*	RB*					
-3				B $\Omega \sim 10^{-19}$ $n \approx 1.1 \times 10^{-7}$ Mpc^{-3} $d \sim 10^{24}$ m $0.5 M_\odot$	B $\Omega \sim 10^{-10}$ $n \approx 1.6 \times 10^{2}$ Mpc^{-3} $d \sim 10^{21}$ m $0.5 M_\odot$	B $\Omega \sim 10^{-4}$ $n \approx 1.1 \times 10^{8}$ Mpc^{-3} $d \sim 10^{19}$ m $0.5 M_\odot$	RB*	RB*	RB*	RB*	RB*				
-2							B $\Omega \sim 10^{-23}$ $n \approx 2.0 \times 10^{-11}$ Mpc^{-3} $d \sim 10^{25}$ m $0.5 M_\odot$	B $\Omega \sim 10^{-13}$ $n \approx 0.1$ Mpc^{-3} $d \sim 10^{22}$ m $0.5 M_\odot$	B $\Omega \sim 10^{-6}$ $n \approx 3.7 \times 10^{5}$ Mpc^{-3} $d \sim 10^{20}$ m $0.5 M_\odot$	B $\Omega \sim 10^{-2}$ $n \approx 8.6 \times 10^{9}$ Mpc^{-3} $d \sim 10^{18}$ m $0.5 M_\odot$ Fig. 71c	RB*	RB*			
-1												R	R	RB $\Omega \sim 10^{-4}$ $n \approx 2.9 \times 10^{5}$ Mpc^{-3} $d \sim 10^{20}$ m $500 M_\odot$ Fig. 72	
0														R	Rea

number of PBHs due to the radiation ($\sim 10^{12}$ PBHs with $5 \times 10^{-5} M_\odot$ ($\approx 0.05 m_J$) and $\sim 10^{11}$ PBHs with $5 \times 10^{-4} M_\odot$ ($\approx 0.5 m_J$)) is also observationally interesting compared with the number of galaxies in the observable Universe. Between the two peaks we have an empty region corresponding to $0.05 M_\odot$ ($\sim 10^{32}$ g). When $n_+ = 1.40$ and $t_+ = 10^{-4}$ s (Figure 71b) the mass spectrum shows only one peak (corresponding to the QCD Bag Model) reaching $\sim 10^{21}$ PBHs corresponding to $n_{PBH} \approx 2.9 \times 10^{10}$ Mpc^{-3}. When $n_+ = 1.50$ and $t_+ = 10^{-2}$ s (Figure 71c) we have a similar situation with a single peak (corresponding to $\sim 0.5 M_\odot$ PBHs) with $N \sim 10^{21}$ PBHs ($n_{PBH} \approx 8.6 \times 10^9$ Mpc^{-3}), with the difference that, in this case, the peak shows an extension to the right corresponding to a small amount ($\sim 10^7$) of $\sim 5 M_\odot$ PBHs.

There are three cases, all giving $N \sim 10^{19}$ PBHs with $0.5 M_\odot$ (mass spectrum analogous to the case $n_+ = 1.40$ and $t_+ = 10^{-4}$ s shown in Figure 71b). These are the cases: $n_+ = 1.38$ and $t_+ = 10^{-6}$ s ($\Omega_{PBH} \sim 10^{-4}$, $n_{PBH} \approx 1.4 \times 10^8$ Mpc^{-3}); $n_+ = 1.38$ and $t_+ = 10^{-5}$ s ($\Omega_{PBH} \sim 10^{-3}$, $n_{PBH} \approx 3.5 \times 10^8$ Mpc^{-3}); $n_+ = 1.42$ and $t_+ = 10^{-3}$ s ($\Omega_{PBH} \sim 10^{-4}$, $n_{PBH} \approx 1.1 \times 10^8$ Mpc^{-3}).

In Figure 72 we show the mass spectrum for the case $n_+ = 1.58$ and $t_+ = 10^{-1}$ s ($\Omega_{PBH} \sim 10^{-4}$, $n_{PBH} \approx 2.9 \times 10^5$ Mpc^{-3}) giving $\sim 10^{16}$ PBHs, mainly with $50 M_\odot$ ($\approx 41\%$) and $500 M_\odot$ ($\approx 59\%$), in the observable Universe. There is also $\sim 10^{13}$ PBHs of $5 \times 10^3 M_\odot$ which is an observationally relevant number (compared with the number of galaxies in the Universe). In this case the contribution from the QCD Bag Model is almost negligible ($< 10^{-6}\%$) compared with the contribution from radiation. However, if one concentrates on $5 M_\odot$ PBHs then the QCD Bag Model contribution rises to $\approx 8\%$ (corresponding to $\sim 10^8$ PBHs).

As we have already seen, when $n_+ = 1.40$ and $t_+ = 10^{-7}$ s (Figure 71a) the mass spectrum shows two peaks with a gap in between. There are other cases, within the QCD Bag Model, with this same feature. As another example, we show, in Figure 73, the case $n_+ = 1.40$ and $t_+ = 10^{-8}$ s (the second in importance in terms of PBH density). In this case the mass spectrum extends from $5 \times 10^{-8} M_\odot$ ($5 \times 10^{-5} m_J$) to $0.5 M_\odot$ ($500 m_J$) with an empty region at $0.05 M_\odot$ ($50 m_J$). The peak from the radiation contribution, located at $5 \times 10^{-6} M_\odot$ ($5 \times 10^{-3} m_J$) corresponds to $\sim 10^{22}$ PBHs. On the other hand the peak due to the QCD Bag Model ($0.5 M_\odot$) gives $\sim 10^{17}$ PBHs which corresponds to $\approx 0.001\%$ of the total number of PBHs.

6.5.2 Lattice Fit

Now we consider the QCD Lattice Fit Model. We tested all the 42 'yellow' cases shown in Table 14 and found out that we have observationally relevant results for Ω_{PBH} in 20 (48%) of them (see Table 21). These 20 cases are, in general, characterized by a peculiar peak located at $\sim 10^{33}$ g ($\sim 0.5 M_\odot$). However, this peak is not so high as in the Bag Model (considering the same (n_+, t_+) combination). To show this we use the same examples as in Figure 71. When $n_+ = 1.40$ and $t_+ = 10^{-7}$ s the QCD peak ($\sim 0.5 M_\odot$) gives, in the Lattice Fit case, $\sim 10^{12}$ PBHs (see Figure

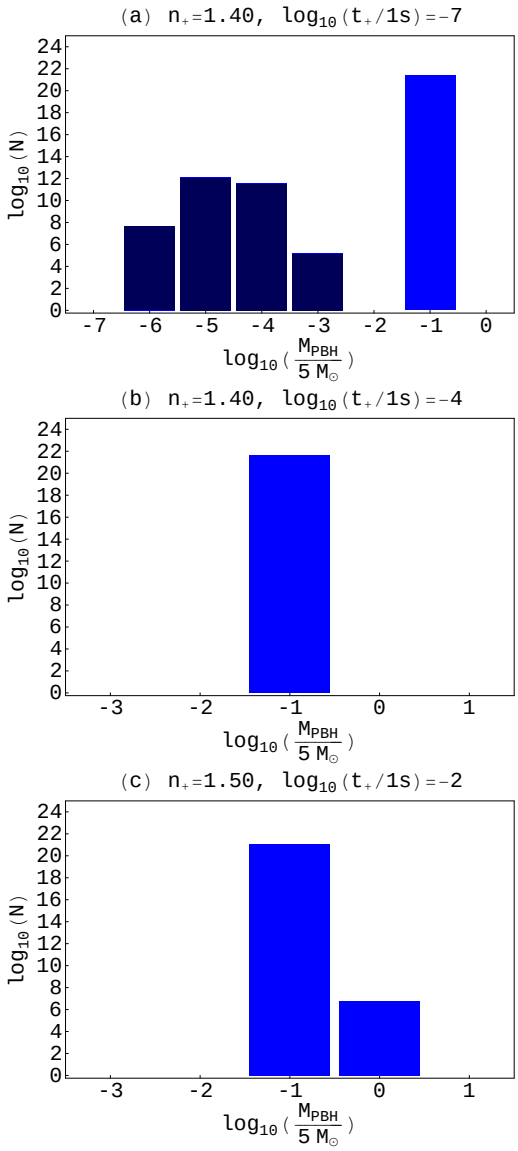

Figure 71: The PBH mass spectrum in the observable Universe due to the QCD Bag Model when: (a) $n_+ = 1.40$ and $t_+ = 10^{-7}$ s; (b) $n_+ = 1.40$ and $t_+ = 10^{-4}$ s; (c) $n_+ = 1.50$ and $t_+ = 10^{-2}$ s. In light–blue we show the contribution from the QCD Bag Model only and in dark–blue the contribution from radiation only.

74a) corresponding to $\approx 66\%$ of the total of PBHs. This is much less than the value predicted by the Bag Model ($\sim 10^{21}$ PBHs with $0.5 M_\odot$ corresponding to $\approx 100\%$ of the totals, cf. Figure 71a). When $n_+ = 1.40$ and $t_+ = 10^{-4}$ s the Lattice Fit predicts $\sim 10^{15}$ PBHs (Figure 74b) against the $\sim 10^{21}$ PBHs predicted by the Bag Model (Figure 71b). Finally, when $n_+ = 1.50$ and $t_+ = 10^{-2}$ s the Lattice Fit predicts $\sim 10^{18}$ PBHs (Figure 74c) against the $\sim 10^{21}$ PBHs predicted by the Bag Model (Figure 71c).

There are some cases for which the peak from the Lattice Fit contribution is higher. In fact, for seven of the cases, out of the 20 (35%), Ω_{PBH} exceeds $\sim 10^{-5}$ (one case

Table 21: The contribution to Ω_{PBH} from the QCD Lattice Fit Model. For more details see Table 19, Table 11 and the Conventions.

	n_+															
$\log_{10}(t_+/1\text{s})$	1.32	1.34	1.36	1.38	1.40	1.42	1.44	1.46	1.48	1.50	1.52	1.54	1.56	1.58	1.60
-10			R												
-9			R	R											
-8				R	RL $\Omega \sim 10^{-5}$ $n \approx 3.6 \times 10^{11}$ Mpc^{-3} $d \sim 10^{18}$ m $5 \times 10^{-6} M_\odot$										
-7				L $\Omega \sim 10^{-21}$ $n \approx 1.1 \times 10^{-9}$ Mpc^{-3} $d \sim 10^{24}$ m $0.5 M_\odot$	RL $\Omega \sim 10^{-11}$ $n \approx 21$ Mpc^{-3} $d \sim 10^{21}$ m $5 \times 10^{-5} M_\odot$ Fig. 74a	RL $\Omega \sim 10^{-4}$ $n \approx 1.9 \times 10^{11}$ Mpc^{-3} $d \sim 10^{18}$ m $5 \times 10^{-5} M_\odot$ Fig. 76									
-6				L $\Omega \sim 10^{-14}$ $n \approx 3.5 \times 10^{-3}$ Mpc^{-3} $d \sim 10^{22}$ m $0.5 M_\odot$	L $\Omega \sim 10^{-7}$ $n \approx 1.2 \times 10^{5}$ Mpc^{-3} $d \sim 10^{20}$ m $0.5 M_\odot$	RL $\Omega \sim 10^{-2}$ $n \approx 6.3 \times 10^{9}$ Mpc^{-3} $d \sim 10^{18}$ m $0.5 M_\odot$ Fig. 75	RL*								
-5				L $\Omega \sim 10^{-12}$ $n \approx 0.3$ Mpc^{-3} $d \sim 10^{22}$ m $0.5 M_\odot$	L $\Omega \sim 10^{-5}$ $n \approx 2.2 \times 10^{6}$ Mpc^{-3} $d \sim 10^{19}$ m $0.5 M_\odot$	L $\Omega \sim 10^{-1}$ $n \approx 4.3 \times 10^{10}$ Mpc^{-3} $d \sim 10^{18}$ m $0.5 M_\odot$	RL*	RL*							
-4				L $\Omega \sim 10^{-16}$ $n \approx 1.4 \times 10^{-4}$ Mpc^{-3} $d \sim 10^{23}$ m $0.5 M_\odot$	L $\Omega \sim 10^{-8}$ $n \approx 1.7 \times 10^{4}$ Mpc^{-3} $d \sim 10^{20}$ m $0.5 M_\odot$ Fig. 74b	L $\Omega \sim 10^{-2}$ $n \approx 1.9 \times 10^{9}$ Mpc^{-3} $d \sim 10^{18}$ m $0.5 M_\odot$	RL*	RL*	RL*						
-3					L $\Omega \sim 10^{-18}$ $n \approx 2.6 \times 10^{-7}$ Mpc^{-3} $d \sim 10^{24}$ m $0.5 M_\odot$	L $\Omega \sim 10^{-9}$ $n \approx 1.8 \times 10^{2}$ Mpc^{-3} $d \sim 10^{21}$ m $0.5 M_\odot$	L $\Omega \sim 10^{-4}$ $n \approx 7.8 \times 10^{7}$ Mpc^{-3} $d \sim 10^{19}$ m $0.5 M_\odot$	RL*	RL*	RL*	RL*			
-2								L $\Omega \sim 10^{-18}$ $n \approx 1.1 \times 10^{-6}$ Mpc^{-3} $d \sim 10^{23}$ m $0.5 M_\odot$	L $\Omega \sim 10^{-10}$ $n \approx 1.3 \times 10^{2}$ Mpc^{-3} $d \sim 10^{21}$ m $0.5 M_\odot$	L $\Omega \sim 10^{-4}$ $n \approx 3.0 \times 10^{7}$ Mpc^{-3} $d \sim 10^{19}$ m $0.5 M_\odot$ Fig. 74c	RL*	RL*			
-1												R	R	RL $\Omega \sim 10^{-4}$ $n \approx 2.9 \times 10^{5}$ Mpc^{-3} $d \sim 10^{20}$ m $500 M_\odot$	
0														R	Rea

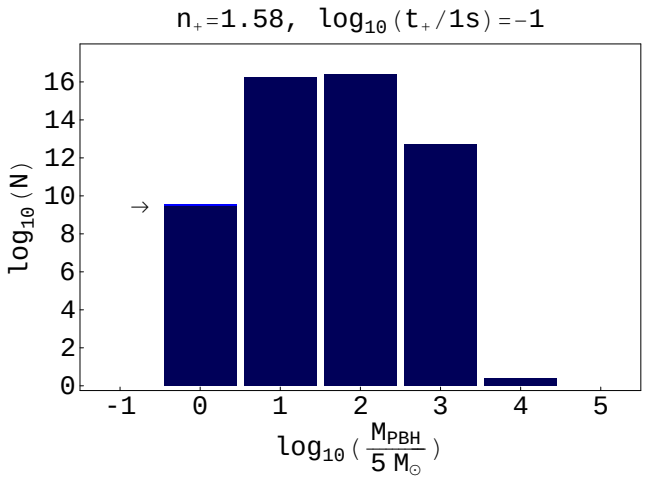

Figure 72: The PBH mass spectrum in the observable Universe due to the QCD Bag Model when $n_+ = 1.58$ and $t_+ = 10^{-1}$ s. In dark–blue we show the contribution from radiation only and in light–blue (see arrow) the contribution from the QCD Bag Model only (corresponding to less than 10^{-6}% of the totals; ≈ 8% of the $5M_\odot$ PBHs).

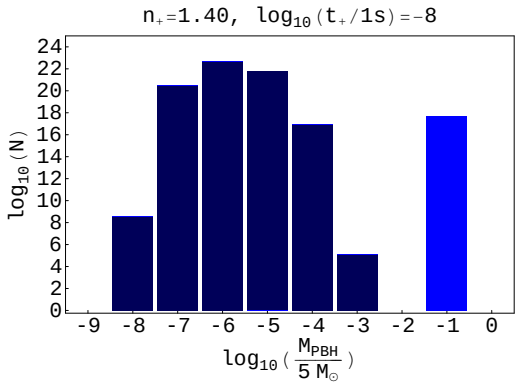

Figure 73: The PBH mass spectrum in the observable Universe due to the QCD Bag Model when $n_+ = 1.40$ and $t_+ = 10^{-8}$ s. See Figure 71 for more details.

giving $\Omega_{PBH} \sim 10^{-1}$, two cases with $\Omega_{PBH} \sim 10^{-2}$ and four cases with $\Omega_{PBH} \sim 10^{-4}$; cf. Table 21).

In Figure 75 we show the mass spectrum for the case $n_+ = 1.42$ and $t_+ = 10^{-6}$ s for which $\Omega_{PBH} \sim 10^{-1}$. In this case the mass spectrum shows two peaks: one located at $0.5M_\odot$ ($N \sim 10^{21}$ PBHs), due to the QCD Lattice Fit, and another, located at $5 \times 10^{-4}M_\odot$ ($N \sim 10^{12}$ PBHs), due to the radiation and Lattice Fit contribution. When $n_+ = 1.42$ and $t_+ = 10^{-5}$ s the mass spectrum shows only one peak (corresponding to the QCD Lattice Fit) reaching $\sim 10^{22}$ PBHs corresponding to $n_{PBH} \approx 4.3 \times 10^{10}$ Mpc^{-3} ($\Omega_{PBH} \sim 10^{-2}$) and when $n_+ = 1.42$ and $t_+ = 10^{-4}$ s we have a similar situation with $N \sim 10^{20}$ PBHs ($n_{PBH} \approx 1.9 \times 10^9$ Mpc^{-3}, $\Omega_{PBH} \sim 10^{-2}$).

We now consider the cases with $\Omega_{PBH} \sim 10^{-4}$. When $n_+ = 1.44$ and $t_+ = 10^{-3}$ s the mass spectrum shows only one peak (corresponding to the QCD Lattice Fit)

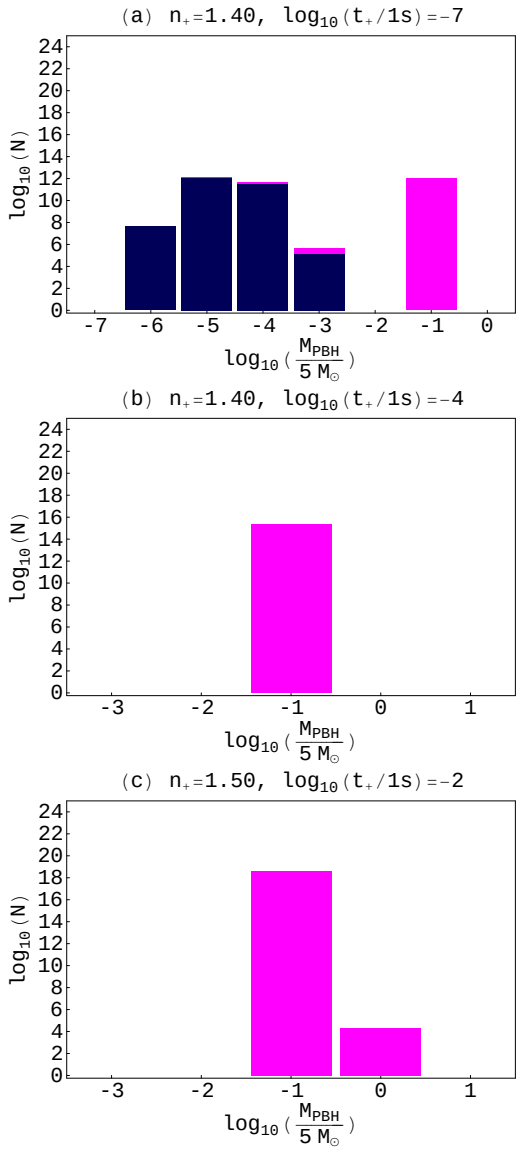

Figure 74: The PBH mass spectrum in the observable Universe due to the QCD Lattice Fit when: (a) $n_+ = 1.40$ and $t_+ = 10^{-7}$ s; (b) $n_+ = 1.40$ and $t_+ = 10^{-4}$ s; (c) $n_+ = 1.50$ and $t_+ = 10^{-2}$ s. In magenta we show the contribution from the QCD Lattice Fit only and in dark–blue the contribution from radiation only. Both add up to the totals shown.

reaching $\sim 10^{19}$ PBHs corresponding to $n_{PBH} \approx 7.8 \times 10^7$ Mpc^{-3}.

When $n_+ = 1.42$ and $t_+ = 10^{-7}$ s (Figure 76) the mass spectrum shows two peaks: one located at $0.5M_\odot$ ($N \sim 10^{18}$ PBHs), due to the QCD Lattice Fit, and another, located at $5 \times 10^{-5}M_\odot$ ($N \sim 10^{22}$ PBHs), due to the radiation contribution.

When $n_+ = 1.50$ and $t_+ = 10^{-2}$ s (Figure 74c) the mass spectrum shows a peak corresponding to $N \sim 10^{18}$ $0.5M_\odot$ PBHs with an extension to the right corresponding to a small amount ($\sim 10^4$) of $5M_\odot$ PBHs. This case is valid for both the QCD Bag Model and the QCD Lattice Fit model. The other cases shown in Figures 75 and 76 are excluded if one chooses the Bag Model instead (cf. Table 20, 'red' cases labeled

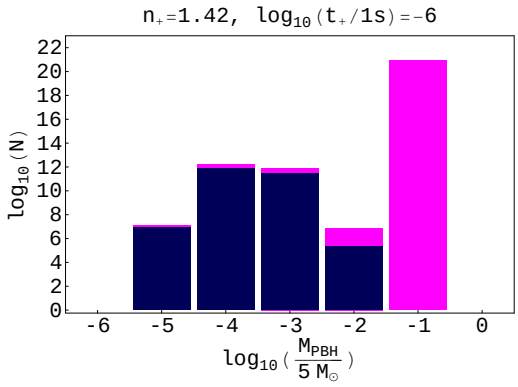

Figure 75: The PBH mass spectrum in the observable Universe due to the QCD Lattice Fit when $n_+ = 1.42$ and $t_+ = 10^{-6}$ s. See Figure 74 for more details.

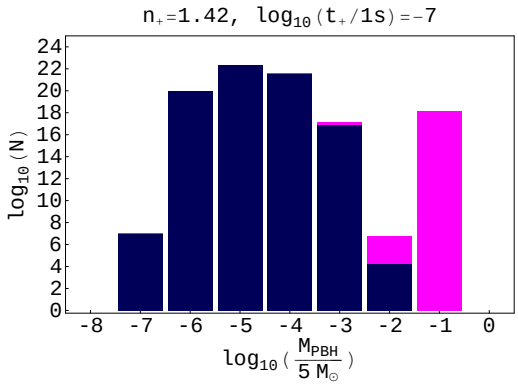

Figure 76: The PBH mass spectrum in the observable Universe due to the QCD Lattice Fit when $n_+ = 1.42$ and $t_+ = 10^{-7}$ s. See Figure 74 for more details.

'RB*').

Another case valid for both the QCD Bag Model and the QCD Lattice Fit model is the one with $n_+ = 1.58$ and $t_+ = 10^{-1}$ s (see Figure 72). In global terms the situation is very similar for both models with the contribution from the QCD Lattice Fit giving less than $10^{-3}\%$ of the PBHs (within the QCD Bag Model this was $< 10^{-6}\%$). However if one concentrates on $5M_\odot$ PBHs then the QCD Lattice Fit model contribution rises to $\approx 49\%$ (corresponding to $\sim 10^9$ PBHs).

Under the QCD Lattice Fit we might get, in some cases, besides the $\approx 0.5M_\odot$ peak, an extension to the left on the mass spectrum resulting from the contribution from the interval $t_1 \leq t \leq t_{QCD-}$ (cf. Section 2.1). The cases $n_+ = 1.42$ and $t_+ = 10^{-6}$ s (Figure 75) and $n_+ = 1.42$ and $t_+ = 10^{-7}$ s (Figure 76) are the ones for which this contribution assumes the largest values in terms of PBH number density.

When $n_+ = 1.42$ and $t_+ = 10^{-6}$ s (Figure 75) almost 100% of the total number of PBHs come from the QCD peak ($0.5M_\odot$ PBHs). Neglecting this peak we still have $\sim 10^{12}$ PBHs (peaking at $5 \times 10^{-4}M_\odot$ ($\approx 0.5m_J$) and $5 \times 10^{-3}M_\odot$ ($\approx 5m_J$)) which is also an observationally interesting number compared with the number of galaxies in the observable Universe. Approximately 44% of these PBHs formed due to the

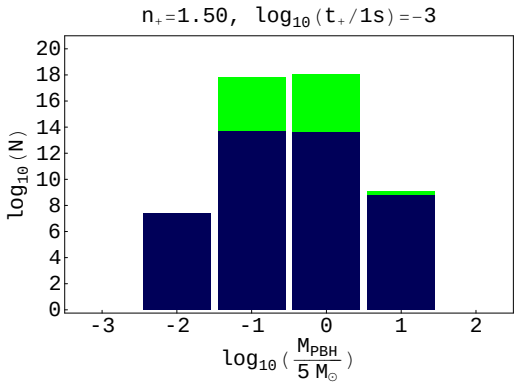

Figure 77: The PBH mass spectrum in the observable Universe due to the QCD Crossover model when $n_+ = 1.50$ and $t_+ = 10^{-3}$ s. In green we show the contribution from the QCD Crossover model only and in dark–blue the contribution from radiation only. Both add up to the totals shown.

radiation contribution. The other 56% come from the QCD Lattice contribution during the interval $t_1 \leq t \leq t_{QCD-}$. When $n_+ = 1.42$ and $t_+ = 10^{-7}$ s (Figure 76) the contribution from the interval $t_1 \leq t \leq t_{QCD-}$ corresponds to $\approx 14\%$ of the totals ($\sim 10^{21}$ PBHs).

6.5.3 Crossover

In the case of a QCD Crossover we found out that 11 of the 26 'yellow' cases (42%) shown in Table 15 lead to observationally relevant results as regards Ω_{PBH} (see Table 22). For five of the cases, out of the 11 (45%), Ω_{PBH} equals or exceeds $\sim 10^{-5}$ with the rest of the cases giving Ω_{PBH} lower than $\sim 10^{-9}$.

When $n_+ = 1.50$ and $t_+ = 10^{-3}$ s the QCD Crossover model gives $\Omega_{PBH} \sim 10^{-4}$. In this case the mass spectrum (Figure 77) shows a peak that extends from $\sim 0.5 M_\odot$ to $5 M_\odot$ giving $N \sim 10^{18}$ PBHs (considering the contribution from radiation only one gets $N \sim 10^{14}$ PBHs). The other case with Ω_{PBH} exceeding $\sim 10^{-5}$ occurs when $n_+ = 1.58$ and $t_+ = 10^{-1}$ s, a case that is valid also within the QCD Bag Model and QCD Lattice Fit Model (cf. Sections 6.5.1 and 6.5.2). The contribution from the QCD corresponds to $\approx 1.5\%$ of the PBHs. However, the QCD Crossover Model contribution rises to $\approx 55\%$ (corresponding to $\sim 10^9$ PBHs) if one concentrates on $5 M_\odot$ PBHs, to $\approx 3\%$ (corresponding to $\sim 10^{14}$ PBHs) if one concentrates on $50 M_\odot$ PBHs and to $\approx 1\%$ (corresponding to $\sim 10^{14}$ PBHs) if one concentrates on $500 M_\odot$ PBHs.

In Figure 78 we show the PBH mass spectrum for the three cases giving $\Omega_{PBH} \sim 10^{-5}$. In general, the contribution from the QCD Crossover is only observationally relevant when there is a significant contribution from radiation. In the case of a Bag Model or Lattice Fit Model this is not always true. In general, the cases which are valid within the QCD Crossover are excluded, due to observational constraints, if one chooses, instead, a Bag Model or a Lattice Fit Model for the QCD phase

Table 22: The contribution to Ω_{PBH} from the QCD Crossover. For more details see Table 19, Table 11 and the Conventions.

	n_+														
$\log_{10}(t_+/1\text{s})$	1.32	1.34	1.36	1.38	1.40	1.42	1.44	1.46	1.48	1.50	1.52	1.54	1.56	1.58	1.60
-10			R												
-9			R	R $\Omega \sim 10^{-6}$ $n \approx 9.1 \times 10^{10}$ Mpc^{-3} $d \sim 10^{18}$ m $5 \times 10^{-7} M_\odot$											
-8				R $\Omega \sim 10^{-16}$ $n \approx 0.7$ Mpc^{-3} $d \sim 10^{22}$ m $5 \times 10^{-6} M_\odot$	R $\Omega \sim 10^{-5}$ $n \approx 3.5 \times 10^{11}$ Mpc^{-3} $d \sim 10^{18}$ m $5 \times 10^{-6} M_\odot$										
-7					R $\Omega \sim 10^{-16}$ $n \approx 10.0$ Mpc^{-3} $d \sim 10^{22}$ m $5 \times 10^{-5} M_\odot$	R $\Omega \sim 10^{-4}$ $n \approx 1.6 \times 10^{11}$ Mpc^{-3} $d \sim 10^{18}$ m $5 \times 10^{-5} M_\odot$								
-6						R $\Omega \sim 10^{-15}$ $n \approx 7.3$ Mpc^{-3} $d \sim 10^{22}$ m $5 \times 10^{-4} M_\odot$	R $\Omega \sim 10^{-4}$ $n \approx 1.4 \times 10^{10}$ Mpc^{-3} $d \sim 10^{19}$ m $5 \times 10^{-4} M_\odot$							
-5							R $\Omega \sim 10^{-14}$ $n \approx 0.4$ Mpc^{-3} $d \sim 10^{22}$ m $5 \times 10^{-3} M_\odot$	RC $\Omega \sim 10^{-5}$ $n \approx 2.6 \times 10^{8}$ Mpc^{-3} $d \sim 10^{19}$ m $5 \times 10^{-3} M_\odot$ Fig. 78a						
-4							C $\Omega \sim 10^{-22}$ $n \approx 5.4 \times 10^{-12}$ Mpc^{-3} $d \sim 10^{25}$ m $0.5 M_\odot$	RC $\Omega \sim 10^{-12}$ $n \approx 0.4$ Mpc^{-3} $d \sim 10^{22}$ m $0.5 M_\odot$	RC $\Omega \sim 10^{-5}$ $n \approx 3.7 \times 10^{6}$ Mpc^{-3} $d \sim 10^{20}$ m $0.5 M_\odot$ Fig. 78b					
-3								C $\Omega \sim 10^{-20}$ $n \approx 1.0 \times 10^{-9}$ Mpc^{-3} $d \sim 10^{25}$ m $5 M_\odot$	RC $\Omega \sim 10^{-10}$ $n \approx 7.1$ Mpc^{-3} $d \sim 10^{21}$ m $5 M_\odot$	RC $\Omega \sim 10^{-4}$ $n \approx 1.2 \times 10^{7}$ Mpc^{-3} $d \sim 10^{19}$ m $5 M_\odot$ Fig. 77	RC*				
-2										RC $\Omega \sim 10^{-21}$ $n \approx 1.9 \times 10^{-11}$ Mpc^{-3} $d \sim 10^{25}$ m $5 M_\odot$	RC $\Omega \sim 10^{-11}$ $n \approx 0.2$ Mpc^{-3} $d \sim 10^{22}$ m $5 M_\odot$	RC $\Omega \sim 10^{-5}$ $n \approx 7.7 \times 10^{5}$ Mpc^{-3} $d \sim 10^{20}$ m $5 M_\odot$ Fig. 78c			
-1												R $\Omega \sim 10^{-16}$ $n \approx 7.2 \times 10^{-8}$ Mpc^{-3} $d \sim 10^{24}$ m $500 M_\odot$	R $\Omega \sim 10^{-9}$ $n \approx 2.5$ Mpc^{-3} $d \sim 10^{22}$ m $500 M_\odot$	RC $\Omega \sim 10^{-4}$ $n \approx 3.0 \times 10^{5}$ Mpc^{-3} $d \sim 10^{20}$ m $500 M_\odot$	
0														R	Rea

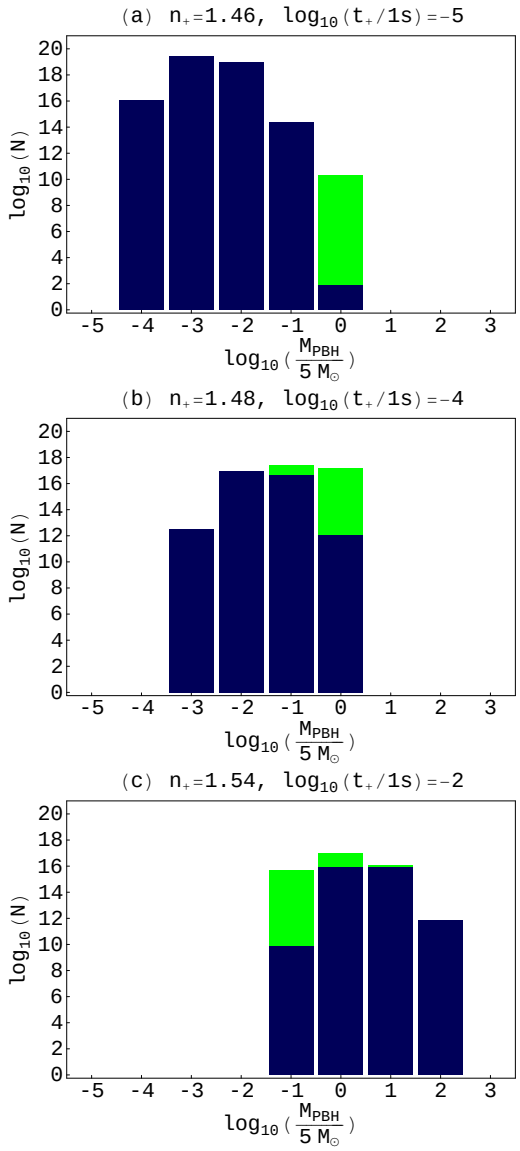

Figure 78: The PBH mass spectrum in the observable Universe due to the QCD Crossover model when: (a) $n_+ = 1.46$ and $t_+ = 10^{-5}$ s; (b) $n_+ = 1.48$ and $t_+ = 10^{-4}$ s; (c) $n_+ = 1.54$ and $t_+ = 10^{-2}$ s. See Figure 77 for more details.

transition (cf. Table 22 with Tables 20 and 21) because these models correspond to a much stronger transition. As an exception to this we mention the case $n_+ = 1.50$ and $t_+ = 10^{-2}$ s for which there is a negligible contribution from radiation and, hence, a negligible contribution from the QCD Crossover as well (less than 10 PHBs in the observable Universe). As another example we have the case $n_+ = 1.58$ and $t_+ = 10^{-1}$ s for which the main contribution to the total number of PBHs is from radiation (see Tables 20, 21 and 22).

Besides the 11 cases with contributions from the QCD Crossover (labeled 'RC' or 'C' in Table 22) we included also in Table 22 the data for other ten cases giving observationally relevant results that arise solely from the radiation contribution.

Namely, these are: the two cases labeled 'R' with $n_+ = 1.38$ that are valid within the QCD Crossover and the QCD Lattice Fit but excluded, due to observational constraints, in the case of a Bag Model (cf. Tables 20, 21 and 22); the six cases labeled 'R' with $1.40 \leq n_+ \leq 1.44$ valid within the QCD Crossover and excluded in the case of a Bag Model or Lattice Fit model (cf. Tables 20, 21 and 22); and the two cases labeled 'R' with $t_+ = 10^{-1}$ s that are valid within the three QCD adopted models (cf. Tables 20, 21 and 22) but with observationally relevant results coming solely from the radiation contribution.

For four of the cases out of the 10 (i.e., 40%) Ω_{PBH} equals or exceeds $\sim 10^{-6}$ with the rest of them giving Ω_{PBH} lower than $\sim 10^{-8}$. In these four cases we have the formation of substellar–mass PBHs and, thus we discuss them in more detail in Section 6.9.

6.6 The effect of the EW phase transition (MSSM) – Bag Model

In this section we consider the contribution from the EW phase transition to the global value of Ω_{PBH}. We studied the 32 'yellow' cases presented in Table 16 and found out that for 17 of them (53%) we have observationally relevant results for the PBH number density in the present day Universe (see Table 23). For some of the cases we might also have contributions from the QCD (cases labeled 'B' (QCD Bag Model) or 'L' (QCD Lattice Fit) in Table 23). However, the numeric values shown correspond to only the contributions from radiation and from the EW Bag Model. Simultaneous contributions from the QCD and from the EW will be discussed later.

In seven of the cases, out of the 17 (41%), Ω_{PBH} exceeds $\sim 10^{-5}$ and, for the rest of the cases, Ω_{PBH} is lower than $\sim 10^{-9}$. Next we describe in more detail those seven cases.

In Figure 79 we show the mass spectrum for the two cases giving $\Omega_{PBH} \sim 10^{-1}$. When $n_+ = 1.34$ and $t_+ = 10^{-11}$ s (Figure 79a) we get $\Omega_{PBH} \approx 0.20$. The peak due to the EW Bag Model, which is located at $5 \times 10^{-7} M_\odot$ (10^{27} g, $\approx 0.2 m_T$), gives $N \sim 10^{27}$ PBHs. On the other hand the peak due to the radiation contribution, which is located in this case at $5 \times 10^{-9} M_\odot$ ($\approx 2 \times 10^{-3} m_T$) gives $\sim 10^{16}$ PBHs. When $n_+ = 1.34$ and $t_+ = 10^{-10}$ s (Figure 79b) we get $\Omega_{PBH} \approx 0.15$, with the peak from the EW Bag Model giving $N \sim 10^{27}$ PBHs. In this case the contribution from radiation is very small (compared to the previous one) reaching only $\sim 10^2$ PBHs (mainly with $\approx 0.02 m_T$) for the observable Universe. In both cases the EW Bag Model contributes also with $N \sim 10^{25}$ PBHs with $5 \times 10^{-6} M_\odot$ (10^{28} g, $\approx 2 m_T$).

In general, the contribution from the EW Bag Model to the PBH mass spectrum shows a characteristic peak at $\sim 10^{27}$ g ($\sim 5 \times 10^{-7} M_\odot$, $\sim 0.2 m_T$) with an extension to the right (10^{28} g, $\sim 5 \times 10^{-6} M_\odot$, $\sim 2 m_T$). In the cases shown in Figure 79 this peak clearly dominates the mass spectrum and for seven of the cases the mass spectrum consists only on these two bars (cases labeled 'E' in Table 23). Here

Table 23: The contribution to Ω_{PBH} from the EW Bag Model. Cases labeled 'B' or 'L' indicate that, for them, we might also have contributions from, respectively, the QCD Bag Model or QCD Lattice Fit. However, the numeric values reflect only the contributions from radiation and from the EW Bag Model. For more details see Table 19, Table 11 and the Conventions.

	n_+											
$\log_{10}(t_+/1\text{s})$	1.26	1.28	1.30	1.32	1.34	1.36	1.38	1.40	1.42	1.44	1.46	1.48
-15			R									
-14			R	R								
-13				RE $\Omega \sim 10^{-11}$ $n \approx 7.2 \times 10^{10}$ Mpc^{-3} $d \sim 10^{18}$ m $5 \times 10^{-11} M_\odot$								
-12				RE $\Omega \sim 10^{-12}$ $n \approx 1.8 \times 10^{5}$ Mpc^{-3} $d \sim 10^{20}$ m $5 \times 10^{-7} M_\odot$	RE $\Omega \sim 10^{-3}$ $n \approx 2.9 \times 10^{15}$ Mpc^{-3} $d \sim 10^{17}$ m $5 \times 10^{-10} M_\odot$ Fig. 80							
-11			E $\Omega \sim 10^{-24}$ $n \approx 4.7 \times 10^{-7}$ Mpc^{-3} $d \sim 10^{24}$ m $5 \times 10^{-7} M_\odot$	E $\Omega \sim 10^{-9}$ $n \approx 1.9 \times 10^{8}$ Mpc^{-3} $d \sim 10^{19}$ m $5 \times 10^{-7} M_\odot$	RE $\Omega \approx 0.20$ $n \approx 2.1 \times 10^{16}$ Mpc^{-3} $d \sim 10^{16}$ m $5 \times 10^{-7} M_\odot$ Fig. 79a	RE*						
-10			E $\Omega \sim 10^{-24}$ $n \approx 1.5 \times 10^{-7}$ Mpc^{-3} $d \sim 10^{24}$ m $5 \times 10^{-7} M_\odot$	E $\Omega \sim 10^{-9}$ $n \approx 1.1 \times 10^{8}$ Mpc^{-3} $d \sim 10^{19}$ m $5 \times 10^{-7} M_\odot$	RE $\Omega \approx 0.15$ $n \approx 1.6 \times 10^{16}$ Mpc^{-3} $d \sim 10^{16}$ m $5 \times 10^{-7} M_\odot$ Fig. 79b	RE*						
-9				E $\Omega \sim 10^{-14}$ $n \approx 2.2 \times 10^{3}$ Mpc^{-3} $d \sim 10^{20}$ m $5 \times 10^{-7} M_\odot$	E $\Omega \sim 10^{-4}$ $n \approx 3.5 \times 10^{13}$ Mpc^{-3} $d \sim 10^{17}$ m $5 \times 10^{-7} M_\odot$	RE*	RBE*					
-8					E $\Omega \sim 10^{-13}$ $n \approx 9.5 \times 10^{3}$ Mpc^{-3} $d \sim 10^{20}$ m $5 \times 10^{-7} M_\odot$	BE $\Omega \sim 10^{-4}$ $n \approx 5.1 \times 10^{13}$ Mpc^{-3} $d \sim 10^{17}$ m $5 \times 10^{-7} M_\odot$	RBE*	RBLE*				
-7						BE $\Omega \sim 10^{-26}$ $n \approx 1.0 \times 10^{-9}$ Mpc^{-3} $d \sim 10^{24}$ m $5 \times 10^{-7} M_\odot$	BLE $\Omega \sim 10^{-11}$ $n \approx 6.5 \times 10^{5}$ Mpc^{-3} $d \sim 10^{20}$ m $5 \times 10^{-7} M_\odot$ Fig. 82b	RBLE $\Omega \sim 10^{-3}$ $n \approx 2.7 \times 10^{14}$ Mpc^{-3} $d \sim 10^{17}$ m $5 \times 10^{-7} M_\odot$ Fig. 82a	RB*LE*			
-6					B	B	BL	B*L	RB*L	RB*L*E $\Omega \sim 10^{-4}$ $n \approx 1.4 \times 10^{10}$ Mpc^{-3} $d \sim 10^{19}$ m $5 \times 10^{-4} M_\odot$ Fig. 81		
-5					B	BL	BL	B*L	B*L	RB*L*	RB*L*C	

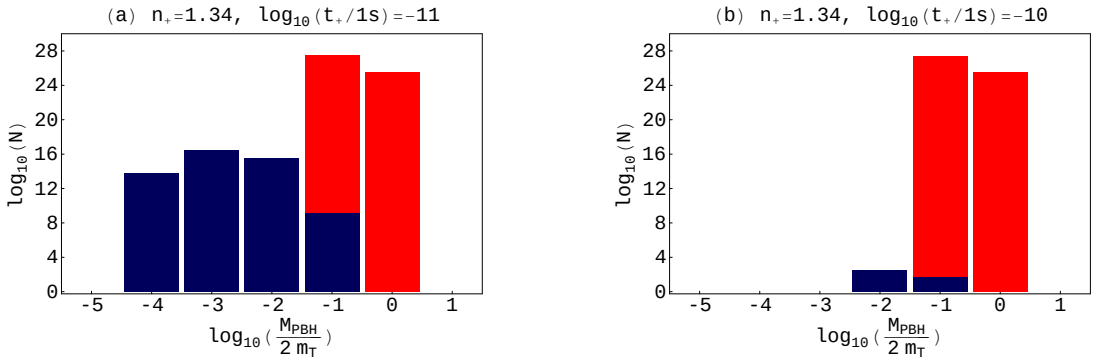

Figure 79: The PBH mass spectrum in the observable Universe due to the EW Bag Model when $n_+ = 1.34$ and: (a) $t_+ = 10^{-11}$ s; (b) $t_+ = 10^{-10}$ s. In red we show the contribution from the EW and in dark–blue the contribution from radiation. Both add up to the totals shown.

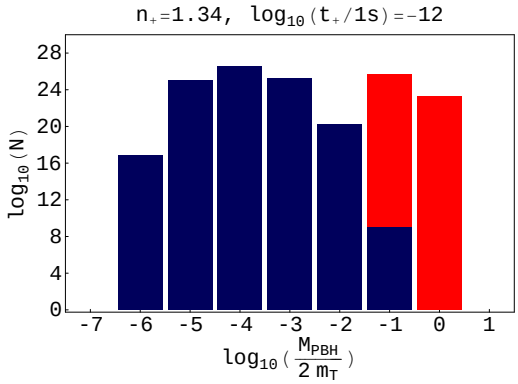

Figure 80: The PBH mass spectrum in the observable Universe due to the EW Bag Model when $n_+ = 1.34$ and $t_+ = 10^{-12}$ s. See Figure 79 for more details.

we consider the two such cases with the highest Ω_{PBH} values ($\sim 10^{-4}$): the case $n_+ = 1.34$ and $t_+ = 10^{-9}$ s (giving $\sim 10^{24}$ PBHs with $0.2m_T$ and $\sim 10^{22}$ PBHs with $2m_T$) and the case $n_+ = 1.36$ and $t_+ = 10^{-8}$ s (giving $\sim 10^{25}$ PBHs with $0.2m_T$ and $\sim 10^{23}$ PBHs with $2m_T$).

In Figure 80 we show the mass spectrum for the case $n_+ = 1.34$ and $t_+ = 10^{-12}$ s, a case with important contributions from both the EW phase transition and from radiation. From radiation we get $\sim 10^{26}$ PBHs, with the peak located at $\approx 2 \times 10^{-4} m_T$, and from the EW Bag Model we get a PBH number of the same order but now peaking at $\approx 0.2m_T$.

In Figure 81 we show the mass spectrum for the case $n_+ = 1.44$ and $t_+ = 10^{-6}$ s ($\Omega_{PBH} \sim 10^{-4}$). This is a valid case as long as one considers for the QCD a Crossover Model (the QCD Bag Model or QCD Lattice Fit model are excluded due to observational constraints – cf. Tables 20, 21 and 22) although with negligible results. Thus, in this case the main contribution comes from radiation (with the peak located at $\approx 0.5m_J$ giving $\sim 10^{21}$ PBHs). The contribution from the EW Bag Model gives $\sim 10^{11}$ PBHs mainly with $\approx 0.2m_T$.

In our sample of cases there are four situations allowing simultaneous contributions

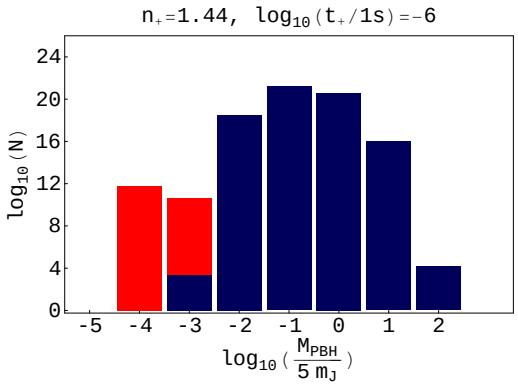

Figure 81: The PBH mass spectrum in the observable Universe due to the EW Bag Model when $n_+ = 1.44$ and $t_+ = 10^{-6}$ s. See Figure 79 for more details.

from both the QCD and the EW transitions if one considers for the QCD phase transition a Bag Model or a Lattice Fit model. These are the three cases with $t_+ = 10^{-7}$ s plus the case $n_+ = 1.36$ and $t_+ = 10^{-8}$ s (this last one already mentioned). In the case of a QCD Crossover the cases for which there is a simultaneous contribution from the EW transition always lead to non–observationally relevant results in terms of PBH number density (cf. Tables 16 and 23).

In Figure 82a we show the mass spectrum for the case $n_+ = 1.40$ and $t_+ = 10^{-7}$ s. If one adopts for the QCD a Bag Model profile then, besides the peak from the EW contribution (located at $\sim 10^{27}$ g, $\sim 5 \times 10^{-4} m_J$) we have another peak due to the QCD (located at $\sim 10^{33}$ g, $\sim 500 m_J$, $0.5 M_\odot$). The contribution from radiation is small if compared with the other two ($\sim 10^{12}$ PBHs due to the radiation contribution, $\sim 10^{21}$ PBHs due to the QCD Bag Model and $\sim 10^{25}$ PBHs due to the EW Bag Model). In terms of PBH number density we get $\approx 2.7 \times 10^{14}$ Mpc^{-3} from the EW and $\approx 1.7 \times 10^{10}$ Mpc^{-3} from the QCD[28]. If one adopts for the QCD a Lattice Fit model instead, then the corresponding PBH number density goes down to ≈ 21 Mpc^{-3} (Figure 82a).

When $n_+ = 1.38$ and $t_+ = 10^{-7}$ s we get $\sim 10^{17}$ PBHs from the EW Bag Model plus $\sim 10^{16}$ PBHs in the case of a QCD Bag Model or $\sim 10^2$ in the case of a QCD Lattice Fit model (Figure 82b). Finally when $n_+ = 1.36$ and $t_+ = 10^{-7}$ s we get $\sim 10^2$ PBHs from the EW Bag Model and $\sim 10^9$ PBHs in the case of a QCD Bag Model.

If the EW phase transition is described by a Crossover, instead of a Bag Model, then the cases labeled 'E*' in Table 23 (that were excluded due to observational constraints) are now allowed. In particular the case $n_+ = 1.42$ and $t_+ = 10^{-7}$ s is allowed if the QCD is not described by a Bag Model as well (cf. Tables 20, 21, 22 and 23). We discuss these cases in Section 6.9.

[28]The values shown in Table 23 refer only to the contribution from the EW phase transition and from radiation. Eventual contributions from the QCD Bag Model or from the QCD Lattice Fit were left outside.

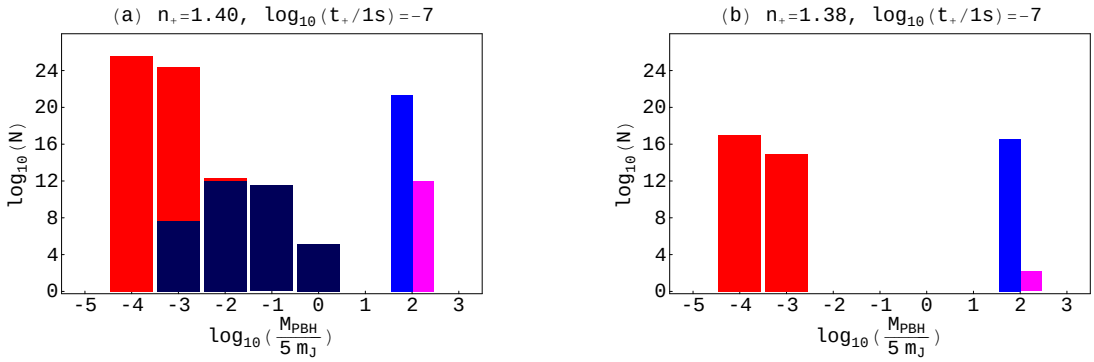

Figure 82: The PBH mass spectrum in the observable Universe due to the EW Bag Model and the QCD phase transition for $t_+ = 10^{-7}$ s: (a) $n_+ = 1.40$ and (b) $n_+ = 1.38$. In red we show the contribution from the EW, in light–blue the contribution from the QCD Bag Model, in magenta the contribution from the QCD Lattice Fit and in dark–blue the contribution from radiation.

Table 24: The eight cases with the largest contribution to the number of IMBHs. For each case we show the PBH number density n_{PBH} (equation 201), the total number of PBHs in the observable Universe N as well as the corresponding average mass. For the cases labeled 'SBHs' the PBH mass spectrum extends to the stellar mass region and, for the cases labeled 'SMBHs' to the SMBH region. For more details see the Conventions and: Table 19 (cases labeled 'Rea'); Tables 20, 21 and 22 (case labeled 'RBLC'); Table 22 (case labeled 'R').

n_+	$\log_{10}(\frac{t_+}{1\ \mathrm{s}})$	$n_{PBH}(\mathrm{Mpc}^{-3})$	N	$M(M_\odot)$	Obs.		Fig.
1.56	-1	2.6	$\sim 10^{11}$	$5 - 5 \times 10^3$	R	SBHs	
1.58	-1	2.9×10^5	$\sim 10^{16}$	$5 - 5 \times 10^4$	RBLC	SBHs	72
1.60	0	2.3	$\sim 10^{11}$	$5 \times 10^2 - 5 \times 10^4$	Rea		
1.62	0	4.8×10^4	$\sim 10^{15}$	$50 - 5 \times 10^5$	Rea	SBHs	68a
1.64	1	2.6	$\sim 10^{11}$	$5 \times 10^3 - 5 \times 10^5$	Rea		69b
1.66	1	6.1×10^3	$\sim 10^{15}$	$5 \times 10^2 - 5 \times 10^5$	Rea		68b
1.70	2	3.0	$\sim 10^{11}$	$5 \times 10^4 - 5 \times 10^6$	Rea	SMBHs	70
1.72	2	2.7×10^3	$\sim 10^{14}$	$5 \times 10^4 - 5 \times 10^7$	Rea	SMBHs	68c

6.7 Intermediate–mass PBHs

In our sample of allowed cases we found out 18 situations ($\approx 23\%$ of the observationally relevant cases) allowing IMBH formation. In six cases, out of the 18, the mass spectrum extends to the stellar mass region (cf. Section 6.8) and, in other six cases, out of the 18, to the SMBH region (cf. Section 6.3). In Table 24 we show the eight cases with the largest contribution to the number of IMBHs (for the rest of the cases N does not exceed $\sim 10^7$). For the cases with extensions to the SMBH or SBH part of the mass spectrum we considered only those with the peak located within the IMBH part of the spectrum.

We start with the cases for which the PBH mass spectrum extends to the SMBH

region. Within this scenario the case with the highest PBH number density (n_{PBH}) corresponds to $n_+ = 1.72$ and $t_+ = 10^2$ s (Figure 68c). In fact, for this case, we have $n_{PBH} \approx 2.7 \times 10^3$ Mpc^{-3} mainly due to IMBHs in the $5 \times 10^4 - 5 \times 10^5 M_\odot$ mass range and $n_{PBH} \approx 3.6$ Mpc^{-3} for $5 \times 10^6 - 5 \times 10^7 M_\odot$ SMBHs.

When $n_+ = 1.66$ and $t_+ = 10$ s all the PBHs are IMBHs with masses within the range $5 \times 10^2 - 5 \times 10^5 M_\odot$ peaking at $5 \times 10^4 M_\odot$(cf. Figure 68b). Among the cases giving only IMBHs (cf. Table 24) this is the one with the highest PBH number density ($n_{PBH} \approx 6.1 \times 10^3$ Mpc^{-3}).

Finally, we consider the case $n_+ = 1.58$ and $t_+ = 10^{-1}$ s that allows simultaneous formation of stellar mass BHs and IMBHs (cf. Figure 72). The mass spectrum, for this case, which is the one with the highest value for the PBH number density in Table 24 ($n_{PBH} \approx 2.9 \times 10^5$ Mpc^{-3}), goes from $5M_\odot$ to $5 \times 10^4 M_\odot$ (peaking at $500M_\odot$ ($N \sim 10^{16}$) but giving also $\sim 10^{16}$ PBHs of $50M_\odot$).

6.8 Stellar mass PBHs

The formation of stellar mass PBHs is closely related to the QCD epoch. In general, the cases allowing the formation of stellar mass PBHs show a peak at $\approx 0.5M_\odot$ corresponding to the QCD contribution (Bag Model, Lattice Fit or Crossover). In Table 25 we compile the 24 cases giving at least one SBH inside our galactic halo (this corresponds to $\approx 11\%$ of the cases giving observationally relevant results).

There are cases for which the mass spectrum consists of a single peak at $\approx 0.5M_\odot$ (e.g., the case when $n_+ = 1.38$ and $t_+ = 10^{-5}$ s). In other cases the mass spectrum extends to the sub–stellar mass region (e.g. the case when $n_+ = 1.40$ and $t_+ = 10^{-7}$ s, Figure 82a) or to the IMBH region (e.g. the case when $n_+ = 1.58$ and $t_+ = 10^{-1}$ s, Figure 72).

Although represented in Table 25, the case $n_+ = 1.42$ and $t_+ = 10^{-5}$ s (obtained within the QCD Lattice Fit) must be excluded because the limits for the CDM halo are exceeded (see Sections 1.1.3 and 7.4).

6.9 Sub–stellar mass PBHs

We are not aware of any process that could lead to the formation of this kind of BHs in the present day Universe. This means that all BHs within this mass range are PBHs. Still, PBHs with $< 10^{15}$ g should have completely evaporated by now (due to the emission of Hawking radiation) with the ones with $\approx 10^{15}$ g exploding right now (cf. Figure 1). Thus, if we want to find sub–stellar PBHs in the Universe then we must look for objects with masses between 10^{15} g and $\lesssim 10^{33}$ g ($1M_\odot \approx 10^{33}$ g), a very large mass range.

We start with the cases giving observationally relevant results for sub–earth mass PBHs (10^{16}–10^{27} g). In Table 26 we show the 21 allowed cases within the context of

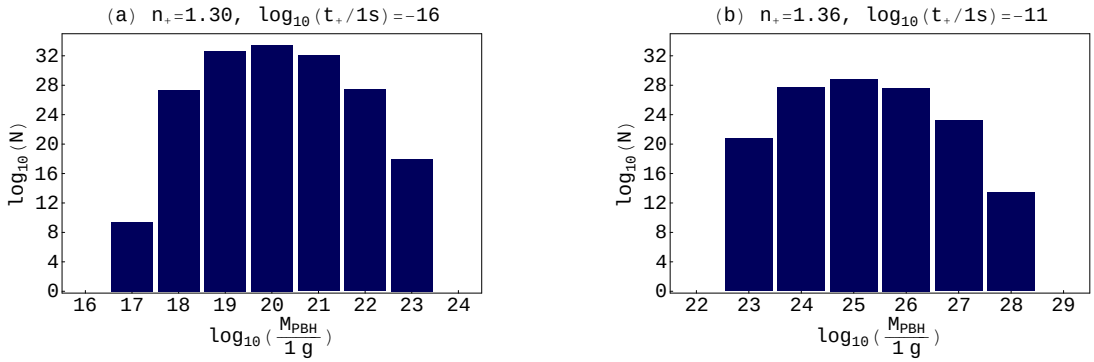

Figure 83: The PBH mass spectrum in the observable Universe when: (a) $n_+ = 1.30$ and $t_+ = 10^{-16}$ s; (b) $n_+ = 1.36$ and $t_+ = 10^{-11}$ s (contribution from radiation only).

an EW Crossover. The cases with $n_+ = 1.36$ are excluded if the EW phase transition is described by a Bag Model instead of a Crossover model (cf. Table 23).

In two of the cases shown in Table 26 we get $\Omega_{PBH} \sim 10^{-2}$ (see Figure 83) and, in two other cases we get $\Omega_{PBH} \sim 10^{-2}$ (see Figure 84). We now discuss these cases in more detail.

When $n_+ = 1.30$ and $t_+ = 10^{-16}$ s we get $\Omega_{PBH} \sim 10^{-2}$ corresponding to a PBH number density $n_{PBH} \approx 2.6 \times 10^{22}$ Mpc^{-3} with the mass spectrum peaking at 10^{20} g (Figure 83a). The other case for which $\Omega_{PBH} \sim 10^{-2}$ occurs when $n_+ = 1.36$ and $t_+ = 10^{-11}$ s (Figure 83b) now with $n_{PBH} \approx 5.8 \times 10^{17}$ Mpc^{-3} and the mass spectrum peaking at 10^{25} g. This case is excluded due to observational constraints if one adopts for the EW a Bag Model.

When $n_+ = 1.28$ and $t_+ = 10^{-18}$ s we get $\Omega_{PBH} \sim 10^{-3}$ with a PBH number density $n_{PBH} \approx 2.6 \times 10^{23}$ Mpc^{-3} with the mass spectrum peaking at 10^{18} g (Figure 84a). This means that, in this case, which is the one giving the highest number of sub–stellar PBHs ($\sim 10^{34}$ PBHs in the Universe), we should expect $\sim 10^{18}$ PBHs inside our galactic halo. These are BHs with $R_s \sim 10^{-14}$–10^{-9} m. The other case giving $\Omega_{PBH} \sim 10^{-3}$ occurs when $n_+ = 1.32$ and $t_+ = 10^{-14}$ s (Figure 84b) now with $n_{PBH} \approx 5.2 \times 10^{19}$ Mpc^{-3} and the mass spectrum peaking at 10^{22} g.

These four cases, that allow the formation of microscopic (or sub–microscopic) PBHs in observationally relevant numbers, are also the single ones giving PBHs within a region of radius 1 pc (cf. Section 6.11).

If the EW phase transition is described by a Bag Model (instead of a Crossover model) then a peak is expected on the mass spectrum at 10^{27}–10^{28} g corresponding to a population of Earth–mass PBHs (e.g. case $n_+ = 1.34$ and $t_+ = 10^{-11}$ s, Figure 79a). In that scenario the cases with $n_+ = 1.36$ shown in Table 26 are excluded due to observational constraints and, in addition, we have six other cases giving observationally relevant results (cases labeled 'E' in Table 23).

There are also five cases allowing simultaneous contributions from both the radiation and the EW Bag Model (cases labeled cases labeled 'RE' in Table 23). For example,

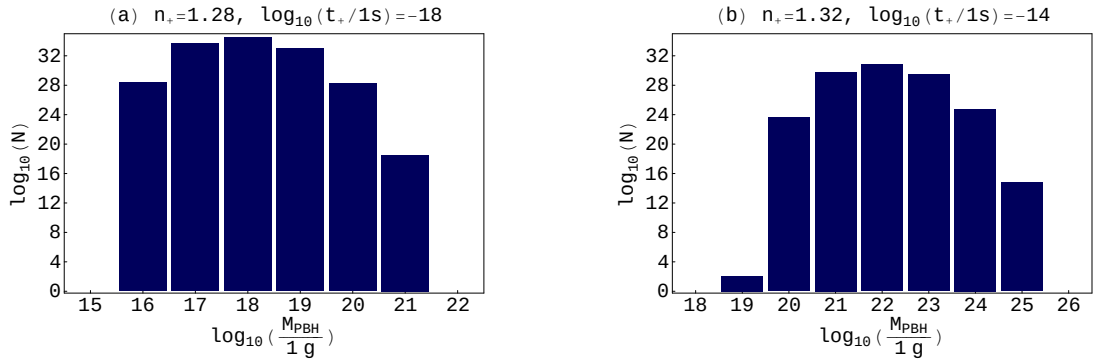

Figure 84: The PBH mass spectrum when: (a) $n_+ = 1.28$ and $t_+ = 10^{-18}$ s; (b) $n_+ = 1.32$ and $t_+ = 10^{-14}$ s (contribution from radiation only).

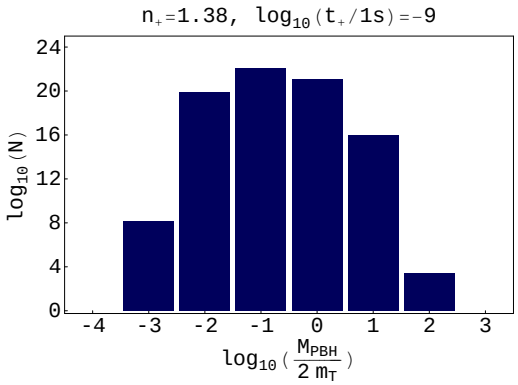

Figure 85: The PBH mass spectrum when $n_+ = 1.38$ and $t_+ = 10^{-9}$ s (contribution from radiation only).

when $n_+ = 1.34$ and $t_+ = 10^{-12}$ s we get from the radiation contribution $\Omega_{PBH} \sim 10^{-5}$. Adding up the EW Bag Model contribution this value rises to $\sim 10^{-3}$ (cf. Tables 23 and 26, Figure 80). When $t_+ = 10^{-11}$ s and $t_+ = 10^{-10}$ s keeping $n_+ = 1.34$ we have even more pronounced variations in the value of Ω_{PBH}: in the first case it rises from $\sim 10^{-14}$ to ~ 0.1 and, in the second case, from $\sim 10^{-27}$ to ~ 0.1 (cf. Tables 23 and 26, Figure 79).

In Table 26 we consider the cases leading to SSBH formation when $1.24 \leq n_+ \leq 1.36$. Moving to higher values of n_+ we still get some cases leading to SSBH formation. However, the allowed cases depend on the model one adopts for the QCD phase transition (Bag Model, Lattice Fit, Crossover).

When $n_+ = 1.38$ and $t_+ = 10^{-9}$ s (Figure 85) we get $\Omega_{PBH} \sim 10^{-6}$ which corresponds to have $n_{PBH} \approx 9.2 \times 10^{10}$ Mpc^{-3} with the mass spectrum peaking at $\sim 10^{27}$ g ($5 \times 10^{-7} M_\odot$, $\approx 0.2 m_T$). This case, valid for the three QCD models, gives a population of $\sim 10^{22}$ SSBHs plus ~ 10 PBHs with $0.5 M_\odot$ in the case of a QCD Bag Model (not shown in Figure 85). In the case $n_+ = 1.38$ and $t_+ = 10^{-8}$ s we have a similar situation now with $\sim 10^{11}$ SSBHs plus $\sim 10^{11}$ PBHs $0.5 M_\odot$ in the case of a QCD Bag Model. The contribution from the QCD Lattice Fit or from the QCD Crossover is, in the two cases, negligible (cf. Tables 20, 21, and 22).

The case $n_+ = 1.44$ and $t_+ = 10^{-6}$ s is excluded, due to observational constraints, if one adopts for the QCD phase transition a Bag Model or a Lattice Fit model. If one adopts a Crossover model instead then, although the contribution from the QCD epoch is negligible, the contribution from radiation gives $\sim 10^{21}$ SSBHs peaking at $0.5m_J$. In addition we might also have a contribution from the EW Bag Model with $\sim 10^{11}$ SSBHs (Figure 81).

There are a few cases for which the mass spectrum extends from the sub–stellar mass region into the stellar mass region. In general, this corresponds to cases with simultaneous contributions from both the EW and the QCD phase transitions (as an example we have the case $n_+ = 1.40$ and $t_+ = 10^{-7}$ s, Figure 82a) or to cases with a strong contribution from radiation plus a contribution from the QCD or from the EW (as an example we have the case $n_+ = 1.46$ and $t_+ = 10^{-5}$ s, Figure 78a).

In Table 27 we compile the 36 cases ($\approx 27\%$ of the observationally relevant cases) giving at least one sub–stellar mass PBH in our galactic halo. Although represented in Table 27, the cases $n_+ = 1.34$ and $t_+ = 10^{-11}$ s and $n_+ = 1.34$ and $t_+ = 10^{-10}$ s (obtained within the EW Bag Model) must be excluded because they exceed the CDM limits for the galactic halo (see Sections 1.1.3 and 7.5).

6.10 PBHs and CDM

If PBHs with masses $> 10^{15}$ g ever formed and exist in the Universe then they are a component of CDM. If this is the case then, how much do they contribute to CDM? We found out that in the studied cases we have situations with PBHs representing an important fraction of CDM ($\geq 1\%$), others where they contribute with a small (but non–negligible) fraction (between $10^{-6}\%$ and 1%) and also some cases for which the contribution is negligible ($< 10^{-6}\%$). In Table 28 we compile the 17 cases ($\approx 13\%$ of the studied cases) contributing with $> 1\%$ to the CDM.

In Figure 86 we show, as an example, the curve $\Omega_{PBH}(t_k)$ for the case when $n_+ = 1.34$ and $t_+ = 10^{-11}$ s since this is the one with the largest contribution from Ω_{PBH} to Ω_{CDM} (Table 28). In fact, when one considers a first–order EW phase transition, integration of the curve $\Omega_{PBH}(t_k)$ (see Figure 86) yields $\Omega_{PBH}(t_0) \approx 0.1955$ which means that these PBHs represent $\approx 99\%$ of all the CDM in the observable Universe[29]. In this situation a large fraction of CDM would be provided by 10^{27} g ($5 \times 10^{-7} M_\odot$) PBHs. However, taking into account that objects with this mass cannot make up more than 25% of the CDM galactic halo we must exclude this case (see Sections 1.1.3 and 7.5). Still, if the EW phase transition consists of a simple crossover, then we get, instead, $\Omega_{PBH}(t_0) \sim 10^{-14}$ (and the case is allowed). The case $n_+ = 1.34$ and $t_+ = 10^{-10}$ s is also excluded for the same reason (cf. Table 28). Another case

[29]This is obtained from (cf. Section 1.1.3, equation 36).

$$\frac{\Omega_{PBH}}{\Omega_{CDM}} \approx \frac{0.1955}{0.1980} \approx 0.987$$

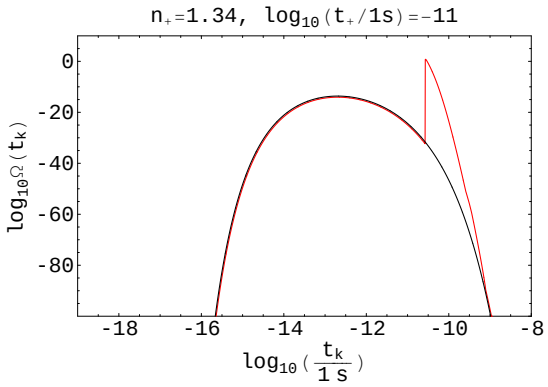

Figure 86: The curve $\Omega_{PBH}(t_k)$ when $n_+ = 1.34$ and $t_+ = 10^{-11}$ s.

that is excluded occurs (within the Lattice Fit) when $n_+ = 1.42$ and $t_+ = 10^{-5}$ s, now because objects with $0.5M_\odot$ cannot contribute with more than 40% to the CDM halo (see Sections 1.1.3 and 7.4).

6.11 Nearby PBHs

From the observational point of view, it is very relevant to determine the probability of finding a PBH within the Solar System neighbourhood. For all the cases that we studied (cf. Tables 19, 20, 21, 22 and 23) we found that the chances of finding a PBH within a distance of the order of the Earth–moon distance are incredibly small and that this picture, in general, does not change significantly if one moves to a region with the size of ~ 50 AU (cf. Section 6.2 and Table O-1).

On the other hand, within a region of radius 1 pc we have *four* cases with interesting results. Perhaps the most interesting one, from the observational point of view, is the case when $n_+ = 1.28$ and $t_+ = 10^{-18}$ s (Figure 84a) with a PBH number density of $\approx 2.6 \times 10^{23}$ Mpc^{-3} peaking at 10^{18} g. This corresponds to having $\sim 10^5$ PBHs within a sphere with radius 0.4 pc (which is aproximately the radius of the *Oort cloud*) or $\sim 10^6$ PBHs inside a sphere with radius 1 pc. The nearest PBH could be as close as 2.8×10^{14} m (0.009 pc or ≈ 50 times the average radius of the orbit of Pluto or ≈ 1885AU). These PBHs have masses in the range 10^{17}–10^{19} g.

The second most important case, as regards PBH number density, with $\approx 2.6 \times 10^{22}$ Mpc^{-3}, is the case $n_+ = 1.30$ and $t_+ = 10^{-16}$ s (Figure 83a). We now have $\sim 10^4$ PBHs inside a sphere with radius 0.4 pc ($\sim 10^5$ PBHs inside a sphere with radius 1 pc) with the nearest one probably at a distance not larger than 6.0×10^{14} m (≈ 0.02 pc). In this case, the PBHs have masses on the range 10^{19}–10^{21} g. The other two cases show more modest values. Those are the cases $n_+ = 1.32$ and $t_+ = 10^{-14}$ s (Figure 84b) with $\sim 10^2$ PBHs (with masses in the range 10^{21}–10^{23} g) inside a sphere with radius 1 pc and the case $n_+ = 1.36$ and $t_+ = 10^{-11}$ s (Figure 83b) with 2 PBHs (with mass 10^{25} g) inside a sphere with radius 1 pc.

Moving to a scale with the size of our galactic halo ($\approx 1.6 \times 10^4$ pc) then we found

out that for $\approx 36\%$ of the cases with observationally relevant results we get at least one PBH inside our galactic halo. These are the 24 cases listed in Table 25 (stellar mass PBHs), together with the 36 cases listed in Table 27 (sub–stellar mass PBHs) and with the case $n_+ = 1.62$ and $t_+ = 1$ s (see Figure 68a) giving a $5 \times 10^3 M_\odot$ PBH in our galactic halo.

Table 25: The 24 cases giving the largest contribution to the number of stellar mass PBHs (giving at least one stellar mass PBH in our galactic halo). For each case we show the PBH number density n_{PBH} (equation 201), the total number of SBHs inside our galactic halo (N_{Halo}) as well as the corresponding mass ranges (only the stellar mass part). For the cases labeled 'SSBHs' the PBH mass spectrum (for the entire Universe) extends to the sub–stellar mass region and, for the cases labeled 'IMBHs' to the IMBH region. For more details see the Conventions and: Table 20 (cases labeled 'RB' or 'B'); Table 21 (cases labeled 'RL' or 'L'); Table 22 (cases labeled 'RC'); Tables 20 and 23 (cases labeled 'BE' and 'RBE').

n_+	$\log_{10}(\frac{t_+}{1\text{ s}})$	$n_{PBH}(\text{Mpc}^{-3})$	N_{Halo}	$M_{Halo}(M_\odot)$	Obs.		Fig.
1.38	-7	2.8×10^5	$\sim 10^1$	0.5	BE	SSBHs	82b
1.38	-6	1.4×10^8	$\sim 10^3$	0.5	B		
1.38	-5	3.5×10^8	$\sim 10^4$	0.5	B		
1.38	-4	5.2×10^5	$\sim 10^1$	0.5	B		
1.40	-8	3.8×10^{11}	$\sim 10^2$	0.5	RB	SSBHs	73
1.40	-7	1.7×10^{10}	$\sim 10^5$	0.5	RBE	SSBHs	82a
1.40	-6	1.2×10^5	$\sim 10^0$	0.5	L		
1.40	-5	2.2×10^6	$\sim 10^1$	0.5	L		
1.40	-4	2.8×10^{10}	$\sim 10^6$	0.5	B		71b
1.42	-7	1.9×10^{11}	$\sim 10^2$	0.5	RL	SSBHs	76
1.42	-6	6.3×10^9	$\sim 10^5$	0.5	RL	SSBHs	75
1.42	-5	4.3×10^{10}	$\sim 10^6$	0.5	L		
1.42	-4	1.9×10^9	$\sim 10^4$	0.5	L		
1.42	-3	1.1×10^8	$\sim 10^3$	0.5	B		
1.44	-3	7.8×10^7	$\sim 10^3$	0.5	L		
1.48	-4	3.7×10^6	$\sim 10^1$	0.5–5	RC	SSBHs	78b
1.48	-2	3.8×10^5	$\sim 10^1$	0.5	B		
1.50	-3	1.3×10^7	$\sim 10^2$	0.5–5	RC	SSBHs	77
1.50	-2	8.5×10^9	$\sim 10^5$	0.5	B		71c
1.50	-2	3.0×10^7	$\sim 10^3$	0.5	L		74c
1.54	-2	7.8×10^5	$\sim 10^1$	0.5–50	RC	IMBHs	78c
1.58	-1	2.9×10^5	$\sim 10^1$	50	RB	IMBHs	72
1.58	-1	2.9×10^5	$\sim 10^1$	50	RL	IMBHs	72
1.58	-1	3.0×10^5	$\sim 10^1$	50	RC	IMBHs	72

Table 26: The contribution to Ω_{PBH} from SSBHs within the mass range 10^{16}–10^{27} g. Cases with a gray background are excluded if one adopts an EW Bag Model. For more details see Table 19, Table 11 and the Conventions.

	n_+								
$\log_{10}(t_+/1\text{s})$	1.22	1.24	1.26	1.28	1.30	1.32	1.34	1.36	1.38
-23		R $\Omega \sim 10^{-16}$ $n \approx 1.7 \times 10^{15}$ Mpc^{-3} $d \sim 10^{17}$ m 10^{16} g							
-22		R $\Omega \sim 10^{-18}$ $n \approx 1.6 \times 10^{13}$ Mpc^{-3} $d \sim 10^{17}$ m 10^{16} g							
-21		R $\Omega \sim 10^{-24}$ $n \approx 2.3 \times 10^{5}$ Mpc^{-3} $d \sim 10^{20}$ m 10^{16} g							
-20		R $\Omega \sim 10^{-39}$ $n \approx 1.1 \times 10^{-9}$ Mpc^{-3} $d \sim 10^{25}$ m 10^{17} g							
-19			R $\Omega \sim 10^{-15}$ $n \approx 3.2 \times 10^{12}$ Mpc^{-3} $d \sim 10^{18}$ m 10^{18} g						
-18			R $\Omega \sim 10^{-28}$ $n \approx 1.5$ Mpc^{-3} $d \sim 10^{22}$ m 10^{18} g	R $\Omega \sim 10^{-3}$ $n \approx 2.6 \times 10^{23}$ Mpc^{-3} $d \sim 10^{14}$ m 10^{18} g Fig. 84a					
-17				R $\Omega \sim 10^{-11}$ $n \approx 5.5 \times 10^{14}$ Mpc^{-3} $d \sim 10^{17}$ m 10^{19} g					
-16				R $\Omega \sim 10^{-21}$ $n \approx 2.5 \times 10^{3}$ Mpc^{-3} $d \sim 10^{21}$ m 10^{20} g	R $\Omega \sim 10^{-2}$ $n \approx 2.6 \times 10^{22}$ Mpc^{-3} $d \sim 10^{15}$ m 10^{20} g Fig. 83a				

(continues on next page)

Table 26 (continued).

$\log_{10}(t_+/1\text{s})$	n_+								
	1.22	1.24	1.26	1.28	1.30	1.32	1.34	1.36	1.38
-15					R $\Omega \sim 10^{-10}$ $n \approx 9.2 \times 10^{13}$ Mpc^{-3} $d \sim 10^{17}$ m 10^{21} g				
-14					R $\Omega \sim 10^{-20}$ $n \approx 5.1 \times 10^{2}$ Mpc^{-3} $d \sim 10^{21}$ m 10^{22} g	R $\Omega \sim 10^{-3}$ $n \approx 5.2 \times 10^{19}$ Mpc^{-3} $d \sim 10^{15}$ m 10^{22} g Fig. 84b			
-13						R $\Omega \sim 10^{-11}$ $n \approx 7.2 \times 10^{10}$ Mpc^{-3} $d \sim 10^{18}$ m 10^{23} g			
-12						R $\Omega \sim 10^{-22}$ $n \approx 6.1 \times 10^{-2}$ Mpc^{-3} $d \sim 10^{22}$ m 10^{24} g	R $\Omega \sim 10^{-5}$ $n \approx 2.5 \times 10^{15}$ Mpc^{-3} $d \sim 10^{17}$ m 10^{24} g Fig. 80		
-11							R $\Omega \sim 10^{-14}$ $n \approx 2.5 \times 10^{5}$ Mpc^{-3} $d \sim 10^{20}$ m 10^{25} g Fig. 79a	R $\Omega \sim 10^{-2}$ $n \approx 5.8 \times 10^{17}$ Mpc^{-3} $d \sim 10^{16}$ m 10^{25} g Fig. 83b	
-10							R $\Omega \sim 10^{-27}$ $n \approx 2.4 \times 10^{-9}$ Mpc^{-3} $d \sim 10^{25}$ m 10^{26} g Fig. 79b	R $\Omega \sim 10^{-11}$ $n \approx 1.3 \times 10^{9}$ Mpc^{-3} $d \sim 10^{19}$ m 10^{26} g	
-9								R $\Omega \sim 10^{-22}$ $n \approx 7.5 \times 10^{-4}$ Mpc^{-3} $d \sim 10^{23}$ m 10^{27} g	RB

Table 27: The 36 cases with the largest contribution to the number of sub–stellar mass PBHs. For each case we show the PBH number density n_{PBH} (equation 201), the total number of PBHs inside our galactic halo N_{Halo} as well as the corresponding mass ranges (only the sub–stellar mass part). For the cases labeled 'SBHs' the PBH mass spectrum extends to the stellar mass region. See Table 25 for more details.

n_+	$\log_{10}(\frac{t_+}{1\ \mathrm{s}})$	$n_{PBH}(\mathrm{Mpc}^{-3})$	N_{Halo}	$M_{Halo}(g)$	Obs.		Fig.
1.24	-23	1.7×10^{15}	$\sim 10^{10}$	10^{15}–10^{16}	R		
1.24	-22	1.6×10^{13}	$\sim 10^{8}$	10^{15}–10^{16}	R		
1.24	-21	2.3×10^{5}	~ 1	10^{15}–10^{16}	R		
1.26	-19	3.2×10^{12}	$\sim 10^{8}$	10^{15}–10^{19}	R		
1.28	-18	2.6×10^{23}	$\sim 10^{18}$	10^{16}–10^{21}	R		84a
1.28	-17	5.5×10^{14}	$\sim 10^{10}$	10^{17}–10^{21}	R		
1.30	-16	2.6×10^{22}	$\sim 10^{17}$	10^{18}–10^{23}	R		83a
1.30	-15	9.2×10^{13}	$\sim 10^{9}$	10^{20}–10^{23}	R		
1.32	-14	5.2×10^{19}	$\sim 10^{15}$	10^{20}–10^{24}	R		84b
1.32	-13	7.2×10^{10}	$\sim 10^{6}$	10^{22}–10^{24}	R		
1.32	-12	1.8×10^{5}	~ 1	10^{27}	RE		
1.32	-11	1.9×10^{8}	$\sim 10^{3}$	10^{27}–10^{28}	E		
1.32	-10	1.1×10^{8}	$\sim 10^{3}$	10^{27}–10^{28}	E		
1.34	-12	2.5×10^{15}	$\sim 10^{10}$	10^{22}–10^{26}	R		80
1.34	-12	2.9×10^{15}	$\sim 10^{10}$	10^{22}–10^{28}	RE		80
1.34	-11	2.5×10^{5}	~ 1	10^{25}	R		79a
1.34	-11	2.1×10^{16}	$\sim 10^{11}$	$10^{25} + 10^{27}$–10^{28}	RE		79a
1.34	-10	1.6×10^{16}	$\sim 10^{11}$	10^{27}–10^{28}	RE		79b
1.34	-9	3.5×10^{13}	$\sim 10^{9}$	10^{27}–10^{28}	E		
1.36	-11	5.8×10^{17}	$\sim 10^{13}$	10^{23}–10^{27}	R		83b
1.36	-10	1.3×10^{9}	$\sim 10^{4}$	10^{25}–10^{27}	R		
1.36	-8	5.1×10^{13}	$\sim 10^{9}$	10^{27}–10^{28}	E		
1.38	-9	9.2×10^{10}	$\sim 10^{6}$	10^{26}–10^{29}	R		85
1.38	-7	6.5×10^{5}	$\sim 10^{1}$	10^{27}–10^{28}	E		82b
1.38	-7	6.5×10^{5}	$\sim 10^{1}$	10^{27}–10^{28}	EB	SBHs	82b
1.38	-7	6.5×10^{5}	$\sim 10^{1}$	10^{27}–10^{28}	EL	SBHs	82b
1.40	-8	3.5×10^{11}	$\sim 10^{7}$	10^{26}–10^{31}	R		73
1.40	-8	3.8×10^{11}	$\sim 10^{7}$	10^{26}–10^{31}	RB	SBHs	73
1.40	-8	3.6×10^{11}	$\sim 10^{7}$	10^{26}–10^{31}	RL	SBHs	73
1.40	-7	2.7×10^{14}	$\sim 10^{9}$	10^{27}–10^{28}	RE		71a
1.40	-7	2.7×10^{14}	$\sim 10^{9}$	10^{27}–10^{28}	REBL	SBHs	71a
1.42	-7	1.6×10^{11}	$\sim 10^{6}$	10^{28}–10^{31}	R		76
1.42	-7	1.9×10^{11}	$\sim 10^{6}$	10^{28}–10^{31}	RL	SBHs	76
1.44	-6	1.4×10^{10}	$\sim 10^{5}$	10^{28}–10^{32}	R	SBHs	81
1.46	-5	2.6×10^{8}	$\sim 10^{3}$	10^{30}–10^{32}	RC	SBHs	78a
1.48	-4	3.7×10^{6}	$\sim 10^{2}$	10^{32}	RC	SBHs	78b

Table 28: The 17 cases with the largest contribution ($\geq 1\%$) to the fraction of CDM in the Universe. For each case we show the PBH number density n_{PBH} (equation 201), $\Omega_{PBH}(t_0)$ (equation 200) and the corresponding fraction of Ω_{CDM} as well as the corresponding mass ranges. Labels 'E', 'B', 'L', 'ea' and 'R' indicate cases for which there is a contribution from the EW phase transition, the QCD Bag Model, the QCD Lattice Fit, the electron–positron annihilation or from radiation, respectively.

n_+	$\log_{10}(\frac{t_+}{1\text{ s}})$	$n_{PBH}(\text{Mpc}^{-3})$	Ω_{PBH}	$\frac{\Omega_{PBH}}{\Omega_{CDM}}(\%)$	$M(g)$	Obs.	Fig.
1.30	-16	2.6×10^{22}	0.00874	4%	10^{17}–10^{23}	R	83a
1.34	-12	1.6×10^{15}	0.00347	2%	10^{22}–10^{28}	RE	80
1.34	-11	2.1×10^{16}	0.1955	99%	10^{24}–10^{28}	RE	79a
1.34	-10	1.6×10^{16}	0.1458	74%	10^{26}–10^{28}	E	79b
1.36	-11	5.8×10^{17}	0.0242	12%	10^{23}–10^{28}	R	83b
1.40	-7	2.7×10^{14}	0.00255	1%	10^{27}–10^{31}	RE	82a
1.40	-7	1.7×10^{10}	0.0268	14%	10^{28}–10^{33}	RB	71a
1.40	-7	2.7×10^{14}	0.0294	15%	10^{27}–10^{33}	REB	82a
1.40	-4	2.9×10^{10}	0.0461	23%	10^{33}	B	71b
1.42	-6	6.3×10^{9}	0.0186	9%	10^{29}–10^{33}	L	75
1.42	-5	4.3×10^{10}	0.1287	65%	10^{33}	L	
1.42	-4	1.9×10^{9}	0.00564	3%	10^{33}	L	
1.50	-2	8.6×10^{9}	0.0143	7%	10^{33}–10^{34}	B	71c
1.72	2	2.7×10^{3}	0.00552	3%	10^{38}–10^{41}	Rea	68c
1.78	3	163	0.00488	3%	10^{39}–10^{41}	R	67b
1.86	4	92.5	0.0337	17%	10^{40}–10^{43}	R	
1.94	5	3.3	0.0152	8%	10^{41}–10^{43}	R	66c

7 Discussion

Here, we summarize and discuss our results. First, in Section 7.1 we review the background theory on PBH formation, and in Section 7.2 we review the methodology that we followed in order to determine the PBH density parameter. In Sections 7.3 to 7.7 we discuss the results obtained taking into account the contributions from radiation, from the cosmological phase transitions (QCD, EW) as well as from the electron–positron annihilation epoch. In Section 7.8 we define a mechanism that allows us to compare, between themselves, PBHs of different masses and located at different distances from us. In Section 7.9 we show that, according to our results, it is possible to directly detect PBHs. Finally, in Section 7.10, we present an overall summary of our results.

7.1 From the inflationary quantum fluctuations to PBH formation (theory)

The Universe is very heterogeneous on the scale of galaxies and smaller formations. This requires that at the beginning of the expansion of the Universe (Section 1.1) there should have existed fluctuations (Section 1.1.5) which lead to the formation of such structures. We now have a successful cosmological paradigm based on the existence of an inflationary stage when the Universe was $\sim 10^{-35}$ s old (Section 1.1.2) which implies a quantum origin for the fluctuations. These are stretched to scales much larger than the Hubble radius (at the time when they are produced) and, as the expansion of the Universe goes on, each fluctuation reenters inside the Hubble radius at some later epoch, depending on its wavelength. With this mechanism we can explain, not only, all the inhomogeneities we see today, even on the largest cosmological scales, but also the production of PBHs.

The inflationary stage is followed by a radiation–dominated era during which the Universe successively visits the different scales at which particle physics predicts symmetry–breaking phase transitions. The SMPP (Appendix C) predicts two phase transitions: first the EW phase transition (Section 1.2.2), at an energy ~ 100 GeV, and later the QCD phase transition (Section 1.2.1), at an energy ~ 170 MeV.

If a perturbation crossing the horizon at some instant t_k is large enough, then it will begin to collapse at some later instant t_c called the *turnaround point* (Section 1.1.5). However, only the fluctuations with amplitude δ above some threshold δ_c (at time t_k) can lead to the formation of PBHs (Section 1.4.1). If $\delta < \delta_c$ the fluctuation dissipates and there is no PBH formation at all. The mass of a PBH forming at instant t_k lays on the range $10^{-4} M_H \leq M_{PBH} \leq M_H$ where M_H represents the horizon mass evaluated at the same instant t_k (Section 1.4.2).

In the case of a radiation–dominated universe we have, from analytical considerations, that $\delta_c = 1/3$ although numerical simulations revealed different values for δ_c, all in the range $1/3$ – 0.7 (Section 1.4.3).

The occurence of a phase transition turns out to be very important in the context of PBH formation. In fact, during such epochs, the sound speed vanishes for some instants (first–order phase transition) or, at least, it suffers, depending on the strength of the transition, a more or less relevant reduction (Crossover) and, as a consequence, the effect of pressure in stopping gravitational collapse becomes less important, decreasing the threshold δ_c and, hence, favouring PBH formation (Section 1.4).

For each phase transition we determined the exact location in terms of time and duration as well as the expression for the sound speed during the transition (Chapter 2) since that is all we needed to determine the behaviour of the threshold δ_c. A crucial parameter that is needed for the calculations is the decrease of the degrees of freedom Δg (Section 1.1.6) during the transitions.

The location of t_k and t_c with respect to the transition epoch allows us to identify, in the case of a first–order phase transition, six different classes of fluctuations (cf. Tables 8 and 9) – A, B, C, D, E, and F. In the presence of a first–order phase transition, the PBH formation threshold δ_c is affected by some factor $(1 - f)$ where f is a function which gives the fraction of the overdense region spent in the dust–like phase of the transition. In the approach considered, f relates the sizes of the overdense region at t_k and t_c (Chapter 4).

7.2 How many PBHs might really be out there?

Having as motivation Hawking radiation and the possibility of direct detection of BHs, we endeavoured into finding out, first, how many PBHs could exist in the Universe. In order to determine the probability of PBH formation at a given t_k or, equivalently, the fraction of the Universe going into PBHs at that epoch ($\beta(t_k)$), we must know the value of the mass variance $\sigma(t_k)$ at that epoch (Section 1.4.4). In order to determine $\sigma(t_k)$ it is also crucial to know the shape of the primordial spectrum of the fluctuations. In Sobrinho & Augusto (2007) we considered different kinds of spectra: i) scale–free power–law spectrum; ii) scale–free power–law spectrum with a pure step; iii) broken scale invariance spectrum; iv) running–tilt power–law spectrum. In the present work we concentrated on the running–tilt power–law spectrum because this seems to be in accordance with WMAP observations (Section 1.3.2) and, besides that, it possesses a variable index $n(k)$ that might be larger during some epochs, relevant to PBH formation.

However, the running–tilt power–law spectrum introduces a pair of additional parameters to the equations: a parameter n_+ giving the maximum value attained by $n(k)$ and a parameter t_+ giving the location of that maximum. At present, the best we can do is to constrain these parameters in accordance with the observational results (Section 1.3.2). We have considered, $1.2 \leq n_+ \leq 2.0$ and 10^{-23} s $\leq t_+ \leq 10^8$ s and we have evenly sampled the (n_+, t_+) parameter space into 1353 different cases (cf. Table 11).

During a phase transition, the background value δ_c, valid for radiation domination,

becomes smaller and, as a consequence, the value of $\beta(t_k)$ (equation 97), which is very sensitive to the threshold δ_c, could show a peak located near the phase transition epoch. Thus, we considered the two cosmological phase transitions experienced by the Universe within the interval 10^{-23} s $\leq t_+ \leq 10^8$ s: the EW phase transition (for which we considered two different models: Crossover and Bag Model) and the QCD phase transition (for which we considered three different models: Crossover, Lattice Fit model and Bag Model). We also considered the cosmological electron–positron annihilation epoch. Putting these all together we considered six different scenarios (see Table 10).

In order to study the distribution of PBHs in the present day Universe one needs to determine the PBH density parameter Ω_{PBH} (Section 1.4.5). Knowing $\beta(t_k)$ then the corresponding value of the PBH density parameter, evaluated at the present epoch, $\Omega_{PBH}(t_0, t_k)$, is given by equation (199). If one wants the global value of Ω_{PBH} (useful, for example, to compare with Ω_{CDM}, see Sections 1.1.3 and 6.10) then one needs to integrate over all epochs (cf. equation 200). Knowing $\Omega_{PBH}(t_0, t_k)$ and assuming that the masses of any PBHs formed at a given epoch $t = t_k$ are predominantly $\sim M_H(t_k)$ we can estimate the PBH number density in the Universe $n_{PBH}(t_0)$ (equation 201) and the PBH mass spectrum for each case (see e.g. Figure 82). On the other hand, assuming a homogeneous and isotropic distribution of PBHs throughout the Universe we can determine the minimum distance to the nearest PBH of a given mass (equation 202).

We have determined the curves $\beta(t_k)$ and $\Omega_{PBH}(t_0, t_k)$ for each one of the 1353 cases and for each of the six scenarios. As a result, the (n_+, t_+) parameter space gets divided into three main regions: i) an excluded region with the cases that violate the observational constraints; ii) an allowed region with the cases giving observationally relevant results – in the case of $\beta(t_k)$ we considered as observationally relevant the cases giving, at least during some epoch, $\beta(t_k) > 10^{-100}$ and, in the case of Ω_{PBH}, we considered as observationally relevant the cases giving at least one PBH within the observable Universe ($N \geq 1$); iii) an allowed region with the cases giving negligible results (i.e. cases giving $\beta(t_k) \approx 0$ or $N = 0$).

In Table 29 we show the number of cases belonging to each region for each of the six scenarios. The number of excluded cases varies from 807 (scenario 3: EW Crossover + QCD Crossover) to 831 (scenario 4: EW Bag Model + QCD Bag Model). The number of cases for which $\beta(t_k) > 10^{-100}$ during some epoch varies from 153 (scenario 6: EW Bag Model + QCD Crossover) to 160 (scenario 5: EW Bag Model + QCD Lattice Fit) and the number of cases for which $\beta(t_k) \approx 0$ at all epochs varies from 363 (scenario 4: EW Bag Model + QCD Bag Model) to 396 (scenario 3: EW Crossover + QCD Crossover).

The number of cases giving at least one PBH in the observable Universe ($N \geq 1$) varies from 70 (scenario 3: EW Crossover + QCD Crossover and scenario 6: EW Bag Model + QCD Crossover) to 75 (scenario 1: EW Crossover + QCD Bag Model) and the number of cases for which $N = 0$ varies from 448 (scenario 4: EW Bag Model + QCD Bag Model) to 476 (scenario 3: EW Crossover + QCD Crossover).

Table 29: Global statistics for the different scenarios (see Table 10). We show the number (absolute and relative) of permitted cases and excluded cases (due to observational constraints). The total number of cases is 1353 (≈ 533 permitted cases plus ≈ 820 excluded cases). Within the permitted ones we show the number of cases giving $\beta(t_k) \approx 0$ for all epochs (cases in cyan in Tables 11, 12, 13, 14, 15 and 16), $\beta(t_k) > 10^{-100}$ during some epoch (cases in white, gray or yellow in Tables 11, 12, 13, 14, 15 and 16, Figures 53b to 64), $N = 0$ (cases in cyan in Tables 18, 19, 20, 21, 22, 23 and 26), where N represents the number of PBHs in the observable Universe, and $N \geq 1$ (cases in white, gray or yellow in Tables 18, 19, 20, 21, 22, 23 and 26, Figures 66 to 85). Excluded cases are the ones in red for the same Tables.

Scenario	$\beta \approx 0$		$\beta \geq 10^{-100}$		$N = 0$		$N \geq 1$		Excluded	
1	371	27%	157	12%	453	33%	75	6%	825	61%
2	377	28%	158	12%	462	34%	73	5%	818	60%
3	396	29%	150	11%	476	35%	70	5%	807	60%
4	363	27%	159	12%	448	33%	74	5%	831	61%
5	368	27%	160	12%	456	34%	72	5%	825	61%
6	386	29%	153	11%	469	35%	70	5%	814	60%

As a global result we see that, for all the considered scenarios, $\approx 61\%$ of the cases are excluded due to observational constraints. The other 39% of the cases are allowed with 12% of the 1353 cases giving $\beta(t_k) > 10^{-100}$ during at least some epoch and 5% of them giving at least one PBH within the observable Universe.

The excluded cases correspond to situations that violate the observational constraints which means that it is reasonable to leave them out of our global statistics. Thus, we have 533 allowed cases (instead of 1353). Doing so we obtain that for ≈ 156 cases ($\approx 29\%$) $\beta(t_k) > 10^{-100}$ at some epoch and that for ≈ 72 cases ($\approx 14\%$) we obtain $N \geq 1$.

We now concentrate on the cases giving observationally relevant results ($N \geq 1$). In Table 30 we show, for each of the six scenarios the different contributions giving $N \geq 1$ and, for each, the absolute and relative number of associated cases. Clearly the predominant contribution is that of radiation. All six scenarios are dominated by the radiation–only contribution, although this predominance is largest for scenario 3 (EW Crossover + QCD Crossover) with 70% of the cases.

The contribution from the QCD Bag Model (valid for scenarios 1 and 4) corresponds to $\approx 29\%$ of the cases. A similar situation occurs for the QCD Lattice Fit model (scenarios 2 and 5) with $\approx 26\%$ of the cases. The contribution from the QCD Crossover (scenarios 3 and 6) corresponds to $\approx 16\%$ of the cases.

The number of cases acounting for the EW Bag Model contribution (valid for scenario 4 – QCD Bag Model, scenario 5 – QCD Lattice Fit and scenario 6 – QCD Crossover) corresponds to ≈ 13 cases out of the 72 ($\approx 18\%$). Finally, in $\approx 13\%$ of the cases we get contributions from the electron–positron annihilation epoch (valid for the six scenarios).

Table 30: The different contributions per scenario (see Table 10) giving $N \geq 1$ and the number of associated cases (cf. Tables which number is shown in column eight). For more information on the labels used in column one see the Conventions.

Cont.	Scenario 1		Scenario 2		Scenario 3		Scenario 4		Scenario 5		Scenario 6		Table	Fig.
R	41	55%	43	59%	49	70%	33	45%	33	46%	35	50%	18, 22, 26	66–67, 83–85
RB	5	7%	–	–	–	–	1	1%	–	–	–	–	20	71a, 72–73
B	19	25%	–	–	–	–	17	23%	–	–	–	–	20	71b,c
RL	–	–	5	7%	–	–	–	–	2	3%	–	–	21	74a, 75, 76
L	–	–	15	21%	–	–	–	–	14	20%	–	–	21	74b,c
RC	–	–	–	–	9	13%	–	–	–	–	9	13%	22	77–78
C	–	–	–	–	2	3%	–	–	–	–	2	3%	22	–
Rea	9	12%	9	12%	9	13%	9	12%	9	13%	9	13%	19	68–70
ea	1	1%	1	1%	1	1%	1	1%	1	1%	1	1%	19	–
RE	–	–	–	–	–	–	5	7%	5	7%	7	10%	23	79–81
E	–	–	–	–	–	–	6	8%	6	8%	7	10%	23	–
REB	–	–	–	–	–	–	1	1%	–	–	–	–	23	82a
EB	–	–	–	–	–	–	1	1%	–	–	–	–	23	82b
REL	–	–	–	–	–	–	–	–	1	1%	–	–	23	82a
EL	–	–	–	–	–	–	–	–	1	1%	–	–	23	82b

7.3 Radiation

The occurence of cosmological phase transitions favours PBH formation. However, we can also get observationally relevant results, in cases for which there is only a contribution from radiation to be taken into account. In particular, there are two regions in the (n_+,t_+) parameter space for which the contribution to PBH formation, in the allowed cases, comes solely from radiation: i) the region $1.72 \leq n_+ \leq 2.00$ and 10^3 s $\leq t_+ \leq 10^6$ s with 17 cases allowing the formation of SMBHs in observationally relevant numbers (cf. Table 18); ii) the region $1.24 \leq n_+ \leq 1.36$ and 10^{-23} s $\leq t_+ \leq 10^{-9}$ s, valid if one adopts the Crossover model for the EW phase transition, with 21 cases allowing the formation of SSBHs in observationally relevant numbers (cf. Table 26). If one adopts a Bag Model instead then we have the region $1.24 \leq n_+ \leq 1.32$ and 10^{-23} s $\leq t_+ \leq 10^{-14}$ s (see Table 23) with 13 cases allowing the formation of SSBHs in observationally relevant numbers.

In terms of distance the nearest primordial SMBH could be as near as $\sim 10^{21}$ m (≈ 32 kpc). In particular, when $n_+ = 1.78$ and $t_+ = 10^3$ s (Figure 67b) a PBH with $5 \times 10^6 M_\odot$ is expected within a radius of 10^{21} m (≈ 32 kpc) which is an interesting distance, in the sense that it is about four times the distance to the galactic centre where a SMBH with $\sim 10^6 M_\odot$ is known to exist. In terms of Ω_{PBH} this case contributes $\approx 2\%$ to the value of Ω_m. Although this is the case giving the largest PBH number density (considering SMBHs only) with $n_{PBH} \approx 1.6 \times 10^2$ Mpc^{-3}, there are two other cases with smaller n_{PBH} but representing larger fractions of Ω_m: namely when $n_+ = 1.94$ and $t_+ = 10^5$ s we get $\Omega_{PBH} \approx 0.06\Omega_m$ and when $n_+ = 1.86$ and $t_+ = 10^4$ s we get $\Omega_{PBH} \approx 0.14\Omega_m$ (cf. Table 18).

Moving now to the second region on the other extreme of the (n_+,t_+) parameter space (see Table 26), we have cases giving the nearest PBH at distances < 1 *pc*. In fact, in this region, we have the cases giving the smallest distances to the nearest PBH (see Section 6.11). The record is reached for the case $n_+ = 1.28$ and $t_+ = 10^{-18}$ s (cf. Figure 84a) which puts the nearest PBH at $\approx 2.8 \times 10^{14}$ m (0.009 pc or ≈ 50 times the average radius of the orbit of Pluto or ≈ 1885AU). This corresponds to having $\sim 10^6$ PBHs inside a sphere with a radius of 1 pc (mainly with 10^{18} g).

Among the cases shown in Table 26 the largest contribution to Ω_{CDM} comes from the case $n_+ = 1.36$ and $t_+ = 10^{-11}$ s (Figure 83b) which accounts for $\approx 12\%$ of all CDM (cf. Table 28). If that is indeed the case, then $\approx 12\%$ of CDM will be in the form of 10^{25} g PBHs. Note that the largest contribution to CDM does not come from the case with the largest n_{PBH} (the case $n_+ = 1.28$ and $t_+ = 10^{-18}$ s with $n_{PBH} \approx 2.6 \times 10^{23}$ Mpc^{-3}). In fact, the distance to the nearest PBH depends directly in the value of n_{PBH} (a larger n_{PBH} shortens the distance to the nearest PBH). On the other hand, the contribution of Ω_{PBH} to the value of Ω_{CDM} depends not only in the value of n_{PBH} but, also in the value of the PBH masses as well. Thus when $n_+ = 1.28$ and $t_+ = 10^{-18}$ s we have $n_{PBH} \approx 2.6 \times 10^{23}$ Mpc^{-3} mainly with 10^{18} g which corresponds to a mass of $\sim 10^{41}$ g Mpc^{-3}. When $n_+ = 1.36$ and $t_+ = 10^{-11}$ s we have $n_{PBH} \approx 5.8 \times 10^{17}$ Mpc^{-3} mainly with 10^{25} g which corresponds to a mass of $\sim 10^{43}$ g Mpc^{-3}.

Between these two (n_+,t_+) regions, completely dominated by the radiation contribution, we have the regions affected by the EW phase transition, the QCD phase transition and the electron–positron annihilation epoch. In the case of a QCD Crossover–like transition, which is smoother than the other two QCD models (Bag Model and Lattice Fit model), we get a few cases for which the PBH mass spectrum is due only to the radiation contribution all giving SSBHs (cf. Table 22). We might get observationally interesting values from these cases as well. For example, when $n_+ = 1.40$ and $t_+ = 10^{-8}$ s (Figure 73) we get $n_{PBH} \approx 3.5 \times 10^{11}$ Mpc^{-3} with the nearest PBH at $\sim 10^{18}$ m (≈ 32 pc).

7.4 The QCD phase transition ($t_U \sim 10^{-4}$ s)

The QCD phase transition is related to the spontaneous breaking of the chiral symmetry of QCD when quarks and gluons become confined into hadrons. The QCD phase transition was suggested, for a long time, as a prime candidate for a first–order phase transition. Recent results provided strong evidence that the QCD transition might be a simple Crossover (Section 1.2.1). Here we have considered the two possibilities. In the case of a first–order phase transition we have considered the Bag Model and the Lattice Fit model, the latter of which is based on LGT results (Section 1.2.1).

In Sections 4.1, 4.2 and 4.3 we determined the values of δ_c during the QCD epoch. In the case of the *Bag Model* (Section 4.1) we divided the study into *before* ($t_k < t_{QCD-}$), *during* ($t_{QCD-} < t_k < t_{QCD+}$) and *after* ($t_{QCD+} < t_k$), since a key–point on the evolution of a fluctuation, besides the amplitude, is the moment t_k when it crosses the horizon (before, during or after the QCD epoch). Before and after the QCD epoch the sound speed remains constant ($1/\sqrt{3}$). However, during the QCD epoch ($t_{QCD-} < t_k < t_{QCD+}$) it completely vanishes. As a result, we found a new window for PBH formation with δ_c reaching values as low as ≈ 0.091 for a background value $\delta_c = 1/3$ (Figure 31).

In Section 4.2 we studied the variation of δ_c during the QCD *Crossover*. Puting $\Delta T = 0.1T_c$ we found out that during the QCD epoch, within this model, the sound speed decreases by about 75% (cf. Figure 11). Taking into account the fact that, during the Crossover, the sound speed decreases but does not vanish, we introduced a new adimensional function α_{sp} (equation 178) which reduces the ratio of the sound speed with respect to the background value ($1/\sqrt{3}$) at a given moment. We found that, in the case of a Crossover, the reduction in the value of δ_c is much less pronounced than in the Bag Model case with $\delta_{c,min} \approx 0.274$ for a background value $\delta_c = 1/3$ (Figure 33).

In Section 4.3 we studied the variation of δ_c during the QCD *Lattice Fit*. In this case we have both, a time range with a vanishing sound speed which is similar to the Bag Model case and, a time range during which the sound speed decreases to zero, resembling the Crossover situation (cf. Figure 13). Thus, we interpret the Lattice Fit as a mixture of both situations and derive an appropriate expression for the

function f (see equations 184 to 192). The study was divided, as in the Bag Model case, into *before*, *during* and *after*. As a result, we obtained a quite pronounced reduction of δ_c from 1/3 to ≈ 0.12 (Figure 40).

Tipically, we have curves for $\beta(t_k)$ with two peaks: one from the radiation contribution and another from the QCD contribution (e.g. Figures 61f and 64c). Contributions from the QCD Bag Model or from the QCD Lattice Fit are, naturally, more visible than those from the QCD Crossover, since, in the latter, the sound speed never reaches zero. Nevertheless, in the case of the QCD Crossover we still might reach high values of $\beta(t_k)$ (e.g. Figure 59).

Especially in the case of a Bag Model or a Lattice Fit we have a few cases for which the contribution from the QCD exceeds the observational constraints. These cases, that were allowed in a radiation–dominated universe, are now excluded. In addition we have new cases, with a contribution from radiation negligible ($\beta(t_k) < 10^{-100}$) for all epochs of interest, but with relevant contributions from the QCD epoch.

Within the QCD Bag Model, 19 ($\approx 13\%$) of the 151 cases shown in Table 11 are excluded due to observational constraints. In addition we have 25 new cases with relevant contributions (i.e., $\beta(t_k) \geq 10^{-100}$ during some interval) from the QCD Bag Model (cf. Table 13) which means that we end up with 157 (i.e., $\approx 4\%$ more) favourable cases for PBH formation.

Within the QCD Lattice Fit model we have 12 cases ($\approx 8\%$ of the 151 cases shown in Table 11) excluded due to observational constraints and 19 additional cases with contributions from the QCD giving a final number of 158 (i.e., $\approx 5\%$ more) favourable cases for PBH formation (cf. Table 14).

If one adopts, instead, a Crossover model for the QCD then the number of cases to be excluded is reduced to a single one with no additional cases (cf. Table 15).

In Section 6.5 we have determined, for each of the cases shown in Tables 13, 14 and 15, the curves $\Omega_{PBH}(t_0, t_k)$, $d(t_0, t_k)$ and $n_{PBH}(t_0, t_k)$. We have also integrated the curves $\Omega_{PBH}(t_0, t_k)$ and $n_{PBH}(t_0, t_k)$ in order to obtain the corresponding values of the PBH density parameter and PBH number density at the present epoch as well as the PBH mass spectrum. We also have determined the minimum value of the curve $d(t_0, t_k)$ in order to obtain the minimum distance to the nearest PBH in each case. Excluding the cases for which $d(t_0, t_k) > 10^{26}$ m at all epochs because for those cases the results are negligible (i.e., the probability of finding one PBH in the entire observable Universe is $\ll 1$), we compiled the results in Tables 20 (Bag Model), 21 (Lattice Fit) and 22 (Crossover), and their discussion follows in the next three paragraphs.

Within the QCD Bag Model, 24 cases out of the 45 (i.e., 53%) presented in Table 13 give observationally relevant results (see Table 20). Within this scenario the PBH mass spectrum shows, in general, a peak located at $\sim 10^{33}$ g ($\sim 0.5 M_{\odot}$). This is the picture for 19 cases ,i.e., $\approx 80\%$ out of the 24. The amplitude of this characteristic peak varies from 2 PBHs ($n_+ = 1.36$ and $t_+ = 10^{-8}$ s) up to $\approx 4 \times 10^{21}$ PBHs ($n_+ = 1.40$ and $t_+ = 10^{-4}$ s, cf. Figure 71b). On the remaining five cases we have

simultaneous contributions from both the radiation and the QCD Bag Model. This cases represent very interesting situations, from the observational point of view, in the sense that now we have, besides the peak from the QCD Bag Model, another peak due to the radiation contribution. Between the two peaks we have an empty region (cases with the two peaks near each other or coincident give rise to situations that are excluded due to observational constraints – cases labeled 'RB*' in Table 20).

Within the QCD Lattice Fit, 20 cases out of the 42 (i.e., 47%) presented in Table 14 give observationally relevant results (see Table 21). Similarly to the Bag Model, now the PBH mass spectrum shows a peak located at $\sim 10^{33}$ g ($\sim 0.5M_{\odot}$). This is the picture for 15 cases, i.e., $\approx 75\%$ out of the 20. The amplitude of this characteristic peak varies from $\sim 10^2$ PBHs ($n_+ = 1.38$ and $t_+ = 10^{-7}$ s) up to $\approx 9 \times 10^{20}$ PBHs ($n_+ = 1.42$ and $t_+ = 10^{-6}$ s). Under the QCD Lattice Fit we might get, in some cases, besides the $\approx 0.5M_{\odot}$ peak, an extension to the left of the mass spectrum resulting from the contribution from the interval $t_1 \leq t \leq t_{QCD-}$. This contribution is particularly important when $n_+ = 1.42$ and $t_+ = 10^{-6}$ s (accounting for $\approx 56\%$ of the PBHs with less than $\approx 0.5M_{\odot}$ – Figure 75) or $t_+ = 10^{-7}$ s (accounting for $\approx 14\%$ of the PBHs with less than $\approx 0.5M_{\odot}$ - Figure 76).

Within the QCD Crossover 11 cases out of the 26 (i.e., 42%) presented in Table 15 give observationally relevant results (see Table 22). Now the $0.5M_{\odot}$ peak is always 'supported' by the radiation contribution (cf. Figures 77 and 78). We have two cases labeled 'C' in Table 15 but they represent very small amounts of PBHs: when $n_+ = 1.46$ and $t_+ = 10^{-3}$ s we have $\sim 10^2$ PBHs ($0.5 - 5M_{\odot}$) and when $n_+ = 1.44$ and $t_+ = 10^{-4}$ s we have just one $0.5M_{\odot}$ PBH.

In the case of a QCD Crossover we have 11 cases giving observationally relevant results against the 24 obtained for the Bag Model (between these two we have the Lattice Fit giving 20 cases). The Bag Model is clearly less demanding in terms of fine–tuning for PBH formation. However, the contribution from the QCD still might give observationally relevant results even in the case of a Crossover model.

Within the QCD Bag Model we found three cases, out of the 24 shown in Table 20 (i.e., 12% of the cases) for which Ω_{PBH} contributes 1% or more to the global value of Ω_{CDM} (cf. Table 28). These are the three cases shown in Figure 71. The largest contribution occurs when $n_+ = 1.40$ and $t_+ = 10^{-4}$ s with $\approx 23\%$ of all CDM provided by $0.5M_{\odot}$ PBHs. Within the QCD Lattice Fit we found, also, three cases (15% of the cases shown in Table 21) for which Ω_{PBH} contributes with 1% or more to the global value of Ω_{CDM} (cf. Table 28). The largest contribution now occurs when $n_+ = 1.42$ and $t_+ = 10^{-5}$ s with $\approx 65\%$ of all CDM provided by $0.5M_{\odot}$ PBHs. However, although the number of PBHs formed within this case do not overclose the Universe, the case must be excluded because $0.5M_{\odot}$ PBHs cannot make up more than 40% of the CDM halo (cf. Section 1.1.3). Thus, the most important contribution to CDM, within the QCD Lattice Fit, occurs when $n_+ = 1.42$ and $t_+ = 10^{-6}$ s with $\approx 9\%$ of all CDM provided mainly by $0.5M_{\odot}$ PBHs (cf. Table 28, Figure 75). Within the QCD Crossover the contribution of PBHs to CDM, for the cases shown in Table 22, is always below 1%.

In terms of distance the nearest PBH due to the QCD contribution could be as near as $\sim 10^{18}$ m (~ 32 pc) if the QCD is described by a Bag Model or Lattice Fit model (cf. Tables 20 and 21). For example, when $n_+ = 1.40$ and $t_+ = 10^{-4}$ s (Figure 71b) we get, within the QCD Bag Model, $n_{PBH} \approx 2.8 \times 10^{10}$ Mpc^{-3} which gives $\sim 10^6$ PBHs with $0.5M_\odot$ in our galactic halo. When $n_+ = 1.42$ and $t_+ = 10^{-6}$ s we get, within the QCD Lattice Fit, $n_{PBH} \approx 6.3 \times 10^9$ Mpc^{-3} which gives $\sim 10^5$ PBHs with $0.5M_\odot$ in our galactic halo. On the other hand if the QCD phase transition is described by a Crossover model then the nearest PBH due to the QCD contribution would be at $\sim 10^{19}$ m, or ~ 320 pc (cf. Table 22).

7.5 The EW phase transition - Bag Model ($t_U \sim 10^{-10}$ s)

The EW phase transition (Section 1.2.2) was responsible for the spontaneous EW symmetry breaking which gave mass to all *massive particles*. Within the context of the SMPP, the EW phase transition is a very smooth Crossover (Section 1.2.2) with $\Delta g \sim 1$, hence a much weaker transition than the QCD phase transition. Taking this into account, we determined $\Delta T \approx 0.013 T_c$ as the value that gives rise to the strongest effect as regards the reduction of δ_c (Section 4.4): for $\delta_c = 1/3$, we get $\delta_{c,min} \approx 0.332$ an almost negligible variation, as expected (Figure 42). Hence, the EW Crossover has no relevant effects as regards PBH production (Section 5.5) – SMPP considered.

However, under the MSSM (Appendix D) a first–order EW phase transition arises. We modelled it by using a Bag Model (Section 2.2.2) with $\Delta g \approx 80$ (cf. Section 1.1.6). In Section 4.5, we determined the values of δ_c during the EW epoch. We divided the study into *before* ($t_k < t_{EW-}$), *during* ($t_{EW-} < t_k < t_{EW+}$) and *after* ($t_{EW+} < t_k$). Before and after the EW epoch the sound speed remains constant ($1/\sqrt{3}$). However, during the EW epoch ($t_{EW-} < t_k < t_{EW+}$) it completely vanishes. The results are now, by far, more obvious than in the Crossover case (Section 4.5): the reduction from $\delta_c = 1/3$ goes down to $\delta_{c,min} \approx 0.17$ (Figure 43).

In Section 5.8 we determined the contribution from the EW Bag Model to the curve $\beta(t_k)$. We found out that for 22 of the 151 cases (i.e., 14%) shown in Table 11 we have non–zero contributions (cases labeled 'RE', 'RBE', 'RBLE', 'RB*LCE' and 'RB*L*CE' in Table 16). We found also that seven of the cases are excluded due to observational constraints (cases labeled 'RE*', 'RBE*', 'RBLE*' and 'RB*LCE*' in Table 16) and that, in addition, we have 10 new cases with non–zero contributions from the EW (cases labeled 'E', 'BE' and 'BLE' in Table 16). Thus, we have a total of 32 cases with non–zero contributions from the EW phase transition.

In Section 6.6 we have determined, for each of the cases shown in Table 16 the curves $\Omega_{PBH}(t_0, t_k)$, $d(t_0, t_k)$ and $n_{PBH}(t_0, t_k)$. We have also integrated the curves $\Omega_{PBH}(t_0, t_k)$ and $n_{PBH}(t_0, t_k)$ in order to obtain the corresponding values of the PBH density parameter and PBH number density at the present epoch as well as the PBH mass spectrum. We also have determined the minimum value of the curve $d(t_0, t_k)$ in order to obtain the minimum distance to the nearest PBH in each case.

We excluded the cases for which $d(t_0, t_k) > 10^{26}$ m at all epochs because for those cases the results are negligible (i.e., the probability of finding one PBH in the entire observable Universe is $\ll 1$). As a result, we found 17 cases out of the 32 (i.e., 53%) giving observationally relevant results. We compiled the results for those 17 cases in Table 23.

In general, the contribution from the EW Bag Model to the PBH mass spectrum shows a characteristic peak at $\sim 10^{27}$ g ($\sim 5\times10^{-7}M_{\odot}$, $\sim 0.2m_T$) with an extension to the right ($\sim 10^{28}$ g, $\sim 5 \times 10^{-6}M_{\odot}$, $\sim 2m_T$). For seven of the cases shown in Table 23 (i.e. $\approx 41\%$ of the cases giving observationally relevant results) the mass spectrum consists only on these two bars (cases labeled 'E').

In five of the cases shown in Table 23 (i.e., 29% of the cases) Ω_{PBH} contributes with 1% or more to the global value of Ω_{CDM} (cf. Table 28). The highest contributions are 99% (when $n_+ = 1.34$ and $t_+ = 10^{-11}$ s) and 74% (when $n_+ = 1.34$ and $t_+ = 10^{-10}$ s). In both cases CDM would be provided mainly by 10^{27} g PBHs (cf. Figure 79). However, these two cases must be excluded because 10^{27} g ($5\times10^{-7}M_{\odot}$) PBHs cannot make up more than 25% of the CDM galactic halo (cf. Section 1.1.3).

In terms of distance, the nearest PBH due to the EW Bag Model contribution could be as near as 10^{17} m (3.2 pc). This would be a SSBH with 10^{27} g ($\sim 5 \times 10^{-7}M_{\odot}$, $\sim 0.2m_T$). The situation occurs when (cf. Table 23): $n_+ = 1.34$ and $t_+ = 10^{-9}$ s, $n_+ = 1.36$ and $t_+ = 10^{-8}$ s, $n_+ = 1.40$ and $t_+ = 10^{-7}$ s. For example, when $n_+ = 1.34$ and $t_+ = 10^{-9}$ s we get $\sim 10^2$ PBHs within 100 pc, $\sim 10^5$ PBHs within 1000 pc and 10^9 PBHs within the galactic halo (cf. Table 27).

Neglecting the EW Bag Model contribution and taking into account solely the contribution from radiation (that would be the case if one adopts for the EW a Crossover model) it turns out that, when $n_+ = 1.34$ and $t_+ = 10^{-11}$ s the nearest PBH would be at a distance $\sim 10^{20}$ m, or ~ 3.2 kpc (giving 4 PBHs in the galactic halo). When $n_+ = 1.34$ and $t_+ = 10^{-10}$ s we found out that, taking into account only the radiation contribution, we would have 10^2 PBHs within the entire observable Universe with the nearest one at $\sim 10^{25}$ m ($\sim$ 320 Mpc). Within this context (EW Crossover) these two cases are not exlcuded. Finally when $n_+ = 1.34$ and $t_+ = 10^{-9}$ s the contribution from radiation give zero PBHs in the observable Universe.

Besides the case $n_+ = 1.34$ and $t_+ = 10^{-9}$ s there are three other cases with the nearest PBH at $\sim 10^{17}$ m ($\sim$ 3.2 pc). These are the cases $n_+ = 1.34$ and $t_+ = 10^{-12}$ s (cf. Figure 80), $n_+ = 1.36$ and $t_+ = 10^{-8}$ s and $n_+ = 1.40$ and $t_+ = 10^{-7}$ s (cf. Figure 82a). When $n_+ = 1.34$ and $t_+ = 10^{-12}$ s we get observationally relevant contributions from both the EW Bag Model and radiation. In fact in this case only 13% of the PBHs are due to the EW Bag Model which means that if one adopts for the EW a Crossover then the results will remain within the some order of magnitude with $n_{PBH} \sim 10^{15}$ Mpc^{-3} (corresponding to have $\sim 10^4$ PBHs within 100 pc, $\sim 10^7$ PBHs within 1000 pc and 10^{10} PBHs within the galactic halo). The other two cases are discussed later, in Section 7.7, because they might include also PBHs formed due to the QCD phase transition.

7.6 Electron–positron annihilation ($t_U \sim 1$ s)

Other possible scenarios during which the sound speed might experience a reduction (besides cosmological phase transitions), are the cosmological particle annihilation epochs. As an example, we considered the electron–positron annihilation epoch during which the sound speed might have decreased by about 20% (Section 1.2.3).

Since Δg is small, we assumed that during this epoch, the sound speed has a 'Crossover'–like profile. We then have found that a reduction of 20% in the value of the sound speed requires $\Delta T \approx 0.115 T_c$ (Section 2.3) and this value, in turn, leads to a reduction in the value of δ_c from 1/3 to ≈ 0.30 (Section 4.6, Figure 45), not so significant. In fact, the electron–positron annihilation epoch is a smooth event with $\Delta g = 3.5$ (cf. Section 1.2.3), even if not as smooth as the EW Crossover.

In Section 5.6 we determined the contribution from the electron–positron annihilation to the curves $\beta(t_k)$. We found that for 26 of the 151 cases (i.e., 17%) shown in Table 11 we have non–zero contributions (cases labeled 'Rea', 'RBLCea' and 'RB*L*Cea' in Table 12). We also found that one of the cases is excluded due to observational constraints (labeled 'Rea*' in Table 12) and that, in addition, we have an extra case (labeled 'ea' in Table 12).

In Section 6.4 we have determined, for each of the cases shown in Table 12 the curves $\Omega_{PBH}(t_0, t_k)$, $d(t_0, t_k)$ and $n_{PBH}(t_0, t_k)$. We have also integrated the curves $\Omega_{PBH}(t_0, t_k)$ and $n_{PBH}(t_0, t_k)$ in order to obtain the corresponding values of the PBH density parameter and PBH number density at the present epoch as well as the PBH mass spectrum. We also have determined the distance to the nearest PBH in each case. We excluded the cases for which $d(t_0, t_k) > 10^{26}$ m at all epochs because for those cases the results are negligible (i.e., the probability of finding one PBH in the entire observable Universe is $\ll 1$). As a result, we found out 10 cases out of the 27 (i.e., 37%) giving observationally relevant results. We compiled the results for those 10 cases in Table 19.

Considering only the contribution from radiation we still get in nine of the 10 cases (shown in Table 19) observationally relevant results (the exception is the case $n_+ = 1.60$ and $t_+ = 10$ s giving a single $5 \times 10^4 M_\odot$ PBH within the observable Universe due to the electron–positron annihilation). However, when one takes into account the contribution from the electron–positron annihilation the number of PBHs increase significantly in most of the cases. In fact, for seven of them the electron–positron annihilation contribution represents more than 30% of the totals with three of them giving contributions higher than 80% (cf. Figures 68, 69 and 70).

The dominant PBH masses as shown in Table 19 (corresponding to the peak of the mass spectrum in each case) are $5 \times 10^3 M_\odot$, $5 \times 10^4 M_\odot$ and $5 \times 10^5 M_\odot$. These masses permit us to classify these PBHs as IMBHs. In fact in Section 6.7 when we consider intermediate–mass PBHs we found out that six of the eight cases giving the largest contributions to the number of IMBHs include contributions from the electron–positron annihilation (cf. Table 24, cases labeled 'Rea').

In terms of distance, the nearest intermediate–mass PBH can be as close as $\sim 10^{20}$ m

(~ 3.2 kpc), i.e., inside our galactic halo. This is the case when $n_+ = 1.62$ and $t_+ = 1$ s (see Figure 68a) for which our results predict the existence of a $5 \times 10^3 M_\odot$ PBH in our galactic halo. This rises to ~ 10 PBHs if one moves to a spherical region with radius of the order of the distance to the Large Magellanic Cloud (≈ 0.055 Mpc) and to $\sim 10^5$ PBHs for a radius of the order of the distance to the Andromeda galaxy (≈ 0.725 Mpc).

When $n_+ = 1.62$ and $t_+ = 1$ s the main contribution to the total number of PBHs ($N \sim 10^{16}$) comes from radiation (the electron–positron annihilation contribution corresponds to less than 0.01%). On the other hand, for example, when $n_+ = 1.66$ and $t_+ = 10$ s we get $N \sim 10^{15}$ PBHs (see Figure 68b) with the electron–positron annihilation providing $\approx 85\%$ of them. This case gives $\sim 10^4$ PBHs in a spherical region with radius of the order of the distance to the Andromeda galaxy. However, considering only the contribution from radiation this number goes down to $\sim 10^3$. This example clearly shows the importance that the electron–positron annihilation epoch might have taken within the context of PBH formation.

7.7 Simultaneous contributuions (EW and QCD)

In some cases we have simultaneous contributions from both the EW phase transition and the QCD phase transition.

As an observationally relevant situation we mention the case when $n_+ = 1.40$ and $t_+ = 10^{-7}$ s for which we have, besides the contribution from the QCD (Bag Model or Lattice Fit), an important contribution from the EW phase transition as well as from radiation (Figure 82a). In this case the mass spectrum spans from $\sim 10^{27}$ g ($5 \times 10^{-4} m_J$) corresponding to the EW contribution (which extends also to $\sim 10^{28}$ g) to $\sim 10^{33}$ g ($5 \times 10^2 m_J$, $0.5 M_\odot$) corresponding to the contribution from the QCD Bag Model or Lattice Fit) with a gap at $\sim 10^{32}$ g ($0.05 M_\odot$, $50 m_J$). Between the two (10^{29}–10^{31} g, 5×10^{-2}–$5 m_J$) we have the contribution from radiation with more modest values.

A similar situation occurs when $n_+ = 1.38$ and $t_+ = 10^{-7}$ s for which we have important contributions from the EW phase transition and from the QCD Bag Model (Figure 82b) now with the empty region between the two peaks spanning four orders of magnitude (10^{29}–10^{32} g, 5×10^{-2}–$50 m_J$). Finally, when $n_+ = 1.36$ and $t_+ = 10^{-8}$ s the main contribution, with 10^{25} PBHs, is due to the EW with the QCD giving (in the case of a Bag Model) only 2 PBHs in the entire observable Universe.

7.8 The most interesting cases

We defined as *observationally relevant* those cases giving at least one PBH in the observable Universe (i.e. cases with $N \geq 1$). However, this quantity N does not allow us to compare properly results from different cases.

What is more interesting from the observational point of view: a $5 \times 10^6 M_\odot$ PBH at a distance of 10^{22} m (≈ 320 kpc) or a 10^{19} g PBH at a distance of 10^{17} m (≈ 3.2 pc)? In order to answer questions like this one we considered, from each observationally relevant case, the distance d to the nearest PBH and the respective mass m and, then, we calculated the ratio m/d^3 (i.e. we spread out the mass of the PBH into a spherical region of radius d centered on the PBH). We consider PBHs with the same m/d^3 ratio as equivalent in terms of observational interest. In order to normalize the results we used a factor $\sim 10^{-23}$ gm^{-3} which gives for the SMBH in our galactic centre ($m \sim 10^6 M_\odot$ and $d \approx 8.5$ kpc) a ratio $m/d^3 \sim 10$. Thus, we consider a PBH with a normalized m/d^3 ratio of ~ 10 equivalent, in observational terms, to the SMBH in our galactic centre.

In Table 31 we show the cases for which the normalized value of m/d^3 is $\sim 10^{-1}$ or larger. In each case we show the mass of the nearest PBH, the scenarios of its validity and the contributions that lead to the formation of PBHs for that particular case. There are six situations giving $m/d^3 \sim 10^2$ corresponding to 12 cases distributed this way: scenarios 1, 4 and 5 – three cases each, scenario 2 – two cases, scenario 6 – one case.

It is very encouraging to see that among the most interesting results (cf. Table 31) we have cases with contributions from radiation, EW Bag Model, QCD Bag Model, QCD Lattice Fit, QCD Crossover and electron–positron annihilation epoch. Besides that, we have cases accounting for PBHs of all mass classes: SSBHs, SBHs, IMBHs and SMBHs, also interesting.

In three of the situations shown in Table 31 the mass spectrum peak is located at $\sim 10^{27}$ g. The existence of a population of 10^{27}–10^{28} g PBHs could give important clues about the EW epoch and the Physics behind it. The absence of this sharp peak indicates that the EW is described by a simple Crossover as predicted by the SMPP. On the other hand, the presence of this peak indicates that the EW was a first–order phase transition, and hence, that the SMPP extends beyond the EW scale.

Perhaps one of the most interesting situations, in terms of PBH mass spectrum, occurs when $n_+ = 1.40$ and $t_+ = 10^{-7}$ s. In fact, within this case, the mass spectrum can exhibit one, two or three peaks (Figure 82a): i) the peak from radiation located at $5 \times 10^{-5} M_\odot$ (10^{29} g) which gives $\sim 10^{12}$ PBHs and is always present; ii) the peak from the EW ($\sim 10^{27}$ g, $5 \times 10^{-4} m_J$), giving 10^{25} PBHs, which is only present if the EW is described by a first–order phase transition; iii) the QCD peak ($\sim 10^{33}$ g, $5 \times 10^2 m_J$, $0.5 M_\odot$) which is present if the QCD phase transition is described by a Bag Model (giving 10^{21} PBHs) or by a Lattice Fit model (giving 10^{12} PBHs). Such a spectrum can give important information about the early Universe, in particular about the interval between the EW and the QCD epochs.

Five of the situations (out of the six) giving $m/d^3 \sim 10^2$ all show mass spectra with a peak located at $0.5 M_\odot$ (cf. Table 30). This $0.5 M_\odot$ peak clearly reflects the contribution from the QCD phase transition. If it is described by a Crossover then this peak is not so significant as it is for the Bag Model or the Lattice Fit model.

The origin of the SMBHs that are observed at the centre of many galaxies remains unknown. They might form inside an existing galaxy or they might have formed long before the epoch of galaxy formation, in the primordial stages of the Universe. It is interesting, from the observational point of view, to find out that for some of the studied cases we get $\sim 10^{11}$ primordial SMBHs, which matches the number of galaxies known to exist in the observable Universe (cf. Figure 66). We also get two cases giving larger numbers ($\sim 10^{13}$ primordial SMBHs). This occurs, for example, when $n_+ = 1.86$ and $t_+ = 10^4$ s (cf. Figure 67c) which happens to be the single case for which we get $m/d^3 \sim 10$ (cf. Table 31). For cases like this one it is plausible to assume a large number of SMBH binaries and/or a huge number of PBH merging before galaxy formation or during the evolution of galaxies. Another possibility is that most of these PBHs remained isolated in space and did not take part in the formation of galaxies.

7.9 Can we directly detect PBHs?

In Section 6.11 we mentioned that the nearest PHB could be at a distance of $\sim 10^{14}$ m (this is the case when $n_+ = 1.28$ and $t_+ = 10^{-18}$ s). This would be probably a 10^{18} g PBH with a surface temperature $\approx 10^8$ K (cf. equation P-4), i.e., with the Hawking blackbody emission peaking at the hard X–ray band (cf. Table P-4). This emission would be peculiar in the sense that it consists in a steady continuous signal, distinguishable from others with transient characteristics.

In Sobrinho (2003) we determined that, in order to detect the electromagnetic component of the Hawking emission of such a BH, the detector (X–ray telescope) should be positioned at a distance no larger than $\sim 10^8$ m (considering the present day best detectors, cf Table P-9). Thus, the probability of detecting the Hawking emission from a PBH within the case $n_+ = 1.28$ and $t_+ = 10^{-18}$ s is

$$p \sim \left(\frac{10^8 \text{ m}}{10^{14} \text{ m}} \right)^3 \sim 10^{-18}.$$

Remembering that the case $n_+ = 1.28$ and $t_+ = 10^{-18}$ s is just one of $\sim 10^3$ possible cases (cf. Table 11) this probability becomes $p \sim 10^{-21}$. We now consider a space probe moving towards the Kuiper–belt. A detector on board would scan $\sim 50\text{AU} \times (10^8 \text{ m})^2$, increasing the probabilitiy of detection to $p \sim 10^{-15}$. In a trip to Sedna ($\sim$ 1000AU) we get $p \sim 10^{-12}$ and in an hypothetical trip to the Oort cloud (≈ 0.4 pc) $p \sim 10^{-11}$.

It is worthwhile to compare these small, but non–null, probabilities with others in Physics. Let us consider, for example, Particle Physics. The *GALLium EXperiment* (GALLEX), was a radiochemical neutrino detection experiment, especially designed to detect solar neutrinos, that operated between 1991 and 1997 (e.g. Anselmann et al., 1992). The experiment was able to detect 300 neutrinos after 1594 days of exposure (e.g. Hampel, 1999). Taking into account that the flux of solar neutrinos reaching the Earth surface is 6×10^{10} cm^{-2} s^{-1} this means that the probability of

detecting a single neutrino with GALLEX was $\sim 10^{-32}$ which is, for example, 17 orders of magnitude smaller than the PBH detection probability in a trip to the Kuiper–belt.

Taking into account that the Oort cloud extends up to ~ 0.4 pc (Dones et al., 2004) and remembering that for $n_+ = 1.28$ and $t_+ = 10^{-18}$ s we have $n_{PBH} \approx 2.6 \times 10^{23}$ Mpc^{-3} we get for the Oort cloud a total of $\sim 10^5$ PBHs mostly with $\sim 10^{18}$ g. Taking into account that the present day estimated number of comets for the Oort cloud is $\sim 10^{12}$ (Dones et al., 2004) this corresponds to (roughly) one PBH for each $\sim 10^7$ comets. It is also interesting to note that the average mass of these PBHs ($\sim 10^{18}$ g) is similar to Halley's comet mass.

It is plausible that, throughout the history of the Solar System, some PBHs might have been thrown into the inner Solar System following the same fate as the comets (i.e., we could have PBHs describing elliptical orbits with semi–major axis 100–200 AU). That would improve the chances of direct detection of a PBH by a space probe. For example, NASA is planing to launch, possibly in 2014, the *Innovative Interstellar Explorer* (IIE) a mission that is expected to reach 200 AU in about 30 years after launch (McNutt et al., 2006). The mission will probe an important Solar System region, with interest within the context of PBH detection.

In this work we considered that the distribution of PBHs throughout the Universe is homogeneous and uniform. Thus, we assumed that the PBH number density, n_{PBH}, stays the same over the galactic disk, on the galactic halo or on the intergalactic medium. However, this is a *conservative assumption*. Perphaps PBHs concentrate around galactic halos during the process of galaxy formation (when PBHs were already present) and around bounded systems such as star clusters. If that was the case then the PBH number density near the Solar System is expected to be a few orders of magnitude above the average value with which we worked with. This would significantly improve the probabilities of PBH direct detection.

Table 31: The most interesting cases from the observational point of view ($m/d^3 \geq 0.1$). For each case we indicate the m/d^3 ratio (normalized such that $m/d^3 \sim 10$ for the SMBH at the centre of our galaxy), the mass of the nearest PBH, the scenarios of validity (cf. Table 10) and the contributions that lead to the formation of PBHs for that particular case. The figures where some cases appear are indicated.

n_+	$\log(\frac{t_+}{1\mathrm{s}})$	$\log(\frac{m}{d^3})$	$m(g)$	$m(M_\odot)$	Scenarios	Cont.	Fig.
1.28	-18	-1	10^{18}	5×10^{-16}	1,2,3,4,5,6	R	84a
1.32	-14	0	10^{22}	5×10^{-12}	1,2,3,4,5,6	R	84b
1.34	-9	-1	10^{27}	5×10^{-7}	4,5,6	E	
1.36	-11	0	10^{25}	5×10^{-9}	1,2,3	R	83b
1.36	-8	-1	10^{27}	5×10^{-7}	4,5,6	E	
1.38	-6	-1	10^{33}	0.5	1,4	B	
1.38	-5	-1	10^{33}	0.5	1,4	B	
1.40	-7	2	10^{33}	0.5	1	RB	71a
1.40	-7	2	10^{27}	5×10^{-7}	4,5,6	REBL	82a
1.40	-5	-1	10^{33}	0.5	2,5	L	
1.40	-4	2	10^{33}	0.5	1,4	B	71b
1.42	-6	2	10^{33}	0.5	2,5	RL	75
1.42	-4	2	10^{33}	0.5	2,5	L	
1.42	-3	-1	10^{33}	0.5	1,4	B	
1.44	-3	-1	10^{33}	0.5	2,5	L	
1.50	-2	2	10^{33}	0.5	1,4	B	71c
1.50	-2	-1	10^{33}	0.5	2,5	L	74c
1.50	-3	0	10^{34}	5	3,6	RC	77
1.58	-1	-1	10^{36}	500	1,2,3,4,5,6	RBLC	72
1.62	0	0	10^{37}	5×10^3	1,2,3,4,5,6	Rea	68a
1.72	2	-1	10^{39}	5×10^5	1,2,3,4,5,6	Rea	68c
1.78	3	0	10^{40}	5×10^6	1,2,3,4,5,6	R	67b
1.86	4	1	10^{41}	5×10^7	1,2,3,4,5,6	R	67c
1.92	5	-1	10^{42}	5×10^8	1,2,3,4,5,6	R	
1.94	5	-1	10^{42}	5×10^8	1,2,3,4,5,6	R	66c

7.10 Summary

Up to now all BH candidates have been identified by indirect processes. In principle a BH can, also, be detected directly by means of its electromagnetic emission (Hawking radiation). However, only small BHs (SSBHs) might be hot enough to be detected at large distances (i.e., greater than the Earth–Moon distance; cf. Appendix P). We are not aware of any process capable of forming such BHs in the present day Universe but we know that they could have formed in the early Universe (PBHs) within some conditions.

With these ideas in mind we moved into the study of PBH formation. We considered, not only, the formation of SSBHs (the ones that offer better chances of direct detection) but also the formation of PBHs of all masses. The key ingredient to know the PBH density at the present epoch is to determine, first, the fraction of the Universe going into PBHs at each epoch, $\beta(t_k)$, during the early stages of the Universe. PBHs form from the gravitational collapse of density fluctuations provided that their amplitude is above some threshold δ_c.

The value of the threshold for PBH formation (valid for a radiation–dominated universe), δ_c, is not a well known value. During this thesis we considered, for most of the time, $\delta_c = 1/3$ (the lower limit). However, according to numerical simulations δ_c could be as large as 0.7 (Section 1.4.1). We have also run our calculations with this upper limit ($\delta_c = 0.7$) and found that the results are similar (cf. Appendix N).

The value of this threshold, that remains constant for a radiation–dominated universe, decreases during cosmological phase transitions which, then, favour PBH formation. Thus, we considered the two phase transitions predicted by the SMPP (the EW phase transition and the QCD phase transition) and, in addition, we also considered the electron–positron annihilation epoch during which δ_c also decreases.

A second key ingredient is an adequate power spectrum for the density fluctuations. The formation of large scale structure in the Universe demands a power spectrum with the spectral index n equal or very close to unity. However, if one wants to get PBH formation in observationally relevant numbers then a power spectrum that gives $n(k) > 1$ at some epoch in the early Universe is needed. We considered here the promissing running–tilt power–law spectrum which introduces a pair of parameters into the equations: n_+ (the maximum of $n(k)$) and t_+ (the location of that maximum).

Then, we have evenly sampled the (n_+, t_+) parameter space (with a total of 1353 cases, cf. Table 11) and determined, for each scenario, the cases that we found observationally relevant for PBH formation: first by determining the curve $\beta(t_k)$ and then the curves for the PBH density parameter $\Omega_{PBH}(t_0, t_k)$. We also determined, for each observationally relevant case, the mass spectrum, the PBH number density, the global value for the PBH density parameter ($\Omega_{PBH}(t_0)$) and the distance to the nearest PBH.

As a result, the (n_+, t_+) parameter space gets divided into three main regions: i) an excluded region with the cases that violate the observational constraints; ii) an

allowed region with the cases giving observationally relevant results (i.e. giving at least one PBH within the observable Universe; $N \geq 1$); iii) an allowed region with the cases giving negligible results ($N = 0$). The excluded cases ($\approx 61\%$ out of the 1353) correspond to situations that violate the observational constraints which means that it is reasonable to leave them out of our global statistics. Thus, we have 533 allowed cases (instead of 1353), which means that, in fact, for ≈ 72 of the cases ($\approx 14\%$) we have $N \geq 1$. Note that the number of observationally relevant cases stays practically the same for all the six scenarios (cf. Table 29).

It is very encouraging to note that among those 72 cases with observationally relevant results we have cases that give important contributions to CDM, PBHs of all masses (SSBHs, SBHs, IMBHs, SMBHs), as well as important contributions to the total population of BHs (within the observable Universe, the galactic halo or the Solar System neighborhood). We also get cases giving important numbers of PBHs formed during different cosmological phase transitions (EW, QCD, electron–positron anihilation).

We consider PBHs with the same m/d^3 ratio as equivalent in terms of observational interest (in order to normalize the results we used a factor $\sim 10^{-23}$ gm^{-3}). In five of the situations giving $m/d^3 \sim 10^2$ the mass spectrum peak is located at $0.5M_{\odot}$. This $0.5M_{\odot}$ peak clearly reflects the contribution from the QCD phase transition. The other situation that gives $m/d^3 \sim 10^2$ shows a peak at $\sim 10^{27}$ g. The existence of a population of 10^{27}–10^{28} g PBHs could give important clues about the EW epoch and the Physics behind it. The absence of this sharp peak indicates that the EW is described by a simple Crossover as predicted by the SMPP. On the other hand, the presence of this peak indicates that the EW was a first–order phase transition, and hence, that the SMPP is extended beyond the EW scale.

In terms of CDM, we found one case accounting for $\approx 23\%$ of all CDM. That occurs when $n_+ = 1.40$ and $t_+ = 10^{-4}$ s (Figure 71b). The contribution to CDM is provided by a population of $0.5M_{\odot}$ PBHs (i.e. SBHs) formed during the QCD epoch within the Bag Model. The nearest PBH could be at $\sim 10^{18}$ m (32 pc) well inside our galactic halo. In fact, within this case the expected number of PBHs in the galactic halo is $\sim 10^6$. There are two other similar cases now giving more modest values of Ω_{PBH} and a smaller, but still important, population of $\sim 10^5$ PBHs within the galactic halo: $n_+ = 1.42$ and $t_+ = 10^{-6}$ s ($\Omega_{PBH} \approx 0.09\ \Omega_{CDM}$, Figure 75), valid within the QCD Lattice Fit model; $n_+ = 1.50$ and $t_+ = 10^{-2}$ s ($\Omega_{PBH} \approx 0.07\,\Omega_{CDM}$, Figure 71c) which is valid within the QCD Bag Model. For all these cases we get $m/d^3 \sim 10^2$.

In some cases we might have simultaneous contributions from both the EW phase transition and the QCD phase transition. As an observationally relevant situation we have the case $n_+ = 1.40$ and $t_+ = 10^{-7}$ s for which we have, besides the contribution from the QCD (Bag Model or Lattice Fit), an important contribution from the EW phase transition as well as from radiation (Figure 82a). In this case the mass spectrum spans from $\sim 10^{27}$ g ($5 \times 10^{-4} m_J$) corresponding to the EW contribution (which extends also to $\sim 10^{28}$ g) to $\sim 10^{33}$ g ($5 \times 10^2 m_J$, $0.5M_{\odot}$) cor-

responding to the contribution from the QCD (Bag Model or Lattice Fit) with a gap at $\sim$ 10^{32} g ($0.05M_{\odot}$, $50m_J$). Between the two (10^{29}–10^{31} g, 5×10^{-2}–$5m_J$) we have the contribution from radiation with more modest values provided by 10^{29}–10^{31} g (5×10^{-2}–$5m_J$) PBHs. In particular, within the QCD Bag Model this case contributes with $\approx 15\%$ to CDM (and gives $m/d^3 \sim 10^2$).

There are other cases giving more modest contributions to Ω_{PBH}, although with important contributions to the population of PBHs within the galactic halo. For example, when $n_+ = 1.40$ and $t_+ = 10^{-8}$ s (Figure 73) we get $\Omega_{PBH} \sim 10^{-5}\ \Omega_{CDM}$ with a population of $\sim 10^7$ PBHs, with masses on the range 10^{26}–10^{31} g ($5{\times}10^{-8}M_{\odot}$–$0.005M_{\odot}$), within the galactic halo. In addition, we might have, still in this case, $\sim 10^2$ PBHs with $0.5M_{\odot}$ due to the QCD Bag Model. In terms of the QCD Crossover the best situation occurs when $n_+ = 1.50$ and $t_+ = 10^{-3}$ s (Figure 77) with $\Omega_{PBH} \sim 10^{-4}\ \Omega_{CDM}$ which gives $\sim 10^2$ PBHs with 0.5–$5M_{\odot}$ within the galactic halo.

We have three cases giving important contributions within the context of IMBHs. For $n_+ = 1.62$ and $t_+ = 1$ s we have, within the observable Universe, $\sim 10^{15}$ PBHs, with masses on the range 50–$5 \times 10^5 M_{\odot}$. For $n_+ = 1.66$ and $t_+ = 10$ s we have a similar global number of PBHs now with masses on the range 5×10^2–$5 \times 10^5 M_{\odot}$. In both cases we have contributions from the electron–positron annihilation epoch (Figures 68a and 68b). In particular when $n_+ = 1.66$ and $t_+ = 10$ s this contribution accounts for $\approx 85\%$ of the PBHs. The other case giving important contributions within the context of IMBHs occurs for $n_+ = 1.58$ and $t_+ = 10^{-1}$ s (Figure 72). Now the mass spectrum spans from $5M_{\odot}$ (SBHs) to $5 \times 10^4 M_{\odot}$ (IMBHs), peaking at 50–$500M_{\odot}$, with a total of $\sim 10^{16}$ PBHs within the observable Universe. It is interesting that the total number of PBHs in all these three cases is four or five orders of magnitude above the number of galaxies known to exist in the observable Universe ($\sim 10^{11}$). In fact, for all of them, the distance to the nearest PBH is well inside our galactic halo (10^{20}–10^{21} m).

The origin of the SMBHs that are observed at the centre of many galaxies remains unknown. They might form inside an existing galaxy or they might have formed long before the epoch of galaxy formation, in the primordial stages of the Universe. It is interesting, from the observational point of view, to find out that for some of the studied cases we get $\sim 10^{11}$ primordial SMBHs, which matches the number of galaxies known to exist in the observable Universe (cf. Figure 66). In particular, when $n_+ = 1.94$ and $t_+ = 10^5$ s (Figure 66c) we have $\sim 10^{11}$ PBHs mainly with $\sim 5 \times 10^8 M_{\odot}$ (corresponding to 8% of all CDM).

We also have cases leading to a number of PBHs by far larger than the number of galaxies. In particular when $n_+ = 1.78$ and $t_+ = 10^3$ s (Figure 67b) we have $\sim 10^{13}$ PBHs with $5 \times 10^6 M_{\odot}$ in the observable Universe ($\Omega_{PBH} \approx 0.03\ \Omega_{PBH}$) and when $n_+ = 1.86$ and $t_+ = 10^4$ s (Figure 67c) we get, also, $\sim 10^{13}$ PBHs mainly with $5 \times 10^7 M_{\odot}$ in the observable Universe ($\Omega_{PBH} \approx 0.17\ \Omega_{PBH}$). For cases like these it is plausible to assume a large number of SMBH binaries and/or a huge number of PBH merging before galaxy formation or during the evolution of galaxies. Another possibility is that most of these PBHs remained isolated in space and did not take

part in the formation of galaxies.

In terms of distances we have three cases giving the nearest PBH at a distance that is well inside the Oort cloud. These are the cases: $n_+ = 1.28$ and $t_+ = 10^{-18}$ s (nearest PBH at $\sim 10^{14}$ m, $\sim 10^5$ PBHs within the Oort cloud); $n_+ = 1.30$ and $t_+ = 10^{-16}$ s (nearest PBH at $\sim 10^{15}$ m, $\sim 10^4$ PBHs within the Oort cloud); $n_+ = 1.32$ and $t_+ = 10^{-14}$ s (nearest PBH at $\sim 10^{15}$ m, ~ 10 PBHs within the Oort cloud).

The case $n_+ = 1.28$ and $t_+ = 10^{-18}$ s is particularly interesting because it is the one that offers the best chances in terms of PBH direct detection. In this case the nearest PBH would have a mass of $\sim 10^{18}$ g and a surface temperature of $\sim 10^8$ K i.e., with the Hawking blackbody emission peaking at the hard X–ray band. In order to detect the electromagnetic component of this emission, the detector (X–ray telescope) should be positioned at a distance no larger than $\sim 10^8$ m (considering the present day best detectors). The probability of detecting the Hawking emission from such a PBH is $p \sim 10^{-21}$ (considering that the case $n_+ = 1.28$ and $t_+ = 10^{-18}$ s is just one of $\sim 10^3$ possible cases). A detector on board of a space probe moving, for example, towards the Kuiper–belt would scan $\sim 50\text{AU} \times (10^8\ \text{m})^2$, increasing the probabilitiy of detection to $p \sim 10^{-15}$. In a trip to Sedna (~ 1000AU) we get $p \sim 10^{-12}$ and in an hypothetical trip to the Oort cloud $p \sim 10^{-11}$. It is worthwhile to compare these small, but non–null, probabilities with others in Physics. For example, the neutrino detector GALLEX was able to capture a solar neutrino with a probability of $\sim 10^{-32}$, i.e., 17 orders of magnitude smaller than the PBH detection probability in a trip to the Kuiper–belt.

It is plausible that, throughout the history of the Solar System, some of these PBHs, initially at the Oort cloud, might have been thrown into the inner Solar System following the same fate as the comets (i.e., we could have PBHs describing elliptical orbits with semi–major axis 100–200 AU). That would improve the chances of direct detection of a PBH by a space probe. For example, with a probe suchs as the IIE (a NASA mission that will be launched hopefully in the next years), that is expected to reach at least 200 AU. It is also interesting to note that these PBHs would have, besides the peculiar blackbody emission, an average mass ($\sim 10^{18}$ g) which is similar to Halley's comet mass.

In this work we considered that the distribution of PBHs throughout the Universe is homogeneous and uniform. Thus, we assumed that the PBH number density, n_{PBH}, stays the same over the galactic disk, on the galactic halo or on the intergalactic medium. However, this is a *conservative assumption*. Perphaps PBHs concentrate around galactic halos during the process of galaxy formation (when PBHs were already present) and around bounded systems such as star clusters. If that was the case then the PBH number density near the Solar System is expected to be a few orders of magnitude above the average value with which we worked with. This would significantly improve the probabilities of PBH direct detection.

8 Conclusions

8.1 Where are we now?

Having as motivation the possibility of direct detection of BHs we endeavoured into finding out, first, how many PBHs exist in the present day Universe. To do that we had to go back to the PBH formation era and determine the fraction of the Universe converted in PBHs at each epoch t_k: $\beta(t_k)$.

The value of $\beta(t_k)$ is very sensitive to the value of the PBH formation threshold δ_c. A decrease in the value of δ_c, which occurs during cosmological phase transitions in the early Universe, may lead to a substantial increase in the value of $\beta(t_k)$. With this idea in mind we paid particular attention to the two phase transitions predicted by the SMPP: EW and QCD. For the QCD we adopted three different models (Bag Model, Lattice Fit and Crossover) and, for the EW two models (Crossover, Bag Model). In addition to these two cosmological phase transitions we consider the electron–positron annihilation epoch during which a decrease in δ_c is also expected. As a consequence of these choices we studied $3 \times 2 \times 1 = 6$ different scenarios for the evolution of the early Universe during the epochs suitable for PBH formation.

In order to determine $\beta(t_k)$ we need to know, first, the mass variance evaluated at the same epoch ($\sigma(t_k)$), i.e., we need to know the behaviour of the density fluctuations in the early Universe at that particular epoch. For the density fluctuations we adopted a running–tilt power–law spectrum because this is in agreement with the observations (we still do not know the exact profile taken by the density fluctuations in those early stages). The running–tilt power–law spectrum introduces a couple of additional parameters to the problem: n_+, which gives the maximum value attained by the spectral index, and t_+, which gives the location of that maximum. The true values of these two parameters are unknown. Thus, we decided to evenly divide the (n_+, t_+) parameter space into 1353 different cases, study each case within the context of each of the six different scenarios, and determine $\beta(t_k)$ for all cases within these. Cases for which $\beta(t_k)$ violates the observational constraints were excluded giving us a total of 533 allowed cases.

The next step consisted of determining how these results are reflected in the present day Universe in terms of the PBH density parameter (Ω_{PBH}), PBH number density (n_{PBH}), total number of PBHs (N), PBH mass spectrum and the distance to the nearest PBH (d). Observationally relevant would only be the cases giving, at least, one PBH inside the observable Universe ($N \geq 1$). This works for 72 of the cases ($\approx 14\%$ out of the 533). It is very encouraging to note that among those 72 cases with observationally relevant results we have cases that give important contributions to CDM, PBHs of all masses (SSBHs, SBHs, IMBHs, SMBHs), as well as important contributions to the total population of BHs (within the observable Universe, the galactic halo or the Solar System neighoorhood). We also have cases giving important numbers of PBHs formed during different cosmological phase transitions (EW, QCD, electron–positron anihilation).

In terms of CDM, we got one case accounting for $\approx 23\%$ of all CDM. That occurs when $n_+ = 1.40$ and $t_+ = 10^{-4}$ s (Figure 71b). The contribution to CDM is provided by a population of $0.5 M_\odot$ PBHs (i.e. SBHs) formed during the QCD epoch within the Bag Model. The nearest PBH could be at $\sim 10^{18}$ m (32 pc) well inside our galactic halo. In fact, within this case the expected number of PBHs in the galactic halo is $\sim 10^6$. There are two other cases giving a smaller, but still important, population of $\sim 10^5$ PBHs within the galactic halo: $n_+ = 1.42$ and $t_+ = 10^{-6}$ s ($\Omega_{PBH} \approx 0.09\, \Omega_{CDM}$, Figure 75), valid within the QCD Lattice Fit model; $n_+ = 1.50$ and $t_+ = 10^{-2}$ s ($\Omega_{PBH} \approx 0.07\, \Omega_{CDM}$, Figure 71c) which is valid within the QCD Bag Model. For all these cases we get $m/d^3 \sim 10^2$.

In some cases we might have simultaneous contributions from both the EW phase transition and the QCD phase transition. As an observationally relevant situation we have the case $n_+ = 1.40$ and $t_+ = 10^{-7}$ s for which we have, besides the contribution from the QCD (Bag Model or Lattice Fit), an important contribution from the EW phase transition as well as from radiation. In this case the mass spectrum spans from $\sim 10^{27}$ g ($5 \times 10^{-4} m_J$) corresponding to the EW contribution (which extends also to $\sim 10^{28}$ g) to $\sim 10^{33}$ g ($5 \times 10^2 m_J$, $0.5 M_\odot$) corresponding to the contribution from the QCD (Bag Model or Lattice Fit) with a gap at $\sim 10^{32}$ g ($0.05 M_\odot$, $50 m_J$). Between the two (10^{29}–10^{31} g, 5×10^{-2}–$5 m_J$) we have the contribution from radiation with more modest values provided by 10^{29}–10^{31} g (5×10^{-2}–$5 m_J$) PBHs. In particular, within the QCD Bag Model this case contributes with $\approx 15\%$ to CDM.

For $n_+ = 1.62$ and $t_+ = 1$ s we have, within the observable Universe, $\sim 10^{15}$ PBHs, with masses in the range 50–$5 \times 10^5 M_\odot$. For $n_+ = 1.66$ and $t_+ = 10$ s we have a similar global number of PBHs now with masses in the range 5×10^2–$5 \times 10^5 M_\odot$ (i.e. IMBHs). In both cases we have contributions from the electron–positron annihilation epoch. In particular when $n_+ = 1.66$ and $t_+ = 10$ s this contribution accounts for $\approx 85\%$ of the PBHs. The other case giving important contributions within the context of IMBHs occurs for $n_+ = 1.58$ and $t_+ = 10^{-1}$ s. Now the mass spectrum spans from $5 M_\odot$ (SBHs) to $5 \times 10^4 M_\odot$ (IMBHs), peaking at 50–$500 M_\odot$, with a total of $\sim 10^{16}$ PBHs within the observable Universe. It is interesting that the total number of PBHs in all these three cases is four or five orders of magnitude above the number of galaxies known to exist in the observable Universe ($\sim 10^{11}$). In fact, for all of them, the distance to the nearest PBH is well inside our galactic halo (10^{20}–10^{21} m).

For some of the studied cases we get $\sim 10^{11}$ primordial SMBHs, which matches the number of galaxies known to exist in the observable Universe. In particular, when $n_+ = 1.94$ and $t_+ = 10^5$ s we have $\sim 10^{11}$ PBHs mainly with $\sim 5 \times 10^8 M_\odot$ (corresponding to 8% of all CDM). We also have cases leading to a number of SMBHs by far larger than the number of galaxies. In particular when $n_+ = 1.78$ and $t_+ = 10^3$ s we have $\sim 10^{13}$ PBHs with $5 \times 10^6 M_\odot$ in the observable Universe ($\Omega_{PBH} \approx 0.03\, \Omega_{PBH}$) and when $n_+ = 1.86$ and $t_+ = 10^4$ s we get, also, $\sim 10^{13}$ PBHs mainly with $5 \times 10^7 M_\odot$ in the observable Universe ($\Omega_{PBH} \approx 0.17\, \Omega_{PBH}$). These cases are important in the sense that the origin of the SMBHs that are observed at the centre of many galaxies remains unknown. They might have formed inside existing

galaxies or they might have formed long before the epoch of galaxy formation, in the primordial stages of the Universe.

In terms of distances we have three cases giving the nearest PBH at a distance of 10^{14}–10^{15} m, i.e., well inside the Oort cloud. For example, when $n_+ = 1.28$ and $t_+ = 10^{-18}$ s we have got a population of $\sim 10^5$ PBHs within the Oort cloud with the nearest one at $\sim 10^{14}$ m. This case $n_+ = 1.28$ and $t_+ = 10^{-18}$ s is particularly interesting because it is the one that offers the best chances in terms of PBH direct detection. In this case the nearest PBH would have a mass of $\sim 10^{18}$ g and a surface temperature of $\sim 10^8$ K, i.e., with the Hawking blackbody emission peaking at the hard X–ray band. In order to detect the electromagnetic component of this emission, the detector (X–ray telescope) should be positioned at a distance no larger than $\sim 10^8$ m. The probability of detecting the Hawking emission from such a PBH, by a detector on board of a space probe moving, for example, towards the Kuiper–belt (50 AU) is $p \sim 10^{-15}$. It is plausible that, throughout the history of the Solar System, some of these PBHs might have been thrown into the inner Solar System following the same fate as the comets (i.e., we could have PBHs describing elliptical orbits with semi–major axis 100–200 AU). That would improve the chances of direct detection of a PBH by a space probe: for example, by the IIE that is expected to reach at least 200 AU. It is also interesting to note that these PBHs would have, besides the peculiar blackbody emission, an average mass ($\sim 10^{18}$ g) which is similar to Halley's comet mass.

In this work we considered that the distribution of PBHs throughout the Universe is homogeneous and uniform. Thus, we assumed that the PBH number density, n_{PBH}, stays the same over the galactic disk, on the galactic halo or on the intergalactic medium. However, this is a *conservative assumption*. Perphaps PBHs concentrate around galactic halos during the process of galaxy formation (when PBHs were already present) and around bounded systems such as star clusters. If that was the case then the PBH number density near the Solar System is expected to be a few orders of magnitude above the average value with which we worked with. This would significantly improve the probabilities of PBH direct detection.

8.2 Where can we go?

We have determined the PBH density parameter and the PBH number density for all observationally relevant cases. Assuming that the distribution of PBHs is homogeneous throught the entire Universe we found Ω_{PBH}, n_{PBH}, and the distance to the nearest PBH, given different post–inflationary phase transition models (QCD, EW, e^+e^-) and the (n_+, t_+) parameter space. We concluded that, provided some fine–tuning to the initial conditions, it is very reasonable to assume the formation and existence of PBHs in observationally relevant numbers in the Universe. We now list some objectives and ideas for future work:

- Exploration of the possibility that PBHs are clustered around galactic halos and see how this affects the distance to the nearest PBH. If PBHs are cre-

ated highly clustered, then this could lead to a huge number of PBH binaries and also to a huge number of PBH mergers (which would lead to the formation of bigger BHs). We plan to determine how this could affect the density distribution function of PBHs in the Universe, possibly through simulations.

- PBHs might be much smaller than the particle horizon at formation, with masses that might be as small as $10^{-4}M_H$ (cf. Section 1.4.2). We plan to explore this subject and how it affects the PBH mass spectrum.

- Our results are clearly dependent on the (n_+, t_+) parameter space. Plus, we have mainly concentrated on a running–tilt power–law spectrum because this seems to be in accordance with WMAP observations. Results from the Planck mission, which is already in space, might provide stronger constraints on the (n_+, t_+) parameter space and on the power–law spectrum: we will, then, refine our results.

- Work with other types of fluctuation spectra and compare the results with the ones achieved so far.

- When a PBH forms at a given epoch it could swallow smaller mass PBHs existing in the neighborhood. We plan to study the importance of this process and evaluate how it affects the value of $\Omega_{PBH}(t_k)$.

- Improve our results by considering a single model that accounts for all of the above ideas; also, by extending our study to the period between the end of inflation ($\sim 10^{-33}$ s) and 10^{-23} s.

- Take into account any LHC results for the production of small BHs. Although within the framework of string and brane Cosmology, these results could reveal important insights into our work.

- Consider possible *space experiments* on board of space probes that could lead to the detection of PBHs. That is, for example, the case of the Innovative Interstellar Explorer (IIE), a NASA probe that is expected to reach 200 AU in about 30 years after launch, or even the current Pluto–Kuiper Express (UV detector), albeit with much smaller probability of success.

A The Universe Timeline

The Big Bang theory is based on the observed Hubble's law redshift of distant galaxies that when taken together with the Cosmological Principle indicate that space is expanding according to the FLRW model of General Relativity (Slipher, 1917; Hubble, 1929). Extrapolated into the past, these observations show that the Universe has expanded from a state in which all its matter and energy had immense temperatures and densities.

In fact, in the very early Universe the temperatures and densities were so high that the photons and the great variety of relativistic particles were in thermodynamic equilibrium. When the mean thermal energy $kT \gg mc^2$, conservation of energy implies that every elementary particle of rest mass m can be converted into every other particle. Creation and annihilation of particle–antiparticle pairs and the interactions with other particles thus keep any particular type of particle of mass m in equilibrium (and in large numbers) above the energy mc^2. As the average energy in the Universe decreased due to its expansion to a value less than the equivalent mass mc^2, particles of mass m which had decayed or been annihilated could no longer be replaced. This point is known as the *threshold* for that particular particle. Cosmic evolution is thus characterized by a sequencial 'dying off' of the various types of particles, beginning with the most massive.

Before one Planck time ($t_P \sim 10^{-43}$ s) all the four fundamental forces were unified into a single force. This phase of the Universe is called the *Planck Era*. During this era the theory of General Relativity, which treats space–time as a continuum, would have to be replaced by a still lacking *Quantum Theory of Gravity*. Only at the end of this era, i.e., when the Universe was $\sim 10^{-43}$ s old, gravity separated from the other three forces (e.g. Unsöld & Bascheck, 2002).

The period 10^{-43} s $< t < 10^{-35}$ s is is called the *Grand Unification Era*. During this era the electromagnetic, strong and weak interactions are unified in a single force mediated by an hypothetical boson X, with mass (energy) of order 10^{14} GeV, which converts leptons into quarks and vice versa. At this stage the Universe consists of a plasma composed of quarks, gluons, leptons, photons, bosons X as well as their respective antiparticles. They are all present in equal abundances and are continuosly being interconverted due to mutual collisions (e.g. Unsöld & Bascheck, 2002).

When the temperature of the Universe drops below 10^{14} GeV it turns out that the decaying X bosons are no longer replaced by new X bosons. As a result, we have the *strong–electroweak phase transition*, i.e., the separation of the strong and EW interactions (e.g. Unsöld & Bascheck, 2002).

In order to explain problems such as 'flatness', 'horizon' and 'monopole', the present paradigm makes use of an inflationary stage of expansion in the very early Universe (Section 1.1.2). During inflation the scale factor $R(t)$ growns exponentially from an initial value R_i, corresponding to the instant $t_i \sim 10^{-35}$ s when the EW and strong forces separate (e.g. Narlikar & Padmanabhan, 1991). The inflationary stage is

followed by a radiation–dominated era after a short period of reheating during which the energy stored in the field that drives inflation decays into quanta of many other fields, which, through scattering processes, reach a state of local thermodynamic equilibrium (e.g. Boyanovsky et al., 2006).

The period which goes from the end of this reheating process up to $t \sim 10^{-5}$ s is known as the *Quark Era*. During this era the Universe consists of a plasma composed of quarks, leptons, photons, gluons and their antiparticles. Particle–antiparticle pairs are constantly being created and annihilated. Conversion between quarks and leptons are not possible because X bosons no longer exist.

When the temperature of the Universe drops to ~ 180 GeV it is no longer possible to create top quarks (or anti–top quarks). Top and anti–top quarks annihilate each other and cease to exist in nature. It is also during the quark era that the tauon, and the bottom and charm quarks thresholds occur (Table A-1). When the Universe temperature reaches ~ 100 GeV (corresponding to the mass of the $W^{\pm}$ and Z^0 bosons) another remarkable effect takes place: the weak force decouples from the electromagnetic force in a process called the *EW phase transition* (Section 1.2.2). It is only now that the four fundamental interactions are separarated (e.g. Unsöld & Bascheck, 2002), as we see them today.

When the temperature of the Universe goes from 2 GeV to 1 GeV almost all the baryons cease to be produced. This applies to the baryons Ω, Ξ, Σ and Λ. Among the decaying products we have neutrons (mean–life ~ 600 s (e.g. Jones & Lambourne, 2004) which is a very long time if compared with the age of the Universe at this stage) and protons. These were the first stable neutrons and protons ever produced in the Universe.

As the temperature falls through ~ 170 MeV the *Quark–Hadron phase transition* occurs (Section 1.2.1), i.e., quarks and gluons bind into stable hadrons (neutrons and protons). This marks the beginning of the *Hadron Era*. During the hadron era the kaons, pions and muons thresholds take place (Table A-1).

When the Universe is 10^{-4} s old, and the last pions have just decayed, the *Lepton Era* begins. The Universe is now composed, according to the SMPP (Appendix C), of photons, protons, neutrons, electrons, positrons, neutrinos and antineutrinos. Protons and neutrons turn into each other through reactions like: $e^- + p \longleftrightarrow \nu_e + n$, $e^+ + n \longleftrightarrow \bar{\nu}_e + p$, $n \longleftrightarrow p + e^- + \bar{\nu}_e$ (e.g. Lyth, 1993; Jones & Lambourne, 2004). When the Universe is ≈ 1 s old neutrinos decouple, i.e., the Universe becomes transparent to neutrinos. Finally, when the Universe is ≈ 3 s old, the electron threshold occurs marking the end of the Lepton Era.

About 200 s after the singularity, the Universe has cooled to $\sim 10^9$ K, allowing the synthesis of nuclei from protons and neutrons in a process called *Primordial Nucleosynthesis*. The first fusion reaction that could occur was that between a proton and a neutron to form a nucleus of deuterium (deuteron): $p + n \leftrightarrows {}^2_1\mathrm{H} + \gamma$. A deuteron can be broken apart by an incident γ–ray photon with energy $\geq$ 2.23 MeV. However at this stage ($t \sim 200$ s) the average photon energy in the Universe decreased

below that limit and hence, deuterium, once formed, would no longer be destroyed (e.g. Jones & Lambourne, 2004).

As soon as there was a significant abundance of deuterium, other nuclear reactions could then proceed with the formation of ${}^{3}_{1}\mathrm{H}$ (tritium), ${}^{3}_{2}\mathrm{He}$, ${}^{4}_{2}\mathrm{He}$, ${}^{6}_{3}\mathrm{Li}$, ${}^{7}_{3}\mathrm{Li}$ and, ${}^{7}_{4}\mathrm{Be}$. The reason why Primordial Nucleosynthesis did not progress to produce elements with higher mass numbers is due to two factors: i) the temperature of the Universe which is by this time lower than required and, ii) there are no stable nuclides with mass number $A = 5$ or $A = 8$. When the Universe become ~ 1000 s old the formation of nuclides effectively ceased leaving a Universe with primary matter content of hydrogen (mainly protons, i.e., ${}^{1}_{1}\mathrm{H}$) and helium (mainly ${}^{4}_{2}\mathrm{He}$), with trace amounts of beryllium and lithium (e.g. Jones & Lambourne, 2004).

The radiation and matter densities in the Universe decrease as the expansion dilutes the number of atoms and photons. Radiation also decreases due to the cosmological redshift (see equation 18), so its density falls faster than that of matter. Looking back in time, there was an instant, which corresponds to an age of the Universe of $\approx 1.1 \times 10^5$ years (redshift $z \approx 3200$, e.g. Bennett et al., 2003; Hinshaw et al., 2009), when matter and radiation densities were just equal (cf. Table A-1). Before that time the Universe was radiation–dominated.

At an age of $\approx 2.8 \times 10^5$ years the Universe had expanded and cooled enough ($T \sim 3800$ K), allowing nuclei and electrons to combine in order to form neutral atoms. This process, which is known as *recombination*[30], can be numerically defined as the instant in time when the number density of ions is equal to the number density of neutral atoms (e.g. Ryden, 2003).

When the Universe was ~ 380000 years old ($z \approx 1090$, e.g. Bennett et al., 2003; Hinshaw et al., 2009) and the temperature had dropped to ~ 3000 K, the number density of free electrons was so low that the Universe essentially became transparent and photons could travel unhindered from this time on. This is known as the *photon decoupling* epoch. The photons released during this epoch become the CMB (Appendix B). Surrounding every observer in the Universe there is a *last scattering surface* from which the CMB photons have been streaming freely (e.g. Ryden, 2003) becoming redshifted due to the expansion of the Universe (Appendix B).

The period between photon decoupling ($z \approx 1090$) and the formation of the first luminous objects ($z \sim 11$) is referred to as the *Cosmic Dark Ages*. That is because, during that period, there were no sources of radiation in the Universe, with the exception of the hyperfine 21–cm line of neutral hydrogen (e.g. Hirata & Sigurdson, 2007).

Reionization is the second of two major phase changes of hydrogen gas in the Universe (the first was recombination). Reionization occurred once objects started to form in the early Universe. As these objects formed and radiated energy, enough

[30]Some authors suggest that we should use the term *combination* instead because this is the very first time in the history of the Universe when electrons and ions combined to form neutral atoms (e.g. Ryden, 2003).

to ionize neutral hydrogen, the Universe went from being neutral back to being an ionized plasma, at redshift $z \sim 11$ according to the (WMAP) results (Hinshaw et al., 2009).

When the Universe was $\approx 2.8 \times 10^{17}$ s old (≈ 0.7 times the present age) it become dark energy–dominated. The true nature of this dark energy, which is responsible for the observed non–linear acceleration of the Universe, remains unknown.

In Table A-1 we present a timeline of the Universe according to the inflationary Big Bang model.

Table A-1: The Universe timeline according to the inflationary Big Bang model (data was taken mainly from Unsöld & Bascheck (2002), Jones & Lambourne (2004) and Ryden (2003).

Era	t(s)	T(K)	T(GeV)	Comments
Planck	–	–	–	Quantum Gravity
GUT	10^{-43}	10^{32}	10^{19}	Gravity separates
Quark	10^{-35}	10^{27}	10^{14}	Strong–electroweak phase transition Inflation begins
	$\sim 10^{-33}$	10^{27}	10^{14}	Inflation ends
	3×10^{-11}		172.5	t quark threshold
	$2.3 - 3.2 \times 10^{-10}$	10^{15}	100	EW phase transition
	10^{-8}		4.2	b quark threshold
	10^{-7}		1.78	Lepton τ threshold
			1.25	c quark threshold
			$1.6 - 1.2$	Hyperons threshold
	1.2×10^{-5}		0.50	Kaons threshold
Hadron	$0.63 - 1.1 \times 10^{-4}$	10^{13}	0.17	Formation of neutrons and protons
	1.6×10^{-4}		0.14	Pions threshold
	2.8×10^{-4}		0.106	Muons threshold
Lepton	3.5×10^{-4}	10^{12}		s quark threshold and last pions decay
	1	10^{10}		Decoupling of ν_e
	2			Neutron production stops
Photon	3	7.3×10^{9}	5×10^{-4}	Electron threshold
	200	10^{9}		Nucleosynthesis of ^2H stable
	10^3			Nucleosynthesis stops
Matter	2.5×10^{12}	9000		Radiation–Matter equality
	9.0×10^{12}	3800		Recombination
	1.2×10^{13}	3000		Photon decoupling
	1.1×10^{16}	30		Reionization
Λ	2.8×10^{17}	≈ 4		Matter–Dark energy equality
	4.3×10^{17}	2.725		Present

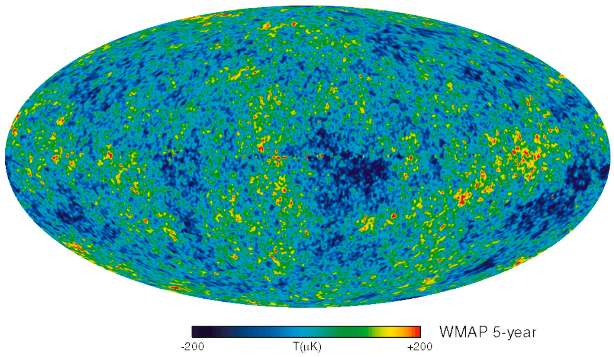

Figure B-1: An all–sky CMB anisotropy map, based on data obtained by the WMAP 5–year. The angular resolution of this map is $\approx 0.1^\circ$ (Hinshaw et al., 2009).

B The Cosmic Microwave Background temperature

The existence of the CMB radiation was first predicted by Gamow et al. (1948) but it was only in 1964 that it was observed (serendipitously) for the first time (Penzias & Wilson, 1965).

In 1989, NASA launched the *Cosmic Background Explorer* satellite (COBE), and the initial findings, released in 1990, were consistent with the Big Bang's predictions regarding the CMB. COBE found a residual temperature of 2.726 K and determined that the CMB was isotropic to about one part in 10^5 (Boggess et al., 1992). During the 1990s, CMB anisotropies were further investigated by a large number of ground–based experiments and the Universe was shown to be almost geometrically flat, by measuring the typical angular size of the anisotropies.

The most recent results are the ones given by WMAP (launched in June 2001). WMAP is the natural sucessor of COBE and, like COBE, it has produced an all–sky anisotropy map, although this time with an angular resolution of $\approx 0.1^\circ$ (the angular resolution of COBE was $\approx 7^\circ$). The WMAP 5–year anisotropy map is shown in Figure B-1. The CMB, viewed from anywhere else in the Universe at the present time, is expected to be similar in its general aspects but different in detail. From a cosmological point of view, what is interesting about any single view is not the detailed information it provides about the directions in which the CMB is slightly warmer or slightly cooler, but the statistical insight it provides into CMB anisotropies in general (e.g. Jones & Lambourne, 2004).

The CMB brings us information about the state of the Universe at the photon decoupling epoch ($z \approx 1090$) when the photons that reach us now had their last scattering (Appendix A). The spectrum of the CMB at the present epoch is well described by a blackbody function with (Mather et al., 1999)

$$T_0 = 2.725 \pm 0.002 \text{ K}. \tag{B-1}$$

Another observable quantity inherent in the CMB is the variation in temperature (or intensity) from one part of the microwave sky to another. Since the first detection of these anisotropies by the COBE satellite in 1992, there has been intense activity to map the sky at increasing levels of sensitivity and angular resolution. Observations have shown us that the CMB contains anisotropies at the 10^{-5} level (e.g. Yao et al., 2006)

$$\frac{\Delta T}{T} \sim 10^{-5}$$

over a wide range of angular scales. Density fluctuations over the plasma in thermal equilibrium gave rise to temperature fluctuations (denser regions were hotter). Hence, the temperature anisotropies in the CMB bring us direct evidence of the density contrast at recombination. This small temperature anisotropy, whose existence is predicted by cosmological models, provides the clue to the origin of structure and is an important confirmation of theories of the early Universe (e.g. Boyanovsky et al., 2006).

These anisotropies are usually expressed by using a spherical harmonic expansion of the CMB sky (e.g. Yao et al., 2006)

$$T(\theta, \phi) = \sum_{l,m} a_{lm} Y_{lm}(\theta, \phi)$$

where $Y_{lm}(\theta, \phi)$ is the so–called spherical harmonic function of degree l and order m[31].

Theoretical models generally predict that the a_{lm} modes are Gaussian random fields. Tests show that this is an extremely good simplifying approximation, with only some relatively weak indications of non–Gaussianity or statistical anisotropy at large scales. With the assumption of Gaussian statistics, and if there is no preferred axis, then it is the variance of the temperature field which carries the cosmological information, rather than the values of the individual a_{lm} coefficients. In other words, the power spectrum in l fully characterizes the anisotropies (e.g. Yao et al., 2006).

On small sections of the sky where its curvature can be neglected, the spherical harmonic analysis becomes ordinary Fourier analysis in two dimensions and l becomes the Fourier wavenumber. Since the angular wavelength $\theta = 2\pi/l$, larger multipole moments correspond to smaller angular scales, with $l \sim 10^2$ representing degree scale separations. In this limit the power spectrum is usually displayed as (e.g. Hu & Dodelson, 2002)

$$\left(\frac{\Delta T}{T}\right)^2 = \frac{l(l+1)}{2\pi} C_l$$

where

$$C_l \equiv \langle |a_{lm}|^2 \rangle.$$

[31] $Y_{lm}(\theta, \phi)$ represents the angular part of the solution of Laplace's equation ($\nabla^2 f(r, \theta, \phi) = 0$). The degree l and order m are integers such that $l \geq 0$ and $|m| \leq l$. The coefficients a_{lm} are constants. The expansion is exact as long as l goes to infinity.

The angular power spectrum indicates how much variation is present in the anisotropy measurements in a particular angular scale. It is constructed from the same data that are used to plot the anisotropy map, but it effectively discards the detail that depends on our particular location, and makes apparent the cosmically important features of the data (e.g. Jones & Lambourne, 2004).

The CMB mean temperature of 2.725 K (cf. equation B-1) can be regarded as the *monopole* component (a_{00}) of CMB maps. Since all mapping experiments involve difference measurements, they are insensitive to this average level. Monopole measurements can only be made with absolute temperature devices, such as the *Far–InfraRed Absolute Spectrophotometer* (FIRAS) instrument on the COBE satellite. Such measurements of the spectrum are consistent with a blackbody distribution over more than three decades in frequency (e.g. Yao et al., 2006).

The largest anisotropy is in the $l = 1$ *dipole* first spherical harmonic, with amplitude 3.346 ± 0.017 mK. The dipole is interpreted to be the result of the Doppler shift caused by the solar system motion relative to the nearly isotropic blackbody field, as confirmed by measurements of the radial velocities of local galaxies (e.g. Yao et al., 2006).

Excess variance in CMB maps at higher *multipoles* ($l \geq 2$) is interpreted as being the result of perturbations in the density of the early Universe, manifesting themselves at the epoch of the last scattering of the CMB photons. In the hot Big Bang picture, this happens at a redshift $z \simeq 1090$, with little dependence on the details of the model (e.g. Yao et al., 2006).

In Figure B-2 we show the theoretical CMB anisotropy power spectrum (according to the standard ΛCDM model). Notice that the physics underlying the C_l's can be separated into four main regions: the *ISW Rise* ($l \gtrsim 2$), the *Sachs–Wolfe plateau* ($l \lesssim 100$), the *acoustic peaks* ($100 \lesssim l \lesssim 1000$) and the *damping tail* ($l \gtrsim 1000$).

The horizon scale at photon decoupling corresponds to $l \approx 100$. Anisotropies at larger scales ($l < 100$) have not evolved significantly, and hence directly reflect the initial conditions. The combination of gravitational redshift and intrinsic temperature fluctuations leads to

$$\frac{\delta T}{T} \simeq \frac{1}{3}\frac{\delta \phi}{c^2}$$

where $\delta\phi$ is the perturbation to the gravitational potential. This is usually referred to as the *Sachs–Wolfe effect*. Assuming, in addition, a nearly scale–invariant spectrum of density perturbations, then $l(l+1)C_l$ is almost constant at large scales ($l < 100$) forming the so–called Sachs–Wolfe Plateau. The dominance of dark energy at low redshift, corresponding to $l \gtrsim 2$, leads to a rise above the Sachs–Wolfe Plateau. This is referred to as the *integrated Sachs-Wolfe effect* or ISW Rise (e.g. Yao et al., 2006).

Before the Universe became neutral the proton-electron plasma was tightly coupled to the photons, and these components behaved as a single photon–baryon fluid. Perturbations in the gravitational potential, dominated by the dark matter component,

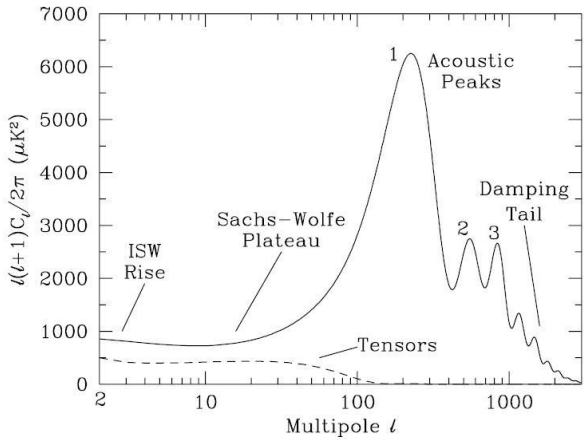

Figure B-2: The theoretical CMB anisotropy power spectrum, using a standard ΛCDM model. The horizontal axis is logarithmic. Four regions, each covering roughly a decade in l, are labeled as: the ISW Rise; Sachs–Wolfe Plateau; Acoustic Peaks (numbers indicate the first, the second and, the third acoustic peak); and Damping Tail. Also shown is the shape of the tensor (gravity wave) contribution, with an arbitrary normalization (adapted from Yao et al., 2006).

were steadily evolving. After recombination and photon decoupling, the phases of the oscillations were frozen–in, and projected on the sky as a harmonic series of acoustic peaks. The main peak (peak 1 at $l \approx 150$ in Figure B-2) is the mode that went through 1/4 of a period, reaching maximal compression. The angular position of the peaks is a sensitive probe of the spatial curvature of the Universe (e.g. Yao et al., 2006). WMAP has provided perhaps the most striking validation of inflation as a mechanism for generating superhorizon fluctuations, through the measurement of the first acoustic peak in the temperature–polarization angular power spectrum at $l \sim 150$ (Spergel et al., 2007).

The recombination process is not instantaneous, giving a thickness to the last scattering surface. This leads to a damping of the anisotropies at the highest multipoles ($l > 1000$), corresponding to scales smaller than that subtended by this thickness. This effect leads to a cut off on the anisotropies for $l \gtrsim 2000$. Also, gravitational lensing, caused by structures at low redshift ($z \ll 1000$), would have the effect of partially flattening the peaks, generating a power-law tail. The WMAP data can reach the multipole $l \simeq 900$, up to the third acoustic peak (see Figure B-2). In order to extend to higher multipoles (including the Damping Tail region), the WMAP team included in their analysis the data of other two CMB ground–based experiments: the *Arcminute Cosmology Bolometer Array Receiver* (ACBAR) and the *Cosmic Background Imager* (CBI) (e.g. Covi, 2003).

Information on the density contrast can also be obtained from the distribution of galaxies in our Universe. The main assumption, in this case, is that the visible matter follows the distribution of the invisible Dark Matter. Recent surveys include the *2 degree Field Galaxy Redshift Survey* (2dFGRS) which released data on 221 414 galaxies with measured redshift (e.g. Colless et al., 2003; Cole et al., 2005). An even larger survey is the *Sloan Digital Sky Survey* (SDSS). Its 6^{th} release of data

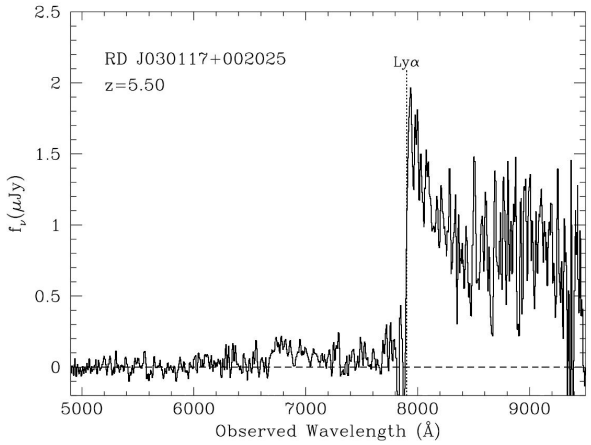

Figure B-3: The spectrum of quasar RD $J030117 + 002025$ with redshift $z = 5.50$. The Lyman α emission line has been shifted from the ultraviolet ($1210\mathring{A}$) to the infrared ($7860\mathring{A}$) and the same happened to the absorption caused by hydrogen clouds between us and the quasar, each at its own redshift (covering $\sim 5000 - 8000\mathring{A}$ in this plot): the Lyα forest (adapted from Stern et al., 2000).

(Adelman–McCarthy et al., 2008) already contains a total of 790 860 galaxies. From the distribution of the galaxies in the sky one can obtain the *two point correlation function* and the density contrast power spectrum (e.g. Covi, 2003).

Other ways to measure the density contrast rely on using photons of distant objects as a probe of the intervening matter or gas densities. *Lyman α forest* data measure the absorption lines in the spectra of distant quasars caused by intergalactic hydrogen and estimate the cosmic gas distribution out to large distances (e.g. Covi, 2003). In Figure B-3 we show, as an example, the Lyman α forest of quasar RD $J030117 + 002025$.

C The Standard Model of Particle Physics

The combination of QCD with the EW theory is known as the SMPP. The SMPP contains a finite number of parameters, which are unrelated, at least within the context of the theory itself. The SMPP is based on only two basic components: the fundamental quantum particles and the concept of interactions between them. A more complete theory of fundamental physics should explain the relationships among these parameters. The ultimate goal would be to determine the values of the parameters from pure mathematics, once the correct theory is discovered (e.g. Scott, 2006).

The current SMPP, experimentally tested with remarkable precision, describes the theory of strong, weak and electromagnetic interactions as a gauge theory[32]. The particle content is (see Figure C-1): three families of *quarks*, three families of *leptons*, and 13 gauge bosons (i.e., particles that act as carriers of the fundamental interactions): eight massless *gluons*, Z^0, $W^{\pm}$; the massless *photon*; the (yet to be discovered) scalar *Higgs* (e.g. Boyanovsky et al., 2006). These particles interact in only three ways: the electromagnetic interaction, the weak interaction and the strong interaction. Note that gravity is left outside the SMPP because we do not yet have a theory of quantum gravity.

The classification of fundamental particles is performed taking into account certain properties such as the rest mass, the electric charge and the spin. The spin must be an integer or an half–integer and is normally expressed in units of $\hbar$. Quantum particles with integer spin are called *bosons* and quantum particles with half–integer spin are called *fermions*. Fermions obey the *Exclusion Principle* (identical fermions cannot be at the same state at the same time) but bosons do not obey the Exclusion Principle.

A particle which does not react to the strong interaction is called a *lepton* (see Table C-1, Figure C-1). In the SMPP six of the 12 fermions are leptons: three electric charged particles (electron – e^-, muon – μ^-, tau – τ^-) and their associated neutrinos (ν_e, ν_μ, ν_τ). The remaining six fermions are quarks – particles which react to the strong interaction (see Table C-2, Figure C-1). Quarks come in six flavours (up – u, down – d, strange – s, charm – c, top – t, bottom – b) and carry, besides a fractional electric charge, a *colour charge*. This colour charge comes in three types: red, green and blue. This means that there are 18 different quarks (6 flavours $\times$ 3 colours).

[32]In Physics, gauge theories are a class of physical theories based on the idea that symmetry transformations can be performed locally as well as globally. Many powerful theories in Physics (e.g. EW theory, Electrodynamics, QCD) are described by Lagrangians which are invariant under certain symmetry transformation groups. When they are invariant under a transformation identically performed at every space–time point they are said to have a global symmetry. Gauge theory extends this idea by requiring that the Lagrangians must possess local symmetries which enable symmetry transformations in a particular region of space–time without affecting what happens in another region. This requirement is a generalized version of the *Equivalence Principle* of general relativity.

Table C-1: The three lepton families of the SMPP. For each particle it is indicated the respective electric charge e, spin s and mass m (according to the Particle Data Group (PDG) results – http://pdg.lbl.gov/2007/listings/contents_listings.html, Yao et al., 2006). For each charged lepton there is an anti–lepton with symmetric charge and the same mass and spin (e.g, the anti–particle of the electron is the positron, e^+, which is a particle with electric charge +1, spin 1/2 and mass 0.511 MeV). At the present it is not known if neutrinos are their own anti–particles (that would depend on the nature of the physics that gives them masses).

Family	Lepton	Symbol	e	s	m(MeV)
1	electron	e^-	-1	1/2	0.511
	electron neutrino	ν_e	0	1/2	$< 2 \times 10^{-6}$
2	muon	μ^-	-1	1/2	105.658
	muon neutrino	ν_μ	0	1/2	< 0.19
3	tau	τ^-	-1	1/2	1776
	tau neutrino	ν_τ	0	1/2	< 18.2

Table C-2: The three quark families of the SMPP. For each particle it is indicated the respective electric charge e, spin s and mass m (according to the PDG results – http://pdg.lbl.gov/2007/listings/contents_listings.html, Yao et al., 2006). For each quark there is an anti–quark with symmetric charge and the same mass and spin (e.g., the up antiquark, $\bar{u}$, is a particle with electric charge $-2/3$, spin 1/2 and mass 1.5 to 3 MeV).

Family	Quark	Symbol	e	s	m(MeV)
1	up	u	2/3	1/2	1.5 to 3
	down	d	$-1/3$	1/2	3 to 7
2	strange	s	$-1/3$	1/2	95 ($\pm$25)
	charm	c	2/3	1/2	1250 ($\pm$90)
3	bottom	b	$-1/3$	1/2	4200 ($\pm$70)
	top	t	2/3	1/2	172500 ($\pm$2700)

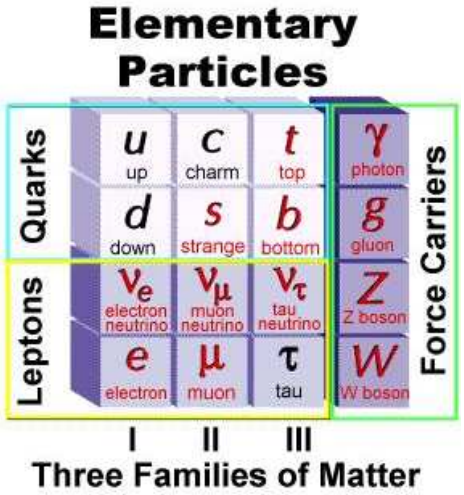

Figure C-1: The particle content of the SMPP (http://www-sldnt.slac.stanford.edu) as regards fundamental fermions and bosons. Since there are eight different types of gluons (g), two W bosons and the (still hypothetical) Higgs boson (H) – not shown – there are a total of 25 particles.

The pairings (e, ν_e) and (u, d) form a family of fundamental particles (Figure C-1). Most of the matter we see around us ultimately consists of this family of four particles. It seems that most matter in the Universe requires representatives from only this family of fundamental particles. Yet, for some reason, this family is reproduced twice over (cf. Figure C-1).

Bosons act as carrier particles of the fundamental forces (see Table C-3). The photon, γ, is the carrier of the electromagnetic interaction. It acts in any particle that possesses electric charge. There are two carrier particles of the weak interaction: the W boson and the Z boson. The W boson is electrically charged and so, there are W^+ and W^- bosons (antiparticles of each other). The Z boson is electrically neutral (Z^0). The weak interaction acts in all particles including neutrinos (the only interaction felt by neutrinos).

The boson responsible for the strong interaction is the *gluon* (g) which couples to the colour charge. The gluon possesses himself a colour charge, i.e. gluons are themselves subject to the strong force. They exchange gluons with other gluons which allows the possibility of *glueballs* (bound states of 'pure glue') and *hybrid mesons* (bound states of a gluon, quark and antiquark).

There are six types of gluons that can change the colour charge of a quark (but not its flavour): red–antigreen, red–antiblue, green–antired, green–antiblue, blue–antired, and blue–antigreen. For example, if a red quark interacts with a red–antigreen quark then it will become a green quark. In addition, there are two different gluons that couple to the color charge in a quark without changing the quark color. These gluons can be regarded as mixtures of blue–antiblue, red–antired, and green–antigreen.

A distinct feature of the EW interactions is that the $W^\pm$ and Z^0 bosons that mediate them are massive which means that it is not possible to describe weak interactions in terms of a gauge field theory. However, although the theory has a symmetry, it

Table C-3: Fundamental Bosons within the SMPP. For each boson it is shown the respective electric charge e, spin s and mass m (according to the PDG results – http://pdg.lbl.gov/2007/listings/contents_listings.html, Yao et al., 2006).

Interaction	Boson	Symbol	q	s	m(MeV)
electromagnetic	photon	γ	0	1	0
weak	W	W^-	-1	1	80403
	Z	Z^0	0	1	91188
	W	W^+	$+1$	1	80403
strong	gluon	g	0	1	0

is not necessary that the ground state of the theory has the same symmetry, that is, the symmetry may be spontaneously broken. This is a suffcient requirement for producing masses for gauge bosons. In the SMPP, this is accomplished by introducing a scalar field, called the *Higgs* scalar, into the theory (e.g. Gynther, 2006).

Associated with this field there is a spin zero boson and charge zero – the *Higgs boson*, H (with a mass yet to be determined – it is still a purely hypothetical particle – the only one of the SMPP). As a quark or lepton moves trough space, it interacts with the Higgs field; the field becomes distorted in the vicinity of the particle. It is this distortion that causes the particle to have mass.

Most of our present experimental knowledge about the SMPP Higgs boson comes from the study of e^+e^- collisions performed at the *Large Electron Positron Collider* (LEP) and the *Stanford Linear Collider* (SLC) between 1988 and 2000. No direct evidence for the existence of the SMPP Higgs has been produced. This allows us to set a lower limit in the Higgs mass of $\sim$ 100 GeV, mainly based of the non–observation of Higgs bosons in association with a Z^0, followed by the eventual decay of the Higgs into a heavy fermion–antifermion pair (e.g. Ellis et al., 2007).

Hadrons are composite particles made up of quarks (as far as we know there are no free quarks in nature at the present stage of the Universe). Hadrons with integer spin are called *mesons* (bosonic hadrons) and those with half–integer spin are called *baryons* (fermionic hadrons).

Every meson consists of a quark–antiquark pair. This means that we have five quark flavours $\times$ five anti–quark flavours = 25 different possible combinations[33].

[33]The top quark is left outside because the probability of formation for top mesons is, according to theory, negligibly small (e.g. Fabiano, 1997). Besides that, there are no reports on the detection

However, the observed number of different mesons is, by far, much larger than this one. That is because, for each quark–antiquark combination, there are, in general, many excited states. For example, the π^+ meson corresponds to the lower energy state (fundamental state) of the $u\bar{d}$ combination ($m \approx 139.57$ MeV). Examples of excited states for the π^+ meson (just to name a few) comprehend the ρ^+ ($m \approx 775.4$ MeV), the $a_0(1450)$ ($m \approx 1474$ MeV), and the $\pi_2(1650)$ ($m \approx 1672.4$ MeV).

Some of the quark–antiquark combinations are observed only in superpositions. That is, for example, the case of the neutral pion (π^0) which is a superposition of the combinations $u\bar{u}$ and $d\bar{d}$. The superposition occurs because the two combinations share the same set of quantum numbers.

The combination $d\bar{s}$ is called the neutral Kaon (K^0). Although the K^0 and its antiparticle $\bar{K}^0$ are usually produced via the strong force, they decay weakly. Thus, once created, the two are better thought of as composites of two weak eigenstates which have vastly different lifetimes: the long–lived (5.116×10^{-8} s) neutral kaon called *K–Long* and the short–lived (8.953×10^{-11} s) neutral kaon called *K–Short*. In Table C-4 we show the fundamental mesons as well as their most common excited states.

A baryon consists of a triplet of quarks. This means that we have 35 different possible combinations[34]. The most common baryons in the present Universe are *nucleons*, i.e., protons and neutrons. The proton consists of two up quarks and one down quark (uud) and the neutron consists of one up quark and two down quarks (udd).

Hyperons are baryons containing at least a strange quark, but no charm or bottom quarks (e.g. Σ^-, Σ^0, Σ^+, Ξ^-, Ξ^0, Λ^0, Ω^-). Charmed baryons are baryons containing at least a charm quark, but no bottom quarks (e.g. Ξ_c^+, Ξ_c^0, Ξ_{cc}^+, Δ_c^+, Ω_c^0). Bottom baryons are baryons containing at least a bottom quark (e.g. Ξ_b^-, Ξ_b^0, Δ_b^0).

Some of the 35 triplets have never been observed (e.g. ubb, sbb). However, the number of known baryons is much larger than the number of different quark triplets. That is due to the existence of many excited states for each configuration. For example, in the case of the proton (uud) there are at least 25 known excited states (e.g. $N(2190)^+$ with mass ≈ 2190 MeV, $N(1710)^+$ with mass ≈ 1710 MeV, Δ^+ with mass ≈ 1232 MeV)[35]. In table C-5 we show the most stable known baryons.

Antibaryons are triplets made of antiquarks. For each baryon there is an antibaryon, which is an antiparticle with the same mass and opposite electric charge, obtained by replacing each quark by the corresponding antiquark[36]. For example, the antiparticle

---

of top mesons (e.g. Yao et al., 2006).

[34]The 35 different quark triplets are: uuu, uud, uus, uuc, uub, udd, uds, udc, udb, uss, usc, usb, ucc, ucb, ubb, ddd, dds, ddc, ddb, dss, dsc, dsb, dcc, dcb, dbb, sss, ssc, ssb, scc, scb, sbb, ccc, ccb, cbb, and bbb. The top quark was left outside because the probability of formation of a *top baryon* is negligibly small.

[35]For a complete list of currently known baryons (including excited states) see http://pdg.lbl.gov/2007/tables/contents_tables.html.

[36]Baryons are matter (they are made of quarks) and antibaryons are antimatter (they are made

Table C-4: The fundamental mesons and their most common excited states. For each meson and antimeson the symbol, the quark content, the electric charge e, the spin s, the mean lifetime t and, whenever possible, the two most probable decaying reactions with corresponding probabilities are displayed (for more data on these and other mesons consult the PDG – http://pdg.lbl.gov/2007/listings/contents_listings.html, Yao et al., 2006).

Name	Meson symbol	Antimeson symbol	quark content		e	s	m(MeV)	$t(s)$	Most probable decaying reaction		Second most probable decaying reaction	
pion	π^+	π^-	$u\bar{d}$	$\bar{u}d$	±1	0	139.57	2.6×10^{-8}	$\pi^\pm \to \mu^\pm + \nu_\mu$	99.99%		
neutral pion	π^0	(self)	$\left(u\bar{u}-d\bar{d}\right)/\sqrt{2}$	–	0	0	134.98	8.4×10^{-17}	$\pi^0 \to \gamma+\gamma$	98.80%		
charged kaon	K^+	K^-	$u\bar{s}$	$\bar{u}s$	±1	0	493.68	1.24×10^{-8}	$K^\pm \to \mu^\pm + \nu_\mu$	63.4%	$K^\pm \to \pi^\pm + \pi^0$	21%
neutral kaon	K^0	$\bar{K}^0$	$d\bar{s}$	$\bar{d}s$	0	0	497.648	–	–	–	–	
K–Short	K^0_S	(self)	$\left(d\bar{s}-s\bar{d}\right)/\sqrt{2}$	–	0	0	497.648	8.953×10^{-11}	$K^0_S \to \pi^+ + \pi^-$	69.2%	$K^0_S \to \pi^0 + \pi^0$	30.7%
K–Long	K^0_L	(self)	$\left(d\bar{s}+s\bar{d}\right)/\sqrt{2}$	–	0	0	497.648	5.116×10^{-8}	$K^0_L \to \pi^\pm + e^\mp + \nu_e$	40.6%	$K^0_L \to \pi^\pm + \mu^\mp + \nu_\mu$	27%
charged rho	ρ^+	ρ^-	$u\bar{d}$	$\bar{u}d$	±1	1	775.4	–	$\rho^\pm \to \pi^\pm + \pi_0$	$\approx 100\%$		
neutral rho	ρ^0	(self)	$\left(u\bar{u}-d\bar{d}\right)/\sqrt{2}$	–	0	1	775.49	–	$\rho^0 \to \pi^+ + \pi^- + \gamma$	–	$\rho^0 \to \pi^0 + \gamma$	–
omega	ω	(self)	$\left(u\bar{u}+d\bar{d}\right)/\sqrt{2}$	–	0	1	782.65	–	$\omega \to \pi^+ + \pi^- + \pi^0$	89.1%	$\omega \to \pi^0 + \gamma$	8.9%
phi	φ	(self)	$s\bar{s}$	–	0	1	1019.46	–	$\varphi \to K^+ + K^-$	49.3%	$\varphi \to K^0_S + K^0_L$	34.0%
eta	η	(self)	$\left(u\bar{u}+d\bar{d}-2s\bar{s}\right)/\sqrt{6}$	–	0	0	547.51	–	$\eta \to \gamma+\gamma$	39.4%	$\eta \to \pi^0+\pi^0+\pi^0$	32.5%
eta prime	η'	(self)	$\left(u\bar{u}+d\bar{d}+s\bar{s}\right)/\sqrt{6}$	–	0	0	957.78	–	$\eta' \to \pi^+ + \pi^+ + \eta$	44.5%	$\eta' \to \rho^0+\gamma+(\pi^+ + \pi^- + \gamma)$	29.4%
charged D	D^+	D^-	$c\bar{d}$	$\bar{c}d$	±1	0	1869.62	1.04×10^{-12}	$D^\pm \to K^0 + ... + \bar{K}^0 + ...$	61%	$D^\pm \to K^\pm + ...$	27%
neutral D	D^0	$\bar{D}^0$	$c\bar{u}$	$\bar{c}u$	0	0	1864.84	4.1×10^{-13}				
strange D	D^+_s	D^-_s	$c\bar{s}$	$\bar{c}s$	±1	0	1968.2	5.0×10^{-13}	$D^\pm_s \to K^0 + ... + \bar{K}^0 + ...$	39%	$D^\pm_s \to K^\pm + ...$	13%
J/Psi	J/ψ	(self)	$c\bar{c}$	–	0	1	396.92	–	$J/\psi \to hadrons$	88%	$J/\psi \to e^+ + e^-$	6%
charged B	B^+	B^-	$u\bar{b}$	$\bar{u}b$	±1	0	5297.0	1.638×10^{-12}	$B^\pm \to l^\pm + \nu_l + ...$	10.9%		
neutral B	B^0	$\bar{B}^0$	$d\bar{b}$	$\bar{d}b$	0	0	5279.5	1.530×10^{-12}	$B^0 \to l^+ + \nu_l + ...$	10.4%		
strange B	B^0_s	$\bar{B}^0_s$	$s\bar{b}$	$\bar{s}b$	0	0	5367.5	1.466×10^{-12}	$B^0_s \to D^-_s + ...$	94%		
charmed B	B^+_c	B^-_c	$c\bar{b}$	$\bar{c}b$	±1	0	6286	4.6×10^{-11}	$B^\pm_c \to J/\psi + l^\pm + \nu_l$	–	$B^\pm_c \to J/\psi + \pi^\pm$	–
Upsilon	Υ	(self)	$b\bar{b}$	–	0	1	9460.3	–	$\Upsilon \to \tau^+ + \tau^-$	2.6%	$\Upsilon \to \mu^+ + \mu^-$	2.5%

of the proton (uud), is the antiproton ($\bar{u}\bar{u}\bar{d}$), an antibaryon with $m \approx 938.272$ MeV and $e = -1$.

of antiquarks). The same idea does not apply to mesons and antimesons. That is because a meson (or antimeson) consists of a quark–antiquark pair.

Table C-5: The most stable known baryons. For each baryon the symbol, the quark content, the electric charge e, the spin s, the mass m, the mean lifetime t, the most probable decaying reaction(s) and probabilities are displayed. In the case of charmed and bottom baryons it is not known, in general, the most probable decaying reaction. In these cases we have selected one or two examples (if available) of possible decaying reactions (according to the PDG results – http://pdg.lbl.gov/2007/listings/contents_listings.html, Yao et al., 2006).

Name	Symbol	quarks	e	s	m(MeV)	$t(s)$	Most probable decaying reaction		Second most probable decaying reaction	
proton	p	uud	$+1$	1/2	938.272	$> 10^{29}$ years				
neutron	n	udd	0	1/2	939.565	885.7	$n \to p + e^- + \bar{\nu}_e$	100%		
sigma	Σ^-	dds	-1	1/2	1197.45	1.48×10^{-10}	$\Sigma^- \to \pi^- + n$	99.8%		
	Σ^0	uds	0	1/2	1192.64	7.4×10^{-20}	$\Sigma^0 \to \Lambda^0 + \gamma$	100%		
	Σ^+	uus	$+1$	1/2	1189.37	8.0×10^{-11}	$\Sigma^+ \to \pi^+ + n$	52%	$\Sigma^+ \to \pi^0 + p$	48%
xi	Ξ^-	dss	-1	1/2	1321.7	1.64×10^{-10}	$\Xi^- \to \Lambda^0 + \pi^-$	99.9%		
	Ξ^0	uss	0	1/2	1314.9	2.9×10^{-10}	$\Xi^0 \to \Lambda^0 + \pi^0$	99.5%		
charmed xi	Ξ_c^+	usc	$+1$	1/2	2467.9	4.42×10^{-13}	$\Xi_c^+ \to \Lambda^0 + \bar{K}^0 + \pi^+$	—	$\Xi_c^+ \to p + K^- + \pi^+$	—
	Ξ_c^0	dsc	0	1/2	2471.0	1.12×10^{-13}	$\Xi_c^0 \to p + K^- + K^- + \pi^+$	—	$\Xi_c^0 \to \Lambda^0 + \bar{K}^0 + \pi^+ + \pi^-$	—
double charmed xi	Ξ_{cc}^+	dcc	$+1$	1/2	3518.9	$< 3.3 \times 10^{-14}$	$\Xi_{cc}^+ \to p + D^+ + \pi^+$	—	$\Xi_{cc}^+ \to \Lambda_c^+ + K^- + \pi^+$	—
bottom xi	Ξ_b^0	usb	0	1/2	—	1.42×10^{-12}	—	—		
	Ξ_b^-	dsb	-1	1/2	—	1.42×10^{-12}	$\Xi_b^- \to J/\psi + \Xi^-$	—		
lambda	Λ^0	uds	0	1/2	1115.68	2.63×10^{-10}	$\Lambda^0 \to p + \pi^-$	63.9%	$\Lambda^0 \to n + \pi^0$	35.8%
charmed lambda	Λ_c^+	udc	$+1$	1/2	2286.46	2.0×10^{-13}	$\Lambda_c^+ \to p + K^- + \pi^+$	5%	$\Lambda_c^+ \to p + \bar{K}^0 + \pi^0$	3.3%
bottom lambda	Λ_b^0	udb	0	1/2	5620.2	1.41×10^{-12}	$\Lambda_b^0 \to \Lambda_c^+ + l^- + \bar{\nu}_l + \pi^+ + \pi^-$ (here l represents any lepton)	5.6%	$\Lambda_b^0 \to \Lambda_c^+ + l^- + \bar{\nu}_l$	5.0%
omega	Ω^-	sss	-1	3/2	1672.5	8.2×10^{-11}	$\Omega^- \to \Lambda^0 + \pi^+$	67.8%	$\Omega^- \to \Xi^0 + \pi^-$	23.6%
charmed omega	Ω_c^0	ssc	0	1/2	2697.5	6.92×10^{-14}	$\Omega_c^0 \to \Xi^0 + K^- + \pi^+$	—	$\Omega_c^0 \to \Omega^- + \pi^+$	—

D The Minimal Supersymmetric extension of the SMPP

Supersymmetry (SUSY) is a generalization of the space–time symmetries of quantum field theory that transforms fermions into bosons and vice versa. SUSY also provides a framework for the unification of particle physics and gravity, which is governed by the Planck energy scale ($\sim 10^{19}$ GeV) where the gravitational interactions become comparable in magnitude to the gauge interactions (e.g. Yao et al., 2006).

The MSSM consists of taking the fields of the two–Higgs–doublet extension of the SMPP[37]

$$H_u = (H_u^+,\, H_u^0) \quad \text{and} \quad H_d = \left(H_d^0,\, H_d^-\right)$$

and adding the corresponding supersymmetric partners (e.g. Yao et al., 2006). The supersymmetric partners of the gauge and Higgs bosons are fermions, whose names are obtained by appending *ino* at the end of the corresponding SMPP particle name (e.g. Yao et al., 2006). In Table D-1 we show a list of the SMPP particles and the respective MSSM *sparticles*.

The enlarged Higgs sector of the MSSM, which constitutes the minimal structure needed to guarantee the cancellation of anomalies from the introduction of the higgsino superpartners (e.g. Yao et al., 2006), corresponds to eight degrees of freedom (cf. Table D-4). When the EW symmetry is broken, three of them are the *would–be Nambu–Goldstone bosons* (G^0, $G^\pm$), which become the longitudinal components of the Z^0 and $W^\pm$ massive vector bosons[38]. The remaining five Higgs scalar mass eigenstates consist of three neutral scalars h^0, H^0, and A^0; and a charge $+1$ scalar H^+, and its conjugate charge -1 scalar H^-. The masses of A^0, H^0 and $H^\pm$ can in principle be arbitrarly large. On the other hand the mass of h^0 is upper bounded around ~ 150 GeV (e.g. Martin, 2006).

The supersymmetric partners of the EW gauge bosons (γ, Z^0 and $W^\pm$) are called *gauginos* and the supersymmetric partners of the Higgs boson are called *higgsinos* (e.g. Yao et al., 2006). Note, however, that before EW symmetry breaking the γ and Z^0 fields are decomposed into a B (superpartner: *Bino* $\tilde{B}$) and W^0 (superpartner: $\tilde{W}^0$) fields. After the EW symmetry breaking, the W^0 and the B fields mix to produce the physical Z^0 and γ fields, while the corresponding *s–fields*[39] mix to produce the zino $\tilde{Z}^0$ and the massless photino $\tilde{\gamma}$ (e.g. Aitchison, 2005).

The higgsinos and EW gauginos mix with each other because of the effects of EW symmetry breaking. The neutral higgsinos ($\tilde{H}_u^0$, $\tilde{H}_d^0$) and the neutral gauginos ($\tilde{B}$,

[37] A general property of any (renormalizable) supersymmetric extension of the SMPP is the presence of, at least, two Higgs doublets, which leads to an *extended Higgs sector* (e.g. Ellis et al., 2007).

[38] A vector boson is a boson with spin 1. A vector boson, A, can be decomposed into a transverse component ($A_\perp$) and a longitudinal component ($A_\parallel$; parallel to the direction of motion) such that the transversality condition ($\nabla . A_\perp = 0$) and the irrotational condition of the longitudinal component ($\nabla \times A_\parallel = 0$) are satisfied.

[39] Super–fields.

Table D-1: The SMPP particles and their supersymmetric partners (sparticles) according to the MSSM. Note, however, that before the EW symmetry breaking the γ (superpartner photino) and Z^0 (superpartner zino) fields are decomposed into a B (superpartner: *Bino* $\tilde{B}$) and W^0 (superpartner: *Wino* $\tilde{W}^0$) fields.

Particle	Symbol	Spin	Sparticle	Symbol	Spin
electron	e	1/2	selectron	$\tilde{e}$	0
muon	μ	1/2	smuon	$\tilde{\mu}$	0
tau	τ	1/2	stau	$\tilde{\tau}$	0
electron neutrino	ν_e	1/2	selectron sneutrino	$\tilde{\nu_e}$	0
muon neutrino	ν_μ	1/2	smuon sneutrino	$\tilde{\nu_\mu}$	0
tau neutrino	ν_τ	1/2	stau sneutrino	$\tilde{\nu_\tau}$	0
top	t	1/2	stop	$\tilde{t}$	0
bottom	b	1/2	sbottom	$\tilde{b}$	0
charm	c	1/2	scharm	$\tilde{c}$	0
strange	s	1/2	sstrange	$\tilde{s}$	0
up	u	1/2	sup	$\tilde{u}$	0
down	d	1/2	sdown	$\tilde{d}$	0
photon	γ	1	photino	$\tilde{\gamma}$	1/2
W	$W^\pm$	1	Wino	$\tilde{W}^0$	1/2
Z	Z^0	1	Zino	$\tilde{Z}$	1/2
gluon	g	1	gluino	$\tilde{g}$	1/2
Higgs	H	0	Higgsino	$\tilde{H}$	1/2

$\tilde{W}^0$) combine to form four mass eigenstates called *neutralinos*. The charged higgsinos ($\tilde{H}_u^+$, $\tilde{H}_d^-$) and winos ($\tilde{W}^+$, $\tilde{W}^-$) mix to form two mass eigenstates with charge ± 1 called *charginos*. We denote the neutralino and chargino mass eigenstates by $\tilde{N}_i$ ($i = 1, 2, 3, 4$) and $\tilde{C}_i^\pm$ ($i = 1, 2$)[40]. By convention, these are labeled in ascending order, so that $m_{\tilde{N}_1} < m_{\tilde{N}_2} < m_{\tilde{N}_3} < m_{\tilde{N}_4}$ and $m_{\tilde{C}_1} < m_{\tilde{C}_2}$. The lightest neutralino, $\tilde{N}_1$, is usually assumed to be the *lightest supersymmetric particle* (LSP), unless there is a lighter gravitino or unless *R–parity*[41] is not conserved, because it is the only MSSM particle that can make a good dark matter candidate (e.g. Martin, 2006).

There is a limit where EW symmetry breaking effects can be viewed as a small perturbation in the neutralino mass matrix. In that limit, the neutralino mass

[40] An alternative notation is: $\tilde{\chi}_i^0$ ($i = 1, 2, 3, 4$) for neutralinos and $\tilde{\chi}_i^\pm$ ($i = 1, 2$) for charginos.

[41] The concept of R–parity was introduced into the MSSM (and other extensions of the SMPP) in order to account to the observed conservation of the baryon number and the lepton number. Particles have $R = +1$ and sparticles have $R = -1$ (e.g. Barbier et al., 2005).

eigenstates are very nearly *bino–like* $\tilde{N}_1 \approx \tilde{B}$, *wino–like* $\tilde{N}_2 \approx \tilde{W}^0$ and *higgsino–like* $\tilde{N}_3, \tilde{N}_4 \approx (\tilde{H}_u^0 \pm \tilde{H}_d^0)/\sqrt{2}$ (e.g. Martin, 2006).

The *gluino* is the superpartner of the gluon. This colour octet fermion is unique among all of the MSSM sparticles because it cannot mix with any other particle in the MSSM. It is reasonable to suspect that the gluino is considerably heavier than the lighter neutralinos and charginos (e.g. Martin, 2006).

The supersymmetric partners of the quarks and leptons are spin–zero bosons: the *squarks*, charged *sleptons*, and *sneutrinos*. For a given fermion f, there are two supersymmetric partners, f_L and f_R which are scalar partners of the corresponding left and right handed fermion. However, in general, f_L and f_R are not mass–eigenstates, since there is $f_L - f_R$ mixing[42] (e.g. Yao et al., 2006).

In the MSSM there are 32 distinct masses corresponding to undiscovered particles, not including the gravitino[43]. Assuming that the mixing of first– and second–family squarks and sleptons is negligible, the mass eigenstates of the MSSM are listed in Table D-2.

The *Snowmass Points and Slopes* (SPS) are a set of benchmark points and parameter lines in the MSSM parameter space corresponding to different scenarios in the search for SUSY at present and future experiments (see e.g. Allanach et al., 2002, for a list of SPS scenarios).

The currently most popular SUSY breaking mechanisms are *minimal supergravity* (mSUGRA), *gauge–mediated SUSY breaking* (GMSB) and *anomaly–mediated SUSY breaking* (AMSB) (e.g. Allanach et al., 2002).

Here we consider, as an example, SPS1 which is a typical mSUGRA scenario. This model features a near–decoupling limit for the Higgs sector, and a bino–like $\tilde{N}_1$ LSP; nearly degenerate wino–like $\tilde{N}_2$, $\tilde{C}_1$; and higgsino–like $\tilde{N}_3$, $\tilde{N}_4$, $\tilde{C}_2$. The gluino is the heaviest superpartner. The squarks are all much heavier than the sleptons, and the lightest sfermion is a stau (e.g. Martin, 2006). The mass spectrum of supersymmetric particles and Higgs boson according to the SPS1a scenario is represented in Figure D-1 and in Table D-3. Note that in this scenario the masses of the second family coincide with the masses of the first family.

At the moment we only have lower limit masses for these particles (cf. Table D-3) and a list of assumptions that we see as reasonable. For example, it is perhaps not unlikely that (e.g. Martin, 2006):

[42] In principle, any scalars with the same electric charge, R–parity, and colour quantum numbers can mix with each other (e.g. Martin, 2006).

[43] If supersymmetry breaking occurs spontaneously, then a massless *Goldstone fermion* called the *goldstino* ($\tilde{G}$) must exist. The goldstino would then be the LSP and could play an important role in supersymmetric phenomenology. However, the goldstino is a physical degree of freedom only in models of spontaneously–broken global supersymmetry. If supersymmetry is a local symmetry, then the theory must incorporate gravity; the resulting theory is called *supergravity*. In models of spontaneously–broken supergravity, the goldstino is absorbed by the *gravitino* (the superpartner of the *graviton*). By this super–Higgs mechanism, the goldstino is removed from the physical spectrum and the gravitino acquires mass (e.g. Yao et al., 2006).

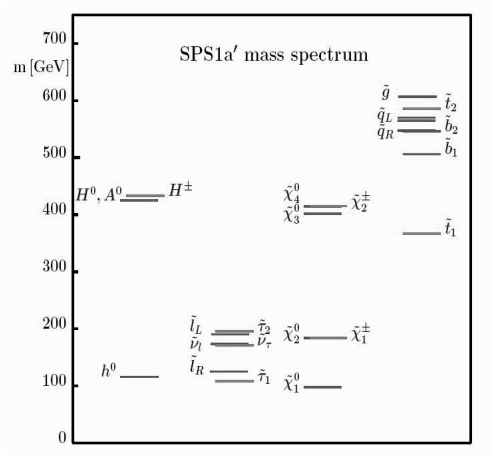

Figure D-1: Mass spectrum of supersymmetric particles and the Higgs boson according to the SPS1a scenario (cf. Table D-3 for mass values). Here ($\tilde{l}_L$,$\tilde{l}_R$, $\tilde{\nu}_l$) and ($\tilde{q}_L$, $\tilde{q}_R$) represent the first and the second families of sleptons and squarks respectively (e.g. Aguilar–Saavedra et al., 2006; Allanach et al., 2002).

- The LSP is the lightest neutralino $\tilde{N}_1$.
- The gluino will be much heavier than the lighter neutralinos and charginos.
- The squarks of the first and second families are nearly degenerate and much heavier than the sleptons.
- The lighter stop $\tilde{t}_1$ and the lighter sbottom $\tilde{b}_1$ are probably the lightest squarks.
- The lightest charged slepton is probably a stau $\tilde{\tau}$.
- The left–handed charged sleptons are likely to be heavier than their right-handed counterparts.
- The lightest neutral Higgs boson h^0 is lighter than about 150 GeV, and may be much lighter than the other Higgs scalar mass eigenstates A^0, $H^\pm$, H^0.

Extensions of the MSSM can be introduced, where the Higgs sector is further enlarged and the Higgs masses are less constrained. As an example we have the so–called *Next–to–Minimal Supersymmetric Standard Model* (NMSSM), whose Higgs sector includes not only two Higgs doublets, but also an additional singlet. Such an extension may slightly decrease the level of fine–tuning required to reconcile the present stringent lower bounds in supersymmetric particles and Higgs boson masses with the measured value of the Fermi scale (e.g. Ellis et al., 2007).

In Table D-4 we list the contribution that each particle and each sparticle species might give to $g(T)$ (see Section 1.1.6). Note that the contributions from squarks, sleptons and gluinos is identical to that of, respectively, quarks, leptons and gluons (apart from the factor 7/8). The Higgs sector now is formed by two doublets which gives 2×4 degrees of freedom. Each neutralino contributes with two degrees of

Table D-2: The MSSM particles in terms of gauge eigenstates and mass eigenstates. In the MSSM there are 32 distinct masses to be determined corresponding to 32 undiscovered particles.

Particles	Spin	Parity	Gauge Eigenstates	Mass Eigenstates
Higgs bosons	0	+1	$H_u^0\ H_d^0\ H_u^+\ H_d^-$	$h^0\ H^0\ A^0\ H^\pm$
squarks	0	−1	$\tilde{u}_L\ \tilde{u}_R\ \tilde{d}_L\ \tilde{d}_R$ $\tilde{s}_L\ \tilde{s}_R\ \tilde{c}_L\ \tilde{c}_R$ $\tilde{t}_L\ \tilde{t}_R\ \tilde{b}_L\ \tilde{b}_R$	(same) (same) $\tilde{t}_1\ \tilde{t}_2\ \tilde{b}_1\ \tilde{b}_2$
sleptons	0	−1	$\tilde{e}_L\ \tilde{e}_R\ \tilde{\nu}_e$ $\tilde{\mu}_L\ \tilde{\mu}_R\ \tilde{\nu}_\mu$ $\tilde{\tau}_L\ \tilde{\tau}_R\ \tilde{\nu}_\tau$	(same) (same) $\tilde{\tau}_1\ \tilde{\tau}_2\ \tilde{\nu}_\tau$
neutralinos	1/2	−1	$\tilde{B}^0\ \tilde{W}^0\ \tilde{H}_u^0\ \tilde{H}_d^0$	$\tilde{N}_1\ \tilde{N}_2\ \tilde{N}_3\ \tilde{N}_4$
charginos	1/2	−1	$\tilde{W}^\pm\ \tilde{H}_u^+\ \tilde{H}_d^-$	$\tilde{C}_1^\pm\ \tilde{C}_2^\pm$
gluino	1/2	−1	$\tilde{g}$	(same)

freedom corresponding to two possible helicity states and each chargino contributes with four degrees of freedom (two charges × two helicity states).

In Table D-5 we show the evolution of $g(T)$ for the MSSM, starting with $g(T) = 228.75$, which corresponds to the case when all particles are present (cf. equation 65), down to $g(T) = 95.25$, when the temperature equals the threshold of the *Lightest Supersymmetric Particle* (LSP). From that point on, the evolution of $g(T)$ proceeds within the SMPP, according to Table 2.

Table D-3: Mass spectrum of the supersymmetric particles and the Higgs boson according to the SPS1a scenario (e.g. Aguilar–Saavedra et al., 2006; Allanach et al., 2002). It is also shown the experimental lower limit for the mass of each particle (in the case of the h^0 we have an upper limit instead). See Yao et al. (2006) for a detailed list of lower mass limits and more details on this subject.

Particle	Spin	Mass (GeV)	Experimental lower limit (GeV)
h^0	0	116.0	< 150
H^0	0	425.0	
A^0	0	424.9	
$H^\pm$	0	432.7	
$\tilde{N}_1$	1/2	97.7	46
$\tilde{N}_2$	1/2	183.9	62
$\tilde{N}_3$	1/2	400.5	100
$\tilde{N}_4$	1/2	413.9	116
$\tilde{C}_1^\pm$	1/2	183.7	94
$\tilde{C}_2^\pm$	1/2	415.4	94
$\tilde{e}_R$	0	125.3	73
$\tilde{e}_L$	0	189.9	107
$\tilde{\nu}_e$	0	172.5	94
$\tilde{\mu}_R$	0	125.3	94
$\tilde{\mu}_L$	0	189.9	94
$\tilde{\nu}_\mu$	0	172.5	94
$\tilde{\tau}_R$	0	107.9	82
$\tilde{\tau}_L$	0	194.9	82
$\tilde{\nu}_\tau$	0	170.5	94
$\tilde{u}_R$	0	547.2	250
$\tilde{u}_L$	0	564.7	250
$\tilde{d}_R$	0	546.9	250
$\tilde{d}_L$	0	570.1	250
$\tilde{s}_R$	0	547.2	250
$\tilde{s}_L$	0	564.7	250
$\tilde{c}_R$	0	546.9	250
$\tilde{c}_L$	0	570.1	250
$\tilde{t}_1$	0	366.5	92
$\tilde{t}_2$	0	585.5	92
$\tilde{b}_1$	0	506.3	89
$\tilde{b}_2$	0	545.7	89
$\tilde{g}$	1/2	607.1	241

Table D-4: The number of degrees of freedom for each kind of particle within the MSSM: g_i is the contribution due to a single particle, N is the number of species of a particular particle and $g_N = Ng_i$ is the total contribution for $g(T)$ of each kind of particle.

Particle	g_i	N	g_N
quark	$12\frac{7}{8}$	6	63.0
charged lepton	$4\frac{7}{8}$	3	10.5
neutrino	$2\frac{7}{8}$	3	5.25
photon	2	1	2
gluon	2	8	16
EW bosons	2	3	6
Higgs	4	2	8
squark	12	6	72
charged slepton	4	3	12
sneutrino	2	3	6
neutralino	$2\frac{7}{8}$	4	7.0
chargino	$4\frac{7}{8}$	2	7.0
gluino	$2\frac{7}{8}$	8	14.0

Table D-5: The evolution of the number of degrees of freedom $g(T)$ in the Universe according to the MSSM (SPS1a scenario) starting with $g(T) = 228.75$, which corresponds to the case when all particles are present. As the expansion goes on, and the temperature T decreases, some particle species cease to exist (because T eventually gets below the particle threshold) lowering the value of $g(T)$. At the bottom we have the case $g(T) = 95.25$ which corresponds to the threshold of the LSP. From that point on, the evolution of $g(T)$ proceeds within the SMPP (Table 2).

Temperature (GeV)	Particles	g_i	$g(T)$
> 607.1			228.75
607.1	$\tilde{g}$	$16\frac{7}{8}$	214.75
585.5	$\tilde{t}_2$	6	208.75
570.1	$\tilde{c}_L\ \tilde{d}_L$	12	196.75
564.7	$\tilde{u}_L\ \tilde{s}_L$	12	184.75
547.2	$\tilde{u}_L\ \tilde{s}_L$	12	172.75
546.9	$\tilde{c}_R\ \tilde{d}_R$	12	160.75
545.7	$\tilde{b}_2$	6	154.75
506.3	$\tilde{b}_1$	6	148.75
432.7	$H^{\pm}$	2	146.75
425.0	H^0	1	145.75
424.9	A^0	1	144.75
415.4	$\tilde{C}_2^{\pm}$	$4\frac{7}{8}$	141.25
413.9	$\tilde{N}_4$	$2\frac{7}{8}$	139.50
400.5	$\tilde{N}_3$	$2\frac{7}{8}$	137.75
366.5	$\tilde{t}_1$	6	131.75
194.9	$\tilde{\tau}_L$	2	129.75
189.9	$\tilde{e}_L\ \tilde{\mu}_L$	4	125.75
183.9	$\tilde{N}_2$	$2\frac{7}{8}$	124.00
183.7	$\tilde{C}_1^{\pm}$	$4\frac{7}{8}$	120.50
172.5	t	$12\frac{7}{8}$	110.00
172.5	$\tilde{\nu}_e\ \tilde{\nu}_\mu$	4	106.00
170.5	$\tilde{\nu}_\tau$	2	104.00
125.3	$\tilde{e}_R\ \tilde{\mu}_R$	4	100.00
107.9	$\tilde{\tau}_R$	2	98.00
116.0	h^0	1	97.00
97.7	$\tilde{N}_1$	$2\frac{7}{8}$	95.25

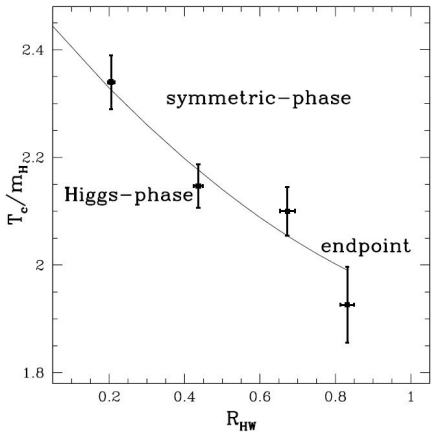

Figure E-1: EW phase diagram in the $T_c/m_H - R_{HW}$ plane with $R_{HW} = m_H/m_W$. The continuous line, representing the phase–boundary, is a quadratic fit to the data points. Above the line we are in the symmetric phase and below we are in the symmetry broken phase. However, this line, as an endpoint at $R_{HW} \approx 0.82$ (Csikor et al., 1998).

E The EW phase transition

The first phase transition predicted by the SMPP is the *EW phase transition* which occurs at a temperature $T_{EW} \sim 100$ GeV and at a time scale $t_{EW} \sim 10^{-10}$ s (e.g. Unsöld & Bascheck, 2002). At this temperature, which corresponds to an energy scale of the order of the masses of the Z^0 and $W^{\pm}$ vector bosons (Table C-3), the weak interactions become short ranged after a symmetry breaking phase transition. For $T < T_{EW}$ the Z^0 and $W^{\pm}$ vector bosons acquire masses through the Higgs mechanism while the photon remains massless, corresponding to the unbroken symmetry of the electromagnetic interactions (e.g. Boyanovsky et al., 2006).

In the EW standard model (*Glashow–Salam–Weinberg model*) the Higgs field is responsible for the dynamical mass generation via spontaneous symmetry breaking. At sufficiently high temperatures, $T > T_{EW}$, the expectation value of the Higgs field is zero, i.e., the symmetry is restored and particles are massless. At $T < T_{EW}$ the symmetry breakes and particle masses become finite (e.g. Kämpfer, 2000). During this transition, according to the SMPP, all particles except the Higgs acquire their mass by the mechanism of spontaneous symmetry breaking (e.g. Schwarz, 2003).

Csikor et al. (1998) obtained, using a nonperturbative analysis, that the phase transition is of first–order for Higgs masses less than 66.5 ± 1.4 GeV while for larger Higgs masses only a rapid crossover is expected (see Figure E-1). This value must be perturbatively transformed to the full Standard Model yielding 72.4 ± 1.7 GeV (Csikor et al., 1998). The exact determination of this critical Higgs–mass value, $m_{H,c}$, at which the first–order EW phase transition changes to a crossover is important given its implications for the standard model (e.g. Karsch et al., 1996).

The location of the endpoint of the first–order phase transition line is seen to move to smaller values of the Higgs mass as the chemical potentials μ are increased, indicating

that the chemical potentials make the transition weaker. At the same time, the critical temperature is slightly increased. The value $m_{H,c} \approx 72$ GeV corresponds to the case $\mu = 0$. If, for example, $\mu \approx 30$ GeV then we have $m_{H,c} \approx 66$ GeV (e.g. Gynther, 2006).

The current mass limit for the Higgs is 114.3 GeV at 95% confidence level (see Yao et al., 2006) suggesting that the standard model does not feature a sharp EW phase transition (either first or second order) but it is rather a smooth Crossover (e.g. Boyanovsky et al., 2006). Since the change in relativistic degrees of freedom is tiny ($\Delta g = 1$, cf. Section 1.1.6) this is also a very boring event from the thermodynamical perspective (e.g. Schwarz, 2003). Since the Higgs sector of the theory carries only four of the total of 106.75 degrees of freedom (see Section 1.1.6), the contribution of the Higgs to the pressure is not easily visible (e.g. Gynther, 2006). Nevertheless, a first–order phase transition is still allowed in several extensions of the SMPP, including the MSSM[44] (e.g. Kajantie et al., 1998, Appendix D).

In the standard model, EW symmetry breaking is induced by the ground state of a single doublet scalar field. We can write the potential for the real scalar component of the doublet which acquires a vacuum expectation value as (e.g. Anderson & Hall, 1992)

$$U(\phi) = \frac{\lambda_0}{4}\left(\phi^2 - \phi_0^2\right)^2$$

where ϕ_0 is the expectation value of the Higgs field and λ_0 is related to the Higgs boson mass by (e.g. Anderson & Hall, 1992)

$$m_H^2 = 2\lambda_0\phi_0^2.$$

The EW phase transition takes place when the expectation value of the Higgs field passes from its high temperature value $\langle\phi\rangle = 0$ to its nonzero value in the low temperature broken phase (e.g. Mégevand, 2000).

To reliably analyze the dynamics of this field, we need to include the interactions of the Higgs field with virtual particles and with the heat bath (Anderson & Hall, 1992). The one–loop, zero temperature potential, $V(\phi)$ can be written as the sum of the classical potential and a one–loop correction (Anderson & Hall, 1992)

$$V(\phi) = U(\phi) + \bar{V}_1(\phi).$$

If we adopt the renormalization prescriptions (e.g. Anderson & Hall, 1992)

$$V''(\phi_0) = m_H^2$$

$$V'(\phi_0) = 0$$

[44] In the case of the MSSM we have to consider two scalars (ϕ_1 and ϕ_2) corresponding to the two complex Higgs doublets H_1 and H_2 (cf. Appendix C) (e.g. Trodden, 1999).

for each degree of freedom to which the Higgs boson is coupled, the zero temperature one–loop correction to the effective potential is (see Anderson & Hall, 1992)

$$\bar{V}_1(\phi) = \pm\frac{1}{64\pi^2}\left[m^4(\phi)\ln\frac{m^2(\phi)}{m^2(\phi_0)} - \right.$$

$$\left. -\frac{3}{2}m^4(\phi) + 2m^2(\phi)m^2(\phi_0) - \frac{1}{2}m^4(\phi_0)\right]$$

where $\pm$ is for bosons (fermions) and $m(\phi)$ is the mass of the particle in the presence of the background field ϕ. In addition to these quantum corrections, we must also include the interaction between the Higgs field and the hot EW plasma. Taking the Higgs boson sufficiently light, the effective potential for the standard model can be reliably written as (e.g. Anderson & Hall, 1992)

$$V(\phi, T) = D(T^2 - T_0^2)\phi^2 - ET\phi^3 + \frac{\lambda_T}{4}\phi^4. \tag{E-1}$$

All the parameters in equation (E-1) depend on the particle content of the theory (e.g. Mégevand, 2000). Parameter D contains contributions from all the particles that acquire their masses through the Higgs mechanism and is given by (Anderson & Hall, 1992)

$$D = \frac{1}{8\phi_0^2}\left(2m_W^2 + m_Z^2 + 2m_t^2\right),$$

while the coefficient of the term linear in temperature, E, which has only boson contributions, is given by (Anderson & Hall, 1992)

$$E = \frac{1}{4\pi\phi_0^3}\left(2m_W^3 + m_Z^3\right).$$

In the SMPP we have $D \sim 10^{-1}$ and $E \sim 10^{-2}$ while in the MSSM, due to the larger particle zoo (see e.g. Table D-3), D and E can be more than an order of magnitude larger than in the SMPP (e.g. Mégevand, 2000).

The temperature–dependent ϕ^4 coupling can be written as (e.g. Gynther, 2006)

$$\lambda_T = \lambda - \frac{3}{16\pi^2\phi_0^4}\left(2m_W^4\ln\frac{m_W^2}{c_B T^2} + m_Z^4\ln\frac{m_Z^2}{c_B T^2} - 4m_t^4\ln\frac{m_t^2}{c_F T^2}\right)$$

where the masses are evaluated at $\langle\phi\rangle = \phi_0$ and we have $c_B \simeq 5.41$ and $c_F \simeq 2.64$ (Anderson & Hall, 1992). Although the parameter λ_T is temperature–dependent, it is almost constant in the range of temperatures in which the phase transition can take place. However, this parameter is very sensitive to the Higgs mass (e.g. Mégevand, 2000).

The potential (E-1) is to be regarded as a phenomenological one, valid in the vicinity of T_c. The parameters T_0, D, E and λ_T are to be chosen so that the potential quantitatively correctly describes the phase transition (Ignatius, 1993).

The physical Higgs mass is related to λ by (Anderson & Hall, 1992)

$$m_H^2 = (2\lambda + 12B)\,\phi_0^2$$

where

$$B = \frac{3}{64\pi^2\phi_0^4}\left(2m_W^4 + m_Z^4 - 4m_t^4\right).$$

The temperature T_0 is defined as the temperature where $V''(\phi = 0) = 0$, i.e., the lowest temperature where the symmetric vacuum can exist (e.g. Ignatius, 1993); it is given by (Anderson & Hall, 1992)

$$T_0^2 = \frac{1}{4D}\left(m_H^2 - 8B\phi_0^2\right) \equiv \chi^2(m_t, m_H)m_H^2. \tag{E-2}$$

Here all the masses are measured at zero temperature and $\phi_0 = 246$ GeV is the value of the scalar condensate at $T = 0$ (e.g. Gynther, 2006).

At high temperatures, i.e., temperatures well above T_0, the only minimum of the potential is achieved when the expectation value of the scalar field vanishes ($\langle\phi\rangle = 0$) and, thus, the symmetry is exact. As the early Universe cools down from this high temperature, a second local minimum of the potential first appears (as an inflection point) when the temperature reaches (Anderson & Hall, 1992)

$$T_* = \frac{T_0}{\sqrt{1 - \frac{9}{8}\frac{E^2}{\lambda_T D}}}. \tag{E-3}$$

The value of the field when $T = T_*$ is given by (Anderson & Hall, 1992)

$$\phi_* = \frac{3ET_*}{2\lambda_T}.$$

At lower temperatures, this point splits into a barrier ϕ_- and a local minimum ϕ_+ which subsequently evolves as (Anderson & Hall, 1992)

$$\phi_\pm = \frac{3ET}{2\lambda_T}\left(1 \pm \sqrt{1 - \frac{8}{9}\frac{\lambda_T D}{E^2}\left(1 - \frac{T_0^2}{T^2}\right)}\right).$$

The cubic term in $V(\phi, T)$ is responsible for the coexistence of two minima separated by a barrier, and subsequently, for the eventual first–order nature of the phase transition. Hence, the strength of the transition depends on the value of the parameter E (e.g. Mégevand, 2000).

The evolution of ϕ_- and ϕ_+ is shown in Figure E-2. We define the temperature T_c to be the temperature at which the second minimum becomes degenerate with the origin: $V(\phi_+(T_c)) = 0$. Hence, if we divide equation (E-1) by ϕ^2, T_c occurs where

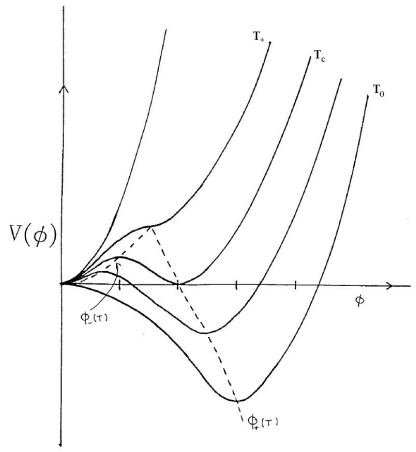

Figure E-2: A schematic plot of the evolution of the scalar potential V for different values of temperature. Also represented is the evolution of ϕ_- and ϕ_+. Here T_0 represents the temperature for which $V''(\phi = 0) = 0$, i.e., the lowest temperature where the symmetric vacuum can exist (equation E-2), T_* is the temperature for which a second local minimum of the potential first appears (equation E-3) and T_c is the temperature at which that second minimum becomes degenerate with the origin (equation E-4) (adapted from Anderson & Hall, 1992).

the resulting quadratic equations have two real equal roots. This gives the relation[45] (Anderson & Hall, 1992)

$$T_c = \frac{T_0}{\sqrt{1 - \frac{E^2}{\lambda_{T_0} D}}}. \tag{E-4}$$

At this critical temperature T_c the two minima become degenerate, and below this temperature the stable minimum of V is at (e.g. Mégevand, 2000)

$$\phi_+ = \frac{3ET}{2\lambda_{T_0}} \left(1 + \sqrt{1 - \frac{8}{9} \frac{\lambda_{T_0} D}{E^2} \left(1 - \frac{T_0^2}{T^2} \right)} \right).$$

When the temperature reaches T_0 the barrier between minima disappears, and $\phi = 0$ becomes a maximum of the potential as it is clear from Figure E-2 (e.g. Mégevand, 2000).

The number $E^2/\lambda_{T_0} D$ is, in general, small, and the difference between T_c and T_0 is $\Delta T \lesssim 10^{-2} T_c$. However, things change rapidly as the temperature falls from T_c to T_0 (e.g. Mégevand, 2000).

The exact temperature of the transition T_t depends on the evolution of the bubbles after they are nucleated, which, in turn, depends on the viscosity of the plasma (e.g. Mégevand, 2000).

[45] Some authors (e.g. Gynther, 2006) prefer to indicate λ_{T_c} instead of λ_{T_0}. In fact, as we shall see, the difference between T_c and T_0 is very small and, hence, $\lambda_{T_c} \approx \lambda_{T_0}$. We prefer to indicate λ_{T_0} because we will determine the value of T_c with the help of the value of T_0.

Considering the present known values for m_W, m_Z, m_t and m_H (see Appendix C) we obtain $D \approx 0.179$, $B \approx -0.00523$, $E \approx 0.0101$, $\lambda \approx 0.1393$, $T_0 \approx$ 137.8 GeV, $\lambda_{T_0} \approx 0.1321$ and $T_c \approx 138.1$ GeV. The value obtained for T_c agrees with the value indicated in the literature which is $T_c \sim 100$ GeV. Thus, we consider

$$T_c = 100 \text{ GeV}.$$

F The quantum–to–classical transition

Although there is a great diversity of inflationary models (Section 1.1.2), they generically predict a gaussian and nearly scale invariant spectrum of primordial fluctuations which is an excellent fit to the highly precise wealth of data provided by the WMAP (e.g. Boyanovsky et al., 2006).

The inhomogeneities that we observe today do not display any property typical of their quantum origin. On the large cosmological scales probed by the observations, the fluctuations appear to us as random classical quantities. This means that there was, at some time in the past, a *quantum–to–classical* transition (Polarski, 2001).

Each field mode can be split into two linearly independent solutions: the *growing mode* and the *decaying mode*. At reentrance inside the Hubble radius, during the radiation–dominated or the matter–dominated stage, the decaying mode is usually vanishingly small, and can, therefore, be safely neglected. As a result, the field mode behaves like a stochastic classical quantity (for more details see Polarski (2001) and Polarski & Starobinsky (1996)).

The classical behaviour of the inflationary fluctuations is very accurate for the description of the CMB temperature anisotropy and LSS formation. In the context of PBH formation this is not always the case. The smallest PBHs can be produced as soon as the fluctuations reenter the Hubble radius right after inflation. However, at this stage the decaying mode still had no time to disappear completely and, as a consequence, one cannot speak about classical fluctuations (Polarski, 2001).

The degree to which the effective quantum–to–classical transition will occur is given by the ratio (Polarski, 2001)

$$D_k = \frac{\phi_{k,gr}}{\phi_{k,dec}} \tag{F-1}$$

of the growing mode (gr) to the decaying mode (dec) of the peculiar gravitational potential $\phi(k)$. Very large values of D_k will correspond to an effective quantum–to–classical transition. Equation (F-1) can be written as a function of the PBH mass (Polarski, 2001)

$$D(M_{PBH}) = 4AGH_k^2 \frac{M_{PBH}}{m_{pl}^2} \tag{F-2}$$

where A is the growth factor of $\phi(k)$ between the inflationary stage and the radiation–dominated stage, H_k is the Hubble parameter at Hubble radius crossing during the inflationary stage and m_{pl} is the Planck mass. The ratio $D(M_{PBH})$ will grow with increasing M_{PBH}, due essentially to the last term in expression (F-2). Clearly, there is a range of scales where D will not be large and the quantum nature of the fluctuations is important (Polarski, 2001).

PBHs with masses less than $M_* \approx 10^{15}$ g will have either completely evaporated or, in any case, be in the latest stage of their evaporation. Expression (F-2) evaluated at

this natural cut–off for PBH masses gives $D(M_*) \simeq 10^{28}$ which means that one can safely use the effective classicality of the fluctuations for PBHs with initial masses $M_{PBH} \geq M_*$, i.e., all the non–evaporated PBHs. Hence, for all PBHs produced after approximately 10^{-23} s (cf. equation 21), the quantum–to–classical transition is already extremely effective. This means that quantum interference for these PBHs is essentially suppressed and one can really work to tremendously high accuracy with classical probability distributions (Polarski, 2001).

G PBHs from collapsing density perturbations

The dynamics of PBH formation from the collapse of density perturbations[46] in the early Universe are fully described by the general relativistic hydrodynamical equations of a perfect fluid, the field equations, the first law of Thermodynamics, and a suitable EoS (e.g. Niemeyer & Jedamzik, 1999a).

The idea is to introduce into the equations, as an initial condition, a density perturbation $\epsilon(R_s)$ superimposed on a uniform background with constant density ϵ_0 and then see the subsequent evolution of that perturbation.

Niemeyer & Jedamzik (1999a) considered three families of curvature perturbations expressed in the form of perturbations on the energy density. The first family of perturbations is described by a Gaussian–shaped overdensity that asymptotically approaches the FLRW solution

$$\epsilon(R_s) = \epsilon_0 \left[1 + A \exp\left(-\frac{R_s^2}{2(R_H/2)^2}\right)\right]. \tag{G-1}$$

The second is described by a mexican–hat function

$$\epsilon(R_s) = \epsilon_0 \left[1 + A\left(1 - \frac{R_s^2}{R_H^2}\right)\exp\left(-\frac{3R_s^2}{2R_H^2}\right)\right], \tag{G-2}$$

and the third by a sixth order polynomial

$$\epsilon(R_s) = \begin{cases} \epsilon_0 \left[1 + \frac{A}{9}\left(1 - \frac{R_s^2}{R_H^2}\right)\left(3 - \frac{R_s^2}{R_H^2}\right)^2\right] & , R_s < \sqrt{3}R_H \\ \epsilon_0 & , R_s \geq \sqrt{3}R_H. \end{cases} \tag{G-3}$$

Here R_H represents the horizon length (see equation 20) at the initial time (the instant when the perturbation begins) and R_s is the circumferential radius. The amplitude A which appears in all the three families of perturbations, is a free parameter used to tune the initial conditions to sub or super criticality with respect to PBH formation. The critical amplitude, A_c, is strongly shape dependent, varying between $A_c = 3.04$ for mexican–hat perturbations and $A_c = 2.05$ for the Gaussian curve (Niemeyer, 1998). The shape of all the three perturbations for the critical case are ilustrated in Figure G-1. For the mexican–hat and polynomial perturbations, the excess energy in the overdense region is exactly balanced by the deficit in the outer underdense region, whereas the Gaussian ones have only an excess, decreasing asymptotically to the background value ϵ_0 (Musco et al., 2005).

Niemeyer & Jedamzik (1999a) found similar values of δ_c for all the three families of perturbations considered – $\delta_c = 0.67$ (mexican–hat), $\delta_c = 0.70$ (Gaussian), and $\delta_c = 0.71$ (polynomial) – suggesting a universal value of $\delta_c \approx 0.7$. The results

[46] For other proposed mechanisms for PBH formation see (e.g. Carr, 2005; Mack et al., 2007).

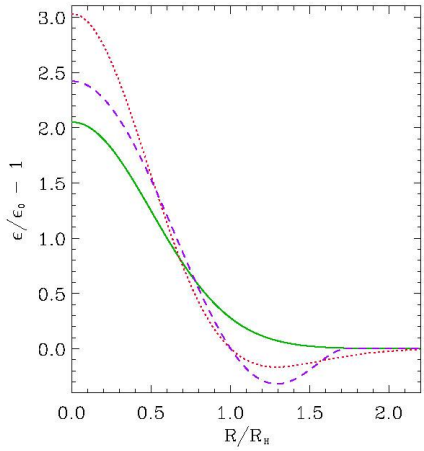

Figure G-1: Shapes of the critical perturbations: Gaussian (solid line, equation G-1), mexican–hat (dotted line, equation G-2), and polynomial (dashed line, equation G-3) (Niemeyer & Jedamzik, 1999a).

were confirmed by Musco et al. (2005) when considering perturbations on length–scales much larger than the horizon scale and well within the linear regime. However, when considering growing–mode perturbations Musco et al. (2005) encountered very similar curves and almost identical values of γ but substantially different values for the critical threshold ($\delta_c \simeq 0.43$ for mexican–hat perturbations and $\delta_c \simeq 0.47$ for polynomial perturbations).

As an example, we consider (Musco et al., 2005) the formation of a $0.4415 M_H$ PBH from a growing–mode mexican–hat perturbation with $R_0 = 5R_H$ (R_0 is the radius of the overdensity) and $\delta - \delta_c = 2.37 \times 10^{-3}$ at horizon crossing. In Figure G-2 we see the behaviour of the fluid worldlines where it is possible to note the separation between the matter which goes to form the PBH and the matter which continues to expand with the rest of the Universe, as well as the semi–evacuated region being formed between them. Notice that some of the outer material first decelerates but then accelerates again before crossing this semi–evacuated region to fall onto the PBH (Musco et al., 2005).

Figure G-3 shows the behaviour of the ratio $2M/R_s$ plotted against R_s at successive times. The event horizon corresponds to the asymptotic location of the outermost trapped surface. Remembering that the PBH only forms asymptotically we may introduce, as an operational definition for M_{PBH}, the condition $(1-2M/R_s) \leq 10^{-4}$ (Musco et al., 2005). Also in Figure G-3 we show a plot of M against R_s. Notice that the profiles for M become very flat just outside the PBH region at late times. This is a consequence of the very low densities reached there ($< 10^{-4}$ times the background density at the horizon–crossing time) (Musco et al., 2005).

Figure G-4 shows, as another example, the evolution of a near critical polynomial perturbation. The curve displays the energy density, ϵ/ϵ_0, at constant proper time, τ, for each mass shell, as a function of the circumferential radius R_s. The initial horizon size, R_H is normalized to unity. Initially, the central overdensity grows in

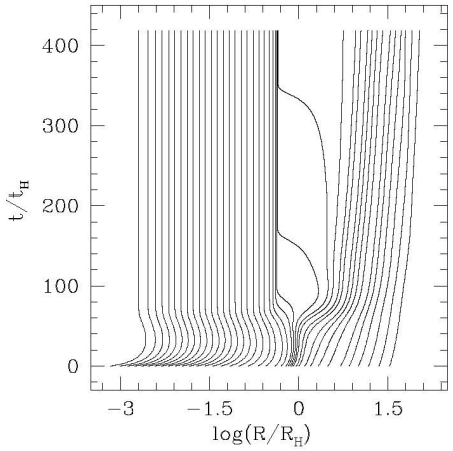

Figure G-2: The fluid element worldlines for a mexican–hat perturbation with $\delta - \delta_c = 2.37 \times 10^{-3}$ at the horizon crossing time. The time is measured in units of the horizon–crossing time t_H (Musco et al., 2005).

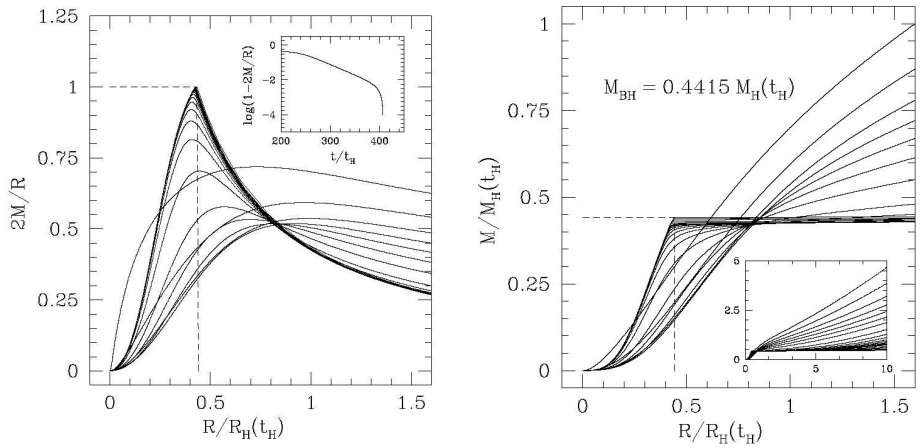

Figure G-3: The evolution of a mexican–hat perturbation with $\delta - \delta_c = 2.37 \times 10^{-3}$ at the horizon crossing time: the profile of $2M/R_s$ at different times, with the inset showing the approach of the maximum value of $2M/R_s \to 1$ (left), and the evolution of the mass–energy (right). In both cases the time sequence of the curves goes from top to bottom on the right hand side. (Musco et al., 2005).

amplitude while the outer underdensity, if present in the initial conditions, gradually widens and levels out. A PBH with $M_{PBH} \approx 0.36 M_H$ forms in the interior. Some time after the initial formation of an event horizon, material close to the PBH, but outside the event horizon, bounces and launches a compression wave traveling outward. This compression wave is connected to the PBH by a rarefaction region that evacuates the immediate vicinity of the PBH (Niemeyer & Jedamzik, 1999a). The shock forms because the pulse moves with a higher velocity than the background material (Hawke & Stewart, 2002).

The bounce of material outside the newly formed PBH is a feature intrinsic only to BHs very close to the formation threshold δ_c. As Figure G-5 demonstrates, no

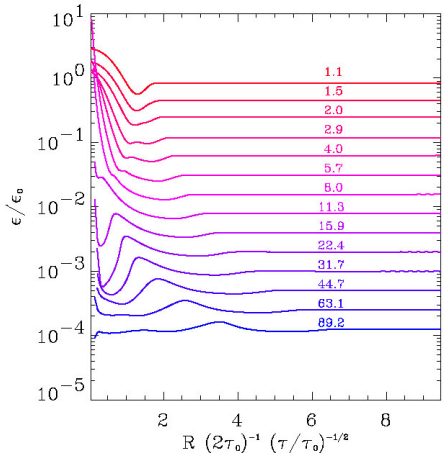

Figure G-4: Time evolution of a near–critical polynomial perturbation with initial $\delta = 0.7175$. A PBH with mass $M_{PBH} = 0.36 M_H$ forms in the interior (Niemeyer & Jedamzik, 1999a).

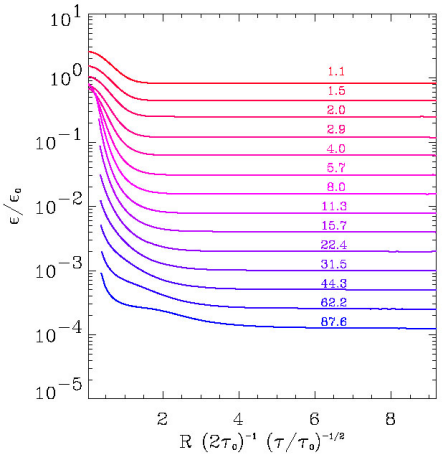

Figure G-5: Time evolution of an overcritical Gaussian perturbation with initial $\delta = 0.7196$. A PBH with mass $M_{PBH} = 2.75 M_H$ forms in the interior (Niemeyer & Jedamzik, 1999a).

bounce occurs if the initial conditions are sufficiently far above the threeshold. In this case a large PBH with $M_{PBH} = 2.75 M_H$ is formed. Here the event horizon reaches further out, encompassing regions where the pressure gradient is smaller, preventing pressure forces from overcoming gravitational attraction (Niemeyer & Jedamzik, 1999a).

The qualitative picture of collapses leadind to PBH formation is not changed very greatly by the presence of a Λ term (Musco et al., 2005).

G.1 PBHs from cosmological phase transitions

The pressure response of a radiation fluid is given by equation (12). Any decrease of the pressure response of the radiation fluid may yield a reduction of the threshold δ_c. Such a behaviour is expected to occur during cosmological first–order phase

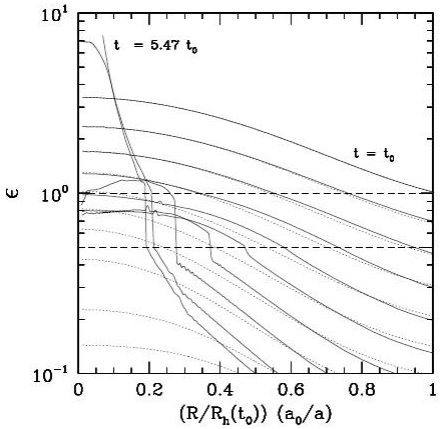

Figure G-6: Energy density, ϵ, as a function of the circumferential radius, $R_s = (R/R_k(t_0))(a_0/a)$, for a fluctuation with initial density contrast $\delta = 0.535$ at horizon crossing. The initial horizon at t_0 is located at $R_s = 1$. From top to bottom, solid lines show the fluctuation at 1.0, 1.22, 1.49, 1.82, 2.22, 2.72, 3.32, 4.06, 4.95, and 5.47 times the initial time t_0. The horizontal dashed lines indicate the energy densities at onset and completion of the phase transition. The dotted lines show, for comparison, the evolution of a fluctuation with the same initial fluctuation parameters, but entering the cosmological horizon during an epoch with EoS $p = \rho/3$. The formation of a PBH with $M_{PBH} \approx 0.34 M_H(t_0)$ results (Jedamzik & Niemeyer, 1999).

transitions (e.g. Jedamzik & Niemeyer, 1999).

A reduction of the PBH formation threshold for fluctuations which enter the cosmological horizon during first–order phase transitions may have cosmological implications. The slightest reduction of δ_c may result in the formation of PBHs with masses of the order of the horizon mass during the first–order phase transition, yielding a highly peaked PBH mass function (e.g. Jedamzik & Niemeyer, 1999).

Jedamzik & Niemeyer (1999) studied the evolution of density fluctuations upon horizon crossing during a cosmological first–order phase transition. In Figure G-6 we show, as an example, the evolution of the radial energy density profile of a fluctuation, with overdensity $\delta = 0.535$, from the initial horizon crossing time t_0 to $5.47 t_0$. The fluctuations self–gravity exceeds pressure forces such that the fluctuation separates from the Hubble flow and recollapses to high–energy densities at the centre until an event horizon forms ($t \approx 5 t_0$). The resulting young PBH rapidly increases its mass up to $M_{PBH} \approx 0.06 M_H(t_0)$. Subsequent accretion of material into the young PBH continues until the immense pressure gradients close to the event horizon launch an outgoing pressure wave which significantly dilutes the PBH environment. Accretion thereafter is negligible. As a result we have, in this example, the formation of a PBH with initial mass $M_{PBH} \approx 0.34 M_H(t_0)$. For comparison, Figure G-6 also shows the evolution of a fluctuation with the same initial conditions, but entering the cosmological horizon during an ordinary radiation–dominated epoch. The strong pressure gradients experienced by the fluctuation entering the horizon during an epoch with an EoS $p = \rho/3$ prevent, in that case, the formation of a PBH (Jedamzik & Niemeyer, 1999).

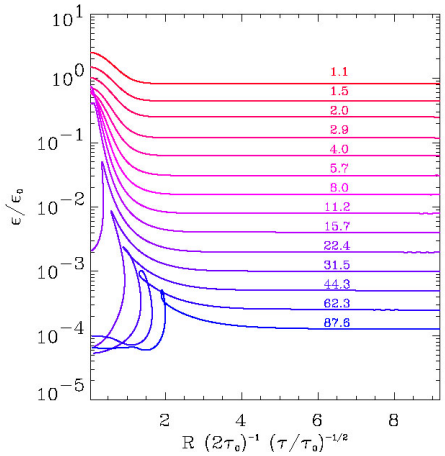

Figure G-7: Time evolution of an undercritical Gaussian perturbation. No PBH is formed (Niemeyer & Jedamzik, 1999a).

G.2 Evolution of subcritical perturbations

We have a subcritical perturbation when $\delta < \delta_c$. If $\delta \ll \delta_c$ the perturbation initially grows but then it vanishes into the surrounding medium. In Figure G-7 a situation where no PBH is formed is shown. The initial density perturbation turns into an acoustic wave or wave–package propagating to infinity (Novikov et al., 1979). Rarefaction waves travel from the fitting region toward the centre of the disturbance and outward. At a certain epoch the expansion in the inner region is replaced by a contraction. As the contraction proceeds, the pressure gradient rises to the point where the central core is dispersed, and a compression wave travels outward (Nadezhin et al., 1978).

H The threshold for PBH formation (variable δ_c)

In Chapter 4 we considered the evolution of the threshold for PBH formation δ_c for a background value $\delta_c = 1/3$. Here, we present some results for other background values of δ_c between 1/3 and 0.7.

H.1 QCD Bag Model

In Figure H-1 we consider, again, the cases $x = 2$, $x = 15$ and $x = 30$ (cf. Figures 23 and 24) but now with δ_c assuming several values between 1/3 and 0.7. Note that the new window for PBH formation, i.e., the region between δ_{c1} and δ_c or δ_{c2}, is larger for smaller values of δ_c (see Section 4.1 for more details). Similarly, in Figure H-2, we consider, again, the cases $x = 0.927$, $x = 0.6$ and $x = 0.308$ (cf. Figure 26) but now with δ_c assuming several values between 1/3 and 0.7 and, in Figure, H-3 we do the same now for the cases $x = 0.26$, $x = 0.22$, and $x = 0.11$ (cf. Figure 28). As a general conclusion we see that the window for PBH formation becomes larger for smaller values of δ_c.

Figure H-4 shows the region in the (x, δ) plane for which collapse to a PBH occurs with $x > 1$ for $\delta_c = 1/3$ and for $\delta_c = 0.7$ (cf. Figure 25). Without the phase transition, these would be two straight horizontal lines at $\delta = 1/3$ and $\delta = 0.7$. The intersection points $\delta_{c1} = \delta_{c2}$ ($x \approx 55$ when $\delta_c = 1/3$; $x \approx 13.8$ when $\delta_c = 0.7$) and $\delta_{c2} = \delta_c$ ($x = 12$ when $\delta_c = 1/3$; $x \approx 3.5$ when $\delta_c = 0.7$) are relevant for the calculation of β (see Chapter 5).

Figure H-5 indicates the region in the (x, δ) plane for which collapse to a PBH occurs with $y^{-1} < x < 1$ for $\delta_c = 1/3$ and for $\delta_c = 0.7$ (cf. Figure 27). Without the phase transition, these would be two straight horizontal lines at $\delta = 1/3$ and $\delta = 0.7$. In Figure H-6 we show the region in the (x, δ) plane for which collapse to a PBH occurs when $x < y^{-1}$ and $\delta_c = 1/3$ and $\delta_c = 0.7$ (cf. Figure 29).

H.2 QCD Crossover

Figure H-7 shows the region of the $(\log_{10}(t_k/1\text{s}), \delta)$ plane for which collapse to PBH occurs for $\delta_c = 1/3$ and for $\delta_c = 0.7$ (cf. Figure 33). Without the phase transition, these would be two straight horizontal lines at $\delta = 1/3$ and $\delta = 0.7$ (see Section 4.2 for more details).

H.3 QCD Lattice Fit

In Figure H-8 we show the region of the (x, δ) plane for which collapse to a PBH occurs when $\delta_c = 0.7$ (compare this with Figure 40). Without the phase transition, this would be a straight horizontal line at $\delta = 0.7$ (see Section 4.3 for more details).

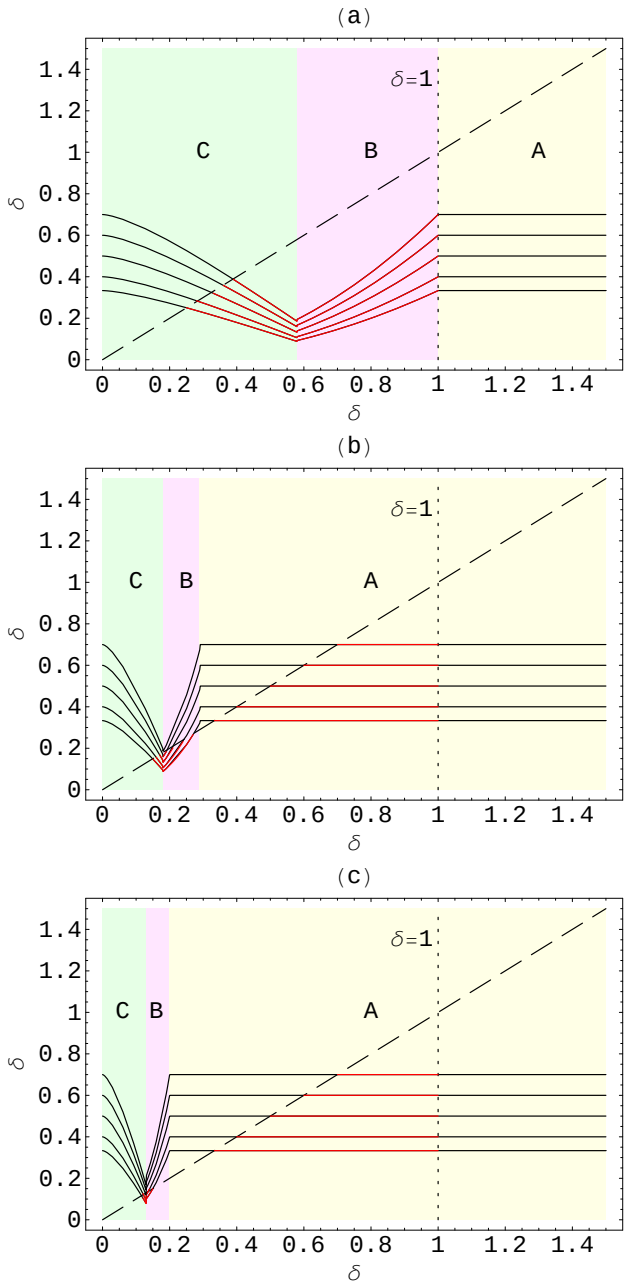

Figure H-1: PBH formation during the QCD transition according to the Bag Model for the cases: (a) $x = 2$, (b) $x = 15$, and (c) $x = 30$. The solid curves correspond to the function $(1 - f)\delta_c$ with, from bottom to top, $\delta_c = 1/3$, $\delta_c = 0.4$, $\delta_c = 0.5$, $\delta_c = 0.6$ and $\delta_c = 0.7$. In red we show the region where PBH formation takes place. The borders between the different classes (which do not depend in the value of δ_c) are given by: (a) $\delta_{AB} = 1$, $\delta_{BC} \approx 0.58$; (b) $\delta_{AB} \approx 0.29$, $\delta_{BC} \approx 0.18$; and (c) $\delta_{AB} \approx 0.20$, $\delta_{BC} \approx 0.13$ (see more details in Figures 23 and 24).

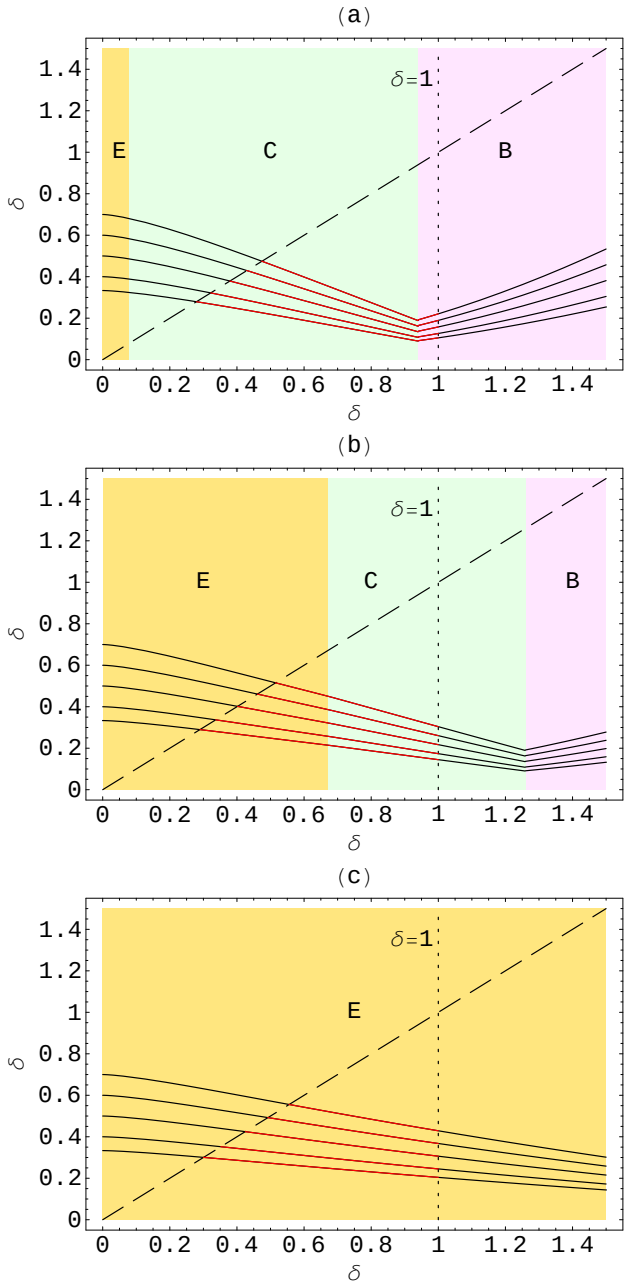

Figure H-2: PBH formation during the QCD transition according to the Bag Model for the cases: (a) $x = 0.927$, (b) $x = 0.6$ and (c) $x = 0.308$. The solid curves correspond to the function $(1 - f)\delta_c$ with, from bottom to top, $\delta_c = 1/3$, $\delta_c = 0.4$, $\delta_c = 0.5$, $\delta_c = 0.6$ and $\delta_c = 0.7$. The dashed line corresponds to the identity δ. The values of the borders between different classes are the same as in Figure 26 (they do not depend in the value of δ_c).

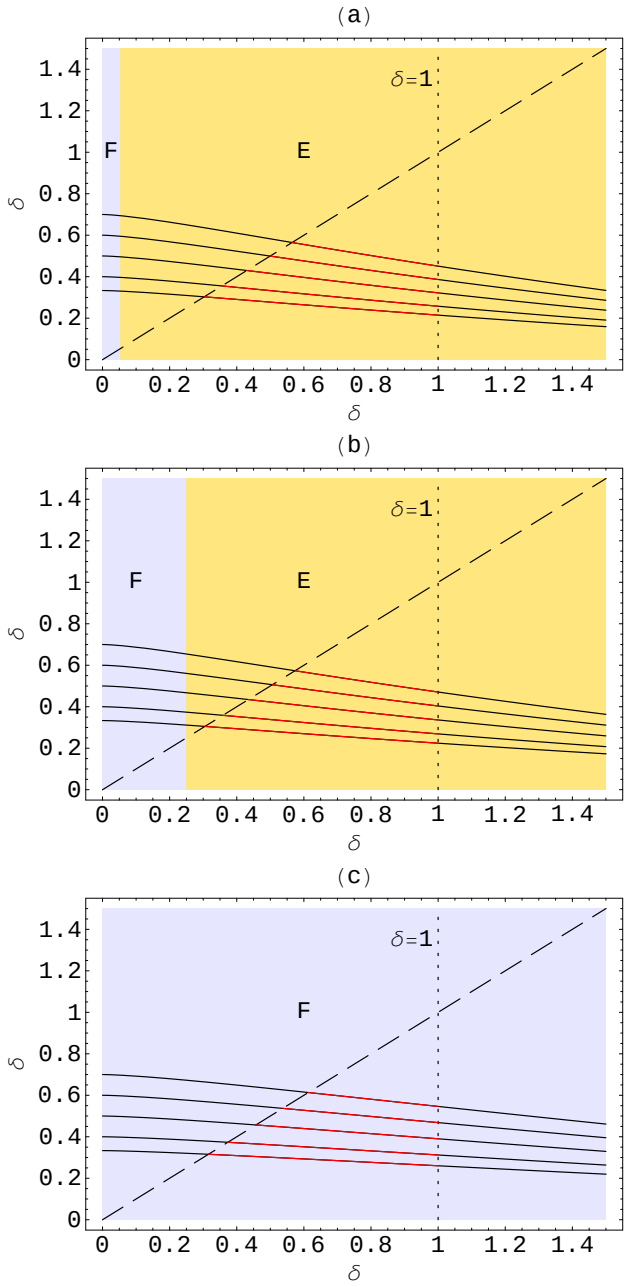

Figure H-3: PBH formation during the QCD transition according to the Bag Model for the cases: (a) $x = 0.26$, (b) $x = 0.22$ and (c) $x = 0.11$. The solid curves correspond to the function $(1 - f)\delta_c$ with, from bottom to top, $\delta_c = 1/3$, $\delta_c = 0.4$, $\delta_c = 0.5$, $\delta_c = 0.6$ and $\delta_c = 0.7$. The dashed line corresponds to the identity δ. The values of the borders between different classes are the same as in Figure 28 (they do not depend in the value of δ_c).

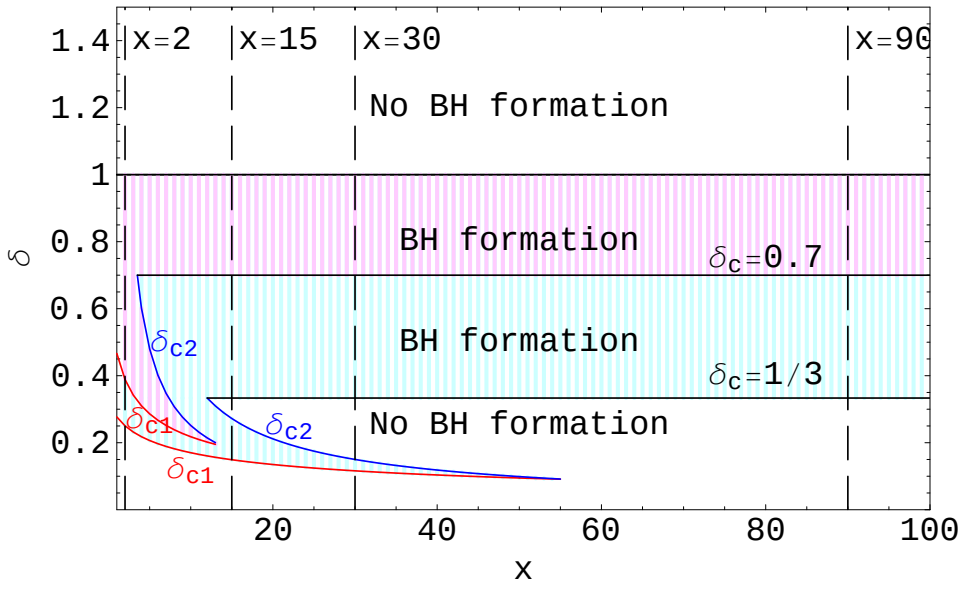

Figure H-4: The curve in the (x, δ) plane indicating which parameter values lead to collapse to a PBH, within the QCD Bag Model, in the case $x > 1$ with $\delta_c = 1/3$ and $\delta_c = 0.7$. We show the values of x corresponding to the cases presented in Figures 23, 24 and H-1. The intersection point $\delta_{c1} = \delta_{c2}$ occurs for $x \approx 55$ when $\delta_c = 1/3$ and $x \approx 13.8$ when $\delta_c = 0.7$. The intersection point $\delta_{c2} = \delta_c$ occurs for $x = 12$ when $\delta_c = 1/3$ and $x \approx 3.5$ when $\delta_c = 0.7$.

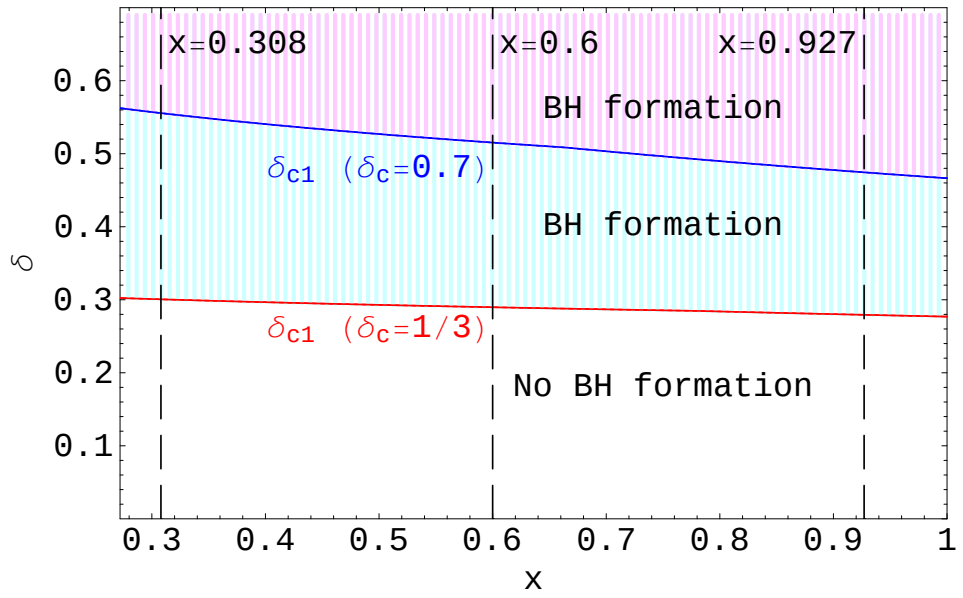

Figure H-5: The curve in the (x, δ) plane indicating which parameter values lead to collapse to a PBH, within the QCD Bag Model, in the case $y^{-1} < x < 1$ with $\delta_c = 1/3$–blue/pink region, and $\delta_c = 0.7$–pink region (note that, in both cases, the PBH formation region extends up to $\delta = 1$). We show the values of x corresponding to the cases presented in Figures 26 and H-2.

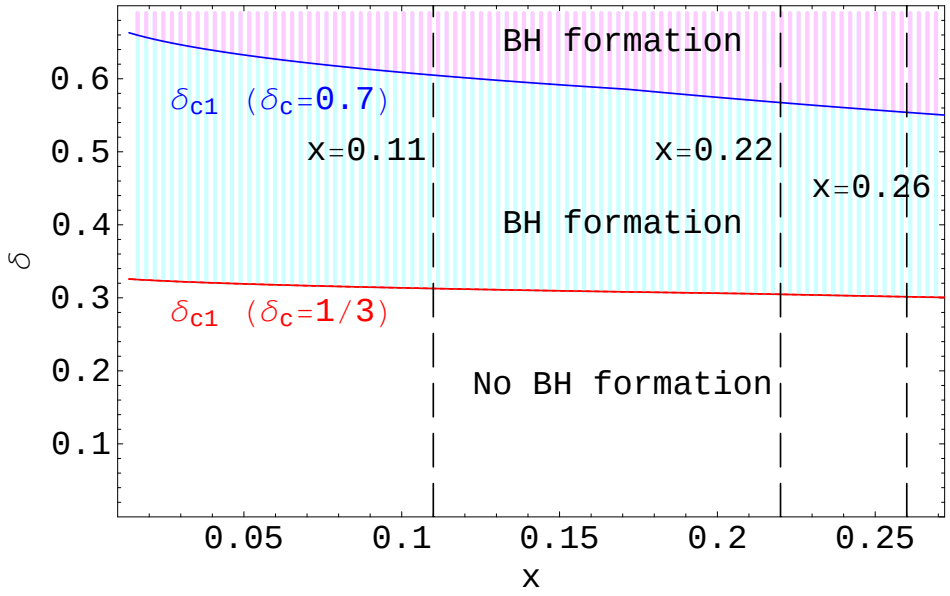

Figure H-6: The curve in the (x, δ) plane indicating which parameter values lead to collapse to a PBH, within the QCD Bag Model, in the case $x < y^{-1}$ with $\delta_c = 1/3$–blue/pink region, and $\delta_c = 0.7$–pink region (note that the PBH formation region extends, in both cases, up to $\delta = 1$). We show the values of x corresponding to the cases presented in Figures 28 and H-3.

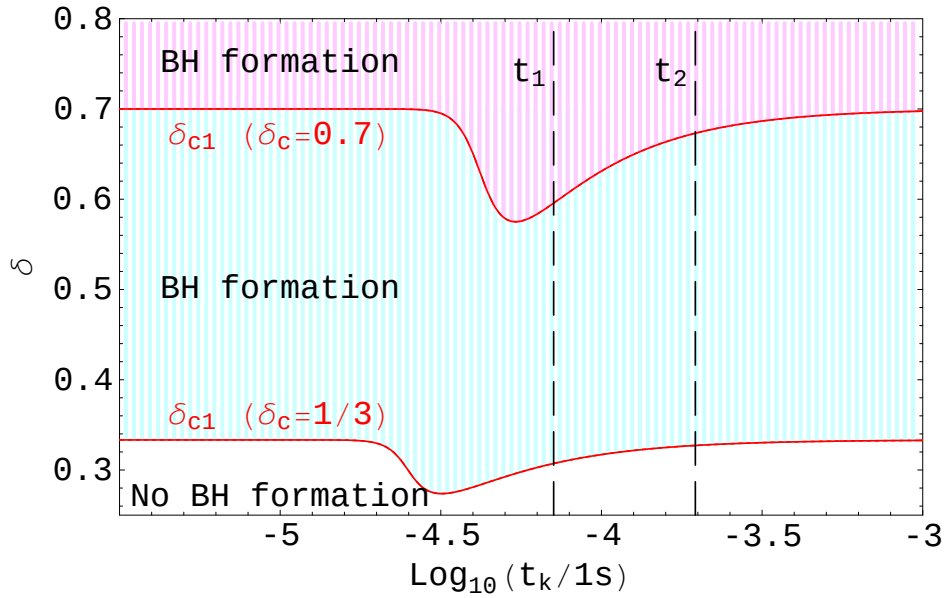

Figure H-7: The curve in the $(\log_{10}(t_k/1\mathrm{s}), \delta)$ plane indicating which parameter values lead to collapse to PBH in the case of a QCD Crossover with $\delta_c = 1/3$ and with $\delta_c = 0.7$. We have also represented, for reference, the values of t_1 and t_2 giving the locus of the transition (note that, in both cases, the PBH formation region extends up to $\delta = 1$).

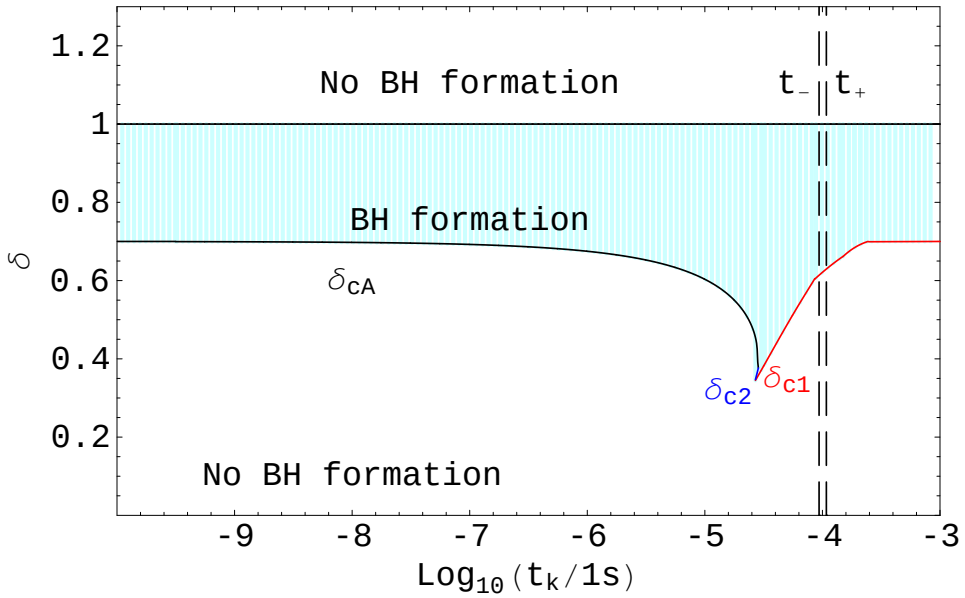

Figure H-8: The curve in the $(\log_{10}(t_k/1s),\ \delta)$ plane indicating which parameter values lead to collapse to a PBH in the case of the QCD Lattice Fit when $\delta_c = 0.7$. The vertical dashed lines correspond to $t_k = t_{QCD-}$ and $t_k = t_{QCD+}$.

H.4 EW Crossover (SMPP)

Figure H-9 indicates the region on the $(\log_{10}(t_k/1\text{s}),\ \delta)$ plane for which collapse to a PBH occurs for $\delta_c = 1/3$ and for $\delta_c = 0.4$. Without the phase transition, these would be two straight horizontal lines at $\delta = 1/3$ and $\delta = 0.4$ (see Section 4.4 for more details).

H.5 EW Bag Model (MSSM)

In Figure H-10 we show the region in the $(\log_{10}(t_k/1\text{ s}),\ \delta)$ plane for which PBH formation is allowed in the case $\delta_c = 0.7$. Without the phase transition this would be a straight horizontal line at $\delta = 0.7$ (see Section 4.5 for more details).

H.6 Electron–positron annihilation

Figure H-11 indicates the region on the $(\log_{10}(t_k/1\text{s}),\ \delta)$ plane for which collapse to a PBH occurs during the electron–positron annihilation epoch with $\Delta T = 0.115 T_c$ and δ_c assuming the values 1/3 and 0.7 (cf. Figure 45). Without the annihilation process these would be two straight horizontal lines at $\delta = 1/3$ and $\delta = 0.7$ (see Section 4.6 for more details).

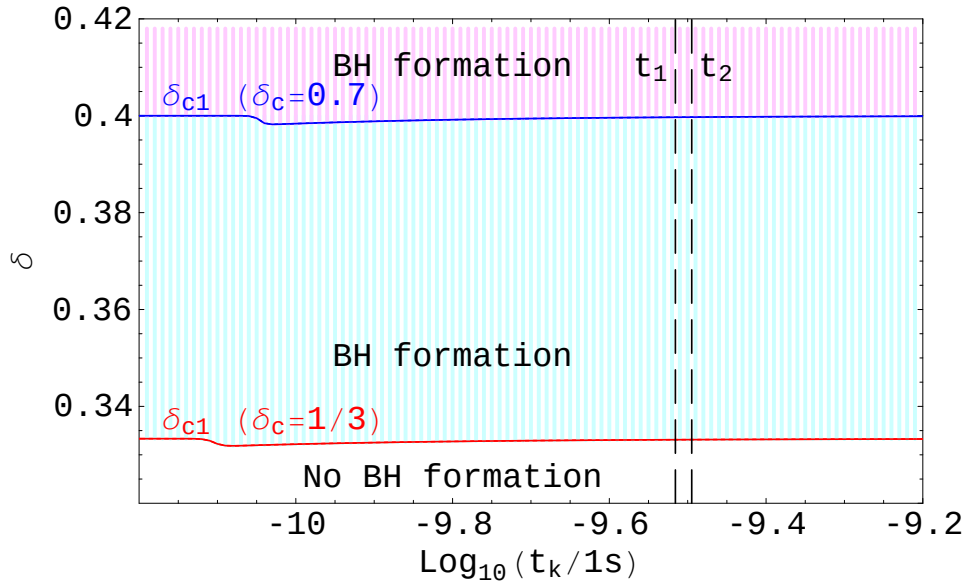

Figure H-9: The curve in the $(\log_{10}(t_k/1\text{s}),\ \delta)$ plane indicating which parameter values lead to collapse to a PBH in the case of the EW Crossover ($\Delta T = 0.013 T_c$) with $\delta_c = 1/3$–blue region, and $\delta_c = 0.4$–pink region (note that, in both cases, the PBH formation region extends up to $\delta = 1$). We have also represented, for reference, the values of t_1 and t_2 giving the locus of the transition (vertical dashed lines).

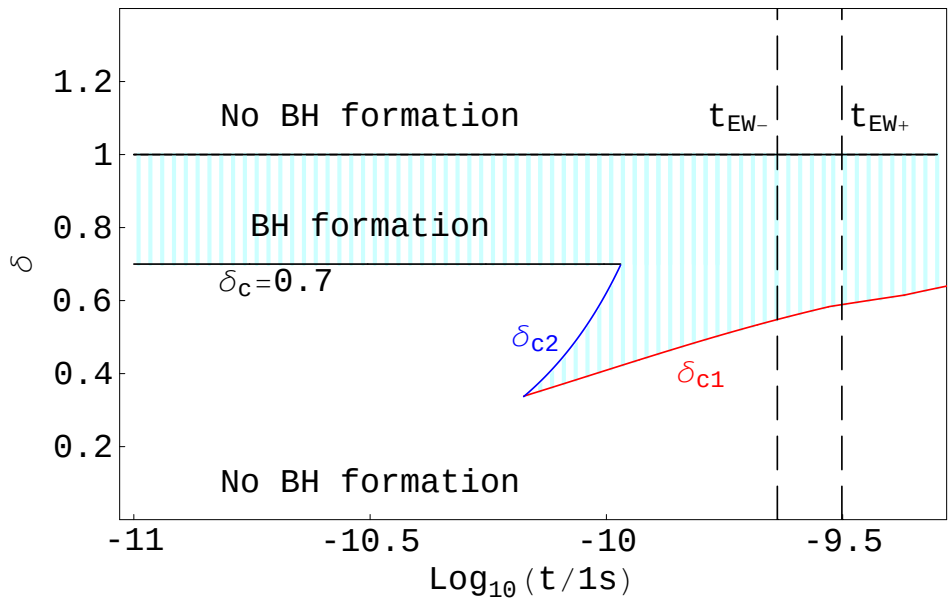

Figure H-10: The curve in the $(\log_{10}(t_k/1\text{ s}), \delta)$ plane indicating which parameter values lead to collapse to a PBH when $\delta_c = 0.7$ during the EW transition within the MSSM.

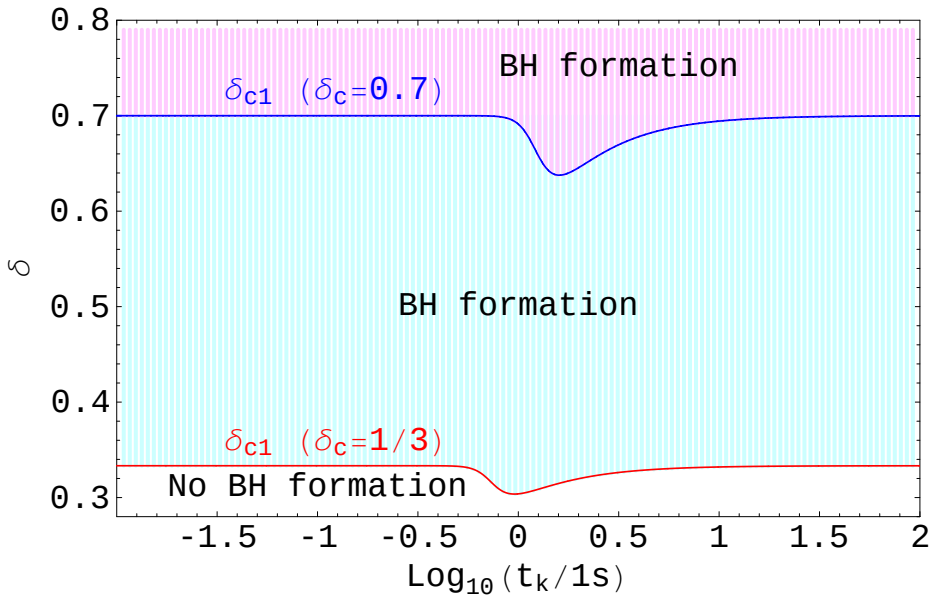

Figure H-11: The curve on the $(\log_{10}(t_k/1\text{s}),\ \delta)$ plane indicating which parameter values lead to collapse to a PBH in the case of the cosmological electron–positron annihilation for the cases $\delta_c = 1/3$ and $\delta_c = 0.7$ when $\Delta T = 0.115 T_c$. Without the annihilation process these would be two straight horizontal lines at $\delta = 1/3$ and $\delta = 0.7$.

I The parameters δ_{c1} and δ_{c2}

During cosmological phase transitions the threshold for PBH formation, δ_c, experiences a reduction. As a result, a new window for PBH formation (between δ_{c1} and δ_c or between δ_{c1} and δ_{c2}) is opened for a brief period.

In Table I-1 we present the new threshold for PBH formation during the QCD transition according to the Bag Model when $\delta_c = 1/3$. We have presented the values of δ_{c1} and δ_{c2} (where applicable) as a function of time and as a function of the parameter x (see Section 4.1 for more details).

In Table I-2 we present the new threshold for PBH formation during the QCD transition according to the Crossover model when $\delta_c = 1/3$ (see Section 4.2 for more details).

In Table I-3 we present the new threshold for PBH formation during the QCD transition according to the Lattice Fit model, when $\delta_c = 1/3$. Note that now there is a window between between δ_{cA} and δ_c. This window does not exist for the Bag Model case because, in that case, we have $f_A = 0$ (see Section 4.3 for more details).

In Table I-4 we present the new threshold for PBH formation during the QCD transition according to the Crossover model when $\delta_c = 1/3$ (see Section 4.4 for more details).

In Table I-5 we present the new threshold for PBH formation during the EW transition according to the Bag Model within the MSSM when $\delta_c = 1/3$. We have presented the values of δ_{c1} and δ_{c2} (where applicable) as a function of time and as a function of the parameter x (see Section 4.5 for more details).

Finally, in Table I-6, we present the new threshold for PBH formation during the electron–positron annihilation epoch when $\delta_c = 1/3$ (see Section 4.6 for more details).

Table I-1: The evolution of δ_{c1} and δ_{c2} (where applicable) as a function of time and as a function of the parameter x for a QCD phase transition according to the Bag Model when $\delta_c = 1/3$ (see Figures 30 and 31).

$\log_{10}(t_k/1\text{ s})$	x	δ_{c1}	δ_{c2}
-5.3	48.1	0.0963	0.102
-5.2	34.0	0.111	0.135
-5.1	24.1	0.126	0.181
-5.0	17.0	0.143	0.244
-4.9	12.0	0.161	0.333
-4.8	8.5	0.179	–
-4.7	6.0	0.197	–
-4.6	4.2	0.215	–
-4.5	2.9	0.233	–
-4.4	2.1	0.249	–
-4.3	1.4	0.264	–
-4.2	0.98	0.278	–
-4.1	0.583	0.290	–
-4.0	0.333	0.299	–
-3.9	0.197	0.307	–
-3.8	0.112	0.315	–

Table I-2: The evolution of δ_{c1} as a function of time for a QCD Crossover with $\Delta T = 0.1T_c$ when $\delta_c = 1/3$.

$\log_{10}(t_k/1\text{ s})$	δ_{c1}	$\log_{10}(t_k/1\text{ s})$	δ_{c1}
-5.0	0.333	-4.9	0.333
-4.8	0.333	-4.7	0.330
-4.6	0.299	-4.5	0.274
-4.4	0.281	-4.3	0.293
-4.2	0.303	-4.1	0.311
-4.0	0.317	-3.9	0.322
-3.8	0.325	-3.7	0.327
-3.6	0.329	-3.5	0.330
-3.4	0.331	-3.3	0.332
-3.2	0.332	-3.1	0.333

Table I-3: The evolution of δ_{cA}, δ_{c1} and δ_{c2} (where applicable) as a function of time for a QCD phase transition according to the Lattice Fit Model when $\delta_c = 1/3$.

$\log_{10}(t_k/1\text{ s})$	δ_{cA}	δ_{c2}	δ_{c1}
-7.5	0.3304	–	–
-7.4	0.3301	–	–
-7.3	0.3297	–	–
-7.2	0.3292	–	–
-7.1	0.3287	–	–
-7.0	0.3281	–	–
-6.9	0.3274	–	–
-6.8	0.3267	–	–
-6.7	0.3258	–	–
-6.6	0.3249	–	–
-6.5	0.3238	–	–
-6.4	0.3226	–	–
-6.3	0.3212	–	–
-6.2	0.3196	–	–
-6.1	0.3178	–	–
-6.0	0.3157	–	–
-5.9	0.3133	–	–
-5.8	0.3105	–	–
-5.7	0.3073	–	–
-5.6	0.3036	–	–
-5.5	0.2992	–	–
-5.4	0.2940	–	–
-5.3	0.2877	–	–
-5.2	0.2800	–	–
-5.1	0.2702	–	–
-5.0	0.2573	0.1450	0.1334
-4.9	0.2381	0.1941	0.1554
-4.8	–	–	0.1784
-4.7	–	–	0.2016
-4.6	–	–	0.2242
-4.5	–	–	0.2453
-4.4	–	–	0.2644
-4.3	–	–	0.2813
-4.2	–	–	0.2960
-4.1	–	–	0.3090
-4.0	–	–	0.3182
-3.9	–	–	0.3236

Table I-4: The evolution of δ_{c1} as a function of time for a EW Crossover with $\Delta T = 0.013 T_c$ when $\delta_c = 1/3$.

$\log_{10}(t_k/1\text{ s})$	δ_{c1}	$\log_{10}(t_k/1\text{ s})$	δ_{c1}
-10.2	0.33333	-10.1	0.33205
-10.0	0.33221	-9.9	0.33254
-9.8	0.33277	-9.7	0.33293
-9.6	0.33305	-9.5	0.33313
-9.4	0.33319	-9.3	0.33323
-9.2	0.33326	-9.1	0.33328
-9.0	0.33330	-8.9	0.33331
-8.8	0.33332	-8.7	0.33332
-8.6	0.33332	-8.5	0.33333

Table I-5: The evolution of δ_{c1} and δ_{c2} (where applicable) as a function of time and as a function of the parameter x for an EW phase transition according to the Bag Model when $\delta_c = 1/3$ (see Figure 43).

$\log_{10}(t_k/1\text{ s})$	x	δ_{c1}	δ_{c2}
-10.5	22.5	0.167	0.191
-10.4	15.9	0.185	0.258
-10.3	11.2	0.203	–
-10.2	7.9	0.221	–
-10.1	5.5	0.238	–
-10	3.9	0.254	–
-9.9	2.7	0.268	–
-9.8	1.9	0.281	–
-9.7	1.3	0.292	–
-9.6	0.81	0.302	–
-9.5	0.46	0.310	–
-9.4	0.28	0.316	–
-9.3	0.15	0.322	–

Table I-6: The evolution of δ_{c1}, as a function of time, for the cosmological electron–positron annihilation with $\Delta T = 0.115 T_c$ when $\delta_c = 1/3$.

$\log_{10}(t_k/1\text{ s})$	δ_{c1}	$\log_{10}(t_k/1\text{ s})$	δ_{c1}
-0.5	0.3333	-0.4	0.3333
-0.3	0.3327	-0.2	0.3273
-0.1	0.3096	0	0.3039
0.1	0.3087	0.2	0.3147
0.3	0.3197	0.4	0.3235
0.5	0.3263	0.6	0.3283
0.7	0.3298	0.8	0.3308
0.9	0.3315	1.0	0.3321
1.1	0.3324	1.2	0.3327
1.3	0.3329	1.4	0.3330
1.5	0.3331	1.6	0.3332
1.7	0.3332	1.8	0.3333

J The parameter ΔT and the EW Crossover

During the EW Crossover a reduction of the value of the PBH formation threshold δ_c is expected due to the decrease in the sound speed. We adopt for f the expression (183) derived for the QCD Crossover (Section 4.2) but now with the sound speed, $c_s(t)$, given by equation (129) in which we have an unkown parameter ΔT. We are particularly interested in a value of ΔT for which the threshold δ_c attains a minimum value (because lower values of δ_c favour PBH formation).

Thus, for a given ΔT we determine, with the help of funtion $(1-f)\delta_c$, the new threshold δ_{c1} as a function of the horizon crossing time t_k. When $t_k \ll t_{EW-}$ or, when $t_k \gg t_{EW+}$, we get $\delta_{c1} = \delta_c$. Between these two extremes there is a value of t_k for which δ_{c1} attains a minimum value $\delta_{c1,min}$. For example, when $\Delta T = 0.001 T_c$ and $\delta_c = 1/3$, we obtain $\delta_{c1,min} \approx 0.33213$ with $t_k \approx 8.32 \times 10^{-11}$ s.

We repeated this procedure for different values of ΔT ($0 < \Delta T \leq T_c$) and concluded that, in the $\delta_c = 1/3$ case, our best value is $\delta_{c1,min} \approx 0.33186$, corresponding to having $\Delta T \approx 0.013 T_c$ and $t_k \approx 8.32 \times 10^{-11}$ s. In Figure J-1 we show a selection of the results obtained.

In Table J-1 we show the results for different values of δ_c. Note that, although, the value of the parameter ΔT remains almost constant the same does not apply to t_k. For a larger value of δ_c, the instant t_k, for which we get the lowest $\delta_{c1,min}$, is closer to t_{EW-}.

Table J-1: The lowest value of $\delta_{c1,min}$ for the EW Crossover for different values of δ_c. It is also shown the corresponding values of $\Delta T/T_c$ and t_k.

δ_c	$\delta_{c1,min}$	$\Delta T/T_c$	$t_k(s)$
1/3	0.33186	0.0131	8.32×10^{-11}
0.4	0.39823	0.0091	9.33×10^{-11}
0.5	0.49778	0.0111	1.10×10^{-10}
0.6	0.59734	0.0101	1.23×10^{-10}
0.7	0.69689	0.0101	1.35×10^{-10}

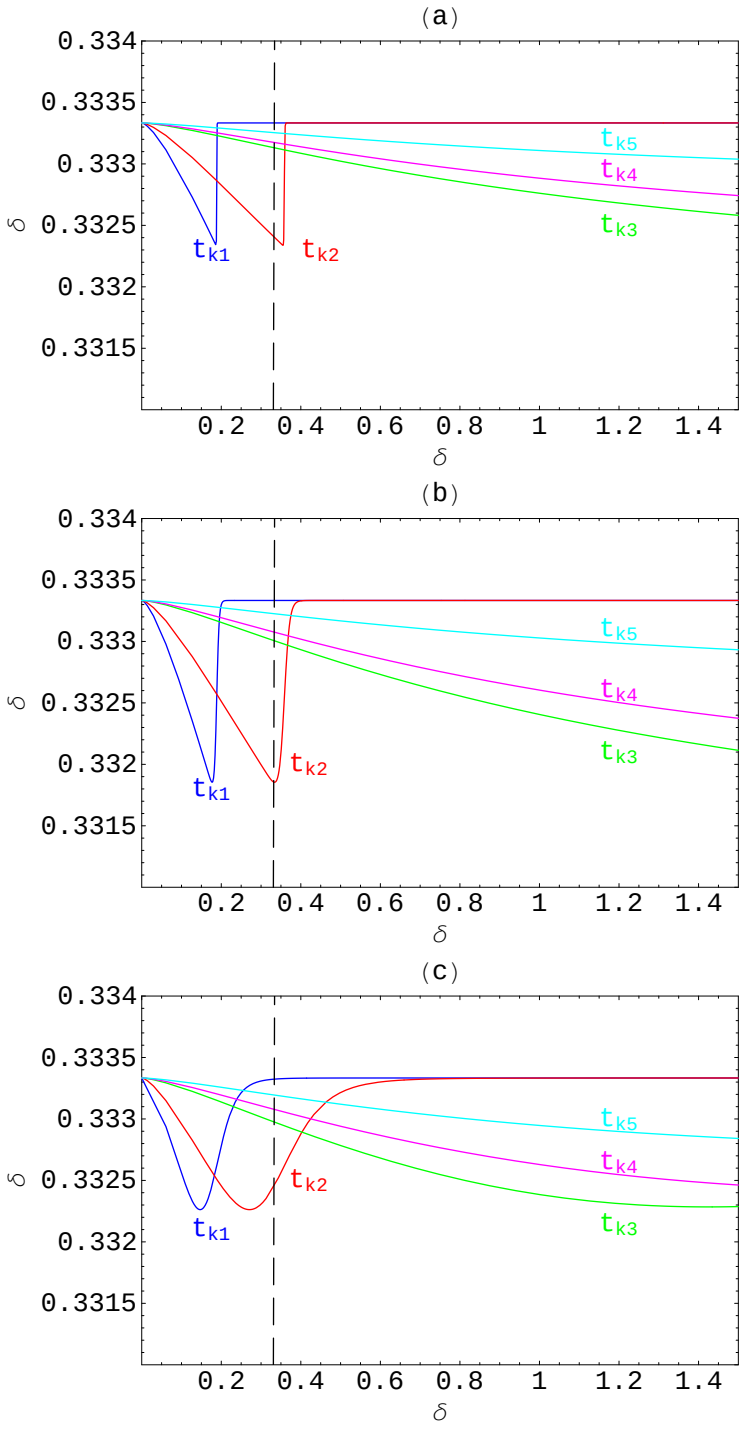

Figure J-1: The curve $(1-f)\delta_c$ for the EW Crossover when $\delta_c = 1/3$ and: (a) $\Delta T = 0.001T_c$, (b) $\Delta T = 0.013T_c$ and (c) $\Delta T = 0.1T_c$. Different lines correspond to different values of t_k: $t_{k1} = 5.0 \times 10^{-11}$ s, $t_{k2} = 8.32 \times 10^{-11}$ s, $t_{k3} = t_{EW-} = 2.3 \times 10^{-10}$ s, $t_{k4} = 2.7 \times 10^{-10}$ s, and $t_{k5} = t_{EW+} = 3.15 \times 10^{-10}$ s.

K The values of n_2 and n_3 when $n_+ = 1.4$

In Table K-1 we show the values for the parameters n_2 and n_3 (cf. equation 193) leading to a blue spectrum with $n_+ = 1.4$ (see Section 5.2 for more details).

Table K-1: The values of n_2 and n_3 which give $n_+ = 1.4$.

$\log_{10}(t_+/1\text{ s})$	$\log_{10}(k_+/1\text{m}^{-1})$	n_2	n_3
-23.0	-6.90	0.0124	-0.000661
-22.0	-7.40	0.0129	-0.000707
-21.0	-7.90	0.0134	-0.000758
-20.0	-8.40	0.0139	-0.000815
-19.0	-8.90	0.0145	-0.000877
-18.0	-9.40	0.0152	-0.000948
-17.0	-9.90	0.0159	-0.00103
-16.0	-10.4	0.0167	-0.00111
-15.0	-10.9	0.0175	-0.00121
-14.0	-11.4	0.0184	-0.00133
-13.0	-11.9	0.0194	-0.00146
-12.0	-12.4	0.0205	-0.00160
-11.0	-12.9	0.0218	-0.00178
-10.0	-13.4	0.0231	-0.00197
-9.00	-13.9	0.0247	-0.00220
-8.00	-14.4	0.0264	-0.00247
-7.00	-14.9	0.0283	-0.00280
-6.00	-15.4	0.0305	-0.00318
-5.00	-15.9	0.0331	-0.00364
-4.00	-16.4	0.0360	-0.00421
-3.00	-16.9	0.0395	-0.00491
-2.00	-17.4	0.0435	-0.00579
-1.00	-17.9	0.0483	-0.00690
0	-18.4	0.0542	-0.00834
1.00	-18.9	0.0613	-0.0102
2.00	-19.4	0.0702	-0.0128
3.00	-19.9	0.0816	-0.0164
4.00	-20.4	0.0963	-0.0215
5.00	-20.9	0.116	-0.0291
6.00	-21.4	0.144	-0.0411
7.00	-21.9	0.184	-0.0611
8.00	-22.4	0.247	-0.0973
9.00	-22.9	0.353	-0.171
10.0	-23.4	0.556	-0.347

L The maximum value of $\sigma^2(t_k)$ for different cases

In Table L-1 we show the maximum values reached by $\sigma^2(t_k)$ for different values of n_+ (corresponding to the value of t_+ right below the forbidden red region in Table 11). For most of the cases we have $\sigma^2_{max}(t_k) \sim 10^{-4}$ (in fact $\sigma^2_{max}(t_k)$ never exceeds 6.5×10^{-4}). This means that, whatever the value of $\delta_c \in [1/3, 0.7]$ we consider, we have $\sigma^2(t_k) \ll \delta_c$ for all the relevant cases (see Section 5.4 for more details).

Table L-1: The maximum value of $\sigma^2(t_k)$ for different cases.

n_+	$\log_{10}(t_+/1\text{ s})$	$\sigma^2_{max}(t_k)(\times 10^{-4})$
1.22	-23	1.7
1.24	-23	4.0
1.26	-19	3.8
1.28	-18	6.0
1.30	-16	6.3
1.32	-14	6.1
1.34	-12	5.3
1.36	-11	6.5
1.38	-9	4.8
1.40	-8	5.2
1.42	-7	5.3
1.44	-6	5.2
1.46	-5	4.8
1.48	-4	4.2
1.50	-3	3.6
1.52	-3	5.3
1.54	-2	4.3
1.56	-1	3.2
1.58	-1	4.6
1.60	0	3.2
1.62	0	4.5
1.64	1	3.0
1.66	1	4.1
1.68	1	5.5
1.70	2	3.3
1.72	2	4.4
1.74	3	2.4
1.76	3	3.1
1.78	3	4.1
1.80	4	2.0
1.82	4	2.6
1.84	4	3.3
1.86	4	4.1
1.88	5	1.8
1.90	5	2.2
1.92	5	2.8
1.94	5	3.4
1.96	6	1.3
1.98	6	1.6
2.00	6	1.9

M The peaks of the curve $\beta(t_k)$

In Table M-2 we list the peaks of the curve $\beta(t_k)$, as well as their locations, for the various cases (and different scenarios) studied in Sections 5.4 to 5.8. The contribution from radiation assumes a radiation–dominated universe ($\delta_c = 1/3$ at all epochs) with the curve $\beta(t_k)$ showing a single peak. In addition we might also have contributions from the QCD phase transition, from the EW phase transition, or from the electron–positron annihilation epoch, each showing its own peak.

If the peak from the radiation contribution is located near the epoch of a particular phase transition then it might be hidden by the corresponding peak. Consider, for example, the case $n_+ = 1.44$ and $t_+ = 10^{-3}$ s (Figure 61e). In this case, we have non–negligible contributions from radiation and from the QCD Lattice Fit or from the QCD Crossover (the QCD Bag Model is excluded due to the observational constraints). Whatever the model one chooses to the QCD phase transition, the peak of the radiation contribution (black curve) remains hidden. Thus, in this case, the curve $\beta(t_k)$ exhibits only one peak. In table M-2 there are other cases for which the peak from the radiation contribution is also hidden. For these cases we show the corresponding value of $\log_{10}\beta_{max}$ inside brackets and labeled with 'A' (meaning *Always* hidden).

As another example, consider the case $n_+ = 1.36$ and $t_+ = 10^{-7}$ s (Figure 64b). In this case we might have one, two or three peaks, depending on the chosen scenario (see Table M-1 and Figure M-1).

When, for example, $n_+ = 1.40$ and $t_+ = 10^{-5}$ s (Figure 61d) we might have one or two peaks. If the QCD phase transition is described by a Crossover model we get two peaks: the peak from radiation and the peak from the Crossover contribution. On the other hand if the QCD phase transition is described by a Lattice Fit model then we get only one peak: the peak from the Lattice Fit contribution which hide the peak from the radiation contribution. This and other similar cases, are shown in Table M-2, with the $\log_{10}\beta_{max}$ value inside brackets and labeled 'S' (meaning *Sometimes* hidden).

When $n_+ = 1.22$ and $n_+ = 1.24$ there are a few cases for which the peak from the radiation contribution occurs for $t_k < 10^{-23}$ s. Taking into account that our expression for $\beta(t_k)$ is classic (Section 1.1.5), not valid for epochs earlier than $\sim 10^{-23}$ s where the maximum is attained, we consider, for these particular cases, the values corresponding to $t_k = 10^{-23}$ s (which correspond to PBHs exploding right now), and we show those values in Table M-2 inside square brackets.

For the QCD Crossover and for the electron–positron annihilation there are a lot of cases for which there is an important contribution to β, similar to the radiation contribution, but without any peak. As an example of this, we mention the case $n_+ = 1.68$ and $t_+ = 100$ s (Figure 56f) for which we have a single peak from the radiation contribution. These cases are labeled, in Table M-2, with 'NA' (meaning *Not Applicable*).

Table M-1: Peaks of the curve $\beta(t_k)$ in the case $n_+ = 1.36$ and $t_+ = 10^{-7}$ s. See Table 10 for the description of different scenarios.

Scenario	Number of peaks	Description	Figure
1	2	Radiation + QCD Bag Model	M-1a
2	2	Radiation + QCD Lattice Fit	M-1b
3	1	Radiation	M-1c
4	3	Radiation + EW Bag Model + QCD Bag Model	M-1d
5	3	Radiation + EW Bag Model + QCD Lattice Fit	M-1e
6	2	Radiation + EW Bag Model	M-1f

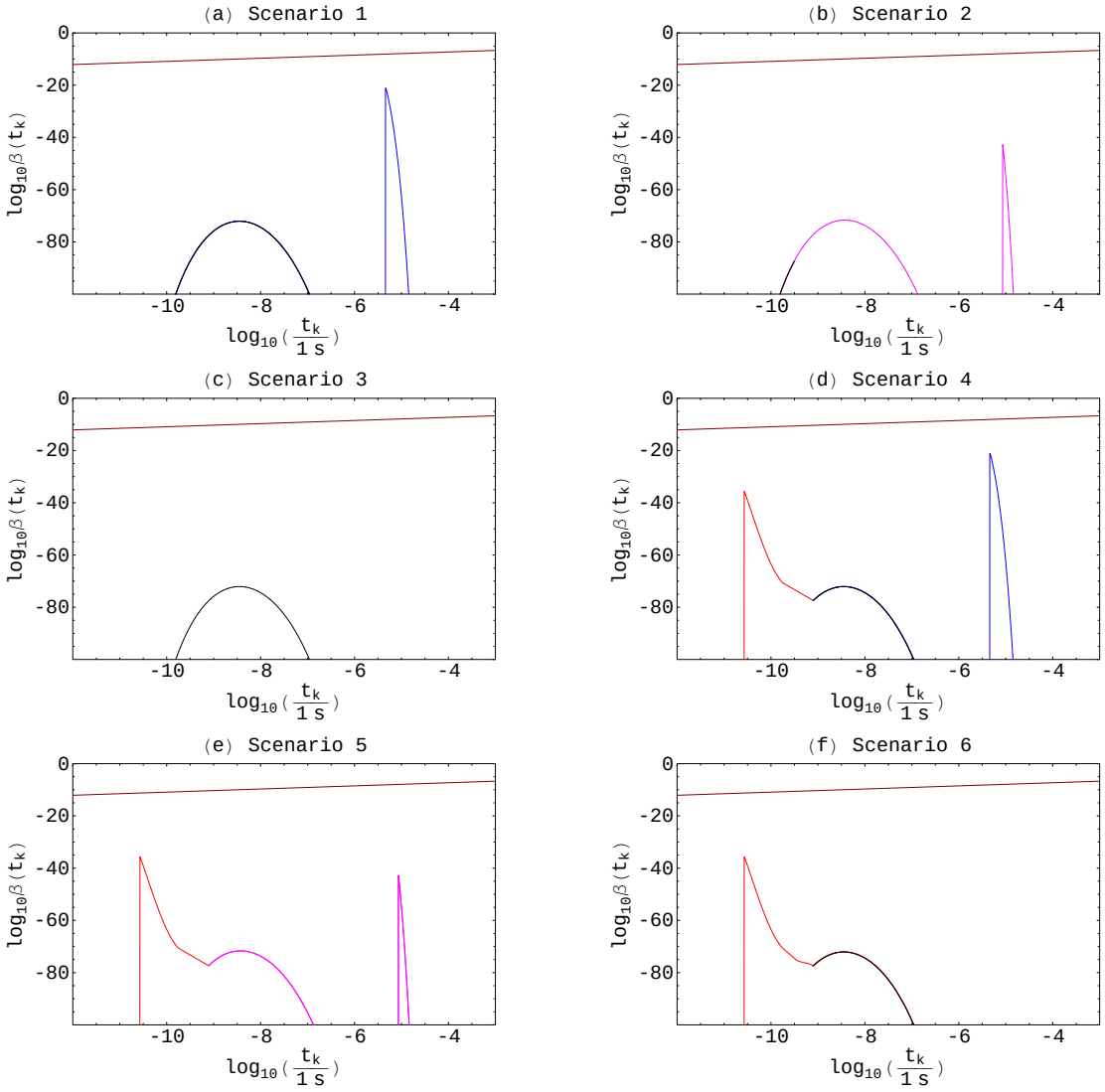

Figure M-1: The fraction of the Universe going into PBHs in a universe with a running–tilt power–law spectrum when $n_+ = 1.36$ and $t_+ = 10^{-7}$ s (see also Figure 64b and Table M-1). The curves represent the contribution from the QCD phase transition (blue – Bag Model; magenta – Lattice Fit), from the EW phase transition (red – Bag Model), and from radiation (black). Also shown (top of figures, in maroon) are the observational constraints. Each Figure represents a different scenario (see Table 10 for the description of different scenarios): (a) Scenario 1; (b) Scenario 2; (c) Scenario 3; (d) Scenario 4; (e) Scenario 5; (f) Scenario 6. The contribution from the QCD Crossover (scenarios 3 and 6) is not shown because it is negligible. The contribution from the electron–positron annihilation is also negligible. Assembling these six Figures into a single one we recover Figure 64b.

Table M-2: The fraction of the Universe going into PBHs during radiation domination and during cosmological phase transitions. The value t_+ corresponds to the instant for which the value of the spectral index attains its maximum n_+. The value $t_{k,max}$ corresponds to the instant for which β attains its maximum value (β_{max}). A gray background means that the value of β_{max} exceeds the observational constraints. A coloured background means that the value of β_{max} belongs to the top ten highest contributions for a particular transition model: EW Bag Model (red), QCD Bag Model (blue), QCD Lattice Fit (magenta), QCD Crossover (green), and electron–positron annihilation (cyan). We have labeled with 'NA' (not applicable) situations for which the curve of $\beta(t_k)$ exists but does not show any maximum, with 'A' the cases for which the radiation peak is always hidden (column 4), and with 'S' the cases for which the radiation peak is only sometimes hidden (column 4). Values inside square brackets correspond to situations for which the peak from radiation occurs for $t_k < 10^{-23}$ s (see text for more details).

		Radiation		EW Bag Model		QCD Bag Model		QCD Lattice Fit		QCD Crossover		e^-e^+ Crossover	
n_+	$\log_{10}(\frac{t_+}{1s})$	$\log_{10}(\frac{t_{k,max}}{1s})$	$\log_{10}\beta_{max}$	$\log_{10}(\frac{t_{k,max}}{1s})$	$\log_{10}\beta_{max}$	$\log_{10}(\frac{t_{k,max}}{1s})$	$\log_{10}\beta_{max}$	$\log_{10}(\frac{t_{k,max}}{1s})$	$\log_{10}\beta_{max}$	$\log_{10}(\frac{t_{k,max}}{1s})$	$\log_{10}\beta_{max}$	$\log_{10}(\frac{t_{k,max}}{1s})$	$\log_{10}\beta_{max}$
1.22	-23	[-23]	[-74]	–	–	–	–	–	–	–	–	–	–
	-22	[-23]	[-79]	–	–	–	–	–	–	–	–	–	–
	-21	-22.6	-98	–	–	–	–	–	–	–	–	–	–
1.24	-23	[-23]	[-31]	–	–	–	–	–	–	–	–	–	–
	-22	[-23]	[-33]	–	–	–	–	–	–	–	–	–	–
	-21	-22.7	-41	–	–	–	–	–	–	–	–	–	–
	-20	-21.7	-54	–	–	–	–	–	–	–	–	–	–
	-19	-20.7	-71	–	–	–	–	–	–	–	–	–	–
	-18	-19.6	-94	–	–	–	–	–	–	–	–	–	–
1.26	-19	-20.7	-31	–	–	–	–	–	–	–	–	–	–
	-18	-19.7	-42	–	–	–	–	–	–	–	–	–	–
	-17	-18.7	-56	–	–	–	–	–	–	–	–	–	–
	-16	-17.6	-76	–	–	–	–	–	–	–	–	–	–
1.28	-18	-19.8	-19	–	–	–	–	–	–	–	–	–	–
	-17	-18.7	-26	–	–	–	–	–	–	–	–	–	–
	-16	-17.7	-36	–	–	–	–	–	–	–	–	–	–
	-15	-16.7	-49	–	–	–	–	–	–	–	–	–	–
	-14	-15.6	-68	–	–	–	–	–	–	–	–	–	–
	-13	-14.6	-94	-10.6	-90	–	–	–	–	–	–	–	–
	-12	–	–	-10.6	-69	–	–	–	–	–	–	–	–
	-11	–	–	-10.6	-60	–	–	–	–	–	–	–	–
	-10	–	–	-10.6	-60	–	–	–	–	–	–	–	–
	-9	–	–	-10.6	-75	–	–	–	–	–	–	–	–

(continues on next page)

Table M-2 (continued).

		Radiation		EW Bag Model		QCD Bag Model		QCD Lattice Fit		QCD Crossover		e^-e^+ Crossover	
n_+	$\log_{10}(\frac{t_+}{1s})$	$\log_{10}(\frac{t_{k,max}}{1s})$	$\log_{10}\beta_{max}$	$\log_{10}(\frac{t_{k,max}}{1s})$	$\log_{10}\beta_{max}$	$\log_{10}(\frac{t_{k,max}}{1s})$	$\log_{10}\beta_{max}$	$\log_{10}(\frac{t_{k,max}}{1s})$	$\log_{10}\beta_{max}$	$\log_{10}(\frac{t_{k,max}}{1s})$	$\log_{10}\beta_{max}$	$\log_{10}(\frac{t_{k,max}}{1s})$	$\log_{10}\beta_{max}$
1.30	-16	-17.8	-17	–	–	–	–	–	–	–	–	–	–
	-15	-16.7	-24	–	–	–	–	–	–	–	–	–	–
	-14	-15.7	-33	-10.6	-72	–	–	–	–	–	–	–	–
	-13	-14.6	-47	-10.6	-50	–	–	–	–	–	–	–	–
	-12	-13.6	-66	-10.6	-38	–	–	–	–	–	–	–	–
	-11	-12.5	-94	-10.6	-33	–	–	–	–	–	–	–	–
	-10	–	–	-10.6	-33	–	–	–	–	–	–	–	–
	-9	–	–	-10.6	-42	–	–	–	–	–	–	–	–
	-8	–	–	-10.6	-71	–	–	–	–	–	–	–	–
	-7	–	–	–	–	-5.3	-85	–	–	–	–	–	–
	-6	–	–	–	–	-5.3	-69	–	–	–	–	–	–
	-5	–	–	–	–	-5.3	-67	–	–	–	–	–	–
	-4	–	–	–	–	-5.3	-84	–	–	–	–	–	–
1.32	-14	-15.7	-17	-10.6	-41	–	–	–	–	–	–	–	–
	-13	-14.7	-24	-10.6	-28	–	–	–	–	–	–	–	–
	-12	-13.6	-36	-10.6	-21	–	–	–	–	–	–	–	–
	-11	-12.6	-49	-10.6	-18	–	–	–	–	–	–	–	–
	-10	-11.5	-71	-10.6	-19	–	–	–	–	–	–	–	–
	-9	–	–	-10.6	-23	–	–	–	–	–	–	–	–
	-8	–	–	-10.6	-40	-5.3	-74	–	–	–	–	–	–
	-7	–	–	–	–	-5.3	-53	–	–	–	–	–	–
	-6	–	–	–	–	-5.3	-43	-5.1	-84	–	–	–	–
	-5	–	–	–	–	-5.3	-41	-5.1	-77	–	–	–	–
	-4	–	–	–	–	-5.3	-52	-5.1	-90	–	–	–	–
1.34	-12	-13.7	-18	-10.6	-12	–	–	–	–	–	–	–	–
	-11	-12.6	-26	-10.6	-11	–	–	–	–	–	–	–	–
	-10	-11.6	-38	-10.6	-11	–	–	–	–	–	–	–	–
	-9	-10.5	$(-57)_S$	-10.6	-13	-5.3	-72	–	–	–	–	–	–
	-8	-9.5	$(-84)_S$	-10.6	-23	-5.3	-47	–	–	–	–	–	–
	-7	–	–	-10.6	-61	-5.3	-33	-5.1	-68	–	–	–	–
	-6	–	–	–	–	-5.3	-27	-5.1	-52	–	–	–	–
	-5	–	–	–	–	-5.3	-26	-5.1	-48	–	–	–	–
	-4	–	–	–	–	-5.3	-33	-5.1	-56	–	–	–	–
	-3	–	–	–	–	-5.3	-63	-5.1	-96	–	–	–	–
1.36	-11	-12.7	-14	-10.6	-6	–	–	–	–	–	–	–	–
	-10	-11.6	-21	-10.6	-7	-5.3	-76	–	–	–	–	–	–
	-9	-10.6	-31	-10.6	-8	-5.3	-46	–	–	–	–	–	–
	-8	-9.5	$(-46)_S$	-10.6	-13	-5.3	-30	-5.1	-63	–	–	–	–
	-7	-8.5	-72	-10.6	-36	-5.3	-21	-5.1	-43	–	–	–	–
	-6	–	–	–	–	-5.3	-17	-5.1	-33	–	–	–	–
	-5	–	–	–	–	-5.3	-16	-5.1	-30	–	–	–	–
	-4	–	–	–	–	-5.3	-21	-5.1	-35	–	–	–	–
	-3	–	–	–	–	-5.3	-40	-5.1	-61	–	–	–	–

(continues on next page)

Table M-2 (continued).

		Radiation		EW Bag Model		QCD Bag Model		QCD Lattice Fit		QCD Crossover		e^-e^+ Crossover	
n_+	$\log_{10}(\frac{t_+}{1s})$	$\log_{10}(\frac{t_{k,max}}{1s})$	$\log_{10}\beta_{max}$	$\log_{10}(\frac{t_{k,max}}{1s})$	$\log_{10}\beta_{max}$	$\log_{10}(\frac{t_{k,max}}{1s})$	$\log_{10}\beta_{max}$	$\log_{10}(\frac{t_{k,max}}{1s})$	$\log_{10}\beta_{max}$	$\log_{10}(\frac{t_{k,max}}{1s})$	$\log_{10}\beta_{max}$	$\log_{10}(\frac{t_{k,max}}{1s})$	$\log_{10}\beta_{max}$
1.38	-9	-10.6	-18	-10.6	-5	-5.3	-30	-5.1	-65	–	–	–	–
	-8	-9.5	-27	-10.6	-8	-5.3	-19	-5.1	-40	–	–	–	–
	-7	-8.5	-42	-10.6	-21	-5.3	-14	-5.1	-27	–	–	–	–
	-6	-7.4	-65	–	–	-5.3	-11	-5.1	-21	–	–	–	–
	-5	–	–	–	–	-5.3	-11	-5.1	-19	–	–	–	–
	-4	–	–	–	–	-5.3	-13	-5.1	-22	–	–	–	–
	-3	–	–	–	–	-5.3	-26	-5.1	-39	–	–	–	–
1.40	-8	-9.6	-16	-10.5	-5	-5.3	-13	-5.1	-26	–	–	–	–
	-7	-8.5	-24	-10.6	-13	-5.3	-9	-5.1	-18	–	–	–	–
	-6	-7.4	-38	-10.6	-69	-5.3	-7	-5.1	-13	-4.5	-92	–	–
	-5	-6.4	$(-61)_S$	–	–	-5.3	-7	-5.1	-12	-4.5	-74	–	–
	-4	-5.3	$(-97)_S$	–	–	-5.3	-9	-5.1	-14	-4.5	-75	–	–
	-3	–	–	–	–	-5.3	-17	-5.1	-25	–	–	–	–
	-2	–	–	–	–	-5.3	-66	-5.1	-83	–	–	–	–
1.42	-7	-8.5	-14	-10.6	-8	-5.3	-6	-5.1	-12	-4.5	-85	–	–
	-6	-7.5	-23	-10.6	-43	-5.3	-5	-5.1	-9	-4.5	-58	–	–
	-5	-6.4	$(-37)_S$	–	–	-5.3	-5	-5.1	-8	-4.5	-46	–	–
	-4	-5.3	$(-60)_S$	–	–	-5.3	-6	-5.1	-10	-4.5	-47	–	–
	-3	-4.3	$(-98)_A$	–	–	-5.3	-11	-5.1	-16	-4.5	-67	–	–
	-2	–	–	–	–	-5.3	-44	-5.1	-55	–	–	–	–
1.44	-6	-7.5	-14	-10.6	-24	-5.3	-4	-5.1	-6	-4.5	-37	–	–
	-5	-6.4	-23	–	–	-5.3	-4	-5.0	-6	-4.5	-29	–	–
	-4	-5.4	-37	–	–	-5.3	-4	-5.1	-6	-4.5	-30	–	–
	-3	-4.3	$(-62)_A$	–	–	-5.3	-8	-5.1	-11	-4.5	-43	–	–
	-2	–	–	–	–	-5.3	-30	-5.1	-36	–	–	–	–
1.46	-5	-6.4	-14	–	–	-5.3	-3	-5.0	-4	-4.5	-19	–	–
	-4	-5.4	-23	–	–	-5.3	-3	-5.0	-5	-4.5	-19	–	–
	-3	-4.3	$(-40)_A$	–	–	-5.3	-5	-5.1	-7	-4.5	-27	–	–
	-2	-3.2	-67	–	–	-5.3	-20	-5.1	-24	-4.4	-70	–	–
1.48	-4	-5.4	-15	–	–	-5.3	-2	-5.0	-3	-4.5	-12	–	–
	-3	-4.3	$(-25)_A$	–	–	-5.3	-4	-5.0	-5	-4.5	-18	–	–
	-2	-3.2	-44	–	–	-5.3	-14	-5.1	-17	-4.4	-45	–	–
	-1	-2.2	-77	–	–	–	–	–	–	–	–	–	–

(continues on next page)

Table M-2 (continued).

		Radiation		EW Bag Model		QCD Bag Model		QCD Lattice Fit		QCD Crossover		e^-e^+ Crossover	
n_+	$\log_{10}(\frac{t_+}{1\text{s}})$	$\log_{10}(\frac{t_{k,max}}{1\text{s}})$	$\log_{10}\beta_{max}$	$\log_{10}(\frac{t_{k,max}}{1\text{s}})$	$\log_{10}\beta_{max}$	$\log_{10}(\frac{t_{k,max}}{1\text{s}})$	$\log_{10}\beta_{max}$	$\log_{10}(\frac{t_{k,max}}{1\text{s}})$	$\log_{10}\beta_{max}$	$\log_{10}(\frac{t_{k,max}}{1\text{s}})$	$\log_{10}\beta_{max}$	$\log_{10}(\frac{t_{k,max}}{1\text{s}})$	$\log_{10}\beta_{max}$
1.50	-3	-4.3	$(-16)_A$	–	–	-5.3	-3	-5.0	-4	-4.5	-11	–	–
	-2	-3.3	-29	–	–	-5.3	-10	-5.1	-11	-4.4	-30	–	–
	-1	-2.2	-51	–	–	–	–	–	–	–	–	–	–
1.52	-3	-4.4	-11	–	–	-5.2	-2	-5.0	-3	-4.5	-8	–	–
	-2	-3.3	-19	–	–	-5.3	-7	-5.0	-8	-4.4	-20	–	–
	-1	-2.2	-34	–	–	–	–	–	–	–	–	-0.1	-84
	0	-1.1	-62	–	–	–	–	–	–	–	–	-0.1	-72
	1	–	–	–	–	–	–	–	–	–	–	0.0	-96
1.54	-2	-3.3	-13	–	–	-5.3	-5	-5.0	-6	-4.4	-13	-0.1	-89
	-1	-2.2	-23	–	–	-5.3	-76	-5.1	-65	NA	NA	-0.1	-58
	0	-1.1	-43	–	–	–	–	–	–	–	–	-0.1	-50
	1	-0.1	$(-80)_A$	–	–	–	–	–	–	–	–	0.0	-67
1.56	-1	-2.2	-15	–	–	-5.3	-55	-5.1	-47	NA	NA	-0.1	-40
	0	-1.1	-29	–	–	–	–	–	–	–	–	-0.1	-34
	1	-0.1	$(-56)_A$	–	–	–	–	–	–	–	–	0.0	-47
1.58	-1	-2.2	-11	–	–	NA	NA	-5.1	-33	NA	NA	-0.1	-28
	0	-1.1	-20	–	–	–	–	–	–	–	–	-0.1	-24
	1	-0.1	$(-39)_A$	–	–	–	–	–	–	–	–	0.0	-33
	2	1.0	-77	–	–	–	–	–	–	–	–	NA	NA
1.60	0	-1.2	-14	–	–	–	–	–	–	–	–	-0.1	-17
	1	-0.1	$(-27)_A$	–	–	–	–	–	–	–	–	0.0	-23
	2	1.0	-55	–	–	–	–	–	–	–	–	NA	NA
1.62	0	-1.2	-10	–	–	–	–	–	–	–	–	-0.1	-12
	1	-0.1	$(-19)_A$	–	–	–	–	–	–	–	–	0.0	-16
	2	1.0	-39	–	–	–	–	–	–	–	–	NA	NA
	3	2.1	-82	–	–	–	–	–	–	–	–	–	–
1.64	1	-0.1	$(-14)_A$	–	–	–	–	–	–	–	–	0.0	-12
	2	1.0	-28	–	–	–	–	–	–	–	–	NA	NA
	3	2.1	-60	–	–	–	–	–	–	–	–	–	–

(continues on next page)

Table M-2 (continued).

		Radiation		EW Bag Model		QCD Bag Model		QCD Lattice Fit		QCD Crossover		e^-e^+ Crossover	
n_+	$\log_{10}(\frac{t_+}{1s})$	$\log_{10}(\frac{t_{k,max}}{1s})$	$\log_{10}\beta_{max}$	$\log_{10}(\frac{t_{k,max}}{1s})$	$\log_{10}\beta_{max}$	$\log_{10}(\frac{t_{k,max}}{1s})$	$\log_{10}\beta_{max}$	$\log_{10}(\frac{t_{k,max}}{1s})$	$\log_{10}\beta_{max}$	$\log_{10}(\frac{t_{k,max}}{1s})$	$\log_{10}\beta_{max}$	$\log_{10}(\frac{t_{k,max}}{1s})$	$\log_{10}\beta_{max}$
1.66	1	-0.1	$(-10)_A$	–	–	–	–	–	–	–	–	0.0	-8
	2	1.0	-20	–	–	–	–	–	–	–	–	NA	NA
	3	2.1	-44	–	–	–	–	–	–	–	–	–	–
1.68	1	-0.1	$(-7)_A$	–	–	–	–	–	–	–	–	0.0	-6
	2	1.0	-15	–	–	–	–	–	–	–	–	NA	NA
	3	2.1	-32	–	–	–	–	–	–	–	–	–	–
	4	3.2	-71	–	–	–	–	–	–	–	–	–	–
1.70	2	1.0	-11	–	–	–	–	–	–	–	–	NA	NA
	3	2.1	-24	–	–	–	–	–	–	–	–	–	–
	4	3.2	-53	–	–	–	–	–	–	–	–	–	–
1.72	2	1.0	-8	–	–	–	–	–	–	–	–	1.0	-8
	3	2.1	-17	–	–	–	–	–	–	–	–	–	–
	4	3.2	-40	–	–	–	–	–	–	–	–	–	–
	5	4.3	-93	–	–	–	–	–	–	–	–	–	–
1.74	3	2.1	-13	–	–	–	–	–	–	–	–	–	–
	4	3.2	-30	–	–	–	–	–	–	–	–	–	–
	5	4.3	-72	–	–	–	–	–	–	–	–	–	–
1.76	3	2.1	-10	–	–	–	–	–	–	–	–	–	–
	4	3.2	-23	–	–	–	–	–	–	–	–	–	–
	5	4.3	-55	–	–	–	–	–	–	–	–	–	–
1.78	3	2.1	-7	–	–	–	–	–	–	–	–	–	–
	4	3.2	-17	–	–	–	–	–	–	–	–	–	–
	5	4.3	-42	–	–	–	–	–	–	–	–	–	–
1.80	4	3.2	-13	–	–	–	–	–	–	–	–	–	–
	5	4.3	-32	–	–	–	–	–	–	–	–	–	–
	6	5.4	-83	–	–	–	–	–	–	–	–	–	–
1.82	4	3.2	-10	–	–	–	–	–	–	–	–	–	–
	5	4.3	-25	–	–	–	–	–	–	–	–	–	–
	6	5.4	-65	–	–	–	–	–	–	–	–	–	–
1.84	4	3.2	-8	–	–	–	–	–	–	–	–	–	–
	5	4.3	-19	–	–	–	–	–	–	–	–	–	–
	6	5.4	-51	–	–	–	–	–	–	–	–	–	–

(continues on next page)

Table M-2 (continued).

		Radiation		EW Bag Model		QCD Bag Model		QCD Lattice Fit		QCD Crossover		e^-e^+ Crossover	
n_+	$\log_{10}(\frac{t_+}{1\mathrm{s}})$	$\log_{10}(\frac{t_{k,max}}{1\mathrm{s}})$	$\log_{10}\beta_{max}$	$\log_{10}(\frac{t_{k,max}}{1\mathrm{s}})$	$\log_{10}\beta_{max}$	$\log_{10}(\frac{t_{k,max}}{1\mathrm{s}})$	$\log_{10}\beta_{max}$	$\log_{10}(\frac{t_{k,max}}{1\mathrm{s}})$	$\log_{10}\beta_{max}$	$\log_{10}(\frac{t_{k,max}}{1\mathrm{s}})$	$\log_{10}\beta_{max}$	$\log_{10}(\frac{t_{k,max}}{1\mathrm{s}})$	$\log_{10}\beta_{max}$
1.86	4	3.2	-6	–	–	–	–	–	–	–	–	–	–
	5	4.3	-15	–	–	–	–	–	–	–	–	–	–
	6	5.4	-40	–	–	–	–	–	–	–	–	–	–
1.88	5	4.3	-12	–	–	–	–	–	–	–	–	–	–
	6	5.4	-32	–	–	–	–	–	–	–	–	–	–
	7	6.5	-89	–	–	–	–	–	–	–	–	–	–
1.90	5	4.3	-9	–	–	–	–	–	–	–	–	–	–
	6	5.4	-25	–	–	–	–	–	–	–	–	–	–
	7	6.5	-72	–	–	–	–	–	–	–	–	–	–
1.92	5	4.3	-7	–	–	–	–	–	–	–	–	–	–
	6	5.4	-20	–	–	–	–	–	–	–	–	–	–
	7	6.5	-58	–	–	–	–	–	–	–	–	–	–
1.94	5	4.3	-6	–	–	–	–	–	–	–	–	–	–
	6	5.4	-16	–	–	–	–	–	–	–	–	–	–
	7	6.5	-46	–	–	–	–	–	–	–	–	–	–
1.96	6	5.4	-12	–	–	–	–	–	–	–	–	–	–
	7	6.5	-37	–	–	–	–	–	–	–	–	–	–
1.98	6	5.3	-10	–	–	–	–	–	–	–	–	–	–
	7	6.5	-30	–	–	–	–	–	–	–	–	–	–
	8	7.6	-96	–	–	–	–	–	–	–	–	–	–
2.00	6	5.3	-8	–	–	–	–	–	–	–	–	–	–
	7	6.5	-24	–	–	–	–	–	–	–	–	–	–
	8	7.6	-79	–	–	–	–	–	–	–	–	–	–

N Using different values for δ_c

We have determined the curve $\beta(t_k)$ assuming a radiation–dominated universe with $\delta_c = 1/3$ (cf. Section 5.4). Here we consider $\delta_c = 0.7$ (still in a radiation–dominated universe) and analyse how this would affect the results. Following the same criteria that we used for the $\delta_c = 1/3$ case (cf. Section 5.4) we obtained 143 cases favourable to PBH formation in a radiation–dominated universe (Table N-1) – eight less than in Section 5.4.

Comparing Tables 11 ($\delta_c = 1/3$) and N-1 ($\delta_c = 0.7$) we see that the favourable cases exhibit a similar pattern in both Tables. The main difference is that, for a given value of n_+, the set of favourable cases is 'pushed' back in time for $\delta_c = 0.7$. Consider, as an example, the case $n_+ = 1.5$. When $\delta_c = 1/3$ and $t_+ = 10^{-5}$ s the curve $\beta(t_k)$ violates the observational constraints (cf. Table 11). This is not the case when $\delta_c = 0.7$. In this situation the observational constraints are violated when $t_+ = 10^{-7}$ s but not when $t_+ = 10^{-6}$ s or $t_+ = 10^{-5}$ s (cf. Table N-1). On the other hand, when $\delta_c = 0.7$ we have $\beta(t_k) \approx 0$ (i.e. $\beta(t_k) < 10^{-100}$) starting at $t_+ = 10^{-2}$ s. On the $\delta_c = 1/3$ case this only happens for $t_+ \geq 10$ s.

Table N-1: The cases for which $\beta > 10^{-100}$ for a radiation–dominated universe with a running–tilt power–law spectrum when $\delta_c = 0.7$ (see Table 11 for more details).

	n_+																																							
$\log_{10}(t_+/1\mathrm{s})$	1.20	1.22	1.24	1.26	1.28	1.30	1.32	1.34	1.36	1.38	1.40	1.42	1.44	1.46	1.48	1.50	1.52	1.54	1.56	1.58	1.60	1.62	1.64	1.66	1.68	1.70	1.72	1.74	1.76	1.78	1.80	1.82	1.84	1.86	1.88	1.90	1.92	1.94	1.96	1.98	2.00
-23	🟦	🟦	🟦	R	🟥	🟥	🟥	🟥	🟥	🟥	🟥	🟥	🟥	🟥	🟥	🟥	🟥	🟥	🟥	🟥	🟥	🟥	🟥	🟥	🟥	🟥	🟥	🟥	🟥	🟥	🟥	🟥	🟥	🟥	🟥	🟥	🟥	🟥	🟥	🟥	🟥
-22	🟦	🟦	🟦	R	🟥	🟥	🟥	🟥	🟥	🟥	🟥	🟥	🟥	🟥	🟥	🟥	🟥	🟥	🟥	🟥	🟥	🟥	🟥	🟥	🟥	🟥	🟥	🟥	🟥	🟥	🟥	🟥	🟥	🟥	🟥	🟥	🟥	🟥	🟥	🟥	🟥
-21	🟦	🟦	🟦	R	R	🟥	🟥	🟥	🟥	🟥	🟥	🟥	🟥	🟥	🟥	🟥	🟥	🟥	🟥	🟥	🟥	🟥	🟥	🟥	🟥	🟥	🟥	🟥	🟥	🟥	🟥	🟥	🟥	🟥	🟥	🟥	🟥	🟥	🟥	🟥	🟥
-20	🟦	🟦	🟦	R	R	🟥	🟥	🟥	🟥	🟥	🟥	🟥	🟥	🟥	🟥	🟥	🟥	🟥	🟥	🟥	🟥	🟥	🟥	🟥	🟥	🟥	🟥	🟥	🟥	🟥	🟥	🟥	🟥	🟥	🟥	🟥	🟥	🟥	🟥	🟥	🟥
-19	🟦	🟦	🟦	🟦	R	R	🟥	🟥	🟥	🟥	🟥	🟥	🟥	🟥	🟥	🟥	🟥	🟥	🟥	🟥	🟥	🟥	🟥	🟥	🟥	🟥	🟥	🟥	🟥	🟥	🟥	🟥	🟥	🟥	🟥	🟥	🟥	🟥	🟥	🟥	🟥
-18	🟦	🟦	🟦	🟦	R	R	🟥	🟥	🟥	🟥	🟥	🟥	🟥	🟥	🟥	🟥	🟥	🟥	🟥	🟥	🟥	🟥	🟥	🟥	🟥	🟥	🟥	🟥	🟥	🟥	🟥	🟥	🟥	🟥	🟥	🟥	🟥	🟥	🟥	🟥	🟥
-17	🟦	🟦	🟦	🟦	🟦	R	R	🟥	🟥	🟥	🟥	🟥	🟥	🟥	🟥	🟥	🟥	🟥	🟥	🟥	🟥	🟥	🟥	🟥	🟥	🟥	🟥	🟥	🟥	🟥	🟥	🟥	🟥	🟥	🟥	🟥	🟥	🟥	🟥	🟥	🟥
-16	🟦	🟦	🟦	🟦	🟦	R	R	R	🟥	🟥	🟥	🟥	🟥	🟥	🟥	🟥	🟥	🟥	🟥	🟥	🟥	🟥	🟥	🟥	🟥	🟥	🟥	🟥	🟥	🟥	🟥	🟥	🟥	🟥	🟥	🟥	🟥	🟥	🟥	🟥	🟥
-15	🟦	🟦	🟦	🟦	🟦	🟦	R	R	🟥	🟥	🟥	🟥	🟥	🟥	🟥	🟥	🟥	🟥	🟥	🟥	🟥	🟥	🟥	🟥	🟥	🟥	🟥	🟥	🟥	🟥	🟥	🟥	🟥	🟥	🟥	🟥	🟥	🟥	🟥	🟥	🟥
-14	🟦	🟦	🟦	🟦	🟦	🟦	R	R	R	🟥	🟥	🟥	🟥	🟥	🟥	🟥	🟥	🟥	🟥	🟥	🟥	🟥	🟥	🟥	🟥	🟥	🟥	🟥	🟥	🟥	🟥	🟥	🟥	🟥	🟥	🟥	🟥	🟥	🟥	🟥	🟥
-13	🟦	🟦	🟦	🟦	🟦	🟦	🟦	R	R	🟥	🟥	🟥	🟥	🟥	🟥	🟥	🟥	🟥	🟥	🟥	🟥	🟥	🟥	🟥	🟥	🟥	🟥	🟥	🟥	🟥	🟥	🟥	🟥	🟥	🟥	🟥	🟥	🟥	🟥	🟥	🟥
-12	🟦	🟦	🟦	🟦	🟦	🟦	🟦	R	R	R	🟥	🟥	🟥	🟥	🟥	🟥	🟥	🟥	🟥	🟥	🟥	🟥	🟥	🟥	🟥	🟥	🟥	🟥	🟥	🟥	🟥	🟥	🟥	🟥	🟥	🟥	🟥	🟥	🟥	🟥	🟥
-11	🟦	🟦	🟦	🟦	🟦	🟦	🟦	🟦	R	R	R	🟥	🟥	🟥	🟥	🟥	🟥	🟥	🟥	🟥	🟥	🟥	🟥	🟥	🟥	🟥	🟥	🟥	🟥	🟥	🟥	🟥	🟥	🟥	🟥	🟥	🟥	🟥	🟥	🟥	🟥
-10	🟦	🟦	🟦	🟦	🟦	🟦	🟦	🟦	R	R	R	R	🟥	🟥	🟥	🟥	🟥	🟥	🟥	🟥	🟥	🟥	🟥	🟥	🟥	🟥	🟥	🟥	🟥	🟥	🟥	🟥	🟥	🟥	🟥	🟥	🟥	🟥	🟥	🟥	🟥
-9	🟦	🟦	🟦	🟦	🟦	🟦	🟦	🟦	🟦	R	R	R	R	🟥	🟥	🟥	🟥	🟥	🟥	🟥	🟥	🟥	🟥	🟥	🟥	🟥	🟥	🟥	🟥	🟥	🟥	🟥	🟥	🟥	🟥	🟥	🟥	🟥	🟥	🟥	🟥
-8	🟦	🟦	🟦	🟦	🟦	🟦	🟦	🟦	🟦	🟦	R	R	R	R	🟥	🟥	🟥	🟥	🟥	🟥	🟥	🟥	🟥	🟥	🟥	🟥	🟥	🟥	🟥	🟥	🟥	🟥	🟥	🟥	🟥	🟥	🟥	🟥	🟥	🟥	🟥
-7	🟦	🟦	🟦	🟦	🟦	🟦	🟦	🟦	🟦	🟦	🟦	R	R	R	R	🟥	🟥	🟥	🟥	🟥	🟥	🟥	🟥	🟥	🟥	🟥	🟥	🟥	🟥	🟥	🟥	🟥	🟥	🟥	🟥	🟥	🟥	🟥	🟥	🟥	🟥
-6	🟦	🟦	🟦	🟦	🟦	🟦	🟦	🟦	🟦	🟦	🟦	R	R	R	R	R	🟥	🟥	🟥	🟥	🟥	🟥	🟥	🟥	🟥	🟥	🟥	🟥	🟥	🟥	🟥	🟥	🟥	🟥	🟥	🟥	🟥	🟥	🟥	🟥	🟥
-5	🟦	🟦	🟦	🟦	🟦	🟦	🟦	🟦	🟦	🟦	🟦	🟦	R	R	R	R	R	🟥	🟥	🟥	🟥	🟥	🟥	🟥	🟥	🟥	🟥	🟥	🟥	🟥	🟥	🟥	🟥	🟥	🟥	🟥	🟥	🟥	🟥	🟥	🟥
-4	🟦	🟦	🟦	🟦	🟦	🟦	🟦	🟦	🟦	🟦	🟦	🟦	🟦	R	R	R	R	R	R	🟥	🟥	🟥	🟥	🟥	🟥	🟥	🟥	🟥	🟥	🟥	🟥	🟥	🟥	🟥	🟥	🟥	🟥	🟥	🟥	🟥	🟥
-3	🟦	🟦	🟦	🟦	🟦	🟦	🟦	🟦	🟦	🟦	🟦	🟦	🟦	🟦	🟦	R	R	R	R	R	🟥	🟥	🟥	🟥	🟥	🟥	🟥	🟥	🟥	🟥	🟥	🟥	🟥	🟥	🟥	🟥	🟥	🟥	🟥	🟥	🟥
-2	🟦	🟦	🟦	🟦	🟦	🟦	🟦	🟦	🟦	🟦	🟦	🟦	🟦	🟦	🟦	🟦	R	R	R	R	R	R	🟥	🟥	🟥	🟥	🟥	🟥	🟥	🟥	🟥	🟥	🟥	🟥	🟥	🟥	🟥	🟥	🟥	🟥	🟥
-1	🟦	🟦	🟦	🟦	🟦	🟦	🟦	🟦	🟦	🟦	🟦	🟦	🟦	🟦	🟦	🟦	🟦	R	R	R	R	R	R	R	🟥	🟥	🟥	🟥	🟥	🟥	🟥	🟥	🟥	🟥	🟥	🟥	🟥	🟥	🟥	🟥	🟥
0	🟦	🟦	🟦	🟦	🟦	🟦	🟦	🟦	🟦	🟦	🟦	🟦	🟦	🟦	🟦	🟦	🟦	🟦	🟦	R	R	R	R	R	R	R	R	🟥	🟥	🟥	🟥	🟥	🟥	🟥	🟥	🟥	🟥	🟥	🟥	🟥	🟥
1	🟦	🟦	🟦	🟦	🟦	🟦	🟦	🟦	🟦	🟦	🟦	🟦	🟦	🟦	🟦	🟦	🟦	🟦	🟦	🟦	🟦	R	R	R	R	R	R	R	R	R	🟥	🟥	🟥	🟥	🟥	🟥	🟥	🟥	🟥	🟥	🟥
2	🟦	🟦	🟦	🟦	🟦	🟦	🟦	🟦	🟦	🟦	🟦	🟦	🟦	🟦	🟦	🟦	🟦	🟦	🟦	🟦	🟦	🟦	🟦	R	R	R	R	R	R	R	R	R	R	🟥	🟥	🟥	🟥	🟥	🟥	🟥	🟥
3	🟦	🟦	🟦	🟦	🟦	🟦	🟦	🟦	🟦	🟦	🟦	🟦	🟦	🟦	🟦	🟦	🟦	🟦	🟦	🟦	🟦	🟦	🟦	🟦	🟦	🟦	R	R	R	R	R	R	R	R	R	R	R	🟥	🟥	🟥	🟥
4	🟦	🟦	🟦	🟦	🟦	🟦	🟦	🟦	🟦	🟦	🟦	🟦	🟦	🟦	🟦	🟦	🟦	🟦	🟦	🟦	🟦	🟦	🟦	🟦	🟦	🟦	🟦	🟦	R	R	R	R	R	R	R	R	R	R	R	R	R
5	🟦	🟦	🟦	🟦	🟦	🟦	🟦	🟦	🟦	🟦	🟦	🟦	🟦	🟦	🟦	🟦	🟦	🟦	🟦	🟦	🟦	🟦	🟦	🟦	🟦	🟦	🟦	🟦	🟦	🟦	🟦	🟦	R	R	R	R	R	R	R	R	R
6	🟦	🟦	🟦	🟦	🟦	🟦	🟦	🟦	🟦	🟦	🟦	🟦	🟦	🟦	🟦	🟦	🟦	🟦	🟦	🟦	🟦	🟦	🟦	🟦	🟦	🟦	🟦	🟦	🟦	🟦	🟦	🟦	🟦	🟦	🟦	🟦	R	R	R	R	R
7	🟦	🟦	🟦	🟦	🟦	🟦	🟦	🟦	🟦	🟦	🟦	🟦	🟦	🟦	🟦	🟦	🟦	🟦	🟦	🟦	🟦	🟦	🟦	🟦	🟦	🟦	🟦	🟦	🟦	🟦	🟦	🟦	🟦	🟦	🟦	🟦	🟦	🟦	🟦	🟦	🟦
8	🟦	🟦	🟦	🟦	🟦	🟦	🟦	🟦	🟦	🟦	🟦	🟦	🟦	🟦	🟦	🟦	🟦	🟦	🟦	🟦	🟦	🟦	🟦	🟦	🟦	🟦	🟦	🟦	🟦	🟦	🟦	🟦	🟦	🟦	🟦	🟦	🟦	🟦	🟦	🟦	🟦
9	🟦	🟦	🟦	🟦	🟦	🟦	🟦	🟦	🟦	🟦	🟦	🟦	🟦	🟦	🟦	🟦	🟦	🟦	🟦	🟦	🟦	🟦	🟦	🟦	🟦	🟦	🟦	🟦	🟦	🟦	🟦	🟦	🟦	🟦	🟦	🟦	🟦	🟦	🟦	🟦	🟦

O The minimum distance $d(t_0, t_k)$

In Table O-1 we list the minimum distance $d(t_0, t_k)$ to the nearest PBH for different scenarios and different cases (see equation 202). Values with a gray background correspond to situations for which the distance to the nearest PBH exceeds the size of the observable Universe. On the other hand values with a red background correspond to situations that are already excluded due to observational constraints. These two extreme situations were included only for illustration purposes.

Table O-1: The distance to the nearest PBH $d(t_0, t_k)$ – equation (202). The value t_+ corresponds to the instant for which the value of the spectral index attains its maximum n_+. A gray background means that the value of $d(t_0, t_k)$ exceeds the size of the observable Universe. Cases with a red background are excluded due to observational constraints. Values inside square brackets correspond to situations for which the peak from radiation occurs for $t_k < 10^{-23}$ s (see Section 6.2 for more details).

		$d(t_0, t_k)$ (m)					
n_+	$\log_{10}(\frac{t_+}{1\text{s}})$	Radiation	EW Bag Model	QCD Bag Model	QCD Lattice Fit	QCD Crossover	e^-e^+ Crossover
1.22	-23	$[1.4 \times 10^{31}]$	–	–	–	–	–
	-22	$[8.3 \times 10^{32}]$	–	–	–	–	–
	-21	3.0×10^{39}	–	–	–	–	–
1.24	-23	$[5.8 \times 10^{16}]$	–	–	–	–	–
	-22	$[3.2 \times 10^{17}]$	–	–	–	–	–
	-21	2.3×10^{20}	–	–	–	–	–
	-20	1.5×10^{25}	–	–	–	–	–
	-19	2.4×10^{31}	–	–	–	–	–
	-18	2.6×10^{39}	–	–	–	–	–
1.26	-19	1.1×10^{18}	–	–	–	–	–
	-18	1.4×10^{22}	–	–	–	–	–
	-17	3.1×10^{27}	–	–	–	–	–
	-16	3.5×10^{34}	–	–	–	–	–
1.28	-18	2.8×10^{14}	–	–	–	–	–
	-17	2.1×10^{17}	–	–	–	–	–
	-16	1.2×10^{21}	–	–	–	–	–
	-15	1.2×10^{26}	–	–	–	–	–
	-14	6.2×10^{32}	–	–	–	–	–
	-13	8.3×10^{41}	8.3×10^{41}	–	–	–	–
	-12	–	5.7×10^{35}	–	–	–	–
	-11	–	4.0×10^{32}	-	–	–	–
	-10	–	8.2×10^{32}	–	–	–	–
	-9	–	6.7×10^{37}	–	–	–	–

(continues on next page)

Table O-1 (continued).

n_+	$\log_{10}(\frac{t_+}{1\text{s}})$	$d(t_0, t_k)$ (m) Radiation	EW Bag Model	QCD Bag Model	QCD Lattice Fit	QCD Crossover	e^-e^+ Crossover
1.30	-16	6.0×10^{14}	–	–	–	–	–
	-15	3.8×10^{17}	–	–	–	–	–
	-14	2.0×10^{21}	2.0×10^{21}	–	–	–	–
	-13	4.0×10^{26}	4.0×10^{26}	–	–	–	–
	-12	2.1×10^{33}	2.9×10^{25}	–	–	–	–
	-11	1.0×10^{43}	5.1×10^{23}	–	–	–	–
	-10	–	7.6×10^{23}	–	–	–	–
	-9	–	4.3×10^{26}	–	–	–	–
	-8	–	2.1×10^{36}	–	–	–	–
	-7	–	–	4.9×10^{43}	–	–	–
	-6	–	–	2.2×10^{38}	–	–	–
	-5	–	–	4.2×10^{37}	–	–	–
	-4	–	–	2.4×10^{43}	–	–	–
1.32	-14	4.8×10^{15}	4.8×10^{15}	–	–	–	–
	-13	4.0×10^{18}	4.0×10^{18}	–	–	–	–
	-12	4.0×10^{22}	8.0×10^{19}	–	–	–	–
	-11	1.5×10^{28}	8.5×10^{18}	–	–	–	–
	-10	1.1×10^{36}	1.1×10^{19}	–	–	–	–
	-9	–	3.6×10^{20}	–	–	–	–
	-8	–	1.1×10^{26}	1.1×10^{40}	–	–	–
	-7	–	–	9.4×10^{32}	–	–	–
	-6	–	–	3.9×10^{29}	3.4×10^{43}	–	–
	-5	–	–	1.4×10^{29}	1.2×10^{41}	–	–
	-4	–	–	6.1×10^{32}	2.4×10^{45}	–	–

(continues on next page)

Table O-1 (continued).

n_+	$\log_{10}(\frac{t_+}{1\text{s}})$	$d(t_0, t_k)$ (m) Radiation	EW Bag Model	QCD Bag Model	QCD Lattice Fit	QCD Crossover	e^-e^+ Crossover
1.34	-12	1.3×10^{17}	7.7×10^{16}	–	–	–	–
	-11	2.6×10^{20}	2.2×10^{16}	–	–	–	–
	-10	1.1×10^{25}	2.4×10^{16}	–	–	–	–
	-9	5.2×10^{31}	1.7×10^{17}	5.2×10^{31}	–	–	–
	-8	2.5×10^{41}	2.4×10^{20}	8.3×10^{30}	–	–	–
	-7	–	1.3×10^{33}	2.6×10^{26}	1.6×10^{38}	–	–
	-6	–	–	1.9×10^{24}	8.4×10^{32}	–	–
	-5	–	–	1.0×10^{24}	2.3×10^{31}	–	–
	-4	–	–	2.0×10^{26}	1.3×10^{34}	–	–
	-3	–	–	2.0×10^{36}	2.9×10^{47}	–	–
1.36	-11	2.1×10^{16}	8.3×10^{14}	–	–	–	–
	-10	1.5×10^{19}	8.8×10^{14}	1.5×10^{19}	–	–	–
	-9	1.7×10^{23}	2.7×10^{15}	1.7×10^{23}	–	–	–
	-8	1.3×10^{29}	1.6×10^{17}	1.9×10^{25}	1.3×10^{29}	–	–
	-7	7.0×10^{37}	4.5×10^{24}	2.5×10^{22}	6.1×10^{29}	–	–
	-6	–	–	1.1×10^{21}	2.7×10^{26}	–	–
	-5	–	–	7.0×10^{20}	2.8×10^{25}	–	–
	-4	–	–	2.3×10^{22}	1.5×10^{27}	–	–
	-3	–	–	5.6×10^{28}	5.7×10^{35}	–	–
1.38	-9	3.7×10^{18}	2.7×10^{14}	3.7×10^{18}	3.7×10^{18}	–	–
	-8	1.8×10^{22}	2.8×10^{15}	5.8×10^{21}	1.8×10^{22}	–	–
	-7	4.9×10^{27}	6.4×10^{19}	8.0×10^{19}	3.9×10^{24}	–	–
	-6	7.8×10^{35}	–	1.1×10^{19}	2.9×10^{22}	–	–
	-5	–	–	8.4×10^{18}	7.0×10^{21}	–	–
	-4	–	–	7.0×10^{19}	8.7×10^{22}	–	–
	-3	–	–	1.0×10^{24}	2.7×10^{28}	–	–

(continues on next page)

Table O-1 (continued).

n_+	$\log_{10}(\frac{t_+}{1\text{s}})$	$d(t_0, t_k)$ (m) Radiation	EW Bag Model	QCD Bag Model	QCD Lattice Fit	QCD Crossover	e^-e^+ Crossover
1.40	-8	2.4×10^{18}	2.8×10^{14}	2.4×10^{18}	2.4×10^{18}	–	–
	-7	7.3×10^{21}	1.0×10^{17}	2.4×10^{18}	2.5×10^{21}	–	–
	-6	1.2×10^{27}	1.2×10^{27}	6.6×10^{17}	1.1×10^{20}	1.2×10^{27}	–
	-5	1.4×10^{35}	–	5.5×10^{17}	4.2×10^{19}	1.4×10^{35}	–
	-4	5.6×10^{47}	–	2.1×10^{18}	2.1×10^{20}	5.2×10^{40}	–
	-3	–	–	1.0×10^{19}	7.1×10^{23}	–	–
	-2	–	–	2.8×10^{37}	1.8×10^{43}	–	–
1.42	-7	3.1×10^{18}	2.5×10^{15}	2.6×10^{17}	3.1×10^{18}	3.1×10^{18}	–
	-6	8.1×10^{21}	8.1×10^{21}	1.2×10^{17}	3.3×10^{18}	8.1×10^{21}	–
	-5	1.4×10^{27}	–	1.0×10^{17}	1.8×10^{18}	1.4×10^{27}	–
	-4	2.4×10^{35}	–	2.4×10^{17}	4.9×10^{18}	2.6×10^{31}	–
	-3	4.2×10^{48}	–	1.3×10^{19}	9.3×10^{20}	2.0×10^{38}	–
	-2	–	–	1.3×10^{30}	6.8×10^{33}	–	–
1.44	-6	7.1×10^{18}	7.1×10^{18}	4.0×10^{16}	3.7×10^{17}	7.1×10^{18}	–
	-5	2.1×10^{22}	–	3.6×10^{16}	2.5×10^{17}	2.4×10^{22}	–
	-4	6.2×10^{27}	–	6.2×10^{16}	4.8×10^{17}	4.3×10^{25}	–
	-3	4.0×10^{36}	–	8.1×10^{17}	1.4×10^{19}	1.2×10^{30}	–
	-2	–	–	1.9×10^{25}	4.9×10^{27}	–	–
1.46	-5	2.6×10^{19}	–	1.9×10^{16}	7.5×10^{16}	2.6×10^{19}	–
	-4	1.3×10^{23}	–	2.7×10^{16}	1.1×10^{17}	1.1×10^{22}	–
	-3	1.1×10^{29}	–	1.4×10^{17}	1.0×10^{18}	8.1×10^{24}	–
	-2	8.2×10^{38}	–	1.2×10^{22}	4.9×10^{23}	5.0×10^{38}	–
1.48	-4	1.6×10^{20}	–	1.6×10^{16}	4.5×10^{16}	6.4×10^{19}	–
	-3	1.9×10^{24}	–	4.6×10^{16}	1.9×10^{17}	4.6×10^{21}	–
	-2	1.1×10^{31}	–	9.0×10^{19}	1.1×10^{21}	7.6×10^{30}	–
	-1	3.7×10^{42}	–	–	–	–	–

(continues on next page)

Table O-1 (continued).

		$d(t_0, t_k)$ (m)					
n_+	$\log_{10}(\frac{t_+}{1\text{s}})$	Radiation	EW Bag Model	QCD Bag Model	QCD Lattice Fit	QCD Crossover	e^-e^+ Crossover
1.50	-3	1.8×10^{21}	–	2.2×10^{16}	6.3×10^{16}	4.1×10^{19}	–
	-2	8.9×10^{25}	–	3.6×10^{18}	2.1×10^{19}	5.5×10^{25}	–
	-1	9.5×10^{33}	–	–	–	–	–
	0	1.3×10^{48}	–	–	–	–	–
1.52	-3	2.2×10^{19}	–	1.4×10^{16}	3.2×10^{16}	2.1×10^{18}	–
	-2	4.6×10^{22}	–	4.2×10^{17}	1.5×10^{18}	2.3×10^{22}	–
	-1	2.0×10^{28}	–	–	–	–	2.0×10^{28}
	0	2.0×10^{38}	–	–	–	–	2.0×10^{38}
	1	–	–	–	–	–	1.1×10^{50}
1.54	-2	3.3×10^{20}	–	1.0×10^{17}	2.7×10^{17}	1.5×10^{20}	3.3×10^{20}
	-1	3.5×10^{24}	–	3.5×10^{24}	3.5×10^{24}	3.5×10^{24}	3.5×10^{24}
	0	4.7×10^{31}	–	–	–	–	4.7×10^{31}
	1	5.8×10^{44}	–	–	–	–	2.1×10^{40}
1.56	-1	1.1×10^{22}	–	1.1×10^{22}	1.1×10^{22}	1.1×10^{22}	1.1×10^{22}
	0	1.5×10^{27}	–	–	–	–	1.5×10^{27}
	1	4.5×10^{36}	–	–	–	–	3.9×10^{33}
1.58	-1	2.5×10^{20}	–	2.5×10^{20}	2.5×10^{20}	2.5×10^{20}	2.5×10^{20}
	0	1.4×10^{24}	–	–	–	–	1.4×10^{24}
	1	1.1×10^{31}	–	–	–	–	8.4×10^{28}
	2	1.9×10^{44}	–	–	–	–	1.2×10^{44}
1.60	0	1.2×10^{22}	–	–	–	–	1.2×10^{22}
	1	1.4×10^{27}	–	–	–	–	4.9×10^{25}
	2	8.0×10^{36}	–	–	–	–	5.6×10^{36}

(continues on next page)

Table O-1 (continued).

n_+	$\log_{10}(\frac{t_+}{1\text{s}})$	$d(t_0, t_k)$ (m) Radiation	EW Bag Model	QCD Bag Model	QCD Lattice Fit	QCD Crossover	e^-e^+ Crossover
1.62	0	4.5×10^{20}	–	–	–	–	4.5×10^{20}
	1	2.7×10^{24}	–	–	–	–	2.8×10^{23}
	2	4.7×10^{31}	–	–	–	–	3.6×10^{31}
	3	2.0×10^{46}	–	–	–	–	–
1.64	1	3.5×10^{22}	–	–	–	–	7.7×10^{21}
	2	9.1×10^{27}	–	–	–	–	7.4×10^{27}
	3	9.3×10^{38}	–	–	–	–	–
1.66	1	1.7×10^{21}	–	–	–	–	6.3×10^{20}
	2	2.1×10^{25}	–	–	–	–	1.8×10^{25}
	3	4.3×10^{33}	–	–	–	–	–
	4	2.2×10^{51}	–	–	–	–	–
1.68	1	2.0×10^{20}	–	–	–	–	1.1×10^{20}
	2	2.7×10^{23}	–	–	–	–	2.4×10^{23}
	3	5.7×10^{29}	–	–	–	–	–
	4	2.2×10^{43}	–	–	–	–	–
1.70	2	1.2×10^{22}	–	–	–	–	1.1×10^{22}
	3	8.6×10^{26}	–	–	–	–	–
	4	2.4×10^{37}	–	–	–	–	–
1.72	2	1.3×10^{21}	–	–	–	–	1.2×10^{21}
	3	7.6×10^{24}	–	–	–	–	–
	4	8.6×10^{32}	–	–	–	–	–
	5	2.1×10^{51}	–	–	–	–	–

(continues on next page)

Table O-1 (continued).

n_+	$\log_{10}(\frac{t_+}{1\text{s}})$	$d(t_0, t_k)$ (m) Radiation	EW Bag Model	QCD Bag Model	QCD Lattice Fit	QCD Crossover	e^-e^+ Crossover
1.74	3	2.4×10^{23}	–	–	–	–	–
	4	4.2×10^{29}	–	–	–	–	–
	5	1.1×10^{44}	–	–	–	–	–
1.76	3	1.9×10^{22}	–	–	–	–	–
	4	1.4×10^{27}	–	–	–	–	–
	5	2.8×10^{38}	–	–	–	–	–
1.78	3	2.9×10^{21}	–	–	–	–	–
	4	2.1×10^{25}	–	–	–	–	–
	5	1.6×10^{34}	–	–	–	–	–
1.80	4	8.8×10^{23}	–	–	–	–	–
	5	9.1×10^{30}	–	–	–	–	–
	6	2.6×10^{48}	–	–	–	–	–
1.82	4	8.1×10^{22}	–	–	–	–	–
	5	3.0×10^{28}	–	–	–	–	–
	6	2.8×10^{42}	–	–	–	–	–
1.84	4	1.4×10^{22}	–	–	–	–	–
	5	3.9×10^{26}	–	–	–	–	–
	6	6.0×10^{37}	–	–	–	–	–
1.86	4	3.5×10^{21}	–	–	–	–	–
	5	1.4×10^{25}	–	–	–	–	–
	6	1.3×10^{34}	–	–	–	–	–

(continues on next page)

Table O-1 (continued).

		$d(t_0, t_k)$ (m)					
n_+	$\log_{10}(\frac{t_+}{1\text{s}})$	Radiation	EW Bag Model	QCD Bag Model	QCD Lattice Fit	QCD Crossover	e^-e^+ Crossover
1.88	5	1.1×10^{24}	–	–	–	–	–
	6	1.9×10^{31}	–	–	–	–	–
	7	1.3×10^{51}	–	–	–	–	–
1.90	5	1.5×10^{23}	–	–	–	–	–
	6	1.1×10^{29}	–	–	–	–	–
	7	1.7×10^{45}	–	–	–	–	–
1.92	5	3.4×10^{22}	–	–	–	–	–
	6	2.0×10^{27}	–	–	–	–	–
	7	3.3×10^{40}	–	–	–	–	–
1.94	5	1.1×10^{22}	–	–	–	–	–
	6	8.5×10^{25}	–	–	–	–	–
	7	5.6×10^{36}	–	–	–	–	–
1.96	6	7.3×10^{24}	–	–	–	–	–
	7	5.4×10^{33}	–	–	–	–	–
1.98	6	1.0×10^{24}	–	–	–	–	–
	7	2.1×10^{31}	–	–	–	–	–
	8	6.2×10^{53}	–	–	–	–	–
2.00	6	2.3×10^{23}	–	–	–	–	–
	7	2.4×10^{29}	–	–	–	–	–
	8	1.3×10^{48}	–	–	–	–	–

P On the possibility of direct detection of BHs by electromagnetic radiation: fundamentals (*)

P.1 Black Hole Thermodynamics

A BH is completely characterized by three parameters only: mass m, electric charge ϵ and angular momentum per unit mass a. These parameters should respect the relation (e.g. Davies, 1978)

$$a^2 + \epsilon^2 \leq m^2$$

with m, ϵ and a writen in geometrized units ($c = G = 1$; G is the gravitational constant; c the speed of light). There is a remarkable analogy between the laws of BH mechanics and the laws of Thermodynamics (e.g. Wald, 1998). It is shown that, when quantum effects are taken into account, BHs radiate like a blackbody (e.g. Hawking, 1974). Thus, it is possible to assign to each BH a temperature (e.g. Wald, 1984)

$$T = \frac{\hbar \Psi}{2\pi k} \tag{P-1}$$

where $\hbar$ is the reduced Planck constant, k is the Boltzmann constant and

$$\Psi = \frac{\left(m^2 - a^2 - \epsilon^2\right)^{1/2}}{2m\left(m + \left(m^2 - a^2 - \epsilon^2\right)^{1/2}\right) - \epsilon^2}, \quad (\epsilon \neq 0, a \neq 0) \tag{P-2}$$

is the surface gravity of the BH ($\Psi_{max} = \frac{1}{4m}$). For a given mass m, the surface gravity (P-2), and hence the temperature (P-1), will be maximum if ϵ and a are both zero, i.e., if we have a Schwarzschild BH. Reissner-Nordström BHs ($m \neq 0, \epsilon \neq 0, a = 0$), Kerr BHs ($m \neq 0, \epsilon = 0, a \neq 0$) or Kerr-Newmann BHs ($m \neq 0, \epsilon \neq 0, a \neq 0$) with the same mass m will have lower temperatures. In fact, for an extreme Reissner-Nordström BH ($\epsilon = \pm m$) or a maximum Kerr BH ($a = \pm m$) we have a null temperature. Thus, for a given mass m, Schwarzschild BHs are the hottest ones and consequently the ones that offer more hypotheses of detection. We shall consider then, from now on, only Schwarzschild BHs.

P.2 The Schwarzschild Black Hole

In terms of structure, the Schwarzschild BH has a central singularity and an infinite redshift surface (event horizon) with a dimension interpreted as radius (Schwarzschild radius) given by (e.g. d'Inverno, 1993)

$$r_s = 2m = \frac{2GM}{c^2} \tag{P-3}$$

(*) This appendix is a summary in English of Sobrinho (2003).

where M is the BH mass in non-geometrized units. The Schwarzschild BH temperature can be written, from equations (P-1) and (P-3), in non–geometrized units, as (e.g. Demianski, 1985)

$$T = \frac{\hbar c^3}{8\pi k G M} \approx 6.2 \times 10^{-8} \frac{M_{M_\odot}}{M} \tag{P-4}$$

Taking into account that a BH emits like a blackbody with the same temperature, we may relate the temperature with the wavelength λ_{max} at which the emission gets its intensity peak. Thus we have according to Wien's Displacement Law (e.g. Eisberg & Resnick, 1985)

$$T\lambda_{max} = 2.898 \times 10^{-3} \tag{P-5}$$

The luminosity of a spherical blackbody with radius r can be written as $L = 4\pi r^2 \sigma T^4$ where σ represents the Stefan-Boltzmann constant (e.g. Harwit, 1998). Taking into account equations (P-3) and (P-4) we can write, for the total luminosity of the Schwarzschild BH

$$L = \frac{\sigma}{\pi^3 G^2 M^2} \left(\frac{\hbar c^2}{4k} \right)^4 \approx \frac{3.6 \times 10^{32}}{M^2} \tag{P-6}$$

All the thermodynamic radiation coming directly from BHs we call *primary* (radio, infrared, visible, ultraviolet, X–ray and γ–ray).

By definition, a Schwarzschild BH gets completely defined given its mass M. All other properties of the BH (e.g. radius, temperature) can be expressed in terms of M. In particular, knowing M, we know the value of λ_{max} (cf. equations P-4 and P-5) which means that we can associate to each wavelength of the electromagnetic spectrum a Schwarzschild BH, i.e., *BHs have colours*. Across the electromagnetic spectrum, from the radio waves to the γ–rays, will take us from the supermassive BHs to the microscopic ones. We then speak about radio, infrared, visible, ultraviolet, X–ray and γ–ray BHs, depending on where their emission spectrum peak is located.

P.3 Secondary γ–rays from BHs

As a BH radiates due to the Hawking process it looses mass or, in other words, it evaporates. The rate at which a BH evaporates can be written as (e.g. Maki et al., 1996)

$$\frac{dM}{dt} = -\frac{5.34 \times 10^{16} f(M)}{M^2} \tag{P-7}$$

where f is a function of the BH mass M. When $M \gg 10^{14}$ kg we have $f(M) \approx 1$ (e.g. Maki et al., 1996) and for $M \ll 10^8$ kg we have $f(M) \approx 15.4$ (e.g. Semikoz,

1994). It is also normally assumed that between these two situations the behaviour is log-linear. The expression giving the evaporation time of an isolated BH can be obtained by integrating equation (P-7). Taking into account that f varies very slowly with the mass M we have (e.g. He & Fang, 2002)

$$t_{evap} \approx \frac{M_i^3 - M_f^3}{1.6 \times 10^{17} f(M)} \tag{P-8}$$

which is the time required for a BH to change its mass from the initial value M_i to the final value M_f. As the evaporation goes on, the BH will start emitting massive particles, besides photons and gravitons (Page & Hawking, 1976). An evaporating BH will emit particles of mass m_0 if its own mass M satisfies the inequality (e.g. Shapiro & Teukolsky, 1983)

$$M \leq \frac{ch}{Gm_0} = \frac{m_p^2}{m_0} \tag{P-9}$$

where m_p is the Planck mass ($m_p \approx 5.46 \times 10^{-8}$ kg). According to equation (P-9), an evaporating BH starts emitting hadrons, starting with the lightest ones which are the π^0 mesons ($m_0 \simeq 2.4 \times 10^{-28}$ kg) when its mass is $\approx 10^{12}$ kg which corresponds to a Schwarzswchild radius of the order of the strong nuclear force range ($\approx 10^{-15}$ m). Because of that, the BH will emit jets of quarks and gluons instead of composed particles (Page & Hawking, 1976). Emitted quarks and gluons develop into hadron jets with a predominance of π mesons (e.g. Semikoz, 1994). An estimation of the total pion flux is (e.g. Belyanin et al., 1996)

$$\frac{dN_\pi}{dt} \approx 2.7 \times 10^6 T^{1.5} \tag{P-10}$$

All the three known kinds of π mesons appear in a jet with the same probability. Every π^+ or π^- meson decays into electrons, positrons and neutrinos. As for the π^0 mesons each one of them decays into two γ–ray photons each one carrying one–half of the π^0 meson energy (≈ 70 MeV) (e.g. Semikoz, 1994). The total number of γ–ray photons emitted per unit time, resulting from the π^0 mesons, can be written as

$$\frac{dN_\gamma}{dt} = \frac{2}{3}\frac{dN_\pi}{dt} \tag{P-11}$$

We will call these *secondary γ–rays* in contrast to the γ–rays emitted directly by the BH (*primary γ-rays*).

The latter equation gives us the number of secondary γ–ray photons emitted per unit time. Thus, the energy flux (F) related to secondary γ–ray emission can be obtained multiplying equation (P-11) with the photons energy (≈ 70 MeV) and dividing by the area of the event horizon of a Schwarzschild BH (πr_s^2)

$$F = \frac{dN_\gamma}{dt}\frac{70MeV}{\pi r_s^2} \tag{P-12}$$

Table P-1: Emission of neutrinos and leptons by BHs. For each particle the respective mass m_0 (see (e.g. Hagiwara et al., 2002) for the neutrinos mass and (e.g. Shapiro & Teukolsky, 1983) for the leptons mass) as well as the mass that a BH should have to start emitting that kind of particle (equation P-9) is shown. The correspondent Schwarzschild radius is also shown.

Particle	m_0 (MeV)	M(kg)	r_s (m)
ν_e neutrino	$< 3 \times 10^{-6}$	$\leq 10^{19}$	10^{-8}
ν_μ neutrino	0.19	$\leq 10^{14}$	10^{-13}
electron	0.511	$\leq 10^{14}$	10^{-13}
ν_τ neutrino	< 18.2	$\leq 10^{12}$	10^{-15}
μ lepton	105.659	$\leq 10^{11}$	10^{-16}
τ lepton	1784	$\leq 10^{10}$	10^{-17}

In Table P-1 the mass magnitude below which an evaporating BH starts emitting specific kinds of leptons and neutrinos is displayed. For the neutrino mass we took, for each type, the respective upper limit as given by (e.g. Hagiwara et al., 2002).

P.4 The possibility of direct detection of BHs

Given that there is little doubt that all BHs emit electromagnetic (Hawking) radiation, it is now our purpose to establish the maximum distance at which each 'colour' might be detected. A BH emits like a blackbody, obeying the Planck radiation law (e.g. Unsöld & Bascheck, 2002)

$$B_\nu(T) = \frac{2h\nu^3}{c^2} \frac{1}{e^{\frac{h\nu}{kT}} - 1} \tag{P-13}$$

with $B_\nu(T)$ the BH brightness, i.e., the energy emitted per unit time, per unit area, per unit frequency ν, per unit solid angle subtended in the sky. Let s_ν be the flux density reaching a detector placed at some distance d from the center of the BH. We shall look for $d \gg r_s$ in order to avoid general relativity effects near the detector. The values of B_ν, s_ν and d are then related by (e.g. Lang, 1999)

$$s_\nu = \Omega_s B_\nu(T) \approx \frac{\pi r_s^2}{d^2} B_\nu(T) \tag{P-14}$$

where r_s is the Schwarzschild radius and Ω_s is the solid angle subtended by the source in the sky. The emited flux density, S_ν, can be obtained from equation (P-14) with $d = r_s$

$$S_\nu = \pi B_\nu(T) = \frac{2\pi h\nu^3}{c^2} \frac{1}{e^{\frac{h\nu}{kT}} - 1} \tag{P-15}$$

Equation (P-14) allows us to relate the flux density emitted by the BH with the flux density measured by a detector through the distance between both, i.e., in the worst case there is a *maximum distance* (d) at which the Hawking radiation could be detected, for a particular wavelength/frequency ν for a particular BH of mass M (equations P-3, P-4 and P-13)

$$d = r_s \left(\frac{2\pi h \nu^3}{s_\nu c^2} \frac{1}{e^{8\pi^2 r_s \nu / c} - 1} \right)^{1/2} \tag{P-16}$$

This means that for distances shorter than this value *we can detect* a Schwarzschild BH of radius r_s (mass M) at a frequency ν (wavelength $\lambda = c/\nu$), using a detector with sensitivity s_ν.

If the sensitivity comes in magnitudes (as at optical wavelengths) we must convert it first to a flux density. In order to express an apparent magnitude m_a as a flux density f we may use the expression (e.g. Zombeck , 1990)

$$m_a - m_0 = -2.5 Log \frac{f}{f_0} \tag{P-17}$$

where m_0 is a reference magnitude (usually $m_0 = 0$) and f_0 is the corresponding flux density. If m_a corresponds to the limiting magnitude of the telescope then f will be the corresponding sensitivity s_ν.

In what follows we will particularize this study by separating the electromagnetic spectrum into six bands, using the current known limitations in sensitivity for each one (Tables P-2 and P-3).

P.5 Present technical limitations to the possibility of direct detection of BHs

In Table P-4 we list 50 Schwarzschild BHs which we will use for the calculations in this Section. They cover 46 decades in λ_{max}, from 10^{12} m (Extremely Low Frequency — radio), which correspond to supermassive BHs, to 10^{-33} m (hard γ–rays) which correspond to Planckian size BHs. For each BH we have also pointed out the calculated values of the temperature (equation P-5), mass (equation P-4), Schwarzschild radius (equation P-3) and total luminosity (equation P-6).

P.5.1 Radio

The radio window (Earth surface) extends from 0.3 mm to 20 m. The short wavelength limit is a function of the atmospheric composition (especially O_2 and H_2O absorptions) while the long wavelength limit depends on the electron density on the atmosphere (Kraus, 1986). There are, at present, several radio telescopes and interferometer arrays operating from the millimeter and sub-mm to metric waves.

Table P-2: Telescopes: summary of the characteristics (bandwidth, central wavelength, and sensitivity) of the instruments considered for the determination of the maximum distances of detection, for BHs, across the electromagnetic spectrum.

Band	$< \lambda >$(m)	s_ν(Jy)	Bandwidth	Telescope
Radio	20 m	1.5×10^{-2}	0.5 MHz	-
	4 m	1.5×10^{-2}	1.5 MHz	VLA
	3.6 cm	5.3×10^{-6}	0.7 GHz	VLA
Infrared	800 μm	10^{-2}	160 μm	SOFIA
	20 μm	10^{-5}	5.5 μm	SST
	3.4 μm	10^{-6}	0.6 μm	SST
Visible	0.70 μm	1.3×10^{-9}	0.21 μm	HST
	0.55 μm	1.1×10^{-9}	0.08 μm	HST
	0.44 μm	8.6×10^{-10}	0.1 μm	HST
Ultraviolet	365 nm	1.9×10^{-7}	145 nm	HST
	105 nm	3.3×10^{-7}	30 nm	FUSE
X–rays	3.5 nm	3.3×10^{-10}	0.3 KeV	XMM
	1 nm	8.6×10^{-11}	1.5 KeV	XMM
	0.167 nm	2.0×10^{-10}	5 KeV	XMM
γ–rays	2.5×10^{-13} m	6.6×10^{-11}	10 MeV	INTEGRAL
	8.3×10^{-17} m	6.7×10^{-13}	50 GeV	AGILE
	2.5×10^{-19} m	1.7×10^{-17}	10 TeV	HESS

Sensitivities vary according to the detector characteristics and, for each one, with the observing wavelength. The archetype of a sensitive radio interferometer is the Very Large Array (VLA), which has sensitivities from $s_\nu = 0.0053$ mJy at 3.6 cm to $s_\nu = 15$ mJy at 4 m, for a long 12 hrs track (http://www.vla.nrao.edu).

Although not all of the 50 BHs of Table P-4 are 'radio' BHs, all emit something at radio wavelengths, even though their peak emissions are elsewhere in the electromagnetic spectrum. Hence, we will use the VLA sensitivities as s_ν in equation (P-14) and extrapolate the 4 m sensitivity up to 20 m (although there are no plans to move towards this end for the enhanced future VLA, the e–VLA). The maximum distances obtained for BHs 13 to 50, using equation (P-16), are presented in Table P-5. BHs 1 to 12 were not included because for each of them, for all the considered wavelengths, we have the maximum distance smaller than the respective Schwarzschild radius. A similar situation occurs for BH 13 when observed at the 3.6 cm wavelength. For $\lambda = 20$ m the BHs 13 and 14 are detectable at distances of, respectively, $1.9r_s$ and $6.4r_s$. Reminding ourselves that we are looking for distances $d \gg r_s$ those values appear in Table P-5 inside parenthesis and will be ignored in the following subsections. Finally, for $\lambda = 4$ m, BH 13 is also detectable at a 'forbidden' distance of $7.3r_s$. Let us see what happens, for example, with BH 15. When $\lambda = 3.6$ cm it

Table P-3: Sensitivities for the UBVR filters (Johnson) derived from equation (P-17). The flux density f_0 corresponds to the reference magnitude $m_0 = 0$ (e.g. Zombeck , 1990).

Filter	$\lambda_{central}(\mu m)$	$\nu_{central}(\times 10^{14} Hz)$	$\Delta\nu(\times 10^{14} Hz)$	m_a (mag)	$f_0(Jy)$	$s_\nu(Jy)$
R	0.70	4.3	1.3	31.3	4270	1.3×10^{-9}
V	0.55	5.5	0.8	31.3	3670	1.1×10^{-9}
B	0.44	6.8	1.6	31.3	2849	8.6×10^{-10}
U	0.365	8.2	44.0	25	1900	1.9×10^{-7}

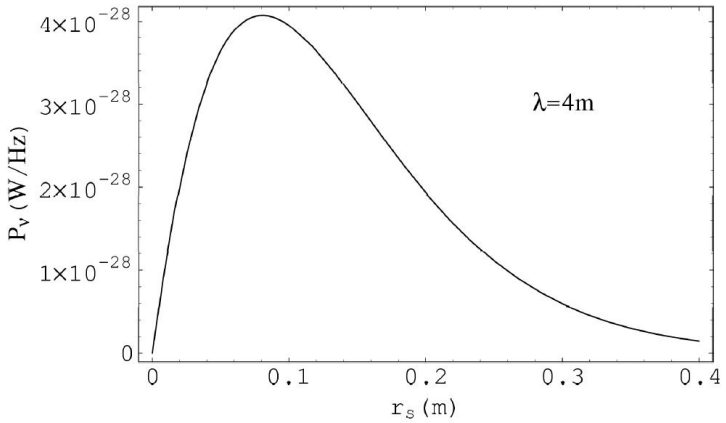

Figure P-1: Luminosity per unit frequency as a function of the Schwarzschild radius for an observing wavelength $\lambda = 4$ m. The peak corresponds to $P_\nu \approx 4.1 \times 10^{-28}$ W/Hz, for a BH with $r_s \approx 0.08$ m.

is detectable at a maximum distance of $d = 2.6 \times 10^2$ m. However for $\lambda = 4$ m, d becomes 6.4 cm and for $\lambda = 20$ m it is 1.3 cm.

Integrating the flux density (equation P-15) over the area of the event horizon of each BH we obtain the luminosity per unit frequency

$$L_\nu = \int S_\nu dA = 4\pi r_s^2 S_\nu$$

Although subatomic size BHs ($r_s \lesssim 10^{-16}$ m; BHs 31 to 50) have high flux densities (Table P-5) their luminosities per unit frequency are, due to their small sizes, very low. In Figure P-1 we plot L_ν as a function of r_s for a wavelength of $\lambda = 4$ m. The maximum value for L_ν is $L_\nu \approx 4.1 \times 10^{-28}$ W/Hz which corresponds to a BH with $r_s \approx 8$ cm ($\approx 2.7 \times 10^{-5} M_\odot$ — see Table P-4) — Table P-5. Taking, for example, a 1.5 MHz bandwidth, this latter value corresponds to a luminosity of $\approx 6.2 \times 10^{-22}$ W.

Let us now consider the study of the function $d(r_s)$ — equation (P-16). We shall use again the 20 m, 4 m and 3.6 cm wavelengths as well as the same values for the detectors sensitivities (VLA style). For the case $\lambda = 20$ m, only BHs with Schwarzschild radius smaller than $\approx 2.6 \times 10^{-3}$ m ($M < 8.8 \times 10^{-7} M_\odot$) could be

Table P-4: List of 50 Schwarzschild BHs. For each case it is indicated the value of the emission intensity peak (λ_{max}), the temperature T (equation P-5), the mass M (equation P-4), the Schwarzschild radius r_s (equation P-3) and the luminosity L (equation P-6).

n	Band	λ_{max}(m)	T(K)	$M(M_\odot)$	r_s(m)	L(W)
1	Radio	10^{12}	2.9×10^{-15}	2.1×10^{7}	6.3×10^{10}	2.0×10^{-43}
2		10^{11}	2.9×10^{-14}	2.1×10^{6}	6.3×10^{9}	2.0×10^{-41}
3		10^{10}	2.9×10^{-13}	2.1×10^{5}	6.3×10^{8}	2.0×10^{-39}
4		10^{9}	2.9×10^{-12}	2.1×10^{4}	6.3×10^{7}	2.0×10^{-37}
5		10^{8}	2.9×10^{-11}	2.1×10^{3}	6.3×10^{6}	2.0×10^{-35}
6		10^{7}	2.9×10^{-10}	2.1×10^{2}	6.3×10^{5}	2.0×10^{-33}
7		10^{6}	2.9×10^{-9}	2.1×10^{1}	6.3×10^{4}	2.0×10^{-31}
8		10^{5}	2.9×10^{-8}	2.1×10^{0}	6.3×10^{3}	2.0×10^{-29}
9		10^{4}	2.9×10^{-7}	2.1×10^{-1}	6.3×10^{2}	2.0×10^{-27}
10		10^{3}	2.9×10^{-6}	2.1×10^{-2}	6.3×10^{1}	2.0×10^{-25}
11		10^{2}	2.9×10^{-5}	2.1×10^{-3}	6.3×10^{0}	2.0×10^{-23}
12		10^{1}	2.9×10^{-4}	2.1×10^{-4}	6.3×10^{-1}	2.0×10^{-21}
13		10^{0}	2.9×10^{-3}	2.1×10^{-5}	6.3×10^{-2}	2.0×10^{-19}
14		10^{-1}	2.9×10^{-2}	2.1×10^{-6}	6.3×10^{-3}	2.0×10^{-17}
15		10^{-2}	2.9×10^{-1}	2.1×10^{-7}	6.3×10^{-4}	2.0×10^{-15}
16	Infrared	10^{-3}	2.9×10^{0}	2.1×10^{-8}	6.3×10^{-5}	2.0×10^{-13}
17		10^{-4}	2.9×10^{1}	2.1×10^{-9}	6.3×10^{-6}	2.0×10^{-11}
18		10^{-5}	2.9×10^{2}	2.1×10^{-10}	6.3×10^{-7}	2.0×10^{-9}
19		10^{-6}	2.9×10^{3}	2.1×10^{-11}	6.3×10^{-8}	2.0×10^{-7}
20	Visible	7.0×10^{-7}	4.1×10^{3}	1.5×10^{-11}	4.4×10^{-8}	4.1×10^{-7}
21		6.0×10^{-7}	4.8×10^{3}	1.3×10^{-11}	3.8×10^{-8}	5.6×10^{-7}
22		5.0×10^{-7}	5.8×10^{3}	1.1×10^{-11}	3.2×10^{-8}	8.0×10^{-7}
23		4.0×10^{-7}	7.2×10^{3}	8.6×10^{-12}	2.5×10^{-8}	1.3×10^{-7}
24	Ultraviolet	10^{-7}	2.9×10^{4}	2.1×10^{-12}	6.3×10^{-9}	2.0×10^{-5}
25		10^{-8}	2.9×10^{5}	2.1×10^{-13}	6.3×10^{-10}	2.0×10^{-3}
26	X–rays	10^{-9}	2.9×10^{6}	2.1×10^{-14}	6.3×10^{-11}	2.0×10^{-1}
27		10^{-10}	2.9×10^{7}	2.1×10^{-15}	6.3×10^{-12}	2.0×10^{1}
28	γ–rays	10^{-11}	2.9×10^{8}	2.1×10^{-16}	6.3×10^{-13}	2.0×10^{3}
29		10^{-12}	2.9×10^{9}	2.1×10^{-17}	6.3×10^{-14}	2.0×10^{5}
30		10^{-13}	2.9×10^{10}	2.1×10^{-18}	6.3×10^{-15}	2.0×10^{7}
31		10^{-14}	2.9×10^{11}	2.1×10^{-19}	6.3×10^{-16}	2.0×10^{9}
32		10^{-15}	2.9×10^{12}	2.1×10^{-20}	6.3×10^{-17}	2.0×10^{11}
33		10^{-16}	2.9×10^{13}	2.1×10^{-21}	6.3×10^{-18}	2.0×10^{13}
34		10^{-17}	2.9×10^{14}	2.1×10^{-22}	6.3×10^{-19}	2.0×10^{15}
35		10^{-18}	2.9×10^{15}	2.1×10^{-23}	6.3×10^{-20}	2.0×10^{17}
36		10^{-19}	2.9×10^{16}	2.1×10^{-24}	6.3×10^{-21}	2.0×10^{19}
37		10^{-20}	2.9×10^{17}	2.1×10^{-25}	6.3×10^{-22}	2.0×10^{21}
38		10^{-21}	2.9×10^{18}	2.1×10^{-26}	6.3×10^{-23}	2.0×10^{23}
39		10^{-22}	2.9×10^{19}	2.1×10^{-27}	6.3×10^{-24}	2.0×10^{25}
40		10^{-23}	2.9×10^{20}	2.1×10^{-28}	6.3×10^{-25}	2.0×10^{27}
41		10^{-24}	2.9×10^{21}	2.1×10^{-29}	6.3×10^{-26}	2.0×10^{29}
42		10^{-25}	2.9×10^{22}	2.1×10^{-30}	6.3×10^{-27}	2.0×10^{31}
43		10^{-26}	2.9×10^{23}	2.1×10^{-31}	6.3×10^{-28}	2.0×10^{33}
44		10^{-27}	2.9×10^{24}	2.1×10^{-32}	6.3×10^{-29}	2.0×10^{35}
45		10^{-28}	2.9×10^{25}	2.1×10^{-33}	6.3×10^{-30}	2.0×10^{37}
46		10^{-29}	2.9×10^{26}	2.1×10^{-34}	6.3×10^{-31}	2.0×10^{39}
47		10^{-30}	2.9×10^{27}	2.1×10^{-35}	6.3×10^{-32}	2.0×10^{41}
48		10^{-31}	2.9×10^{28}	2.1×10^{-36}	6.3×10^{-33}	2.0×10^{43}
49		10^{-32}	2.9×10^{29}	2.1×10^{-37}	6.3×10^{-34}	2.0×10^{45}
50		10^{-33}	2.9×10^{30}	2.1×10^{-38}	6.3×10^{-35}	2.0×10^{47}

Table P-5: Maximum distances (d) for detection at the radio wavelengths 3.6 cm ($s_\nu = 0.0053$ mJy; VLA), 4 m ($s_\nu = 15$ mJy; VLA) and 20 m ($s_\nu = 15$ mJy; extrapolated). It is also shown the flux density (S) for each BH in each case. The d values inside parenthesis do not obey $d \gg r_s$. Ignored here the results for BHs 1–12 (Table P-4) which, like for BH 13 and $\lambda = 3.6$ cm, gave nonsense results of $d < r_s$.

		$\lambda = 20$ m		$\lambda = 4$ m		$\lambda = 3.6$ cm	
n	$r_s(m)$	S(Jy)	d(m)	S(Jy)	d(m)	S(Jy)	d(m)
13	6.3×10^{-2}	5.5×10^{-2}	(1.2×10^{-1})	7.9×10^{-1}	(4.6×10^{-1})	–	$< r_s$
14	6.3×10^{-3}	6.2×10^{-1}	(4.1×10^{-2})	15	2.0×10^{-1}	2.7	4.5
15	6.3×10^{-4}	6.3	1.3×10^{-2}	1.6×10^{2}	6.4×10^{-2}	9.0×10^{5}	2.6×10^{2}
16	6.3×10^{-5}	63	4.1×10^{-3}	1.6×10^{3}	2.0×10^{-2}	1.8×10^{7}	1.2×10^{2}
17	6.3×10^{-6}	6.3×10^{2}	1.3×10^{-3}	1.6×10^{4}	6.5×10^{-3}	1.9×10^{8}	38
18	6.3×10^{-7}	6.3×10^{3}	4.1×10^{-4}	1.6×10^{5}	2.0×10^{-3}	1.9×10^{9}	12
19	6.3×10^{-8}	6.3×10^{4}	1.3×10^{-4}	1.6×10^{6}	6.5×10^{-4}	1.9×10^{10}	3.8
20	6.3×10^{-8}	9.0×10^{4}	1.1×10^{-4}	2.2×10^{6}	5.4×10^{-4}	2.8×10^{10}	3.2
21	6.3×10^{-8}	1.0×10^{5}	1.0×10^{-4}	2.6×10^{6}	5.0×10^{-4}	3.2×10^{10}	3.0
22	6.3×10^{-8}	1.3×10^{5}	9.1×10^{-5}	3.1×10^{6}	4.6×10^{-4}	3.9×10^{10}	2.7
23	6.3×10^{-8}	1.6×10^{5}	8.2×10^{-5}	3.9×10^{6}	4.1×10^{-4}	4.8×10^{10}	2.4
24	6.3×10^{-9}	6.3×10^{5}	4.1×10^{-5}	1.6×10^{7}	2.0×10^{-4}	1.9×10^{11}	1.2
25	6.3×10^{-10}	6.3×10^{6}	1.3×10^{-5}	1.6×10^{8}	6.5×10^{-5}	1.9×10^{12}	3.8×10^{-1}
26	6.3×10^{-11}	6.3×10^{7}	4.1×10^{-6}	1.6×10^{9}	2.0×10^{-5}	1.9×10^{13}	1.2×10^{-1}
27	6.3×10^{-12}	6.3×10^{8}	1.3×10^{-6}	1.6×10^{10}	6.5×10^{-6}	1.9×10^{14}	3.8×10^{-2}
28	6.3×10^{-13}	6.3×10^{9}	4.1×10^{-7}	1.6×10^{11}	2.0×10^{-6}	1.9×10^{15}	1.2×10^{-2}
29	6.3×10^{-14}	6.3×10^{10}	1.3×10^{-7}	1.6×10^{12}	6.5×10^{-7}	1.9×10^{16}	3.8×10^{-3}
30	6.3×10^{-15}	6.3×10^{11}	4.1×10^{-8}	1.6×10^{13}	2.0×10^{-7}	1.9×10^{17}	1.2×10^{-3}
31	6.3×10^{-16}	6.3×10^{12}	1.3×10^{-8}	1.6×10^{14}	6.5×10^{-8}	1.9×10^{18}	3.8×10^{-4}
32	6.3×10^{-17}	6.3×10^{13}	4.1×10^{-9}	1.6×10^{15}	2.0×10^{-8}	1.9×10^{19}	1.2×10^{-4}
33	6.3×10^{-18}	6.3×10^{14}	1.3×10^{-9}	1.6×10^{16}	6.5×10^{-9}	1.9×10^{20}	3.8×10^{-5}
34	6.3×10^{-19}	6.3×10^{15}	4.1×10^{-10}	1.6×10^{17}	2.0×10^{-9}	1.9×10^{21}	1.2×10^{-5}
35	6.3×10^{-20}	6.3×10^{16}	1.3×10^{-10}	1.6×10^{18}	6.5×10^{-10}	1.9×10^{22}	3.8×10^{-6}
36	6.3×10^{-21}	6.3×10^{17}	4.1×10^{-11}	1.6×10^{19}	2.0×10^{-10}	1.9×10^{23}	1.2×10^{-6}
37	6.3×10^{-22}	6.3×10^{18}	1.3×10^{-11}	1.6×10^{20}	6.5×10^{-11}	1.9×10^{24}	3.8×10^{-7}
38	6.3×10^{-23}	6.3×10^{19}	4.1×10^{-12}	1.6×10^{21}	2.0×10^{-11}	1.9×10^{25}	1.2×10^{-7}
39	6.3×10^{-24}	6.3×10^{20}	1.3×10^{-12}	1.6×10^{22}	6.5×10^{-12}	1.9×10^{26}	3.8×10^{-8}
40	6.3×10^{-25}	6.3×10^{21}	4.1×10^{-13}	1.6×10^{23}	2.0×10^{-12}	1.9×10^{27}	1.2×10^{-8}
41	6.3×10^{-26}	6.3×10^{22}	1.3×10^{-13}	1.6×10^{24}	6.5×10^{-13}	1.9×10^{28}	3.8×10^{-9}
42	6.3×10^{-27}	6.3×10^{23}	4.1×10^{-14}	1.6×10^{25}	2.0×10^{-13}	1.9×10^{29}	1.2×10^{-9}
43	6.3×10^{-28}	6.3×10^{24}	1.3×10^{-14}	1.6×10^{26}	6.5×10^{-14}	1.9×10^{30}	3.8×10^{-10}
44	6.3×10^{-29}	6.3×10^{25}	4.1×10^{-15}	1.6×10^{27}	2.0×10^{-14}	1.9×10^{31}	1.2×10^{-10}
45	6.3×10^{-30}	6.3×10^{26}	1.3×10^{-15}	1.6×10^{28}	6.5×10^{-15}	1.9×10^{32}	3.8×10^{-11}
46	6.3×10^{-31}	6.3×10^{27}	4.1×10^{-16}	1.6×10^{29}	2.0×10^{-15}	1.9×10^{33}	1.2×10^{-11}
47	6.3×10^{-32}	6.3×10^{28}	1.3×10^{-16}	1.6×10^{30}	6.5×10^{-16}	1.9×10^{34}	3.8×10^{-12}
48	6.3×10^{-33}	6.3×10^{29}	4.1×10^{-17}	1.6×10^{31}	2.0×10^{-16}	1.9×10^{35}	1.2×10^{-12}
49	6.3×10^{-34}	6.3×10^{30}	1.3×10^{-17}	1.6×10^{32}	6.5×10^{-17}	1.9×10^{36}	3.8×10^{-13}
50	6.3×10^{-35}	6.3×10^{31}	4.1×10^{-18}	1.6×10^{33}	2.0×10^{-17}	1.9×10^{37}	1.2×10^{-13}

detected at a distance $d > 10r_s$ (Figure P-2a), as also would approximately be inferred from Table P-5. This is the case for BHs 15 to 50. For the case $\lambda = 4$ m only BHs with radius smaller than ≈ 4 cm ($M < 1.4 \times 10^{-5} M_\odot$) could be detected at a distance $d > 10r_s$ (Figure P-2b). This is the case for BHs 14 to 50 from Table P-4. The graphic in Figure P-2c shows the curve for $\lambda = 3.6$ cm. The distance of maximum detection, which corresponds to the peak of the curve, is 2.6×10^2 m for a BH with $r_s \approx 7.3 \times 10^{-4}$ m ($M \approx 2.5 \times 10^{-7} M_\odot$). The intersection point $d = 10r_s$ occurs for $r_s \approx 1.0 \times 10^{-2}$ m ($M \approx 3.4 \times 10^{-6} M_\odot$). This means that BHs with $r_s < 1.0 \times 10^{-2}$ m are detectable at distances higher than $10r_s$ for the 3.6 cm wavelength. This is the case for BHs 14 to 50 in Table P-4.

P.5.2 Infrared

Due to the atmospheric absorption of infrared rays by water vapor, carbon dioxide and ozone ground based infrared astronomy turns out to be a possible task only for some windows (which are wider in dry, high mountains). Of course, space or high atmosphere is ideal. The Stratospheric Observatory For Infrared Astronomy (SOFIA), (http://www.sofia.usra.edu), works in the entire infrared band ([0.7,1000] μm) while the Spitzer Space Telescope (SST), covers [1,180] μm.

We will consider the possibility of detecting the Hawking radiation emitted by the 50 BHs in Table P-4, on the wavelengths of 800 μm (submillimeter), 20 μm (mid-infrared — Filter Q) and 3.4 μm (near infrared — Filter L). For 800 μm we will consider a sensitivity of 10 mJy (like the one of SOFIA) while for 20 μm and 3.4 μm we will consider sensitivities of, respectively, 10^{-2} mJy and 10^{-3} mJy (like the ones of SST). The maximum distances obtained for BHs 16 to 50, using equation (P-16) are presented in Table P-6. The other BHs (1 to 15) have no valid values (d is not greater than $10r_s$ for them). In Figure P-3 we show the function $d(r_s)$ (equation P-16) for the wavelengths considered in Table P-6 (3.4 μm, 20 μm, 800 μm).

P.5.3 Visible

Although the transition from visible light and the adjacent bands is not an abrupt one we shall consider that visible light lies between the wavelengths 0.4 μm and 0.7 μm (those are the values suggested by the Institute for Telecommunications Sciences of the United States – http://its.bldrdoc.gov). Visible light is not significantly blocked by the Earth's atmosphere and we have both large ground and space based facilities in this region of the electromagnetic spectrum. The sensitivity of optical detectors is normally expressed in terms of apparent magnitude and the current best (e.g. Advanced Camera for Surveys and Wide Field and Planetary Camera 2 on the Hubble Space Telescope) is ~ 31.3 mag.

We will consider the possibility of detecting the Hawking radiation emitted by the 50 BHs from Table P-4, at the central wavelengths of 0.70 μm (Johnson filter R – (Johnson, 1966); see Table P-3 for bandwidths), 0.55 μm (V) and 0.44 μm (B).

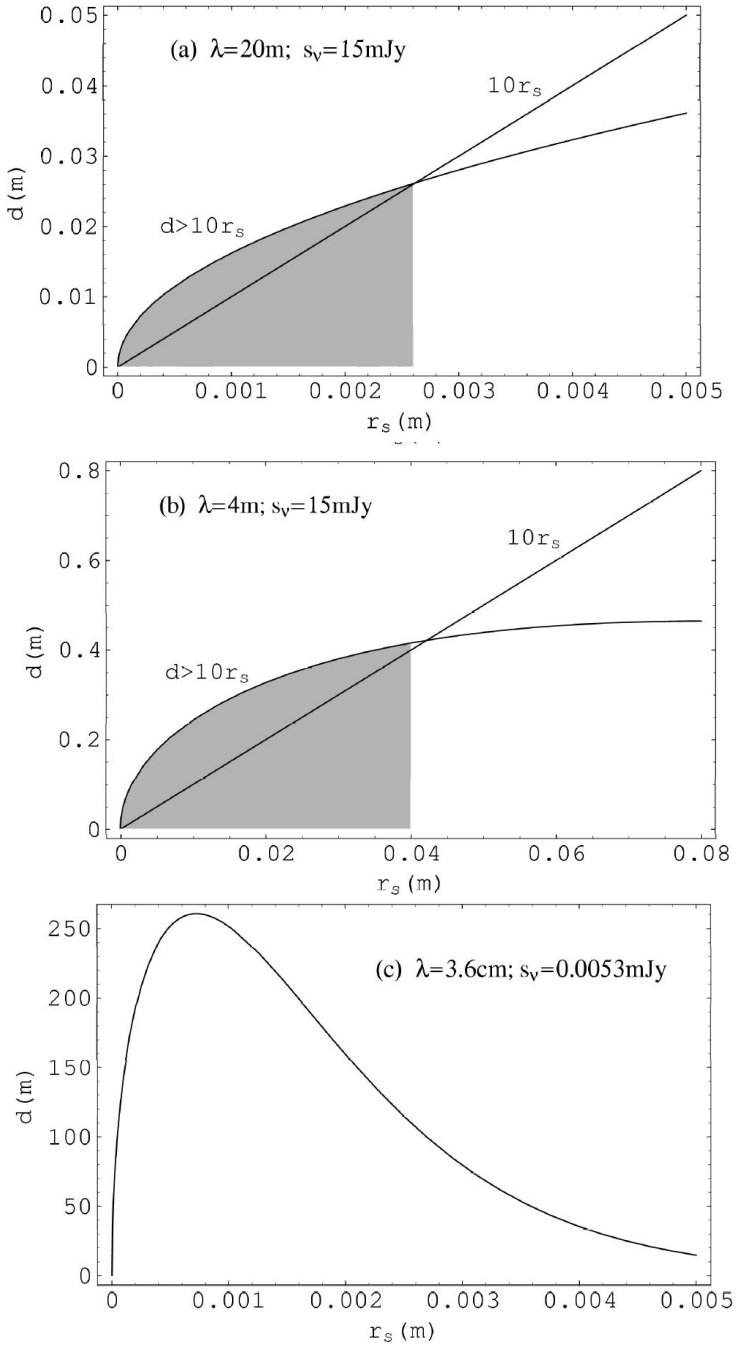

Figure P-2: Maximum distance for detecting the Hawking radiation as a function of the Schwarzschild radius for the radio wavelengths of 20 m, 4 m and 3.6 cm. The grey part in cases (a) and (b) corresponds to values of r_s for which $d > 10r_s$. The intersection point ($d = 10r_s$) corresponds to a BH with: (a) $r_s \approx 2.6 \times 10^{-3}$ m and $M \approx 8.8 \times 10^{-7} M_\odot$ (approx. BH 14 in Table P-4); (b) $r_s \approx 0.04$ m and $M \approx 1.4 \times 10^{-5} M_\odot$ ($\approx$ BH 13). The peak of the curve $d(r_s)$ in case (c) occurs for $r_s \approx 7.3 \times 10^{-4}$ m, $d \approx 2.6 \times 10^2$ m, $M \approx 2.5 \times 10^{-7} M_\odot$ ($\approx$ BH 15).

Table P-6: Maximum distances (d) for detection at the infrared wavelengths 800 μm ($s_\nu = 10$ mJy; SOFIA), 20 μm ($s_\nu = 0.01$ mJy; SST) and 3.4 μm ($s_\nu = 0.001$ mJy; SST). The flux density (S) for each BH is also shown in each case. The results for BHs 1–15 (Table P-4) which, like for BH 16 and $\lambda = 20$ μm, BHs 16–17 and $\lambda = 3.4$ μm, gave nonsense results of $d < r_s$ are ignored here.

		$\lambda = 800$ μm		$\lambda = 20$ μm		$\lambda = 3.4$ μm	
n	$r_s(m)$	S(Jy)	d(m)	S(Jy)	d(m)	S(Jy)	d(m)
16	6.3×10^{-5}	4.9×10^{8}	13	–	–	–	–
17	6.3×10^{-6}	2.8×10^{11}	31	2.6×10^{5}	1.8×10^{-1}	–	–
18	6.3×10^{-7}	3.8×10^{12}	11	1.4×10^{15}	1.4×10^{3}	1.4×10^{12}	2.4×10^{2}
19	6.3×10^{-8}	3.9×10^{13}	3.6	5.5×10^{16}	8.6×10^{2}	9.6×10^{17}	2.0×10^{4}
20	6.3×10^{-8}	5.6×10^{13}	3.0	8.2×10^{16}	7.3×10^{2}	1.8×10^{18}	1.9×10^{4}
21	6.3×10^{-8}	6.5×10^{13}	2.8	9.7×10^{16}	6.8×10^{2}	2.3×10^{18}	1.8×10^{4}
22	6.3×10^{-8}	7.8×10^{13}	2.6	1.2×10^{17}	6.3×10^{2}	3.0×10^{18}	1.7×10^{4}
23	6.3×10^{-8}	9.8×10^{13}	2.3	1.5×10^{17}	5.6×10^{2}	4.0×10^{18}	1.6×10^{4}
24	6.3×10^{-9}	3.9×10^{14}	1.1	6.2×10^{17}	2.9×10^{2}	2.0×10^{18}	9.0×10^{3}
25	6.3×10^{-10}	3.9×10^{15}	3.6×10^{-1}	6.3×10^{18}	91	2.2×10^{20}	2.9×10^{3}
26	6.3×10^{-11}	3.9×10^{16}	1.1×10^{-1}	6.3×10^{19}	29	2.2×10^{21}	9.3×10^{2}
27	6.3×10^{-12}	3.9×10^{17}	3.6×10^{-2}	6.3×10^{20}	9.1	2.2×10^{22}	2.9×10^{2}
28	6.3×10^{-13}	3.9×10^{18}	1.1×10^{-2}	6.3×10^{21}	2.9	2.2×10^{23}	93
29	6.3×10^{-14}	3.9×10^{19}	3.6×10^{-3}	6.3×10^{22}	9.1×10^{-1}	2.2×10^{24}	30
30	6.3×10^{-15}	3.9×10^{20}	1.1×10^{-3}	6.3×10^{23}	2.9×10^{-1}	2.2×10^{25}	9.3
31	6.3×10^{-16}	3.9×10^{21}	3.6×10^{-4}	6.3×10^{24}	9.1×10^{-2}	2.2×10^{26}	2.9
32	6.3×10^{-17}	3.9×10^{22}	1.1×10^{-4}	6.3×10^{25}	2.9×10^{-2}	2.2×10^{27}	9.3×10^{-1}
33	6.3×10^{-18}	3.9×10^{23}	3.6×10^{-5}	6.3×10^{26}	9.1×10^{-3}	2.2×10^{28}	2.9×10^{-1}
34	6.3×10^{-19}	3.9×10^{24}	1.1×10^{-5}	6.3×10^{27}	2.9×10^{-3}	2.2×10^{29}	9.3×10^{-2}
35	6.3×10^{-20}	3.9×10^{25}	3.6×10^{-6}	6.3×10^{28}	9.1×10^{-4}	2.2×10^{30}	2.9×10^{-2}
36	6.3×10^{-21}	3.9×10^{26}	1.1×10^{-6}	6.3×10^{29}	2.9×10^{-4}	2.2×10^{31}	9.3×10^{-3}
37	6.3×10^{-22}	3.9×10^{27}	3.6×10^{-7}	6.3×10^{30}	9.1×10^{-5}	2.2×10^{32}	2.9×10^{-3}
38	6.3×10^{-23}	3.9×10^{28}	1.1×10^{-7}	6.3×10^{31}	2.9×10^{-5}	2.2×10^{33}	9.3×10^{-4}
39	6.3×10^{-24}	3.9×10^{29}	3.6×10^{-8}	6.3×10^{32}	9.1×10^{-6}	2.2×10^{34}	2.9×10^{-4}
40	6.3×10^{-25}	3.9×10^{30}	1.1×10^{-8}	6.3×10^{33}	2.9×10^{-6}	2.2×10^{35}	9.3×10^{-5}
41	6.3×10^{-26}	3.9×10^{31}	3.6×10^{-9}	6.3×10^{34}	9.1×10^{-7}	2.2×10^{36}	2.9×10^{-5}
42	6.3×10^{-27}	3.9×10^{32}	1.1×10^{-9}	6.3×10^{35}	2.9×10^{-7}	2.2×10^{37}	9.3×10^{-6}
43	6.3×10^{-28}	3.9×10^{33}	3.6×10^{-10}	6.3×10^{36}	9.1×10^{-8}	2.2×10^{38}	2.9×10^{-6}
44	6.3×10^{-29}	3.9×10^{34}	1.1×10^{-10}	6.3×10^{37}	2.9×10^{-8}	2.2×10^{39}	9.3×10^{-7}
45	6.3×10^{-30}	3.9×10^{35}	3.6×10^{-11}	6.3×10^{38}	9.1×10^{-9}	2.2×10^{40}	2.9×10^{-7}
46	6.3×10^{-31}	3.9×10^{36}	1.1×10^{-11}	6.3×10^{39}	2.9×10^{-9}	2.2×10^{41}	9.3×10^{-8}
47	6.3×10^{-32}	3.9×10^{37}	3.6×10^{-12}	6.3×10^{40}	9.1×10^{-10}	2.2×10^{42}	2.9×10^{-8}
48	6.3×10^{-33}	3.9×10^{38}	1.1×10^{-12}	6.3×10^{41}	2.9×10^{-10}	2.2×10^{43}	9.3×10^{-9}
49	6.3×10^{-34}	3.9×10^{39}	3.6×10^{-13}	6.3×10^{42}	9.1×10^{-11}	2.2×10^{44}	2.9×10^{-9}
50	6.3×10^{-35}	3.9×10^{40}	1.1×10^{-13}	6.3×10^{43}	2.9×10^{-11}	2.2×10^{45}	9.3×10^{-10}

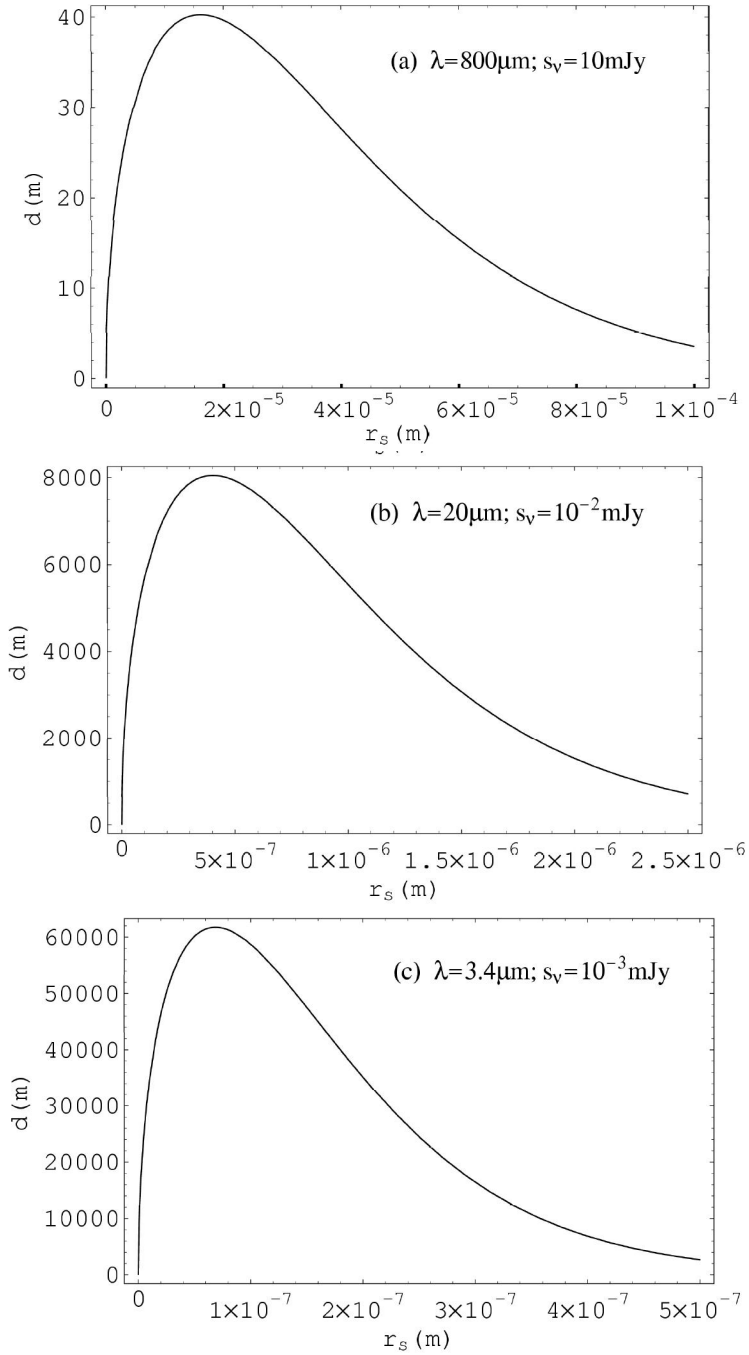

Figure P-3: Maximum distance for detecting the Hawking radiation as a function of the Schwarzschild radius for the wavelengths 800 μm (submilimeter waves), 20 μm (mean infrared – filter Q) and 3.4 μm (near infrared – filter L). Note the different instrument sensitivities (s_ν) in each case. The values for each peak are as follows: (a) $r_s = 1.6 \times 10^{-5}$ m, $d = 40.3$ m, $M = 5.4 \times 10^{-9} M_\odot$ (approx. BH 17 in Table P-4); (b) $r_s = 4.0 \times 10^{-7}$ m, $d = 8.0 \times 10^3$ m, $M = 1.4 \times 10^{-10} M_\odot$ ($\approx$ BH 18); (c) $r_s = 6.9 \times 10^{-8}$ m, $d = 6.2 \times 10^4$ m, $M = 2.3 \times 10^{-11} M_\odot$ ($\approx$ BH 19).

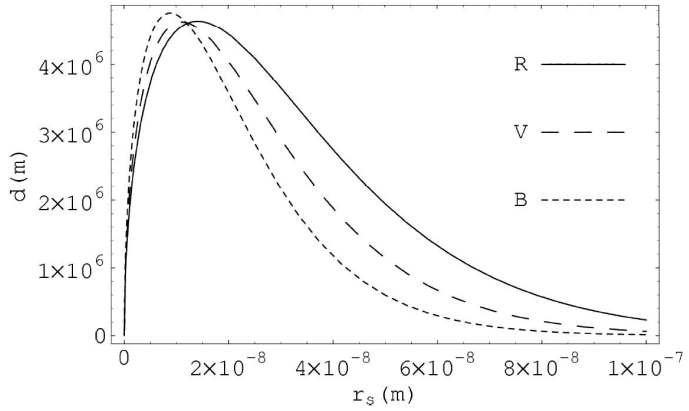

Figure P-4: Maximum distance for detecting the Hawking radiation as a function of the Schwarzschild radius for the visible wavelengths 0.70 μm (filter R), 0.55 μm (filter V) and 0.44 μm (filter B). The values for each peak are as follows: (R) $r_s = 1.4 \times 10^{-8}$ m, $d = 3.8 \times 10^6$ m, $M = 4.7 \times 10^{-12} M_\odot$ (approx. 'between' BHs 23 and 24 in Table P-4); (V) $r_s = 1.1 \times 10^{-8}$ m, $d = 4.6 \times 10^6$ m, $M = 3.7 \times 10^{-12} M_\odot$ ($\approx$ 'between' BHs 23 and 24); (B) $r_s = 8.9 \times 10^{-9}$ m, $d = 5.9 \times 10^6$ m, $M = 3.0 \times 10^{-12} M_\odot$ ($\approx$ BH 24).

For each case we will consider as the sensitivity limit the apparent magnitude $m_a = 31.3$ mag. In order to apply equation (P-16), we use equation (P-17) with $m_a = 31.3$ and f_0 equal to the flux density corresponding to the reference magnitude $m_0 = 0$ (which depends on the optical band used—Table P-3). The flux density f obtained from equation (P-17) corresponds in fact to the sensitivity s_ν. Table P-7 shows the maximum distances for detecting, at visible wavelengths, BHs 19 to 50 (1 to 18 have no valid values). Presented in Figure P-4 are the curves for the function $d(r_s)$ (equation P-16) for the same wavelengths considered for Table P-7 and for the detector sensitivities indicated on Table P-3.

P.5.4 Ultraviolet

Ultraviolet (UV) radiation from outer space is blocked by the ozone layer, which is why UV astronomy has been exclusively done from space. HST instruments are able to detect radiation at near–UV and mid–UV wavelengths down to $m_a \approx 25$ mag. The Far Ultraviolet Spectroscopic Explorer (FUSE) satellite, launched in 1999, allows observations between 90 nm (extreme–UV) and 120 nm (far–UV) with a sensitivity limit of $s_\nu \approx 0.33$ μJy. We will consider the possibility of detecting the Hawking radiation emitted by the 50 BHs in Table P-4, at the wavelengths 365 nm (near–UV) and 105 nm (far–UV). For the 365 nm we will consider $s_\nu = 1.9 \times 10^{-7}$ Jy (Johnson Filter U (Johnson, 1966); see Table P-3) and for the 105 nm $s_\nu = 3.3 \times 10^{-7}$ Jy (FUSE). The maximum distances obtained for BHs 19 to 50 (remaining have no valid values), using equation (P-16), as well as the flux density emitted by each BH in each case, are those presented in Table P-8. Presented in Figure P-5 are the curves for the function $d(r_s)$ (equation P-16) for the same wavelengths considered for Table P-8.

Table P-7: Maximum distances (d) for detection in the visible wavelengths 0.70 μm ($s_\nu = 1.3 \times 10^{-9}$ Jy; filter R), 0.55 μm ($s_\nu = 1.1 \times 10^{-9}$ Jy; filter V) and 0.44 μm ($s_\nu = 8.6 \times 10^{-10}$ Jy; filter B). It is also shown the flux density (S) for each BH in each case. The results for BHs 1–18 (Table P-4) which gave nonsense results of $d < r_s$ are ignored here.

		$\lambda = 0.70\ \mu m$		$\lambda = 0.55\ \mu m$		$\lambda = 0.44\ \mu m$	
n	$r_s(m)$	S(Jy)	d(m)	S(Jy)	d(m)	S(Jy)	d(m)
19	6.3×10^{-8}	3.0×10^{17}	9.6×10^{5}	9.0×10^{16}	5.7×10^{5}	1.8×10^{16}	2.9×10^{5}
20	6.3×10^{-8}	2.6×10^{18}	2.0×10^{6}	1.4×10^{18}	1.6×10^{6}	5.4×10^{17}	1.1×10^{6}
21	6.3×10^{-8}	5.2×10^{18}	2.4×10^{6}	3.3×10^{18}	2.1×10^{6}	1.7×10^{18}	1.7×10^{6}
22	6.3×10^{-8}	1.1×10^{19}	2.9×10^{6}	8.3×10^{18}	2.7×10^{6}	5.2×10^{18}	2.5×10^{6}
23	6.3×10^{-8}	2.3×10^{19}	3.3×10^{6}	2.1×10^{19}	3.5×10^{6}	1.6×10^{19}	3.5×10^{6}
24	6.3×10^{-9}	3.5×10^{20}	3.3×10^{6}	5.1×10^{20}	4.3×10^{6}	7.0×10^{20}	5.7×10^{6}
25	6.3×10^{-10}	4.9×10^{21}	1.2×10^{6}	7.9×10^{21}	1.7×10^{6}	1.2×10^{22}	2.4×10^{6}
26	6.3×10^{-11}	5.1×10^{22}	4.0×10^{5}	8.3×10^{22}	5.5×10^{5}	1.3×10^{23}	7.7×10^{5}
27	6.3×10^{-12}	5.1×10^{23}	1.3×10^{5}	8.3×10^{23}	1.7×10^{5}	1.3×10^{24}	2.5×10^{5}
28	6.3×10^{-13}	5.1×10^{24}	4.0×10^{4}	8.3×10^{24}	5.5×10^{4}	1.3×10^{25}	7.8×10^{4}
29	6.3×10^{-14}	5.1×10^{25}	1.3×10^{4}	8.3×10^{25}	1.7×10^{4}	1.3×10^{26}	2.5×10^{4}
30	6.3×10^{-15}	5.1×10^{26}	4.0×10^{3}	8.3×10^{26}	5.5×10^{3}	1.3×10^{27}	7.8×10^{3}
31	6.3×10^{-16}	5.1×10^{27}	1.3×10^{3}	8.3×10^{27}	1.7×10^{3}	1.3×10^{28}	2.5×10^{3}
32	6.3×10^{-17}	5.1×10^{28}	4.0×10^{2}	8.3×10^{28}	5.5×10^{2}	1.3×10^{29}	7.8×10^{2}
33	6.3×10^{-18}	5.1×10^{29}	1.3×10^{2}	8.3×10^{29}	1.7×10^{2}	1.3×10^{30}	2.5×10^{2}
34	6.3×10^{-19}	5.1×10^{30}	40	8.3×10^{30}	55	1.3×10^{31}	78
35	6.3×10^{-20}	5.1×10^{31}	13	8.3×10^{31}	17	1.3×10^{32}	25
36	6.3×10^{-21}	5.1×10^{32}	4.0	8.3×10^{32}	5.5	1.3×10^{33}	7.8
37	6.3×10^{-22}	5.1×10^{33}	1.3	8.3×10^{33}	1.7	1.3×10^{34}	2.5
38	6.3×10^{-23}	5.1×10^{34}	4.0×10^{-1}	8.3×10^{34}	5.5×10^{-1}	1.3×10^{35}	7.8×10^{-1}
39	6.3×10^{-24}	5.1×10^{35}	1.3×10^{-1}	8.3×10^{35}	1.7×10^{-1}	1.3×10^{36}	2.5×10^{-1}
40	6.3×10^{-25}	5.1×10^{36}	4.0×10^{-2}	8.3×10^{36}	5.5×10^{-2}	1.3×10^{37}	7.8×10^{-2}
41	6.3×10^{-26}	5.1×10^{37}	1.3×10^{-2}	8.3×10^{37}	1.7×10^{-2}	1.3×10^{38}	2.5×10^{-2}
42	6.3×10^{-27}	5.1×10^{38}	4.0×10^{-3}	8.3×10^{38}	5.5×10^{-3}	1.3×10^{39}	7.8×10^{-3}
43	6.3×10^{-28}	5.1×10^{39}	1.3×10^{-3}	8.3×10^{39}	1.7×10^{-3}	1.3×10^{40}	2.5×10^{-3}
44	6.3×10^{-29}	5.1×10^{40}	4.0×10^{-4}	8.3×10^{40}	5.5×10^{-4}	1.3×10^{41}	7.8×10^{-4}
45	6.3×10^{-30}	5.1×10^{41}	1.3×10^{-4}	8.3×10^{41}	1.7×10^{-4}	1.3×10^{42}	2.5×10^{-4}
46	6.3×10^{-31}	5.1×10^{42}	4.0×10^{-5}	8.3×10^{42}	5.5×10^{-5}	1.3×10^{43}	7.8×10^{-5}
47	6.3×10^{-32}	5.1×10^{43}	1.3×10^{-5}	8.3×10^{43}	1.7×10^{-5}	1.3×10^{44}	2.5×10^{-5}
48	6.3×10^{-33}	5.1×10^{44}	4.0×10^{-6}	8.3×10^{44}	5.5×10^{-6}	1.3×10^{45}	7.8×10^{-6}
49	6.3×10^{-34}	5.1×10^{45}	1.3×10^{-6}	8.3×10^{45}	1.7×10^{-6}	1.3×10^{46}	2.5×10^{-6}
50	6.3×10^{-35}	5.1×10^{46}	4.0×10^{-7}	8.3×10^{46}	5.5×10^{-7}	1.3×10^{47}	7.8×10^{-7}

Table P-8: Maximum distances (d) for detection at the UV wavelengths of 365 nm ($s_\nu = 1.9 \times 10^{-7}$ Jy; HST) and 105 nm ($s_\nu = 3.3 \times 10^{-7}$ Jy; FUSE). It is also shown the flux density (S) for each BH in each case. Ignored here the results for BHs 1–18 (Table P-4) which gave nonsense results of $d < r_s$.

		$\lambda = 365$ nm		$\lambda = 105$ nm	
n	r_s(m)	S(Jy)	d(m)	S(Jy)	d(m)
19	6.3×10^{-8}	3.2×10^{15}	8.1×10^{3}	3.1×10^{2}	1.9×10^{-3}
20	6.3×10^{-8}	1.9×10^{17}	4.4×10^{4}	4.5×10^{8}	1.6
21	6.3×10^{-8}	7.3×10^{17}	7.4×10^{4}	5.1×10^{10}	15
22	6.3×10^{-8}	2.9×10^{18}	1.2×10^{5}	5.8×10^{12}	1.3×10^{2}
23	6.3×10^{-8}	1.1×10^{19}	1.9×10^{5}	6.5×10^{14}	1.1×10^{3}
24	6.3×10^{-9}	8.9×10^{20}	4.3×10^{5}	9.6×10^{20}	3.4×10^{5}
25	6.3×10^{-10}	1.8×10^{22}	1.9×10^{5}	1.8×10^{23}	4.6×10^{5}
26	6.3×10^{-11}	1.9×10^{23}	6.3×10^{4}	2.2×10^{24}	1.6×10^{5}
27	6.3×10^{-12}	1.9×10^{24}	2.0×10^{4}	2.3×10^{25}	5.2×10^{4}
28	6.3×10^{-13}	1.9×10^{25}	6.3×10^{3}	2.3×10^{26}	1.7×10^{4}
29	6.3×10^{-14}	1.9×10^{26}	2.0×10^{3}	2.3×10^{27}	5.2×10^{3}
30	6.3×10^{-15}	1.9×10^{27}	6.3×10^{2}	2.3×10^{28}	1.7×10^{3}
31	6.3×10^{-16}	1.9×10^{28}	2.0×10^{2}	2.3×10^{29}	5.2×10^{2}
32	6.3×10^{-17}	1.9×10^{29}	63	2.3×10^{30}	1.7×10^{2}
33	6.3×10^{-18}	1.9×10^{30}	20	2.3×10^{31}	52
34	6.3×10^{-19}	1.9×10^{31}	6.3	2.3×10^{32}	17
35	6.3×10^{-20}	1.9×10^{32}	2.0	2.3×10^{33}	5.2
36	6.3×10^{-21}	1.9×10^{33}	6.3×10^{-1}	2.3×10^{34}	1.7
37	6.3×10^{-22}	1.9×10^{34}	2.0×10^{-1}	2.3×10^{35}	5.2×10^{-1}
38	6.3×10^{-23}	1.9×10^{35}	6.3×10^{-2}	2.3×10^{36}	1.7×10^{-1}
39	6.3×10^{-24}	1.9×10^{36}	2.0×10^{-2}	2.3×10^{37}	5.2×10^{-2}
40	6.3×10^{-25}	1.9×10^{37}	6.3×10^{-3}	2.3×10^{38}	1.7×10^{-2}
41	6.3×10^{-26}	1.9×10^{38}	2.0×10^{-3}	2.3×10^{39}	5.2×10^{-3}
42	6.3×10^{-27}	1.9×10^{39}	6.3×10^{-4}	2.3×10^{40}	1.7×10^{-3}
43	6.3×10^{-28}	1.9×10^{40}	2.0×10^{-4}	2.3×10^{41}	5.2×10^{-4}
44	6.3×10^{-29}	1.9×10^{41}	6.3×10^{-5}	2.3×10^{42}	1.7×10^{-4}
45	6.3×10^{-30}	1.9×10^{42}	2.0×10^{-5}	2.3×10^{43}	5.2×10^{-5}
46	6.3×10^{-31}	1.9×10^{43}	6.3×10^{-6}	2.3×10^{44}	1.7×10^{-5}
47	6.3×10^{-32}	1.9×10^{44}	2.0×10^{-6}	2.3×10^{45}	5.2×10^{-6}
48	6.3×10^{-33}	1.9×10^{45}	6.3×10^{-7}	2.3×10^{46}	1.7×10^{-6}
49	6.3×10^{-34}	1.9×10^{46}	2.0×10^{-7}	2.3×10^{47}	5.2×10^{-7}
50	6.3×10^{-35}	1.9×10^{47}	6.3×10^{-8}	2.3×10^{48}	1.7×10^{-7}

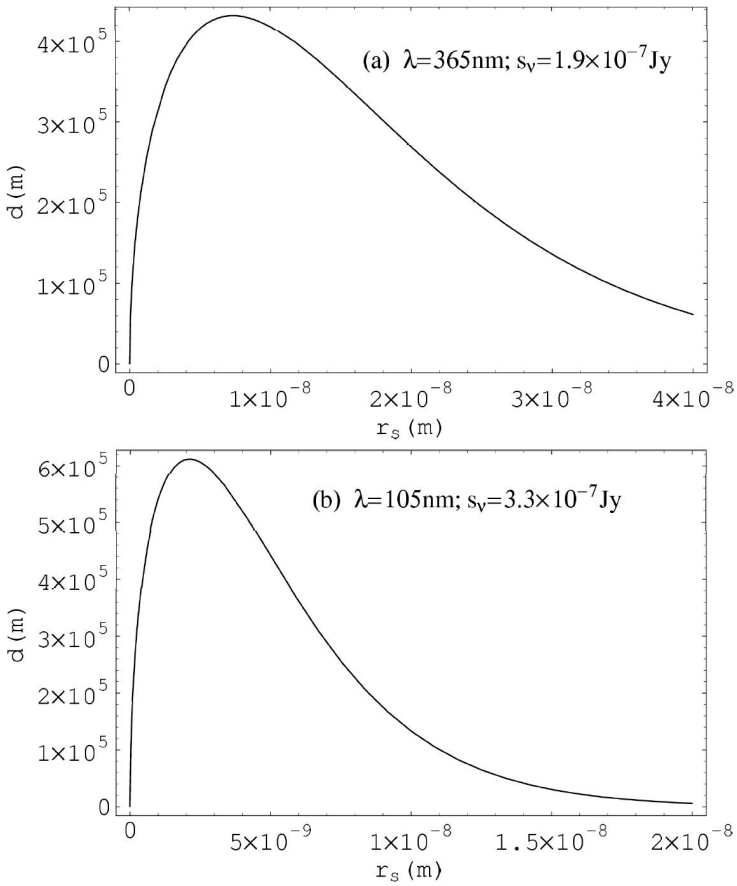

Figure P-5: Maximum distance for detecting the Hawking radiation as a function of the Schwarzschild radius for the wavelengths 365 nm (near UV) and 105 nm (extreme UV). The values for each peak are as follows: (a) $r_s = 7.4 \times 10^{-9}$ m, $d = 4.3 \times 10^5$ m, $M = 2.5 \times 10^{-12} M_\odot$ (approx. BH 24 in Table P-4); (b) $r_s = 2.1 \times 10^{-9}$ m, $d = 6.1 \times 10^5$ m, $M = 7.1 \times 10^{-13} M_\odot$ ($\approx$ 'between' BHs 24 and 25).

P.5.5 X–Rays

X–ray photons interact strongly with matter by means of photo electronic absorption. The mean free path of X–ray photons in the air is therefore limited to a few centimeters and that is why X–ray astronomy has always been done from space. During the last few years several X–ray telescopes have been placed into orbit. One of the most sensitive in operation is the Newton X–ray Multi–mirror Mission (XMM). It has, for example (http://heasarc.gsfc.nasa.gov/docs/xmm/), a sensitivity $s_\nu = 3.3 \times 10^{-10}$ Jy at 0.2–0.5 keV (6.2 nm $> \lambda >$ 2.5 nm — soft X–rays), $s_\nu = 8.6 \times 10^{-11}$ Jy at 0.5–2.0 keV (2.5 nm $> \lambda >$ 0.6 nm — soft and mid X–rays), and $s_\nu = 2.0 \times 10^{-10}$ Jy at 0.2–0.5 keV (0.25 nm $> \lambda >$ 0.13 nm — mid X–rays)[47].

We will consider the possibility of detecting the Hawking radiation emitted by the

[47]Sensitivities in Jy were obtained dividing the given value in erg $cm^{-2}s^{-1}$ by the correspondent bandwidth (http://heasarc.gsfc.nasa.gov/docs/xmm/).

Table P-9: Maximum distances (d) for detection at the X–rays wavelengths 3.5 nm ($s_\nu = 3.3 \times$ 10−10 Jy; XMM), 1 nm ($s_\nu = 8.6 \times 10^{-11}$ Jy; XMM) and 0.167 nm ($s_\nu = 2.0 \times 10^{-10}$ Jy; XMM). The flux density (S) for each BH in each case is also shown. Ignored here the results for BHs 1–24 (Table P-4) which, like for BH 25 and $\lambda = 0.167$ nm, gave nonsense results of $d < r_s$.

		$\lambda = 3.5$ nm		$\lambda = 1$ nm		$\lambda = 0.167$ nm	
n	$r_s(m)$	S(Jy)	d(m)	S(Jy)	d(m)	S(Jy)	d(m)
25	6.3×10^{-10}	2.3×10^{21}	1.7×10^{6}	3.2×10^{7}	3.8×10^{-1}	–	–
26	6.3×10^{-11}	9.1×10^{26}	1.0×10^{8}	8.7×10^{26}	2.0×10^{8}	3.2×10^{18}	8.0×10^{3}
27	6.3×10^{-12}	1.9×10^{28}	4.7×10^{7}	1.9×10^{29}	3.0×10^{8}	1.4×10^{30}	5.4×10^{8}
28	6.3×10^{-13}	2.0×10^{28}	1.5×10^{7}	2.5×10^{30}	1.1×10^{8}	7.7×10^{31}	3.9×10^{8}
29	6.3×10^{-14}	2.0×10^{30}	4.9×10^{6}	2.5×10^{31}	3.4×10^{7}	8.9×10^{32}	1.3×10^{8}
30	6.3×10^{-15}	2.0×10^{31}	1.5×10^{6}	2.5×10^{32}	1.1×10^{7}	9.0×10^{33}	4.2×10^{7}
31	6.3×10^{-16}	2.0×10^{32}	4.9×10^{5}	2.5×10^{33}	3.4×10^{6}	9.0×10^{34}	1.3×10^{7}
32	6.3×10^{-17}	2.0×10^{33}	1.5×10^{5}	2.5×10^{34}	1.1×10^{6}	9.0×10^{35}	4.2×10^{6}
33	6.3×10^{-18}	2.0×10^{34}	4.9×10^{4}	2.5×10^{35}	3.4×10^{5}	9.0×10^{36}	1.3×10^{6}
34	6.3×10^{-19}	2.0×10^{35}	1.5×10^{4}	2.5×10^{36}	1.1×10^{5}	9.0×10^{37}	4.2×10^{5}
35	6.3×10^{-20}	2.0×10^{36}	4.9×10^{3}	2.5×10^{37}	3.4×10^{4}	9.0×10^{38}	1.3×10^{5}
36	6.3×10^{-21}	2.0×10^{37}	1.5×10^{3}	2.5×10^{38}	1.1×10^{4}	9.0×10^{39}	4.2×10^{4}
37	6.3×10^{-22}	2.0×10^{38}	4.9×10^{2}	2.5×10^{39}	3.4×10^{3}	9.0×10^{40}	1.3×10^{4}
38	6.3×10^{-23}	2.0×10^{39}	1.5×10^{2}	2.5×10^{40}	1.1×10^{3}	9.0×10^{41}	4.2×10^{3}
39	6.3×10^{-24}	2.0×10^{40}	49	2.5×10^{41}	3.4×10^{2}	9.0×10^{42}	1.3×10^{3}
40	6.3×10^{-25}	2.0×10^{41}	15	2.5×10^{42}	1.1×10^{2}	9.0×10^{43}	4.2×10^{2}
41	6.3×10^{-26}	2.0×10^{42}	4.9	2.5×10^{43}	34	9.0×10^{44}	1.3×10^{2}
42	6.3×10^{-27}	2.0×10^{43}	1.5	2.5×10^{44}	11	9.0×10^{45}	42
43	6.3×10^{-28}	2.0×10^{44}	4.9×10^{-1}	2.5×10^{45}	3.4	9.0×10^{46}	13
44	6.3×10^{-29}	2.0×10^{45}	1.5×10^{-1}	2.5×10^{46}	1.1	9.0×10^{47}	4.2
45	6.3×10^{-30}	2.0×10^{46}	4.9×10^{-2}	2.5×10^{47}	3.4×10^{-1}	9.0×10^{48}	1.3
46	6.3×10^{-31}	2.0×10^{47}	1.5×10^{-2}	2.5×10^{48}	1.1×10^{-1}	9.0×10^{49}	4.2×10^{-1}
47	6.3×10^{-32}	2.0×10^{48}	4.9×10^{-3}	2.5×10^{49}	3.4×10^{-2}	9.0×10^{50}	1.3×10^{-1}
48	6.3×10^{-33}	2.0×10^{49}	1.5×10^{-3}	2.5×10^{50}	1.1×10^{-2}	9.0×10^{51}	4.2×10^{-2}
49	6.3×10^{-34}	2.0×10^{50}	4.9×10^{-4}	2.5×10^{51}	3.4×10^{-3}	9.0×10^{52}	1.3×10^{-2}
50	6.3×10^{-35}	2.0×10^{51}	1.5×10^{-4}	2.5×10^{52}	1.1×10^{-3}	9.0×10^{53}	4.2×10^{-3}

50 BHs in Table P-4, at the wavelengths 3.5 nm ($s_\nu = 3.3 \times 10^{-10}$ Jy), 1 nm ($s_\nu = 8.6 \times 10^{-11}$ Jy) and 0.167 nm ($s_\nu = 2.0 \times 10^{-10}$ Jy). The maximum distances obtained for BHs 25 to 50 (remaining have no valid values), using equation (P-16), as well as the flux density emitted by each BH in each case, are presented in Table P-9. Presented in Figure P-6 we have the curves for the function $d(r_s)$ (equation P-16) for the same wavelengths considered in Table P-9.

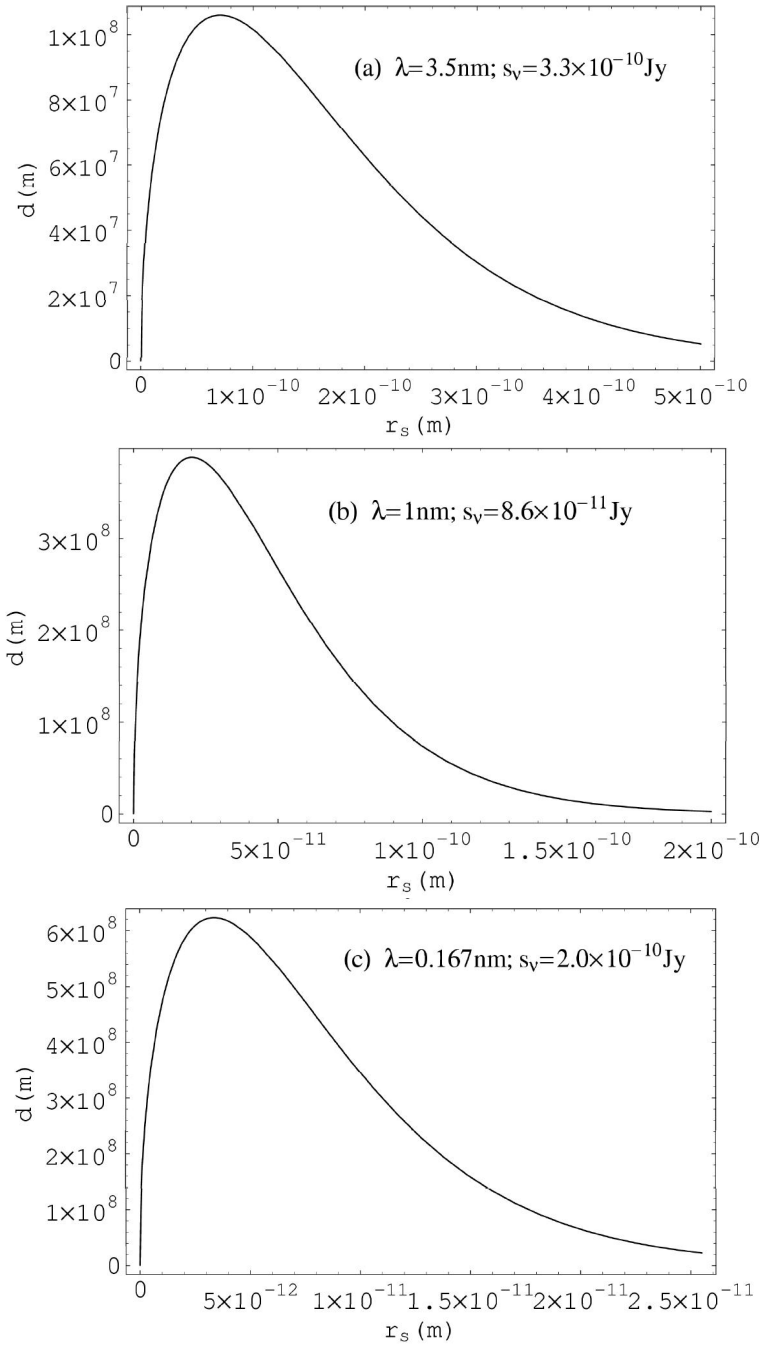

Figure P-6: Maximum distance for detecting the Hawking radiation as a function of the Schwarzschild radius for the wavelengths 3.5 nm (soft X–rays), 1 nm (mid X–rays) and 0.167 nm (hard X–rays). The values for each peak are as follows: (a) $r_s = 7.1 \times 10^{-11}$ m, $d = 1.1 \times 10^8$ m, $M = 2.4 \times 10^{-14} M_\odot$ (approx. BH 26 in Table P-4); (b) $r_s = 2.0 \times 10^{-11}$ m, $d = 3.9 \times 10^8$ m, $M = 6.8 \times 10^{-15} M_\odot$ ($\approx$ 'between' BHs 26 and 27); (c) $r_s = 3.4 \times 10^{-12}$ m, $d = 6.2 \times 10^8$ m, $M = 1.2 \times 10^{-15} M_\odot$ ($\approx$ BH 27).

P.5.6 γ–rays

γ–ray observations must also be made from space because, like X–rays, γ–rays interact strongly with matter in the atmosphere. An exception are hard γ–rays with energies higher than 100 GeV which can penetrate the atmosphere and reach the ground (where Čerenkov detectors are used to detect them).

In the soft γ–ray domain the INTErnational Gamma-Ray Astrophysics Laboratory (INTEGRAL) is already in operation. The detectors on board INTEGRAL allow for observations between 15 keV ($\lambda = 8.3 \times 10^{-11}$ m; hard X–rays) and 10 MeV ($\lambda = 1.2 \times 10^{-13}$ m; soft γ–rays) with a sensitivity of aproximately[48] 6.6×10^{-11} Jy (e.g. Winkler, 2000). For the observation of mid–γ–rays, launched in 2007, we have the Astro-revilatore Gamma a Immagini LEggero (AGILE). Its instruments are able to observe in the 30 MeV–50 GeV (4.1×10^{-14} m $> \lambda > 2.5 \times 10^{-17}$ m; mid–γ–rays) band with a sensivity[49] of $\approx 6.7 \times 10^{-13}$ Jy (e.g. Morselli, 2003). Operating on the hard γ–ray we have in Namibia the High Energy Stereoscopic System (HESS). The system has a sensitivity of 1.7×10^{-17} Jy when operating at 0.1–10 TeV (1.2×10^{-17} m $> \lambda > 1.2 \times 10^{-19}$ m; hard γ–rays) band (e.g. Morselli, 2003)[50].

We will consider the possibility of detecting the Hawking radiation emitted by the 50 BHs in Table P-4, at the wavelengths 2.5×10^{-13} m ($s_\nu = 6.6 \times 10^{-11}$ Jy), 8.3×10^{-17} m ($s_\nu = 6.7 \times 10^{-13}$ Jy) and 2.5×10^{-19} m ($s_\nu = 1.7 \times 10^{-17}$ Jy). The maximum distances obtained for BHs 29 to 50 (the only ones with valid values), using equation (P-16), as well as the flux density emitted by each BH in each case, are those presented in Table P-10. In Figure P-7 we show the curves for the function $d(r_s)$ (equation P-16) for the same wavelengths considered for Table P-10.

P.5.7 Black Holes in their Terminal Phases

Knowing its mass we can estimate, with the help of equation (P-8), the BH evaporation time. In Table P-11 we show these for BHs 31 to 50 (the ones with evaporation times smaller than the age of the Universe). The diversity of time scales from this table urges us to operationally define *terminal BHs* as the ones with evaporation times ≤ 1 year (i.e., BH 34 onwards). The maximum distances for the detection of the Hawking radiation, emitted by terminal BHs, of all colours, were already calculated (Tables P-5, P-6, P-7, P-8, P-9 and P-10).

P.5.8 Emission of Massive Particles and Secondary γ–rays

As presented in Section P.3, BHs also emit massive particles which, in turn, give way to γ–ray emission (secondary γ–rays). We will consider the possibility of detecting

[48] Average of the values in the INTEGRAL which cover two magnitudes (e.g. Winkler, 2000).

[49] Average of the values in the AGILE which cover one magnitude (e.g. Morselli, 2003).

[50] Sensitivities in Jy were obtained dividing the given value in photon $cm^{-2}s$ by the correspondent bandwidths.

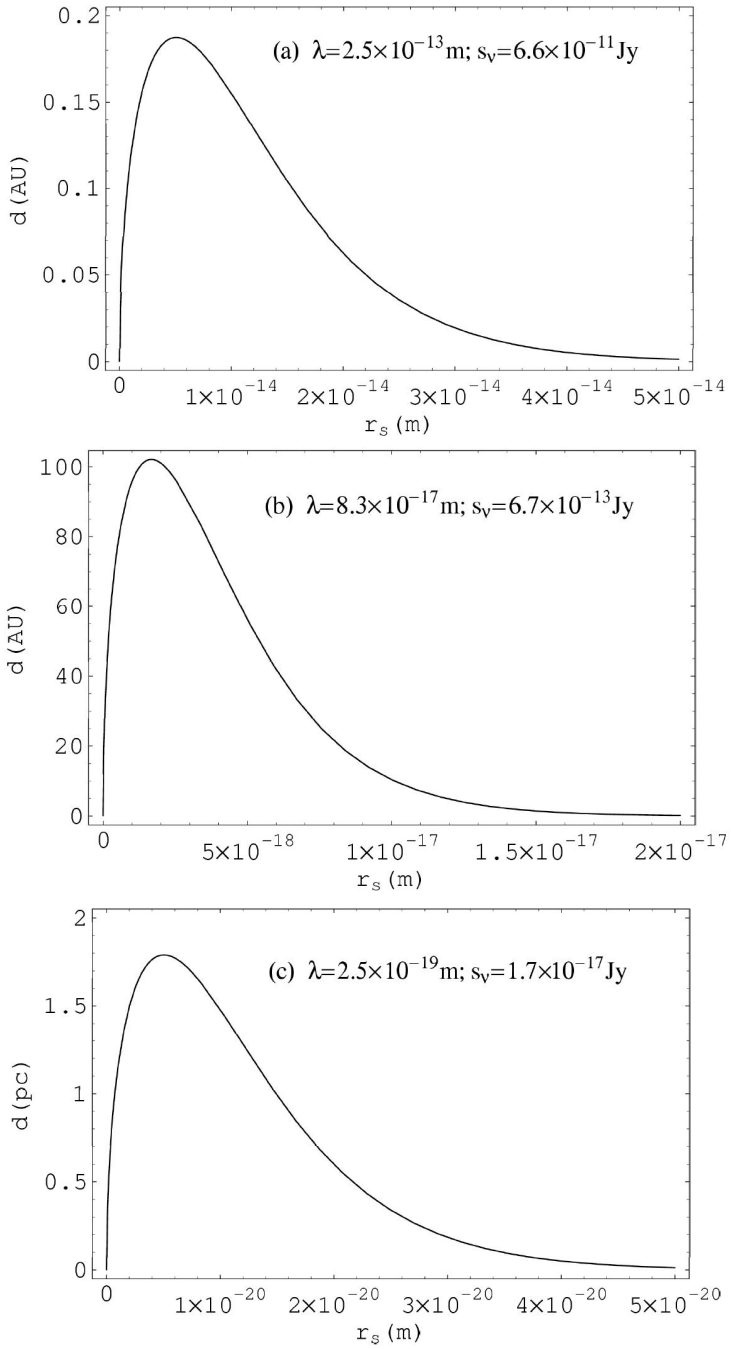

Figure P-7: Maximum distance for detecting the Hawking radiation as a function of the Schwarzschild radius for the wavelengths 2.5×10^{-13} m (soft γ–rays), 8.3×10^{-17} m (mid γ–rays) and 2.5×10^{-19} m (hard γ–rays). The values for each peak are as follows: (a) $r_s = 5.0 \times 10^{-15}$ m, $d = 2.8 \times 10^{10}$ m, $M = 1.7 \times 10^{-18} M_\odot$ (approx. BH 32 in Table P-4); (b) $r_s = 1.7 \times 10^{-18}$ m, $d = 1.5 \times 10^{13}$ m, $M = 5.8 \times 10^{-22} M_\odot$ ($\approx$ BH 34); (c) $r_s = 5.0 \times 10^{-21}$ m, $d = 5.5 \times 10^{16}$ m, $M = 1.7 \times 10^{-24} M_\odot$ ($\approx$ BH 36).

Table P-10: Maximum distances (d) for detection at the γ–ray wavelengths 2.5×10^{-13} m ($s_\nu = 6.6 \times 10^{-11}$ Jy; INTEGRAL), 8.3×10^{-17} m ($s_\nu = 6.7 \times 10^{-13}$ Jy; AGILE) and 2.5×10^{-19} m ($s_\nu = 1.7 \times 10^{-17}$ Jy; HESS). The flux density (S) for each BH in each case is also shown. Ignored BHs 1–28 for $\lambda = 2.5 \times 10^{-13}$ m, BHs 1–31 for $\lambda = 8.3 \times 10^{-17}$ m and BHs 1–34 for $\lambda = 2.5 \times 10^{-19}$ m which gave nonsense results of $d < r_s$. The values for the AGILE case are shown in italic because the detection of primary γ–rays in the 30 MeV–50 GeV bandwith turns out to be not possible.

		$\lambda = 2.5 \times 10^{-13}$ m		$\lambda = 8.3 \times 10^{-17}$ m		$\lambda = 2.5 \times 10^{-19}$ m	
n	$r_s(m)$	S(Jy)	d(m)	S(Jy)	d(m)	S(Jy)	d(m)
29	6.3×10^{-14}	1.9×10^{31}	3.3×10^{7}	–	–	–	–
30	6.3×10^{-15}	1.3×10^{39}	2.8×10^{10}	–	–	–	–
31	6.3×10^{-16}	3.6×10^{40}	1.5×10^{10}	–	–	–	–
32	6.3×10^{-17}	4.0×10^{41}	4.9×10^{9}	*2.2×10^{24}*	*1.2×10^{2}*	–	–
33	6.3×10^{-18}	4.0×10^{42}	1.6×10^{9}	*5.5×10^{47}*	*5.7×10^{12}*	–	–
34	6.3×10^{-19}	4.0×10^{43}	4.9×10^{8}	*2.7×10^{50}*	*1.3×10^{13}*	–	–
35	6.3×10^{-20}	4.0×10^{44}	1.6×10^{8}	*3.5×10^{51}*	*4.6×10^{12}*	1.9×10^{49}	6.7×10^{13}
36	6.3×10^{-21}	4.0×10^{45}	4.9×10^{7}	*3.6×10^{52}*	*1.5×10^{12}*	1.3×10^{57}	5.5×10^{16}
37	6.3×10^{-22}	4.0×10^{46}	1.6×10^{7}	*3.6×10^{53}*	*4.7×10^{11}*	3.6×10^{58}	3.0×10^{16}
38	6.3×10^{-23}	4.0×10^{47}	4.9×10^{6}	*3.6×10^{54}*	*1.5×10^{11}*	4.0×10^{59}	9.8×10^{15}
39	6.3×10^{-24}	4.0×10^{48}	1.6×10^{6}	*3.6×10^{55}*	*4.7×10^{10}*	4.0×10^{60}	3.1×10^{15}
40	6.3×10^{-25}	4.0×10^{49}	4.9×10^{5}	*3.6×10^{56}*	*1.5×10^{10}*	4.0×10^{61}	9.9×10^{14}
41	6.3×10^{-26}	4.0×10^{50}	1.6×10^{5}	*3.6×10^{57}*	*4.7×10^{9}*	4.0×10^{62}	3.1×10^{14}
42	6.3×10^{-27}	4.0×10^{51}	4.9×10^{4}	*3.6×10^{58}*	*1.5×10^{9}*	4.0×10^{63}	9.9×10^{13}
43	6.3×10^{-28}	4.0×10^{52}	1.6×10^{4}	*3.6×10^{59}*	*4.7×10^{8}*	4.0×10^{64}	3.1×10^{13}
44	6.3×10^{-29}	4.0×10^{53}	4.9×10^{3}	*3.6×10^{60}*	*1.5×10^{8}*	4.0×10^{65}	9.9×10^{12}
45	6.3×10^{-30}	4.0×10^{54}	1.6×10^{3}	*3.6×10^{61}*	*4.7×10^{7}*	4.0×10^{66}	3.1×10^{12}
46	6.3×10^{-31}	4.0×10^{55}	4.9×10^{2}	*3.6×10^{62}*	*1.5×10^{7}*	4.0×10^{67}	9.9×10^{11}
47	6.3×10^{-32}	4.0×10^{56}	1.6×10^{2}	*3.6×10^{63}*	*4.7×10^{6}*	4.0×10^{68}	3.1×10^{11}
48	6.3×10^{-33}	4.0×10^{57}	49	*3.6×10^{64}*	*1.5×10^{6}*	4.0×10^{69}	9.9×10^{10}
49	6.3×10^{-34}	4.0×10^{58}	16	*3.6×10^{65}*	*4.7×10^{5}*	4.0×10^{70}	3.1×10^{10}
50	6.3×10^{-35}	4.0×10^{59}	4.9	*3.6×10^{66}*	*1.5×10^{5}*	4.0×10^{71}	9.9×10^{9}

the secondary γ–rays emitted after the π^0 mesons decay. Using equation (P-12) we compute the energy flux (F) related to secondary γ–ray emission by a particular BH. Dividind this by the detector bandwidth ($\Delta\nu$) we obtain the corresponding flux density (S_ν) emitted by the BH on that bandwidth. Using equation (P-14), with $\pi B_\nu(T)$ given by S_ν, in Table P-12 we show the maximum distances at which it is possible to detect secondary γ–rays for a sensor with a sensitivity $s_\nu = 6.7 \times 10^{-13}$ Jy (the same as AGILE for the 30 MeV–50 GeV bandwidth) from BHs 31 to 46 only. BHs 47 to 50 are excluded because the luminosity distances we are using loose meaning when the space-time geometry of the Universe clearly shows its presence (for $d \gtrsim 400$ Mpc). The remaining BHs (1 to 30) do not emit hadron jets ($M > 10^{11}$ kg; cf. equation P-9).

AGILE is able to detect signal variations as short as 1 μs (e.g. Tavani et al., 2001).

Table P-11: Evaporation times for Schwarzschild BHs that do it in less time than the current known age of the Universe ($\sim 10^{10}$ yrs), from equation (P-8). It was assumed for $f(M)$ a log–linear behaviour between $M = 10^7$ kg and $M = 10^{15}$ kg.

n	r_s(m)	M(kg)	t_{evap}
31	6.3×10^{-16}	4.3×10^{11}	10^9 years
32	6.3×10^{-17}	4.3×10^{10}	10^6 years
33	6.3×10^{-18}	4.3×10^{9}	10^3 years
34	6.3×10^{-19}	4.3×10^{8}	1 year
35	6.3×10^{-20}	4.3×10^{7}	8.7 hours
36	6.3×10^{-21}	4.3×10^{6}	31 s
37	6.3×10^{-22}	4.3×10^{5}	3.1×10^{-2} s
38	6.3×10^{-23}	4.3×10^{4}	3.1×10^{-5} s
39	6.3×10^{-24}	4.3×10^{3}	3.1×10^{-8} s
40	6.3×10^{-25}	4.3×10^{2}	3.1×10^{-11} s
41	6.3×10^{-26}	43	3.1×10^{-14} s
42	6.3×10^{-27}	4.3	3.1×10^{-17} s
43	6.3×10^{-28}	4.3×10^{-1}	3.1×10^{-20} s
44	6.3×10^{-29}	4.3×10^{-2}	3.1×10^{-23} s
45	6.3×10^{-30}	4.3×10^{-3}	3.1×10^{-26} s
46	6.3×10^{-31}	4.3×10^{-4}	3.1×10^{-29} s
47	6.3×10^{-32}	4.3×10^{-5}	3.1×10^{-32} s
48	6.3×10^{-33}	4.3×10^{-6}	3.1×10^{-35} s
49	6.3×10^{-34}	4.3×10^{-7}	3.1×10^{-38} s
50	6.3×10^{-35}	4.3×10^{-8}	3.1×10^{-41} s

BH 38, with an evaporation time of 31 μs (cf. Table P-11), can de detected within the AGILE technical limits at a maximum distance of 6.2×10^{17} m ($\approx$ 20 pc) (cf. Table P-12). For smaller BHs we have evaporation times smaller than 1 μs (cf. Table P-11) which means that AGILE will not be able to detect their secondary γ–rays even if they are at smaller distances than $\approx$ 20 pc. The maximum distances for the secondary γ–ray detection varies between 3.5×10^{12} m ($\approx$ 23 AU, BH 31) and 6.2×10^{17} m ($\approx$ 20 pc, BH 38).

P.5.9 Summary

In Table P-2 we present a summary of the state-of-the-art instruments considered for the determination of the maximum distances of detection, for BHs, across the electromagnetic spectrum. In Table P-13 we summarise, for each BH 'colour', the maximum distance of detection with the instruments of Table P-2. These range from 1 mm to 1 pc.

Table P-12: Maximum distances for detection of secondary γ–rays ($s_\nu = 6.7 \times 10^{-13}$ Jy; the same as AGILE for the 30 MeV–50 GeV bandwidth). BHs 47 to 50 are excluded because the luminosity distances we are using loose meaning when the space-time geometry of the Universe clearly shows its presence (for $d \gtrsim 400$ Mpc). BHs 1 to 30 are excluded because they do not emit hadron jets ($M > 10^{11}$ kg; cf. equation P-9). It is also indicated the secondary γ–ray emission rate (equation P-11) as well as the correspondent energy flux (equation P-12).

n	r_s(m)	$dN_\gamma/dt(s^{-1})$	$F(Wm^{-2})$	$d(m)$	
31	6.3×10^{-16}	2.8×10^{23}	2.5×10^{42}	3.5×10^{12}	
32	6.3×10^{-17}	8.9×10^{24}	7.9×10^{45}	1.9×10^{13}	
33	6.3×10^{-18}	2.8×10^{26}	2.5×10^{49}	1.1×10^{14}	
34	6.3×10^{-19}	8.9×10^{27}	7.9×10^{52}	6.2×10^{14}	
35	6.3×10^{-20}	2.8×10^{29}	2.5×10^{56}	3.5×10^{15}	0.1 pc
36	6.3×10^{-21}	8.9×10^{30}	7.9×10^{59}	1.9×10^{16}	0.6 pc
37	6.3×10^{-22}	2.8×10^{32}	2.5×10^{63}	1.1×10^{17}	3.5 pc
38	6.3×10^{-23}	8.9×10^{33}	7.9×10^{66}	6.2×10^{17}	20.0 pc
39	6.3×10^{-24}	2.8×10^{35}	2.5×10^{70}	3.5×10^{18}	112.2 pc
40	6.3×10^{-25}	8.9×10^{36}	7.9×10^{73}	1.9×10^{19}	631.0 pc
41	6.3×10^{-26}	2.8×10^{38}	2.5×10^{77}	1.1×10^{20}	3.5 kpc
42	6.3×10^{-27}	8.9×10^{39}	7.9×10^{80}	6.2×10^{20}	20.0 kpc
43	6.3×10^{-28}	2.8×10^{41}	2.5×10^{84}	3.5×10^{21}	112.2 kpc
44	6.3×10^{-29}	8.9×10^{42}	7.9×10^{87}	1.9×10^{22}	631.0 kpc
45	6.3×10^{-30}	2.8×10^{44}	2.5×10^{91}	1.1×10^{23}	3.5 Mpc
46	6.3×10^{-31}	8.9×10^{45}	7.9×10^{94}	6.2×10^{23}	20.0 Mpc

P.6 Discussion and conclusions

We have considered the detection of BHs by the electromagnetic component of the Hawking Radiation for several wavelengths (from long radio waves to hard γ–rays). For that, we took a list of 50 Schwarzschild BHs covering 46 decades in λ_{max} (Table P-4) and the respective most sensitive detectors operating at the present date whenever possible[51], for each BH we have determined the maximum distance d (equation P-16) at which each detector must be in order to detect the electromagnetic emission of the BH.

We notice that, for a given observing wavelenght λ, the maximum distance d is larger when both λ (observing wavelength) and λ_{max} (which characterizes the BH; equation P-5) are of the same order. For instance, BH 20, which has $\lambda_{max} = 0.7$ μm could be

[51]For all the considered observing wavelengths λ there are some BHs which could not be detected because, for them, the maximum distance d is smaller than the respective Schwarzschild radius r_s (nonsense). For all the considered radio wavelengths, BH 13 cannot be detected at a distance larger than $10r_s$ (Table P-5). The same goes for BH 14 when $\lambda = 20$ m. We have discarded these situations in order to avoid strong gravity effects.

Table P-13: Maximum distances (in meters) for detection of the Hawking radiation emitted by BHs of different colours (λ_{max}) for various spectral bands (their numbers, as listed in Table P-4, are in brackets). We also present the observing wavelengths (λ).

BH color	d_{max} (m)					
(λ_{max})	Radio	Infrared	Visible	UV	X–rays	γ–rays
	$\lambda = 3.6$ cm	$\lambda = 3.4$ μm	$A_\lambda = 0.70$ μm	$C_\lambda = 365$ nm	$E_\lambda = 3.5$ nm	$\lambda = 2.5 \times 10^{-19}$ m
			$B_\lambda = 0.44$ μm	$D_\lambda = 105$ nm	$F_\lambda = 0.167$ nm	
Radio	(15) 260	-	-	-	-	-
Infrared	(16) 120	(19) 2.0×10^4	(19)^A 9.6×10^5	(19)^D 8.1×10^3	-	-
Visible	(20) 3.2	(20) 1.9×10^4	(23)^B 3.5×10^6	(23)^D 1.9×10^5	-	-
UV	(24) 1.2	(24) 9.0×10^3	(24)^C 5.7×10^6	(25)^E 4.6×10^5	(25)^F 1.7×10^6	-
X–rays	(26) 1.2×10^{-1}	(26) 9.3×10^2	(26)^C 7.7×10^5	(26)^E 1.6×10^5	(27)^G 5.4×10^8	-
γ–rays	(28) 1.2×10^{-2}	(28) 93	(28)^C 7.8×10^4	(28)^E 1.7×10^4	(28)^G 3.9×10^8	(36) 5.5×10^{16}

detected at a maximum distance of 2.0×10^6 m for an observing wavelength of 0.7 μm (see Table P-7). The same BH observed at $\lambda = 0.55$ μm and $\lambda = 3.4$ μm is detectable at maximum distances of, respectively, 1.6×10^6 m and 1.9×10^4 m (Tables P-6 and P-7). Moving to smaller observing wavelengths, we also obtain larger values for the maximum distance d. This is only due to the fact that, in general, the sensitivity of a detector is better at the shortest wavelengths (e.g. Table P-2, for radio vs. γ–ray there is a 15 orders of magnitude difference). We have decided to compile this graphically and, for each given pair of λ and s_ν (Table P-2), we have drawn the curve $d(r_s)$ (equation P-16) presented, for each of the Table P-2 pairs, in Figures P-2–P-7. The peak in each curve corresponds to the BH that can be detected farthest for the corresponding(λ,s_ν) pair. Notice that in Figure P-2, for $\lambda = 20$ m and $\lambda = 4$ m, the distance d correspondent to the peak is less than $10r_s$: we do not consider such cases, in order to avoid strong gravity complications. We confirm that the smaller the wavelength is, the higher the peak (distance) will be and the smaller the BH will be (e.g. Figure P-3).

BHs 1 to 12, i.e., BHs with masses $> 10^{-4}M_{\odot}$ (which include all currently known BH candidates), are undetectable for all the considered situations, since their maximum detection distances (equation P-16) are always smaller than the respective Schwarzschild radius (equation P-3). BH 13 ($\lambda_{max} = 1$ m, $M = 2.1 \times 10^{-5}M_{\odot}$, $r_s = 6.3 \times 10^{-2}$ m) is the largest one detectable (longest wavelength only), with maximum distances for detection of 12 cm and 46 cm ($\lambda = 20$ m and $\lambda = 4$ m, respectively).

As regards individual BH 'colour' analysis, starting with radio BHs, the one detectable farthest is BH 15 at 260 m for $\lambda = 3.6$ cm (Table P-5, cf. Figure P-2), while for IR this is BH 19, 9.6×10^5 m for $\lambda = 0.70$ μm, (actually detectable from the radio to the UV)—cf. Figure P-3. Visible BHs are detectable from the radio to the UV, and have largest maximum distances of the order of 10^6 m (cf. Figure P-4). UV BHs 24 and 25 are detectable up to 10^5 m (UV) and 10^6 m (visible), (cf. Figure P-5), while the two X–ray BHs from Table P-4 are detectable (at their wavelengths) up to distances of the order of 10^8 m (same order of the Earth–Moon distance) (cf. Figure P-6). Finally, BHs 28 to 50 are γ–ray BHs, although BH 28 is not detectable at γ–rays; it is detectable in hard X–rays up to a maximum distance of 3.9×10^8 m ($\approx$ Earth–Moon distance). The BHs detected farther are the ones with strong emission at $\lambda = 2.5 \times 10^{-19}$ m (cf. Table P-10), e.g. BH 36 ($r_s = 6.3 \times 10^{-21}$ m, $T = 2.9 \times 10^{16}$ K, $M = 4.3 \times 10^6$ kg) is detectable at a distance of 5.5×10^{16} m (≈ 1.8 pc), decreasing to ≈ 10 AU and $8R_{earth}$ (at mid and soft γ–rays, respectivly) (cf. Figure P-7).

In Table P-13 we show, for each type of BH (radio, IR, visible, UV, X–ray and γ–ray), the one which is detectable at the largest distance when observed at a given wavelength. It is possible to detect BHs farther and farther as we move our observations into shorter and shorter wavelengths. In fact, we move from the possibility of laboratorial detection of Hawking Radiation emitted by Schwarzschild BHs (at radio wavelengths) up to satellite use for detection of interplanetary and interstellar BHS at X–Ray or γ–ray wavelengths. However in the case of laboratory detection only, we can, in fact, explore the full electromagnetic spectrum[52] and BHs 14–50 studied in this paper as is apparent from Tables P-5 to P-10.

BHs in their *terminal phases*, i.e. BHs with evaporation times equal or inferior to one year (cf. Table P-11 : BHs 34 to 50), are detectable, for the studied γ–ray wavelengths, at distances much greater than the Moon ($\geq 10^7$ km), with the one possible to detetect farthest BH 36 ($t_{evap} = 31$ s) up to ≈ 0.6 pc. This means that once detected a terminal BH, we could follow the respective evolution towards the final γ–ray explosion.

Since BHs 31 to 50 from Table P-4 emit *secondary γ–rays* they deserve a specific study, the results of which we present in Table P-12. The maximum distances for the detection of secondary γ–rays are always larger (by a large factor) than the ones

[52]Although some maximum distances seem very small, notice that their values are still several magnitudes greater than the Schwarzschild radius in each case. For example, in the case of BH 36 ($r_s = 6.3 \times 10^{-21}$ m) we have $d = 2.0 \times 10^{-10}$ m $\approx 3.2 \times 10^{10} r_s$.

correspondent to primary γ–rays originating at the same type of BH (cf. Tables P-10 and P-12): for example, primary γ–rays emited by BH 39 are detectable at a maximum distance of 3.1×10^{15} m (≈ 0.1 pc) when $\lambda = 2.5 \times 10^{-19}$ m while the secondary γ–rays emitted by the same BH are detectable at a maximum distance of 3.5×10^{18} m (≈ 112 pc). There is, however, one exception, concerning BH 36 which is detectable up to half the maximum distance when emitting primary γ–rays (because for BH 36 the value of λ_{max} (cf. Table P-4) is of the same order of the observed $\lambda = 2.5 \times 10^{-19}$ m). With secondary γ–rays, we reach distances of ~ 20 pc for the detection of (the smallest) BHs by the emission of Hawking Radiation.

Notice that each BH emits always some amount of primary γ–rays on the bandwidth used to detect the secondary γ–rays (in our case 30 MeV–50 GeV) and that in practice we cannot distinguish between primary and secondary γ–rays. However, for the considered BHs, the contribution of primary γ–rays to the flux is always much smaller than the one corresponding to secondary γ–rays ($\approx 10^3$ times smaller for BHs 33 and 34 which are the cases where the contribution of primary γ–rays is more significant). This is why we have ignored the contribution of primary γ–rays in Table P-12, and also the reason for the detection of primary γ–rays with AGILE (30 MeV–50 GeV bandwidth) not being possible (although still considered in Table P-10).

It is important to notice that each BH detectable on the 0.1–10 TeV bandwidth (HESS), in terms of primary γ–rays, is also detectable on the 30 MeV–50 GeV bandwidth (AGILE) in terms of secondary γ–rays, at distances of the same or higher order (see Tables P-10 and P-12). For example, BH 37, which is detectable with HESS at a maximum distance of 3.0×10^{16} m, is also detectable with AGILE at a distance of 1.1×10^{17} m.

References

Adelman–McCarthy J. K., et al. 2008, *The Sixth Data Release of the Sloan Digital Sky Survey*, ApJS, 175, 297, [arXiv:0707.3413].

Afshordi, N., McDonald, P. & Spergel, D. N. 2003, *Primordial black holes as dark matter: the power spectrum and evaporation of early structures*, ApJL, 594, 74 [arXiV: astro-ph/0302035].

Aguilar–Saavedra J. A., et al. 2006, *Supersymmetry Parameter Analysis: SPA Convention and Project*, Eur. Phys. Jour. C, 46, 43 [hep-ph/0511344].

Aitchison I. J. R., 2005, *Supersymmetry and the MSSM: An Elementary Introduction*, hep-ph/0505105v1.

Alcock C., et al. 1997, *The MACHO Project LMC Microlensing Results from the First Two Years and the Nature of the Galactic Dark Halo*, ApJ, 486, 697 [astro–ph/9606165].

Alcock C., et al. 1998, *EROS and MACHO Combined Limits on Planetary Mass Dark Matter in the Galactic Halo*, ApJL, 499, 9 [astro–ph/9803082].

Alcock C., et al. 2001, *MACHO Project Limits on Black Hole Dark Matter in the 1-30 Solar Mass Range*, ApJL, 169, 550 [astro–ph/0011506].

Allanach B. C., et al. 2002, *The Snowmass Points and Slopes: Benchmarks for SUSY Searches*, Eur. Phys. Jour. C, 25, 113 [hep–ph/0202233].

Anchordoqui L. A., et al. 2002, *Black holes from cosmic rays: probes of extra dimensions and new limits on TeV-scale gravity*, PhRvD, 65, 124027 [het–ph/0112247].

Anderson G. W. & Hall, L. J., 1992, *The electroweak phase transition and baryogenesis*, PhRvD, 45, 2685.

Anselmann et al., 1992, *Solar neutrinos observed by GALLEX at Gran Sasso*, Phys. Let. B, 285, 376.

Aoki Y. et al., 2006a, *The QCD transition temperature: Results with physical masses in the continuum limit*, Phys. Let. B, 643, 46 [hep–lat/0609068].

Aoki Y. et al., 2006b, *The order of the quantum chromodynamics transition predicted by the standard model of particle physics*, Nature, 443, 675 [hep–lat/0611014].

Baierlein R., 2001, *The elusive chemical potential*, Am. J. Phys., 69, 423.

Barbier B. et al. 2005, *R–parity violating supersymmetry*, Phys. Rep., 420, 1 [hep–ph/0406039].

Bardeen, J. M., et al. 1986, *The statistics of peaks of Gaussian random fields*, ApJ, 304, 15.

Barrau A., 2000, *Primordial black holes as a source of extremely high energy cosmic rays*, Astroparticle Physics, 12, 269 [astro–ph/9907347].

Belyanin A. A., Kocharovsky V. V., Kocharovsky V1. V., 1996, *Gamma-ray bursts from the final stage of primordial black hole evaporation*, MNRAS, 283, 626.

Bennett C. L. et al. 2003, *First year Wilkinson Microwave Anisotropy Probe (WMAP) observations: Preliminary Maps and Basic Results*, ApJS, 148, 1 [astro-ph/0302207].

Bennett D. P. et al., 2002, *Gravitational Microlensing Events Due to Stellar–Mass Black Holes*, ApJ, 579, 639 [astro-ph/0109467].

Bernard C. et al., 1997, *Kaon interferometry as signal for the QCD phase transition at RHIC*, Nuc. Phys. A, 625, 473 [nucl-th/9703017].

Bernard C. et al. (the MILC collaboration), 2004, *QCD thermodynamics with three flavours of improved staggered quarks*, PhRvD, 71, 034504 [hep-lat/0405029].

Bertone G., Hooper, D. & Silk, J., 2005, *Particle dark matter: evidence, candidates and constraints*, Phys. Rep., 405, 279 [hep-ph/0404175].

Blais D., Bringmann T., Kiefer C. & Polarski D., 2003, *Accurate results for primordial black holes from spectra with a distinguished scale*, PhRvD, 67, 024024 [astro-ph/0206262].

Boggess N. W., 1992, *The COBE mission: its design and performance two years after launch*, ApJ, 397,420.

Boyanovsky D., Vega H. J. & Schwarz D. J., 2006, *Phase transitions in the early and present Universe* , Ann. Rev. Nucl. Part. Sci., 56, 441 [hep-ph/0602002].

Bridle S.L., Lewis A.M., Weller J. & Efstahiou G., 2003, *Reconstructing the primordial power spectrum*, MNRAS, 342, L72 [astro–ph/0302306].

Bringmann T., Kiefer C. & Polarski D., 2002, *PBHs from inflationary models and without broken scale invariance*, PhRvD, 65, 024008 [astro–ph/0109404].

Bunn E. F. et al. 1996, *Four–year COBE normalization of inflationary cosmologies*, PhRvD, 54, 5917 [astro–ph/9607038].

Cardall C. Y. & Fuller G. M., 1998, *Semianalytic Analysis of Primordial Black Hole Formation During a First–order QCD Phase Transition*, astro–ph/9801103.

Carr B. J., 1975, *The PBH mass spectrum*, ApJ, 201, 1.

Carr B. J., 1976, *Some cosmological consequences of primordial black–hole evaporations*, ApJ, 206, 8.

Carr B. J., 2003, *Primordial Black Holes as a Probe of Cosmology and High Energy Physics*, Lect. Notes Phys., 631, 301 [astro–ph/0310838].

Carr B. J., 2005, *Primordial black holes: recent developments*, 22nd Texas Symposiun at Stanford, Dec. 2004 [astro–ph/0504034].

Carr B. J. et al., 2010, *New cosmological constraints on primordial black holes*, PhRvD, 81, 104019 [arXiv:0912.5297].

Carr B. J. & Goymer C., 1999, *Primordial Black Holes and gravitational memory*, Progress of Theoretical Physics Supplement, 136, 321 [astro–ph/0003027].

Carr B. J. & Hawking S. W., 1974, *BHs in the early Universe*, MNRAS, 168, 399.

Carr B.J., Gilbert J. H. & Lidsey J. E., 1994, *Black hole relics and Inflation: limits on blue perturbation spectra*, PhRvD, 50, 4853 [astro-ph/9405027].

Cavaglia M., Das, S. & Maartens, R. 2003, *Will we observe black holes at the LHC?*, CQGra, 20, L205 [hep-ph/0305223].

Choptuik M. W., 1993, *Universality and scaling in gravitational collapse of a massless scalar field*, PhRvD, 70, 9.

Choptuik M. W., 1998, *The (unstable) threshold of BH formation*, Talk given at 15th International Conference on General Relativity and Gravitation (GR15), Pune, India, 16-21 Dec 1997 [gr–qc/9803075].

Christiansen M. B. & Madsen J., 1996, *Large nucleation distances from impurities in the cosmological quark-hadron transition*, PhRvD, 53, 5446 [astro-ph/9602071].

Cole S. et al., 2005, *The 2dF Galaxy Redshift Survey: power–spectrum analysis of the final data set and cosmological implications*, MNRAS, 362, 505 [astro-ph/0501174].

Coleman T. S. & Roos M., 2003, *Effective degrees of freedom during the radiation era*, PhRvD, 68, 27702 [astro-ph/0304281].

Colless M. et al., 2003, *The 2dF Galaxy Redshift Survey: Final Data Release*, astro–ph/0306581 (accompanies the 2dFGRS Final Data Release available at http://www.mso.anu.edu.au/2dFGRS/).

Combes F. et al., 2002, *Galaxies and Cosmology*, Astronomy & Astrophysics Library, Springer–Verlag, London.

Covi L., 2003, *Status of Observational Cosmology and Inflation*, Physics in Collision, Proceedings of the XXIII International Conference, Edited by S. Riemann and W. Lohmann. SLAC, p. 67 (http://www.slac.stanford.edu/econf/C030626) [hep-ph/0309238].

Cox A. N., Editor, 2000, *Allen's Astrophysical Quantities*, 4th Ed., Springer–Verlag, New York.

Csikor F. et al., 1998, *Endpoint of the hot electroweak phase transition*, PhRvL, 82 ,21 [hep-ph/9809291].

Davies P. C. W., 1978, Rep. Prog. Phys. *Thermodynamics of black holes*, 41, 1313.

Demianski M., 1985, *Relativistic Astrophysics*, Polish Scientific Publishers, Warswaza.

Dimopoulos, S. & Landsberg, G. 2001 *Black Holes at the Large Hadron Collider*, PhRvL, 87, 161602 [hep–ph/0106295].

d'Inverno R., 1993, *Introducing Einstein's relativity*, Oxford, Claredon Press.

Dones L., et al., 2004, *Oort Cloud Formation and Dynamics*, Star Formation in the Interstellar Medium: In Honor of David Hollenbach, Chris McKee and Frank Shu, ASP Conference Proceedings, Vol. 323. Edited by D. Johnstone, F.C. Adams, D.N.C. Lin, D.A. Neufeld, and E.C. Ostriker. San Francisco: Astronomical Society of the Pacific, p. 371.

Düchting N., 2004, *Supermassive black holes from primordial black hole seeds*, PhRvD, 70, 064015 [astro–ph/0406260].

Easther R., 2005, *Folded Inflation, Primordial Tensors, and the Running of the Scalar Spectral Index*, hep–th/0407042.

Ejiri S., 2007, *Lattice QCD thermodynamics with Wilson quarks*, Progress of Theoretical Physics Supplement, 168, 245 [astro-ph/0704.3747].

Eisberg R., Resnick R., 1985, *Quantum Physics*, John Wiley & Sons, New York.

Ellis J. et al., 2007, *Higgs Boson Properties in the Standard Model and its Supersymmetric Extensions*, Comptes Rendus – Physique, 8, 999 [hep-ph/0702114].

Evans C. R. and Coleman J. S., 1994, *Observation of critical phenomena and self–similarity in the gravitational collapse of radiation fluid*, Phys. Rev. Let., 37, 72, 1782 [gr–qc/9402041].

Fabiano N., 1997, *Top mesons*, Eur. Phys. Jour. C, 2, 345 [hep–ph/9704261].

Gamow G., Alpher R. A. & Bethe H., 1948, *The Origin of Chemical Elements*, Phys. Rev., 73, 803.

Gillessen S., et al. 2009, *Monitoring Stellar Orbits Around the Massive Black Hole in the Galactic Center*, ApJ, 692, 1075 [arXiv:0810.4674].

Green A. M. and Liddle A. R., 1997, *Constraints on the density perturbation spectrum from PBHs*, PhRvD, 56, 6166, [astro–ph/9704251].

Green A. M. and Liddle A. R., 1999, *Critical collapse and the primordial black hole initial mass function*, PhRvD, 60, 63509, [astro–ph/9901268].

Green A. M., Liddle A. R., Malik K. A. & Sasaki M., 2004, *A new calculation of the mass fraction of PBHs*, PhRvD, 70, 041502 [astro–ph/0403181].

Greene, J. E. & Ho, L. C., 2004, *Active Galactic Nuclei with Candidate Intermediate–Mass Black Holes*, ApJ, 610, 722 [astro–ph/0404110].

Gundlach C., 1998, *Critical phenomena in gravitational collapse*, Adv. Theor. Math. Phys., 2, 1 [gr–qc/9712084].

Gundlach C. & Martín-García J. M., 2007, *Critical phenomena in gravitational collapse*, Living Rev. Rel., 10, 5, [arXiv:0711.4620].

Gupta S., 2003, *The quark gluon plasma: lattice computations put to experiment test*, Pramana, 61, 877 [hep-ph/0303072].

Guth A. H., 2000, *Inflation and eternal inflation*, Phys. Rep., 333, 555 [astro-ph/0002156].

Gynther A., 2006, *Thermodynamics of electroweak matter*, PhD Thesis, University of Helsinki, HU-P-D130 [hep–ph/0609226].

Habib et al. 2005, *Inflationary perturbations and precision Cosmology*, PhRvD, 71, 43518 [astro–ph/0501130].

Hagiwara K. et al., 2002, *Review of Particle Properties*, Phys. Rev. D, 66, 1.

Hampel W. et al., 1999, *GALLEX solar neutrino observations: results for GALLEX IV*, Phys. Let. B, 447, 127.

Hands S., 2001, *The phase diagram of QCD*, Comtemp. Phys., 42, 209 [physics/0105022].

Harada T. & Carr B. J., 2005, *Growth of PBHs in a universe containing a massless scalar field*, PhRvD, 71, 104010 [astro–ph/0412135].

Harrison, E. R. 1970, *Fluctuations at the threshold of Classical Cosmology*, PhRvD, 1, 2726.

Harwit M., 1998, *Astrophysical Concepts*, Springer, New York.

Hawke I. and Stewart J. M., 2002, *The dynamics of PBH formation*, CQGra, 19, 3687.

Hawking S., 1971, *Gravitationally collapsed objects of very low mass*, MNRAS, 152, 75.

Hawking S., 1974, *Black Hole Explosions?*, Nature, 248, 30.

He P., Fang L., 2002, *Constraints on Primordial Black Holes and Primordial Density Perturbations from the Epoch of Reionization*, ApJ, 568, L1.

Hinshaw G. et al. 2009, *Five–Year Wilkinson Microwave Anisotropy Probe (WMAP) Observations: Data Processing, Sky Maps, & Basic Results*, ApJS, 180, 225 [arxiv:0803.0732].

Hirata C. M. & Sigurdson K., 2007, *The spin–resolved atomic velocity distribution and 21–cm line profile of dark–age gas*, MNRAS, 375, 1241 [astro-ph/0600507].

Hu W. & Dodelson S., 2002, *Cosmic Microwave Background Anisotropies*, ARA&A, 40, 171 [astro-ph/0110414].

Huang, Q.-G., 2007, *Simplified chain inflation*, JCAP, 05, 9 [hep-th/0704.2835v2].

Hubble E., 1929, *A Relation between Distance and Radial Velocity among Extra–Galactic Nebulae*, Proceedings of the National Academy of Sciences of the United States of America, 15, 168.

Ignatius J., 1993, *Cosmological phase transitions*, Academic Dissertation, University of Helsinky, HU-TFT-IR-3-1 [hep–ph/9312293].

Jedamzik K., 1997, *Primordial black hole formation during the QCD epoch*, PhRvD, 55, 5871 [astro-ph/9605152].

Jedamzik K., 1998, *Could MACHOs be primordial black holes formed during the QCD epoch?*, Phys. Rep., 307, 155 [astro-ph/9805147].

Jedamzik K. & Niemeyer J. C., 1999, *PBH formation during first–order phase transitions*, PhRvD, 59, 124014 [astro–ph/9901293].

Jones M. H., & Lambourne R. J. A., 2004, *An introduction to galaxies and cosmology*, by Mark H. Jones and Robert J.A. Lambourne. Co-published with The Open University, Milton Keynes. Cambridge, UK: Cambridge University Press.

Johnson H. L., 1966, *Astronomical Measurements in the Infrared*, ARA&A, 4, 193.

Kajantie K., et al., 1998, *The universal properties of the electroweak phase transition*, Talk presented by K.R. at the 5th International Workshop on Thermal Field Theory and their applications, Regensburg, Germany, August 1998 [hep-ph/9809435].

Kämpfer B., 2000, *Cosmic phase transitions*, Annalen der Physik, 9, 605 [astro-ph/0004403].

Karsch F. et al., 1996, *Critical Higgs Mass and Temperature Dependence of Gauge Boson Masses in the SU(2) Gauge-Higgs Model*, Nuc. Phys. B - Proc. Supp., 53, 623 [hep-lat/9608087].

Karsch F., 2002, *Lattice Results on QCD Thermodynamics*, Nuc. Phys. A, 698, 199 [hep-ph/0103314].

Karsch F. et al., 2000, *QCD Thermodynamics with 2 and 3 quark flavors*, Presented at the conference on *Strong and Electroweak Matter*, SEWM 2000, Marseille, June 13–17th, 2000 [hep-lat/0010027].

Kiefer C., 2003, *Quantum aspects of black holes*, In *The Galactic black hole*–Lectures on general relativity and astrophysics; Edited by Heino Falcke & Friedrich W. Hehl; Series in high energy physics, cosmology and gravitation; Bristol: IoP; Institute of Physics Publishing [astro–ph/0202032].

Koch V., 1997, *Aspects of Chiral Symmetry*, Int. Jour. Mod. Phys. E, 6, 203 [nucl–th/9706075].

Koike T., Hara T., and Adachi S., 1995, *Critical behaviour in gravitational collapse of radiation fluid A renormalization group (linear perturbation) analysis*, PhRvL, 74, 5170 [gr-qc/9503007].

Koike T., Hara T., and Adachi S., 1999, *Critical behaviour in gravitational collapse of a perfect fluid*, PhRvD, 59, 104008.

Kopp M., Hofmann S. & Weller J., 2011, *Separate Universes Do Not Constrain Primordial Black Hole Formation*, PhRvD, 83, 124025 [arXiv:1012.4369v2, astro–ph.CO].

Kormendy, J. 2004, *The Stellar–Dynamical Search for Supermassive Black Holes in Galactic Nuclei* in Coevolution of Black Holes and Galaxies, from the Carnegie Observatories Centennial Symposia., ed. L. Ho (Cambridge University Press), 1 [astro–ph/0306353].

Kormendy J. and Richstone D., 1995, *The Search For Supermassive Black Holes In Galactic Nuclei*, ARA&A, 33, 581.

Kraus J. D., 1986, *Radio Astronomy* - 2nd edition, Cygnus-Quasar Books.

Kribs G. D., Leibovich A. K. and Rothstein I. Z., 1999, *Bounds from PBHs with a near critical collapse IMF*, PhRvD, 60, 103510 [astro–ph/9904021].

Lang K. R., 1999, *Astrophysical Formulae*, Volume 1-3rd edition, Springer Verlag, Berlin.

Lemos, J. P. S. 1996, *Black Holes: From galactic nuclei to elementary particles*, astro–ph/9612220.

Liddle A. R. et al. 2006, *WMAP normalization of inflationary cosmologies*, PhRvD, 74, 83512 [astro–ph/0607275].

Liddle A. R. & Lyth D. H., 1993, *The cold dark matter density perturbation*, Phys. Rep., 231, 1 [astro–ph/9303019].

Linde A. D., 1990, *Particle Physics and Inflationary Cosmology*, Contemporary Concepts in Physics, 5, 1 [hep–th/0503203].

Longair M. S., 1998, *Galaxy formation*, Astronomy & Astrophysics Library, Springer–Verlag, Berlin.

Lyth D. H., 1993, *Introduction to Cosmology*, Lectures given at the *Summer School in High Energy Physics and Cosmology*, ICTP (Trieste) 1993 [astro-ph/9312022].

MacGibbon, J. H. and Carr, B. J. 1991, *Cosmic rays from primordial black holes*, ApJ, 371, 447.

Mack K. J. et al., 2007, *Growth of Structure Seeded by Primordial Black Holes*, ApJ, 665, 1277 [astro-ph/0608642].

Maison D., 1996, *Non–universality of critical behaviour in spherically symmetric gravitational collapse*, Phys. Let. B, 366, 82 [gr–qc/9504008].

Maki K., Mitsui T., Orito S., 1996, *Local Flux of Low-Energy Antiprotons from Evaporating Primordial Black Holes*, Phys. Rev. Let., 76, 3474.

Martin S. P., 1998 (version 4, June 2006), *A Supersymmetry Primer*, Perspectives on Supersymmetry, Advanced Series on Directions in High Energy Physics, Vol. 18, Edited by Gordon L. Kane, Published by World Scientific Publishing Company, Singapore (1998), p.1 [hep–ph/9709356].

Mather, J. C. et al., 1999, *Calibrator Design for the COBE Far-Infrared Absolute Spectrophotometer (FIRAS)*, ApJ, 512, 511 [astro–ph/9810373].

McNutt R. L., et al., 2006, *Innovative interstellar explorer*, Physics of the Inner Heliosheath: Voyager Observations, Theory, and Future Prospects; 5th Annual IGPP International Astrophysics Conference; AIP Conference Proceedings, Vol. 858, p. 341.

Mégevand A., 2000, *Development of the electroweak phase transition and baryogenesis*, Int. Jour. Mod. Phys. D, 9, 733 [hep-ph/0006177].

Misner, C. W., Thorne, K. S. & Wheeler, J. A. 1973, *Gravitation*, Freeman, San Francisco.

Morselli A., 2003, *Gamma ray astroparticle physics with GLAST*, Frascati Physics Series, XXIV, 363, International School of Space Science 2001 [astro–ph/0202340].

Musco I., Miller J. C. & Rezzolla L., 2005, *Computations of PBH formation*, CQGra, 22, 1405 [gr–qc/0412063].

Nadëzhin D. K., Novikov I. D. and Polnarev A. G., 1978, *The hydrodynamics of PBH formation*, SvA, 22, 129.

Narlikar J. V., 2002, *An Introduction to Cosmology*, Cambridge University Press, Cambridge.

Narlikar J. V. & Padmanabhan T., 1991, *Inflation for Astronomers*, ARA&A, 29, 325.

Natarajan, P., & Treister, E. 2009, *Is there an upper limit to black hole masses?*, MNRAS, 393, 838 [arXiv:0808.2813].

Niemeyer J. C., 1998, *Numerical investigation of the threshold for PBH formation*, proceedings of Dark Matter 98, Los Angeles (ed. D. Cline) [astro–ph/9806043].

Niemeyer J. C. and Jedamzik K., 1998, *Near–critical gravitational collapse and the IMF of PBHs*, PhRvL, 80, 5481 [astro–ph/9709072].

Niemeyer J. C. and Jedamzik K., 1999a, *Dynamics of PBH formation*, Phys. Rev D, 59, 124013 [astro–ph/9901292].

Novikov I. D., Polnarev A. G., Starobinsky A. A. & Zeldovich Ya. B., 1979, *Primordial Black Holes*, A&A, 80, 104.

Page, D. N. & Hawking, S. W. 1976, *Gamma Rays from Primordial Black Holes*, ApJ, 206, 1.

Penzias A. A. & Wilson R. W., 1965, *A measurement of excess antenna temperature at 4080 Mc/s* , ApJL, 1, 419.

Polarski D., 2001, *Classicality of primordial fluctuations and primordial black holes*, Int. Jour. Mod. Phys. D, 10, 927 [astro-ph/0109388].

Polarski D., 2002, *Primordial black holes in an accelerating Universe*, Phys. Let. B, 528, 193 [astro–ph/0112328].

Polarski D. & Starobinsky A. A., 1996, *Semiclassicality and decoherence of cosmological perturbations*, CQGra, 13, 377.

Portegies Zwart, S. F. 2004, *Formation of massive black holes through runaway collisions in dense young star clusters*, Nature, 428, 724 [astro-ph/0402622].

Ricotti M., Ostriker J. P., and Mack K. J., 2008, *Effect of Primordial Black Holes on the Cosmic Microwave Background and Cosmological Parameter Estimates*, ApJ, 680, 829 [arXiv:0709.0524].

Ryden B., 2003, *Introduction to Cosmology*, Pearson Eduction, Inc., publishing as Addison Wesley, San Francisco.

Schmid C., Schwarz D. J. & Widerin P., 1997, *Peaks above the Harrison-Zel'dovich spectrum due to the Quark-Gluon to Hadron Transition*, PhRvL, 78, 791 [astro-ph/9606125].

Schmid C., Schwarz D. J. & Widerin P., 1999, *Amplification of cosmological inhomogeneities by the QCD transition*, PhRvD, 59, 43517 [astro-ph/9807257].

Schwarz D. J., 1998, *Evolution of gravitational waves through the cosmological QCD transition*, Mod. Phys. Lett. A, 13, 2771 [gr-qc/9709027].

Schwarz D. J., 2003, *The first second of the Universe*, Annalen der Physik, 12, 220 [astro-ph/0303574].

Schutz B. F., 1985, *A first course in General Relativity*, Cambridge University Press, Cambridge.

Scott D., 2006, *The standard cosmological model*, Canadian Journal of Physics, 84, 419 [astro-ph/0510731].

Semikoz D. V., 1994, *On the detection of individual primordial black hole explosions*, ApJ, 436, 254.

Shapiro S. L., Teukolsky S. A., 1983, *Black Holes White Dwarfs and Neutron Stars*, John Wiley & Sons, New York.

Slipher V. M., 1917, *Nebulae*, Proceedings of the American Philosophical Society, 56, 403.

Sobrinho J. L. G., 2003, *Possibilidade de detecção directa de Buracos Negros por radiação electromagnética*, Tese submetida nas Provas de Aptidão Pedagógica e Capacidade Científica para habilitação à categoria de Assistente, Universidade da Madeira [see Appendix P for a summary in English].

Sobrinho J. L. G. & Augusto P., 2007, *The fraction of the Universe going into Primordial Black Holes*, Internal Report, CCM, 126/07 [`http://ccm.uma.pt/publications/ccm-126-07.pdf`].

Spergel D. N., et al. 2003, *First-Year Wilkinson Microwave Anisotropy Probe (WMAP) Observations: Determination of Cosmological Parameters*, ApJS, 148, 175 [astro–ph/0302209].

Spergel D. N., et al. 2007, *Three-Year Wilkinson Microwave Anisotropy Probe (WMAP) Observations: Implications for Cosmology*, ApJS, 170, 337 [astro-ph/0603449].

Starobinsky A. A., 1992, *Spectrum of adiabatic perturbations in the universe when there are singularities in the inflaton potential*, JETP Lett., 55, 489.

Stern D. et al., 2000, *Discovery of a color–selected Quasar at* $z = 5.50$, ApJL, 533, 75.

Tavani M. et al., 2001, *Science with AGILE* in AIP Conf. Proc. 587, Gamma–Ray Astrophysics Symposium 2001, ed. S. Ritz, N. Gehrels, & C. R. Schrader (New York: AIP), 729.

Tegmark M. et al., 2004, *Cosmological parameters from SDSS and WMAP*, PhRvD, 69, 103501 [astro–ph/0310723].

Trodden M., 1999, *Electroweak baryogenesis*, Reviews of Modern Physics, 71, 1463 [hep-ph/9803479].

Tsujikawa S., 2003, *Introductory review of cosmic inflation*, lecture notes given at The Second Tah Poe School on Cosmology "Modern Cosmology", Naresuan University, Phitsanulok, Thailand, April 17 -25, 2003 [hep-ph/0304257].

Unsöld A. & Bascheck B., 2002, *The new Cosmos*, Springer Verlag, Berlin.

Verde L., et al. 2003, *First-Year Wilkinson Microwave Anisotropy Probe (WMAP) Observations: Parameter Estimation Methodology*, ApJS, 148, 195 [astro–ph/0302218].

Weinberg S., 2000, *The Cosmological Constant Problems* (Talk given at Dark Matter 2000, February, 2000), astro-ph/0005265.

Winkler C., 2000, *The INTEGRAL Mission*, INTEGRAL Spring School (Les Diablerets–Switzerland), http://isdc.unige.ch/Conf/observing/Viewgraphs/ChrisWinkler.pdf.

Wald R. M., 1984, *General Relativity*, University of Chicago Press, Chicago.

Wald R. M., 1998, *Black Holes and Relativistic Stars*, Edited by Robert M. Wald, University of Chicago Press, Chicago.

Yao W.-M., et al., 2006, *Review of Particle Physics*, Journal of Physics G, 33, 1 [also available on the *Particle Data Group* pages: http://pdg.lbl.gov/].

Yokoyama J., 1998, *Cosmological constraints on PBHs produced in the near–critical gravitational collapse*, PhRvD, 58, 107502 [gr–qc/9804041].

Zeldovich, Y. B. 1970, *Gravitational instability: an approximate theory for large density perturbations*, A&A, 5, 84.

Zeldovich Ya. B. and Novikov I. D., 1967, *The hypothesis of cores retarded during expansion and the hot cosmological model*, SvA, 10, 602.

Zhang S. N. et al., 1997, *Black Hole Spin in X–Ray Binaries: Observational Consequences*, ApJL, 482, 155 [astro-ph/9704072].

Zimdahl W. & Pavón D., 2001, *Cosmological two–fluid thermodynamics*, GR&G, 33, 791 [astro-ph/0005352].

Zombeck M. V., 1990, *Handbook of Astronomy and Astrophysics*, Second Edition (Cambridge, UK: Cambridge University Press).